METHODS IN THE PHYSICS OF POROUS MEDIA

Volume 35

Po-zen Wong

Experimental Methods in the Physical Sciences

VOLUME 35

METHODS IN THE PHYSICS OF
POROUS MEDIA

EXPERIMENTAL METHODS IN THE PHYSICAL SCIENCES

Volume 35

Methods in the Physics of Porous Media

Edited by

Po-zen Wong
Department of Physics and Astronomy
University of Massachusetts
Amherst, Massachusetts

ACADEMIC PRESS

San Diego London Boston New York Sydney Tokyo Toronto

Academic Press
A Harcourt Science and Technology Company
525 B Street, Suite 1900, San Diego, CA 92101-4495, USA
http://www.academicpress.com

Academic Press
24–28 Oval Road, London NW1 7DX, United Kingdom
http://www.hbuk.co.uk/ap/

International Standard Serial Number: 1079-4042/99

International Standard Book Number: 0-12-475982-3

PRINTED IN THE UNITED STATES OF AMERICA
99 00 01 02 03 EB 9 8 7 6 5 4 3 2 1

CONTENTS

This Page Intentionally Left Blank

CONTRIBUTORS

Numbers in parentheses indicate the pages on which the authors' contributions begin.

DALE P. BENTZ (1), *Building Materials Division, National Institute of Standards and Technology, Gaithersburg, Maryland 20899-8621*

C. T. PHILIP CHANG (387), *Department of Chemical Engineering and Engineering Imaging Laboratory, Texas A&M University, College Station, Texas 77843-3122*

MARY E. COLES (301), *Mobil Technology Company, Mobil Exploration and Production Technical Center, Dallas, Texas 75244-4390*

CARL M. EDWARDS (387), *Baker Atlas Logging Services, Houston, Texas 77210*

EDWARD J. GARBOCZI (1), *Building Materials Division, National Institute of Standards and Technology, Gaithersburg, Maryland 20899-8621*

JEAN-PIERRE HULIN (425), *Laboratoire FAST, Pierre et Marie Curie and Paris-Sud Universities, and CNRS (UMR 7608), Orsay, France*

ROBERT L. KLEINBERG (337), *Schlumberger-Doll Research, Ridgefield, Connecticut 06877*

KENNETH H. LANGLEY (263), *Department of Physics and Astronomy, University of Massachusetts, Amherst, Massachusetts 01003*

ROLAND LENORMAND (43), *Institut Français du Pétrole, Rueil Malmaison, France*

NICOS S. MARTYS (1), *Building Materials Division, National Institute of Standards and Technology, Gaithersburg, Maryland 20899-8621*

PETER B. NAGY (161), *Department of Aerospace Engineering and Engineering Mechanics, University of Cincinnati, Cincinnati, Ohio 45221-0070*

DOMINIQUE SALIN (425), *Laboratoire FAST, Pierre et Marie Curie and Paris-Sud Universities, and CNRS (UMR 7608), Orsay, France*

SUNIL K. SINHA (223), *Advanced Photon Source, Argonne National Laboratory, Argonne, Illinois 60439*

IWAO TERAOKA (263), *Department of Chemical Engineering, Chemistry, and Materials Science, Polytechnic University, Brooklyn, New York 11201*

A. TED WATSON (387), *Department of Chemical Engineering and Engineering Imaging Laboratory, Texas A&M University, College Station, Texas 77843-3122*

PO-ZEN WONG (119), *Department of Physics and Astronomy, University of Massachusetts, Amherst, Massachusetts 01003*

YANIS C. YORTSOS (69), *Department of Chemical Engineering and Petroleum Engineering Program, University of Southern California, Los Angeles, California 90089-1211*

VOLUMES IN SERIES

EXPERIMENTAL METHODS IN THE PHYSICAL SCIENCES

(formerly Methods of Experimental Physics)

Editors-in-Chief
Robert Celotta and Thomas Lucatorto

Volume 1. Classical Methods
Edited by Immanuel Estermann

Volume 2. Electronic Methods, Second Edition (in two parts)
Edited by E. Bleuler and R. O. Haxby

Volume 3. Molecular Physics, Second Edition (in two parts)
Edited by Dudley Williams

Volume 4. Atomic and Electron Physics—Part A: Atomic Sources and Detectors; Part B: Free Atoms
Edited by Vernon W. Hughes and Howard L. Schultz

Volume 5. Nuclear Physics (in two parts)
Edited by Luke C. L. Yuan and Chien-Shiung Wu

Volume 6. Solid State Physics—Part A: Preparation, Structure, Mechanical and Thermal Properties; Part B: Electrical, Magnetic and Optical Properties
Edited by K. Lark-Horovitz and Vivian A. Johnson

Volume 7. Atomic and Electron Physics—Atomic Interactions (in two parts)
Edited by Benjamin Bederson and Wade L. Fite

Volume 8. Problems and Solutions for Students
Edited by L. Marton and W. F. Hornyak

Volume 9. Plasma Physics (in two parts)
Edited by Hans R. Griem and Ralph H. Lovberg

Volume 10. Physical Principles of Far-Infrared Radiation
By L. C. Robinson

Volume 11. Solid State Physics
Edited by R. V. Coleman

Volume 12. Astrophysics—Part A: Optical and Infrared Astronomy
Edited by N. Carleton

Part B: Radio Telescopes; Part C: Radio Observations
Edited by M. L. Meeks

Volume 13. Spectroscopy (in two parts)
Edited by Dudley Williams

Volume 14. Vacuum Physics and Technology
Edited by G. L. Weissler and R. W. Carlson

Volume 15. Quantum Electronics (in two parts)
Edited by C. L. Tang

Volume 16. Polymers—Part A: Molecular Structure and Dynamics; Part B: Crystal Structure and Morphology; Part C: Physical Properties
Edited by R. A. Fava

Volume 17. Accelerators in Atomic Physics
Edited by P. Richard

Volume 18. Fluid Dynamics (in two parts)
Edited by R. J. Emrich

Volume 19. Ultrasonics
Edited by Peter D. Edmonds

Volume 20. Biophysics
Edited by Gerald Ehrenstein and Harold Lecar

Volume 21. Solid State: Nuclear Methods
Edited by J. N. Mundy, S. J. Rothman, M. J. Fluss, and L. C. Smedskjaer

Volume 22. Solid State Physics: Surfaces
Edited by Robert L. Park and Max G. Lagally

Volume 23. Neutron Scattering (in three parts)
Edited by K. Sköld and D. L. Price

Volume 24. Geophysics—Part A: Laboratory Measurements; Part B: Field Measurements
Edited by C. G. Sammis and T. L. Henyey

Volume 25. Geometrical and Instrumental Optics
Edited by Daniel Malacara

Volume 26. Physical Optics and Light Measurements
Edited by Daniel Malacara

Volume 27. Scanning Tunneling Microscopy
Edited by Joseph Stroscio and William Kaiser

Volume 28. Statistical Methods for Physical Science
Edited by John L. Stanford and Stephen B. Vardaman

Volume 29. Atomic, Molecular, and Optical Physics—Part A: Charged Particles; Part B: Atoms and Molecules; Part C: Electromagnetic Radiation
Edited by F. B. Dunning and Randall G. Hulet

Volume 30. Laser Ablation and Desorption
Edited by John C. Miller and Richard F. Haglund, Jr.

Volume 31. Vacuum Ultraviolet Spectroscopy I
Edited by J. A. R. Samson and D. L. Ederer

Volume 32. Vacuum Ultraviolet Spectroscopy II
Edited by J. A. R. Samson and D. L. Ederer

Volume 33. Cumulative Author Index and Tables of Contents, Volumes 1–32

Volume 34. Cumulative Subject Index

Volume 35. Methods in the Physics of Porous Media
Edited by Po-zen Wong

This Page Intentionally Left Blank

PREFACE

The initiative to put together this volume came from Zvi Ruder, senior editor of physical sciences at Academic Press. He observed that *porous media* had been an active area of research in condensed-matter physics in the last two decades, yet there has not been an introductory text for physics students at the undergraduate level, nor has there been a more advanced text that gives an overview of the frontiers of research. When we discussed his ideas of meeting these needs, my immediate reaction was that these would be formidable challenges for one or two authors to take on. The difficulty is partly due to the intrinsic breadth of any interdisciplinary field, but more importantly, despite the progress made on many fronts, the amount of fundamental physical understanding is still far from mature and there is a wealth of unexplained empirical data. As a result, most people engaged in porous media research rely on a collection of monographs [1–8], handbooks [9–11], and conference proceedings [12–17] as sources for reference. A more concise text would be useful not only for students entering the field, but for seasoned researchers as well. One way of achieving the goal is to have a dozen or so chapters that cover different aspects of porous media. If each chapter were written by someone experienced in that topic, it would break down the difficult task into more manageable pieces. As we explored this model for a text further, we were also drawn to the idea of having an experimental emphasis, as it would best complement other existing monographs; the readers would gain a better sense of what is actually done in the research. All too often, we take for granted that the equations and data we see in books are proven truths, but for a field that is still developing, having some knowledge of the experimental details would help us make more critical judgments and identify opportunities for further work. With these considerations in mind, the *Experimental Methods in the Physical Sciences* series seemed like a natural place for a volume such as this.

As the editor, my role was to construct the table of contents, solicit contributors for each chapter, and add some coherence to the largely independent writings. The interdisciplinary nature of the field is reflected in the diverse backgrounds of the authors: They come from academia and industry as well as government laboratories. While many would describe themselves as physicists, others consider themselves as engineers, chemists, or applied scientists. The experimental emphasis is reflected in the fact that

they are predominantly experimentalists and each chapter is devoted to a particular class of experiments. The authors were specifically asked to include some description of the experimental methods in addition to the usual presentation of theoretical principles and illustrative data. To make this volume viable as an introductory text, the length of each chapter is limited to about 35 pages. A comprehensive bibliography at the end of each chapter serves as a road map for readers who want to have a more thorough understanding of the topic or delve into the most recent literature. The principal guideline I gave to the authors was to consider how they would introduce the topic to students or nonexperts in three to four lectures. Clearly, each author approached the task somewhat differently. But collectively, the eleven chapters contained in this volume may be thought of as the lecture notes of a one-semester course taught by eleven guest lecturers. Their different backgrounds and emphases ensure that the audience is exposed to a broad spectrum of perspectives, which is essential in learning about any interdisciplinary subject. At the same time, efforts were made to have the chapters organized in a logical and coherent fashion so that the basic concepts are introduced in the early chapters and applied in the later ones.

The first chapter by Edward Garboczi, Dale Bentz, and Nicos Martys deals with the applications of digital imaging techniques. As thin sections have always been widely used to give visual and intuitive information of pore structure, the arrival of the computer age has made it possible to extract quantitative information conveniently. Several important concepts, such as correlation functions, self-similar fractals, and the percolation model are introduced to describe the microgeometry. The authors do not stop at just quantifying 2-D images; they show how such images can be used to build representative 3-D structures on the computer and use them to compute macroscopic properties to compare with experiments. Several theoretical models used for computation are discussed. Continuing on the theme of imaging, Roland Lenormand discusses in Chapter 2 how video imaging is used to study multiphase fluid flow phenomena in artificially constructed 2-D micromodels. This offers a natural platform to explain the competing roles of wetting properties, surface tension, viscosity, gravity, and diffusion in determining the flow pattern and dynamics, including the central ideas of viscous fingering, invasion percolation, and interface pinning. Although the focal point of this chapter is on the difference between *drainage* (nonwetting fluid invasion) and *imbibition* (wetting fluid invasion) in two-phase capillary displacement, highlights of several other types of more complicated flow problems are given. These include three-phase flow, foam flow, flow in fractures, critical (or almost miscible) flow, and tracer dispersion in miscible flow.

Chapters 3 to 5 address several traditional types of experiments used to characterize porous media. Continuing along the ideas introduced in the first two chapters, Yanis Yortsos discusses in Chapter 3 how the adsorption–desorption of gases and the injection of mercury are used to probe the pore structure. The definitions of pore size and throat size are given, and the concept of self-affine fractal surfaces is introduced. The main emphases of this chapter are on the effects of fractal surface roughness within a single pore and the overall connectivity of the pore network. In the latter, the invasion percolation model is used to understand both the desorption and mercury injection experiments because both involve the displacement of a wetting fluid by a nonwetting one. In Chapter 4, I give an integrated discussion of electrical conductivity, hydraulic permeability, and electrokinetic measurements. Several key concepts such as tortuosity, pressure diffusion, and viscous relaxation are introduced in the context of bulk conductivity and permeability measurements, which prepare the readers for the next chapter on acoustic and ultrasonic wave propagation. One of my main emphases is the important roles of the surface counterions in causing surface conductivity, induced polarization, and electrokinetic phenomena. I show that, despite the highly disordered nature of the pore network, transport phenomena are governed by a characteristic pore radius. While other techniques such as image analysis and mercury injection can give *estimates* of this radius, electrokinetic measurements can determine it *exactly* and give a simple relationship between the conductivity and permeability of brine-saturated porous media. For two-phase flow systems, the drainage-imbibition hysteresis discussed in the preceding chapters is demonstrated in conductivity measurements with simultaneous x-ray imaging. In Chapter 5, on acoustic and ultrasonic waves, Peter Nagy reviews the basics of bulk, surface, interfacial, and guided waves before introducing the important concept of Biot slow waves that correspond to out-of-phase motions of the pore fluid and the solid matrix. Results of reflection and transmission measurements on air-filled and water-filled samples are used to compare with the Biot theory in the limits of rigid frame and elastic frame. They are shown to be useful in determining bulk material properties such as porosity, tortuosity, and permeability. Using collimated and focused beams of ultrasonic waves, spatial variations of these properties in thin slabs can be imaged. Guided waves along planar surfaces and cylindrical boreholes can be exploited in geophysical applications.

Scattering experiments are among the most powerful tools for determining microscopic structures. The wavelength of the radiation sets the length scale of investigation. In Chapter 6, Sunil Sinha discusses how small-angle scattering of x rays and thermal neutrons are used to study structures

between 1 and 100 nm, a range inaccessible by imaging. Because the scattering is very weak and almost completely elastic, the scattered intensity is directly proportional to the Fourier transform of the geometric correlation function introduced in Chapter 1. Sinha reviews the scattering theory with particular emphasis on probing pore structures with either a spatial modulation or random fractal geometry. He shows that neutron scattering is particularly useful for studying the behavior of two fluids inside the pores. By suitable substitution of hydrogen by deuterium in one of the fluids, its scattering power can be made to match the solid so that the three-phase system (two fluids and one solid) looks like a two-phase system. This simplifies the data interpretation. For example, it is possible to observe the preferential adsorption of certain molecules on the pore surface out of a uniformly mixed fluid that is matched to the solid. Similar *contrast matching* techniques are essential in using light to probe porous media, because light is strongly scattered even for a small difference in refractive index between the pore fluid and the solid matrix. In Chapter 7, Kenneth Langley and Iwao Teraoka discuss the principles and applications of several optical techniques. In index-matched systems, they show that dynamic light scattering, fluorescence, interferometry, and forced Rayleigh scattering can be used to study a variety of dynamical phenomena in the pore space; for example, diffusion of macromolecules and phase separation of binary fluids. In unmatched systems where multiple scattering dominates, they show how the technique of diffusion-wave spectroscopy can be used to study the dynamics of foam, colloids, and flowing granular materials.

A large part of the physics of porous media occurs at macroscopic length scales that cannot be probed by scattering. While Chapters 1 and 2 deal with imaging of 2-D samples, there is really no substitute for nondestructive 3-D imaging for obtaining the full structural information. In Chapter 8, Mary Coles gives a concise review of x-ray imaging with emphasis on petrophysical applications. Unlike scattering experiments that use low-energy monochromatic x rays, radiography and tomographic imaging typically utilize high-energy polychromatic x rays that can penetrate solid samples several centimeters in thickness. The image is essentially a spatial map of the attenuation coefficient of the sample. Coles describes the basic principles and many practical considerations that are critical in getting the best image quality. Average properties such as porosity and density can be easily extracted from the images. In multiphase flow studies, doping one fluid with heavy ions to increase attenuation can discriminate it from the other fluid. A quantitative knowledge of how the fluids are distributed can be used to understand other experiments; for example, electrical conductivity as described in Chapter 4. Even the qualitative images are useful for identifying heterogeneities such as geological bedding planes and fractures in the

sample. State-of-the-art microtomography performed at national synchrotron facilities can now achieve spatial resolutions of a few microns.

The other powerful 3-D imaging technique is magnetic resonance imaging (MRI). It utilizes nuclear magnetic resonance (NMR) of hydrogen or other light elements. This feature makes NMR and MRI most useful for studying the behavior of pore fluids such as water and hydrocarbons. In Chapter 9, Robert Kleinberg explains that the amplitude of the NMR signal is useful for determining fluid saturation, but the relaxation times for fluid molecules are shortened inside small pores due to interactions with the pore surface. The latter makes the measurement sensitive to the specific area and pore size distribution of the sample. Comparing the results to other measurements such as nitrogen adsorption and mercury injection (as described in Chapter 3) determines the strengths of the fluid–solid interactions. A number of materials processing and petrophysical applications are described. Instrumental considerations specific to the study of porous media and implementation for field measurements in boreholes are discussed. Following this introduction to NMR, Philip Chang, Ted Watson, and Carl Edwards describe how it is used in 3-D imaging and applied to the study of porous media. After explaining how a spatially varying but unidirectional magnetic field is used to mark the positions inside the sample, the authors discuss the complications caused by the fluid–solid interactions and various ways to discriminate one pore fluid from another. In addition to obtaining static information such as porosity and saturation, pulsed field-gradient (PFG) methods are shown to be useful for obtaining velocity maps of the different fluids. Examples of using this information to study multiphase flow are given.

In the final chapter, Jean-Pierre Hulin and Dominique Salin focus on issues related to the mixing of flowing fluids in porous media and show how some of the techniques described in the earlier chapters can be applied. They begin by describing the phenomenology of passive tracer dispersion and the basic mechanisms involved. This is followed by a discussion of the different techniques that are used to study dispersion at microscopic and macroscopic length scales, with particular emphases on PFG–NMR, electrochemical, acoustic, and conductivity echo techniques. Experiments aimed at understanding the origin of non-Gaussian dispersion and the effects of large viscosity or density contrast between the mixing fluids are discussed.

Although these eleven chapters cover a wide range of the research activities on porous media in recent years, they are by no means complete. Nevertheless, it is my hope that some will find this compilation useful as the basis for a one-semester course in which physics students will be exposed to practical applications, engineering students will learn about the fundamental physics, and all will develop an appreciation of the role of experimentation.

The bibliographies given below and in each chapter offer additional sources of information.

I owe much to my friends and former colleagues at Schlumberger–Doll Research for introducing me to the physics of porous media. It has been a wonderful learning experience to work on this volume and interact with all the authors. They have been most gracious and accommodating to my suggestions in their writings. I am also indebted to several anonymous referees who helped in reviewing the early drafts and offered their thoughtful comments.

PO-ZEN WONG
Amherst, Massachusetts

1. A. E. Scheidegger, *The Physics of Flow Through Porous Media* (MacMillan, New York, 1960).
2. F. A. L. Dullien, *Porous Media: Fluid Transport and Pore Structure* (Academic Press, San Diego, 1992).
3. M. Sahimi, *Flow and Transport in Porous Media and Fractured Rock: From Classical Methods to Modern Approaches* (VCH, Weinheim, 1995).
4. Y. Guéguen and V. Palciauskas, *Introduction to the Physics of Rocks* (Princeton University Press, Princeton, 1994).
5. N. R. Morrow, ed., *Interfacial Phenomena in Petroleum Industry* (Marcel Dekkar, New York, 1991).
6. G. Uehara and G. Gillman, *The Mineralogy, Chemistry, and Physics of Tropical Soils with Variable Charge Clays* (Westview Press, Boulder, Colorado, 1981).
7. J. Bear and A. Verruijt, *Modeling Groundwater Flow and Pollution* (Reidel, Dordrecht, 1987).
8. J. Bear, *Dynamics of Fluids in Porous Media* (American Elsevier, New York, 1971).
9. J. H. Schön, *Physical Properties of Rocks: Fundamentals and Principles of Petrophysics* (Pergamon-Elsevier, Tarrytown, N.Y., 1996).
10. Y. S. Touloukian, W. R. Judd, and R. F. Roy, eds., *Physical Properties of Rocks and Minerals* (McGraw-Hill, New York, 1981).
11. *Flow Through Porous Media* (American Chemical Society Publications, Washington, D.C., 1970).
12. D. L. Johnson and P. N. Sen, eds., *Physics and Chemistry of Porous Media*, AIP Conf. Proc. **107** (AIP, New York, 1984).
13. J. Banavar, J. Koplik, K. Winkler, eds., *Physics and Chemistry of Porous Media II*, AIP Conf. Proc. **154** (AIP, New York, 1987).
14. J. Klafter, R. J. Rubin, and M. F. Shlesinger, eds., *Transport and Relaxation in Random Materials* (World Scientific, Singapore, 1986).

15. J. Klafter and J. M. Drake, eds., *Molecular Dynamics in Restricted Geometries* (Wiley, New York, 1989).

16. J. M. Drake, J. Klafter, and R. Kopelman, eds., *Dynamics in Small Confining Systems II & III*, Mater. Res. Soc. Symp. Proc., **366** & **464** (MRS, Pittsburgh, 1995 & 1998).

17. T. J. Pinnavaia and M. F. Thorpe, eds., *Access in Nanoporous Materials*, (Plenum, New York, 1995).

This Page Intentionally Left Blank

1. DIGITAL IMAGES AND COMPUTER MODELING

Edward J. Garboczi, Dale P. Bentz, and Nicos S. Martys

National Institute of Standards and Technology
Building Materials Division
Building and Fire Research Laboratory
Gaithersburg, Maryland

Abstract

This chapter describes how digital images of porous materials can be analyzed to give information about the structure and properties of the material and the various ways 3-D digital-image-based models can be generated to help understand real porous materials.

1.1 Introduction to Porous Materials and Digital Images

Holes in objects may be desirable or undesirable. For instance, when we unwrap a piece of clothing that was ordered from an expensive mail-order catalog, and find that there are unwanted holes in it, we usually send it right back, with a more or less polite demand for a refund or an exchange. And everyone knows the effect of holes in bicycle or automobile tires. However, holes in the middle of records (remember records?) enable them to be played on a phonograph, and holes in the middle of bagels and doughnuts not only eliminate the hard-to-cook part, but also allow ease of handling by clumsy fingers. So holes can indeed sometimes be useful.

A *porous material* is simply some kind of solid material that has holes in it. The holes are also called pores. However, if asked, most people would make a distinction between a pair of socks with three holes in the toes, an empty closed cardboard box, and a household sponge. The socks and the box would not generally be considered to be porous materials, while the sponge would be. To call a material a porous material, there is usually some kind of implicit assumption of homogenization and length scale.

Attempting to state this intuitive feeling more quantitatively is difficult. We might in general say that the holes must be small enough, compared to the typical size of the piece of material that is considered, so that it is reasonable to consider the material as a mixture of solid framework and

EXPERIMENTAL METHODS IN THE PHYSICAL SCIENCES
Vol. 35
ISBN 0-12-475982-3

ISSN 1079-4042/99 $30.00

pores. Also, the holes must be distributed fairly evenly throughout the material. Therefore, if the length scale of the sample is large compared to the typical pore size, and the pores are distributed reasonably uniformly throughout the material, then the material is a porous material. We use these qualitative ideas as a working definition of most porous materials in this and later chapters.

Common porous materials, some of which are considered in the chapters of this book, include concrete [1]; paper [2]; ceramics (with natural [3] or artificially created pores [4]); clays [5]; porous semiconductors [6]; chromotography materials [7]; and natural materials such as coral, bone, sponges, rocks, and shells. Porous materials can also be reactive, such as in charcoal gasification, acid rock dissolution, catalyst deactivation [8], and concrete [1].

The purpose of this chapter is to describe a "tool kit" of mathematical and computational tools that are available for use on digital images, in general, and digital images of porous materials, in particular. These include tools for measuring geometrical and morphological quantities, tools for computing physical properties of various kinds, and tools for generating 3-D images, either from 2-D images or using models of various kinds. There are many standard review papers and monographs in this area. Sahimi's book, in particular, is a good overall reference that covers some of the same material as this chapter [9].

1.1.1 Porous Materials

Consider a sample of total volume V. Define the volume of the solid phase to be V_s, and the volume of the pore phase (the holes) to be V_p, with $V = V_s + V_p$. The volume fraction is a normalized variable that is generally more useful. The volume fraction of the pore phase is commonly called the porosity, and is denoted $\phi = V_p/V$. The solid volume fraction is then $(1 - \phi)$.

Since a porous material is a two-phase material (at least), a surface separating the pore phase from the solid phase can be defined, with its area denoted S_p. This quantity is often called the pore surface area. A normalized variable common for this quantity is called the specific surface area, $s_p = S_p/V$. Note that the dimension of $1/s_p$ is length, so that sometimes it is thought of as a length that characterizes the length scale of the pores. A simple example would be a collection of N mono-sized nonoverlapping spherical pores of radius r. The inverse of the specific surface area, $1/s_p = V/S_p$, would be $r/(3\phi)$, which is obviously a length characteristic of the pores. Other ways to form a length scale from pore space characteristics are covered later in this chapter and in other chapters of this book dealing with the transport properties of porous materials.

In thinking about the microgeometry of porous materials, a common approach is to consider them to be two-phase solid–pore composites, even though the solid phase can be heterogeneous. Properties such as elastic moduli are essentially functions of the solid phase, but are reduced and modified by the presence of the pores. If there is a fluid that fills the pore space, which can modify the dynamic elastic response, then both solid and pore characteristics must be dealt with in understanding the elastic properties [10]. Elastic moduli decrease as the porosity increases. Properties such as diffusivity and permeability are functions of pore size, shape, and connectivity and increase as the porosity increases.

The topology of the pore space of a porous material is very important in determining the properties of the material, and even in properly formulating ideas about the pore space in the first place. By topology we mean how the pores are connected, if at all. If the pores are completely isolated from each other, then clearly one can discuss the shape and size of individual pores. The left side of Fig. 1 shows an example of this case, in two dimensions, where the pores are random-size, nonoverlapping circular holes. It is clear in this case how to define the pore size distribution, a quantity that gives the number or volume of pores of a given size.

If the pores are fully connected to each other, as shown in the right side of Fig. 1, then there is really only one multiply connected "pore" in the material. The number of pores is no longer a meaningful quantity, and it becomes difficult to talk about the shape and size of the "pores." However, in this case, the idea of "throats" can be important. If the pore space in many areas is shaped like the cartoon shown in Fig. 2, then the idea of a throat shape and size can be loosely defined. The size of the "throat" limits the

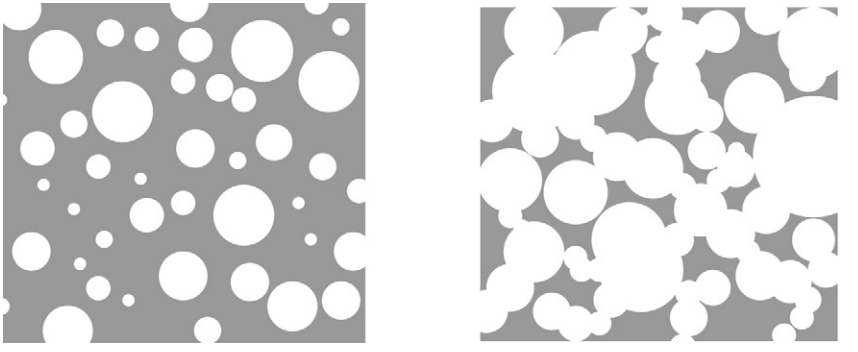

FIG. 1. Two-dimensional picture of (left) isolated circular pores and (right) connected pores (gray = solid, white = pores).

FIG. 2. Schematic picture defining a throat and pore in the pore space of a porous material.

accessibility of the larger "pore" and is then the size of importance for many properties of the material.

If there is such a throat structure, then a *pore throat size distribution*, usually but erroneously called the pore-size distribution, can be defined. Techniques such as nitrogen BET and mercury intrusion porosimetry (see Chapter 3) measure a pore throat size distribution that is convolved with the cross-sectional throat shape and the topology of the pore–throat network [7, 11]. These techniques measure an equivalent circular cross-sectional throat diameter [7, 11]. In practice, pore–throat combinations can only really be separated in terms of grossly simplified geometrical models of the pore microgeometry.

In most cases, porous materials are random materials, with random pore sizes, shapes, and topology. Because of this fact, most porous materials tend to be isotropic. This is not always the case, however. Many rocks have anisotropy built into them from how they were formed due to deposition of sediment [12]. When looking at a slice of a porous material, one must of course be aware whether the material is or is not isotropic. We assume isotropy in the remainder of this chapter.

1.1.2 Digital Images

To our eye's perception, an artist painting a watercolor or oil picture makes an analog picture, although it is actually finely divided at the scale of individual, overlapping paint pigment particles. A digital image is a collection of individual, nonoverlapping elements or pixels that have distinct intensities (gray scale or color) indicating the solid and pore phases of the material. The spatial resolution of the image indicates the size of the pixels, with high resolution meaning a small pixel is used. As the pixel size decreases, the number of pixels per unit length increases, hence the designation "high." A digital image can be a gray-scale image, where the intensity of each pixel ranges from black (0) to white (N). For many imaging systems (microscopes etc.), $N = 255$, corresponding to 8 bits of intensity resolution.

A digital image can also be a color image, where each pixel contains three values, say from 0 to 255, for red, green, and blue, forming 24 bits of color resolution. For porous materials, if the solid part is a uniform material, all a digital image requires is 1 bit per pixel, where pore is black (0) and solid is white (1), or vice versa. The importance of digital images in science, as opposed to analog paintings, is that digital images enable quantitative analysis. Old-fashioned photographs and videos also must be digitized before analysis. Modern digital cameras and scanning and transmission electron microscopes can produce digital images directly.

Usually a rectangular array of square pixels is used in two dimensions, although other shapes, such as a triangular lattice of hexagonal pixels, are also possible and can be useful for special applications [13]. Actually any area-filling collection of random shapes, on a random lattice, could be used to make a digital image. Requiring that the pixels have uniform shape restricts us to having them be a unit cell of one of the five Bravais lattices in two dimensions [14]. The further requirement that the pixels be equilateral forces the choice of square lattices of square pixels and triangular lattices of hexagonal pixels. For the rest of this chapter, we discuss only digital images made from square pixels, and in 3-D cubic lattices made up of cubic pixels.

In two dimensions, digital images at sufficient spatial resolution portray areas well. Figure 3 shows the same physical size circle, but digitized at higher and higher resolutions. The real circle is centered on the middle of a pixel. If the circles were to be centered on a pixel corner, the digitized image would look slightly different, with no significant changes. The image appears more circular as the resolution increases. Simple calculations show that when 15 or more pixels are used per circle diameter, the error in the area is always less than 1% [15].

However, the perimeter of a curved surface is usually off by a large amount, no matter what the resolution. In Fig. 3, it is easy to see that the perimeter of a digital circle P, obtained by counting pixel edges, is given by $P = 8r$, not $P = 2\pi r$ [16]. In the same way, for a 3-D digital image, where the pixels (or voxels) are now cubes, volumes are well represented at high resolutions, but the surface area of a sphere, obtained by counting pixel faces, is always approximately $6\pi r^2$, not $4\pi r^2$. These corrections must be kept in mind when trying to analyze pore surfaces based on digital images [17].

Another important issue in analyzing digital images of random porous materials is the ratio of image size to pore size. To get statistically meaningful results, the image must sample a representative area of the porous material. A more rigorous way of stating this can be formulated using the porosity. For a random porous material, the measured porosity

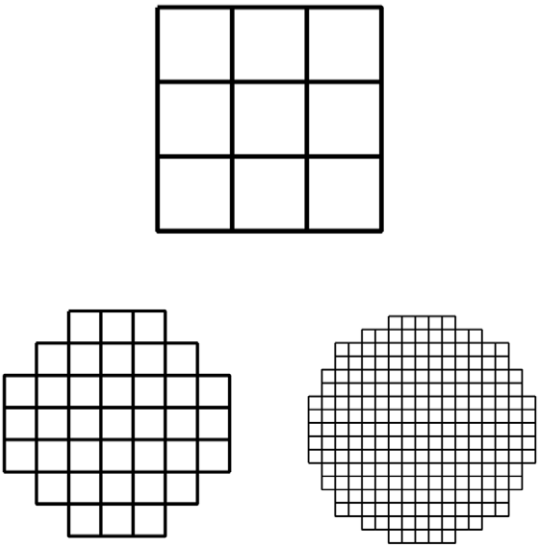

FIG. 3. Example of the effect of digital resolution on how a circle of diameter d is represented (top: pixel length = $d/3$, lower left: pixel length = $d/7$, lower right: pixel length = $d/17$).

will vary from image to image due to the randomness of the material. The smaller the image compared to the average length scale of the pores, the greater this fluctuation will be [18]. If the size of the images used is such that this fluctuation from image to image is small enough, then the image is considered to be large enough to be representative [18]. The terms "small enough" and "large enough" are defined for the application at hand. A rough rule of thumb is that the image should be 5–10 times the typical pore size.

1.2 Geometrical and Topological Analysis

Assume a digital image of a cut through a porous material has been obtained, in the form of a gray-scale image. Often the first step is to make it into a two-phase black and white image. There are many ways this can be done, based on analysis of the gray-scale histogram (distribution) of the image [19]. This histogram simply tells what fraction of the pixels have which gray-scale value. If the density of the solid phase is known, then the porosity can also be directly measured from some kind of physical bulk density measurement. If ρ_s is the solid density, and ρ is the measured

empty-pore or bulk density, then the porosity is simply $\phi = 1 - \rho/\rho_s$. A threshold gray scale can then be chosen, so that all pixels with gray levels above this threshold are white (solid) and all below are black (porosity), such that the correct porosity is achieved. Once a correct binary image has been made, further analysis can be carried out. Often, one will want to remove isolated pixels due to noise in the image acquisition process. Median filtering or other image processing algorithms can be utilized for this purpose [19].

The top left of Fig. 4 shows an example of a random image generated by convolving a Gaussian function with a random noise image (see Section

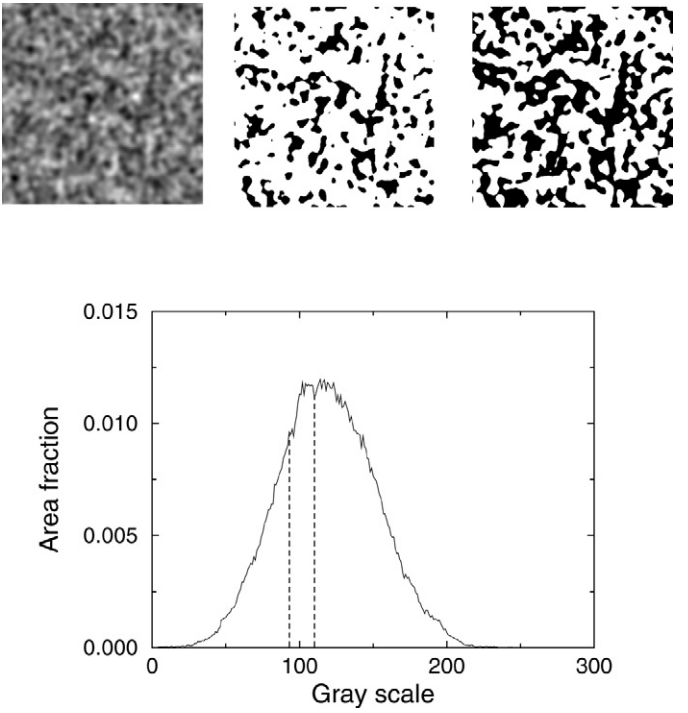

FIG. 4. Top left: an artificial gray-scale image generated from a Gaussian convolution process; middle top: the same image thresholded at a gray level of 93, so that all pixels with a gray level less than or equal to 93 are turned black and all others are turned white; black area fraction = 22%. Right top: the same image thresholded at a gray level of 110, with black area fraction of 41%. Bottom: gray-scale histogram of the original image. The *y*-axis is the area fraction of the image having a given gray scale, and the gray scale runs from 0 to 255. The values of 93 and 110 are marked by dashed lines.

1.5.2). The bottom of Fig. 4 shows the gray-scale histogram for this image, with dashed lines marking the gray scales of 93 and 110. In the graph, there is a single maximum at a gray scale of about 125, out of 255. Many porous material images would have two peaks in the gray-scale histogram, one for each phase. The middle top image of Fig. 4 shows the result of choosing a threshold gray level of 93, where every pixel with a gray scale lower than this is turned to black, and every other pixel is turned to white. The resulting porosity (black phase) is about 22%. If the threshold is chosen to be 110, in the top right part of Fig. 4, then the porosity turns out to be about 41%. In these 2-D sections, the pore phase is isolated and the solid phase is connected. The isolated islands of solid trapped within the pore phase are 2-D artifacts.

1.2.1 Stereology, Mathematical Morphology, and Fractal Analysis

There are several bodies of mathematical knowledge and techniques that have been developed and that are actively used to mathematically analyze and characterize the microstructure of porous materials, or indeed any material.

Stereology is the mathematical science of predicting 3-D quantities by measuring 2-D quantities. Books are available on this topic [20, 21], with many new articles produced each year. Stereology, combined with image analysis [22, 23], can be a powerful tool for inferring quantities such as ϕ and s_p that are the same in two as in three dimensions. Stereology cannot, however, analyze quantities that change between dimensions, such as percolation quantities (see Section 1.2.3). Mathematical morphology is a related and powerful tool for studying images of porous materials [24].

Another body of knowledge available for analyzing and characterizing random materials is that of fractal mathematics. Making use of the techniques of stereology, mathematical morphology, and image analysis, questions of fractal geometry [25–29] can be explored in digital images of porous materials, whether these images are 2-D or 3-D. For an object to be fractal, it must display scale invariance over a range of length scales. A given digital image must have enough resolution so that it can display a reasonable range of length scales, in order that its potential fractal character can be analyzed. A rough rule of thumb is that scale invariance must be displayed over at least one order of magnitude of length scale for an object to be considered to have fractal character. Therefore the image must contain at least that much resolution. In a digital image of a porous material, the size of the image is $L \times L$, and the pixel length is p. Clearly then we must have $L \gg 10p$, since looking at length scales too close to the digital resolution will bring in the digital "graininess," and looking at length scales too close to L will bring in finite size effects.

Assuming that the image is adequate in terms of length scales and resolution, one way to examine the possible fractal nature of an object in a digital image is to measure how the object fills Euclidean space as a function of the size of the region being examined. Such a property is characterized by the mass fractal dimension d_m. In the case of a digital image, we can count the number of pixels that are contained within a given radius. The number of points $M(r) \sim r^{d_m}$. Certainly, the range of r over which this relationship could hold would be for $p < r < L$. If the object did fill space uniformly, then $d_m = d$, the Euclidean dimension. As an example of fractal objects, objects built up in three dimensions by diffusion-limited aggregation or percolation networks at the percolation threshold have $d_m \simeq 2.54$.

Another way of determining d_m is to construct a grid that covers the digital image, of box size l. It would be easiest, in the case of a digital image, to choose l to be an integer number times p. By counting the number of boxes that included part of the object, as a function of grid spacing l, one obtains the box dimension, $d_b = d_m$, from the relation $M(l) \sim l^{-d_b}$. Once again, the range of grid spacing that would produce such a relation would be between the pixel size p and the image size L.

A surface can be rough in a way such that it can also be characterized by a fractal dimension, this time a surface fractal dimension. In a 2-D digital image, a "compass" of opening t can be used to step around the surface (perimeter) and measure its apparent length $S(t)$. If the surface fractal dimension is d_s, then $S(t) \sim t^{-d_s}$. A grid method can also be used, similar to the determination of the mass fractal dimension, which is defined for a 2-D or 3-D digital image. One counts how many grid boxes have surface within them, $S(l)$, for various grid sizes l. If the surface is fractal, then $S(l) \sim l^{-d_s}$, where d_s is again the fractal dimension of the surface.

Experimentally, one can directly determine the fractal dimension by use of small angle scattering, whether neutron or x-ray scattering. Further details can be found in Chapter 6.

For porous materials, the pore space itself, if it has pores over a wide range of length scales, can be a mass fractal [30–33]. If the pore surface is very rough, which would be the case for a high-surface-area material, then the pore surface could form a surface fractal [30–33]. Studies of fractal geometry have been carried out for rocks [26, 34], aerogels [35], and cement-based materials [36]. The transport properties of fractal pore spaces have also been studied theoretically [37, 38].

1.2.2 Correlation Functions and Bounds

Beyond the empirical characterization of pore and throat sizes, the pore geometry can be characterized in a rigorous way mathematically using

correlation functions, which can be measured using image analysis. Since they are used for bounds and the reconstruction of images, topics that are covered later in this chapter, we review them in some detail.

In 2-D, we define a function $f(i, j)$, where (i, j) indicates the location of a pixel in the $M \times N$ image, $i = 1, \ldots, M$ and $j = 1, \ldots, N$, and $f(i, j) = 0$ for solids, and $f(i, j) = 1$ for pores. Then the first-order pore correlation function is $S_1 = \langle f(i, j) \rangle = \phi$, where

$$\langle f(i, j) \rangle \equiv \frac{1}{A} \sum_{i,j} f(i, j), \tag{1}$$

and where $A = M \times N$ is the number of pixels in the image. A similar definition holds in d dimensions. The second-order correlation function, $S_2(x, y)$, is defined similarly, by

$$S_2(x, y) = \langle f(i, j) f(i + x, j + y) \rangle. \tag{2}$$

Writing the preceding equation in this way assumes that the system is translation invariant, so that only the difference vector between two pixels matters, and not the absolute location of the two pixels. If the image is also isotropic, then with $r = |(x,y)|$, $S_2(x, y) = S_2(r, \theta) = S_2(r)$, so that S_2 is a function of distance only.

The value of $S_2(r)$ carries information about how far away different parts of the microstructure still "feel" each other. When $r \to 0$, $S_2 \to \phi$, since $f(i, j)^2 = f(i, j)$. For nonzero values of r, one can think of $f(i + x, j + y)$ as a weighting probability factor for $f(i, j)$. At a given value of (i, j), such that $f(i, j) = 1$, if there is a correlation in the system up to a distance r_c, and if $r = \sqrt{x^2 + y^2} < r_c$, then $f(i + x, j + y)$ has a better than average $(> \phi)$ chance of also having the value of 1. The overall integral will still be less than ϕ, however. As $r \to \infty$, there is no causal connection between the points (i, j) and $(i + x, j + y)$, as long as there is no long-range order, so the probability associated with the pixel at $(i + x, j + y)$ being equal to unity is just ϕ, independent of (i, j). Therefore $S_2 \to \phi^2$ in this limit. A simple physical way of understanding S_2 is to think of it as the probability of finding two randomly selected points that are both in the pore space. This probability turns out to depend on the distance between the two points. Clearly, $S_2 = \phi$ when $r = 0$ and decays to the value ϕ^2 as $r \to \infty$. The decay length is a measure of the pore size. Because digital images have a finite size $(M \times N)$, the actual evaluation of the two-point correlation function can be achieved using

$$S_2(x, y) = \sum_{i=1}^{M-x} \sum_{j=1}^{N-y} \frac{f(i, j) f(i + x, j + y)}{(M - x)(N - y)}. \tag{3}$$

A simple mathematical exercise is the case of overlapping spheres, where each identical sphere is randomly placed in three dimensions without regard to any of the other spheres. The volume outside the solid spheres is the pore space. This case has been solved analytically [39, 40]. If ρ is the number of overlapping spheres per unit volume, and R is the radius of the spheres, then

$$\phi = \exp\left(-\rho\frac{4\pi R^3}{3}\right), \tag{4}$$

$$S_2(r) = \exp\left[-\rho\frac{4\pi}{3}\left(R^3 + \frac{3rR^2}{4} - \frac{r^3}{16}\right)\right] \qquad r < 2R, \tag{5}$$

$$S_2(r) = \exp\left(-\rho\frac{8\pi}{3}R^3\right) \qquad r \geqslant 2R. \tag{6}$$

Figure 5 shows $S_2(r)$ plotted as a function of r, where $R = 1$ is the radius of the spheres and $\rho = 0.29$, so that $S_2(0) = \phi \simeq 0.3$. One can see that S_2 decreases as r increases from zero, and is always monotonically decreasing. For systems where there are distinct grains, there are usually oscillations after the first large decrease in S_2. In this exactly solvable case, S_2 actually reaches the value ϕ^2, as can be seen in Eq. (6) and comparing with Eq. (4).

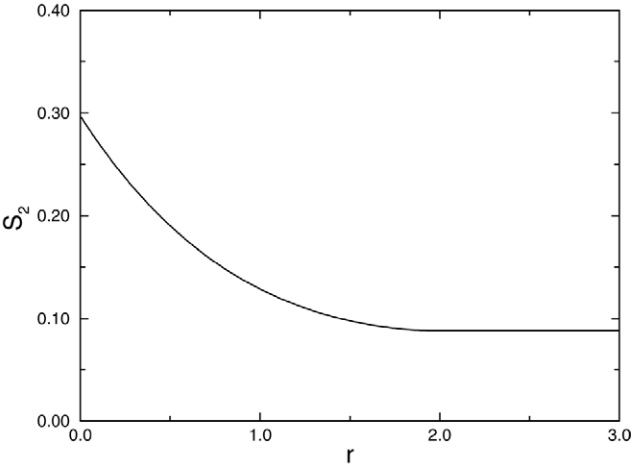

FIG. 5. Two-point correlation function for overlapping spheres (exact theoretical result). The sphere radius is $R = 1$, and the number density of spheres was 0.29, so the volume fraction of pore space ϕ, which is the space surrounding the solid spheres, is approximately 0.3.

For any random isotropic pore space with smooth surfaces, the slope of the two-point correlation function at $r = 0$ is given exactly by [41–43]

$$\frac{\partial S_2}{\partial r}|_{r\to 0} = \frac{-S_p}{4V} = -4s_p. \tag{7}$$

Therefore S_2 is always a decreasing function of r for small r, because of this negative initial slope.

Note that $S_2(r)$ also contains additional information when fractal geometry is present [29]. In the case where the material phase considered is a mass fractal, $S_2(r) \sim r^{d_m - 3}$ when r is in the fractal limit (less than the image size and greater than the pixel size), where d_m is the mass fractal dimension (see Section 1.2.1).

When the material phase is Euclidean, but its surface is fractal, with dimension d_s, the small r limit is given in terms of the surface fractal dimension: $S_2(r) \sim \phi B r^{3-d_s} + \cdots$, where B is a constant [29]. When the material phase is a mass fractal with a fractal surface, then other mathematical forms must be considered [29].

Higher-order correlation functions are defined similarly. Although in practice, two-point functions are most used, three-point functions are fairly common, but correlations past three-point are rarely used. For an isotropic translationally invariant material, the three-point correlation function, S_3, is a function of three variables, r_1, r_2, and θ where these can be thought of as defining a triangle with two sides of length of r_1 and r_2, with θ being the angle between these two sides. Then $S_3(r_1, r_2, \theta)$ is the probability of finding the three vertices of this triangle all in the pore phase [39].

When computing correlation functions from digital images, it is important to correctly handle certain technical issues such as converting to polar coordinates, especially at small r, and to consider the limitations of digital images, such as digitizing curved surfaces, which were mentioned earlier. References [40, 44, 45] give explanations of the methods that must be used, the pitfalls of which to be wary, and the sources and magnitudes of possible errors.

Other than characterizing pore geometry, one of the principal uses of correlation functions is in the area of computing bounds for the effective properties of composite materials [46, 47]. Bounds are analytical formulas that, for some particular property such as elastic moduli or electrical conductivity, give the upper and lower limits for what the effective composite property can be.

Bounds are classified by their order. An nth-order bound usually includes information from the nth order correlation function [46, 47]. Of course, if there are more than two phases, there will be more than one nth-order correlation function. However, the second-order bounds for elastic moduli and

electrical–thermal conductivity, commonly called the Hashin–Strichkman bounds [47], are unusual in that they do not explicitly contain information from S_2, the second-order correlation function, other than $S_2(0) = \phi$. But the third-order bounds for these properties do have parameters computed from S_3. The first-order bounds are simply the parallel (Voigt) upper bound and series (Reuss) lower bounds, for which the phases are arranged in a parallel or series microstructure. These use the same information as the second-order bounds, the volume fraction and properties of each phase, but are wider apart than the Hashin–Strichkman bounds.

As bounds incorporate higher and higher correlation functions, they are known to become tighter and tighter, increasing their usefulness at the expense of a great increase of computational difficulty. In fact, it is known that the isotropic and anisotropic electrical conductivity [46, 48] and isotropic elastic moduli [49] of a random isotropic two-phase composite can be written down exactly in powers of the difference of the properties of the two phases. The coefficients in the power series are functions of all the correlation functions of any order for the composite. So, in general, the properties of a porous material will depend on all order correlation functions.

Bounds are most useful for composite materials where none of the phases have zero properties. They are less useful for air-filled porous materials. This is because in the array of nth-order bounds, the lower bound always has something of a series character and the upper bound always has something of a parallel character. For air-filled porous materials, this means that the lower bound is always close to zero, because air approximates a zero-property phase. So there is really only an upper bound for air-filled porous materials, which may or may not be very close to the actual effective properties. For a liquid-filled porous media, a meaningful lower bound can exist. However, for elastic properties, a zero shear modulus in the liquid phase causes both the lower shear modulus and Young's modulus bounds to be zero.

There has been much work in the past decade or so on bounding the permeability, which is a more difficult problem than that of bounding the effective electrical conductivity or elastic moduli [46, 50–53]. Permeability is different from quantities like electrical conductivity and elastic moduli. The conductivity, for example, is defined at every point of the material, and the overall effective conductivity is found by solving Laplace's equation [Eq. (9)], for the composite and averaging over this solution and the microscopic conductivities. However, there is no microscopic permeability, because permeability cannot be defined at a point, even in the pore space, but is defined instead by averaging over solutions of the Navier–Stokes equations in a porous material.

1.2.3 Pore Connectivity

Assessing the connectivity of any phase is simple in a digital image of a porous material. Usually, we want to know this for the pore phase, as the solid phase must be connected to have mechanical integrity of the sample. A simple method to use on a digital image is called a "burning algorithm" [54, 55]. In two dimensions, only one phase at a time in a porous material can be percolated [54, 56]. In three dimensions, several phases can simultaneously percolate. This fact reduces, but does not eliminate, the usefulness of the burning algorithm in two dimensions.

The burning algorithm is a way of identifying all members of a cluster of connected pixels that span the image. Starting on one side of an image, "burn" one pore pixel by setting its gray scale to another number that is not in the existing range; for example, not in the range 0–255. Then any pore pixel that touches this pixel is also set to the same number. Continue this process until there are no more "unburned" pore pixels left that are touching the last burned pixels. The process is similar to classifying all pixels of a certain gray value as being combustible, and then touching a match to one of them. If the "fire" burns from one side of the image to the opposite side, then the burned pixels are said to form a spanning cluster, or percolate. This process can be repeated by starting the fire at any unburned pixel to identify all connected clusters, and all nonspanning clusters as well. This is an efficient way to determine if the pore space percolates through the digital image.

In performing the burning algorithm, one issue to consider is which pixels constitute a neighboring pixel for propagation of the "fire." The most common case is to consider the immediate nearest neighbors (4 in two dimensions, 6 in three dimensions). Alternately, the second nearest neighbors (4 in two dimensions), or the second and third nearest neighbors (20 in three dimensions) can also be considered. The connectivity of a phase in a digital image with square or cubic pixels has this degree of uncertainty. We note, however, that using only the first nearest neighbors in two dimensions resulted in good agreement of percolation thresholds, determined on digital images, with their continuum counterparts [15]. Different numerical techniques for discretizing continuum equations on a digital image have natural definitions of connectivity connected with them, as we see in the next section.

It is important to note that percolation thresholds are usually larger in two than in three dimensions. For instance, if one carries out site percolation on a square lattice digital image, considering only nearest neighbor connections, where a random fraction x of the pixels are white and $(1 - x)$ are black, then the white pixels will percolate only when $x \geqslant x_c$, where $x_c = 0.59$

in two dimensions, but $x_c = 0.31$ in a 3-D simple cubic lattice [56]. If the pore space of a real material followed these site percolation statistics, and had a porosity of 35%, it would have a percolated pore space, but, seen in the microscope, a 2-D slice would appear to have a disconnected pore space, as a porosity of 35% is much less than $x_c = 0.59$. Thus it is incorrect to study 3-D percolation quantities using 2-D images. Stereology breaks down in this instance, as the connectivity in three dimensions and two dimensions is fundamentally different. Real pore spaces, which generally have different kinds of percolation statistics, will also show difference. Since the connectivity of the pore space has a critical influence on transport properties such as permeability [57], its quantification can be critical for understanding microstructure–transport property relationships.

1.3 Computing Material Properties from Images

By the fact that it is already divided into pixels, a digital image is easily adapted to discrete computational methods, such as finite difference, finite element, and lattice Boltzmann methods. Since there is an underlying lattice, any known algorithm for lattice problems can be applied. A manual available through the Internet describes a collection of various programs [58] that apply finite difference and finite element methods to any 2-D or 3-D digital images. These programs can be used to compute a variety of material properties to compare with experiment. Later in the chapter we discuss how the different methods can be applied to two-phase pore–solid images, representing materials in which either the solid or the pores have a uniform property, and the other is zero. An example of the case where the solid is insulating and the pores are filled with a conductive fluid is Vycor™ glass filled with a liquid metal [59]. On the other hand, we could have a conducting granular backbone and insulating pores [60]. Similarly for elastic properties, the solid is assumed to have a uniform elastic modulus tensor, while the pores have zero elastic modulus. For hydraulic permeability, the fluid can only flow in the pores.

Both finite element and finite difference methods are simply means of converting partial differential equations into a set of approximate algebraic equations. At this point, however, it is worth noting some of the differences between the finite element and finite difference methods discussed in this chapter. The linear electrical conduction and linear elasticity problems can be formulated either directly as a set of linear partial differential equations or, indirectly, as an energy functional of partial derivatives that obeys a variational principle. We present finite difference methods for the electrical conduction case, and finite element methods for the elasticity case. The full

Navier–Stokes equations are nonlinear and do not have an associated variational principle [61]. The linearized forms of these equations, the Stokes equations, do have a variational formulation [62]. However, we present only finite difference methods for the fluid flow case.

In the various methods presented in this chapter, there also can be differences in node placement. In a digital image, we want to use no more than one node per pixel, if possible, to conserve memory. Philosophically, this is also desirable since having more than one node per pixel would seem to imply that more information is available than is really present in the pixel structure. In a digital image, there are as many pixel corners as there are pixels or pixel centers, so a reasonable choice of node location would be either pixel corners or pixel centers. Of course, just as one can use any coordinate system to solve a physical problem, the node placement can be arbitrary as well. However, for example, one would not choose parabolic coordinates to solve a problem involving the surface of an ellipsoid, because ellipsoidal coordinates result in algebra that is much easier to work with than parabolic coordinates in this case. In the same way, for the finite difference and finite element methods, certain ways of choosing the node placement result in much simpler equations.

1.3.1 Steady-State Conduction

The important problem of steady-state conduction is a good case in which to see the differences between finite difference and finite element methods. The partial differential equation to solve is

$$\nabla \cdot \vec{j} = 0, \tag{8}$$

where $\vec{j} = \sigma \vec{E}$ is the current flux, and $\vec{E} = -\nabla V$, with V being the potential of the problem, and σ the local conductivity. Inside a constant conductivity material phase, this equation becomes the same as Laplace's equation,

$$\nabla^2 V = 0. \tag{9}$$

Between phases with different values of σ, the normal flux, along with the potential, must be continuous at a phase boundary. The energy functional that obeys a variational principle is given as

$$\frac{1}{2} \int \vec{j} \cdot \vec{E} d^3 r. \tag{10}$$

When this functional is extremized, the preceding differential equation results, with the correct boundary conditions.

In a digital image, all phase boundaries are also pixel boundaries. Having a square array (in two dimensions) or a cubic array (in three dimensions)

of pixels means that locally all boundaries are oriented in one of the principal directions. Since in a direct finite difference formulation of the partial derivatives of the problem, the derivatives are thought of as being between the nodes, it makes sense in the finite difference formulation to place the nodes at pixel centers, so that the boundaries are always located exactly between nodes. To get a finite difference form of Eq. (8), we simply expand the partial derivatives of the potential around the center of the pixel of interest, pixel m, to obtain

$$\Sigma_j S_{m,j}(V_j - V_m) = 0, \tag{11}$$

where $S_{m,j}$ is the conductance connecting pixels m and j, and V_m is the voltage at pixel m. For a porous two-phase material, if pixels m and j are both conductors, then $S_{m,j}$ is just the conductance of one conducting pixel. Otherwise, $S_{m,j} = 0$. For an electrolyte-filled rock, in the case of electrical conductivity, the pore phase is the conductor and the solid phase is the insulator. In the case of steady-state thermal conduction of a rock with empty pores, the solid phase becomes the conductor and the pore phase becomes the insulator. When there are two types of conductors, the finite difference formulation implies that $S_{m,j}$ becomes a series combination of the conductances of one-half of pixel m and one-half of pixel j [58, 63]. Figure 6 shows a piece of a finite difference network superimposed on a random image, where the gray pixels are conducting and the white pixels are insulating. The bonds indicate conducting connections between nodes.

A finite element solution of Laplace's equation can also be generated using the variational principle that the correct solution gives the minimum energy dissipated, averaged over the random structure [58]. Now the finite

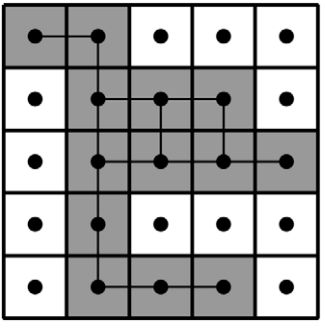

FIG. 6. Finite difference grid for a piece of a digital image. The gray area has nonzero conductivity, and the white area is insulating. The nodes are at pixel centers, and the lines connecting the nodes indicate mathematical "bonds."

element nodes are placed on the corners of the pixels, with the voltages given at the pixel corners instead of at the pixel centers. The voltage at the interior of the pixel is found by linear interpolation of the corner voltages. Equation (10) is then approximately computed, pixel by pixel, by integrating over each pixel and then summing over all pixels. This converts the energy functional into a quadratic form that involves the nodal voltages. This functional is minimized to solve for the nodal voltages and the approximate solution to the conduction problem. In many cases, the finite difference method is simpler and gives results that are just as accurate. For the case where two or more phases have a nonzero conductivity, sometimes the finite element method can be more accurate [58]. Figure 7 shows some of the finite element nodes superimposed on the same digital image as was shown in Fig. 6. Again, the gray phase is the conducting phase.

As mentioned earlier, the connectivity of a digital image can vary when different sets of neighbors are defined to be connected [64]. This can affect the result of computations. In the finite difference cases already described, the only mathematical connections are between nearest neighbor pixels. In the finite element method, however, since the nodes are at the corners of a pixel, and all the nodes on the corners of a given pixel are mathematically connected in the quadratic form, the result is that in two dimensions, each node is mathematically connected to nine different nodes, itself and its four nearest and four second nearest neighbors, which are the nodes in the corners of the four pixels that share a corner. In three dimensions, each node is mathematically connected to 26 other nodes plus itself. Therefore a conducting structure that is physically made up of pixels connected only by corners would be connected electrically when using finite elements but

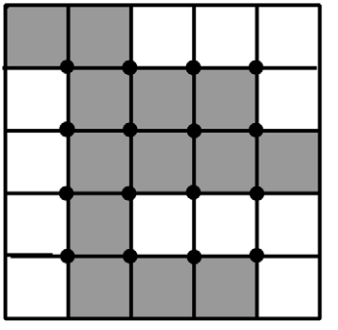

FIG. 7. Finite element grid for the same digital image as shown in Fig. 6. The nodes are now at pixel corners, where variables such as voltages and elastic displacements are evaluated. Both gray and white regions can have nonzero elastic moduli.

disconnected electrically when using finite differences. There is not much difference when the image resolution is high enough so that even the smallest feature is made up of many pixels. However, for low-resolution digital images, there can be a difference between the answer that these two methods give, with generally no way of distinguishing which is preferred. If the real pixel-to-pixel connections are defined beforehand in some way, so that only certain neighbors are "really" connected, this will give insight into which method to use. Otherwise, the choice is arbitary. However, exact solutions for various nontrivial systems can be used to check the accuracy of these different methods [58], in some cases distinguishing between them in a quantitative way.

1.3.2 Fluid Flow

Fluid flow in porous materials is of great interest for many practical reasons, including the service life of building materials, petroleum recovery, waste containment, catalysis, and filtering [7, 26, 65]. The continuum equation for calculating flow properties is the Navier–Stokes equation [65]. The Stokes equation is the slow-flow linearized version of the full Navier–Stokes equations. For flow through porous materials, in almost all cases, one is just interested in this slow-flow limit. The Stokes equation, in the steady-state limit, is given by [65]

$$\nabla^2 \vec{v}\,(\vec{r}\,) = \frac{1}{\mu} \nabla P(\vec{r}\,), \tag{12}$$

where $\vec{v}\,(\vec{r}\,)$ is the fluid velocity at the point $\vec{r}$, $P(\vec{r}\,)$ is the pressure at the point $\vec{r}$, and μ is the fluid viscosity. For incompressible fluids, an additional condition,

$$\nabla \cdot \vec{v}(\vec{r}\,) = 0, \tag{13}$$

applies.

There are many different ways to solve the Stokes equations [66], including both the finite difference and finite element methods. One way of solving the Stokes equation that is well adapted to a digital image uses a "marker-and-cell" (MAC) mesh [66]. Figure 8 shows the same image as in Figs. 6 and 7, where gray is the pore phase through which the fluid flows. The nodes indicate where the pressures are determined, and arrows show where the fluid velocities are determined, in the middle of pixel sides [16]. All fluid velocities right at a gray–white (pore–solid) boundary are set to zero, so no arrows are shown at these points in Fig. 8. This algorithm is similarly constructed in three dimensions [57].

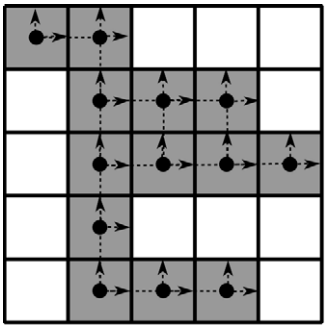

FIG. 8. Part of the MAC mesh for the same digital image as was used in Figs. 6 and 7. The pressure is evaluated at the nodes, and the fluid velocities are evaluated at the arrow tips, at pixel boundaries. The gray area is pore space and contains fluid, and the white areas are solid. Fluid velocities are forced to be zero (no arrows shown) at fluid–solid boundaries.

Darcy's law [65] is found to describe macroscopic flow through porous media:

$$\vec{v} = \langle \vec{v}(\vec{r}) \rangle = \frac{k\Delta P}{\mu L}, \tag{14}$$

where k, the permeability, has dimensions of length squared, $\vec{v}$ is the average fluid velocity in the entire volume of the sample (not just the pores), and ΔP is the pressure drop over the sample length L. Darcy's law is a macroscopic equation, obtainable from the Stokes equation [67], which treats the porous material as a homogeneous material defined by a certain bulk resistance to fluid flow through it. Darcy's law is mathematically analogous to Ohm's law, with μ/k playing the role of the resistivity.

Since permeability has units of length squared, and the conductivity, normalized by the conductivity of the conducting phase, is something like a dimensionless tortuosity, there have been many attempts to generate a length scale from the pore space that can relate the two quantities. The most widely used of these length scales are based on the specific surface area [65], an electrically weighted specific surface area that comes from solutions of Laplace's equation in the conducting pore phase [68] and a length scale based on mercury injection [69]. A common idea has been to find a length scale that correctly weights the parts of the pore space where the fluid actually goes. These length scales are all reviewed and compared on the same set of digital images in Ref. [16].

1.3.3 Linear Elasticity

The linear elastic properties of porous media can be computed by finite difference or a finite element methods applied to digital images. Expressed in terms of the elastic vector displacement, $\vec{u}(\vec{r})$, the Poisson's ratio ν of an isotropic solid, and ignoring the effect of gravity, the vector equation to be solved is [70]

$$(1 - 2\nu)\nabla^2\vec{u} + \vec{\nabla}(\vec{\nabla}\cdot\vec{u}) = 0. \tag{15}$$

For a two-phase image (solid and pores), where the solid has a uniform elastic moduli tensor and both elastic moduli are zero in the pore space, a finite difference approach can be used [71]. The boundary condition of zero normal force at a solid–pore boundary is automatically satisfied in the finite difference formulation [71]. When there are two or more kinds of solid materials, or when the pore space is filled with an incompressible fluid, it is difficult to incorporate into a finite difference formulation the boundary conditions of continuity of elastic displacement and normal stress at boundaries between different elastic moduli regions. It is easier to use a finite element formulation, which makes use of the variational principle that the correct displacement solution minimizes the elastic energy under an applied strain [58, 72]. The finite difference method would use a grid just like that shown in Fig. 6 with elastic displacements determined at the nodes in the pixel centers, while the finite element method would use a grid like that in Fig. 7 with elastic displacements determined at the pixel corners. In the displacement formulation [73] of the finite element method, continuity of displacement is satisfied automatically, but continuity of normal stresses is only approximate.

Figure 9 shows the component σ_{xx} of the computed stress tensor throughout the 22% porosity microstructure shown in Fig. 4, where the solid (white) phase was fully connected with a Poisson ratio of 0.2 and a Young's modulus of 1.0 in arbitrary units. A horizontal strain (ε_{xx}) of 0.01 has been applied across the sample. Figure 9 was obtained using a finite element method [58]. The brighter the gray scale, the higher the stress. The pores are shown in black, and the compressed regions are shown in an uniform dark gray. Because of the randomness of the porous material, even though the average strain is tensile, there will still be regions of compressive stress. Notice that the areas of compressive stress are always near a pore. On the other hand, the areas of high tensile stress are almost always at the bottom or top of a pore, due to the stress concentration effects of a cavity in a tensile strain field [74]. Figure 10 shows the corresponding stress histogram. The area under the histogram has been adjusted to be 1, rather than 1 − porosity, because the zero stresses in the (empty) pores have been

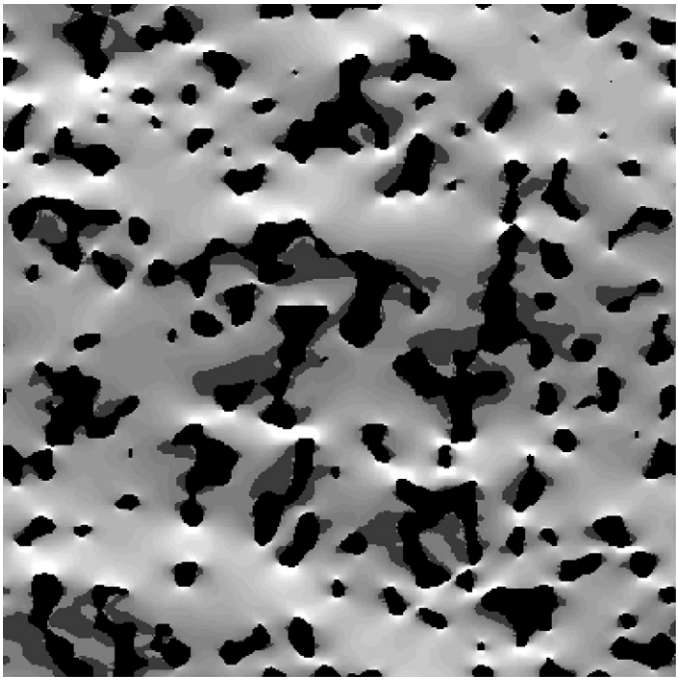

FIG. 9. The horizontal tensile stresses (σ_{xx}) for the 22% porosity microstructure shown in Fig. 4, where the solid phase (white in Fig. 4) has a Poisson's ratio of 0.2. The brightness is proportional to the tensile stress magnitude, with pores shown in black. Areas of compressive stress are in dark gray.

ignored. The effective Young's modulus of this porous material was about $\frac{1}{3}$. The effective moduli are easily determined by computing the average stress tensor and then extracting the effective moduli using the applied strain and well-known composite theory [46, 47]. Reference [75] describes a successful comparison with experiment using the finite element elastic technique to compute the effective elastic and shrinkage properties of porous Vycor™ glass.

1.3.4 Nonwetting Fluid Injection

A simple simulation of injection of a nonwetting fluid has been developed in two dimensions [76] and three dimensions [77, 78]. The results can be compared with mercury porosimetry experiments. The idea is to apply the "equivalent sphere" concept to digital images in the following way [79]. For

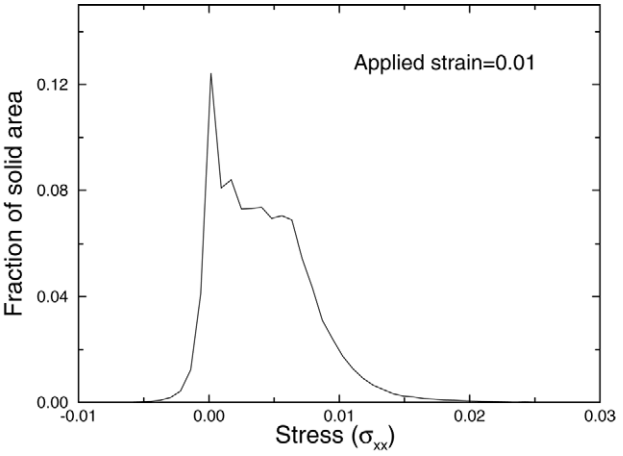

FIG. 10. Showing a stress histogram for the computed stress fields shown in Fig. 9. The applied strain was 0.01, and Young's modulus of the solid phase was 1.0 in arbitrary units.

a given injection pressure P, there is a corresponding pore radius R, $P \sim 1/R$. In three dimensions, a sphere with radius R is put into the image from the outside, and moved around to cover as much volume as possible without overlapping the solid. As the injection pressure is increased, the size of the sphere is decreased. The amount of additional volume swept out at each progressively smaller value of R is the pore space assigned to that pore size or to its equivalent pressure [11, 76], just as in mercury injection porosimetry. In two dimensions, this technique is fairly accurate, as there is only one radius of curvature for a meniscus, and it is reasonably approximated by a circular arc. In three dimensions, however, there are two principal radii of curvature at any point on the surface of a liquid meniscus. Thus using a sphere to simulate the meniscus is much less reliable. Mathematical morphology techniques can also be utilized in simulating these processes in porous media [80].

Figure 11 shows a simulation of mercury intrusion (gray) in a material in which the solid frame (white) is made up of randomly placed, rigid overlapping monosize circles (white) [76]. The uninvaded pores are in black. The left-hand side is for a lower pressure, where only surface intrusion has occurred. The right-hand side shows the intrusion that occurs at higher injection pressure, where the nonwetting fluid can get into smaller pores. Clearly, there are large pores that are not invaded because they are only accessible by small throats. This is the well-known "ink bottle" effect [81].

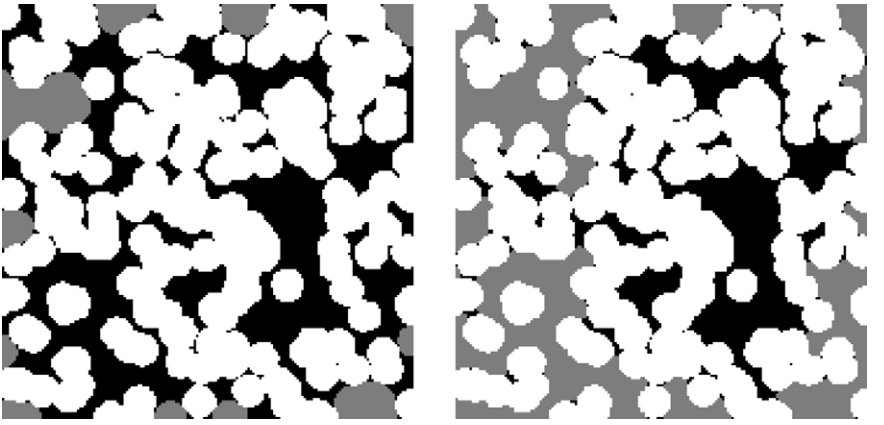

FIG. 11. Example of the intrusion of a nonwetting fluid (gray) into the empty pore space (black) around the solid (fixed) circles (white). Left: low-pressure intrusion; right: high-pressure intrusion.

Moisture absorption is important in the study and use of porous materials in atmospheric conditions (see Chapter 3). A typical quantity measured is the sorption isotherm, which is the amount of moisture absorbed as a function of the partial pressure of the absorbing vapor, at a fixed temperature. A simple variation of the mercury injection simulation can be made so as to simulate the moisture absorption–desorption processes in any digital image of a porous material in two or three dimensions [75, 78, 80].

1.3.5 Cellular Automaton Fluid Methods

Two additional computational fluid dynamics algorithms, originally based on cellular automaton ideas, that are alternative to the direct finite difference solution of the Stokes equation are the lattice gas [82] and lattice Boltzmann methods [82–84], as applied to porous materials. These methods, in contrast to the finite difference and finite element methods, do not directly discretize the continuum Navier–Stokes equations but rather operate at the "fluid particle" level.

The lattice gas method tracks the motion of particles moving on a lattice that are subject to collison rules that guarantee conservation of mass and momentum. Macroscopic variables such as density and flow velocity are obtained from statistical analysis of the particle motions.

In contrast, the lattice Boltzmann method solves for the time evolution of

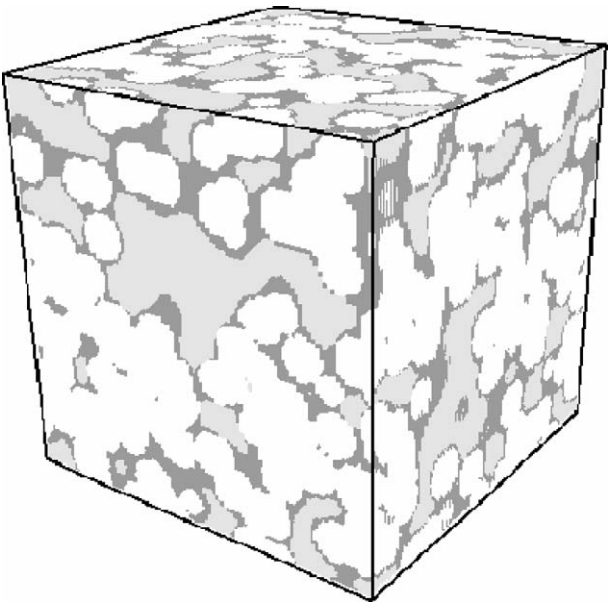

FIG. 12. A 3-D lattice Boltzmann simulation of the phase separation of two immiscible fluids in a porous material, where one fluid wets the solid phase (solid = white, dark gray = wetting fluid) and the other does not (light gray = nonwetting fluid).

the fluid particle velocity distribution function, which evolves due to the "collision" of fluid particles. Quantities such as fluid density and velocity can be easily obtained from moments of the distribution function. The method can be applied to any digital image of a porous material, and the resulting fluid behavior proves to satisfy the Navier–Stokes equations. Due to ease of implementation, the lattice Boltzmann method is much more frequently used than the lattice gas method.

For a given digital image and the simple problem of saturated single-fluid flow driven by a small pressure gradient, it may be easier to use a finite difference code for the Stokes equations. However, the lattice Boltzmann method is much more useful in treating multiphase flow problems because interfacial forces between liquid, gas, and solid phases can be more easily incorporated. Thus flow and wetting properties in partially saturated porous materials can be obtained in two or three dimensions [82–84].

One example is shown in Fig. 12, which depicts a 3-D computation of the phase separation of two immiscible fluids inside a model porous material. One fluid (dark gray) wets the solid (white), and one does not (light gray).

The simulation starts with the fluids homogeneously mixed and present everywhere in the pore space. The lattice Boltzmann algorithm causes the two fluids to phase separate, with the wetting fluid preferentially moving to the solid surface.

1.4 Creating Isotropic 3-D Structures from 2-D Images

There are various ways to obtain 3-D images from 2-D images. Experimentally, 3-D images may be built up from a set of 2-D serial sections [85]. This is a tedious and time-consuming task, even with an automated system. X-ray tomography offers one possibility for rapidly obtaining a 3-D image of a microstructure. Resolution limits of several micrometers per pixel can be achieved. This is adequate for many porous materials [86–88] (see Chapter 8). Sample sizes of a few millimeters or centimeters can be accommodated, depending on the needed resolution. The acquisition and processing of such images are rapid because no physical slicing of the sample is involved. The rest of this section describes a method for generating 3-D images from 2-D images in cases where 3-D images are not readily or directly obtainable.

1.4.1 Quiblier Method

An interesting theoretical approach to generating 3-D images is to generate a representative 3-D porous medium from a single 2-D view of the system, such as that provided by a conventional micrograph illustrating the pore system. Based on the work of Joshi [89], Quiblier developed a computational technique for creating a 3-D microstructure based on two-point correlation function (S_1) analysis of a 2-D image [90]. The main principle is that a 3-D image is produced that has the same one-point and two-point correlation functions as did the real material, as determined in the 2-D image. In essence, S_2 obtained from the 2-D image is introduced into a 3-D image by convoluting an initial image consisting of Gaussian noise. The resulting image is then filtered so as to have the same S_2 as the original image. This involves solving a large number of nonlinear equations [90]. In his original paper, Quiblier performed some stress calculations on a slice of the generated 3-D medium. Adler et al. [91] utilized this technique to generate 3-D images of Fontainebleau sandstones. They computed permeabilities [91] and conductivities [92], but the results were consistently lower than measurements on real samples. This is probably due to differences in the pore space connectivity since S_2 does not contain such information. The evidence of this weakness is the difference in percolation thresholds. Pores in sandstone are known to become disconnected at a few

percent porosity, but the 3-D generated images tend to have percolation thresholds near 10% porosity [91].

1.4.2 Simplified Method

A simplified version of the approach outlined by Quiblier has been developed that modifies the generated 3-D structure based on analysis of the hydraulic radius of the pore space [93, 94]. Transport properties such as permeability and conductivity and the critical pore diameter can be computed to evaluate the merit of the generated 3-D microstructure. An example in Fig. 13 shows the original scanning electron micrograph (SEM) of a porous clinker brick, along with a thresholded and two-phase view of solid plus pores [94]. In the modified generation procedure, S_2 is calculated using Fig. 13 (right) and then used to generate a 3-D microstructure. The value of s_p for this structure is not equal to the original value. The hydraulic radius of the 3-D structure is then modified so as to force its value of s_p to match that of the real image [93], which also makes the two-point correlation function approximately match the real one as well. A 3-D view of the final generated brick microstructure is shown in Fig. 14, with the pores in black. As pointed out earlier in Section 1.2.3, while the pores appear discontinuous in the 2-D image, they are actually connected in the generated 3-D image.

1.4.3 Limitations of 2-D to 3-D Image Generation Methods

There are advantages and drawbacks to generating 3-D porous microstructures from 2-D images. If the geometrical characteristics of a porous

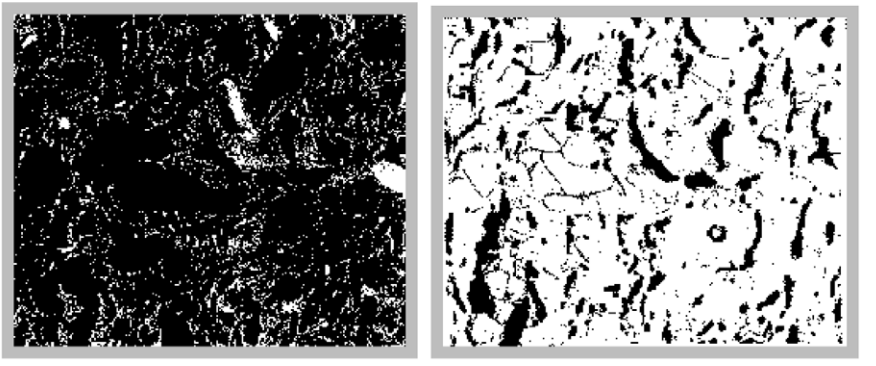

FIG. 13. A starting 2-D SEM image of the clinker brick (left) and a thresholded binary image showing pore regions in black (right). Each image is about 500 μm wide.

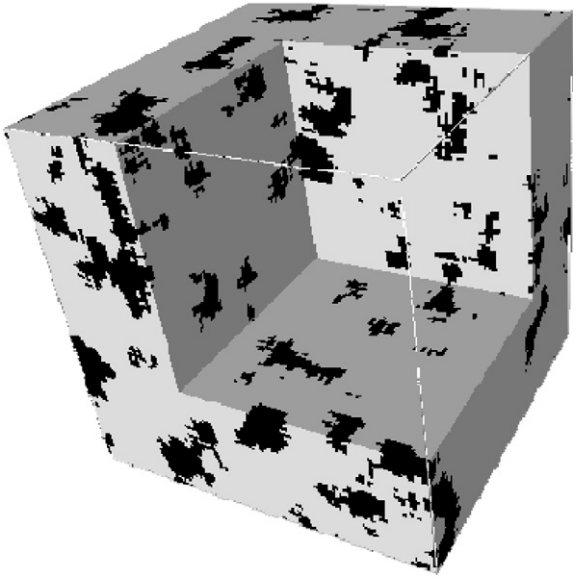

FIG. 14. A cutaway view of a 3-D reconstructed image of the clinker brick with the same porosity (black) as the original 2-D image.

material are well captured by S_2, then the generated image can be used to compute other properties as well. If the geometrical information in $S_3, S_4, \ldots$ or the connectivity of the pore space is important for the computed properties, then there is no substitute for the real 3-D image [75].

1.5 Microstructure Models in Three Dimensions

Besides using digital images of real materials to compute their various physical properties, it is often useful to construct artificial models to elucidate the essential physics. There are three broad classes of 3-D models for porous materials.

The first kind of model is called a *percolation-type* model. Here, one builds up a structure using randomly or regularly deposited shapes of various kinds within a finite imaging field; for example, overlapping ellipsoids, lattices of overlapping spheres, or a random or regular lattice of tubes. The result is a 3-D structure that bears some similarities to real materials and is easy to generate on a computer. They can give real insight into parameters such as percolation thresholds, transport properties, and their interrelation-

ships. However, the values of parameters in the models are not to be compared with real materials.

The second type of model is usually based on smoothing of a random noise image. A random noise image is first created, and then mathematical operations are carried out to transform it into something that resembles a real material. There is no attempt to simulate the actual physical and chemical processes that create the porous material. Cellular automaton methods can also be used to generate images that look like the "real thing" without attempting to duplicate the actual physics and chemistry [95].

The third kind of model is a microstructure development model that tries to simulate the actual processes by which the material is made. Examples, to be discussed further later in the chapter, include models for the formation of cement-based materials, sintered ceramic materials, and sedimentary rocks. These kinds of models are usually harder to create than the first two kinds, requiring insights into the physical and chemical processes, and the algorithms are more complicated. However, their output can be compared directly to images of the real materials and their measured properties. An image of the actual starting materials, as we shall see, can often be used as the starting point for these kinds of models. The outcome of a microstructure development model can be visually compared to images of the real material. At the crudest level, this is the "duck" test: If it looks like a duck, then it is a duck. However, using the tools developed in Sections 1.2 and 1.3, more quantitative tests can be conducted; for example, various correlation functions can be compared and other properties can be computed and compared against experimental data. Good agreement validates the assumed physical and chemical processes contained in the model.

1.5.1 Percolation-type Models

Percolation theory is a well-studied topic, with many excellent reviews [54, 56, 96–98]. The early studies of percolative structures and their effects on bulk physical properties were made on random lattice structures, thus making them relevant to structures seen in digital images, which are typically square or cubic lattice structures. A digital image approximates a continuum structure when the geometric features of interest each occupy many pixels. In this sense, a useful digital image is a lattice structure with spatial correlations among the pixels [99, 100].

There has been less, but still substantial work, on generating 3-D continuum models using continuum objects placed at random or regular positions within the image frame. Many references can be found in the reviews cited earlier. One example is to build microstructures out of overlapping, randomly placed and oriented ellipsoids [101]. Figure 15

shows a 2-D section of such a 3-D model. The prolate ellipsoids used were of the same size with an aspect ratio of 10. The volume fraction of ellipsoids in Fig. 15 is approximately 7%. Even though in the image, the ellipsoids appear to be mostly isolated, over half of them are connected in three dimensions and form a spanning cluster. Note that a similar model with ellipses in two dimensions having the same aspect ratio would percolate at an area fraction of about 30% [102].

Building continuum models with other objects in three dimensions was reviewed by Balberg [103] and they are relevant to real processes. Cubes were used to study percolation processes in the combustion of carbon [104], and regular lattice packings of spheres have been used to study capillary condensation hysteresis loops [105]. A regular lattice packing of spheres that can consequently grow and overlap, called the grain consolidation model, has been used to gain insight into transport processes in sedimentary

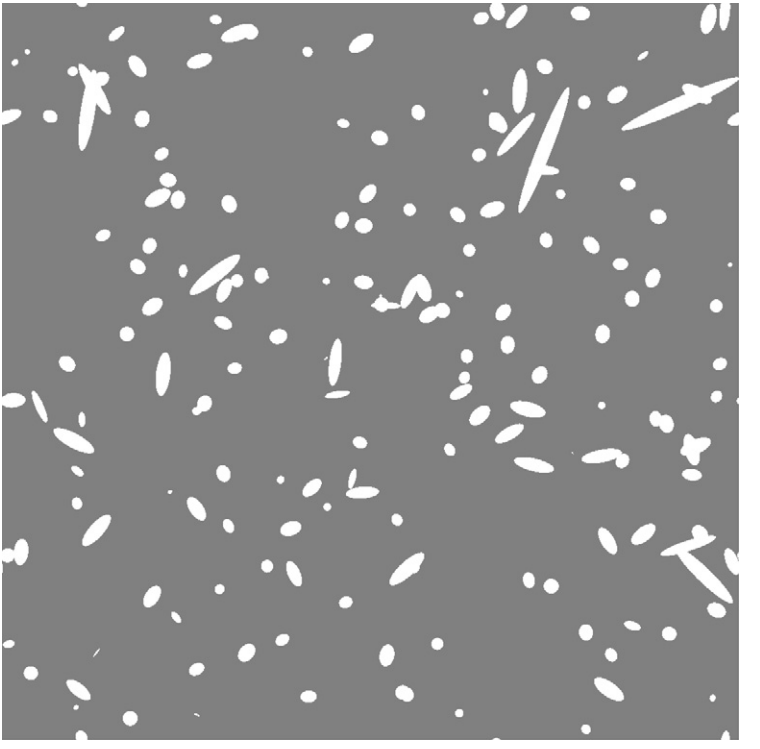

FIG. 15. Slice through a 3-D model of overlapping prolate ellipsoids (white) having an aspect ratio of 10. The volume fraction of ellipsoids is 7%.

rocks [106]. Two-dimensional lattices of disks that can rub against each other have been used to simulate the elastic properties of sandstone [107]. Other discussions of percolative-type models can be found in Ref. [46].

A subset of this approach, mostly used for simulating fluid flow in porous materials, is the use of tube networks, both regular [108] and random [109]. In some sense, this is similar to using discrete conductor networks to solve the continuum Laplace equation [100]. However, setting up a finite difference solution of the continuum Stokes equation in a porous material does not result mathematically in equations that resemble those for a network of tubes. Nevertheless, a great deal can be found about flow in porous materials from this approach [110]. More details can be found in Chapter 2.

1.5.2 Artificial Image Models

The second set of models are what we call artificial image models. In Section 1.4, the measured two-point correlation function, S_2, measured on a 2-D digital image of a real material, was used to convolve a random noise image to obtain an artificial 3-D microstructure that had approximately the same porosity and functional form of S_2 as did the 2-D image. There are other ways of operating directly on random images to produce artificial structures. These methods are not based on the actual formation processes of the real material, and they may not even use a real image in the convolution algorithm. They are, however, useful because they can be easily generated and often bear reasonable resemblances to real microstructures.

One method is to take a random white noise image, convolve it with some other function, and then threshold it to solid and pore phases to give the desired porosity. This has been done using a Gaussian convolution function and, remarkably, provided images that resembled thin sections of carbonate rock [111]. If the convolution function is the Laplacian of a Gaussian, the resulting images exhibit features of Vycor™ [111, 112]. The microstructures in Fig. 4 are from Gaussian convolutions of a white noise image.

A variation of the preceding method uses two thresholds, x_1 and x_2. All pixels with values of x, $0 < x < 1$, below x_1 and above x_2 are designated pores, and pixels with $x_1 < x < x_2$ are designated as solid. This algorithm turned out to generate images that resembled foam-like and aerogel-like structures [113, 114]. The conductivity of these structures has been computed along with the two- and three-point correlation functions and resulting three-point bounds, and showed reasonable agreement with experimental measurements [113, 115].

This kind of model shows that as long as the correlation functions are similar to the real materials, artificial image models can be used productively to understand other material properties.

1.5.3 Microstructure Development Models

It is desirable to generate porous microstructures based on actual physical and chemical processes. This is often very difficult because of the complexity of these processes. Natural materials such as sandstone are not made under a controlled laboratory environment, so our quantitative knowledge of the processes involved is weak. However, man-made materials such as concrete (5 billion tonnes per year worldwide) and ceramics (including bricks) and various gels are manufactured according to well-defined processes, so in principle, it should be possible to simulate these processes by a 3-D microstructure model. The success of the model is, in fact, a test of our understanding of the processes.

Consider the case of the porous material concrete. It is made up of cement, water, sand, and pebbles (aggregates). It is formed by the hydration of cement, the most common variant of which, known as portland cement, consists of mainly calcium silicates with minor amounts of aluminate, sulphate, and ferrite phases [116]. When water is mixed with the cement, the various phases of the cement undergo hydration reactions, each at a different rate and interacting with each other. The initial viscous mixture of liquid and particulates grows into a rigid solid that keeps increasing its strength as the hydration progresses, which can continue for months. The cement paste (cement plus water) turns into a solid matrix, in which the sand and pebbles are embedded.

The main geometrical feature that must be understood about concrete microstructure to be able to optimize concrete properties is the development of the cement paste microstructure during hydration, because the cement paste matrix governs the properties of concrete. This is a microstructure made up of unhydrated cement grains, reaction products, and water-filled pore space. The starting cement grains have an average size of about 20–50 μm, so that the length scale that initially characterizes the primary cement paste pores is of the order of micrometers. These pores do, however, become as small as a tenth of a micrometer as hydration progresses. There are smaller secondary pores present, called gel pores, inherent in the main reaction product, amorphous calcium silicate hydrate. Their diameters are of the order of tens of nanometers [78, 116], but we ignore them in considering the primary cement paste microstructure. Cement paste is thus a porous material whose solid phase is not uniform. This has a sensitive effect on many concrete properties such as elastic moduli and thermal conductivity.

Models have been made to simulate the evolution of the cement paste microstructure from a mixture of water and cement grains to the final hydrated product [55, 117, 118]. These models incorporate only some of the relevant cement chemistry and physics. The amounts and volume of reac-

tants and products are correctly handled. The randomness of the original multiphase composite cement particles is realistically taken into account by using 2-D scanning electron microscope digital images of real particles as a basis for constructing 3-D particles [118]. The randomness in the growth process and the topology of the various reaction products are also realistically simulated.

Figure 16 (right) shows an SEM micrograph of a real cement paste, compared to the model equivalent in Fig. 16 (left) [55, 117]. The gray scales indicate the different phases. The darkest gray pixels contain other minority phases, including gel pores, which are not shown. The pores are black. For calculating composite properties such as elastic moduli, the different phases in the solid framework must be identified, as they all have different elastic moduli. Color pictures that reveal more details of the various stages of cement hydration can be found in Refs. [117–119].

Properties that have been computed using the various methods described in Section 1.3 of this chapter include the connectivity of both the solid and pore phases of hydrated cement [55], diffusivity of the pore space [63], and how the cement paste matrix in concrete is modified by the nearby presence of aggregates [119, 120]. Comparison with experimental data has been quite favorable.

Another example of a microstructural development model has to do with the high-temperature sintering of powders into ceramics and metals. The powder particles change shape, and the powder compact densifies to minimize surface energy [121]. This process has been simulated by a cellular

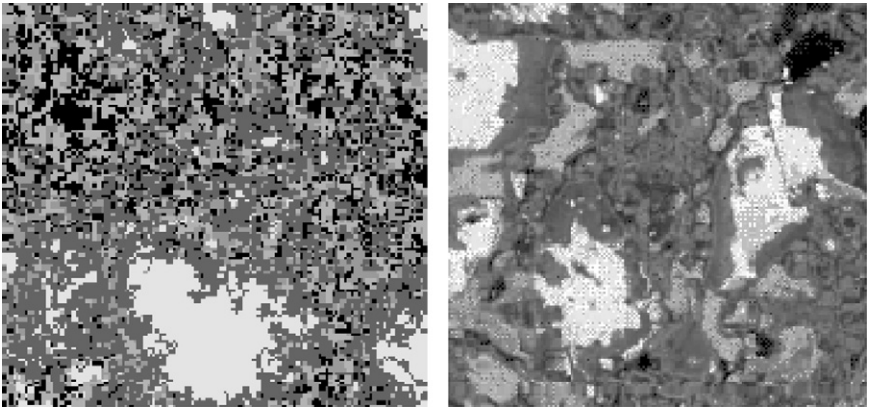

FIG. 16. A real hydrated cement paste (right) and its model equivalent (left). The different gray levels indicate the principal different solid phases of unhydrated cement and its reaction products. Porosity is black. The darkest gray level contains minor phases that are not shown.

automaton model that minimizes the surface area of a digital image of particles [122, 123]. A simple algorithm that transfers pixels from areas of high curvature to areas of low curvature captures the essence of the process. It is clear that by moving mountains to fill valleys, surface area is reduced, which is the main driving force for sintering. To implement the model on a digital image requires a simple algorithm to measure curvature, which is illustrated in Fig. 17. The solid pixels in this figure are shown with heavy black lines and the pore space pixels with thin black lines. A circular template (shown in gray) is centered at the point of interest on the surface. The local curvature is estimated by counting the number of pore pixels in the circular template. It is intuitively obvious that a flat surface would have 50% pore pixels in the circle, with less than 50% for negative curvature, and more than 50% for positive curvature. It can be proved mathematically [123] that this procedure is asymptotically exact, in the limit where the template radius is much smaller than the local radius of curvature. Other ways of measuring curvature in a digital image are described in Ref. [124]. The algorithm is applicable in three dimensions as well, but it gives only the average of the two principal radii of curvature [123].

Figure 18 shows the evolution (from left to right) of a collection of circular grains as the curvature and therefore surface area is reduced by the algorithm. The collection of grains is gradually becoming a circle, which has

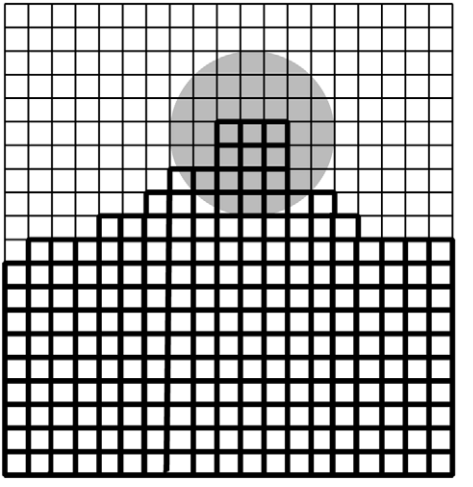

FIG. 17. The circular template algorithm in two dimensions. Thick black lines denote solid pixels, and thin black lines denote pore pixels. The circular template is shown in gray.

FIG. 18. The evolution of a collection of circular particles (left to right) under the sintering algorithm described in the text.

the minimum perimeter of a given surface area of any finite area shape in two dimensions [125]. This growth model can be applied directly to a digital image that has been acquired experimentally.

The sintering model described does not contain all of the relevant dynamics. When material is removed from a high-curvature surface, it must be transported to the low-curvature surface by either vapor transport through the pores, surface diffusion, volume diffusion, or diffusion through any grain boundaries. There are also elastic forces that arise from the tendency of the particles to coalesce to minimize surface area [126, 127].

1.5.4 Summary

With the rapid advance in computing and imaging tools, 2-D and 3-D digital images of porous materials can be readily obtained by a variety of techniques. Mathematical and computational techniques have been adapted to work with these images. In this chapter, we surveyed many of the techniques that have been applied to porous materials and showed the results. Although this is a rapidly advancing field, the essence is that a digital image converts a continuum picture into a lattice of discrete pixels, so that all lattice computational techniques are applicable.

The rapid growth of computing power will lead to more realistic models, and more 3-D experimental data, using x-ray tomography, nuclear magnetic resonance (NMR) imaging, and other methods. The improved characterization of pore geometry will result in more accurate calculation and prediction of material properties, which ultimately will aid in materials engineering via microstructural design.

Acknowledgments

We thank the NIST High-Performance Construction Materials and Systems program and the National Science Foundation Science and Tech-

nology Center for Advanced Cement-Based Materials for support of this work, M. F. Thorpe for useful conversations, and the NIST Scientific Visualization Group for help with many of the 3-D figures.

References

1. P. Hirsch, J. D. Birchall, D. D. Double, A. Kelly, G. K. Moir, and C. D. Pomeroy, *Phil. Trans. Roy. Soc. Lond.* **310**, 1–207 (1983).
2. S. Sapieha and P. Lepoutre, *Tappi* **65**, 99–101 (1982).
3. R. L. Coble and W. D. Kingery, *J. Am. Ceram. Soc.* **39**, 377–385 (1956).
4. J. Rodel and A. M. Glaeser, *J. Am. Ceram. Soc.* **70**, C172–C175 (1987).
5. R. L. Johnson, J. A. Cherry, and J. F. Pankow, *Environ. Sci. Technol.* **23**, 340–349 (1989).
6. R. L. Smith and S. D. Collins, *J. Appl. Phys.* **71**, R1–R2 (1992).
7. F. A. L. Dullien, *Porous Media: Fluid Transport and Pore Structure*, 2nd ed. (Academic Press, San Diego, 1992).
8. M. Sahimi, *Phys. Rev. A* **43**, 5367–5376 (1991).
9. M. Sahimi, *Flow and Transport in Porous Media and Fractured Rock* (VCH, New York, 1996).
10. M. A. Biot, *J. Appl. Phys.* **33**, 1482–1498 (1962); M. A. Biot, *J. Acoust. Soc. Am.* **34**, 1254–1264 (1962).
11. E. J. Garboczi, *Powder Tech.* **67**, 121–130 (1991). Also available at http://ciks.cbt.nist.gov/garboczi/, Chap. 11.
12. B. E. Hornby, L. M. Schwartz, and J. A. Hudson, *Geophysics* **59**, 1570–1583 (1994).
13. K. A. Snyder, E. J. Garboczi, and A. R. Day, *J. Appl. Phys.* **72**, 5948–5955 (1992).
14. C. Kittel, *Introduction to Solid State Physics*, 5th ed. (John Wiley & Sons, New York, 1979).
15. E. J. Garboczi, M. F. Thorpe, M. S. DeVries, and A. R. Day, *Phys. Rev. A* **43**, 6473–6482 (1991). Also available at http://ciks.cbt.nist.gov/garboczi/, Chap. 3.
16. N. Martys and E. J. Garboczi, *Phys. Rev. B* **46**, 6080–6090 (1992). Also available at http://ciks.cbt.nist.gov/garboczi/, Chap. 11.
17. J. Berryman, E. Garboczi, and N. Martys, unpublished.
18. B. Lu and S. Torquato, *J. Chem. Phys.* **93**, 3452–3459 (1990).
19. K. R. Castleman, *Digital Image Processing* (Prentice-Hall, Englewood Cliffs, NJ, 1981).
20. E. E. Underwood, *Quantitative Stereology* (Addison-Wesley, Reading, MA, 1970).

21. R. T. DeHoff and F. N. Rhines, *Quantitative Microscopy* (McGraw-Hill, New York, 1968).
22. John C. Russ, *The Image Processing Handbook* (CRC Press, Cleveland, OH, 1994).
23. V. Cantoni, S. Levialdi, and G. Musso, eds., *Image Analysis and Processing* (Plenum, New York, 1986).
24. J. Serra, *Image Analysis and Mathematical Morphology* (Academic Press, London, 1982); *Image Analysis and Mathematical Morphology Volume II: Theoretical Advances* (Academic Press, London, 1988).
25. B. B. Mandelbrot, *The Fractal Geometry of Nature* (W. H. Freeman, New York, 1983).
26. P. Wong, *Phys. Today* **41**, 24–25 (1988).
27. P. Wong, *Phys. Rev. B* **32**, 7417–7424 (1985).
28. P. Wong and A. J. Bray, *J. Appl. Cryst.* **21**, 786–794 (1988).
29. P. Wong and Q. Cao, *Phys. Rev. B* **45**, 7627–7632 (1992).
30. H. E. Stanley and N. Ostrowsky, eds., *Random Fluctuations and Pattern Growth* (Kluwer Academic, Dordrecht, 1988).
31. T. Vicsek, *Fractal Growth Phenomena* (World Scientific, Singapore, 1989).
32. F. Family and T. Vicsek, eds. , *Dynamics of Fractal Surfaces* (World Scientific, Singapore, 1991).
33. J. Feder, *Fractals* (Plenum, New York, 1988).
34. A. H. Thompson, A. J. Katz, and C. E. Krohn, *Adv. Phys.* **36**, 625–694 (1987).
35. D. W. Schaefer and K. D. Keefer, *Phys. Rev. Lett.* **56**, 2199–2202 (1986).
36. D. N. Winslow, J. M. Bukowski, and J. F. Young, *Cem. Conc. Res.* **25** (1), 147–156 (1995).
37. R. Lemaitre and P. M. Adler, *Transp. Porous Media* **5**, 325–340 (1990).
38. J. K. Williams and R. A. Dawe, *Transp. Porous Media* **1**, 201–209 (1986).
39. S. Torquato and G. Stell, *J. Chem. Phys.* **79**, 1505 (1983).
40. J. G. Berryman, *J. Appl. Phys.* **57**, 2374–2384 (1985).
41. P. Debye, H. R. Anderson, and H. Brumberger, *J. Appl. Phys.* **28**, 679 (1957).
42. J. G. Berryman, *J. Math. Phys.* **28**, 244–245 (1987).
43. J. G. Berryman and S. C. Blair, *J. Appl. Phys.* **60**, 1930–1938 (1986).
44. D. A. Coker and S. Torquato, *J. Appl. Phys.* **77**, 6087–6099 (1995).
45. D. A. Coker and S. Torquato, *J. Appl. Phys.* **77**, 955–964 (1995).
46. S. Torquato, *Appl. Mech. Rev.* **44**, 37–76 (1991).
47. Z. Hashin, *Appl. Mech.* **50**, 481–505 (1983).
48. W. F. Brown, *J. Chem. Phys.* **23**, 1514–1517 (1955).
49. S. Torquato, *J. Mech. Phys. Solids* **45**, 1421–1448 (1997).
50. J. G. Berryman and G. W. Milton, *J. Chem. Phys.* **83**, 754–760 (1985).
51. J. Rubinstein and S. Torquato, *J. Fluid Mech.* **206**, 25–46 (1989).

52. S. Torquato, *Phys. Rev. Lett.* **64**, 2644– 2646 (1990).

53. M. Avellaneda and S. Torquato, *Phys. Fluids A* **3**, 2529–2540 (1991).

54. D. Stauffer, *Percolation Theory* (Taylor and Francis, London, 1985).

55. D. P. Bentz and E. J. Garboczi, *Cem. Conc. Res.* **21**, 325–344 (1991). Also available at http://ciks.cbt.nist.gov/garboczi/, Chap. 5.

56. R. Zallen, *The Physics of Amorphous Solids* (John Wiley & Sons, New York, 1983), Chap. 4.

57. N. S. Martys, S. Torquato, and D. P. Bentz, *Phys. Rev. E* **50**, 403–408, 1994.

58. E. J. Garboczi, Finite element and finite difference programs for computing the linear electrical and elastic properties of digital images of random materials, National Institute of Standards and Technology Internal Report NISTIR 6269 (1999). Also available at http://ciks.cbt.nist.gov/garboczi/, Appendix 3.

59. M. J. Graf, C. A. Huber, T. E. Huber, and A. P. Salzberg, in *MRS Proc.* Vol. 195 *Physical Phenomena in Granular Materials*, edited by G. D. Cody, T. H. Geballe, and P. Sheng, pp. 397–402 (1991).

60. K. Kendall, *Powder Technol.* **62**, 1147–154 (1990).

61. C. B. Millikan, *Phil. Mag. S.* **7**, 641–662 (1929).

62. H. Helmholtz, *Wiss. Abh.* **1**, 223–230 (1868); J. B. Keller, L. A. Rubenfeld, and J. E. Molyneux, *J. Fluid Mech.* **30**, 97–125 (1967).

63. E. J. Garboczi and D. P. Bentz, *J. Mater. Sci.* **27**, 2083–2092 (1992). Also available at http://ciks.cbt.nist.gov/garboczi/, Chap. 5.

64. M. A. Ioannidis, M. J. Dwiecien, and I. Chatzis, *Transp. Porous Media* **29**, 61–83 (1997).

65. A. E. Scheidegger, *The Physics of Flow Through Porous Media* (University of Toronto Press, Toronto, 1974).

66. R. Peyret and T. D. Taylor, *Computational Methods for Fluid Flow* (Springer-Verlag, New York, 1983).

67. S. Whitaker, *Trans. Porous Media* **1**, 3 (1986).

68. D. L. Johnson, J. Koplik, and L. M. Schwartz, *Phys. Rev. Lett.* **57**, 2564 (1986).

69. A. J. Katz and A. H. Thompson, *Phys. Rev. B* **34**, 8179 (1986); *J. Geopys. Res.* **92**, 599 (1987).

70. L. D. Landau and E. M. Lifshitz, *Theory of Elasticity*, 3rd ed. (Pergamon Press, Oxford, 1986).

71. J. Poutet, D. Manzoni, F. Hage-Chehade, C. J. Jacquin, M. J. Bouoteca, J.-F. Thovert, and P. M. Adler, *Int. J. Rock Mech. Min. Sci. Geomech. Abstr.* **33**, 409–415 (1996); The effective mechanical properties of random porous media, *J. Phys. Mech. Solids* **44**, 1587–1620 (1996).

72. E. J. Garboczi and A. R. Day, *J. Phys. Mech. Solids* **43**, 1349–1362 (1995). Also available at http://ciks.cbt.nist.gov/garboczi/, Chap. 11.

73. R. D. Cook, D. S. Malkus, and M. E. Plesha, *Concepts and Applications of Finite Element Analysis*, 3rd ed. (John Wiley & Sons, New York, 1989).

74. S. P. Timoshenko and J. N. Goodier, *Theory of Elasticity*, 3rd ed. (McGraw-Hill Book Co., New York, 1970), 90–97.

75. E. J. Garboczi and D. P. Bentz, *Model. Sim. Mater. Sci. Eng.* **6**, 211–236 (1998). Also available at http://ciks.cbt.nist.gov/garboczi/, Chap. 11.

76. E. J. Garboczi and D. P. Bentz, *Ceram. Trans.* **16**, 365–379 (1991). Also available at http://ciks.cbt.nist.gov/garboczi/, Chap. 11.

77. J. A. Lewis, M. A. Galler, and D. P. Bentz, *J. Am. Ceram. Soc.* **79**, 1377–1388 (1996).

78. D. P. Bentz, D. A. Quenard, V. Baroghel–Bouny, E. J. Garboczi, and H. M. Jennings, *Mater. Struct.* **28**, 450–458 (1995). Also available at http://ciks.cbt.nist.gov/garboczi/, Chap. 4.

79. J. F. Thovert, J. Salles, and P. M. Adler, *J. Microsc.* **170**, 65–79 (1993).

80. D. A. Quenard, D. P. Bentz, and E. J. Garboczi, Capillary condensation, hysteresis, and image analysis, in *Drying 92*, A. S. Mudjumdar, ed. Pt. A, 252–262, (Elsevier Press, Amsterdam, 1992).

81. J. van Brakel, S. Modry, and M. Svata, *Powder Technol.* **29**, 1–12 (1981). This is the first article in a special issue devoted to mercury porosimetry.

82. D. H. Rothman, *Geophysics* **53**, 509 (1988); D. H. Rothman and S. Zaleski, *Rev. Mod. Phys.* **66**, 1417–1479 (1994).

83. N. S. Martys and H. Chen, *Phys. Rev. E* **53**, 743–750 (1996).

84. R. Benzi, S. Succi, and M. Vergassola, *Phys. Rep.* **222**, 145–197 (1992).

85. P. E. Stutzman, *Ceram. Trans.* **16**, 237 (1991).

86. B. P. Flannery, H. W. Deckman, W. G. Roberge, and K. L. D'Amico, *Science* **237**, 1439–1444 (1987).

87. D. P. Bentz, N. S. Martys, P. Stutzman, M. S. Levenson, E. J. Garboczi, J. Dunsmuir, and L. M. Schwartz, X-ray microtomography of an ASTM C-109 mortar exposed to sulfate attack, in *Microstructure of Cement-Based Systems/Bonding and Interfaces in Cementitious Materials*, edited by S. Diamond et al. (Materials Research Society Vol. 370, Pittsburgh, 1995), pp. 77–82. Also available at http://ciks.cbt.nist.gov/garboczi/, Chap. 9.

88. F. M. Auzerais, J. Dunsmuir, B. B. Ferreol, N. Martys, J. Olson, T. S. Ramakrishman, D. H. Rothman, and L. M. Schwartz, *Geophys. Res. Lett.* **23**, 705–708 (1996).

89. M. Joshi, *A Class of Stochastic Models for Porous Media*, Ph.D. Thesis, Univ. of Kansas, 1974.

90. J. A. Quiblier, *J. Colloid Interf. Sci.* **98** 84–102 (1984).

91. P. M. Adler, C. G. Jacquin, and J. A. Quiblier, *Int. J. Multiphase Flow* **16**, 691–712 (1990).

92. P. M. Adler, C. G. Jacquin, and J. F. Thovert, *Wat. Res. Res.* **28**, 1571–1576 (1992).

93. D. P. Bentz and N. S. Martys, *Transp. Porous Media* **17**, 221–238 (1994).
94. D. A. Quenard, K. Xu, H. M. Kunzel, D. P. Bentz, and N. S. Martys, *Mater. Struct.* **31**, 317–324 (1998).
95. D. A. Young and E. M. Corey, *Phys. Rev. A* **41**, 7024–7032 (1990).
96. M. B. Isichenko, *Rev. Mod. Phys.* **64**, 961 (1992).
97. J. W. Essam, *Rep. Prog. Phys.* **43**, 833–912 (1980).
98. J. M. Hammersley and D. J. A. Welsh, *Contemp. Phys.* **21**, 593–605 (1980).
99. P. Renault, *Transp. Porous Media* **6**, 451–468 (1991).
100. S. Kirkpatrick, *Rev. Mod. Phys.* **45**, 574–588 (1973).
101. E. J. Garboczi, K. A. Snyder, J. F. Douglas, and M. F. Thorpe, *Phys. Rev. E* **52**, 819–828 (1995). Also available at http://ciks.cbt.nist.gov/garboczi/, Chap. 3.
102. W. Xia and M. F. Thorpe, *Phys. Rev. A* **38**, 2650–2655 (1988).
103. I. Balberg, *Phil. Mag. B* **56**, 991–1003 (1987).
104. P. Salatino and L. Massimilla, *Powder Technol.* **66**, 47–52 (1991).
105. M. Yanuka, *J. Coll. Inter. Sci.* **127**, 48–58 (1989).
106. L. M. Schwartz and S. Kimminau, *Geophysics* **52**, 1402–1411 (1987).
107. L. M. Schwartz, D. L. Johnson, and S. Feng, *Phys. Rev. Lett.* **52**, 831–834 (1984).
108. R. Lenormand, *Proc. Roy. Soc. London A* **423**, 159 (1989).
109. M. Blunt and P. King, *Phys. Rev. A* **42**, 4780–4787 (1990).
110. P. Wong, J. Koplik, and J. P. Tomanic, *Phys. Rev. B* **30**, 6066 (1984).
111. P. A. Crossley, L. M. Schwartz, and J. R. Banavar, *Appl. Phys. Lett.* **59**, 3553–3555 (1991).
112. R. Blumenfeld and S. Torquato, *Phys. Rev. E* **48**, 4492–4500 (1993).
113. A. P. Roberts and M. A. Knackstedt, *J. Mater. Sci. Lett.* **14**, 1357–1359 (1995).
114. A. P. Roberts and M. Teubner, *Phys. Rev. E* **51**, 4141–4154 (1995).
115. A. P. Roberts and M. A. Knackstedt, *Phys. Rev. E* **54**, 2313 (1996).
116. H. F. W. Taylor, *Cement Chemistry* (Academic Press, London, 1990).
117. D. P. Bentz, P. V. Coveney, E. J. Garboczi, M. F. Kleyn, and P. E. Stutzman, *Model. Simul. Mater. Sci. Eng.* **2**, 783–808 (1994).
118. D. P. Bentz, *J. Am. Ceram. Soc.* **80**, 3–21 (1997).
119. D. P. Bentz, E. Schlangen, and E. J. Garboczi, in *Materials Science of Concrete IV*, edited by J. Skalny and S. Mindess (American Ceramic Society, Westerville, Ohio, 1995).
120. D. P. Bentz, P. E. Stutzman, and E. J. Garboczi, *Cem. Conc. Res.* **22** (5), 891–902 (1992). Also available at http://ciks.cbt.nist.gov/garboczi/, Chap. 6.
121. W. D. Kingery, H. K. Bowen, and D. R. Uhlman, *Introduction to Ceramics*, 2nd ed. (John Wiley & Sons, New York, 1976).

122. P. Pimeinta, W. C. Carter, and E. J. Garboczi, *Comp. Mater. Sci.* **1**, 63–77 (1992). Also available at http://ciks.cbt.nist.gov/garboczi/, Chap. 10.

123. J. W. Bullard, E. J. Garboczi, W. C. Carter, and E. R. Fuller, *Comp. Mater. Sci.* **4**, 103–116 (1995). Also available at http://ciks.cbt.nist.gov/garboczi/, Chap. 10.

124. J. C. Russ, *J. Computer-Assisted Microsc.* **1**, 39–77 (1989).

125. G. Polya and G. Szego, *Isoperimetric Inequalities in Mathematical Physics* (Princeton University Press, Princeton, NJ, 1951).

126. J. W. Bullard and W. C. Carter, in *Sintering Technology*, edited by R. M. German, G. L. Messing, and R. G. Cornwall (Marcel Dekker, New York, 1996), 45–52.

127. J. W. Bullard, *J. Appl. Phys.* **81**, 159–168 (1997).

This Page Intentionally Left Blank

2. VISUALIZATION OF FLOW PATTERNS IN 2-D MODEL NETWORKS

Roland Lenormand

Institut Français du Pétrole, Rueil Malmaison, France

This chapter is devoted to the visualization of fluid displacements in two-dimensional porous media. The different techniques are presented, but the main objective of the chapter is to show how pore-scale visualizations have contributed to the understanding of the mechanisms involved in fluid displacements.

The chapter is organized as follows. I first describe the different techniques for making the micromodels used for two-dimensional visualizations. I then present some examples where visualizations have contributed to the understanding of the mechanisms: immiscible displacements, tracer flow, critical flows (nucleation, condensation), etc.

2.1 Visualization Tools

Various transparent models have been used to study the properties of flow in porous media, from 1-D capillary tubes of different shapes to 2-D networks of capillaries made by glass etching or resin molding and 3-D visualizations using transparent media, and more recently high-resolution x-ray tomography. The 2-D micromodels are most useful in identifying microscopic mechanisms that are essential in interpreting 3-D data in practical applications.

2.1.1 Capillary Tubes

A circular capillary tube is the simplest model of a porous medium. It enables the observation of phenomena including the displacement of a meniscus between two immiscible fluids, the measurement of the effects of velocity on the contact angle, the hysteresis between advancing and receding contact angles, and the spreading of a tracer (Taylor dispersion [1]).

Roof [2] studied the snap-off of a nonwetting fluid displacing a wetting fluid in a capillary tube with periodic variable cross section. He showed that snap-off occurs when the ratio between large and small sections is larger than 1.5.

EXPERIMENTAL METHODS IN THE PHYSICAL SCIENCES
Vol. 35
ISBN 0-12-475982-3

ISSN 1079-4042/99 $30.00

A capillary tube with a square cross section allows the simultaneous flow of two immiscible fluids, with the nonwetting fluid flowing in the center part and the wetting fluid in the corners of the duct (Fig. 1). The technique used by Legait *et al.* [3] consists in molding a Pyrex tube around a square stainless-steel stem that is then dissolved by acid. The smallest size is of the order of 1 mm. To obtain a smaller internal diameter, the square capillary is heated and stretched, but the shape of the cross section is no longer well defined. This square tube has also been used by Kalaydjian and Legait [4] to study the viscous coupling between two fluids flowing in the same capillary. Li and Wardlaw [5] studied the collapse of wetting films in a rectangular throat for different wettabilities.

A "doublet" of two connected capillaries of different sizes (Fig. 2) was used by Engoy *et al.* [6] to study the drying of a fluid. In this simple geometry, there is a competition between viscous flow in the tubes, capillary forces due to the difference of diameter, and molecular diffusion in the gas phase.

These 1-D models cannot account for the interconnection of the pore structure leading not only to fluid bypassing and trapping but also to original cooperative mechanisms. For this purpose, 2-D models have been developed. Among the more often used techniques, I describe glass and resin micromodels and monolayers of glass beads.

2.1.2 Glass Micromodels

In 1961, Mattax and Kyte [7] used chemical etching of glass plates. A glass plate is coated with a thin layer of wax and lines are scribed on the wax with a stylus. Then the glass is etched with hydrofluoric acid. The

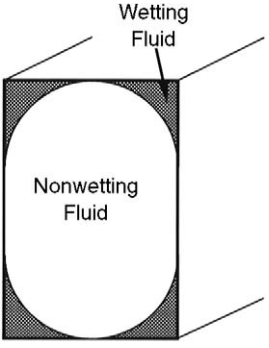

FIG. 1. Flow of two immiscible fluids in a square capillary tube. The nonwetting fluid flows in the center part and the wetting fluid along the corners of the capillary tube.

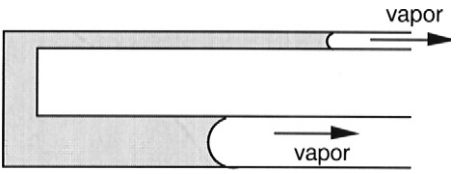

FIG. 2. Doublet of two capillary tubes used for studies of drying in porous media.

drawing is a square grid with 350 × 350 lines. Intermediate wettability was obtained by saturating the model with crude oil and it was left in contact for several hours. The authors made several observations on the effect of wettability, especially, flow of oil by films in the case of mixed wettability and large-scale fingering. They also measured relative permeabilities and found that the curves were similar to those of real rocks.

Davis and Jones [8] made 2-D networks using a photosensitive resist that enables the reproduction of any network pattern made from a photograph or generated by computer. The technique, which was improved by McKellar and Wardlaw [9] and is still in use, is as follows:

- A piece of mirror is placed in a hot solution of NaOH to remove the backing protection.
- A photoresist coating (photosensitive polymer) is applied to the copper backing.
- A film of the pattern is applied on the photoresist and exposed to ultraviolet light. The channels are in black and are not exposed.
- The image is developed (the unexposed photoresist is removed).
- Exposed copper is removed by a nitric acid solution (channels).
- The exposed portion of the glass is then etched by hydrofluoric acid.
- The remaining copper and photoresist are removed.
- A cover is fused on the top of the etched plate.

The etching has a V shape with a typical size in the range 10–100 μm and separation of 0.1 to 1 mm.

One of the main problems when flowing oil and water is cleaning and the restoration of wettability properties. Trygstad *et al.* [10] took apart the plates of their model and cleaned them with a solution of saturated NaOH. The plates were also made oil-wet using a chemical treatment.

Payatakes and coworkers have worked on two-layer glass micromodels [11]. Two etched plates are separated by a thin glass plate and interconnected with small holes drilled at the node positions. The main conclusion of a study in micromodel containing 24 × 20 nodes and 120 perpendicular 0.7-mm-diameter throats is that the nonplanarity of the medium has small

qualitative but significant quantitative effects on displacements, especially on relative permeabilities. These results confirm that topological effects lead to different results in three dimensions than in two dimensions.

Glass micromodels are also used at a high pressure (around 100 bar) for studies of miscible flooding [12]. They are placed in a high-pressure chamber and surrounded by a transparent confining fluid.

An updated version of glass etching and the references for the chemical products can be found in Wan *et al.* [13]. These authors also developed an original method to visualize and measure the velocity of fluorescent colloid particles.

2.1.3 Silicon Wafer Micromodels

Two-dimensional micromodels with very fine structure, down to 1 μm, have been successfully prepared by Hornbrook *et al.* [14] using a silicon wafer instead of glass. With their technique, the pore size in the micromodels is comparable to the pores of a real rock. In addition, the etching process oxidizes the silicon, producing a surface that is uniformly wettable, but not strongly water-wet. In addition, the cross section is rectangular, almost perfect. The cover plate is attached by anodic bonding.

2.1.4 Resin Micromodels

The resin technique developed by Bonnet and Lenormand [15] provides much better control of the shape and size of the channels. This is important when experiments are compared to computer simulations. The principle of this technique is as follows:

- A negative film is made of a computer-generated network (the black parts will be the micromodel channels).
- A photosensitive plastic plate used for making printing plates is illuminated by ultraviolet light through the negative. The plastic under the transparent parts of the negative polymerizes and becomes hard.
- The soft part of the plate is washed out by a chemical solution.
- The plate is not transparent. Thus, a transparent replica made of polyester resin is cast in a rubber mold of the plate.
- The channels are filled with paraffin wax in a vacuum, and the surface is carefully cleaned.
- A thick layer of polyester resin is cast on this polyester plate to make the cover. After polymerization, a block of transparent resin is obtained, with the inside of the channels filled with paraffin wax.
- The paraffin is removed by heating and rinsing with toluene.

One advantage of this technique is the well-controlled shape of the channels: a rectangular cross section with a constant depth of 1 mm and a minimum width of 0.2 mm. Another advantage is that the relatively large thickness (1 mm) enables easy visualization, even with a low concentration of dye in the fluids. Dawe and Wright [16] obtained a channel depth of 50 μm by choosing a different kind of photosensitive plate. Oxaal [17] directly used polymer etching without the replica. The process of sealing with a transparent plate is accomplished using a Mylar membrane and compressed air.

The main drawback of using resin is the wettability hysteresis when oil and water are used together. Thus, the application is mainly limited to oil and gas or oil and mercury.

2.1.5 Glass Bead Monolayers

Several authors have developed models containing a monolayer of glass beads between two glass plates (for instance, Chatenever [18] and Moulu [19]). Generally, the main problem is a bypass between the plates and the beads. Even if the beads are well packed, the average pore diameter between the beads and the plates is larger than that between the beads. This problem was solved by Feder *et al.* [20] and Oxall *et al.* [21] who used a thin plastic sheet pressurized by compressed air. This sheet made contact with all the beads and kept them in place. A very large sample (of the order of 1 m) was achieved.

2.1.6 Image Analysis

As described in Chapter 1, digital image analysis is used to study the fluid distribution inside micromodels. For instance, Soll *et al.* [22] were able to measure three-phase saturations from video images taken from the micromodels. Water and oil were dyed respectively with ethylene glycol-based blue food coloring for water and Oil Red O dye for oil. Using image analysis they were able not only to calculate the fluid saturations but also to identify and analyze the size distribution of the trapped phases.

2.2 Capillary Displacements

This section shows how the simple physical effect of capillarity at the pore level can explain the complicated flow patterns observed in porous media. First, the main properties of capillarity and wettability are reviewed.

2.2.1 Notion of Capillarity

A key element in considering immiscible fluids in a pore is the presence of a curved meniscus between the fluids. This leads to a pressure difference between the fluids related to the curvature across the interface. This pressure difference, called capillary pressure Pc, is inversely proportional to the radius of curvature r of the interface if the meniscus is spherical (Laplace's law): $Pc = 2\gamma/r$. The surface tension γ is a physical parameter that characterizes the interactions between the fluids. A typical value for surface tension at the water–air interface at standard temperature and pressure is $0.072\,\mathrm{N}\cdot\mathrm{m}^{-1}$.

When the meniscus is in contact with a solid surface, there is a contact angle θ that depends on the balance of molecular forces between the two liquids and the solid. In a circular capillary tube of radius R (Fig. 3), the radius of curvature is $R/cos\,\theta$ and therefore the capillary pressure $Pc = (2\gamma \cos\theta)/R$. The solid is generally preferentially wetted by one of the fluids, called the "wetting fluid," for which the contact angle is less than 90°. Wettability depends on the two fluids and the solid. For example,

- With air and water, most solids are wetted by water, except Teflon (Goretex membranes for raincoats).
- Mercury is a nonwetting fluid on glass with air or water.
- "Clean" sedimentary rocks are preferentially wetted by water in presence of oil and water. After being in contact with crude oil for a few weeks, however, they can become of intermediate wettability (θ around 90°).

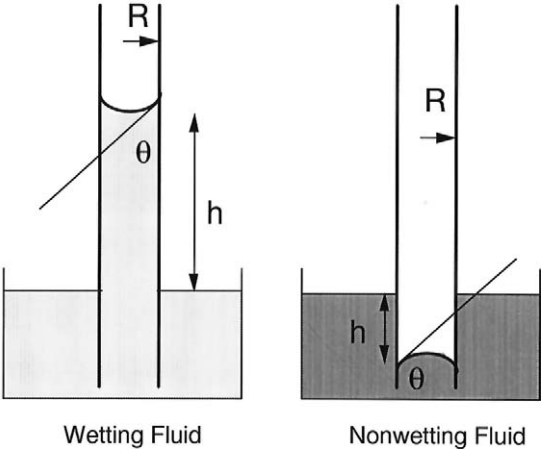

FIG. 3. Capillary rise in a tube.

Laplace's law also explains the capillary rise of a liquid in a capillary tube (Fig. 3). In this simple experiment, the hydrostatic pressure balances the capillary pressure:

$$\rho g h = \frac{2\gamma \cos\theta}{R},$$

where ρ is the liquid density and g is the gravitational acceleration.

In porous media, capillary forces are relatively large because of the small size of the pores. In many cases, especially in oil reservoirs, capillary forces between oil and water control the displacement. For instance, for a 1-μm pore the capillary pressure is around 1 atm ($=10^5$ Pa). In a tube of 1-μm diameter, the capillary rise of a wetting fluid would be of 10 m.

During fluid displacements, capillary forces are generally in competition with viscous and gravitational forces. Two dimensionless numbers are used to characterize the relative importance of the different forces. The capillary number Ca is the ratio between viscous forces (acting at the pore level) and capillary forces:

$$Ca = \frac{\mu V}{\gamma}$$

where μ is the fluid viscosity and V is the mean velocity inside a pore.

The Bond number B is the ratio between gravity forces acting at the pore level and capillary forces:

$$B = \frac{\Delta\rho g D^2}{\gamma},$$

where D is a mean pore diameter and $\Delta\rho$ the difference of density between the fluids.

In addition to the displacements taking place in the bulk of the pores, the wetting fluid can also flow along the roughness of the solid grains. This mechanism, generally called "film flow," has been studied experimentally in square capillaries [23] and theoretically for rough surfaces [24] and fractal media [25, 26].

2.2.2 Drainage: Invasion of the Nonwetting Fluid

A typical situation of two immiscible fluids in a micromodel is shown in Fig. 4. The picture represents a cluster of air surrounded by water. The size of the "grains" is about 1 mm. The displacement mechanism depends on the wettability of the fluid that is pushing the other.

The displacement of a wetting fluid by a nonwetting fluid is generally called "drainage." The displacement of the meniscus is very simple in

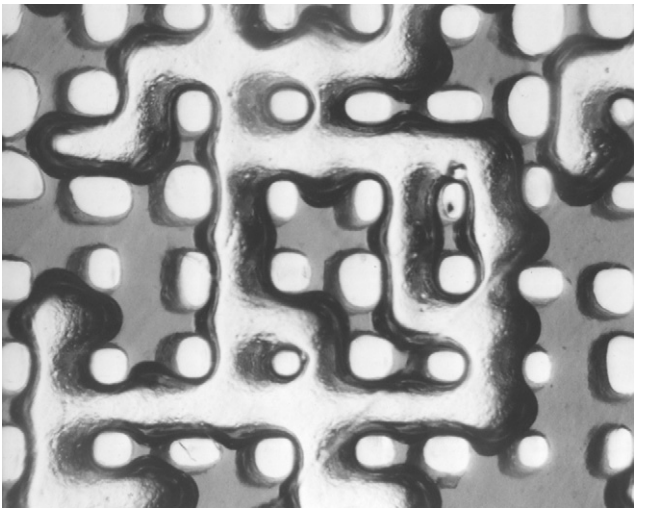

FIG. 4. Distribution of oil and air in the pores of an etched micromodel.

drainage (Lenormand *et al.* [27], Mahers and Dawe [28], Chen [29]). The nonwetting fluid is stopped by a throat (Fig. 5) until the pressure exceeds the threshold value (given by Laplace's law). After passing this throat, the nonwetting fluid spontaneously invades all the adjacent pores (intersections of the channels) and other throats larger than the original throat.

This sequential pore-by-pore invasion is known as invasion percolation. In essence, capillary forces prevent the nonwetting fluid from spontaneously

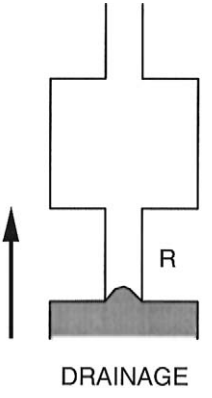

FIG. 5. Fluid invasion in a simple pore.

entering a porous medium. It can enter only a throat with diameter D when the pressure in the fluid exceeds the threshold pressure. If P_0 is the pressure, the threshold corresponds to D_0 and the fluid can enter all the throats that are larger than D_0.

To make an analogy with a percolation network, we can consider a throat with $D > D_0$ as a *conductive* bond and a throat with $D < D_0$ an *insulating* bond. The fraction p of conductive bonds at a given pressure P_0 can easily be deduced from the throat size distribution. At that pressure, the injected fluid invades the cluster formed by the connected conductive bonds. This is standard *percolation* except that the clusters must be connected to the inlet to be invaded. Hence, this model of invasion has been called *invasion percolation* [30, 31]. In Fig. 6 (after Lenormand [32]) where air displaces oil, the pattern shows the ramified structure of the air cluster and also the trapped oil clusters, which span a wide range of sizes.

Invasion percolation can be studied by computer simulations using simple rules. The throats of the network are numbered acccording to their size (1 is the largest). The numbers are randomly generated and distributed on the network. The invading fluid is injected from one side of the network (or at any node to simulate a local injection) and the invasion is simulated channel by channel. The largest accessible throat, which corresponds to the

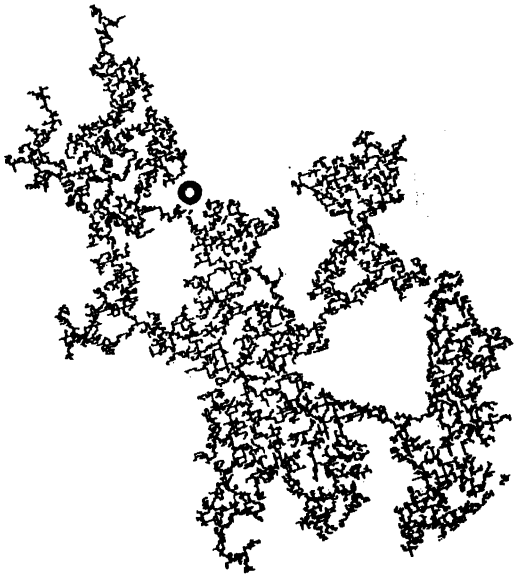

FIG. 6. Experimental invasion percolation cluster. Reprinted with permission from R. Lenormand, *Physica* **140A**, 114 (1986).

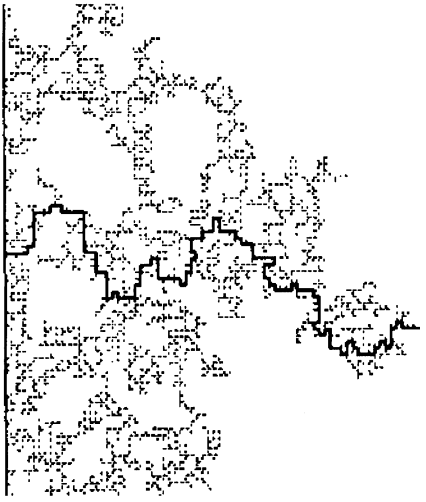

FIG. 7. Network simulation of invasion percolation. Reprinted with permission from R. Lenormand and S. Bories, *C. R. Acad. Sci. Paris*, **B291**, 279 (1980).

smallest number, is invaded until the exit is reached. The bold line in Fig. 7 shows the continuous path between the inlet and the outlet on a computer simulation.

Invasion percolation has been shown to have some properties in common with standard percolation, especially the fractal structure of the infinite cluster at the percolation threshold. We evaluated this property with micromodels [33] using a large network containing 250,000 channels with seven classes of widths (from 0.27 to 0.51 mm). The wetting fluid was a paraffin oil (viscosity $0.020\,\mathrm{N}\cdot\mathrm{m}$) displaced by air at three different flow rates. Photographs were taken at the end of displacement (Fig. 8). The fractal dimension was obtained by counting the number N of filled channels in boxes of different sizes L (in lattice spacing unit) using the relation $N \propto L^D$, where D is the fractal dimension (Fig. 9). The results show that, on a log-log scale, the plot of N vs L was linear over 1 decade and the slope was 1.82. This value agrees with the result of numerical simulations [34]. The difference from standard percolation ($D = 1.89$) is believed to be a finite-size effect.

2.2.3 Imbibition: Invasion of the Wetting Fluid

For this reverse displacement (called imbibition), the pore-scale mechanisms are more complicated than in drainage. There are two additional effects due to pore geometry and also to the flow by films along the roughness of

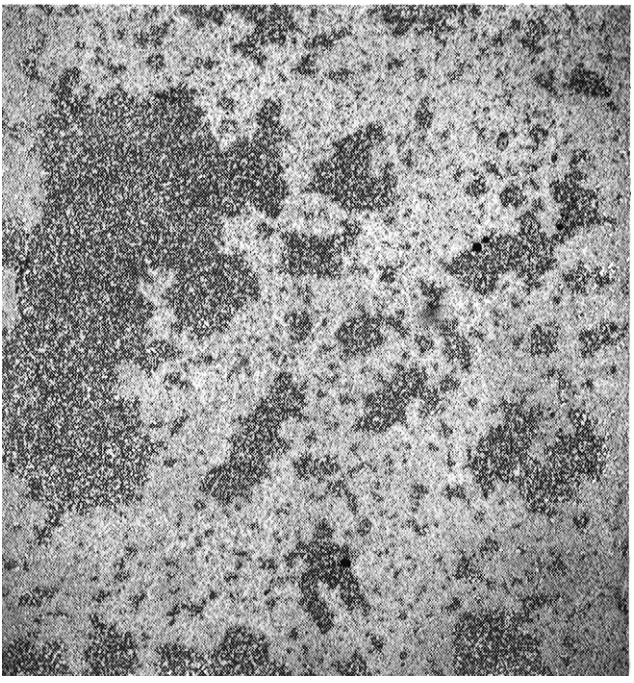

FIG. 8. Displacement of the wetting fluid (black) by the nonwetting fluid (white) in a large network (Ref. [33]). Copyright 1985 by the American Physical Society.

the solid. The first obervations were made with oil displacing air in resin micromodels of large size with various heterogeneities and pore topologies [35]. Chen [29] used a small network containing only 16 pores and accurately measured all the throat dimensions and followed the displacements at various flow rates. Wardlaw and coworkers [5, 36, 37] studied mercury withdrawal in glass micromodels. Liquid mercury is the nonwetting fluid when in equilibrium with its vapor or with any gas. Billiotte *et al.* [38] studied in detail the role of film flow for trapping during gas–water injection and withdrawal. The results of the different studies can be summarized as follows.

There are mainly two kinds of displacement at the pore level.

Pore invasion (Fig. 10a). Initially, the wetting fluid occupies two adjacent channels. During invasion of the wetting fluid, the capillary pressure decreases, and consequently the radius of curvature of the meniscus increases in the pore. At a given pressure P_1, the meniscus touches the

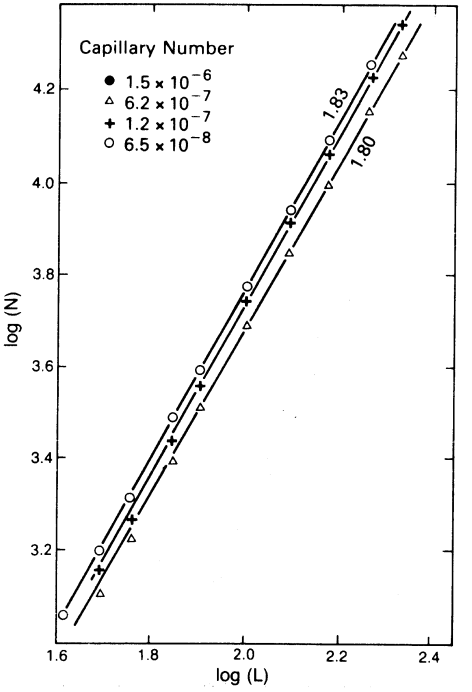

FIG. 9. A log-log plot of the number of invaded pores as function of the size of the box. (Ref. [33]). Copyright 1985 by the American Physical Society.

wall (point A), and the wetting fluid then invades the whole pore (the intersection of the four channels) and the two other adjacent channels.

Collapse in a channel (Fig. 10b). The wetting fluid can flow along the roughness of the walls and surround the solid grains. At a given pressure P_2, the fluid that accumulates on the walls of a channel becomes unstable and fills the channel (snap-off).

At the scale of a micromodel, the invaded patterns depend on the details of the pore geometry, contrary to the drainage displacement.

During imbibition, the wetting fluid is injected and the capillary pressure decreases. Consequently the dominant displacement mechanism corresponds to the higher of P_1 and P_2; that is, the displacement mechanism that occurs first as the capillary pressure is decreased. For simple geometries, these pressures P_1 and P_2 can be calculated if the contact angle is known. Generally, due to broad pore size distribution, both mechanisms occur during imbibition in real porous media. With micromodels, we can control the pore geometry to demonstrate the two idealized cases. The key par-

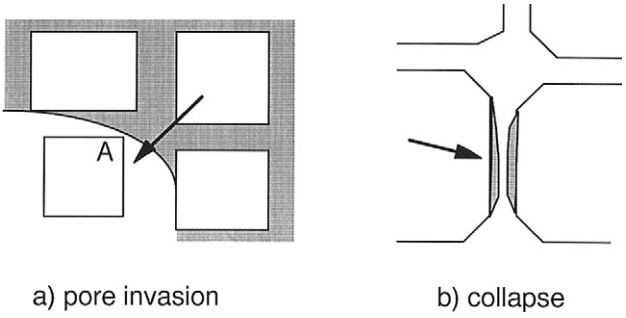

FIG. 10. Two mechanisms of pore invasion during imbibition. Reprinted with permission from R. Lenormand, *Physica* **140A**, 114 (1986).

ameter is the pore-to-throat-size ratio, or aspect ratio. Figure 10a represents the limiting case where the pores and throats are of the same size (aspect ratio of the order of unity). In Fig. 10b, the aspect ratio is larger than unity.

Small aspect ratio. With no flow by films, when the size of the pore is small compared with channel diameters, the meniscus touches the wall very quickly and P_1 is higher than P_2. Imbibition takes place by a succession of pore invasions (as previously described). This leads to a kind of *faceted crystal* growth developing at the point of injection [39]. The compact shape of the *crystal* is related to the network mesh: rectangular for a square mesh or triangular for a triangular mesh (Fig. 11).

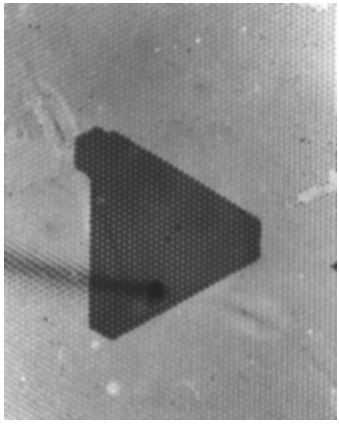

FIG. 11. Capillary imbibition with a triangular mesh. Reprinted with permission from R. Lenormand, *J. Phys. Condens. Matter* **2**, SA79 (1990).

With flow through films, the same mechanism occurs anywhere in the network, without any apparent connectivity with the injection face. The result is a set of *compact clusters* [40] (Fig. 12) for a square network. The process can be simulated by a mechanism similar to nucleation. When two clusters are in contact, they grow until they form only one rectangular cluster. However, the critical fraction for forming an infinite cluster of collapsed channels (which is around 0.12 in Fig. 13) decreases with the size of the network and the threshold is zero in the limit of an infinite network.

Large aspect ratio. Now P_2 is larger than P_1 and the collapse inside a channel is the dominant mechanism. The injected fluid invades the network by a succession of collapses in the channels. Due to pressure effects, the smallest channel is filled first. This channel is a *bond* between two grains. Consequently, imbibition is related to a bond percolation process but, contrary to drainage, it takes place in the network of grains and not in the network of pores (*dual* network) [41].

Without flow through films, the need for continuity requires that the filled channel is adjacent to the interface: The process is *invasion bond percolation in the dual network*. With flow through films, the collapse can occur anywhere in the network, and the process is *bond percolation in the dual network*.

For micromodels with a broad pore size distribution, both mechanisms take place at the same time in different pores. The result is a ramified cluster, like that in percolation but with a much more compact shape due to the effect of local faceted growth. The different mechanisms are shown in Table I.

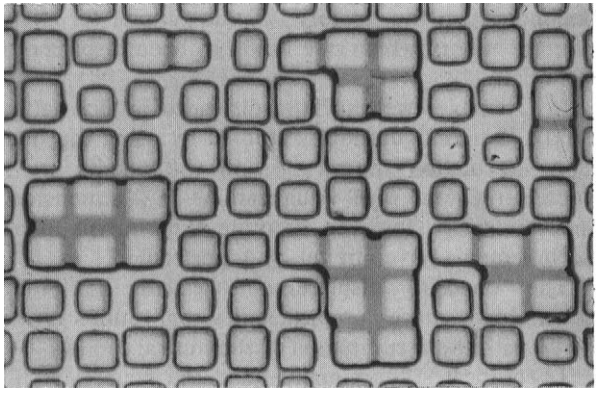

FIG. 12. Formation of compact oil clusters during imbibition with flow by film (Ref. [33]). Copyright 1985 by the American Physical Society.

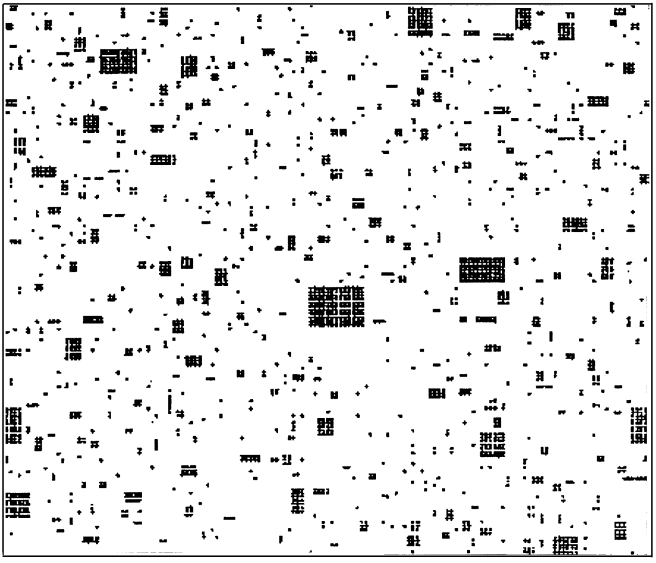

FIG. 13. Computer simulation of compact cluster growth. Reprinted from R. Lenormand and C. Zarcone, in *Kinetics of Aggregation and Gelation*, F. Family and D. P. Landau, eds., © 1984, with permission of Elsevier Science.

TABLE I. Various imbibition mechanisms.

	Small aspect ratio	Large aspect ratio
No flow by films	Compact growth (faceted)	Invasion percolation in dual network
Flow by films	Faceted clusters	Bond percolation in dual network

Cieplak and Robbins [42] studied the crossover between drainage and imbibition by varying the contact angle in a pore-scale simulation. In the nonwetting limit, the structures formed by the injected fluid are fractal as in invasion percolation. As the injected fluid becomes more wetting, the cooperative mechanisms lead to more compact structures. Below a given critical contact angle, the structure is compact.

2.2.4 Effects of Viscous Forces in Drainage

During a displacement in an aquifer or oil reservoir, there is always the interplay of viscous and capillary forces. I discuss only the case of drainage,

when a nonwetting fluid is displacing a wetting fluid. Two different effects can be observed, depending on the value of the viscosity ratio M, defined as viscosity of displaced fluid over viscosity of displacing fluid [43].

$M \ll 1$. An example is air displacing a viscous oil (viscosity ratio $M \approx 10^{-5}$). Figure 14 shows the experimental (not computer simulation) patterns for radial drainage at three different flow rates. The lower flow rate is a capillary displacement and corresponds to *invasion percolation*. The highest one, dominated by viscous forces, shows *viscous fingering*, which can be modeled by a statistical process called *diffusion-limited aggregation* (DLA) [44]. This statistical mechanism is linked to the shape of a growing interface in a Laplacian field, which is the case for the pressure field during displacement of a viscous fluid by an inviscid one in porous media. Figure 15b shows a similar displacement with a linear injection.

$M \gg 1$. An example is mercury displacing air. Here viscosity has a stabilizing effect. At low flow rates, the pattern corresponds to *invasion percolation* (Fig. 15a). At higher rates, the displacement is more stable (Fig. 15c). This process can be modeled by a statistical process called *anti*-DLA [43]. This model is the reverse of DLA. The inviscid fluid filling the

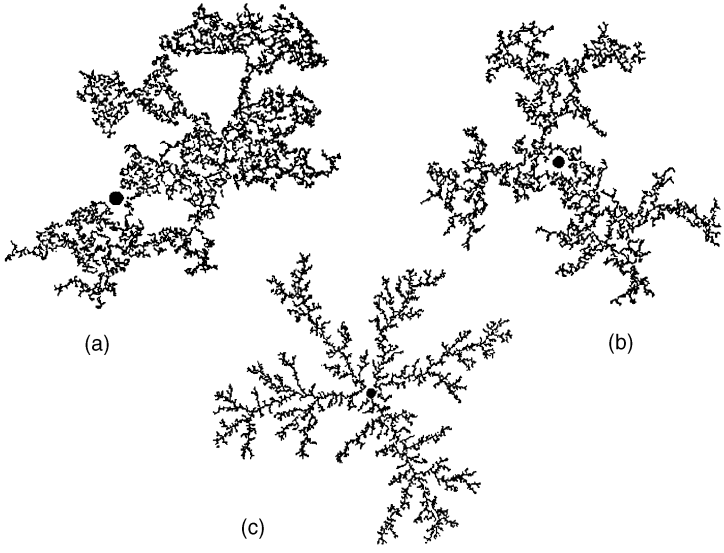

FIG. 14. Crossover between invasion percolation and DLA by changing the injection flow rate during experiments in a radial micromodel. Reprinted with permission from R. Lenormand, *Physica* **140A**, 114 (1986).

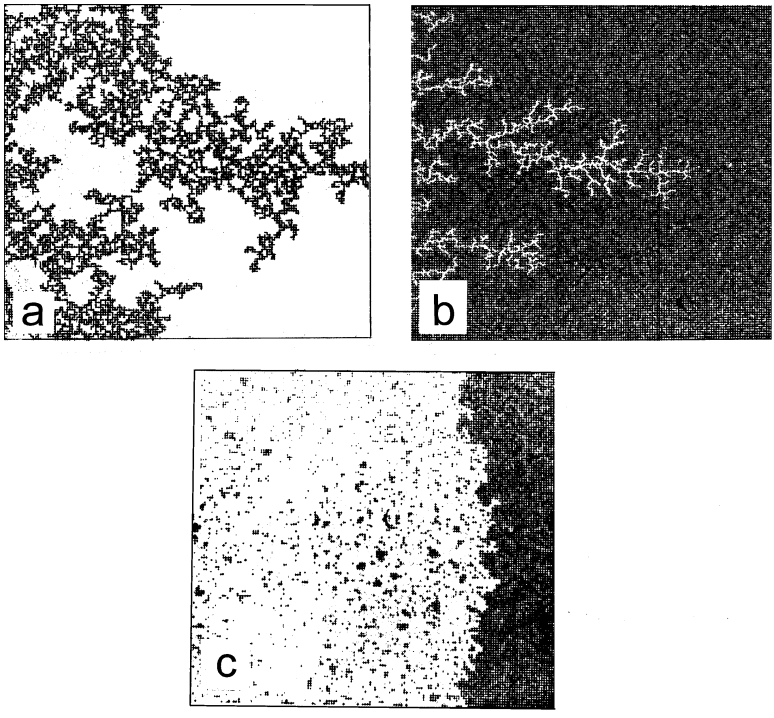

FIG. 15. Various kinds of drainage in a micromodel with linear injection (a) percolation (no viscous effect), (b) DLA (less viscous fluid injected), and (c) anti-DLA (more viscous fluid injected) (Ref. [43]). Copyright 1989 Cambridge University Press.

medium is represented by particles placed at each node of the network. The injected viscous fluid is represented by "antiparticles," which are released one by one at the inlet. Each antiparticle moves at random and, when it reaches a particle, both are removed. The similarity in the mechanisms comes from the diffusion of the antiparticles, which leads to a Laplacian probability field analogous to the pressure field in the viscous fluid.

2.2.5 Dynamics of Imbibition

The rise of a wetting fluid in a vertical capillary tube of radius R is derived by writing the balance between viscous, capillary, and gravitational forces on the liquid column at any time t. The rate of advance of the

meniscus is then given by the following Washburn equation [45, 46]:

$$\frac{dh}{dt} = \frac{1}{8\mu h}\left(\frac{2\gamma}{R} - \Delta\rho h\right) R^2.$$

Experiments in 2-D media such as paper sheets [47] or 3-D beads packs [48] show that the data are well described by the Washburn equation at early times. At late times, the kinetics are governed by the randomness of the capillary pressure. The rate of rise can be interpreted in terms of critical pinning, similar to a phase transition. The velocity of the meniscus is then proportional to $(P - Pt)^{\beta}$, where P is capillary pressure, Pt is the critical pressure, and β is a critical exponent larger than 1.

In a more classical approach, capillary rise in a porous medium can be interpreted using the standard concepts of capillary pressure curves and relative permeabilities [45].

2.3 Tracer Dispersion

A tracer is a soluble chemical product that does not change the fluid properties and is not adsorbed on the solid walls of the porous medium. The simplest example of tracer spreading is a dye in a straight capillary tube. A fluid (say water) is flowing at a constant rate and at time $t = 0$, a spike of tracer is injected at the inlet, uniformly over the cross section. Without any molecular diffusion, the tracer is transported by the flowing fluid (pure convection or advection). The velocity profile is parabolic with zero velocity at the walls. Consequently, the tracer near the walls will not be displaced (Fig. 16a). In the opposite limit, if molecular diffusion is dominant, the tracer concentration will be uniform across the tube (Taylor's regime, Fig. 16b). The relative importance of convective to diffusive transport is characterized

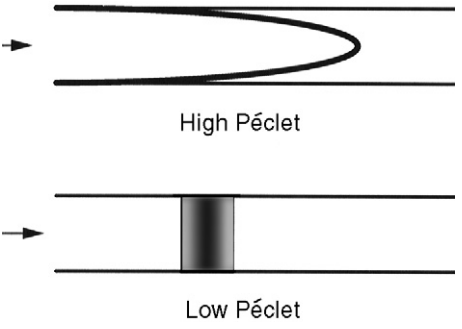

FIG. 16. Spreading of a tracer in a tube.

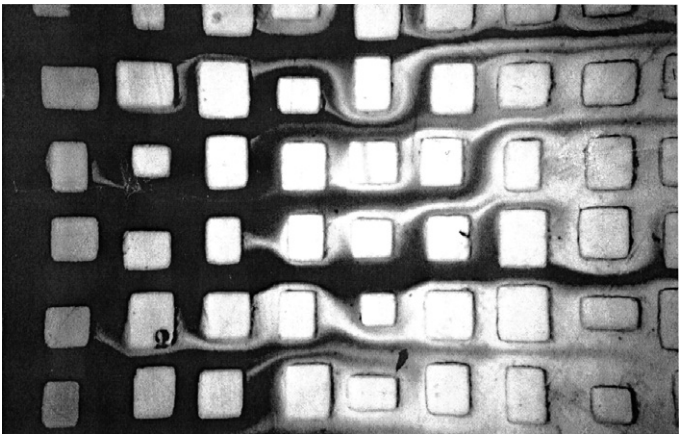

FIG. 17. Detail of tracer flow in a micromodel. Reprinted with permission from R. Lenormand, in *Fractals and Functional Calculus in Continuum Mechanics*, A. Carpinteri and F. Mainardi eds., Springer Wien, New York. Copyright 1997 Springer Wien.

by the Péclet number

$$Pe = VR/D_m,$$

where V is the fluid velocity, R, is a characteristic length, and D_m is the molecular diffusion coefficient.

In a more complicated geometry, such as a two-dimensional micromodels, the flow lines separate at each grain and the velocity field is much more complicated. Charlaix *et al.* [49] studied the effect of heterogeneities in micromodels formed by a partially connected network. They have shown that the tracer present in a channel follows different trajectories (in black in Fig. 17, after Lenormand [50]). However, molecular diffusion enables the transfer of tracer molecules across the flow lines.

At the scale of a large network, Maloy *et al.* [51] found that the dispersion front has a fractal structure (Fig. 18). Using transparent 2-D models and a radial injection, they calculated the fractal dimension of the interface. They found that the contour of the concentration equal to 0.5 has a fractal dimension of $D = 1.42$. The problem of interpreting this fractal dimension and the corresponding statistical process remains an open question [52].

2.4 Three-phase Flow

A description of three-phase flow — oil, water, and gas in porous media — is required in several domains of oil production (production by

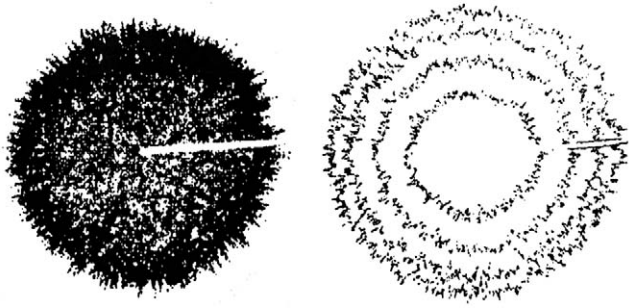

FIG. 18. Fractal contour of a tracer front in a radial geometry. Reprinted with permission from K. J. Maloy *et al.*, *Phys. Rev. Lett.* **61**, 2925. Copyright 1988 by the American Physical Society.

solution gas drive, gas injection) and for studies related to pollution of aquifers with organic liquids. Since real experiments are difficult to realize, network simulations are often used to derive such macroscopic properties as capillary pressure and the relative permeability curves. However, a network simulator is based on a set of physical rules that must be inferred from micromodel visualizations. The recent study by Pereira *et al.* [53] presents a review of the various physical mechanisms and the capabilities of network simulations.

In the case of two-phase flow, the pore-scale displacements are controlled by "wettability" (the difference between wetting and nonwetting fluids). For three-phase flow, the situation is more complicated: It concerns the relative magnitudes of surface tension between the fluids and with respect to the solid. If we assume that the solid is preferentially wetted by water, there are two different cases:

1. Oil spreads on water (positive spreading coefficient).
2. Oil does not spread and forms a lens on the surface of water (negative spreading coefficient).

The main purpose of micromodel observation was to establish the rules for building a three-phase network simulator. These rules are a combination of drainage and imbition events of the three different pairs of fluids, depending of the respective values of interfacial tension, and wettability.

Kantzas *et al.* [54] and Chatzis *et al.* [55] have used micromodels to explain the good efficiency of oil recovery by gas injection. For strongly water-wet reservoirs and positive spreading coefficients, oil forms a continuous film on the water, which reconnects the trapped oil droplets. Pore-level mechanisms for positive and negative spreading coefficients were also confirmed by Oren *et al.* [56]. They concluded that oil recovery was higher for positive spreading.

More recently, Dong *et al.* [57] observed that even nonspreading oil can form films over water films in micromodels. The mechanism is capillary imbibition of oil against gas and is linked to the curvature of the water film, which follows the pore geometry.

Soll *et al.* [22] used glass micromodels for capillary pressure measurements. Using image analysis, they were able to measure the fluid saturations and identify the type of displacement (double drainage etc.) at the pore level and then determined the statistics of the various events.

Keller *et al.* [58] also observed films of nonspreading oil in a silicon micromodel (made using the technique developed by Hornbrook *et al.* [14] with pore diameters in the range of 3–30 μm). They observed displacements as double drainage (gas displacing oil displacing water) and double imbibition (a terminology introduced by Oren *et al.* [56]). However, they concluded that the presence of a film of oil precludes any possibility of simultaneous drainage and imbibition, regardless of the value of spreading coefficient.

These observations have been used as inputs to numerical simulations. For instance, Fenwick and Blunt [59] calculated relative permeabilities similar to what is found experimentally. They also showed that relative permeabilities for gas injection were different from water flooding.

2.5 Critical Flows

In petroleum engineering, there are often situations where fluids are near critical conditions: when oil pressure decreases below the bubble point (gas nucleation), when gas forms liquid condensates, or when the surface tension becomes very low (transition from miscibility to immiscibility).

Modeling of gas production by pressure decline requires an accurate description of the physical mechanisms involved in the appearance of gas bubbles. The few existing models found in the petroleum literature are contradictory. The classical model is derived from "homogeneous nucleation" [60], whereas Firoozabadi and Kashiev [61] propose an approach based on instantaneous nucleation.

To understand the mechanisms of nucleation by pressure decline, El Yousfi *et al.* [62, 63] performed experiments in transparent glass and resin micromodels with a CO_2–water solution. The main results were the following:

- The bubbles appear progressively with time during approximately 1 h. After this time, no new bubbles are created.
- The final number of bubbles increases with supersaturation.

- Results are reproducible. The first bubble and several of the following ones always appear in the same pores when the same experiment is repeated. In addition, the sites are also the same for different pressure drop values.
- The inverse of time of appearance of the first bubble $1/\tau$ is roughly proportional to the dimensionless supersaturation $\Delta P/P$ and is similar for glass and resin micromodels.
- There is a threshold in supersaturation for bubble appearance. For $\Delta P < 0.4$ bar for resin and $\Delta P < 0.8$ bar for glass micromodels, there is no bubble creation, even after waiting more than 1 week. Just beyond the threshold, the time of appearance is of the order of 1 minute.

All these observations can be interpreted by a process that consists of the following succession of steps:

1. Stabilized microbubbles (order of magnitude of 1 μm) are always present before the pressure declines.
2. There is growth of the microbubbles by diffusion in a very large number of sites and trapping by capillary forces in the roughness of the solid walls of the pores (the microbubbles are much smaller than the pore).
3. Some of these sites are activated when pressure drawdown balances capillary trapping. This step explains the observed threshold in supersaturation.
4. Growth of these bubbles by gas diffusion reaches a size that enables observation (around 30 μm).

The preceding process is similar to one found in the literature that explains the boiling process on rough surfaces.

Micromodels have also been used to study the growth of bubbles inside the pores. When the bubble is small compared to the pore, the growth is described by molecular diffusion with some correction factors to account for the presence of the porous medium [64]. Satik *et al.* [65] observed ramified patterns and a transition from percolation to DLA patterns as the cluster size increased and occupied several pores. Using these observations, they developed a general theory for the scaling of bubble growth using numerical simulations.

For studies of near-critical conditions, Williams and Dawe [66, 67] and Gray and Dawe [68] developed an original system of two partially miscible liquids (2–6 lutinine and water) observed in micromodels. With this system, it is possible to cross the phase boundary just by varying the temperature. They showed that the appearance of a phase was strongly dependent on wettability. For the wetting phase, the small droplets spread on the pore walls, while nonwetting droplets grow by coalescence inside the wetting liquid. They also showed that at low interfacial tension, the nonwetting phase flows in ganglia and is not in hydraulic continuity below a given

saturation (near 10%). Under the same conditions, the wetting phase coats the matrix and can flow by films.

2.6 Flow in Fractured Media

Haghighi *et al.* [69] used a glass micromodel representing a porous matrix with a high permeability channel representing a fracture. Two-phase flows were performed and the displacement of oil in the matrix was studied. They observed a critical rate in the fracture for displacement in the matrix. The main conclusion of the work is that observations can be modeled using macroscopic equations ("mean field approach"). The physics is similar to blob displacements; that is, a balance between viscous pressure drop in the fracture and capillary forces in the matrix. Good agreement with macroscopic laws was found.

2.7 Foam Flow in Porous Media

A foamed gel material is often used to plug high-permeability streaks. Micromodels have contributed to the understanding of the physical mechanisms. Miller and Fogler [70] have shown that there is a percolation threshold in pressure corresponding to the rupture of the gel into a larger number of pores along a connected path through the micromodel.

Manlowe and Radke [71] studied the destabilizing effect of crude oil on foams. Previous studies suggested several destabilizing mechanisms, including the depletion of surfactant by formation of oil–water emulsion and oil spreading at the gas–water interface. Observations in glass micromodels have shown no difference for spreading and nonspreading oil. In fact, foam stability is directly related to the stability of a film of water between oil and gas (and is called a "pseudoemulsion film").

Hornbrook *et al.* [14] used an etched silicon micromodel with a pore size of the same order as real sandstone (3–30 μm) and a low surfactant concentration. Gas bubbles are separated by thick water lenses. The gas occupied several pores and moved by invasion of the water filled throats followed by reinvasion by water. Contrary to other observations in larger micromodels, thin lamellae were rarely seen.

2.8 Conclusion

The main information gained from micromodel observations is that we cannot forget that the porous medium has a granular structure and a network structure. Even if the transport properties of porous media are

described by "continuum" laws such as Darcy's law, there is a strong geometrical disorder at the pore scale. This "quenched disorder" leads to very specific behavior. Using a macroscopic approach for capillary or viscous fingering is misleading. For instance, percolation and DLA patterns cannot be described by macroscopic equations.

References

1. T. Korenaga, F. Shen, and T. Takahashi, *AIChE J*. **35**, 1395 (1989).
2. J. G. Roof, *Soc. Petr. Eng. J*., **85**, 10 (1970).
3. B. Legait, P. Sourieau, and M. Combarnous, *J. Coll. Int. Sci.* **91**, 400 (1983).
4. F. Kalaydjian and B. Legait, *C. R. Acad. Sci. Paris*, **304**, II, 869 (1987).
5. Y. Li and N. C. Wardlaw, *J. Coll. Int. Sci.* **109**, 461 (1986).
6. T. Engoy, J. Feder, and T. Jossang, *Phys. Scripta* **T38**, 99 (1991).
7. C. C. Mattax and J. R. Kyte, *Oil Gas J*. October, 115 (1961).
8. J. A. Davis and S. C. Jones, *J. Petr. Tech.* Dec., 1415 (1968).
9. M. McKellar and N. C. Wardlaw, *J. Can. Petr. Tech.* **21**, 81 (1987).
10. J. C. Trygstad, R. Ehrlich, and N. C. Wardlaw, SPE/DOE paper no. 14891, presented at the 5th Symposium on Enhanced Oil Recovery, Tulsa, Okla. (1986).
11. D. G. Avraam, G. B. Kolonis, T. C. Roumeliotis, G. N. Constantinides, and A. C. Payatakes, *Trans. Porous Media* **16**, 75 (1994).
12. K. K. Mohanty, A. Gupta, and R. A. Deruiter, *J. Coll. Int. Sci.* **163**, 199 (1994).
13. J. Wan, T. K. Tokunaga, C-F. Tsang, and G. S. Bodvarsson, *Wat. Res. Res.* **32**, 1955 (1996).
14. J. W. Hornbrook, L. M. Castanier, and P. A. Pettit, SPE 22631, Proceedings of the 66th Annual Technical Conference and Exhibition of the Society of Petroleum Engineers, Dallas, Tex. (1991).
15. J. Bonnet and R. Lenormand, *Rev. Inst. Fr. Pétrole* **42**, 477 (1977) (in French).
16. R. A. Dawe and R. J. Wright, *Roy. School Mines J*. **33**, 25 (1983).
17. U. Oxaal, *Phys. Rev. A* **44**, 5038 (1991).
18. A. Chatenever, *Petr. Trans. AIME* **195**, 149 (1952).
19. J. C. Moulu, *Rev. Inst. Fr. Pétrole* **39**, 67 (1984).
20. J. Feder, K. J. Maloy, and T. Jossang, in *Hydrodynamics of Dispersed Media*, J. P. Hulin, A. M. Cazabat, E. Guyon, and F. Carmona (eds.), North-Holland, Amsterdam (1990).
21. U. Oxaal, M. Murat, F. Boger, A. Aharony, J. Feder, and T. Jossang, *Nature* **329**, 32 (1987).
22. W. E. Soll, M. A. Celia, and J. L. Wilson, *Wat. Res. Res.* **29**, 2963 (1993).
23. R. Lenormand and C. Zarcone, SPE 13264, Houston meeting, 1984.
24. M. O. Robbins, D. Andelman, and J.-F. Joanny, *Phys. Rev. A* **43**, 4344 (1991).

25. R. Lenormand, in *European Oil and Gas Conference*, G. Imarisio, M. Frias, and J. M. Bemtgen, eds., Graham and Trotman, London (1991).
26. P.-G. de Gennes, in *Physics of Disordered Media*, D. Adler, H. Fritzsche, and S. R. Ovshinsky, eds., Plenum, New York (1985).
27. R. Lenormand, C. Zarcone, and A. Sarr, *J. Fluid Mech.* **135**, 337 (1983).
28. E. G. Mahers and R. A. Dawe, Proceedings of the 3rd European Meeting on Improved Oil Recovery, Rome, April, 1985.
29. J. D. Chen, *J. Coll. Int. Sci.* **110**, 488 (1986).
30. R. Lenormand and S. Bories, *C. R. Acad. Sci. Paris*, **B291**, 279 (1980).
31. R. Chandler, J. Koplik, K. Lerman, and J. F. Willemsen, *J. Fluid Mech.* **119**, 249 (1982).
32. R. Lenormand, *Physica* **140A**, 114 (1986).
33. R. Lenormand and C. Zarcone, *Phys. Rev. Lett.* **54**, 2226 (1985).
34. D. Wilkinson and G. Willemsen, *J. Phys. A.* **16**, 3365 (1983).
35. R. Lenormand and C. Zarcone, SPE 13264, Houston meeting, (1984).
36. N. C. Wardlaw, *Transp. Porous Media* **3**, 17 (1988).
37. N. C. Wardlaw and M. McKellar, *Powder Tech.* **29**, 127 (1981).
38. J. A. Billiotte, H. de Moegen, and P. E. Oren, SPE 20765, New Orleans meeting, 1990.
39. R. Lenormand, *J. Phys. Condens. Matter* **2**, SA79 (1990).
40. R. Lenormand and C. Zarcone, in *Kinetics of Aggregation and Gelation*, F. Family and D. P. Landau, eds., Elsevier, Amsterdam (1984).
41. R. Lenormand, *C. R. Acad. Sci. Paris* **297**, 437 (1983).
42. M. Cieplak and M. O. Robbins, *Phys. Rev. Lett.* **43,** 4344 (1988).
43. R. Lenormand, E. Touboul, and C. Zarcone, *J. Fluid Mech.* **189**, 159 (1989).
44. T. A. Witten and L. M. Sander, *Phys. Rev. Lett.* **47**, 1400 (1981).
45. F. A. L. Dullien, *Porous Media, Fluid Transport and Porous Structures*, Academic Press, London (1991).
46. E. W. Washburn, *Phys. Rev.* **17**, 273 (1921).
47. F. Family, K. C. B. Chan, and J. G. Amar, in *Surface Disordering: Growth, Roughening and Phase Transition*, R. Hullien et al., eds., Nova Science, Commack, NY (1992).
48. T. Delker, D. B. Pengra, and P.-z. Wong, *Phys. Rev. Lett.* **76**, 2902 (1996).
49. E. Charlaix, J. P. Hulin, C. Leroy, and C. Zarcone, *J. Phys. D Appl. Phys.* **21**, 1727 (1988).
50. R. Lenormand, in *Fractals and Fractional Calculus in Continuum Mechanics*, A. Carpinteri and F. Mainardi, eds., Springer Wien, New York (1997).
51. K. J. Maloy, J. Feder, F. Boger, and T. Jossang, *Phys. Rev. Lett.* **61**, 2925 (1988).
52. J. Feder, *Fractals*, Plenum, New York (1988).
53. G. G. Pereira, W. V. Pinczewski, D. Y. C. Chan, L. Paterson, and P. E. Oren, *Transp. Porous Media* **24**, 167 (1996).

54. A. Kantzas, I. Chatzis, and F. A. L. Dullien, SPE 17506, proceedings of the SPE Rocky Mountain Regional Meeting, Casper, Wyo. (1988).
55. I. Chatzis, A. Kantzas, and F. A. L. Dullien, SPE 18284, Proceedings of the 63rd Annual Technical Conference and Exhibition of the Society of Petroleum Engineers, Houston, Tex., 1988.
56. P. E. Oren, J. Billiotte, and W. V. Pinczewski, *SPE Form. Eval.* 70 (March 1992).
57. M. Dong, F. A. L. Dullien and I. Chatzis, *J. Coll. Int. Sci.* **172**, 21 (1995).
58. A. A. Keller, M. J. Blunt, and P. V. Roberts, *Transp. Porous Media* **27**, 266 (1998).
59. D. H. Fenwick and M. J. Blunt, *SPE J.*, 86 (1998).
60. X. Li and Y. C. Yortsos, Paper SPE 26662, Houston, Tex., 1993.
61. A. Firoozabadi and Kashiev, *SPE J.* 219–227 (September 1996).
62. A. El Yousfi, C. Zarcone, S. Bories, and R. Lenormand, *C. R. Acad. Sci. Paris* **313**, II, 1093 (1991).
63. A. El Yousfi, C. Zarcone, S. Bories, and R. Lenormand, SPE 38921, San Antonio meeting, 1997.
64. X. Li and Y. C. Yortsos, *AIChE J.* **41**, 214 (1995).
65. C. Satik, X. Li, and Y. C. Yortsos, *Phys. Rev. E* **51**, 3286 (1995).
66. J. K. Williams and R. A. Dawe, *J. Coll. Int. Sci.* **117**, 81 (1987).
67. J. K. Williams and R. A. Dawe, *J. Petr. Sci. Eng.* **2**, 225 (1989).
68. J. D. Gray and R. A. Dawe, SPE 19696, San Antonio meeting, 1989.
69. M. Haghighi, B. Xy, and Y. C. Yortsos, *J. Coll. Int. Sci.* **166**, 168 (1994).
70. M. J. Miller and H. S. Fogler, SPE 24662, Washington meeting, 1992.
71. D. J. Manlowe and C. J. Radke, *SPE Reserv. Eng.*, November, 495 (1990).

3. PROBING PORE STRUCTURES BY SORPTION ISOTHERMS AND MERCURY POROSIMETRY

Yanis C. Yortsos

Department of Chemical Engineering and Petroleum Engineering Program
University of Southern California
Los Angeles, California

3.1 Introduction

The objective of this chapter is to provide a review of the use of (physi)sorption isotherms and mercury porosimetry to identify geometric and pore-structural parameters of porous media. Physisorption refers to the reversible adsorption or desorption of a gas in a porous medium at constant temperature, as a result of an incremental increase or decrease of its pressure, respectively. Its origin is the binding of the gas molecules at the solid surface, typically by van der Waals forces. Mercury porosimetry refers to the process of the slow intrusion or extrusion of liquid mercury in the porespace of a porous medium in response to an incremental increase or decrease in the applied pressure, respectively. This process is also controlled by interfacial (capillary) forces at the advancing or receding interface. Adsorption and mercury extrusion conceptually correspond to the displacement of a nonwetting phase (vapor or mercury, in the respective processes) by a wetting phase (liquid or air, respectively). This is also known as an imbibition process. Conversely, the processes of desorption and mercury intrusion conceptually correspond to the displacement of a wetting by a nonwetting phase, also known as drainage. The information on the pore structure is obtained from the inversion of experimental isotherms and measuring the mass or volume adsorbed or penetrated in sorption or mercury porosimetry, respectively, as a function of the applied pressure. The two methods have been widely used in the past and they constitute standard surface science tools for porous media characterization [1–5].

In the absence of other information on the history of the pore-structure evolution (whether chemical, biological, or geological), the task of providing a complete representation of the pore structure is very complex. Typically, two main variables are probed: the (accessible) pore surface and the "pore-size" distribution. Information on the pore surface can be provided by

EXPERIMENTAL METHODS IN THE PHYSICAL SCIENCES
Vol. 35
ISBN 0-12-475982-3

ISSN 1079-4042/99 $30.00

the adsorption of single-component gases at low pressures or by mercury porosimetry at high pressures. Under these conditions, the surface may be unfolded into an object that can be studied independently of the complicated three-dimensional pore structure. Here, the key task is to relate the experimental measurements to quantities such as the surface area per unit mass, its roughness, or its fractal characteristics, if appropriate. In this context, the surface is often modeled as a statistically self-affine object.

For the characterization of porous media containing mesopores or macropores (see later in this chapter), sorption processes at relative pressures in the capillary condensation regime or mercury porosimetry at relatively low pressures, respectively, are used. The accurate interpretation of these measurements, however, requires the representation of the porespace in terms of a pore network. The latter is described by the size distribution of pore bodies and pore throats, their connectivity, and their spatial correlations. The use of network theories, such as percolation theory [6] and its variants, can be quite beneficial in this context.

The information extracted from sorption or mercury porosimetry experiments is based on the analysis of a few isotherms. A forward and an inverse problem must be formulated. The forward problem involves the modeling of the process assuming a certain representation of the porous medium. The inverse problem involves identifying the assumed properties of the porous medium by inverting the experimental measurements. Because the latter reflect the integrated response of the system, which is also influenced by heterogeneities in geometry, size, connectivity, and accessibility, the inversion of the experimental isotherms is not unique. The corresponding limitations are important and are addressed in this chapter. Even though the information on the pore structure is not as detailed as one may desire, sorption and mercury porosimetry methods can be quite useful for porous media characterization, provided that their strengths and limitations are properly recognized.

This chapter is organized as follows: First, background material is provided on porous media description with a focus on the pore surface and the pore network, and on the basic aspects of sorption isotherms and mercury porosimetry. The next section deals with the characterization of the pore surface and its chemical and geometric heterogeneity. We discuss adsorption over a surface (or, equivalently, adsorption in a porous medium at low relative pressures) and capillary invasion at high capillary pressures to identify pore surface characteristics. Multilayer adsorption and condensation are also reviewed. The next section involves sorption processes and capillary invasion in single pores and pore networks. We review fundamentals of capillary condensation in confined geometries and capillary equilibria and discuss their applicability for infering pore-size distributions. The use of

percolation approaches to interpret the effect of the pore network on sorption isotherms and mercury porosimetry data is particularly emphasized. Various issues related to pore and throat size distributions and their spatial correlations are also discussed.

3.2 Background

Understanding the macroscopic behavior of sorption isotherms and capillary phenomena in porous media requires conceptual models of the pore surface and the pore structure. In general, porous media and pore surfaces are geometrically and chemically heterogeneous, as a result of their formation and evolution history [7, 8]. For example, porous materials prepared by methods such as coagulation, controlled growth, precipitation, or aging have different geometric and chemical properties, in general. The same is true for geologic porous media, the particular history of the formation of which (sedimentation, compaction, diagenesis, etc.) leads to specific pore-structural characteristics. Given the large diversity in these media, an inclusive description, although desirable, is rather impractical. Here, we comment instead on the representation of two key aspects of porous media — the pore surface and the pore network — the identification of some of the properties of which are the objectives of sorption isotherm and mercury porosimetry methods. Following this description, basic experimental procedures in adsorption–desorption processes and in mercury porosimetry are reviewed.

3.2.1 Representation of Porous Media

Pore surfaces are, in general, rough with features in the form of cavities, peaks, and pits at various scales. For the purposes of this section, we assume that the surface can be unfolded into a topologically two-dimensional object, so that its height z can be expressed as a function of local Cartesian coordinates x and y (Fig. 1), namely,

$$z = h(x, y). \tag{1}$$

The function h certainly depends on the history of the formation of the surface. An increasing amount of evidence has accumulated (e.g., see reviews by Barabasi and Stanley [9] and Halpin-Healy and Zhang [10]), suggesting that surfaces evolving from various different processes (from molecular beam epitaxy to displacements in random media) are actually self-affine fractals (Fig. 1). Self-affinity is a generalization of self-similarity (which is more commonly associated with a fractal description, see Mandelbrot [11]),

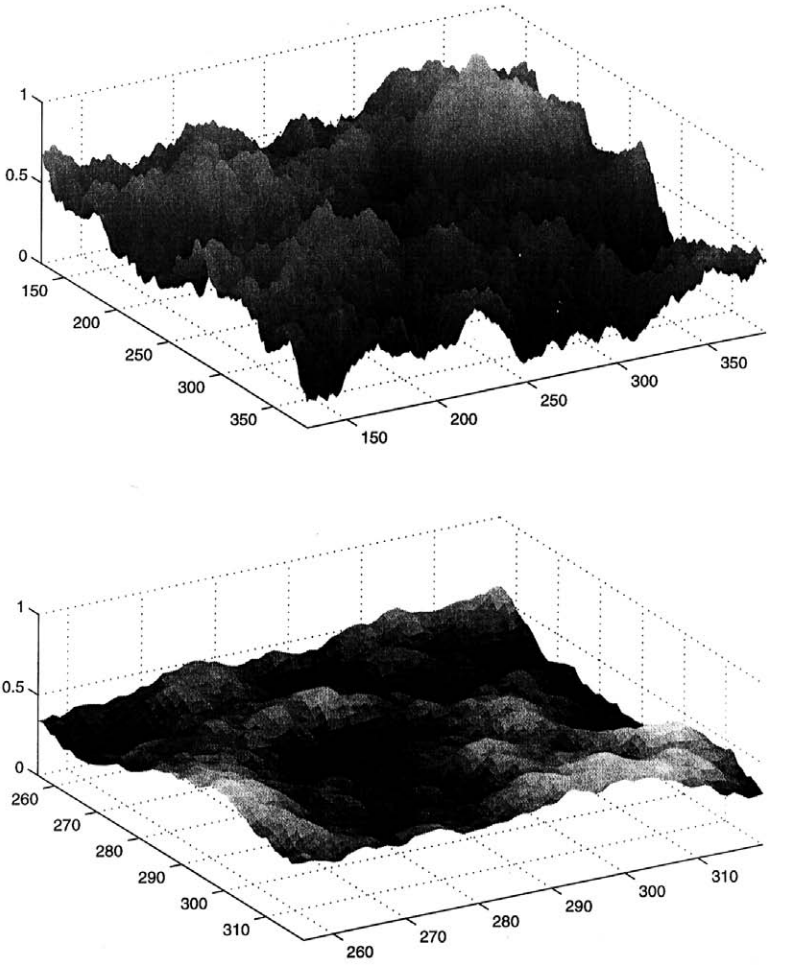

FIG. 1. Schematic description of a pore surface as a self-affine surface of the fBm (fractional Brownian motion type) with $H = 0.7$. Two different regimes corresponding to two different scales are shown.

in that self-affine objects preserve statistical similarity only if their scaling response is different in different directions. For example, a self-affine surface of the type of Eq. (1) satisfies the anisotropic scaling

$$z \sim \frac{1}{b^H} h(bx, by), \tag{2}$$

where $b > 0$ is the scale expansion (or reduction). The affine exponent, $H\,(0 < H < 1)$, is known as the Hurst or Hölder exponent [12] and reflects the relative roughness, surfaces with higher values of H being smoother with long-range trends. In the preceding, we implicitly assumed isotropy in the x and y directions. Barabasi and Stanley [9] have reviewed the various mechanisms, including ballistic deposition, solid-on-solid models, propagation of interfaces, that lead to the formation of self-affine surfaces.

An important characteristic of self-affine objects is that their scaling behavior is different, depending on the range investigated [12–14] (Fig. 1). In general, two limiting regimes exist: a local one at small length scales, $\delta \ll \delta_{cr}$, where the surface can be viewed as a self-similar fractal with fractal dimension $D = 1 + d - H$, where d is the topological dimension (hence, $D = 3 - H$ for a surface); and a global one at large length scales, $\delta \gg \delta_{cr}$, where the surface is not fractal (of dimension d, hence equal to 2 for a surface). The crossover length δ_{cr} demarcates the two regimes. Recall that in real systems, fractal behavior is typically displayed in a finite region, between upper and lower cutoff scales d_{up} and d_{lo}, respectively. In this region, the measured surface area is not a constant, but varies depending on the ruler used for its measurement, according to the power law:

$$S(\delta) \sim \delta^{2-D}, \quad d_{lo} < \delta < d_{up}. \tag{3}$$

This is the behavior expected in the local regime of a self-affine surface. Adamson [2] was among the first to recognize the relevance of a multiscale, fractal description in the context of surface chemistry. Pioneering work in the application of fractal concepts to porous media was also conducted by Feder [12], Avnir [15], and de Gennes [16].

Neimark [14] investigated the characterization of self-affine surfaces in the global regime and considered the scaling of the excess area S_{ex} (namely, that in excess over a reference planar surface), of smoothed surfaces, obtained from the actual rough surface after small-scale fluctuations below a smoothing scale Δx_s are eliminated. In particular, he considered the scaling of S_{ex} with the mean radius of curvature of the smooth surface δ_c and demonstrated the scaling behavior

$$S_{ex} \sim \left(\frac{\delta_c}{\delta_{cr}}\right)^{-(1-H)} \quad \text{for } \delta \ll \delta_{cr} \quad \text{and} \quad S_{ex} \sim \left(\frac{\delta}{\delta_{cr}}\right)^{-[2(1-H)]/(2-H)} \quad \text{for } \delta \gg \delta_{cr} \tag{4}$$

in the two limiting regimes of self-affinity, respectively. Note that the first scaling is the same with that for a self-similar surface [Eq. (3)] in the local regime (where $D = 3 - H$). However, the scaling of S_{ex} in the global regime is different. Neimark [14] noted that the latter exponent is more properly

related to an "excess dimension," $2 + [2(1 - H)]/(2 - H)$, rather than to a fractal dimension. Related are the observations of Pfeifer and Cole [17] who argued that in the regime of self-similarity, any fractal dimension obtained experimentally must be the local fractal dimension $3 - H$ and that a different exponent should apply in the global regime (but see also Kardar and Indekeu [18]).

The fact that self-affine objects involve power-law scalings in various regimes makes self-affinity a good working model for surface roughness. Its implications to sorption at low pressures and mercury porosimetry at high pressures are discussed in the next section.

In addition to the pore surface, sorption and mercury intrusion are significantly affected by the three-dimensional aspects of porous media, specifically the characteristics of pores and throats: their size distributions, connectivity, and spatial correlation (see the schematic in Fig. 2). For a detailed geometrical description, consult references such as Dullien [4] and Adler [19]. In the context of sorption, IUPAC has recommended the following classification of pores based on their size:

- Micropores with sizes in the range $\leqslant 2$ nm
- Mesopores with sizes in the range 2–50 nm
- Macropores with sizes in the range $\geqslant 50$ nm

However, Balbuena and Gubbins [20] have argued in favor of a different classification, which would also depend on the particular intermolecular interaction between the adsorbed gas and the adsorbent solid, rather than size alone.

For the purposes of this chapter, we model the local pore geometry in terms of a converging–diverging cross section, which is the simplest model for describing fundamental aspects of equilibrium and transport in porous media [4, 21, 22] (Fig. 2). We define pores (also termed sites or cavities or chambers) as the geometrical elements in which an inscribed sphere has the locally largest radius; and throats (also termed bonds or windows or necks) as the elements joining adjacent sites, and which are characterized by the locally smallest radius of an inscribed sphere (Fig. 2). Pores contain most of the information on volume (or capacity) and they are most important in adsorption and extrusion (imbibition). Throats contain mostly information on transport properties and they are important in desorption and mercury intrusion (drainage). The statistical distributions of pore and throat sizes are described by the two cumulative probability density functions

$$q = \int_r^\infty \alpha_s(r)\, dr \quad \text{and} \quad p = \int_r^\infty \alpha_b(r)\, dr, \tag{5}$$

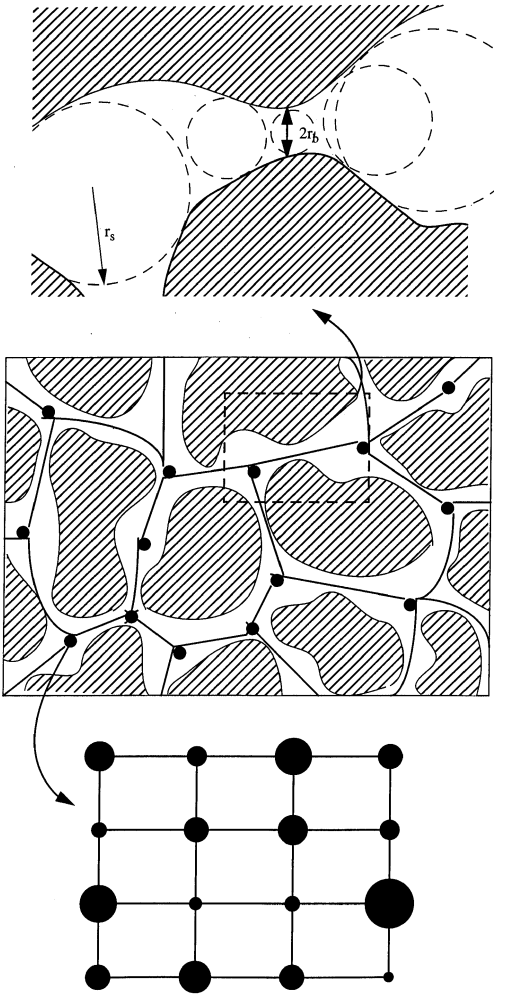

FIG. 2. Schematic of a porous medium. Highlighted are the converging–diverging geometry nature of the cross sections and the pore–network representation of the porespace.

respectively, where $\alpha_i(r)$ ($i = s, b$ for site or bond) is the respective probability density function. (We also ocasionally denote by r_s or r_b the corresponding sizes.) In many applications, it is these two probability functions that are needed for a basic formulation of forward and inverse problems. A variety of other models have also been used in the literature [23–26]. Geometric,

volume, transport, and capillary properties associated with these elements can be distributed randomly or by spatial correlation.

In some applications, however, additional simplifications are introduced. In the context of adsorption, for example, Seaton and coworkers [27–32] take the porous medium to consist of pores of a slitlike (parallel plates) geometry, which contain all the volume of the porous material, and which join at junctions to form a pore network. In this approach, it is only the throat size distribution $\alpha_b(r)$ that characterizes the pore geometry. A slitlike geometry has been proposed to model the pore structure of activated carbon. On the other hand, Mason [33–36], Zhdanov *et al.* [37], and Parlar and Yortsos [38, 39] consider both pores and throats, with all the volume contained in the sites and throats controlling the onset of desorption. Two size distributions are necessary in the latter models.

The graph that connects adjacent pores in the porous medium comprises the pore network (Fig. 2). It is characterized by its coordination number Z (which is the average number of neighboring pores adjacent to a given pore), its dimension (two or three dimensions), and its linear size L (which expresses the number of pores along a coordinate direction). The need for a pore network representation to capture percolationlike processes, which are associated with the onset of connectivity of a phase (and may be controlling desorption and mercury intrusion), was recognized since the late 1950s by Fatt [40]. However, a systematic application of pore network models, and specifically of percolation theory, to porous media processes started only several years later [4, 41, 42]. Wall and Brown [43] were among the first to recognize the importance of percolation theory in interpreting adsorption–desorption curves. Regular lattices (2-D square, 3-D cubic, etc.), but also the less realistic but analytically tractable Bethe lattices (which lack reconnections), have been used in computational and analytical studies.

Having defined some key aspects of porous media, we next proceed with a description of the basic characteristics of sorption isotherms and of mercury porosimetry.

3.2.2 Sorption Isotherms and Their Classification

Sorption isotherms correspond to single-component gas (physi)sorption in a porous medium. Physisorption is a result of long-range attractive interactions and short-range repulsion between the molecules of the gas and the solid that makes up the porous medium. For nonmetallic surfaces, a Lennard–Jones 6–12 intermolecular potential, which translates into a 3–9 potential for the interaction between an atom and a flat surface, provides an often used model of this combined interaction. When chemisorption or chemical reactions are important, however, a different approach is necessary, as described in detail in Masel [44].

The experimental procedure involves exposing the porous medium to a single-component gas at constant temperature T and incrementally increasing–decreasing its pressure until an equilibrium state is reached. The quantity measured is the amount adsorbed (usually per unit volume of the adsorbent) as a function of pressure P, or more appropriately of the relative pressure $P/P^0(T)$, where $P^0(T)$ is the bulk vapor pressure. With increasing pressure, adsorption coverage of the surface proceeds in the form of a submonolayer, first, followed by the formation of a monolayer and then multilayer condensation. Over a flat surface, progressively thicker liquid films would form as the bulk vapor pressure is approached. In a porous medium, however, adsorption will give rise to the filling of micropores, followed by capillary condensation in larger pores. When the pressure is decreased, desorption occurs. Because of the lack of reversibility in the capillary condensation regime, at both the single-pore and the pore network levels, however, adsorption–desorption isotherms show a characteristic hysteresis, the origin of which has been the subject of numerous studies. A compilation of the adsorption behavior of various gases in various media can be found in the review of Valenzuela and Meyers [45].

It is conventional to classify sorption isotherms in porous media according to their qualitative behavior, following the recommendations of the IUPAC Commission on Colloid and Surface Chemistry [46], as shown in Fig. 3. According to this classification, type I corresponds to monolayer coverage (and filling of micropores). Types II and III are characteristic of multilayer adsorption in nonporous materials (with type II corresponding to strong and type III to weak gas–solid attractive forces, respectively). Isotherms I–III are reversible. Isotherms of types IV and V occur when multiple layers of gas adsorb in a porous solid containing mesopores, and correspond to strong and weak fluid–solid interactions, respectively. These types involve a reversible part at low pressures, where filling of micropores occurs, and an irreversible part at higher pressures, due to capillary condensation, which exhibits hysteresis. They are typical of many industrial applications. Finally, type VI occurs in nonporous materials with strong fluid–wall interactions at a temperature close to the melting point of the adsorbed gas. Based on calculations in slit pores using nonlocal DFT (density functional theory), Balbuena and Gubbins [20] proposed yet another type corresponding to capillary evaporation.

To interpret the sorption isotherms, the adsorption–desorption behavior over a surface in single pores and in a network of pores is analyzed in the sections to follow. Under thermodynamic equilibrium conditions, all these isotherms manifest the underlying equality of the chemical potential between adsorbed and bulk phases.

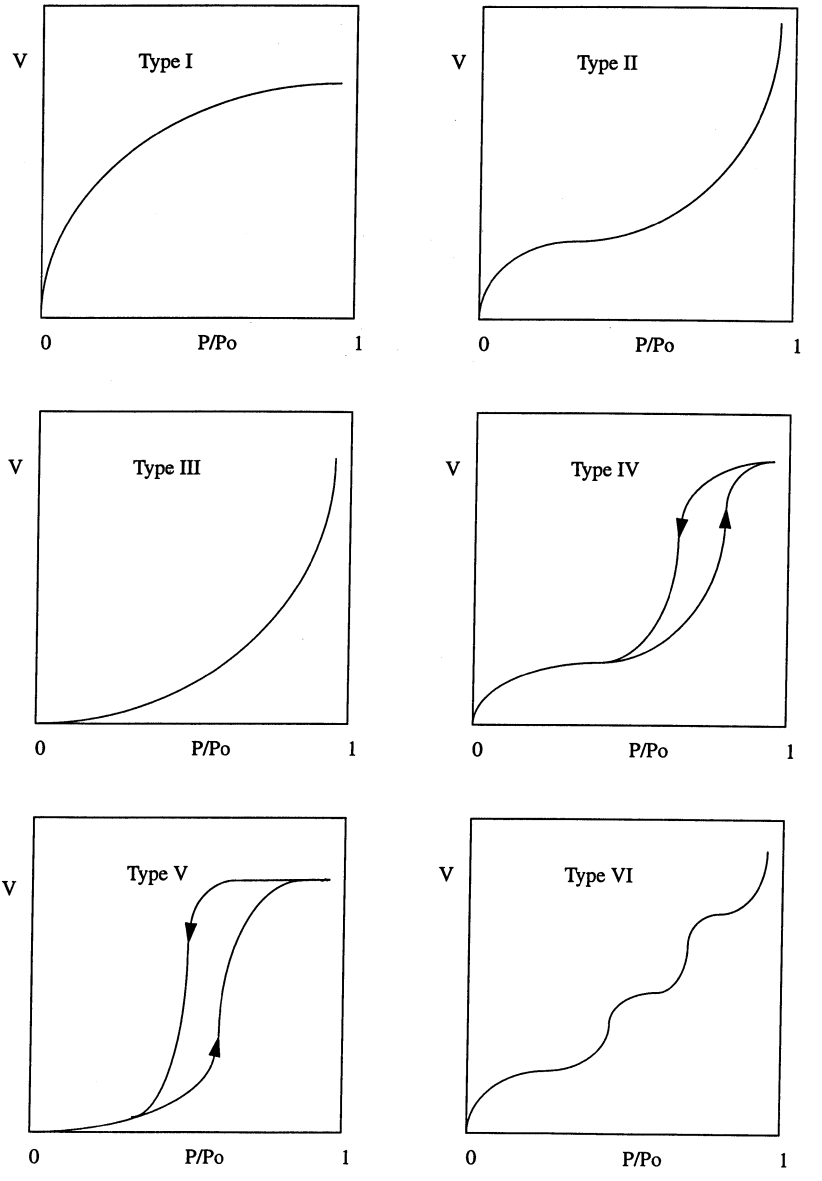

FIG. 3. Schematics of adsorption isotherms according to the IUPAC classification [46].

3.2.3 Mercury Porosimetry Curves

Mercury porosimetry is an experimental tool for the characterization of the pore structure of porous media containing macropores. It is routinely used in the characterization of catalysts, soils, geologic porous media, etc. The conventional experimental procedure consists of conducting cycles of intrusion or extrusion of liquid mercury in an initially dry porous sample, at constant temperature, by incrementally increasing or decreasing its pressure. In these applications, mercury is the nonwetting phase. After equilibrium is reached, the volume of mercury occupying the porespace at equilibrium is plotted as a function of the pressure. Conventionally, the results are presented in a capillary pressure–saturation diagram, where the capillary pressure $P_c = P_{nw} - P_w$ is the difference between the pressures of nonwetting and wetting phases (namely, of mercury and air, respectively), and the nonwetting saturation S_{nw}, is the volume fraction of the porespace occupied by the nonwetting phase (namely, mercury, in the present application). Repeated intrusion–extrusion cycles give rise to scanning curves, as shown in Fig. 4. In analogy with sorption isotherms, the hysteresis exhibited in mercury porosimetry has its origin both at the single-pore and at the pore network levels, as discussed later in the chapter.

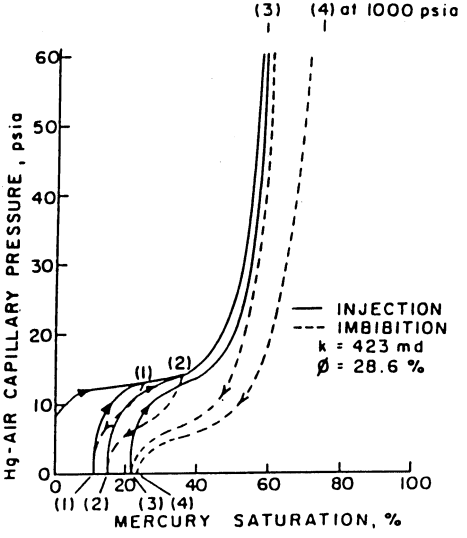

FIG. 4. Characteristic mercury intrusion–extrusion curves (denoted as injection–imbibition, respectively), for Dalton sandstone with the permeability and porosity indicated. Reprinted with permission from J. J. Pickell *et al.*, *Soc. Pet. Eng. J.*, 55. Copyright 1966 SPE.

During the primary cycle of mercury intrusion, significant penetration of the porous sample occurs only after a certain threshold in the capillary pressure is reached (Fig. 4). This threshold reflects the facts that mercury, being a nonwetting phase, preferably invades larger pore throats and that for a significant penetration, a connected pathway of these large pore throats must exist. As pressure increases, mercury invades progressively smaller pore throats, and at sufficiently large pressures, the penetration of small cavities and other features of roughness at the pore surface will take place. In this regime, the characteristics of the pore surface can be uncovered. Note that because of its compressibility, the volume of air can be constantly reduced, even when the latter becomes topologically disconnected by the advancing mercury. However, this is not the case during extrusion, where liquid mercury–air menisci can become trapped as isolated blobs (ganglia) of mercury. As a result, a significant residual, trapped saturation of mercury (of the order of 15–20% in Fig. 4), will exist at the termination of the extrusion process.

The preceding description pertains to constant pressure porosimetry. An alternative method, known as APEX, was developed based on controlled-volume porosimetry [48]. Here, it is the volume rate of intrusion that is held constant. As a result of the constant rate invasion (or withdrawal) of menisci in pores and throats, the pressure undergoes rapid fluctuations, which reflect the characteristics of pore geometry [26]. The envelope of the pressure–saturation curve in APEX is the mercury porosimetry curve in the conventional approach. Thus, the information obtained from APEX includes, in principle, that from the more conventional approach.

In the sections to follow, we discuss in sequence the behavior of sorption and mercury intrusion–extrusion in pore surfaces, single pores, and pore networks.

3.3 Probing Pore Surfaces

The identification of the characteristics of the pore surface by sorption and mercury porosimetry methods is possible using adsorption at low relative pressures and/or capillary invasion at high capillary pressures. These two applications are discussed separately.

3.3.1 Langmuir Adsorption

Consider, first, adsorption over a flat, smooth surface at low pressures. The resulting submonolayer coverage can be described by the well-known

Langmuir's model [5, 44]:

$$\theta = \frac{K_L(E)\,P}{1 + K_L(E)\,P}, \tag{6}$$

which expresses the equilibrium between adsorption and desorption rates under the conditions of submonolayer coverage. Here, $\theta = V/V_M$ is the surface fractional coverage, V is the volume adsorbed, V_M is the monolayer volume, P denotes pressure, and the equilibrium constant $K_L(E)$ depends on the binding energy E between adsorbate and adsorbent. Langmuir-type models produce adsorption isotherms of type I. Langmuir's equation enables the estimation of the monolayer volume V_M, which is best accomplished by rearranging the V, P data in the form

$$\frac{1}{V} = \frac{1}{V_m} + \frac{1}{V_M K_L P}, \tag{7}$$

and using linear regression. A direct estimation of the surface area of the adsorbent follows, provided that the surface coverage σ of the adsorbate molecules per site is known (e.g., estimated [49] to be equal to 16.2 Å^2 for N_2 at 77 K).

The Langmuir model and its modifications apply to noncompetitive, nondissociative adsorption in chemically homogeneous surfaces [44]. When the surface is chemically heterogeneous or has geometric roughness, however, the low-pressure adsorption data can be further analyzed as follows.

3.3.1.1 Chemical Heterogeneity. In the presence of chemical (energetic) heterogeneity of the surface, the binding energy E, hence the equilibrium constant K_L, is distributed, and adsorption models of the type of Eq. (6) must be modified. A direct extension is to assume a linear superposition of the effects of the various sites, in which case Langmuir's model yields

$$\theta(P) = \int_0^\infty \frac{K_L(E)\,P}{1 + K_L(E)\,P}\, f(E)\, dE. \tag{8}$$

Here, the chemical heterogeneity of the surface is represented in terms of a probability density function (pdf) $f(E)$, where $f(E)dE$ expresses the fraction of the surface area with binding energies in the interval $(E, E + dE)$. The basis of Eq. (8) is the assumption that effects of different sites are independent of neighboring interactions.

The effect of the particular distribution $f(E)$ can be significant and may change the qualitative features of the composite adsorption isotherm. In fact, by combining the local Langmuir model with an assumed form of heterogeneity, as expressed in Eq. (8), one can derive various empirical

expressions [5] commonly used. These include the Freundlich isotherm

$$\theta = aP^n, \tag{9}$$

where a and n are fitting constants, obtained from Eq. (8) using an exponential distribution, and the multisite model

$$\theta = \sum \frac{\chi_i K_L(E_i) P}{1 + K_L(E_i) P}, \tag{10}$$

where χ_i is the fraction of sites with constant $K_L(E_i)$ obtained using patch coverage. Equations of the type of Eqs. (9) and (10) are examples of the forward problem in adsorption in heterogeneous surfaces.

Conversely, Eq. (8) can be inverted with respect to $f(E)$ to identify the chemical heterogeneity of the surface. The problem posed is to find $f(E)$, satisfying Eq. (8), given experimental data $\theta(P)$ and the kernel function $K_L(E)$. An extensive discussion of the various inversion techniques used can be found in Jaroniec and Madey [8]. Similar inverse problems also arise in the estimation of the pore-size distribution of micro-, meso-, and macropores, as is shown later, as well as in other fields (for example, in the context of identifying the permeability heterogeneity of porous media [50]). Equation (8) is a Volterra integral equation of the first kind (e.g., see Carrier *et al.* [51]). Because of its ill-posedness, the inversion being sensitive to experimental and numerical noise, however, some regularization method is needed for its solution [52, 53]. Another approach is to assume an a priori pdf (e.g., Gaussian, log-normal, etc.) with a few adjustable parameters, which are then estimated by various best-fit routines. Figure 5 shows pdfs obtained from the inversion of data for adsorption of nitrogen on Aerosil A at 78 K, using two different algorithms.

3.3.1.2 Surface Roughness. Adsorption at low pressures will also be affected by the geometric heterogeneity of the surface. Consider, in particular, adsorption on a self-similar fractal surface, first discussed by Avnir *et al.* [54, 55]. These authors reasoned that the size of the molecule of the adsorbate δ is effectively a ruler measuring the area of the self-similar surface. They found experimentally that the monomolecular coverage (molecular tiling) of the surface by various species of different molecular weight (and hence of presumed different surface coverage per site, $\sigma \sim \delta^2$) scales as a power law of δ, namely,

$$N_M(\delta) \sim \sigma^{-n/2} \sim \delta^{-n}, \tag{11}$$

where $N_M(\delta)$ denotes the amount adsorbed at the end of monolecular coverage. Because Eq. (11) can be interpreted as a power law between the number N_M of "spheres" that cover the surface (actually its active sites) and their size δ, it also serves to define the box-counting fractal dimension of the

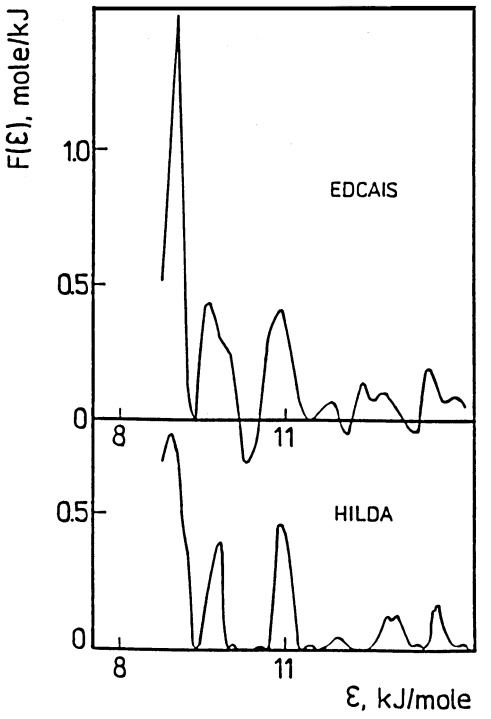

FIG. 5. The pdf of the binding energy in a chemically heterogeneous surface obtained from the inversion of adsorption data of nitrogen on Aerosil A at 78 K using two different inversion algorithms. Reprinted from Jaroniec and Madey, *Physical Adsorption on Heterogeneous Solids*, © 1988, with permission from Elsevier Science.

surface (namely, we have $D = n$). A list of widely different surfaces were probed and found to have a fractal dimension in the range between 2 and 3. In most of these experiments, however, the range of scales where fractal behavior was identified was quite narrow (less than a decade in terms of δ, for example, for N_2, $d_{lo} = 0.2$ nm and $d_{up} < 1$ nm). The limitation of small range is clearly important as far as a fractal characterization is concerned. It must be also kept in mind that the fractal dimension thus identified may well pertain to the local regime of a generally self-affine pore surface with self-affine exponent $H = 3 - D$. In this context, the dimension D identified would reflect the roughness of the various surfaces tested, which will increase (lower H) as D increases. The molecular tiling approach for estimating the fractal dimension of the surface was critically reviewed by Drake *et al.* [56].

An alternative approach for the determination of various characteristics of the pore surface involves the use of an isotherm of a single species in the multilayer region, rather than of multiple isotherms of different adsorbates. This is discussed in the following section.

3.3.2 Multilayer Adsorption

In multilayer adsorption, adsorbate–adsorbate interactions cannot be ignored and, in fact, control the adsorption process. Brunauer, Emmett, and Teller [57] proposed the simple, but still widely used, BET model for multilayer adsorption over a flat surface, based on which the pore surface area can be estimated. The BET equation has the simple form

$$\frac{V}{V_M} = \frac{Cx}{(1-x)[1+(C-1)x]}, \tag{12}$$

where $x = P/P^0$ is the relative pressure and C is a parameter depending on temperature, the binding energy, and the latent heat. The approach follows assumptions similar to Langmuir's, namely, localized adsorption over a homogeneous, flat surface and the absence of lateral interactions. Depending on the value of C, the BET model can cover the range of adsorption isotherms of types II ($C > 1$) and III ($C < 1$) (see Fig. 6). As in the Langmuir model, the BET equation is reversible. By rearranging it in the linear form,

$$\frac{x}{V(1-x)} = \frac{1}{CV_M} + \frac{x(C-1)}{CV_M}, \tag{13}$$

we can estimate the monolayer volume, V_M (and C), by parameter fitting, from which the pore surface area follows, as in the case of Langmuir adsorption.

When multilayer adsorption occurs over a rough surface, models that account for the potential energy of the adsorbate due to its attraction to the rough surface are required. One such class makes use of the "equipotential" assumption, in which the potential of the interaction depends only on the distance from the surface, while the film thickness remains the same irrespective of surface curvature. We note that the thickness t of a liquid film over a flat surface is obtained by a simple balance in the chemical potential between adsorbed and bulk gas phases:

$$\frac{A_H}{6\pi t^3} = -\frac{kT}{V_{m,l}} \ln x \equiv \Pi(t), \tag{14}$$

where van de Waals attraction was assumed. Here A_H is the Hamaker

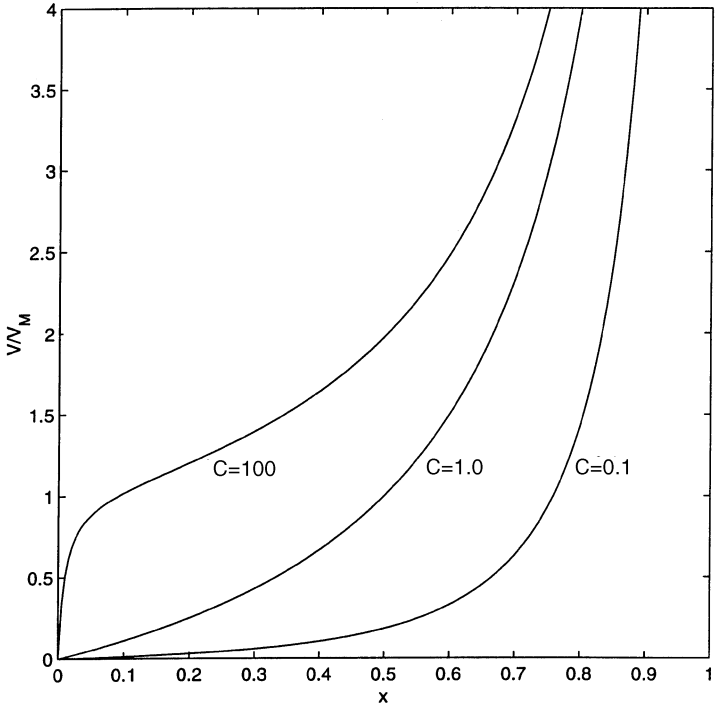

FIG. 6. Adsorption isotherms described by the BET model for different values of C.

constant, $V_{m,l}$ is the molar volume of the liquid, and we also introduce the disjoining pressure $\Pi(t)$ for later use. The latter is the pressure of the nonwetting phase in equilibrium over a flat wetting film of thickness t. Under the equipotential assumption, adsorption over a rough surface of area S can be described by generalizing Eq. (14):

$$\frac{\beta}{t^3} = -RT \ln x, \tag{15}$$

where β is a constant. Then, multilayer adsorption of volume V over a surface area S is expressed as

$$\frac{V}{S} = \left[\frac{A}{\beta}\right]^{-1/3} \tag{16}$$

where we have used the conventional notation, $A = RT \ln(P^0/P)$, for the adsorption potential.

In practice, however, isotherms over rough surfaces display power laws with an exponent in a range of values rather than the specific value of 3 suggested in Eq. (16). To account for such behavior, semiempirical isotherms of the type

$$\frac{V}{V_M} = \left[\frac{A}{\beta'}\right]^{-1/n} \tag{17}$$

have been proposed, in which exponent n is now an adjustable parameter (and β' is another constant). Equations of the type of Eq. (17) are known as Frenkel–Halsey–Hill (FHH) equations. Other semiempirical models for multilayer adsorption over rough surfaces have also been proposed, for example, the Dubinin–Radushkevich (DR) equation,

$$\frac{V}{V_M} = \exp[-bA^2], \tag{18}$$

where b is another adjustable parameter [3] (although the latter is actually more appropriate for the filling of micropores, see later).

Pfeifer *et al.* [58] combined the equipotential approach with van der Waals attraction to describe adsorption over a self-similar fractal surface, and derived the following result:

$$V \sim t^{3-D} \sim A^{-[(3-D)/3]}, \tag{19}$$

for the volume V contained in cavities and pits of size less than t. The first part of this equation reflects the surface self-similarity and was derived previously by de Gennes [16] (see later). The second reflects equation Eq. (14). Comparison with Eq. (17) shows that Eq. (19) has the form of an FHH equation, now with exponent $n = 3/(3 - D)$, thus providing a possible interpretation of the empirical FHH exponent in terms of the degree of roughness. Indeed, according to this model, $n = 3$ is obtained in the Euclidean limit of flat surfaces, $D = 2$. Pfeifer *et al.* [58] fitted Eq. (19) to experimental results for the adsorption of N_2 on silver and reported a surface fractal dimension of 2.3 in the range 0.8–4.5 nm. This range is larger than that for the molecular tiling approach, giving confidence to the estimated fractal dimension. However, the method neglects capillary condensation, which will likely occur in pores in the upper limit of the range investigated, and the consideration of which will change the scaling behavior, while the adsorbate–adsorbent interaction for this system may not necessarily be of the van der Waals type [59]. In a subsequent paper, Pfeifer and Cole [17] presented an extensive discussion of the adsorption and capillary equilibria over a self-affine surface and discussed the various regimes that may arise.

3.3.3 Capillary Effects and Surface Roughness

In the previous sections, the intermolecular forces between bulk and condensed phases (essentially the effect of the meniscus) were neglected. As adsorption proceeds and films thicken, however, their contribution becomes important. It is well known that across a macroscopic interface separating two immiscible phases in equilibrium, the capillary pressure between the two phases, $P_c = P_{\mathrm{nw}} - P_w$, is related to the mean curvature, $C^{\mathrm{nw},w}$, through the Laplace equation

$$P_c = 2C^{\mathrm{nw},w}\gamma \tag{20}$$

where γ is the interfacial tension between the fluids. Here, we defined $C^{\mathrm{nw},w} = 1/2(1/R_1 + 1/R_2)$, where R_1 and R_2 are the principal radii of curvature measured from the side of the nonwetting phase. The interface is stable provided that

$$\frac{dC^{\mathrm{nw},w}}{dV_{\mathrm{nw}}} > 0, \tag{21}$$

namely, that $C^{\mathrm{nw},w}$ increases with an increase in the volume V_{nw}. Equation (20) contains the well-known result,

$$P_c = \frac{2\gamma}{r}, \tag{22}$$

for spherical interfaces of radius r. It is important to note the different power-law dependences between the pressure (disjoining or capillary) and the length scale (film thickness or radius of curvature) expressed in the two Eqs. (14) and (20) [or (22)], respectively. In relating surface roughness with adsorption data at higher relative pressures (which give rise to a capillary condensation) or mercury porosimetry at high capillary pressures, therefore, the different power law, Eq. (20) [or (22)] must also be considered.

This problem was considered by de Gennes [16], who studied the displacement of a wetting fluid from the cavities of a self-similar fractal surface. He derived the following scaling law for the wetting fluid saturation (namely, the pore volume fraction occupied by the wetting phase) contained in pits and cavities of radius less than r:

$$S_w \sim \left(\frac{r}{r_{\mathrm{up}}}\right)^{3-D}, \tag{23}$$

where D is the fractal dimension of the pore surface and r_{up} is the upper cutoff limiting the fractal behavior. We recognize Eq. (23) as the first part of Eq. (19) of Pfeifer *et al.* [58]. Now, when macroscopic curvature effects dominate over adsorbed films, the radius r is related to the capillary

pressure P_c via Eq. (22). Then, the following scaling law between S_w and P_c can be derived [60]

$$S_w \sim P_c^{-n} \qquad \text{where } n = 3 - D. \tag{24}$$

This power law is consistent with the experimental data of Melrose [61] for describing the dependence of the capillary pressure curve in the low S_w regime (Fig. 7), where the exponent n was found to be in the range 0.38–0.46. From this analysis, Davis [60] concluded that the pore surface in these experiments has a fractal dimension in the range 2.54–2.60.

Neimark [59] combined de Gennes's approach with capillary condensation to interpret adsorption data at higher pressures. Using Kelvin's equation (see later) and neglecting the adsorbed film in comparison to the capillary-condensed adsorbate, he obtained the following relation between adsorbed volume and adsorption potential:

$$V \sim A^{-(3-D)}. \tag{25}$$

Like Eq. (19), this is also an equation of the FHH type, but now with the different exponent $n = 1/(3 - D)$, reflecting the dominance of macroscopic curvature over thin film effects. The same exponent was also derived by

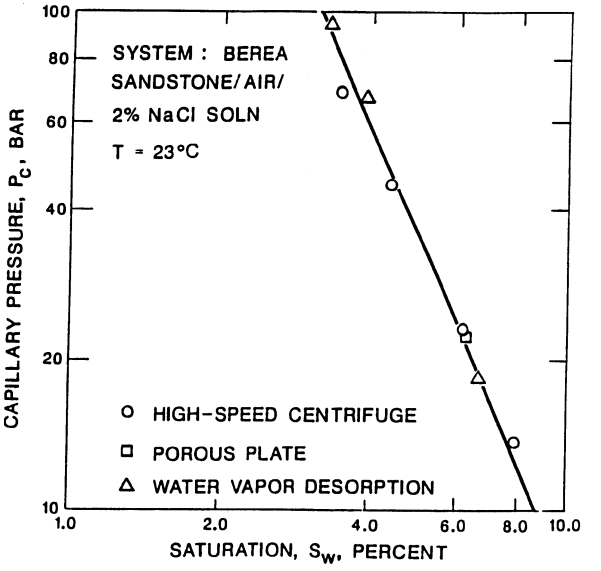

FIG. 7. Experimental data showing the power-law scaling of the capillary pressure curve at low values of the wetting saturation. Reprinted with permission from J. C. Melrose, SPE18331, 63rd SPE Annual Fall Meeting, Houston, TX (1988).

Avnir and Jaroniec [62] and Yin [63] (but for a different system), as discussed in the next section.

A more general method for probing the characteristics of surfaces was proposed by Neimark [59, 64]. The key to his approach is the following general thermodynamic relation between the interfacial excess area S_{ex} of an adsorbate and the chemical potential [64], $S_{ex} \sim \int_{N(\mu)}^{N_{max}} \mu \, dN$, where N_{max} is the maximum extent of adsorption. For the particular case of the capillary condensation regime, where Kelvin's equation is used, this reads as

$$S(N) = \frac{1}{\gamma} \int_{N}^{N_{max}} A \, dN. \tag{26}$$

Implicit in Eq. (26) is the assumption of a spatially constant curvature and negligible wall–adsorbate interactions. Now, assuming a fractal surface with the properties of Eq. (3), use of Kelvin's equation in Eq. (26) enables one to calculate the fractal dimension from the adsorption (or desorption) data via

$$D = 2 + \frac{d[\ln \int_{N}^{N_{max}} A \, dN]}{d \ln A} \quad \text{or} \quad D = 2 + \frac{d[\ln \int_{N}^{N_{max}} |\Delta\mu| dN]}{d \ln |\Delta\mu|} \tag{27}$$

(note the generalization expressed in the second equality). From an analysis of experimental data of sorption of nitrogen in an activated carbon sample, Neimark reported the values 2.73 and 2.71 from the two respective branches, adsorption and desorption, over a range covering about 2 decades in pore sizes. He also remarked that because of its general validity [note the second equality in Eq. (27)] this approach can also be applied to other processes, for example, to mercury porosimetry in macropores (see later).

We conclude that adsorption or capillary pressure data in the appropriate regimes can be inverted to yield information on surface roughness. However, because surfaces are likely to be self-affine, power laws can be interpreted as pertaining to either the local or the global regimes, and an appropriate distinction is necessary. In particular, the exponent at small scales would give the local fractal dimension D, namely, the growth exponent $H = 3 - D$, while the probing of scales in the global regime can also be expressed in terms of a power law, following Neimark's approach [14], except that now the apparent fractal dimension D would actually reflect exponent H through the relationship $H = (6 - 2D)/(4 - D)$. The latter is derived by equating the exponent of the second part of Eq. (4) with $2 - D$. Assuming a global regime, Neimark [14, 64] interpreted experimental data of low-temperature nitrogen adsorption on 1000-Å-thick silver film and found a surface roughness with $H = 0.36$. This value is consistent with the roughness exponent $\frac{1}{3}$ that characterizes the formation of self-affine surfaces according to the Kardar–Parisi–Zhang (KPZ) model [65].

We should add that the wetting of a rough (but not self-affine or self-similar) surface by a liquid was considered by Sweeney *et al.* [66], who used the augmented Laplace-Young equation,

$$P_c = 2C^{g,l}\gamma + \frac{A'_H}{t^n}, \tag{28}$$

to account for both macroscopic curvature effects as well as for adsorbed films (and where A'_H is a Hamaker constant). This is a composite expression that patches two different limiting behaviors (macroscopic interfaces and thin films) into a single expression. In Eq. (28), the disjoining pressure was approximated by a power-law function of the film thickness, while $C^{g,l}$ is the mean curvature of the macroscopic gas–liquid interface (measured from the side of the gas). At conditions of capillary equilibrium, where P_c is constant, the shape of the interface over the rough surface can be determined by solving Eq. (28). Numerical results showed the existence of two regimes, one in which the equilibrium shape is dominated by thin films (for example, over surface peaks) and another in which it is dominated by pendular structures (over valleys). In an earlier paper, Melrose [67] also considered separate contributions from pendular rings and adsorbed films (which he modeled using an FHH equation) to describe capillary equilibria in a model of densely packed spheres.

3.4 Probing Porous Media

Sorption and capillary invasion–retraction in a porous medium is complicated by the presence of pores of various sizes, shapes, and connectivities. Sorption in micropores is affected by the confinement of the fluid in a pore space of thickness of a few layers and the strong interaction between pore walls and the fluid over the entire range of the pore. Sorption in mesopores gives rise to capillary condensation and a characteristic hysteresis in the adsorption–desorption loop. Capillary invasion–withdrawal in macropores is affected by the pore geometry, which also gives rise to hysteresis. Finally, the connectivity of the pore network plays an important role in the accessibility of the porespace and further contributes to the macroscopic response. This section provides a description of these processes first in single pores and subsequently in a network of pores and discusses the identification of the various parameters by inverting the experimental response. Sorption and capillary invasion–withdrawal are discussed separately. We begin with an analysis of sorption isotherms.

3.4.1 Adsorption–Desorption in Single Pores

Adsorption–desorption processes in micropores occur at sufficiently low relative pressures and they are reversible. This reversibility is due to the fact that the fluid in the micropores is in a supercritical state as a result of the lowering of its critical temperature by the confinement and the interaction with the pore walls (the lowering increases with a decrease in the pore size). Termination of micropore filling is signaled by the decrease of the slope of the adsorption isotherm in the low-pressure regime. Adsorption–desorption in larger pores (mesopores) involves capillary condensation.

Various semiempirical expressions, such as the DR Eq. (18), have been proposed to describe micropore filling. However, a more exact description can be obtained using recent advances in modeling based on DFT in sufficiently small pores, to be discussed later. For the filling of mesopores, where capillary condensation takes place, the contribution of the interfacial energy of the gas–liquid meniscus must be also considered in the thermodynamic equilibrium. Two different approaches have been used for its description.

Everett and Haynes [68] analyzed the thermodynamic equilibrium of a vapor–liquid interface confined in a cylindrical pore by neglecting pore wall–adsorbate interactions. For its description they used Laplace's Eq. (20) along with Kelvin's equation:

$$\ln x = \frac{2\gamma V_{m,l} C^{l,v}}{RT}, \tag{29}$$

where $C^{l,v}$ is the mean curvature from the side of the liquid (note that in a liquid film on the walls of a cylindrical pore, $C^{l,v}$ is negative). Several pore network studies [33–39, 69–72] are based on Kelvin's equation, as discussed later in the chapter. The condition for interface stability is now $(dC^{l,v}/dV_l) > 0$, where V_l is the volume of the condensed liquid. Based on the representation of the vapor–liquid interface by an unduloid inside a cylindrical pore of size r (Fig. 8) and making use of Eqs. (20), (21), and (29), Everett and Haynes [68] showed that as the pressure increases, the interface remains stable until the unduloid takes the shape of a cylindrical surface with curvature $C^{l,v} = -1/(2r)$ (point A in Fig. 8). Following this point, the gas–liquid interface is unstable to further increases in volume (path ABDHIJ in Fig. 8). In this scenario, therefore, pore-filling will occur at a relative pressure corresponding to a cylindrical meniscus geometry:

$$\ln \frac{P_A}{P^0(T)} = -\frac{\gamma V_{m,l}}{rRT}. \tag{30}$$

By similar arguments, the reverse process (pore-emptying or desorption) as

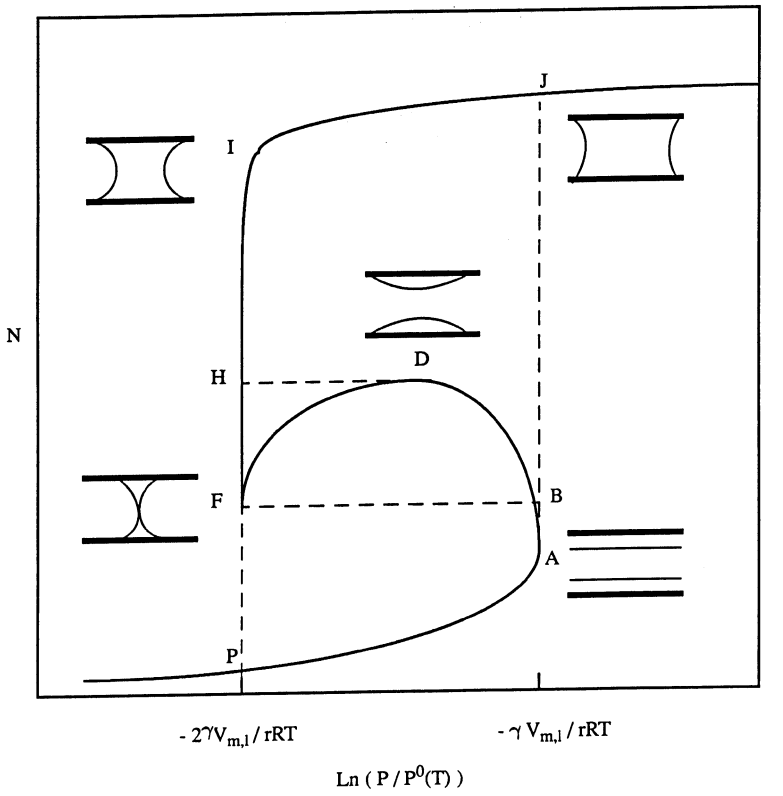

FIG. 8. Single-pore hysteresis during adsorption–desorption in a cylindrical capillary according to Everett and Haynes [68].

the relative pressure decreases, is stable for an interface configuration involving semispherical menisci with curvature $C^{l,v} = -1/r$ (at the pore mouths, point I, and until the two menisci are in contact, point F, in Fig. 8). Following point F, however, the equilibrium is unstable (path FDBAP in Fig. 8) and rapid pore-emptying will occur. In this scenario, therefore, desorption will occur at a relative pressure corresponding to a spherical meniscus geometry:

$$\ln \frac{P_D}{P^0(T)} = -\frac{2\gamma V_{m,l}}{rRT}. \tag{31}$$

The difference between the two expressions, Eqs. (30) and (31), shows that capillary condensation in a single pore is hysteretic, with pore-filling (adsorption) occuring at a higher relative pressure.

In the preceding theory, the presence of pore walls, which is likely to affect the interfacial tension and the molar volume, is not considered. An improved modification [3], the so-called t-plot approach, makes use of the effective radius $r - t$, instead of r, where t is the thickness of the adsorbed layer. This thickness is independently measured as a function of the relative pressure over a nonporous, flat surface with otherwise identical properties. Although accounting for part of the wall–adsorbate interaction, however, this method still fails to account for the interaction between the film and the opposite wall.

Cole and Saam [73] proposed a different interpretation, which accounts for the wall interaction, and it is based on the metastability of the liquid–vapor coexistence in confined pores. In sufficiently small pores, the proximity of the pore walls affects the vapor–liquid transition so that the capillary can support metastable states in a manner analogous to the superheating or supercooling of bulk fluids [74, 75]. Here, the interactions with the walls are also accounted in the stability of the adsorbed film using an "extended" Kelvin equation:

$$RT \ln x = 2\gamma V_{m,l} C^{l,v} + U_m(t), \tag{32}$$

where the molar energy of the adsorbed condensed phase $U_m(t)$ depends on the film thickness t. Pores with adsorbing walls effectively shift the liquid–vapor coexistence curve to lower pressures. A stability analysis shows that during adsorption the film becomes unstable at a critical thickness t_c, which depends on fluid–fluid and fluid–solid interactions and the interfacial tension. In desorption, the liquid is in a metastable equilibrium with an asymmetric meniscus, with the liquid film thickness t_m now being larger, $t_m > t_c$. This thickness also depends on the molecular interaction parameters. Due to the difference between t_m and t_c, complete emptying (desorption) of a filled pore occurs at a pressure lower than pore filling, thus resulting in hysteresis. Due to the account of the liquid–solid interaction, the onset of adsorption and desorption predicted by this theory is different from that of Everett and Haynes [68].

More modern treatments make use of DFT and molecular dynamics simulations. The significant advantage of the molecular models is that they can cover the size distribution over a large range, including micropores (which do not involve capillary condensation) and macropores (which involve capillary condensation). Evans *et al.* [76] applied local DFT in slit and cylindrical pore geometries. As in Cole and Saam [73], they attributed hysteresis to the metastability of thick films and obtained hysteresis loops for the amount adsorbed as a function of pressure. Their theory shows explicitly how the vapor–liquid coexistence in confined geometries depends on the pore radius. In effect, the constricted geometry leads to a lowering of

the critical temperature of the fluid (T_{cc}), compared to the bulk (T_c), which in certain limiting cases can be described with the approximate expression

$$\frac{T_{cc}}{T_c} \approx 1 - \frac{1}{\lambda r}, \tag{33}$$

where r is the pore size and $1/\lambda$ is the decay length of the intermolecular potential. Thus, for sufficiently small pores at a sufficiently high temperature, the confined fluid is in a supercritical state, and the adsorption–desorption process is reversible. This is the case of adsorption in micropores. Figure 9 shows experimental results for adsorption in porous media [77], which clearly demonstrate the diminishing of the hysteresis loop as the temperature increases and the existence of a capillary critical point.

We conclude that the single-pore adsorption–desorption behavior in the capillary condensation regime can be modeled only approximately with the use of Kelvin's equation and, more accurately, by molecular models. Use of Kelvin's equation, however, leads to simple analytical estimates for the relative pressure at which a pore of size r fills (or empties). For example, one has

$$\ln(P/P^0) = -\frac{r_c}{r} \qquad \text{where } r_c = \frac{2s\gamma V_{m,l}}{RT}, \tag{34}$$

and the geometry-dependent index is equal to $s = 1$ in spherical pores for either adsorption or desorption, while in cylindrical elements (throats), $s = 1$ for desorption, and $s = 1/2$ for adsorption. A number of single-pore studies have been conducted using molecular models, an important by-product of which has been the assessment of the validity of Kelvin's equation.

Ball and Evans [74, 75] used local DFT, in which the adsorption branch was assumed to "nucleate" at the limit of metastability (namely, at the spinoidal pressure) and the transition from liquid to gas was assumed to occur at the bulk equilibrium coexistence point. In a related study, Seaton *et al.* [28] used local DFT in slitlike pores. To obtain expressions for the intermolecular potential parameters they fitted their DFT results for large pores (which effectively mimic a flat surface) to a t-plot-like curve. They showed that Kelvin's equation deviates significantly from the DFT predictions for small pores, although the modified equation that includes the t correction gives better agreement (with a deviation that does not exceed 10% in small pore sizes). Balbuena and Gubbins [20] applied nonlocal DFT to slitlike pores to characterize adsorption–desorption isotherms in terms of pressure, temperature, the pore width H, and the intermolecular (fluid–fluid and solid–fluid) parameter ratios. Their results covered the range of

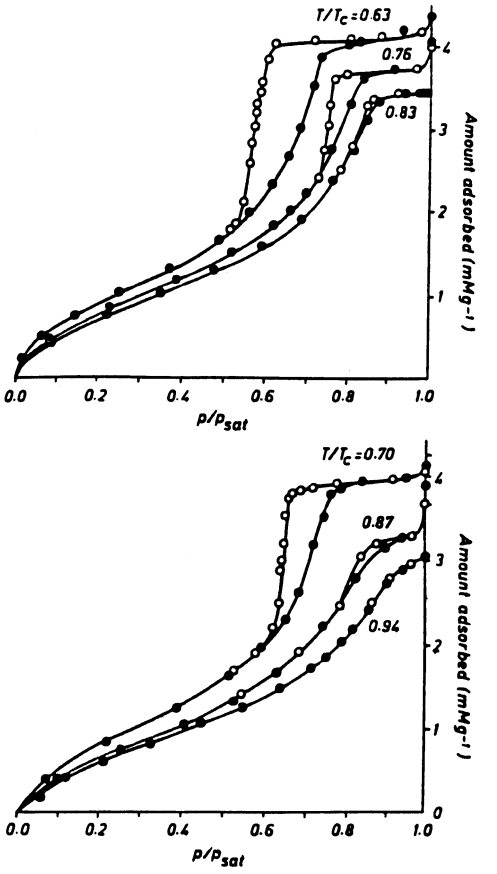

FIG. 9. Experimental sorption isotherms of Xe on Vycor demonstrating the dependence of hysteresis loops on temperature and the existence of a capillary critical temperature. Solid circles denote adsorption and open circles denote desorption. Reprinted with permission from Burgess *et al.*, *Pure Appl. Chem.* **61**, 1845 (1989).

the six IUPAC types of Fig. 3, all of which were found in the simulations. They found that the classification of the various types correlated well with the reduced thickness $H^* = H/\sigma_{ff}$, where σ_{ff} is a characteristic length of the Lennard–Jones potential, and they recommended specifying values of H^* rather than the IUPAC absolute size scale to classify pores in the micropore, mesopore, and macropore classes. These authors also commented on the inadequacy of Kelvin's equation for micropores and in a certain range of mesopores.

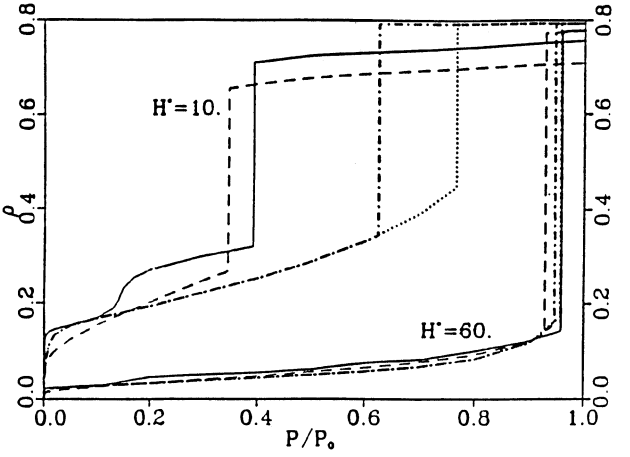

FIG. 10. Predictions of single-pore isotherms for the adsorption of nitrogen in carbon slit pores based on different approaches (dotted line, Kelvin equation; dash-dotted line, modified Kelvin equation; dashed line, local DFT; and solid line, nonlocal DFT). Here H^* is a dimensionless pore width. Reprinted with permission from Lastoskie *et al.*, *J. Phys. Chem.* **97**, 4786. Copyright 1993 American Chemical Society.

Lastoskie *et al.* [78] applied nonlocal DFT theory to examine adsorption in carbon slitlike pores. They particularly emphasized the filling of micropores and identified various filling regimes. In a separate study, Lastoskie *et al.* [79] compared the predictions of pore-filling with the various different approaches (Kelvin, modified Kelvin, DFT, and nonlocal DFT). Their results (reprinted in Fig. 10) show that the various forms of Kelvin's equation misrepresent pore-filling, particularly of micropores, although they appear adequate for mesopores of larger size. Using lattice gas simulations, Binder and Landau [80] also commented on the validity of Kelvin's equation in sufficiently large capillaries. Nonlocal DFT in cylindrical pores was also used by Ravikovitch *et al.* [81]. Interestingly, however, adsorption–desorption processes in converging–diverging pore geometries, which are typical of porous media, have not yet been simulated at the time of writing this chapter.

Direct experimental determination of capillary condensation in slit geometries was obtained by Christenson and coworkers [82–85] using the surface force apparatus.

3.4.2 Adsorption–Desorption in a Pore Network

Sorption isotherms in porous media reflect the overall response of the multitude of pores comprising the porous medium. The pore structure gives rise to issues of heterogeneity and accessibility. In formulating forward and inverse problems in pore networks, the typical approach taken is to assign local conditions for adsorption or desorption in a pore element, as described earlier, and then to consider the composite behavior of the system subject to various assumptions. In analyzing the composite response of porous media, we consider adsorption and desorption separately.

As the relative pressure increases, multilayer adsorption proceeds uniformly over all surfaces. At some stage, the filling of micropores and mesopores will commence. Assuming that pores fill independently of each other, elements with smaller radii fill first, regardless of their accessibility. Then, we can take the linear superposition [28]

$$N(P) = \int_{r_{\min}}^{r_{\max}} \rho(P,r)\, f(V)\, dV \tag{35}$$

to express the adsorbed amount N in terms of the molar density $\rho(P, r)$ of the fluid at pressure P in a pore of size r. Here f is the pdf of pores with volume V (which can be related to the size distributions, depending on the geometric model used). We recognize Eq. (35) as belonging to the same class as Eq. (8), describing the effect of chemical and geometric heterogeneity of the pore surface. To construct adsorption isotherms in the forward problem, two additional items are required: relating the number fraction of liquid-occupied sites to the throat statistics and assigning a volume distribution.

Considerable attention has been paid to pdfs with power-law scaling. Avnir and Jaroniec [62] considered the filling of micropores. They used Dubinin's approach for the liquid density, by taking

$$N \sim \int_{r_{\max}}^{r_{\max}} \exp(-mr^2A^2)\, f(r)\, dr, \tag{36}$$

and assumed that the pore-size distribution satisfies a power-law scaling, namely, $f(r) \sim r^{2-D}$, where $f(r)\, dr$ is the volume fraction contributed by pores with sizes in the interval $(r, r + dr)$. Based on these assumptions, they obtained the result

$$N \sim A^{-(3-D)}. \tag{37}$$

Equation (37) is of the FHH type with exponent $n = 1/(3 - D)$, which is

identical to Neimark's Eq. (25). However, the two objects to which power-law characteristics are attributed are different, with Neimark's equation pertaining to a fractal surface, while Avnir and Jaroniec's was the micropore size distribution. Yin [63] also used the same assumption for the power-law scaling of f. However, instead of assuming micropore filling, he considered a capillary condensation regime, in which pores fill when the Kelvin threshold for adsorption is reached, and neglected any contributions from the adsorbed film. His result is also an FHH equation of the same type as Eq. (37). Later, Jaroniec [86] pointed out the equivalence of the two approaches for deriving Eqs. (25) and (37).

When a pore network model representation of the porous medium is used, formulating the forward and, most important, the inverse problems depends on the assumptions made about the pore structure. As noted, a basic element of the latter is the pore–throat converging–diverging geometry. However, capillary condensation in a converging–diverging geometry has not been rigorously analyzed. A plausible assumption is that pore-filling in the latter occurs when the radius of curvature of the meniscus becomes equal to the pore radius, as further condensation will lead to a smaller radius of curvature, hence to a smaller (more negative) $C^{l,v}$. However, this presupposes that all throats adjacent to the pore under consideration have already been filled. Given that cylindrical pore throats fill at a higher relative pressure than spherical sites of the same radius [compare with Eq. (34)], the filling of a pore could be delayed, in principle, until its largest adjacent pore throat has been filled first [69–72]. For this scenario to apply, the following constraint must hold, $r_s < 2r_{b,\max}$, where $r_{b,\max}$ is the maximum size of the throat adjacent to a pore. Thus, the pore–throat aspect ratio becomes an important parameter in the filling sequence. Mayagoitia *et al.* [69–72] have discussed the possibility that such pore–throat interactions may, in fact, have a long-range effect on the overall adsorption pattern. Interactions of this type develop in imbibition, which is the counterpart of adsorption, and drastically affect the displacement patterns [87]. However, the two processes differ in at least one respect: that imbibition has mainly invasion characteristics, in contrast to adsorption, where condensation does not necessitate connectivity to an invading front. The issue of pore–throat correlation appears again in the discussion of desorption and mercury porosimetry.

Zhdanov *et al.* [37] proceeded with the assumption that pore filling is only controlled by their own radius, and accounted for the density of the adsorbed films using a t-plot approach. Then Eq. (35) can be used directly to obtain the pore size distribution $\alpha_s(r)$. Mason [33–36] (and, subsequently, Parlar and Yortsos [38, 39]), on the other hand, modeled adsorption based on the premise that a pore is filled when its largest adjacent throat is

filled. Then, the fraction of occupied sites X_s is

$$X_s = 1 - (1 - p)^Z, \tag{38}$$

where p is implicitly related to the relative pressure via Eqs. (5) and (34) and Z is the coordination number (the notation C, instead of Z, is also used in the adsorption literature). The appearance of Z in modeling adsorption makes this model qualitatively different from that of Zhdanov *et al.* [37] (and also of Seaton *et al.* [28], see later). By further equating the pore-volume fraction with the number fraction of liquid-occupied sites (in which it is tacitly assumed that the site volume is uncorrelated with its radius r_s), a predictive model for the composite response during adsorption can be obtained using Eq. (38). Given adsorption data and an assumed (or estimated) value of Z, the pore-size distribution $\alpha_b(r)$ can be thus estimated. Mason further postulated that Eq. (38) actually serves to relate pore and throat size distributions, namely,

$$q = 1 - (1 - p)^Z, \tag{39}$$

from which the pore size distribution, $\alpha_s(r)$, can be obtained given $\alpha_b(r)$. In a subsequent study, Parlar and Yortsos [39] analyzed the effect of relaxing the assumption of Eq. (39). Although not explicitly accounted for in these models, the contribution of the adsorbed film to the total volume can be readily incorporated using the *t*-plot approach.

In studies where molecular models are used to describe the local behavior, the density function $\rho(P, r)$ is computed directly. Because the single-pore geometries studied are of only two types (slitlike and cylindrical), however, all volume is allocated to the throats, hence only the pore size distribution of throats $\alpha_b(r)$ is used (or inverted). Seaton *et al.* [28] considered slitlike geometries and applied local DFT to obtain the pore size distribution of porous carbons from nitrogen adsorption isotherms. Lastoskie *et al.* [78, 79] applied nonlocal DFT to slitlike geometries. Their results showed that the former is generally better than DFT and that both are preferred over Kelvin-type equations. A comparison of the different pdfs obtained based on the different local models is shown in Fig. 11 (reprinted from Lastoskie *et al.* [79]). Nonlocal DFT was also used by Ravikovitch *et al.* [81] to study adsorption in distributed cylindrical pores of near uniform sizes in the range 18–80 Å.

Adsorption terminates upon the complete filling of all pores (or of some fraction q_i, corresponding to fraction p_i, if secondary desorption is to be investigated). Desorption starts upon reversal of the pressure. Conventionally [27, 33–38, 43, 88], nucleation is neglected (but see Ref. [39]), and according to the single-pore analyses, largest-size elements (namely, pores)

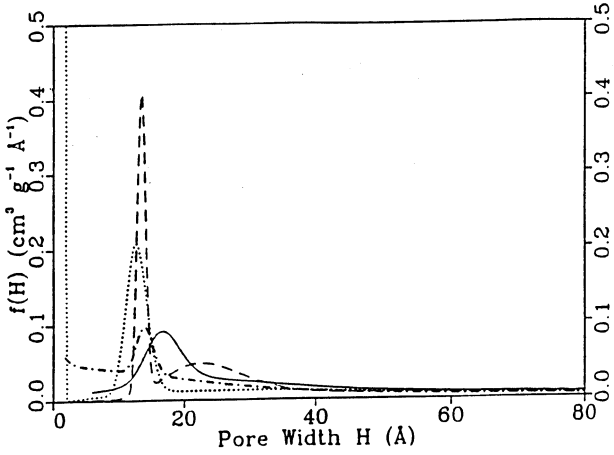

FIG. 11. Comparisons of the pdfs of the pore size obtained by inverting adsorption data for noninteracting slitlike pores based on different approaches (dotted line, Kelvin's equation; dash-dotted line, modified Kelvin's equation; dashed line, local DFT; and solid line, nonlocal DFT). Reprinted with permission from Lastoskie *et al.*, *J. Phys. Chem.* **97**, 4786. Copyright 1993 American Chemical Society.

empty first. However, unlike adsorption, desorption (emptying) of a pore requires access to vapor-occupied sites. These can be sites at the outside surface of the sample (the fraction of which can be significant for pore networks of relatively small size), sites belonging to a cluster spanning the sample, or sites that are not connected to bulk vapor, but contain vapor either as a result of incomplete termination of adsorption (in the case of secondary processes) or as a result of nucleation (Fig. 12). Thus, desorption is affected by the network connectivity. The resulting hysteresis in the adsorption–desorption curves is now due to the limited accessibility, rather than the local geometry.

The requirement of accessibility to external (or internal) sources attributes to desorption invasion percolation (IP) characteristics similar to the extrusion part of mercury porosimetry (discussed later). The process is mixed bond-site percolation, in which we are interested in the fraction of vapor-occupied (empty) sites, the occupancy of which is controlled by bonds. This brings about the important question of whether or not the geometrical parameters of pores and throats are interrelated. Bond-percolation or site-percolation models, where only throats or pores, respectively, are considered, have also been suggested as desorption models. Most studies in this area have used ordinary percolation (OP) rather than IP models (the difference between the two in three dimensions being negligible, for practical

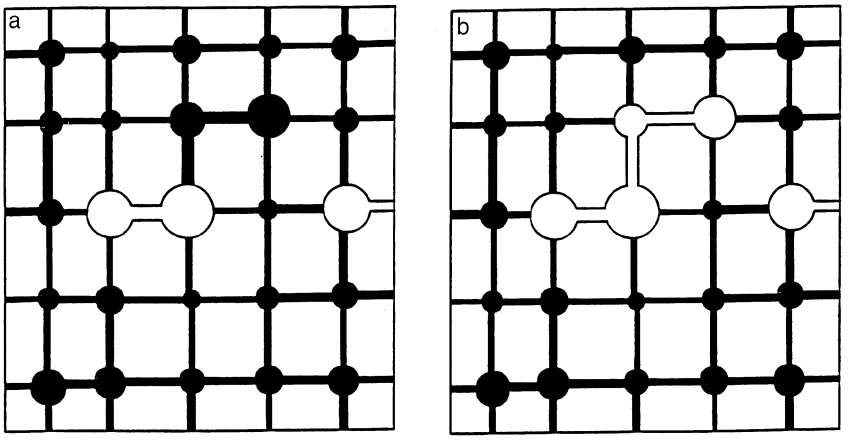

FIG. 12. Schematic of the requirement for accessibility to bulk vapor or an internal source before a site can empty during desorption. Two successive steps of desorption are shown. Reprinted with permission from Parlar and Yortsos, *J. Colloid Interface Sci.* **124**, 162 (1988).

purposes). The implicit assumption in all percolation models is that the pressure decreases in infinitesimally small intervals and that dynamic effects during the process are absent. This issue appears again in mercury porosimetry.

Whether of the site, bond, or mixed site–bond type, the application of percolation theories results in a set of curves for the fraction of vapor-occupied elements. The curves can be obtained by numerical simulation for regular networks and analytically for Bethe lattices and also depend on the pore network coordination number Z, its dimension, and the size L. Mason [33] developed a differential description of such processes. Parlar and Yortsos [38] solved Mason's differential equations exactly and provided various analytical solutions of different percolation problems (site-only, bond-only, and mixed site–bond percolation) to model primary and secondary adsorption and desorption in a Bethe lattice, and presented numerical solutions for a square lattice. Typical adsorption–desorption curves for the condensed liquid saturation as a function of the relative pressure for a Bethe lattice [38] are shown in Fig. 13. Similar results are obtained for regular lattices [89] (the main differences are related to the behavior of the primary desorption curve near the onset of connectivity).

In these percolation-type models, larger-scale hysteresis associated with connectivity and topology is assumed to dominate over local, single-pore hysteresis (earlier suggested as the reason for the hysteresis loops). Ball and Evans [75] provided a comparative study to probe the origin of hysteresis.

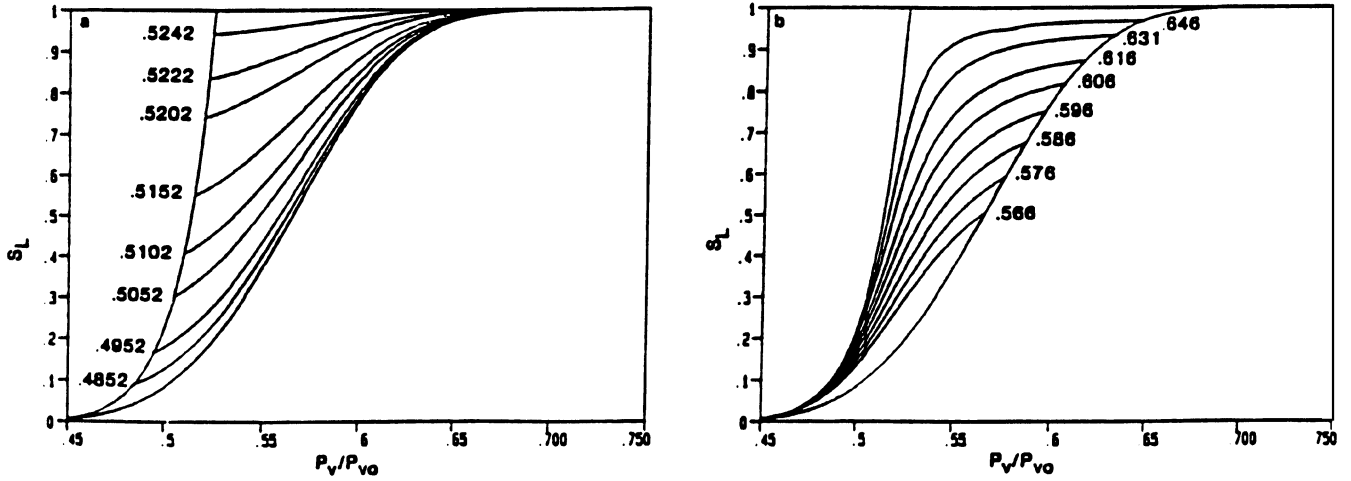

FIG. 13. Predictions of primary and secondary adsorption curves (left diagram) and desorption curves (right diagram) for the adsorption of xenon in Vycor glass at 151 K based on a Bethe lattice model with $Z = 4$ and an assumed pore size distribution. The numbers indicate the relative pressure values at the onset of secondary adsorption or desorption. Reprinted with permission from Parlar and Yortsos, *J. Colloid Interface Sci.* **124**, 162 (1988).

They used a Gaussian pore size distribution and a Bethe lattice of coordination number 4 (similar to Refs. [33, 38]), to model desorption. Contrary to the latter studies, however, they used results from DFT rather than Kelvin's equation. They showed that the percolation approach matched the qualitative behavior of the experimental data of Burgess *et al.* [77] much better than the single-pore hysteresis models and concluded in favor of a percolation approach. Nonetheless, approaches that do not recognize accessibility or connectivity issues are still used. Essentially, these are equivalent to representing the pore network in terms of a bundle of parallel capillaries. Using a percolation approach, Seaton [27] interpreted the various types of hysteresis in the IUPAC classification.

By neglecting nucleation and spatial correlations (see also later), primary desorption curves can be inverted as follows:

1. For fixed Z and L, obtain from simulations a percolation probability curve $P(p;\ L)$ expressing the fraction of occupied sites in terms of the percolation variable p and the size L. Such curves can, in fact, be cataloged.
2. Convert desorption data into an equivalent liquid saturation vs pore radius curve, S_L vs r, using information on the pore volume of the sample and Kelvin's equation or other expressions.
3. Obtain $p(r)$, thus, the cumulative distribution function (cdf) $F_p(r) = \int_0^r \alpha_b(r)\, dr = 1 - p$, by making the identification $S_L(r) = 1 - P(p; L)$. Differentiation of this curve produces the desired pdf $\alpha_b(r)$.

An essentially identical approach is used to infer the pore-size distribution from mercury intrusion porosimetry (see later). An example illustrating the application of this algorithm using synthetic data is presented during the discussion of mercury porosimetry. The success of this method, however, relies on several assumptions, including the premise that pores are uncorrelated in space and that the coordination number Z and lattice size L are known. Correlation issues are also discussed later in the chapter.

The coordination number affects the percolation probability curve, mainly through its effect on the bond percolation threshold p_c, which for regular lattices in three dimensions has the approximate dependence

$$p_c \approx \frac{1.5}{Z}. \tag{40}$$

Larger Z leads to a smaller p_c, hence to a less sharp primary desorption curve. Can the coordination number be obtained from adsorption–desorption data? If one assumes that Mason's relation [Eq. (38)] is valid, then the simultaneous use of both primary adsorption and desorption data can be iteratively used to infer Z. In particular, Eq. (40) can be usefully employed

to match the point where the knee in the primary desorption forms. An alternative approach for estimating Z is based on secondary desorption curves. Using a Bethe lattice, Parlar and Yortsos [38, 39] found that the tangent of the local angle formed by secondary desorption (originating at fractions q_i and p_i) and primary adsorption curves satisifies

$$\frac{dS_{L,\mathrm{SD}}}{dS_{L,A}} = Z\frac{dp_i}{dq_i}\frac{(1-q_i)(q_i-p_i)}{(1-p_i)^2} \tag{41}$$

for arbitrary pore and throat size distributions. In conjuction with available adsorption–desorption scanning loops, Eq. (41) can then be used to estimate Z, without the need to rely on the restrictive assumption of Eq. (39). Du [89] performed simulations of primary adsorption and secondary desorption in regular lattices and found that the value of Z estimated using this approach (which is based on a Bethe lattice representation) is quite close to that assumed for a variety of lattices and coordination numbers. An analogous approach, but based on Mason's [36] results, was proposed by Rajniak and Yang [90].

Another method for the estimation of both Z and L makes use of the finite-size scaling of percolation [27, 29–31]. Proceeding with the assumption that industrially relevant porous particles are actually collections of smaller porous agglomerates with the same Z and L, Seaton and coworkers [27, 29–31] suggested that primary desorption data actually reflect finite-size effects, and proposed the following relation:

$$ZP(p;L) = L^{p-d}h[(Zp-1.5)L^{1/\nu}]. \tag{42}$$

Here h is a crossover function, depending only on the dimensionality of the lattice, D is the percolation cluster mass fractal dimension, d is the embedding (Euclidean) dimension, and ν is the correlation length exponent. Given that in Seaton's approach, the information on pore-size distribution is already available from the primary adsorption data, P is available as a function of p. Then the estimation of Z and L follows by matching experimental results with Eq. (42), where the function h is obtained independently from numerical simulations. Various estimates for Z (although some unrealistically large) and L were obtained with this procedure.

The application of percolation approaches has been very useful for elucidating the effect of connectivity during desorption in pore networks. However, as discussed, the data interpretation still relies on several assumptions on the pore–throat size relationships and on the assumed lack of spatial correlations. These issues are generic to mercury porosimetry, as well, and are further discussed in the following.

3.4.3 Mercury Intrusion–Extrusion

Mercury intrusion–extrusion in a pore network shares many common aspects with sorption, capillary intrusion being analogous to desorption and extrusion being analogous to adsorption, respectively. As in the case of adsorption, to formulate forward and inverse problems in mercury porosimetry, we must consider phenomena at the two different scales, the single pore and the pore network. We also assume that capillary forces dominate over other forces, such as viscous and buoyancy.

The advance of a meniscus at the single-pore scale is best captured by considering a converging–diverging geometry of a circular cross section, as shown in Fig. 14. At conditions of capillary equilibrium, the mercury–air interface has a locally spherical shape with mean curvature

$$C^{m,a} = \frac{\cos(\theta + \phi)}{r}, \tag{43}$$

where θ is the contact angle of the meniscus (measured from the air side), ϕ is the local angle formed by the tangent to the pore surface at the contact line, and r is the radius of the cross section at the same point. As long as $\theta + \phi < \pi/2$, the interface curvature is positive. During drainage (depicted on the right schematic of Fig. 14), the interface configuration is stable before the meniscus reaches the pore throat (path AB in Fig. 14), since the curvature increases with an increase of the volume of the displacing phase, due to the decrease of both r and ϕ, and the condition of Eq. (21) is satisfied. At the point where the meniscus reaches the minimum pore throat radius r_b (point B in Fig. 14), however, further penetration leads to an unstable interface (dashed lines in the menisci of Fig. 14) as the curvature now decreases with increasing volume. As a result of this instability a nonequilibrium jump of the interface will ensue (path BCED in Fig. 14), until a new stable equilibrium position is reached downstream of the throat (point D in Fig. 14). This jump (B $\rightarrow$ D), known as Haines's jump or a rheon event [1], effectively corresponds to the penetration of the throat and the filling of the adjacent pore. Thus, filling of the downstream pore by the nonwetting phase occurs when the capillary pressure reaches the threshold

$$P_{cd} = \frac{2\gamma \cos\theta}{r_b}. \tag{44}$$

This step is the counterpart of pore-emptying in desorption.

Conversely, during imbibition in the same geometry (for example, by reversing the displacement, see schematic on the left in Fig. 14), the interface remains stable as long as withdrawal of the meniscus results in an increasing radius of curvature (path DE in Fig. 14). At the point where the maximum

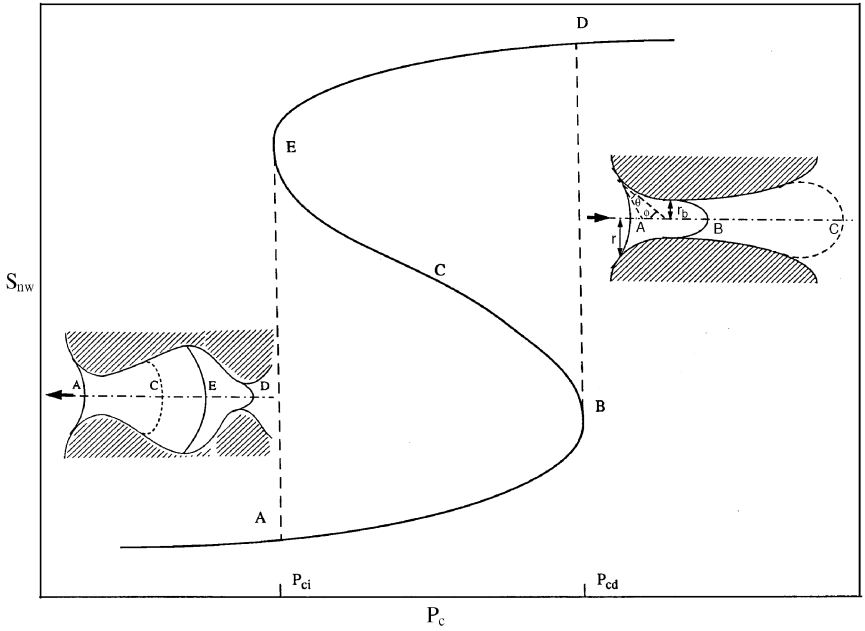

FIG. 14. Schematic of single-pore hysteresis during drainage–imbibition in a pore with converging–diverging geometry.

radius of the cross section is reached (point E in Fig. 14), however, further retraction will result in an unstable configuration (path ECBA in Fig. 14) and an interface jump (E → A) will occur. This Haines jump or hygron event [1] is the analogue of the pore-filling step in adsorption. Thus, in the geometry of Fig. 14, the emptying of the pore by the nonwetting phase is dictated by the maximum pore body size

$$P_{ci} = \frac{2\gamma \cos \theta}{r_s}. \tag{45}$$

Comparison of Eqs. (44) and (45) shows that the process is hysteretic ($P_{cd} > P_{ci}$) at the pore level. We recognize a close analogy with the single-pore hysteresis in sorption processes depicted in Fig. 8.

The stability of menisci in capillary equilibria in a variety of pore geometries has been studied by various authors [23–26, 87, 91]. Realistic geometries, however, involve pore junctions (as shown schematically in Figs. 2 and 12). Thus, the retraction of the interface during imbibition will also be affected by the interaction with other throats adjoining the pore. Indeed,

the filling state of adjacent throats affects the value of the capillary pressure at the point where the interface loses stability, leading to different withdrawal mechanisms and affecting the overall imbibition pattern [87]. Furthermore, the receding interface is subject to snap-off instabilities during retraction, the likelihood of which is primarily a function of the size aspect ratio between pores and throats. Consideration of these different mechanisms will give rise to cooperative phenomena between pores, as analyzed for the first time in square channel networks by Lenormand *et al.* [87]. These mechanisms have been incorporated in various pore network models developed since [24, 25, 92].

Consider, now, pore network effects during mercury intrusion. Early models of the intrusion curve were based on the model of noninteracting parallel capillaries (model of the bundle of tubes), where accessibility and percolation phenomena were ignored. In fact, such models formally correspond to pore networks with $Z = \infty$. Fatt [40] and Dullien [4] were among the first to recognize the need for a pore network description. In parallel with various numerical models [4, 24, 25, 92, 93], percolation-type approaches have also been proposed to model the forward and inverse problems [4, 91, 94–97]. Both bond percolation [94, 95, 98, 99] and mixed site–bond percolation [89, 91, 96] have been used. In these approaches, the volume of the invading nonwetting phase is related to the applied capillary pressure as follows. Assuming that all invaded elements (sites or bonds) have the same volume, percolation probability curves relate the saturation to the capillary pressure. For example, in simple bond-percolation models, we have

$$S_{\mathrm{nw}} = P(p) \quad \text{and} \quad P_c = \frac{2\gamma \cos\theta}{r}, \tag{46}$$

where P is the percolation probability curve (obtained by various authors using ordinary percolation [98] or invasion percolation [99] without trapping) and P_c is related to p through Eqs. (44) and (45). The implicit assumption is that of infinitesimally small pressure increments, such that only one pore throat (in fact the largest one available) is invaded at a time. Geometrical (but not kinetic) aspects of percolation during mercury invasion were demonstrated by Thompson *et al.* [100, 101], who analyzed the electrical resistance of invaded mercury as a function of the pressure step size (see also Ref. [102]). These authors also found important effects of gravity during the invasion and suggested that invasion percolation in a gradient may be better suited as a model of the process.

Volume-controlled mercury porosimetry [48, 92] (the APEX method) is also affected by pore network effects. This process can be connected to invasion percolation in the theoretical limit where the injection rate is

sufficiently small to allow for the resolution of the front as it advances one pore at a time. During mercury intrusion, the capillary pressure fluctuates in the form of bursts of variable size, the characteristics of which reflect single-pore processes and have been analyzed in detail [48, 92]. We note that the analogous problem of fluctuations in IP (where, however, the pore is structureless) was analyzed by Roux and Guyon [103] (see also Maloy *et al.* [104]), who related the pressure jumps to percolation exponents. Constant pressure intrusion is, in principle, a subset of APEX in the sense that the envelope of the pressure fluctuations of APEX is the intrusion curve of constant-pressure porosimetry. An example of the use of a pore network model to simulate mercury intrusion–withdrawal in the APEX method is shown in Fig. 15 (from Ref. [92]). In addition to the intrusion part, simulations of withdrawal and scanning loops are shown. The withdrawal algorithm includes snap-off of the retracting interfaces and the entrapmemt of mercury ganglia.

Inverting the intrusion data from porosimetry to obtain information on the pore-size distribution was suggested early [105–107]. The use of percolation theory facilitates this analysis, just as in the case of primary desorption. As long as P_c remains below a threshold level $P_{cd} = 2\gamma \cos\theta / r_c$, corresponding through Laplace's [Eq. (20)] to a bond radius r_c, significant (sample-spanning) penetration of the sample by mercury will not occur (see Figs. 4 and 15). The threshold r_c is related to the percolation threshold of the pore network p_c, here taken to be bond percolation

$$\int_{r_c}^{\infty} \alpha_b(r)\, dr = p_c \tag{47}$$

which for cubic lattices is approximately equal to 0.25. Clearly, larger values of the coordination number lead to smaller p_c, hence to larger r_c, and to smaller P_{cd}. Scaling the capillary pressure curve with the threshold P_{cd} has been found to effectively collapse mercury-porosimetry data in many sandstones [91] and it is the basis (along with the relation between r_c and the medium permeability, e.g., see Ref. [108]) of the so-called Leverett function. The subsequent filling of the pore space is dictated by its accessibility. As in desorption, the algorithm for inverting mercury intrusion data is straightforward.

Given a lattice type and size, the fraction of the sites X_s occupied during percolation can be computed and stored as a function of p. Assuming that pores are random and uncorrelated and that the volume of sites is unrelated to their nominal size r_s, the saturation of the invading phase can be identified with the fraction of sites invaded. Using the relationship between X_s and r from the experimental data and the relationship between X_s and

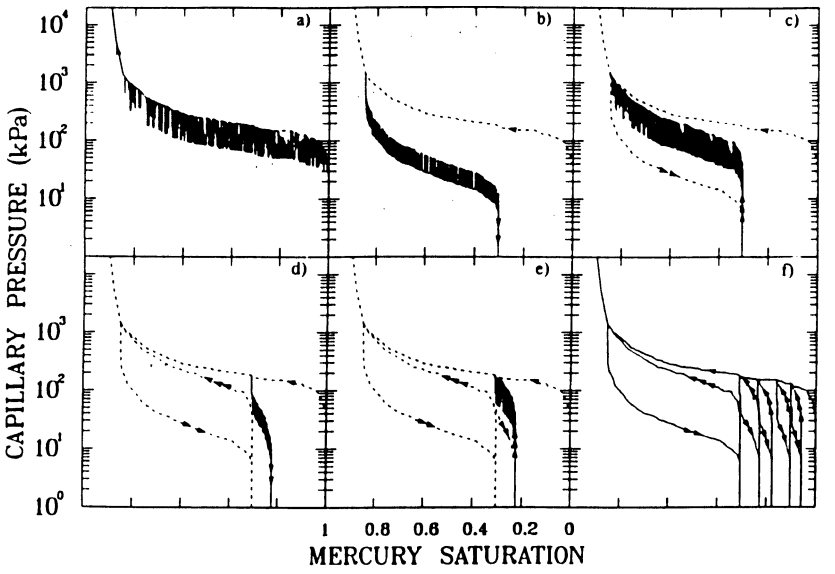

FIG. 15. Pore network simulation of various scanning loops of the APEX process in a cubic lattice with low-aspect ratio biconical pore segments. Reprinted with permission from Toledo *et al.*, *SPE Form. Eval.*, 46. Copyright 1994 SPE.

p from the network model, the curve $p(r)$ can then be reconstructed. Thus, the pdf of the throat size distribution $\alpha_b(r)$ can be obtained. As an example, we have for the simple percolation model [Eq. (46)]:

$$\alpha_b(r) = \frac{dS_{\mathrm{nw}}}{dP_c}\frac{dp}{dP}\frac{P_c^2}{2\gamma\cos\theta}. \tag{48}$$

The parallel tube model is included in Eq. (48) in the limit $P = p$. As in desorption, however, effective use of this inversion algorithm necessitates knowledge of Z. Typical results for the cdf of throat sizes from the inversion of the intrusion part of a mercury porosimetry curve using mixed site–bond percolation and $Z = 5$ are shown in Fig. 16. Results corresponding to the common method of the bundle of capillary tubes are also plotted. It is clear that the latter results in a narrower distribution, underestimating the width of the true distribution [4]. This mismatch increases as the coordination number decreases.

Information on the pore size distribution must be sought either by assuming a certain relation between q and p (see also later) or by methods other than constant-pressure mercury porosimetry. Inversion of the extru-

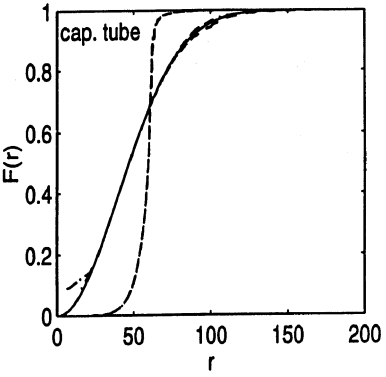

FIG. 16. The cdf of pore throat sizes, $F(r) = 1 - p(r)$, obtained by inverting a simulated capillary pressure curve using 3-D mixed bond-site invasion percolation in a $40 \times 40 \times 40$ lattice with average coordination number $Z = 5$. The solid line is the input cdf. The inverted data for three different realizations of invasion practically coincide with the assumed cdf, except near small sizes. The predictions of the capillary tube model are also shown as a dashed line (reprinted from Du [89]).

sion curve is subject to the additional complications of size aspect ratio and it is difficult to apply in practice. However, assuming a certain pore throat geometry, Toledo *et al.* [92] simulated volume-controlled porosimetry. Inversion of the pressure–saturation curve, which now involves pressure fluctuations, was done by interpreting the fluctuations of pressure according to local pore models. Both intrusion and withdrawal curves were analyzed and led to the distributions shown in Fig. 17. This approach appears to have considerable merit, compared to constant-pressure porosimetry, as it requires less restrictive assumptions. On the other hand, important assumptions on the correlation between pores and throats and the lack of spatial correlations still apply.

3.4.4 Some Additional Issues

The preceding inversion techniques are based on certain approximations. These include the relation between pores and throats and the absence of spatial correlations.

The question of the particular relation between the size distributions of pores and throats has been repeatedly raised in the literature. Typically, the following relations:

$$q \geqslant 1 - (1 - p)^Z, \qquad q^2 \geqslant p, \qquad q \geqslant p \tag{49}$$

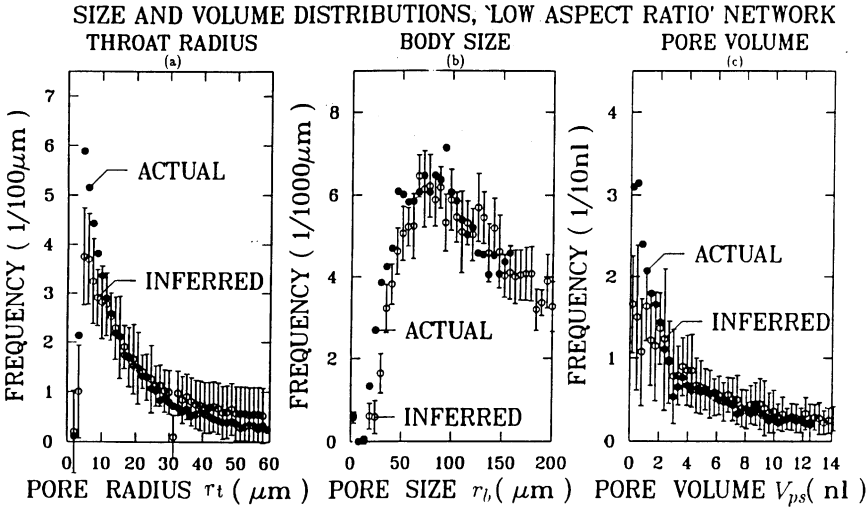

FIG. 17. Actual and inferred pore size and volume distributions from the inversion of simulated APEX in a cubic lattice with low-aspect-ratio biconical pore segments. Reprinted with permission from Toledo *et al.*, *SPE Form. Eval.*, 46. Copyright 1994 SPE.

have been postulated by Mason [33], Chatzis and Dullien [91], and Mayagoititia *et al.* [69–72] (their "first law"), respectively. Actually, in a pore network, two conditions are required: (i) a throat selected at random must have a size smaller than its adjacent two pores and (ii) a pore selected at random must have a size larger than its adjacent Z throats. These two conditions can be expressed by the following two relations between the pore size distributions:

$$\alpha_b(r) = 2 \int_r^\infty q(y)\, \alpha_s(y)\, g(y - r)\, dy, \tag{50}$$

where $g(x) \geqslant 0$ is the pdf of the difference between the size of a throat and its smallest adjacent pore, with the property $g(x) = 0$ for $x < 0$, and

$$\alpha_s(r) = Z \int_0^r [1 - p(y)]^{Z-1}\, \alpha_b(y)\, k(r - y)\, dy, \tag{51}$$

where $k(x) \geqslant 0$ is the pdf of the difference between the size of a pore and the largest of its adjacent throats, with the same properties as g, namely, $k(x) = 0$ for $x < 0$. Mason's results follow by taking $k(x) = \delta(x)$ in Eq. (51), while Chatzis and Dullien's expression results by taking $g(x) = \delta(x)$ in Eq.

(50), where $\delta(x)$ is the Dirac delta function. Specifying these two functions will lead to different relations between the pore size distributions.

The behavior of the processes will also be influenced by possible spatial correlations. These can develop either because adjacent pores and throats have a certain correlation, which may then propagate to create large-range spatial correlations in the network (e.g., see Zgrablich *et al.* [109] for sorption and Li *et al.* [23], and Tsakiroglou and Payatakes [110] for mercury porosimetry), or because spatial correlations exist as a result of the history of the formation of the medium (for example, due to diagenesis, chemical alteration, etc.). The effect of pore–throat correlations on mercury porosimetry has been numerically simulated and found to be important [110]. More generally, desorption and mercury intrusion in correlated systems must be analyzed by correlated percolation [111–117]. Aspects of this process have been studied by Renault [111] and Prakash *et al.* [112], who found that percolation thresholds depend on the structure of the correlation function. For example, for a correlation function with a slow (algebraic) decay (scaling as $\sim|\xi|^{-H}$, $H > 0$), Prakash *et al.* [112] found that the site percolation threshold in a square lattice decreases with H and approaches the value of 0.5 at $H = 0$ (compared to its random value of 0.59). For the case of growing spatial correlations, as is the case with self-affine fields of the fBm type, percolation thresholds become random variables with a variance that increases with the Hurst exponent [114–117]. Ensemble-average percolation probability curves were computed as a function of the Hurst exponent [117]. These curves have an effectively lower percolation threshold and near the threshold display a behavior similar to a finite-size effect in uncorrelated percolation. Given the stochastic aspects of this problem and its similarity to a finite-size effect, the unmasking of long-range correlations by inverting desorption or mercury intrusion data would be a difficult undertaking.

3.5 Conclusions

Sorption isotherms and mercury porosimetry are quite useful tools for the identification of key properties of pore surfaces and porous media in general. Surface roughness, pore size distributions, and possibly pore network connectivity can be probed by such methods. Given the nonuniqueness in the inversion of the data in various cases and the use of various assumptions in the forward modeling, however, interpretations using the current methods must be done carefully. These include identifying the various regimes for which a scaling behavior applies at low pressures in sorption or at high capillary pressures in mercury porosimetry, assessing the

relative volume contributions of pores and throats from the analysis of adsorption data, and identifying throat size distributions and the connectivity of the porous medium for desorption and mercury intrusion data. Despite the significant progress that has been made, important issues still remain open, including the particular interrelation in the sizes of pores and throats and the identification of spatial correlations.

Acknowledgments

The author would like to acknowledge the assistance of Lang Zhan in composing some of the figures of this chapter. The constructive criticism of an earlier draft by R. A. Guyer is also acknowledged. Given the space limitations, the references cited form only a partial list of the extensive literature of the various fields treated in this chapter.

References

1. N. R. Morrow, *Ind. Eng. Chem.* **62**, 32 (1970).
2. A. W. Adamson, *Physical Chemistry of Surfaces*, Wiley, New York (1990).
3. S. J. Gregg and K. S. W. Sing, *Adsorption, Surface Area and Porosity*, Academic Press, New York (1982).
4. F. A. L. Dullien, *Porous Media: Fluid Transport and Pore Structure*, Academic Press, New York (1st ed., 1979; 2nd ed., 1991).
5. J. Lyklema, *Fundamentals of Interface and Colloid Science. Volume II: Solid-Liquid Interfaces*, Academic Press, London (1995).
6. D. Stauffer and A. Aharony, *Introduction to Percolation Theory*, Taylor and Francis, London (1992).
7. D. H. Everett, *Langmuir* **9**, 2586 (1993).
8. M. Jaroniec and R. Madey, *Physical Adsorption on Heterogeneous Solids*, Elsevier, New York (1988).
9. A.-L. Barabasi and H. E. Stanley, *Fractal Concepts in Surface Growth*, Cambridge University Press, Cambridge (1995).
10. T. Halpin-Healy and Y.-C. Zhang, *Phys. Rep.* **254**, 215 (1995).
11. B. Mandelbrot, *The Fractal Geometry of Nature*, W. H. Freeman, New York (1982).
12. J. Feder, *Fractals*, Plenum Press, New York (1988).
13. H.-O. Peitgen and D. Saupe (eds.), *The Science of Fractal Images*, Springer Verlag, New York (1986).
14. A. V. Neimark, *Phys. Rev. B* **50**, 15435 (1994).

15. D. Avnir (ed.), *The Fractal Approach to Heterogeneous Chemistry*, Wiley, New York (1989).
16. P. G. de Gennes, in *Physics of Disordered Materials*, D. Adler, H. Fritzche, and S. R. Ovskinsky, eds., p. 227, Plenum Press, New York (1985).
17. P. Pfeifer and M. W. Cole, *New J. Chem.* **14**, 221 (1990).
18. M. Kardar and J. O. Indekeu, *Europhys. Lett.* **12**, 161 (1990).
19. P. Adler, *Porous Media: Geometry and Transports*, Butterworth-Heinemann, London (1992).
20. P. B. Balbuena and K. E. Gubbins, *Langmuir* **9**, 1801 (1993).
21. A. C. Payatakes, C. Tien, and R. M. Turian, *AIChEJ* **19**, 58 (1973).
22. K. K. Mohanty, H. T. Davis, and L. E. Scriven, *SPE Res. Eng.*, 113 (1987).
23. Y. Li, W. G. Laidlaw, and N. C. Wardlaw, *Adv. Colloid Interface Sci.* **26**, 1 (1986).
24. C. D. Tsakiroglou and A. C. Payatakes, *J. Colloid Interface Sci.* **137**, 315 (1990).
25. M. A. Ioannidis and I. Chatzis, *J. Colloid Interface Sci.* **161**, 278 (1993).
26. P. G. Toledo, L. E. Scriven, and H. T. Davis, *SPE Form. Eval.*, 61 (1994).
27. N. A. Seaton, *Chem. Eng. Sci.* **46**, 1895 (1991).
28. N. A. Seaton, J. P. R. B. Walton, and N. Quirke, *Carbon* **27**, 853 (1989).
29. H. Liu, L. Zhang, and N. A. Seaton, *Chem. Eng. Sci.* **47**, 4393 (1992).
30. H. Liu, L. Zhang, and N. A. Seaton, *Langmuir*, **9**, 2576 (1993).
31. H. Liu, L. Zhang, and N. A. Seaton, *J. Colloid Interface Sci.* **48**, 285 (1993).
32. H. Liu, L. Zhang, and N. A. Seaton, *Chem. Eng. Sci.* **49**, 1869 (1994).
33. G. Mason, *J. Colloid Interface Sci.* **88**, 36 (1982).
34. G. Mason, *Proc. R. Soc. London A* **390**, 47 (1983).
35. G. Mason, *J. Colloid Interface Sci.* **95**, 277 (1983).
36. G. Mason, *Proc. R. Soc. London A* **415**, 453 (1988).
37. V. P. Zhdanov, V. B. Fenelonov, and D. K. Efremov, *J. Colloid Interface Sci.* **120**, 218 (1987).
38. M. Parlar and Y. C. Yortsos, *J. Colloid Interface Sci.* **124**, 162 (1988).
39. M. Parlar and Y. C. Yortsos, *J. Colloid Interface Sci.* **132**, 425 (1989).
40. I. Fatt, *Trans. AIME* **207**, 144 (1956).
41. R. G. Larson, L. E. Scriven, and H. T. Davis, *Nature* **286**, 409 (1977).
42. P. G. de Gennes and E. Guyon, *J. Mec.* **17**, 403 (1978).
43. G. C. Wall and R. J. C. Brown, *J. Colloid Interface Sci.* **82**, 141 (1981).
44. R. I. Masel, *Principles of Adsorption and Reaction on Solid Surfaces*, Wiley, New York (1996).
45. D. P. Valenzuela and A. L. Meyers, *Adsorption Equilibrium Data Book*, Prentice Hall, Englewood Cliffs, NJ (1989).
46. K. S. W. Sing, D. H. Everett, R. A. W. Haul, L. Moscou, R. A. Pierotti, J. Rouquerol, and T. Siemineiewska, *Pure Appl. Chem.* **57**, 603 (1985).

47. J. J. Pickell, B. F. Swanson, and W. B. Hickman, *Soc. Pet. Eng. J.*, 55 (1966).
48. H. H. Yuan and B. F. Swanson, *SPE Form. Eval.*, 17 (1989).
49. D. Dollimare, P. Spooner, and A. Turner, *Surface Tech.* **4**, 121 (1976).
50. D. Oliver, *SPE Form. Eval.*, 290 (1992).
51. G. F. Carrier, M. Krook, and C. E. Pearson, *Functions of a Complex Variable*, McGraw-Hill, New York (1966).
52. C. W. Groetsch, *The Theory of Tikhonov Regularization for Fredholm Integral Equations of the First Kind*, Pitman, London (1984).
53. V. S. Mamleev and E. A. Bekturov, *Langmuir* **12**, 441 (1996).
54. D. Avnir, D. Farin, and P. Pfeifer, *J. Chem. Phys.* **79**, 13566 (1983).
55. D. Avnir, D. Farin, and P. Pfeifer, *J. Colloid Interface Sci.* **103**, 112 (1985).
56. J. M. Drake, P. Levitz, and J. Klafter, *New J. Chem.* **17**, 77 (1990).
57. S. Brunauer, P. H. Emmett, and E. Teller, *J. Amer. Chem. Soc.* **60**, 309 (1938).
58. P. Pfeifer, Y. J. Wu, M. W. Cole, and J. Krim, *Phys. Rev. Lett.* **62**, 1997 (1989).
59. A. V. Neimark, *Ads. Sci. Tech.* **7**, 210 (1990).
60. H. T. Davis, *Europhys. Lett.* **8**, 629 (1989).
61. J. C. Melrose, paper no. SPE18331 presented at the 63rd SPE Annual Fall Meeting, Houston, TX (1988).
62. D. Avnir and M. Jaroniec, *Langmuir* **5**, 1431 (1989).
63. Y. Yin, *Langmuir* **7**, 216 (1991).
64. A. V. Neimark, in *Fundamentals of Adsorption*, M. D. Le Van (ed.), Kluwer Academic, Boston (1996).
65. M. Kardar, G. Parisi, and Y.-C. Zhang, *Phys. Rev. Lett.* **56**, 889 (1986).
66. J. B. Sweeney, H. T. Davis, L. E. Scriven, and J. A. Zasadzinski, *Langmuir* **9**, 1551 (1993).
67. J. C. Melrose, *Langmuir* **3**, 661 (1987).
68. D. H. Everett and J. M. Haynes, *J. Colloid Interface Sci.* **38**, 125 (1972).
69. V. Mayagoitia, F. Rojas, and I. Kornhauser, *J. Chem. Soc. Faraday Trans. 1* **81**, 2931 (1985).
70. V. Mayagoitia, F. Rojas, and I. Kornhauser, *J. Chem. Soc. Faraday Trans. 1* **84**, 785 (1988).
71. V. Mayagoitia, B. Gilot, F. Rojas, and I. Kornhauser, *J. Chem. Soc. Faraday Trans. 1* **84**, 801 (1988).
72. V. Mayagoitia, M. J. Cruz, and F. Rojas, *J. Chem. Soc. Faraday Trans. 1* **85**, 2071 (1989).
73. M. W. Cole and W. F. Saam, *Phys. Rev. Lett.* **32**, 985 (1974).
74. P. C. Ball and R. Evans, *Europhys. Lett.* **4**, 715 (1987).
75. P. C. Ball and R. Evans, *Langmuir* **5**, 714 (1989).
76. R. Evans, U. M. B. Marconi, and P. Tarazona, *J. Chem. Soc. Faraday Trans. 2* **82**, 1763 (1986).

77. C. G. V. Burgess, D. H. Everett, and S. Nutall, *Pure Appl. Chem.* **61**, 1845 (1989).
78. C. Lastoskie, K. E. Gubbins, and N. Quirke, *Langmuir* **9**, 2693 (1993).
79. C. Lastoskie, K. E. Gubbins, and N. Quirke, *J. Phys. Chem.* **97**, 4786 (1993).
80. K. Binder and D. P. Landau, *J. Chem. Phys.* **96**, 1444 (1992).
81. P.I. Ravikovitch, S. C. O. Domhnaill, A. V. Neimark, F. Schuth, and K. K. Unger, *Langmuir* **11**, 4765 (1995).
82. D. Beaglehole and H. K. Christenson, *J. Phys. Chem.* **96**, 3395 (1992).
83. E. J. Wanless and H. K. Christenson, *J. Chem. Phys.* **101**, 4260 (1994).
84. H. K. Christenson, *Phys. Rev. Lett.* **73**, 1821 (1994).
85. J. E. Curry and H. K. Christenson, *Langmuir* **12**, 5729 (1996).
86. M. Jaroniec, *Langmuir* **11**, 2316 (1995).
87. R. Lenormand, C. Zarcone, and A. Sarr, *J. Fluid Mech.* **135**, 337 (1983).
88. A. V. Neimark, *Colloid J.* **46**, 813 (1984).
89. C. Du, PhD Dissertation, University of Southern California (1996).
90. P. Rajniak and R. T. Yang, *AIChEJ* **39**, 774 (1993).
91. I. Chatzis and F. A. L. Dullien, *Int. Chem. Eng.* **25**, 47 (1985).
92. P. G. Toledo, L. E. Scriven, and H. T. Davis, *SPE Form. Eval.*, 46 (1994).
93. G. P. Androutsopoulos and R. Mann, *Chem. Eng. Sci.* **34**, 1203 (1979).
94. R. G. Larson and N. R. Morrow, *Powder Tech.* **30**, 123 (1981).
95. A. A. Heiba, M. Sahimi, L. E. Scriven, and H. T. Davis, *SPE Res. Eng.*, 7 (1992).
96. C. E. Diaz, I. Chatzis, and F. A. L. Dullien, *Transp. Porous Media* **2**, 215 (1987).
97. G. P. Matthews, C. J. Ridgway, and M. C. Spearing, *J. Colloid Interface Sci.* **171**, 8 (1995).
98. B. K. Mishra and M. M. Sharma, *AIChEJ* **34**, 684 (1988).
99. Z. Zhou and E. H. Stenby, *Transp. Porous Media* **11**, 17 (1993).
100. A. H. Thompson, A. J. Katz, and R. A. Raschke, *Phys. Rev. Lett.* **58**, 29 (1987).
101. A. J. Katz, A. H. Thompson, and R. A. Raschke, *Phys. Rev. A* **38**, 4901 (1988).
102. J.-N. Roux and D. Wilkinson, *Phys. Rev. A* **37**, 3921 (1988).
103. S. Roux and E. Guyon, *J. Phys. A: Math. Gen.* **22**, 3693 (1989).
104. K. J. Maloy, L. Furuberg, J. Feder, and T. Jossang, *Phys. Rev. Lett.* **68**, 2161 (1992).
105. E. W. Washburn, *Proc. Natl. Acad. Sci.* **7**, 115 (1921).
106. W. R. Purcell, *Trans. AIME* **186**, 39 (1949).
107. N. T. Bourdine, L. S. Gournay, and P. P. Reichertz, *Trans. AIME* **189**, 195 (1950).
108. A. J. Katz and A. H. Thompson, *Phys. Rev. B* **34**, 8179 (1986).
109. G. Zgrablich, S. Mendioroz, L. Daza, J. Pajares, V. Mayagoitia, F. Rojas, and W. C. Conner, *Langmuir* **12**, 179 (1996).
110. C. D. Tsakiroglou and A. C. Payatakes, *J. Colloid Interface Sci.* **146**, 471 (1991).

111. P. Renault, *Transp. Porous Media* **6**, 451 (1991).
112. S. Prakash, S. Havlin, M. Schwartz, and H. E. Stanley, *Phys. Rev. A* **64**, 1724 (1992).
113. M. B. Isichenko, *Rev. Mod. Phys.* **64**, 961 (1992).
114. J. Schmittbuhl, J.-P. Vilotte, and S. Roux, *J. Phys. A: Math. Gen.* **26**, 6115 (1993).
115. M. A. Ioannidis and I. Chatzis, *Water Resour. Res.* **29**, 1777 (1993).
116. M. Sahimi, *AIChEJ* **41**, 229 (1995).
117. C. Du, C. Satik, and Y. C. Yortsos, *AIChEJ* **42**, 2392 (1996).

This Page Intentionally Left Blank

4. CONDUCTIVITY, PERMEABILITY, AND ELECTROKINETICS

Po-zen Wong

Department of Physics and Astronomy
University of Massachusetts
Amherst, Massachusetts

4.1 Introduction

The flow of fluids and ions in porous media occur in many natural and industrial processes; for example, filtration, catalytic reactions, and the spreading of contaminants in ground water [1–9]. The electrical conductivity σ and the hydraulic permeability k are defined by the usual Ohm's law and Darcy's law, which are similar in form:

$$\mathbf{J}_e = -\sigma \nabla \Phi \tag{1}$$

$$\mathbf{J}_f = -\frac{k}{\eta} \nabla P. \tag{2}$$

Here $\mathbf{J}_e$ denotes the macroscopic electric current density, $\mathbf{J}_f$ is the fluid-volume current density and η is the fluid viscosity, Φ and P are the scalar potential and pressure fields that drive the flow, and $\mathbf{J}_f$ has the unit of velocity and its magnitude is called the Darcy velocity v_{D}. The real fluid velocity in the pore v_p is related to v_{D} by $v_{\mathrm{D}} = \phi v_p$, where ϕ is the porosity. In petroleum exploration, the conductivity and permeability of sedimentary rock formations are routinely measured. Much of the discussion in this chapter is given in this context, but the principles and techniques are applicable to other systems.

In petrophysical studies, the rock conductivity σ is used in conjunction with other measurements to estimate the porosity ϕ and the water saturation S_w of the formation. For brine-saturated rock, the solid matrix is insulating and the pore fluid is conductive. The empirical correlation between the conductivity and porosity is known as the Archie's relation [10]:

$$\sigma \equiv \sigma_w / F \approx A \sigma_w \phi^m, \tag{3}$$

where σ_w is the conductivity of the brine and the dimensionless constant F

EXPERIMENTAL METHODS IN THE PHYSICAL SCIENCES
Vol. 35
ISBN 0-12-475982-3

ISSN 1079-4042/99 $30.00

is called the *formation factor*. For sandstones, Archie found that $m \approx 2$ and $A \approx 1$. This behavior is illustrated in Fig. 1 where the formation factors of artificial rocks made by fused glass beads (FGBs) are plotted against their porosities on log-log scales. We note that the data roughly follow the straight line that represents $m = 2$, and the size of the beads used to make the samples appears to have no effect [11]. Similar experiments using mixtures of different size beads confirmed this finding [12]. Since hydrocarbons can also be present in the pores and they are electrically insulating like the solid matrix, Archie suggested an extension of Eq. (3) for oil-bearing rocks:

$$\sigma' \equiv \sigma/I \approx \sigma S_w^n, \tag{4}$$

where $S_w < 1$ is the water saturation (the oil saturation is $S_o \equiv 1 - S_w$) and $n \approx 2$. The dimensionless constant $I \approx S_w^{-n}$ is known as the *resistivity index* [13]. The physical basis for this second relation is much less certain, however. As we saw in Chapter 2, fluids can have very different spatial distributions for a given saturation due to the displacement history, and the conductivity should vary correspondingly. Nevertheless, these equations

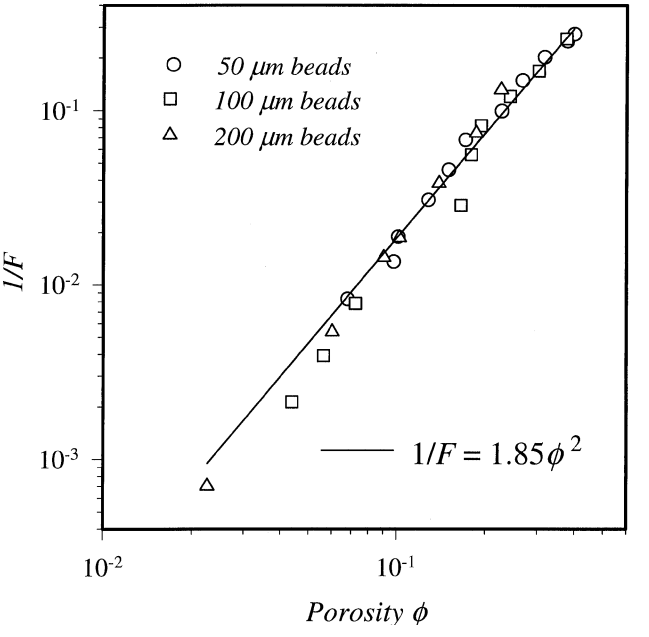

FIG. 1. The formation factor and porosity of fused-glass-bead samples follow the empirical Archie's relation [Eq. (3)] with $m \approx 2$ (from Ref. [9]).

show that rock conductivity plays an important role in estimating petroleum reserves. This is why a great deal of effort has gone into improving the measurements and studying the underlying physics.

For petroleum to be extracted, it must flow through the pores in the rock. The economic feasibility of a well depends critically on the permeability k of the formation. Oil shales, for example, have high oil contents that are difficult to extract due to their extremely low permeability. The management of the reservoirs would generally benefit from a good knowledge of the formation permeability, yet there is no simple way to measure it directly in the field. Permeability is usually inferred from other measurable quantities. It is reasonable to expect that k and σ are correlated because fluid and electric currents flow through the same network of pores. Archie actually suggested a correlation between k and ϕ analogous to Eq. (3), but it was not supported by his data and was never adopted in practice. How these quantities should be related remained unclear for a long time. A long-standing goal in the industry is to find a scientifically sound approach to determine k through other measurements. A notable suggestion is to use nuclear magnetic resonance (NMR) and porosity (or conductivity) [14, 15] (see Chapter 9). Another new approach is to use electrokinetic measurements (see Section 4.4) [16, 17]. These would not have been possible without a basic understanding of the underlying physics.

Theoretical understanding aside, no genuine progress can be made without good experimental data. Given the long history of conductivity and permeability measurements, one might think that the experimental techniques are standard affairs that require little discussion. This, however, is not quite the case. If different laboratories were asked to determine the formation factor of the same rock sample independently, chances are that the results would vary much more than those for an ordinary resistor. Part of the difficulty has to do with sample handling [18, 19]; for example, the pore fluid may interact with the rock so that the fluid salinity and pore geometry can change with time, and the sample may not be in a simple ideal shape. Some problems are related to the measurement details such as sample cell design, choice of electrode material, and driving frequency. Additionally, there are issues related to the intrinsic physics of porous media. For example, permeability measurements are made by applying a pressure gradient across the sample, which inevitably distorts the pore geometry in a nonuniform way. Section 4.5 shows that the conductivity of rocks with partial oil and water saturations depends on the flow history. Taken together, one can see that reliable measurements of σ and k require considerable care.

This chapter describes some of the basic issues associated with both experimental techniques and theoretical understanding, focusing mainly on brine-saturated samples. Conductivity and permeability are separately ad-

dressed in Sections 4.2 and 4.3. In addition to the steady-state (DC) behavior, we discuss how AC measurements can give useful information. Several theoretical models are used to provide an understanding of the physical meaning of empirical parameters such as F and m. These models enable us to see that relationships between σ and k require additional knowledge of either the pore size or grain size. Data obtained on FGB and rock samples are used to illustrate the general idea. (Chapters 3 and 9 describe how mercury injection and NMR can be used to estimate the pore size, respectively.) Section 4.4 shows that the *effective pore size* can be determined *exactly* by *electrokinetic* measurements. *Electrokinetic phenomena* arise from the coupling between charge and fluid flow due to the presence of excess ions at the fluid–solid interface [20–23]. Using nonequilibrium thermodynamics, the linear response coefficients, called electrokinetic coefficients, can be used to relate k to σ rigorously, independent of any detail of the pore geometry. This theoretical prediction has been borne out by experiments on real rock and FGB samples. This chapter concludes with a discussion of the difficulties associated with multiphase flow measurements due to the nonequilibrium nature of the problem. We give an example of using x-ray imaging (see Chapter 8) in a conductivity experiment to account for the history dependence and large-scale spatial inhomogeneity in multiphase systems [24, 25]. Other examples of using magnetic resonance and acoustic imaging to study fluid flow are given in Chapters 10 and 11.

4.2 Electrical Conductivity

4.2.1 AC Technique

Conductivity measurements based on Ohm's law are simple in principle. However, when electrolytes are involved, they are somewhat more complicated. Because the current is carried by ions, a DC measurement would cause charge transfer across the interface that can only occur through redox reactions at the electrodes. This is generally undesirable and hence AC measurements are standard. On the other hand, AC impedance of the metal–electrolyte interface has unusual characteristics of its own that are not well understood [26]. In the standard two-terminal configuration, in which the same pair of electrodes are used to send current through the sample and sense the voltage drop, the applied voltage is kept well below 1 V to prevent electrolysis, but the interfacial impedance is in series with the sample impedance and the two are unseparable in the measurement. Figure 2a shows the result of such a measurement on a Berea sandstone sample

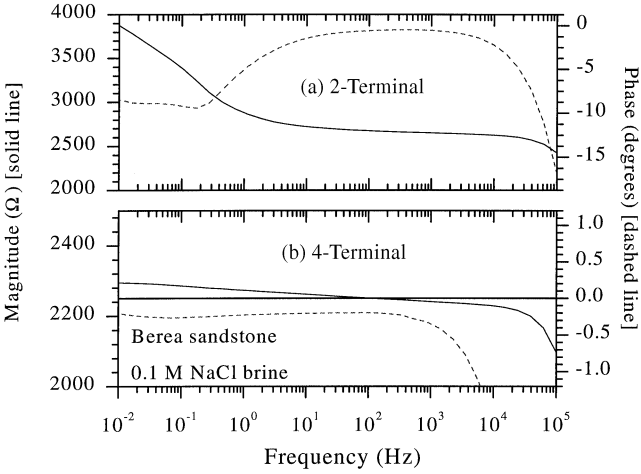

FIG. 2. Impedance measurements on a brine-saturated Berea sandstone using Ag/AgCl electrodes show that a two-terminal configuration (a) would result in anomalous frequency dependence due to electrode polarization. A four-terminal configuration (b) would avoid this artifact and reveal the small but nonzero phase angle due to the induced polarization (IP) of the sandstone. Why the phase angle is constant over a wide range of frequency is not fully understood, but is probably due to adsorption–desorption of counterions on the pore surface when an electric field is applied.

saturated with 0.1-M NaCl brine. There is a strong frequency dependence from 10 mHz to 100 kHz, which is caused by ions interacting with the electrodes and not a property of the sample. This can be easily verified by changing either the ion species or the electrode material. The electrodes used to obtain the data here were made of Ag/AgCl, which is regarded as a good reversible electrode that minimizes the interfacial polarization. The reason is that AgCl is a conducting material and it does not block the passage of charge. When an electrode has fine grains of silver and silver chloride on the surface, the presence of excess Cl^- or Ag^+ ions results in redox reactions that convert one material into the other, thereby reducing the charge accumulation, or electrode polarization. Indeed, we note that the magnitude of the conductivity in Fig. 2a varies by less than 10% from 10 Hz to 10 kHz, which covers the most commonly used frequencies. Suitable Ag/AgCl electrodes can be prepared by different means. The simplest and quickest approach we found was to apply household chlorine bleach on cleaned silver plates until they turn dull and gray. These plates are stored in NaCl solutions and kept electrically connected to each other. After a long time,

the surface conditions of the two electrodes become quite similar and, if disconnected, the DC voltage between them should be less than 50 mV.

The electrode polarization problem can be avoided by using a four-terminal configuration, that is, separate pairs of electrodes for sending the current and detecting the voltage drop. Figure 2b shows the data obtained on the same sample as in Fig. 2a with this approach. We note that there is only a very weak frequency dependence from 10 mHz to 10 kHz, which is a true property of the sample and not an artifact due to the electrodes. A small phase angle, roughly 0.2° in this case, remains constant below 1 kHz, and is common among shaley sandstone. This has to do with excess ions at the pore surface [27–30]. More concerning this is discussed in Section 4.2.3. The construction of a typical sample cell is shown in Fig. 3a. The rock or FGB samples are cut into cylinders about 4 cm in length and 2 cm in diameter, mounted into a Lucite sleeve of outer diameter 1.25 in. (3.175 cm) with epoxy cement [31]. After curing the epoxy, the sample is saturated with

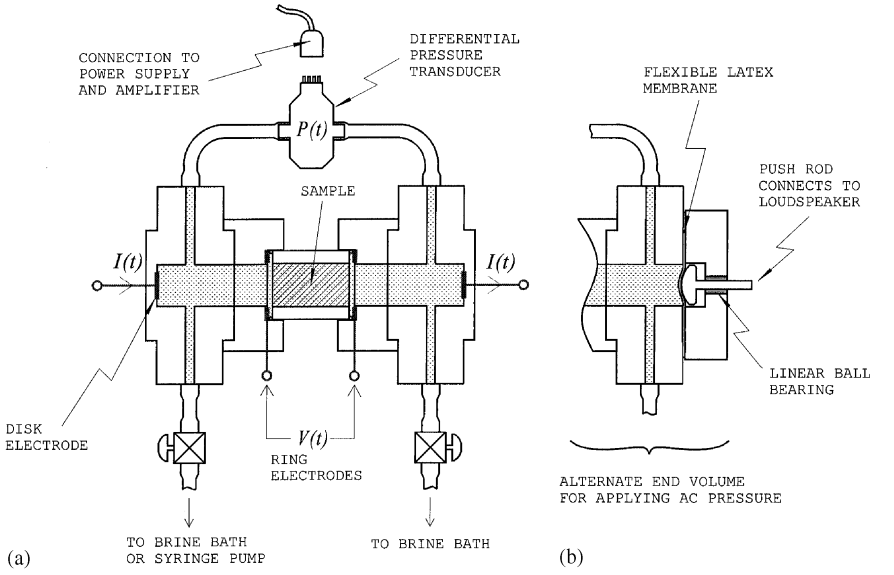

FIG. 3. An example of a sample cell that can be used for making transport measurements. The configuration on the left (a) has separate pairs of electrodes for sensing the current and voltage, and a differential pressure transducer across the sample. It can be used for AC conductivity, AC electroosmosis and DC permeability measurements. By replacing one of the end pieces with the one on the right (b), an oscillating pressure can be applied. This can be used for AC streaming potential and AC permeability measurements. Reprinted from Wong and Pengra, in *Access in Nanoporous Materials*, Pinnavaia and Thorpe, eds., © 1995, with permission of Plenum Publishing.

the desired brine and mounted into the cell. It is clamped between two Lucite collars fitted with Ag/AgCl *ring electrodes* for sensing the voltage across the sample. The collars are held in place by two rigid Lucite blocks, each of which has a fluid cavity, and within it a Ag/AgCl *disk electrode* for passing electric current. The diameters of the disks and the cavities closely match that of the sample so that the electric current is uniformly distributed over the circular cross-sectional area. Any deviation from a perfectly cylindrical shape would result in error when the measured conductance is converted to conductivity. In Fig. 3a, the distance between disk electrodes is approximately 13 cm and each end cavity holds about 15 ml of brine. The overall dimensions of the cell are approximately $25 \times 10 \times 10\,\text{cm}^3$.

The circuit used for the measurement is shown in Fig. 4a. The AC voltage between the ring electrodes and that across a current-sensing precision resistor are sent to two isolation preamplifiers with unity gain. The preamplifiers convert the differential voltage inputs to single-ended outputs, referenced to a common ground. A digital frequency response analyzer (FRA) (e.g., Solartron 1255 [32]) is used to compare the phase and amplitude of the two voltages and to compute the sample impedance. The digital lock-in circuit [33] used in the FRA can determine the magnitude to better than 0.01% and the phase angle to better than 0.01° over a broad frequency range. The electrode polarization effect is removed in this method because the interfacial impedance of voltage electrodes are in series with the much larger input impedance of the preamplifier (typically greater than $10^9\,\Omega$). Hence, the voltage drop due to the interfacial impedance is a negligible part of the total signal. In addition, because the preamplifier is in parallel with the sample, the current that passes through the voltage electrodes is very small relative to what goes through the sample. This is the main reason for using the four-terminal configuration. Even if the electrodes were not carefully prepared or made of Ag/AgCl, the effect is minimal as long as the polarization voltage is not so large as to cause the preamplifier to overload and misbehave.

4.2.2 Tortuosity, Formation Factor, and Archie's Exponent

Although the data in Fig. 2b show a very weak frequency dependence, they give a sufficiently good approximation of the DC resistance of the sample from which the formation factor F is computed. The usual assumption is that F depends only on the porosity ϕ. Figure 1 is a plot of F versus ϕ for a set of FGB samples made of different size beads [11]. It shows a behavior similar to what Archie originally observed for a diverse suite of sandstones, and is reasonably well represented by Eq. (3). Whether Eq. (3) has a deep physical meaning has been a subject of much discussion. Initial

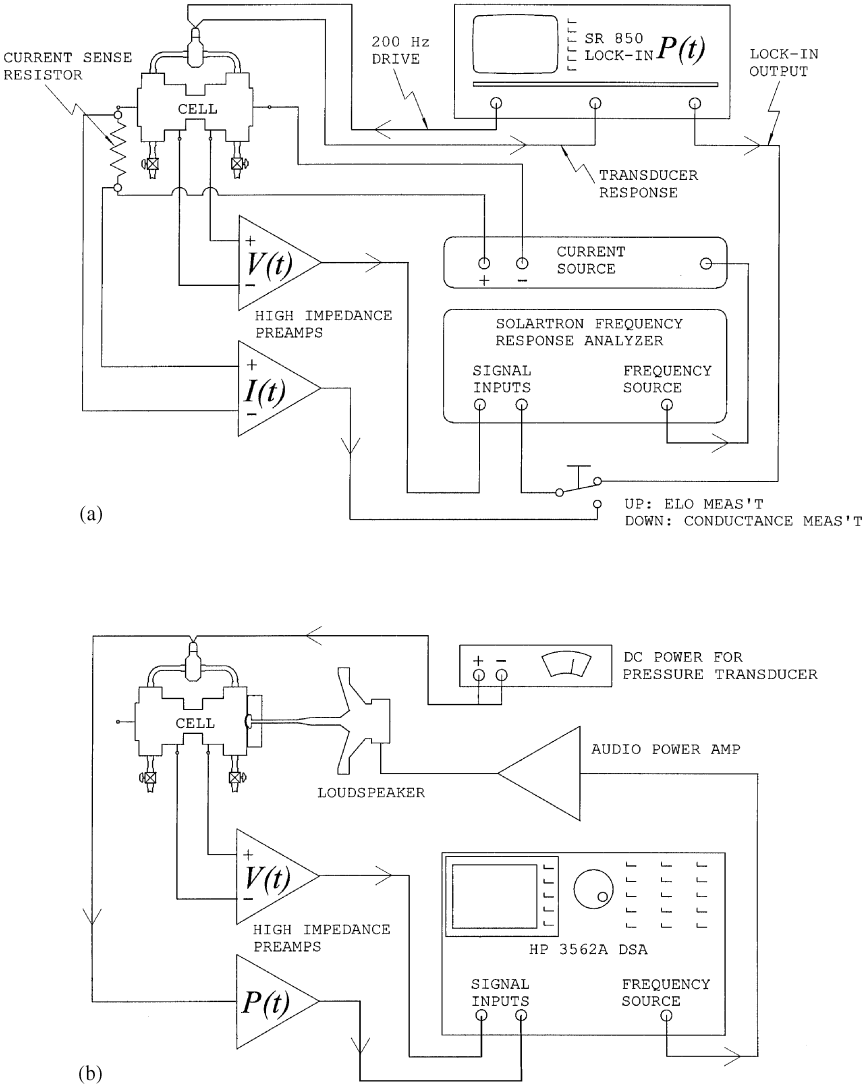

FIG. 4. Schematic circuits for (a) AC conductivity and AC electroosmosis measurements and (b) AC streaming potential and AC permeability measurements.

attempts to explain this empirical relation involve the use of various effective medium theories to calculate the complex dielectric constant of random two-component systems [34]. This works well for dilute colloidal suspensions in which the volume fraction of the insulating solid phase $(1 - \phi)$ is less than 40%, and $m \leqslant 1.5$ is observed [35]. However, they do not give a satisfactory account of well-consolidated porous media that have $\phi < 40\%$ and $m \approx 2$. These theories are also unable to provide a clear physical picture of the transport process. We describe here several models that have led to an intuitive understanding of the empirical behavior. In Section 4.3.2, we show that these models also enable us to establish simple relationships between σ and k.

The most primitive model for understanding transport phenomena in porous media treats the pores as a collection of tiny nonintersecting *wormholes* that meander through the solid matrix [36]. While this picture is overly simplistic, it introduces the important concept of *tortuosity*. In this model, we consider a slab of area A and thickness L, with N nonintersecting winding tubes going through it. If each tube has an effective length L_e and uniform cross-sectional area $A_e = \pi r_e^2$, the conductance is $\sigma_w A_e / L_e$. It is straightforward to show that the formation factor, as defined by Eq. (3), is

$$F = \frac{L_e / N A_e}{L / A}. \tag{5}$$

The porosity of the slab is given by $\phi = N L_e A_e / LA$ and the *tortuosity* α is defined by

$$\alpha \equiv F\phi = (L_e / L)^2. \tag{6}$$

Thus α is a measure of the tortuous nature of the flow paths. Since $L_e \geqslant L$ is always true, it follows that $\alpha \geqslant 1$. Using Eq. (3) for F, we can also write $\alpha \approx \phi^{1-m}$. Hence, $m \geqslant 1$ is always true and larger values of m imply more tortuous paths.

The parameters α and m take on quite different meanings if the pore space is modeled as a random network. A simple model that has been studied both numerically and analytically is known as the *shrinking-tube* (ST) *model* [11]. It treats the pore space as a set of straight pipes that are either connected in series in one dimension, or as a network on a square or cubic lattice in two and three dimensions. The pipes have identical radius r_o initially and they are reduced randomly by a multiplicative factor $a < 1$ to lower the porosity. The conductivity was computed numerically and analytically as a function of porosity and it was found to obey Archie's relation. The physical reason for this is that the random reduction process

resulted in a broad log-normal pore-size distribution. In the 1-D model, the narrow pipes dominate the resistance due to the series connection, but the wide pipes contribute more to the porosity. This is an explicit demonstration of the different effects of *throat size* and *pore size*. Large values of α and m indicate a large difference between the pore and throat sizes. We note that while the qualitative idea of *throat size* and *pore size* are well recognized, this model shows how they can affect the empirical parameters α and m. In the 2- and 3-D network models, it was found that Archie's behavior was also obeyed, but it resulted from the contrast between the *most-probable* radius r_{mp} and the *average* radius $\bar{r}$ of the random distribution. For a fully connected network with a broad distribution, the most-probable conductance ($\propto r_{mp}^2$) is a good estimate of the network conductance. In contrast, the porosity is directly related to $\bar{r}^2$ because the average volume of the pipe is $\pi\bar{r}^2\ell_g$, where ℓ_g is the length of the pipes (the lattice constant) in the model. In real rock, ℓ_g is roughly given by the size of the grains. Large values of m and α imply large differences between r_{mp} and $\bar{r}$ in a skewed pore-size distribution. Although the ST model is artificial, it shows that when the flow paths are connected like a network, it is not necessary to think about the tortuous nature of the flow paths. Instead, it is more useful to consider the formation factor F as the fundamental quantity that contains information about pore and grain sizes. The random simple cubic network can be replaced by a uniform one consisting of identical building blocks of size ℓ_g^3, each of which has a cylindrical pipe of radius r_{mp} along the flow direction. With this simplification, we have

$$F = \ell_g^2/\pi r_{mp}^2. \tag{7}$$

Another noteworthy model, called the *grain consolidation* (GC) *model* [37], treats a more realistic pore geometry than the ST model, but the main conclusion is similar. This model creates a porous medium by forming a dense random packing of uniform spheres on the computer and then allowing the sphere diameter to increase uniformly to mimic grain growth. The porosity is reduced by the growth. The conductivity σ and porosity ϕ were calculated during the growth process and the results fit the FGB data in Fig. 1 quite well. Like the ST model, the main conclusion is that the Archie's behavior results from the variations in the pore size. It is of interest to note that although σ was originally calculated by reducing the pore space into a network, subsequently it was improved by digitizing the pore space on a fine grid and performing random walk simulations [38]. The latter yields a diffusion constant (D) for ions in the porous media that is lower than the value in water (D_w). Using Einstein's relation, $\sigma \propto nD$, where n is

the density of the ions, we see that

$$\alpha = \phi F = \phi \frac{\sigma_w}{\sigma} = \frac{\phi n_w D_w}{nD} = \frac{D_w}{D}. \tag{8}$$

Thus the random walk simulations not only provide an efficient and accurate way to obtain the conductivity in arbitrary pore geometry, but they also actually give a new meaning to α as a ratio of diffusion constants [39], just as F is the ratio of the conductivities in Eq. (3). In this connection, we can understand why α in Eq. (6) is the square of two lengths, but L_e and L should be interpreted as the *diffusion lengths* in bulk water and in water saturated porous media.

4.2.3 Surface Conduction and Transport Radius Λ

An implicit assumption made in the preceding discussion is that the brine conductivity in the pores is uniform, which requires the ion concentrations to be uniform. This is generally not true because excess ions always accumulate at the interface between dissimilar materials. The abundance of internal surface area in porous media implies that the surface ions can contribute significantly to the overall conductivity. In shaley sandstone, for example, the clay minerals carry *exchangeable* cations on the surface and some of them become solvated in the presence of water [40]. The solvated ions are lifted off the surface to form a diffuse charge layer. They can move within the layer, *exchange* position with ions in the bulk solution, and respond to applied electric fields. For other solids without such exchangeable ions, the free ions in the brine are attracted to the solid surface by electrostatic forces. One of the ionic species (e.g., Cl^-) can be chemically adsorbed in a tightly bound layer, called the Stern layer. The other ionic species (e.g., Na^+) then form a diffuse layer known as the Guoy–Chapman layer. The combination is often referred to as the *electrochemical double layer* [20–23]. The dividing plane between the two layers is known as the outer Helmholtz plane (OHP). The details of the layer structure depend on many factors, such as the adsorption energy on the surface, the solvation energy in water, the temperature and the brine concentration. For our purpose, it is useful to give a simple picture based on the Debye–Hückel theory that treats only the diffuse layer. It assumes that the ions in the brine are point particles that bear charge $\pm q$, and that the surface charge density qN_s is small enough to not cause a large potential change at the interface. For a simple 1,1-valent electrolyte (e.g., NaCl) of concentration N_0, the thickness of the diffuse layer (the *Debye–Hückel screening length* λ) for a

planar surface is

$$\lambda = \left(\frac{\varepsilon k_B T}{2q^2 N_0}\right)^{1/2}, \tag{9}$$

where ε is the dielectric permittivity of the brine and T is the absolute temperature. For a 0.2-M NaCl solution at room temperature ($N_0 \approx 1.2 \times 10^{26}\,\mathrm{m}^{-3}$, $T \approx 300$ K, $\varepsilon \approx 80\varepsilon_0 \approx 7.1 \times 10^{-10}$ F/m, and $q = e = 1.6 \times 10^{-19}$ C), Eq. (9) gives $\lambda \approx 7$ Å. The electrostatic potential at the hydrodynamic slipplane, called the *zeta potential* (ζ), obeys the relation [20]

$$\frac{2k_B T}{q} \sinh\left(\frac{q\zeta}{2k_B T}\right) = \frac{qN_s\lambda}{\varepsilon}, \tag{10}$$

which reduces to

$$\zeta = qN_s\lambda/\varepsilon \tag{11}$$

for $\zeta \ll 2k_B T/q$. Since $2k_B T/q \approx 50$ mV at room temperature, this requires $N_s \ll 3.1 \times 10^{17}\,\mathrm{m}^{-2}$, or less than one ion in an area of $(18\,\text{Å})^2$. We note that the amount of exchangeable cations in shaley sandstones are often measured in milliequivalents per milliliter of pore volume (meq/ml), denoted by Q_v [41]. A shale sample with 10% porosity, specific area of $1\,\mathrm{m}^2/\mathrm{cm}^3$ and Q_v of 1meq/ml would have a surface charge density of $6 \times 10^{19}\,\mathrm{m}^{-2}$, about 200 times larger than the preceding estimate. Clearly, in many practical situations, the assumptions of the Debye–Hückel theory are unrealistic. On the other hand, Section 4.4 shows that ζ can be determined from electrokinetic measurements and typical values are indeed below 50 mV [16, 17]; ζ was also found to be quite insensitive to the total cation density on the surface. This implies that only a small fraction of the surface ions are solvated. The fraction is determined by the relative strength of the adsorption and solvation energies and the temperature. Thus Eqs. (9–11) are still useful approximations to reality.

Experimentally, surface conduction manifests itself in two different ways. Fig. 5 illustrates how the conductivity of a shaley sandstone σ increases with the conductivity σ_w of the brine that fills the pores [39]. We note that the increases are nonlinear with brines of sodium chloride, but linear with tetraethylammonium chloride. The reason is that Na^+ ions have a large solvation energy, and some of the surface ions become mobile at room temperature. In contrast, $(C_2H_5)_4^+$ ions have negligible solvation energy and they remain tightly bound to the surface [30]. The difference between the two curves is generally attributed to *surface conductivity* σ_s. Since parallel conductances add, the surface conduction paths are considered to be in parallel with the bulk conduction paths. In reality, there are no clear

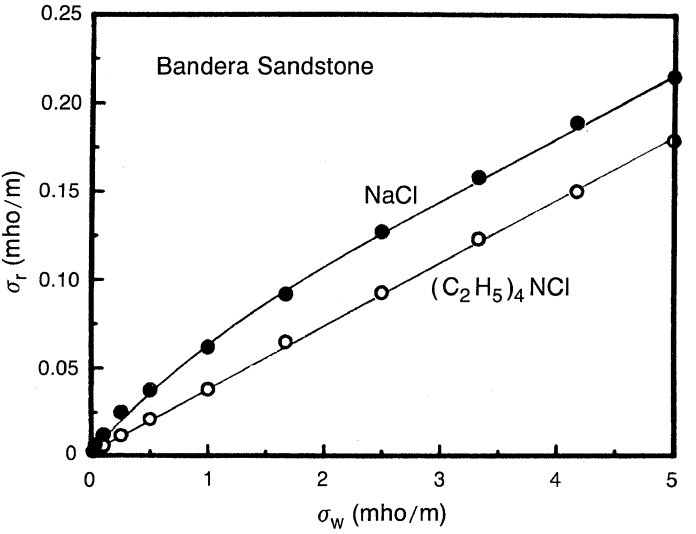

FIG. 5. Conductivity of brine-saturated sandstone shows a large difference depending on the cations in the solution. This is attributed to the mobility of the ions on the pore surface (from Ref. [39]).

divisions between these paths. Every ion can travel partly along the surface and partly in the interior of the pores as it moves through the sample. The second manifestation of surface conduction is the small phase angle seen in Fig. 2b, which remains roughly constant down to 10 mHz [27–30]. If the Na^+ is replaced by $(C_2H_5)_4^+$, this angle would become immeasurably small [30]. In samples with small surface charge densities such as fused glass beads, the angle is also much smaller. These observations indicate that the finite phase angle, or quadrature conductivity, is caused by the movement of surface ions.

In electrochemical studies, *constant-phase-angle* behavior observed in electrolytic cells has often been attributed to the geometric roughness of electrode surfaces [42], and sedimentary rocks are known to have fractal pore surfaces [43, 44]. Fractally rough surfaces are naturally associated with a wide range of length and time scales, hence having a frequency dependence that extends over several decades seem reasonable [39, 45]. However, more recent studies show that the behavior may simply result from the adsorption and desorption of ions on the surface [46, 47], that is, surface ions can go between the Stern layer and the diffuse layer as the concentration of the latter is disturbed by the flow of electric current. Since the adsorption–desorption process is thermally activated, on a heterogenous surface where

the variation in adsorption energy is large compared to $k_B T$, a broad frequency response is expected. Empirically, the complex rock conductivity data in Fig. 2b can be represented as the sum of a DC term and an AC term:

$$\begin{aligned}\sigma &= \sigma^{DC} + \sigma_s^{AC}\log(i\omega\tau) \\ &= \sigma_p^{DC} + \sigma_s^{DC} + \sigma_s^{AC}\log\omega\tau + i\pi\sigma_s^{AC}/2. \end{aligned} \tag{12}$$

The DC term, as depicted in Fig. 5, can be separated into pore volume and surface parts, σ_p^{DC} and σ_s^{DC}, respectively. The AC term is entirely due to the surface ions, with a logarithmic real part and a constant imaginary part. The phase angle of σ shown in Figs. 2b is

$$\theta = \tan^{-1}\frac{\pi\sigma_s^{AC}}{2(\sigma_p^{DC} + \sigma_s^{DC} + \sigma_s^{AC}\log\omega\tau)} \approx \tan^{-1}\frac{\sigma_s^{AC}}{2(\sigma_p^{DC} + \sigma_s^{DC})}. \tag{13}$$

That θ is small implies that $\sigma_p^{DC} \gg \sigma_s^{AC}$ in the brine saturated sandstone. Thus θ generally decreases with increasing water salinity, but its value also depends on the ionic species [30]. The value of θ is larger if part of the pore space is filled with oil, because σ_p^{DC} would be reduced and charged layers are present at the oil–water interfaces. If there are metallic minerals such as pyrite (FeS) present, the effect would also be stronger because metal–electrolyte interfaces are more highly charged [28]. The logarithmic change in the real part of σ is typically very weak and difficult to detect; for example, it is less than 0.5%/decade in Fig. 2b. Historically, it was the presence of an imaginary part in σ at very low frequencies that drew attention. It is commonly referred to as the *induced polarization* phenomenon and used in mineral exploration [28]. The physics of this phenomenon is not fully understood, but we expect ionic diffusion and thermally activated adsorption–desorption to occur when the charge density in the diffuse layer is disturbed. Clearly, at low enough frequencies ($\omega\tau \ll 1$) when all the relaxation mechanisms are exhausted, the imaginary part must vanish and the real part must tend to a constant.

The DC part of σ in Eq. (12) is reasonably well understood. Within the wormhole model, if we assume that each tube is coated with a thin layer of conductor with surface conductivity Σ_s, it simply adds a parallel conductance $2\pi r_e\Sigma_s/L_e$. The conductivity that results from having N such tubes in parallel in a slab with area A and thickness L is

$$\sigma^{DC} = \frac{\sigma_w N}{A/L}\left(\frac{\pi r_e^2}{L_e} + \frac{2\pi r_e\Sigma_s}{L_e}\right) = \frac{\sigma_w}{F}\left(1 + \frac{2\Sigma_s}{r_e}\right), \tag{14}$$

where we have used Eq. (5) for F. Despite the unrealistic nature of the model, this turns out to have captured the essential physics and Eq. (16) is consistent with empirical relations that had been widely used in the

petroleum industry [41, 48]. For arbitrary pore geometry, Johnson *et al.* [49] introduced a pore-size parameter Λ that plays the role of r_e. The parameter Λ is defined by

$$\Lambda \equiv 2\frac{\int |E_o|^2 \, dV_p}{\int |E_o|^2 \, dS_p}, \tag{15}$$

where E_o is the electric field strength in the pores in the absence of any interfacial charge (determined by solving the Laplace's equation for the given pore geometry), and the integrals are taken over the pore volume V_p and the pore surface S_p. In essence, this is a weighted average of the volume–surface ratio. The narrow throats of the pore space, where the field is strong and the current density is high, are weighted more strongly. Intuitively, Λ can be regarded as an *effective transport radius* that controls the current flow. Treating the surface layer as a perturbation, Johnson *et al.* [49] showed that, in the limit of large σ_w,

$$\sigma^{DC} \approx \frac{\sigma_w}{F}\left(1 + \frac{2\Sigma_s}{\Lambda}\right) \tag{16}$$

This result is identical to Eq. (14) except for a change from r_e to Λ, and F is defined by Eq. (3). It predicts that the slope of σ^{DC} versus σ_w is $1/F$ in the high-salinity limit, which agrees with the NaCl data in Fig. 5. The theory has been extended to explain the convex curvature seen in the NaCl data [50]. The asymptotic behavior in the low-salinity limit has also been studied with various models of surface roughness [51].

4.3 Hydraulic Permeability

4.3.1 DC Technique

Like conductivity measurements, measuring Darcy permeability is simple in principle, but the data are often not very reproducible. There are many factors that can cause complications, especially the chemical or physical interactions between the fluid and solid; for example, water can cause certain clays to swell, or hydrocarbons can have molecules that are not much smaller than some of the pores [52]. Gas is sometimes used to speed up the measurements as it is much less viscous than liquid, but flow with a high Reynolds number has many complications. These include turbulent effects and the fact that the density and viscosity of gas change with pressure throughout the sample [6]. Despite the fact that there are schemes to correct for some of these complications [53], permeability measured with gas and liquid flow can disagree considerably [41]. These complications are beyond

the scope of this chapter. We assume here that the measurements are made in the low-Reynolds-number limit, with an inert liquid that has molecules much smaller than the pore size, and that the liquid properties are uniform everywhere in the pores. Even with this idealization, there is the fundamental problem that most porous media are quite *soft* (compressible). Since the flow of liquid is driven by a pressure gradient, the sample is inevitably deformed more at one end than the other [54, 55]. Although the viscous pressure gradient in rock formation is very small, laboratory measurements of core samples are typically made with much stronger gradients to achieve a flow rate high enough to be measured accurately. The resulting distortion of the pore geometry would depend on the rigidity of the rock matrix. For example, we note that the typical figure for Darcy velocity in producing oil fields is $v_D = 1$ ft/day (about 1.3 cm/h or 3 μm/s). Clearly, it would take many hours to collect enough fluid to determine the flow rate accurately. A valid measurement of permeability requires applying several pressure gradients to generate different flow rates, and then using a linear regression to verify the proportionality in Eq. (2) [56]. Quite often, however, when the flow rate is plotted against pressure, the data do not fall on a straight line through the origin; that is, Darcy's law is *not* obeyed. Figure 6 illustrates this problem in a Berea sandstone sample with $k \approx 0.4$ D (1 D = 1 darcy = $0.987\,\mu m^2 \approx 1\,\mu m^2$). We note that even though the pressure difference across the 4-cm-long sample was quite modest (less than 0.5 bar), v_D ($\sim 10^2$ μm/s) is much larger than the 3 μm/s reference figure given earlier. A nonlinear behavior is evident in Fig. 6 where the slope of the plot varies by about 30%. Only the data points in the lower half of the range fit a straight line through the origin. In the upper half of the range, v_D increases faster than linearly, which implies that the applied fluid pressure opened up the pores and made the sample more permeable [16].

The data in Fig. 6 were obtained using the cell design shown in Fig. 3a. Contrary to the common practice of applying a pressure and measuring the volume of fluid that passes through in a given time, we used a microprocessor-controlled syringe pump [57] that could be set to deliver fluid at precise and constant flow rates. An Omega PX160 [58] piezoresistive transducer was used to detect the differential pressure across the sample. It has a sensitivity of 10 mV/psi ($\sim 1.5\,\mu V/Pa$) when powered by a 10-V DC voltage. The pressure as a function of time $P(t)$ was recorded by a computer during the flow. We observed that even though the flow rate was held constant, it took a finite amount of time after the flow started for the pressure to reach a steady value. The reason is that a finite amount of fluid must be injected to establish a compression that corresponds to the steady-state pressure. If the fluid cavity shown in Fig. 3a is large and the injection rate is low, then the waiting time can be very long. Since the speed of the syringe pump can be set by the computer, it is possible to program it with a higher flow rate

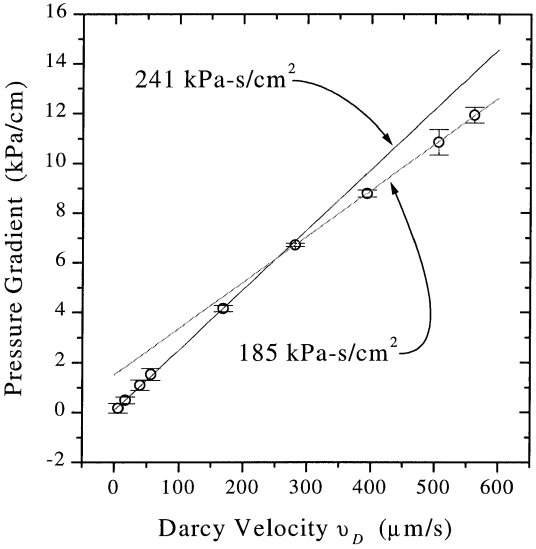

FIG. 6. In a typical laboratory measurement of brine permeability of of sandstone, the flow rate and pressure gradient can deviate from a linear dependence even with quite modest applied pressure. This plot, taken from Ref. [16], shows that the nonlinear behavior is noticeable in a 400-mD Berea sandstone sample when the pressure difference across a 4-cm sample is less than 0.5 bar. Copyright 1995 by the American Physical Society.

initially to achieve the desired pressure and then reduce the speed to a lower value for the actual measurement. It is important that the cell is constructed with a minimal amount of compliant materials (e.g., gaskets and tubing) so that a small volume of injected fluid can produce a large pressure change. In our cell, we found that the effective bulk modulus of the cavity ($\kappa \equiv V\delta P/\delta V$) was in the range of 10^5–10^7 Pa, which is much smaller than the bulk modulus for water ($\kappa_f \approx 2 \times 10^9$ Pa). This means that to obtain a pressure rise of 10^5 Pa in the 15-ml cavity, approximately 0.75 ml of fluid should be injected quickly. Some of the compressed fluid must go into the sample to establish a pressure gradient, and that also requires a finite amount of time. In the low-frequency limit, the propagation of the pressure field into the sample is known to be described by a diffusion equation [59, 60]:

$$D_p \nabla^2 P - \frac{\partial P}{\partial t} = 0, \tag{17}$$

where D_p is a diffusion constant. In the rigid frame limit where the rock is

assumed to be incompressible compared to the water, $D_p = k\kappa_f/\eta\phi$ [61]. For the general case in which both the solid frame and the fluid are compressible, the expression for D_p is more complicated [62], but Eq. (17) still holds. The time for building up the steady-state pressure gradient in a sample of length L_S may be estimated by the diffusion time

$$\tau_p = L_S^2/D_p. \tag{18}$$

Here τ_p sets the minimum time for a real measurement. It cannot be shortened significantly by using a computer because it is limited by how fast fluid can flow into the sample. For a sample with $L_S = 4\,\text{cm}$, $k = 100\,\text{mD}$, and $\phi = 0.2$, using $\kappa_f = 2 \times 10^9\,\text{Pa}$ and $\eta = 0.01$ for water, the rigid frame limit gives $D_p \approx 10^4\,\text{cm}^2/\text{s}$ and $\tau_p \approx 1.6\,\text{ms}$, which is short compared to typical DC measurement times. However, if the sample and the cell are compliant and the permeability is low, the equilibration can be much longer. For our apparatus, 10 min is typical.

4.3.2 Pore Size, Grain Size, and Permeability

Since fluid and electric currents flow through the same pore space, and Darcy's law and Ohm's law are similar in form, one would naturally expect a simple relationship between permeability and conductivity. However, such a relationship must involve the pore size. This can be seen most easily in the wormhole model where the permeability is simply determined by the Poiseuille flow in N parallel capillary tubes. Following the notation in Section 4.2.2, if a pressure difference ΔP is applied across a slab of area A and thickness L, the Darcy velocity is

$$v_{\text{D}} = \frac{1}{A}\frac{dQ}{dt} = \frac{N}{A}\cdot\frac{A_e^2}{8\pi\eta}\cdot\frac{\Delta P}{L_e} = \frac{N}{A}\cdot\frac{A_e^2 L}{8\pi\eta L_e}\cdot\frac{\Delta P}{L}. \tag{19}$$

Using Eqs. (2) and (5), we have

$$k = \frac{N}{A}\cdot\frac{A_e^2 L}{8\pi L_e} = \frac{A_e}{8\pi F} = \frac{r_e^2}{8F}. \tag{20}$$

This shows that k has an explicit dependence on the effective pore radius. It is also why the unit of permeability, darcy, has the dimension of length squared, as opposed to F, which is a dimensionless number. For more complicated pore geometry, as discussed in Section 4.3.3, Johnson *et al.* [49] suggested that a good approximation is to replace r_e by the effective transport radius Λ:

$$k \approx \frac{\Lambda^2}{8F}. \tag{21}$$

This prediction has been tested out in several theoretical models, including the GC model. Essentially the same result can be obtained in the ST model [11], in which a random network is replaced by a uniform one where all the tubes have the same length and radius. Letting $A/N = \ell_g^2$, $A_e = \pi r_{\mathrm{mp}}^2$, and $L = L_e$ in the first part of Eq. (20), we have

$$k = \pi r_{\mathrm{mp}}^4 / 8\ell_g^2 = r_{\mathrm{mp}}^2 / 8F, \tag{22}$$

where F is defined by Eq. (7).

A semiempirical approach was adopted by Katz and Thompson who arrived at a similar conclusion [63, 64]. They performed mercury injection (see Chapter 3) on rock samples and determined the critical pressure P_c at which the mercury first penetrated across each sample. Since mercury may be regarded as a perfectly nonwetting fluid, this defines a critical throat radius $\ell_c \equiv 4\gamma/P_c$, where γ is the surface tension of mercury. Using percolation theory, Katz and Thompson argued that

$$k \approx \frac{\ell_c^2}{226F}. \tag{23}$$

Their data, shown in Fig. 7, follow this approximate relationship quite well,

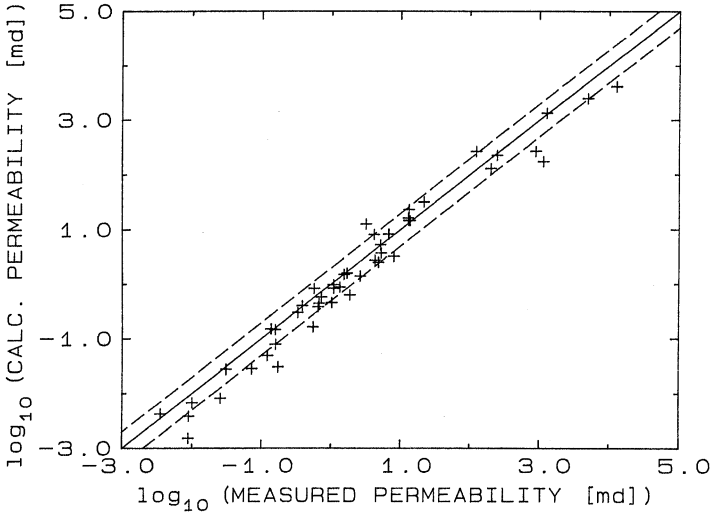

FIG. 7. The gas permeability of a large number of sandstones and carbonates show a good correlation with values calculated from Eq. (23). The dashed lines indicate departure from the calculated values by a factor of 2. Reprinted with permission from Katz and Thompson, *Phys. Rev. B* **34**, 8179. Copyright 1986 American Physical Society.

except that the correct prefactor given by percolation theory is actually 1/130 and not 1/226 [65]. The seemingly large difference in the numerical prefactors in Eqs. (21) and (23) is due to the theoretical definition of Λ and the empirical definition of ℓ_c. Since ℓ_c is a diameter, the ratio of the two length scales is $(2\Lambda/\ell_c) = (32/226)^{1/2} = 0.38$. That this value is of the order of unity shows that the underlying physical pictures are qualitatively the same.

The common element in all the preceding models is that the random pore space is represented by two quantities: the formation factor F and an effective pore size. Although these quantities are defined differently in each model, the resulting relationships between k and F in Eqs. (20–23) are of the same form. The main difference is in the meaning of the pore-size parameter that appears in the numerator. Since F is known from the conductivity ratio in Eq. (3), any measure of the pore size could be used to give an estimate of the permeability, provided that some empirical adjustment is made in the prefactor. The good correlation seen in Fig. 7 is one such example. The essential picture that emerges from various models allows one to find other sensible empirical correlations. For example, if the grain size instead of the pore size is known, we can substitute Eq. (7) into Eq. (22) and write

$$k = \ell_g^2/8\pi F^2. \tag{24}$$

This has been tested out in FGB samples made with different bead diameters D_b. Figure 8 shows data that span over 5 decades of permeability and they are well represented by the equation

$$k \approx D_b^2/76F^2, \tag{25}$$

consistent with Eq. (24) [9]. Chapter 9 describes empirical correlations between NMR relaxation time T_1 and k in real rocks, which are analogous to Eqs. (23) and (25) [14, 15]. The success in fitting the data shows that, despite the complicated geometry, the pore space can be conceptually replaced by an equivalent *uniform* network of cylinders. The relationships between k and F follow from the properties of a single cylinder in this uniform network. Other than a change in the prefactor, these relationships hold for real samples, provided that the pores are well connected. As discussed in Chapter 1, k and F can be calculated numerically by solving Laplace's and Stokes's equations using digital images of real materials. The results are also in good agreement with these relationships

4.3.3 Viscous Relaxation and Dynamic Permeability

Although permeability is usually measured under steady-state flow condition, AC measurements can yield useful information about the porous

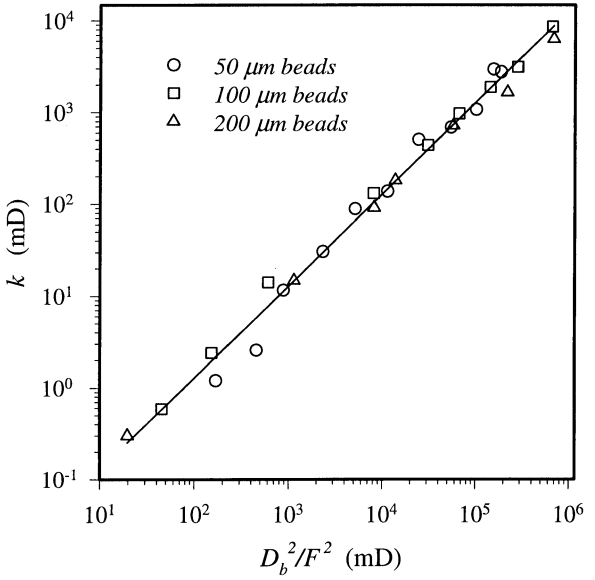

FIG. 8. Brine permeability of fused-glass-bead samples shows a good correlation with values calculated from Eq. (25), as indicated by the solid line (from Ref. [9]).

media. The essence of such measurements is to apply an oscillating pressure gradient ($\mathbf{V}Pe^{-i\omega t}$) on the sample and detect the corresponding flow current ($\mathbf{J}_f e^{-i\omega t}$), much like the AC conductivity measurement described in Section 4.2.1. The dynamic permeability $k(\omega)$ is defined by the Darcy's law in Eq. (2). Various groups have used AC techniques to study flow in capillary tubes [66]. Their techniques can be adapted quite straightforwardly for porous media using the sample cell and circuits that have already been described. Specifically, the cell in Fig. 3 may have one of the end pieces replaced by another one that is sealed with a flexible latex membrane. A linear bearing embedded in the Lucite block allows a push-rod to be placed against the membrane from the outside. The rod is attached to a loudspeaker that is driven by an audio power amplifier. This simple mechanism enables one to conveniently apply a small oscillating pressure on one side of the sample. The other side of the cell is connected in series to a small capillary tube of known permeability. Two separate pressure transducers are used to detect the pressure drops across the sample and the tube, the relative amplitude and phase of which can be determined with the digital lock-in circuit shown in Fig. 4a. There are two main cautions to observe in the measurement. First, the connection between the cell and the capillary must be made of

rigid materials, and the system should be free of trapped air bubbles. This ensures that all the fluid that flows through the sample also flows through the capillary; that is, the system is as close to being incompressible as possible. In reality, any finite compressibility implies a nonzero pressure diffusion time τ_p as given by Eq. (18). Thus the second caution is that the angular frequency ω must be small compared to $1/\tau_p$ so that a linear pressure drop is fully established inside the sample. (AC flow under more general conditions is considered in Chapter 5.)

Within the limits already defined, the fluid flow is well described by the Navier–Stokes equations:

$$\nabla \cdot \boldsymbol{v} = 0 \tag{26}$$

and

$$\nabla P = -\rho \dot{\boldsymbol{v}} + \eta \nabla^2 \boldsymbol{v}, \tag{27}$$

where ρ is the fluid density and $\boldsymbol{v}$ is the vector velocity field. If the fluid is at rest ($\boldsymbol{v} = 0$), upon the application of a pressure gradient, the initial response is governed by the inertial term $-\rho\dot{\boldsymbol{v}}$. After the flow reaches the steady state, $\dot{\boldsymbol{v}}$ is zero and only the viscous term remains. For a finite measurement frequency ω, the fluid is on average accelerated in one direction for a time $\tau \sim 1/\omega$. The velocity variation transverse to the flow direction occurs over a distance called the *viscous skin depth* ξ. A dimensional analysis of the two terms in Eq. (27) predicts [67, 68]

$$\rho/\tau = \rho\omega \sim \eta/\xi^2. \tag{28}$$

As the frequency is decreased, the velocity field has enough time to reach the steady-state configuration, ξ grows to the radius of the pore and $k(\omega)$ tends to a DC value k_o. In the high-frequency limit, $k(\omega)$ can be obtained by ignoring the viscous term in Eq. (27). Using the wormhole model, we note that the magnitude of ∇P in a fluid-filled winding tube is reduced from the macroscopic value by the length ratio L/L_e, and the real fluid velocity inside the pore is related to the Darcy velocity by $v = (v_D/\phi)(L_e/L)$. Substituting these in Eq. (27), and comparing it to Eq. (2), we can identify $\eta/k(\omega)$ with $-i\omega\rho(L_e/L)^2/\phi$. Using Eq. (6), we have

$$\lim_{\omega \to \infty} k(\omega) = i\eta/\omega\rho F. \tag{29}$$

Equating the magnitude of this high-frequency limit to k_o (the low-frequency limit) gives the characteristic relaxation frequency

$$\omega_c = \eta/\rho k_o F. \tag{30}$$

This proved to be a useful general result, because Eq. (20) for the wormhole

model is essentially the same as Eq. (21) for arbitrary porous media. The viscous relaxation time is defined by $\tau_c \equiv 1/\omega_c$.

Johnson *et al.* [68] suggested the complete viscous relaxation in $k(\omega)$ can be described by a simple function of the scaled frequency $\tilde{\omega} \equiv \omega/\omega_c$:

$$k(\omega) = \frac{k_o}{(1 - iM\tilde{\omega}/2)^{1/2} - i\tilde{\omega}}, \tag{31}$$

where $M \equiv 8kF/\Lambda^2$. Since Eq. (21) is a good approximation for most porous media, $M \approx 1$ holds true, and hence this function may be regarded as universal. Charlaix *et al.* [69] confirmed this prediction by measuring $k(\omega)$ on several water saturated samples. Figure 9 shows their data on three bead packs and two crushed glass samples with different particle sizes. A plot of the scaled permeability $k(\omega)/k_o$ versus the scaled frequency $\tilde{\omega}$ collapses all the data on to a universal curve. Fitting the individual data set to Eq. (31) gave M between 0.99 and 1.25. However, it should be noted that all the samples had high enough permeability so that the condition $\omega \ll 1/\tau_p$ was satisfied; ω_c also fell within the measurement window so that the entire relaxation behavior was revealed. Sheng *et al.* [70] studied several theoretical models and found that $M \approx 1$ held if the pore size varied smoothly near the throat region, but it failed if the throat size was defined by acute edges such that the flow field had to undergo abrupt changes. This is understandable because the former can be approximated by the behavior of a capillary tube and the latter cannot. According to Section 4.2.2, the pore space is usually a well-connected network and its behavior is much like that of a single capillary tube.

4.4 Electrokinetics

While we have emphasized the analogy between the flow of electric and fluid currents in the preceding sections, there is actually a direct coupling between the two currents due to the existence of the interfacial charge layer. This gives rise to electrokinetic phenomena. Textbook discussions of electrokinetics are usually given in the context of capillary tube geometry [20–23], but many laboratory studies have been carried out for random porous media [16, 17, 71–78]. It has also been proposed for use in large-scale geological survey [79–81]. In this section, we focus on high-precision laboratory measurements of the coupling constants and explain how they are related to σ and k. As we see, the coupling constants can be used to determine the effective pore radius r_e in Eq. (20) and ζ potential in Eq. (10). From these quantities, we can obtain the permeability k and surface charge density in the diffuse layer for any brine-saturated system.

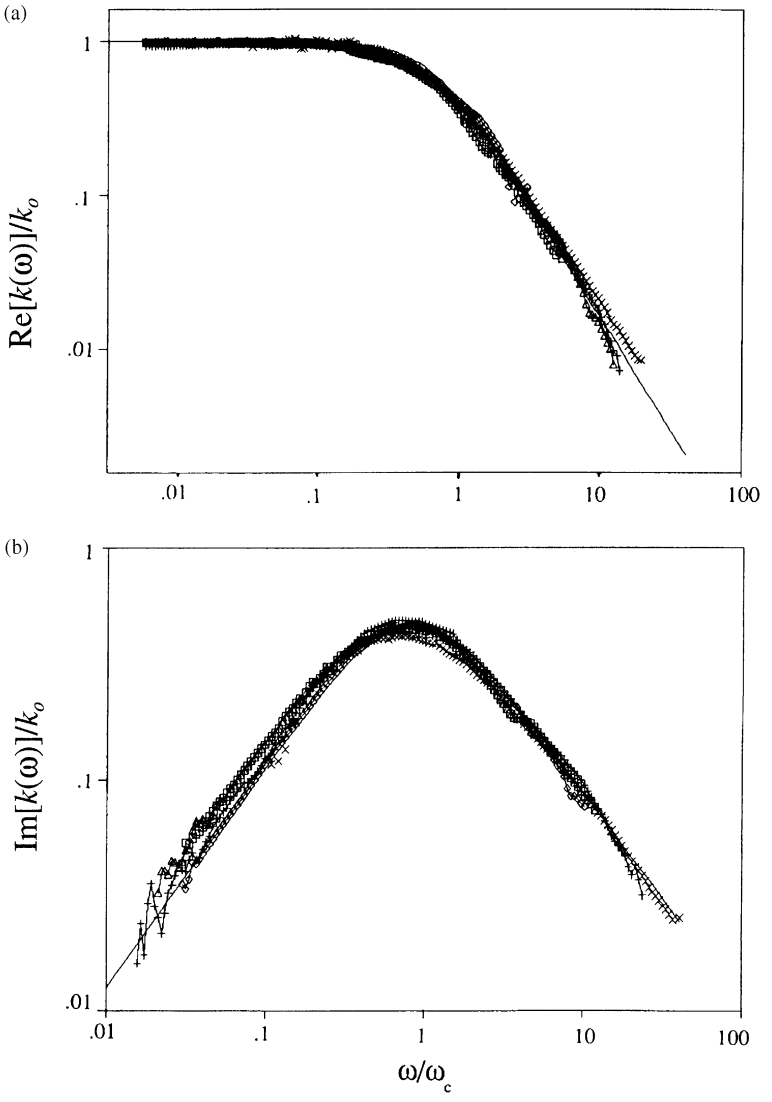

FIG. 9. AC permeability measurements made on three water saturated glass bead packs (diameter = 0.5, 0.95 and 1.7 mm) and two crushed glass packs (size range 0.35–0.71 mm and 0.71–1.05 mm) show that both the real and imaginary parts are well described by Eq. (31). Reprinted with permission from Charlaix *et al.*, *Phys. Rev. Lett.* **61**, 1595. Copyright 1988 American Physical Society.

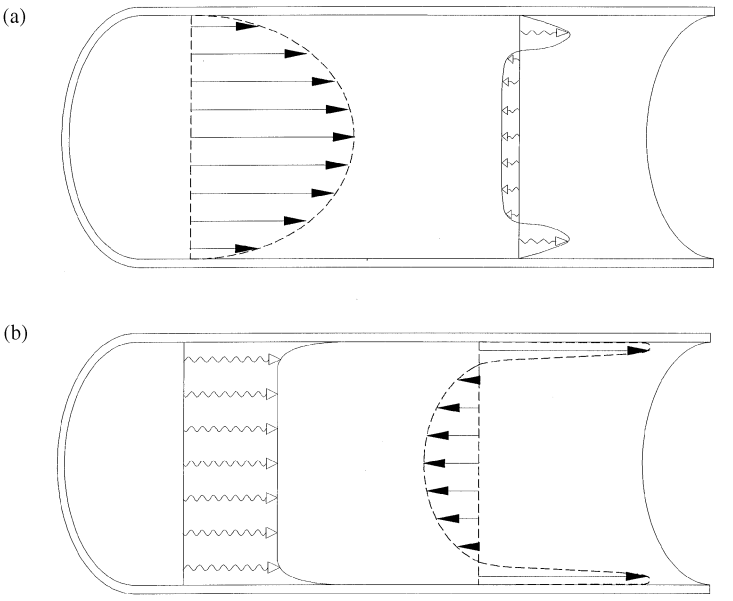

FIG. 10. Illustrations of electrokinetic couplings in a capillary tube. The solid arrows represent the fluid velocity field and the wiggly arrows represent the electric current density. (a) The situation when a streaming potential is established in response to a Poisueille flow of viscous fluid and (b) the situation when an electroosmotic counterpressure is developed in response to an applied electric current. Reprinted from Wong and Pengra, in *Access in Nanoporous Materials*, Pinnavaia and Thorpe, eds., © 1995, with permission of Plenum Publishing.

4.4.1 Streaming Potential, Electroosmosis, and Onsager's Relation

Since the ion densities in the diffuse charge layer are not uniform, the flow of fluid can lead to an electric current along the surface, and vice versa. Figure 10 illustrates the effect in a straight capillary, where the fluid velocity profile is represented by the straight arrows, and electric current density by the wiggly arrows. In Fig. 10a, a pressure difference ΔP_a applied across the tube drives the fluid to flow with a parabolic velocity profile. Assuming that the diffuse layer has excess cations, the viscous drag causes them to migrate in the same direction and results in a surface electric current, called the *streaming current*. As the cations accumulate downstream and excess anions are left upstream, a potential difference $\Delta\Phi_s$, called the *streaming potential* (STP), is developed and it drives a countercurrent in the bulk fluid. In the steady state, the total electric current is zero. The net effect is that an applied pressure generates a response voltage. The linear response coefficient K_S is

defined by

$$K_S \equiv -\Delta\Phi_s/\Delta P_a. \tag{32}$$

Figure 10b shows the reciprocal process known as *electroosmosis* (ELO). When a voltage $\Delta\Phi_a$ is applied across the tube, the excess cations in the diffuse layer give rise to a higher electric current density near the surface, and it drags along a fluid current, called the *electroosmotic current*. The flow would continue until an opposing pressure difference ΔP_e, called the *electroosmotic pressure*, is established. The linear response coefficient K_E is defined by

$$K_E \equiv -\Delta P_e/\Delta\Phi_a. \tag{33}$$

Similar effects exist in porous media due to their large internal surface area. We can measure K_S and K_E using the experimental cell depicted in Fig. 3 for conductivity and permeability measurements. For STP, a pressure difference ΔP_a is applied and the resulting voltage difference $\Delta\Phi_s$ is detected. For ELO, a voltage $\Delta\Phi_a$ is applied and the resulting pressure difference ΔP_e is detected. We note that ELO measurements must be made in a closed cell so that the induced fluid flow creates a compression in one cavity and a decompression in the other, thereby generating a counterpressure.

The significance of K_S and K_E can be first understood by considering Poiseuille flow in a uniform capillary tube, which can be extended to the *wormhole model* of porous media. Assuming that the tube wall is smooth and the tube radius is much larger than the screening length ($r \gg \lambda$), it can be shown that [20]

$$K_S^{\text{cap}} = \varepsilon\zeta/\eta\sigma_w \tag{34}$$

and

$$K_E^{\text{cap}} = 8\varepsilon\zeta/r^2. \tag{35}$$

These results are independent of the details of the potential and charge density variations in the diffuse layer. From these equations, we can see that by measuring two macroscopic coefficients, K_S^{cap} and K_E^{cap}, one can determine ζ and r for the tube. Adapting these results in the wormhole model for porous media, we can define an *effective zeta potential* [16, 17]

$$\zeta_e \equiv \eta\sigma_w K_S/\varepsilon \tag{36}$$

and an *effective pore radius*

$$r_e^2 \equiv 8\eta\sigma_w \frac{K_S}{K_E}. \tag{37}$$

According to Eq. (20), the permeabilty is

$$k = \frac{r_e^2}{8F} = \frac{\eta \sigma_w K_S}{F K_E} = \eta \sigma \frac{K_S}{K_E}. \tag{38}$$

Thus, within the *wormhole model*, the several *macroscopic* transport coefficients are directly related to each other. This result turns out to be a general relationship that can be proven on the basis nonequilibrium thermodynamics. Consequently, it is appropriate to regard Eqs. (36) and (37) as the definitions of the *effective zeta potential and throat radius* for random porous media.

To prove that Eq. (38) is a general result, we note that the presence of streaming current and electroosmotic current means that Eqs. (1) and (2) must be generalized to

$$I_e = -L_{11}\Delta\Phi - L_{12}\Delta P \tag{39}$$

and

$$I_f = -L_{21}\Delta\Phi - L_{22}\Delta P, \tag{40}$$

where I_e and I_f are the total electric and fluid currents. The L_{12} term represents the streaming current and the L_{21} term represents the electroosmotic fluid current. Also, $L_{11} = A\sigma_0/L$ is the uniform-pressure conductance of the system, and $L_{22} = Ak_0/L\eta$, where k_0 is the zero-electric-field permeability. The STP coefficient K_S is obtained when there is only fluid flow and no net electric current. Setting Eq. (39) to zero gives

$$K_S = -\left.\frac{\Delta\Phi}{\Delta P}\right|_{I_e=0} = \frac{L_{12}L}{\sigma_0 A}. \tag{41}$$

Similarly, K_E is obtained when there is only electric current and no net fluid current. Setting Eq. (40) to zero gives

$$K_E = -\left.\frac{\Delta P}{\Delta\Phi}\right|_{I_f=0} = \frac{L_{21}L\eta}{k_0 A}. \tag{42}$$

A celebrated result in nonequilibrium thermodynamics known as the *Onsager relation* states that $L_{12} = L_{21}$ in the steady state [82–84]. Using it in Eqs. (41) and (42), we obtain

$$\frac{k_0}{\eta} = \sigma_0 \frac{K_S}{K_E}, \tag{43}$$

which is almost (but not exactly) the same as Eq. (38), because k_0 and σ_0 do not have quite the same meanings as k and σ. The former are theoretical quantities for ideal situations with either $\Delta P = 0$ or $\Delta\Phi = 0$, but the latter

are measured quantities under the condition that both gradients are present. Using Eqs. (41) and (42) to eliminate $\Delta\Phi$ and L_{12} in Eq. (40), we have

$$I_f = -\frac{k_0}{\eta}\left(1 - \frac{L_{12}^2\eta}{k_0\sigma_0}\right)\Delta P = -\frac{k_0}{\eta}(1 - K_S K_E)\Delta P. \tag{44}$$

Similarly, using Eqs. (41) and (42) to eliminate ∇P and L_{12} in Eq. (39) gives

$$I_e = -\sigma_0\left(1 - \frac{L_{12}^2\eta}{k_0\sigma_0}\right)\Delta\Phi = -\sigma_0(1 - K_S K_E)\Delta\Phi. \tag{45}$$

Compared to Eqs. (1) and (2) that define σ and k, we see that

$$k = k_0(1 - K_S K_E) \tag{46}$$

and

$$\sigma = \sigma_0(1 - K_S K_E). \tag{47}$$

Substituting Eqs. (46) and (47) into Eq. (43) recovers Eq. (38), proving that it is a general property of the steady state, independent of any model. The wormhole model was used only to give a simple and more concrete physical picture. We should note that, using Eqs. (11), (34), and (35), the correction factor $(1 - K_S K_E)$ can be written as

$$1 - K_S K_E = 1 - \frac{L_{12}L_{21}}{L_{11}L_{22}} = 1 - \frac{8q^2N_s^2}{\eta\sigma_w}\left(\frac{\lambda}{r_e}\right)^2. \tag{48}$$

Clearly, the deviation from unity is important only if the surface charge density qN_s is high and the pores radius r_e is not much larger the screening length λ. In practice, this factor is close to unity for most situations, and hence the distinction between (k_0, σ_0) and (k, σ) is not widely appreciated. By the same token, this implies that K_S and K_E are small quantities that are not easy to measure. This is why high-precision data of K_S and K_E are scarce even though the existence of electrokinetic phenomena has been known for more than a century [85].

4.4.2 Experimental Method and Results

The primary difficulty in measuring the electrokinetic coefficients is that the induced voltage and pressure are quite small compared to typical experimental errors. In Wyllie's 1951 investigations of STP [86], fluid pressure up to a few hundred pounds per square inch (psi) was used to produce a voltage of about 10 mV, but the two signals are not linearly proportional to each other. This implies that K_S in Eq. (32) was not a constant. This may be attributed to the problems discussed in the preceding sections; for example, the pore structure can change with pressure and

electrode polarization effect can overwhelm the STP signal. Clearly, to make good measurements, one must keep the fluid pressure low and be able to detect voltage signals that are masked by a large background. Both of these goals can be accomplished with the cell and circuits shown in Figs. 3 and 4. The key point is to make AC measurements [87, 88, 89] using a lock-in technique [33]. In this method, the system is driven at a fixed frequency and the detector is an amplifier that is phase and frequency locked to the drive signal. By integrating the signal over enough cycles, noise that is uncorrelated with the driving signal is averaged out and a small signal hidden under the noise can be measured. The high sensitivity of the technique, in turn, enables one to drive the system with a small signal. The specifics given next are based on Refs. [16] and [17].

In our experimental cell, room noise and temperature drift of the pressure transducer give roughly 10 Pa pressure noise in the frequency window of the transducer ($\sim 15\,\mu$V root-mean-square [rms] over the range of 0–10 Hz), and electrode polarization produces broadband voltage noise at low frequencies (< 1 Hz) that varies by tens of millivolts. These have made electrokinetic measurements unreliable historically because typical values of K_S and K_E are of the order of 10^{-8} V/Pa and 1 Pa/V, respectively. Using the lock-in technique, we can detect STP voltage oscillations below 1 μV and ELO pressure oscillations below 1 Pa, well below the noise level. The measurements can be made over a spectrum of frequencies, as low as 1 mHz, to determine the DC limit where Eq. (20) is valid. The conductivity–permeability cell depicted in Fig. 3 can be used directly for ELO experiments because it is already fitted with electrodes and a pressure transducer. These can be used to measure the voltage and pressure across the sample simultaneously. The circuit shown in Fig. 4a requires only one small change: An AC current is still applied through the disk electrodes, but the FRA compares the AC pressure against the AC voltage across the sample. To achieve the necessary pressure sensitivity, the Wheatstone bridge built in to the piezoresistive transducer is driven by a 200-Hz AC voltage in a separate lock-in circuit. A lock-in amplifier (e.g., Stanford Research 850 [90]) is used as the null detector of the bridge and its output, which oscillates at the much lower frequency of the applied AC current, is sent to the FRA. This two-stage lock-in approach can detect pressure down to 100 mPa rms (or 15 nV output from the PX160 transducer when it is driven by a 1-V rms AC signal).

Figure 11b shows the ELO data for Berea sandstone saturated with 0.1-M NaCl brine. The frequency range of 1 mHz to 10 Hz is limited by the practical integration time at the lower end and the mechanical response time of the transducer at the upper end. A relaxation behavior is evident within this range and it is not seen in the conductivity data in Fig. 11a. It arises

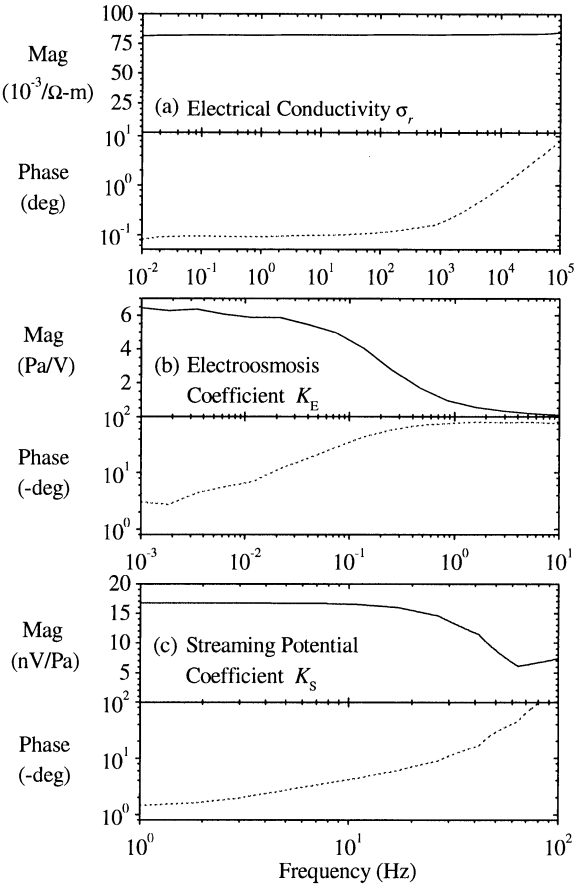

FIG. 11. The complex frequency response (magnitude and phase) of a Berea sandstone saturated with 0.1-M NaCl brine. (a) Conductivity σ, (b) electroosmotic coefficient K_E, and (c) streaming potential coefficient K_S (from Ref. [16]). Copyright 1995 by the American Institute of Physics.

from the fact that a finite amount of time is necessary to move enough fluid across the sample to create the counterpressure. It can be shown that the frequency response takes the form of a Debye relaxation [17]

$$K_E(\omega) = \frac{K_E}{1 + i\omega/\omega_r} \equiv B(\omega)e^{-i\delta}, \tag{49}$$

where ω_r is a characteristic angular relaxation frequency, or inverse relax-

ation time. The phase angle δ is given by

$$\tan \delta = \omega/\omega_r, \tag{50}$$

and the magnitude $B(\omega)$ is given by

$$B(\omega) = \frac{K_E}{\sqrt{1 + (\omega/\omega_r)^2}}. \tag{51}$$

For our cell, which has cylindrical cavities with the same cross-sectional area as the sample, it can be shown that

$$\omega_r \equiv \frac{2\kappa k}{\eta L_S L_F}. \tag{52}$$

where κ is the bulk modulus of the cavity (the fluid is assumed to be incompressible) and L_S and L_F are the lengths of the sample (~ 4 cm) and the cavity (~ 4.5 cm), respectively. Thus ω_r can be made higher if the cavities are smaller or more rigid, or if the sample is more permeable. As in AC permeability measurements, it is important to avoid air bubbles trapped in the fluid cavities because they would reduce the effective bulk modulus κ; that is, for a given amount of fluid movement, the pressure change would be much less. The cell was designed to have fluid inlets and outlets for each cavity so that air can be purged from the system. Figure 11b shows that the DC value is reached when the measurement frequency is well below ω_r. However, it is possible to measure δ and B at a higher frequency and use Eqs. (50) and (51) to solve for ω_r and K_E. If multiple frequencies are used, a least-squares fit can be made to improve the precision. It is of interest to note that the data in Fig. 11b give $\omega_r \approx 0.04$ Hz and $K_E \approx 6$ Pa/V. Using $k \approx 300$ mD in Eq. (52), we find that $\kappa \approx 10^5$ Pa for our cell. With an applied voltage of 1 V, about 0.1 µl of fluid moved across the sample. These figures demonstrate the high sensitivity of the AC method in detecting fluid flow.

For AC STP measurements, an oscillating pressure gradient must be applied. This is accomplished by using the modified end cavity in Fig. 3 for AC permeability measurements. We were able to achieve a pressure oscillation of 5 kPa rms (7.5 mV rms voltage output from the PX160 transducer) over the 0–10 Hz range. Since this signal is sufficiently high compared to the noise background, the transducer was driven with a 10-V DC power supply without using a second lock-in amplifier. The resulting AC STP voltage is detected by the ring electrodes. We obtain K_S by comparing this voltage against the applied pressure using the circuit shown in Fig. 4b. Just as in the circuit in Fig. 4a, the two signals go through a pair of isolation preamplifiers and then into an FRA (an HP3562A Dynamic Signal Analyzer [91] in this

case) for phase and amplitude comparison. Figure 11c shows the data obtained on Berea sandstone saturated with 0.1-M NaCl brine. Unlike the ELO data, the response is flat below 10 Hz, so there is no need to go to lower frequencies. The apparent relaxation above 10 Hz is due to the mechanical behavior of the transducer and the cell, not a property of the sample. The intrinsic STP relaxation is governed by the viscous relaxation frequency ω_c. According to Eq. (30), a pore radius of 10 μm corresponds to $\omega_c \sim 10^5$ Hz for water. Thus the AC data in Fig. 11c are indeed the steady-state property of the sample. It should also be noted that, unlike the dynamic permeability measurement, the frequency does not have to be small compared to $1/\tau_p$. Provided that the sample is uniform, because we measure only the voltage difference across the sample, whether it decreases linearly inside the sample is irrelevant. An important feature in Fig. 11 is that all three measurements show a small but finite phase angle at the low frequency. As discussed in Section 4.2.3, this is likely to be due to the adsorption and desorption of surface ions when the nearby charge density is disturbed. Some experiments have been done to investigate the effect by changing salinity, temperature, and cation species [92], but more is needed before a clear understanding can be reached.

For any sample, when K_E, K_S, and σ, are known, Eqs. (36–38) enable us to determine the effective zeta potential ζ_e, throat radius r_e, and permeability k. We refer to the latter as the *electrokinetic permeability* and denote it by k_e, as opposed to the Darcy permeability k_d obtained in the manner described in Section 4.3.1. For example, the data in Fig. 11 give $\zeta_e = 22$ mV, $r_e = 4.5$ μm, and $k_e = 220$ mD. Figure 12 shows a comparison between k_e and k_d for 12 samples with very different characteristics. Over 4 decades of permeability, the agreement is excellent. The electrokinetic approach is actually more reliable because it applies a much smaller pressure gradient and the pore geometry would not be deformed in any significant way.

4.5 Multiphase Systems

In this chapter, we have focused on the transport properties of insulating porous media saturated with conducting fluids, using mainly brine-saturated rocks and glass bead packs as examples. In general, the measurements can be done with high accuracy and the results are quite well understood. Empirical observations can be explained in simple physical terms and new quantitative predictions have been verified. The major puzzle that remains to be solved is the constant-phase-angle behavior associated with surface ions. To fully understand this phenomenon would require knowledge of the dynamics of the surface ions at a microscopic level. We have avoided discussion of multiphase systems — for example, rocks with partial oil and

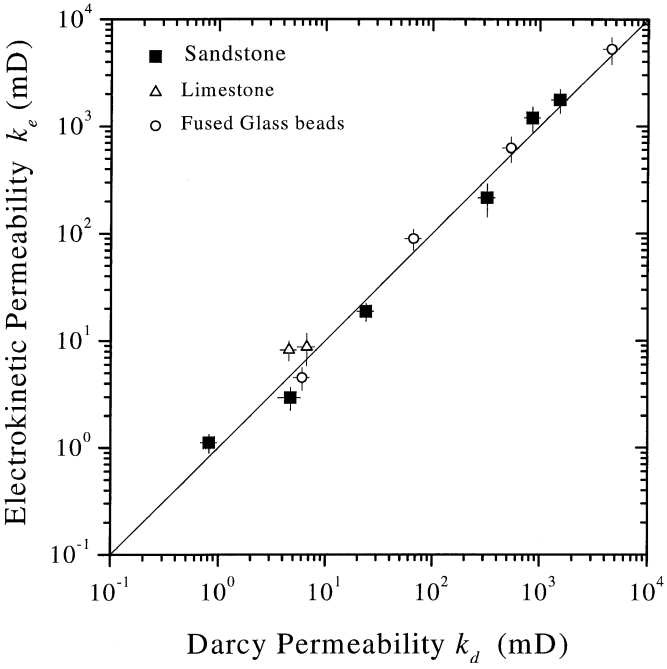

FIG. 12. A comparison between the electrokinetic permeability and the Darcy permeability confirms the prediction of Eq. (38). All measurements were made on samples saturated with 0.1-M NaCl brines (from Ref. [16]). Copyright 1995 by the American Institute of Physics.

water saturations in the pores—even though such systems are of great practical importance and measurements are routinely made. The reason is that the fundamental *physics* is much more complicated and the significance of the data is not easy to grasp. We offer here only a brief discussion of the problems to illustrate the challenges for future studies.

There are two major problems associated with multiphase systems. The first is the appearance of oil–water interfaces that are highly charged. Sprunt *et al.* [79] have observed large STP signals and have attributed them to the interfacial charge, but the physics is not fully understood. We can expect large effects on the surface conductivity and ELO as well. The second problem with multiphase systems is the difficulty of reproducing the experimental results. As shown in Chapter 2, fluid distribution in immiscible flow exhibits inhomogeneities on a wide range of length scales. It also depends critically on the flow history of the sample, because the presence of microscopic wetting films on the pore surface can have profound effects on

the macroscopic flow pattern. In other words, the fluid distribution is always out of equilibrium. There is no assurance that the data taken on a sample is either reproducible or representative of even *that* sample. Although Eq. (4) appears to be a logical extension of Eq. (3), the meaning of the resistivity index I is far less certain than the formation factor F. Because of the nonequilibrium nature of the system, one should not expect a simple correlation between the conductivity and the water saturation S_w without some further specifications. Different fluid configurations for a given saturation are expected to give rise to different conductivities. To understand such systems, the experiments should include characterization of the large-scale inhomogeneity as well as the flow history. The best way to approach such a study is to include some form of imaging to complement the transport measurements.

Figure 13 shows an apparatus that was developed to study vertical drainage and imbition [24, 25]. A cylindrical cell, 20 cm in length and 4.4 cm in diameter, filled with glass beads, has an array of voltage electrodes implanted along its length and a pair of current electrodes placed at the two ends. Using the four-terminal circuit shown in Fig. 4, the resistance of each section of the sample could be measured and the spatial variation characterized. 0.5-M potassium iodide solution was used as the wetting fluid and air as the nonwetting fluid. Two syringe pumps were used to maintain a constant flow rate in either direction. When one pump is injecting, the other refills. A set of switching valves and pressure transducers are controlled by a computer to ensure that the pressure changes smoothly. At any stage of the process, the flow could be made to pause and x-ray imaging could be carried out to determine the saturation profile along the cell (see Chapter 8). Figure 14a shows the data taken at 10-min intervals at a flow rate of 0.4 ml/min ($v_D \approx 4.4\,\mu m/s$). The range of bead diameters is 210–297 μm, which corresponds to a capillary number $Ca \equiv D_b^2 \eta v_D/\gamma k \approx 4.3 \times 10^{-5}$ and Bond number $Bo \equiv D_b^2 \rho g/\gamma \approx 8.5 \times 10^{-3}$, where γ is the surface tension. The three panels from top to bottom correspond to the first drainage from 100% water saturation, imbibition from irreducible water saturation, and second drainage from irreducible air saturation, respectively. The time sequence of evolution is indicated by the arrows. Figure 14b shows the resistance profiles that correspond to each of the saturations profiles. It is evident that there are large spatial variations along the sample. However, for a single section of the sample — for example, that indicated by the boxes drawn in dashed lines — the variation is not too large and a meaningful average value can be taken. Figure 15a shows how the resistivity index I varies with S_w for that section. A large hysteresis between drainage and imbibition is evident but the first and second drainage yielded almost the same result. The dotted line corresponds to $n = 1.85$ in Eq. (4), but offset

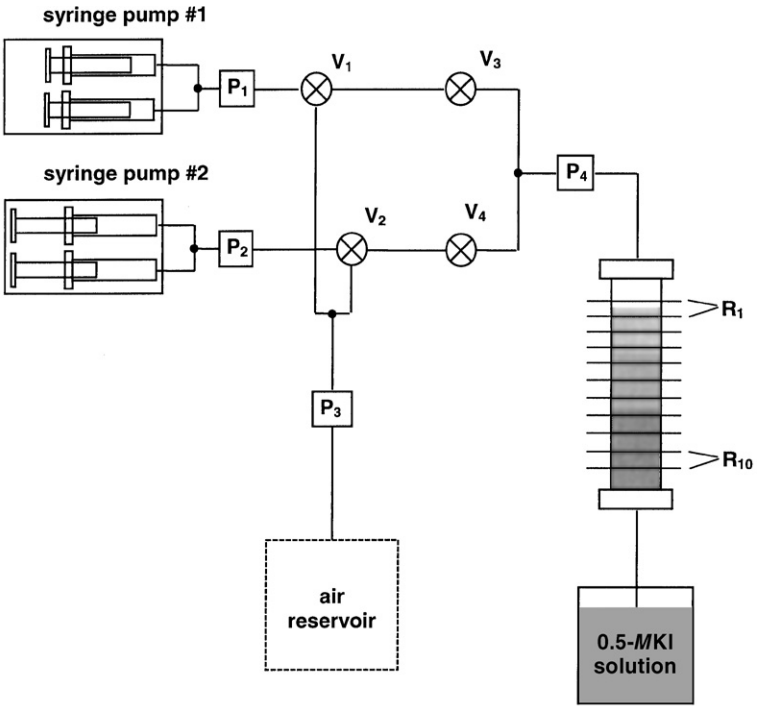

FIG. 13. Schematic diagram for an experimental setup for performing conductivity measurement during drainage and imbibition. Two syringe pumps and a set of valves are used to maintain a constant flow rate. A uniformly spaced array of electrodes is used to detect the variation in the sample along the flow direction. X-ray imaging can be made simultaneously to detect the saturation gradient (from Ref. [24]).

from the data to show the slope. Without the offset, all the drainage data points with $S_w > 0.2$ would lie on the dotted line; that is, the empirical Eq. (4) fits the data over much of the drainage cycle. This has also been observed in studies on sandstones [13, 93]. However, deviation occurs at low saturation. Figure 15b shows that if the drainage process did not pass the threshold at $S_w \approx 0.2$, the imbibition data would follow Eq. (4) as well. This example shows that it is important to explicitly take into account the large-scale *spatial variations* and *history dependence* that invariably exist in multiphase systems. Only with this additional information can we begin to characterize the system in a meaningful way and search for a physical understanding. X-ray imaging is used here for conductivity studies because the presence of metallic electrodes preclude the use of magnetic resonance

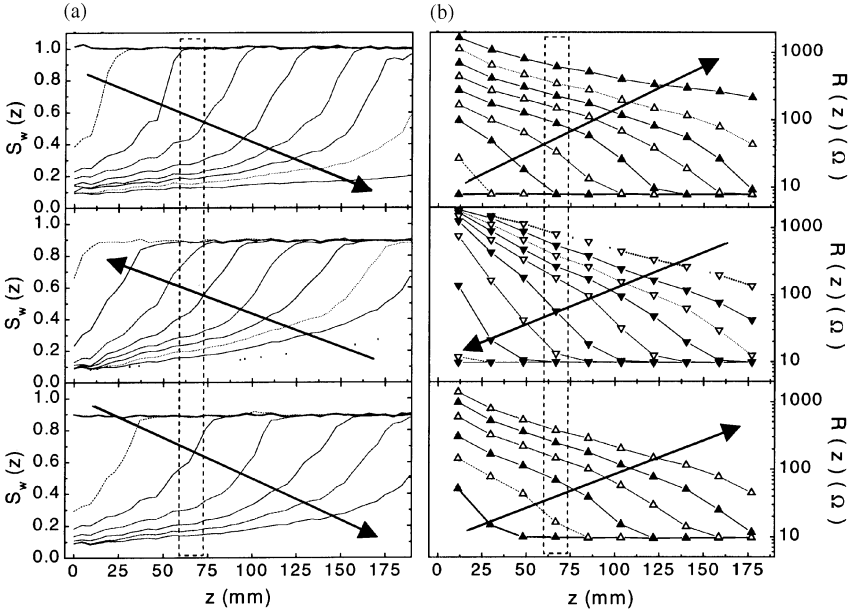

FIG. 14. (a) Saturation and (b) resistance profiles obtained on a column of glass beads saturated with 0.5-M KI brine using the apparatus of Fig. 13. The profiles were taken every 10 min and the distance z is measured from the top of the cell. The three panels from the top down correspond to the first drainage, the reimbibition, and the second drainage. The flow rate was 0.4 ml/min and the bead diameters were in the range 210–297 μm. The total pore volume of the samples was 140 ml (from Ref. [24]).

imaging (MRI). In Chapters 10 and 11, MRI and acoustic imaging are shown to be useful for measuring fluid velocity distribution and relative permeability.

Acknowledgments

My work in the topics discussed has benefited from collaborations and interactions with many students, postdoctoral associates, and colleagues over the years, especially Jaynath Banavar, Qizhong Cao, Peter Dimon, Robert Farrell, David L. Johnson, Eric Kawamoto, J. Koplik, Sidney X. Li, David B. Pengra, Lawrence M. Schwartz, Pabitra N. Sen, Arthur H. Thompson, and Joseph P. Tomanic. Some of the published works reviewed

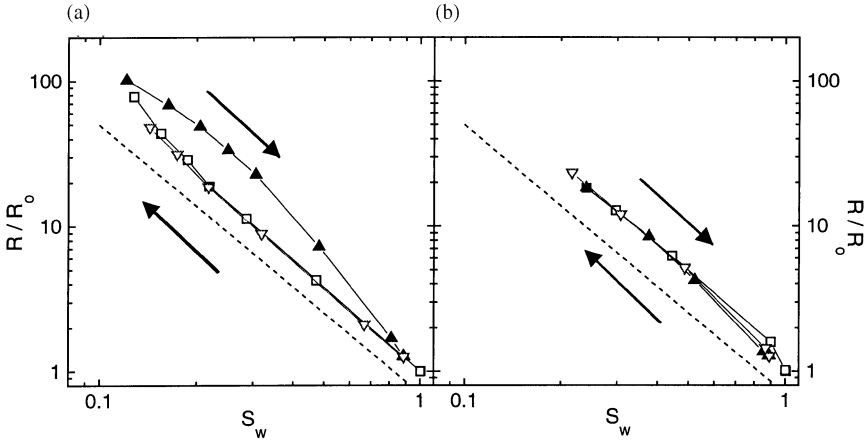

FIG. 15. The resistivity index and water saturation data extracted from the profiles in Fig. 14 for a single section of the column (bounded by the dashed lines in Fig. 14). (a) Over much of the drainage cycle, the data follow Eq. (4) with $n \approx 2$, but there is a large hysteresis in the imbibition cycle. (b) When the drainage cycle was not carried to irreducible saturation, the hysteresis in the imbibition data was insignificant (from Ref. [24]).

here received support from the Gas Research Institute, the National Science Foundation, and the American Chemical Society. I am indebted to David Pengra, Rosemary Sult, and Erik Spangenberg for their critical readings of the manuscript and many helpful suggestions.

References

1. F. A. L. Dullien, *Porous Media: Fluid Transport and Pore Structure* (Academic Press, San Diego, 1992).
2. M. Sahimi, *Flow and Transport in Porous Media and Fractured Rock: From Classical Methods to Modern Approaches* (VCH, Weinheim, 1995).
3. N. R. Morrow, ed., *Interfacial Phenomena in Petroleum Industry* (Marcel Dekker, New York, 1991).
4. J. Bear and A. Verruijt, Modeling Groundwater Flow and Pollution (Reidel, Dordrecht, 1987).
5. G. Dagan, *Flow and Transport in Porous Formations* (Springer-Verlag, New York, 1989).
6. A. E. Scheidegger, *The Physics of Flow Through Porous Media* (MacMillan, New York, 1960).

7. *Flow Through Porous Media* (American Chemical Society, Washington, D.C., 1970).
8. P.-z. Wong, *Physics Today*, **41** No. 12, 24 (1988).
9. P.-z. Wong, *Mater. Res. Soc. Bull.* **XIX** No. 5 (May), 32 (1994).
10. G. Archie, *Trans. AIME* **146**, 54 (1942). See also, A. M. Borai, *SPE Form. Eval.* (Dec. 1987), 495.
11. P.-z. Wong, J. Koplik, and J. P. Tomanic, *Phys. Rev. B* **30**, 6606 (1984).
12. E. Guyon, L. Oger, and T. J. Plona, *J. Phys. D* **20**, 1637 (1987).
13. M. H. Waxman and E. C. Thomas, *J. Pet. Tech.* (Feb. 1974), 213; *Trans. AIME* **257**.
14. W. E. Kenyon, P. I. Day, C. Straley, and J. F. Willemsen, SPE paper no. 15643 (1986).
15. A. H. Thompson, S. W. Sinton, S. L. Huff, A. J. Katz, R. A. Raschke, and G. A. Gist, *J. Appl. Phys.* **65**, 3259 (1989).
16. S. X. Li, D. B. Pengra, and P.-z. Wong, *Phys. Rev. E* **51**, 5748 (1995).
17. P.-z. Wong and D. B. Pengra, in *Access in Nanoporous Materials*, T. J. Pinnavaia and M. F. Thorpe, eds. (Plenum, New York, 1995); see also D. B. Pengra and P.-z. Wong, in *Disordered Materials and Interfaces*, H. Z. Cummins, D. J. Durian, D. L. Johnson, and H. E. Stanley, eds., *MRS Symp. Proc.* **407**, 3 (MRS, Pittsburgh, 1996).
18. D. C. Thomas and V. J. Pugh, *The Log Analyst* (Mar.–Apr., 1989), 71.
19. P. F. Worthington, ed., *Advances in Core Evaluation: Accuracy and Precision in Reserves Estimation* (Gordon and Breach, Philadelphia, 1990).
20. See, for example, G. Kortüm, *Treatise on Electrochemistry* (Elsevier, Amsterdam, 1965).
21. R. J. Hunter, *Zeta Potential in Colloid Science: Principles and Applications* (Academic Press, London, 1981).
22. V. G. Levich, *Physicochemical Hydrodynamics* (Prentice-Hall, Englewood Cliffs, N.J., 1962).
23. J. S. Newman, *Electrochemical Systems* (Prentice-Hall, Englewood Cliffs, N.J., 1973).
24. E. H. Kawamoto and P.-z. Wong, in *Dynamics in Small Confining Systems III*, J. M. Drake, J. Klafter, and R. Kopelman, eds., *MRS Symp. Proc.* **464**, 371 (1997).
25. P.-z. Wong, Gas Research Institute Report No. GRI-96/0377 (GRI, Chicago, 1996).
26. J. R. Macdonald, ed., *Impedance Spectroscopy* (John Wiley & Sons, New York, 1987).
27. D. J. Marshall and T. R. Madden, *Geophysics* **24**, 790 (1959).
28. W. H. Pelton, W. R. Sill, and B. D. Smith, *Geophy. Trans.* **30**, 11 (1984); W. H.

Pelton, S. H. Ward, P. G. Hallof, W. R. Sill, and P. H. Nelson, *Geophysics* **43**, 588 (1978).

29. G. R. Oelhoeft, *Geophysics* **50**, 2492 (1985).
30. H. J. Vinegar and M. H. Waxman, *Geophysics* **49**, 1267 (1984); SPWLA 25th Logging Symp., paper no. LLL (1984).
31. For example, Epoxy 907 from Miller-Stephenson Chemicals, George Washington Highway, Danbury, CT 06810.
32. Schlumberger Technologies, Instruments Division, Victoria Road, Farnborough, Hampshire, England GU14 7PW.
33. P. Horowitz and W. Hill, *The Art of Electronics*, 2nd ed. (Cambridge University Press, Cambridge 1989).
34. P. N. Sen, C. Scala, and M. H. Cohen, *Geophysics* **46**, 781 (1981); P. N. Sen, ibid., 1714 (1981).
35. R. E. de LaRue and C. W. Tobias, *J. Electrochem. Soc.* **106**, 827 (1959).
36. See, for example, M. R. J. Wyllie and M. B. Spangler, *Bull. AAPG* **36**, 359 (1952), and reference therein.
37. J. N. Roberts and L. M. Schwartz, *Phys. Rev. B* **31**, 5990 (1985).
38. L. M. Schwartz and J. R. Banavar, *Phys. Rev. B* **39**, 11965 (1989).
39. P.-z. Wong, in *Physics and Chemistry of Porous Media II*, J. Banavar, J. Koplik, K. Winkler, eds., *AIP Conf. Proc.* **154**, 304 (AIP, New York, 1987).
40. See for example, G. Uehara and G. Gillman, *The Mineralogy, Chemistry, and Physics of Tropical Soils with Variable Charge Clays* (Westview Press, Boulder, CO., 1981); D. J. Greenland and M. H. B. Hayes, eds., *The Chemistry of Soil Constituents*, (Wiley, Chichester, England, 1978); H. van Olphen, H., *An Introduction to Clay Colloid Chemistry: For Clay Technologists, Geologists, and Soil Scientists*, 2nd ed. (Wiley, New York, 1977).
41. M. H. Waxman and L. J. M. Smits, *SPE J.* **8**, 107 (1968).
42. A. LeMehaute and G. Crepy, *Solid State Ionics* **9**–**10**, 17 (1983).
43. P.-z. Wong, J. Howard, and J.-S. Lin, *Phys. Rev. Lett.* **57**, 637 (1986).
44. A. H. Thompson, A. J. Katz, and C. E. Krohn, *Adv. Phys.* **36**, 625 (1987).
45. T. C. Halsey and M. Leibig, *Ann. Phys.* **219**, 109 (1992); *J. Electroanal. Chem.* **358**, 77 (1993).
46. Q.-z. Cao, P.-z. Wong, and L. M. Schwartz, *Phys. Rev. B* **50**, 5771 (1994).
47. T. Pajkossy, *J. Electroanal. Chem.* **364**, 111 (1994).
48. C. Clavier, G. Coates, and J. Dumanoir, *SPE J.* **24**, 153 (1984).
49. D. L. Johnson, J. Koplik, and L. M. Schwartz, *Phys. Rev. Lett.* **57**, 2564 (1986).
50. D. L. Johnson and P. N. Sen, *Phys. Rev. B* **37**, 3502 (1988).
51. L. M. Schwartz, P. N. Sen, and D. L. Johnson, *Phys. Rev. B* **40**, 2450 (1989).
52. P. Debye and R. L. Cleland, *Phys. Rev.* **30**, 843 (1959).
53. L. J. Klinkenberg, A.P.I., *Drilling and Production Practice*, 200 (1941).

54. J. O. Amaefule, K. Wolfe, J. D. Walls, A. O. Ajufo, and E. Peterson, paper no. 15149, SPE 56th California Regional Meeting, Oakland, April 2–4, 1986.

55. J. Geertsma, *SPE J*, 445 (Oct. 1974).

56. R. D. Wyckoff, H. G. Botset, M. Muskat, and D. W. Reed, *Rev. Sci. Instr.* **4**, 394 (1933).

57. Harvard Apparatus, Inc., 22 Pleasant Street, South Natick, MA 01760.

58. Omega Engineering, Inc., P.O. Box 4047, Stamford, CT 06907.

59. M. A. Biot, *J. Appl. Phys.* **12**, 155 (1941); *J. Acoust. Soc. Am.* **28**, 168 (1956); **28**, 179 (1956).

60. R. N. Chandler and D. L. Johnson, *J. Appl. Phys.* **52**, 3391 (1981).

61. W. E. Culham, *SPE J.* **14**, 545 (1974).

62. R. Chandler, *J. Acoust. Soc. Am.* **70**, 116 (1981).

63. A. J. Katz and A. H. Thompson, *Phys. Rev. B* **34**, 8179 (1986).

64. *See also* B. F. Swanson, *J. Petr. Tech.* (Dec. 1981), 2498.

65. J. R. Banavaar and D. L. Johnson, *Phys. Rev. B* **35**, 7283 (1987).

66. P. Dimon, A. P. Kushnick, and J. P. Stokes, *J. Physique*, **49**, 777 (1988); J. P. Stokes, M. J. Higgins, A. P. Kushnick, and S. Bhattacharya, *Phys. Rev. Lett.* **65**, 1885 (1990); S. Kumar, D. H. Reich, and M. O. Robbins, *Phys. Rev. E* **52**, R5776 (1995).

67. T. J. Plona and D. L. Johnson, in *1980 Ultrasonics Symposium*, 868 (IEEE, 1980).

68. D. L. Johnson, J. Koplik, and R. Dashen, *J. Fluid Mech.* **176**, 379 (1987); D. L. Johnson, *Phys. Rev. Lett.* **63**, 580 (1989).

69. E. Charlaix, A. P. Kushnick, and J. P. Stokes, *Phys. Rev. Lett.* **61**, 1595 (1988).

70. P. Sheng and M.-Y. Zhou, *Phys. Rev. Lett.* **61**, 1591 (1988); P. Shang, M.-Y. Zhou, E. Charlaix, A. P. Kushnick, and J. P. Stokes, *Phys. Rev. Lett.* **63**, 581 (1989).

71. T. S. Berlin and A. V. Khabakov, *Geochemistry* **3**, 215 (1961).

72. T. Ishido and H. Mizutani, *J. Geophys. Res.* **86**, 1763 (1981).

73. J.-F. Kuo, M. M. Sharma, and T. F. Yen, *J. Colloid Interf. Sci.* **126**, 537 (1988).

74. F. D. Morgan, E. R. Williams, and T. R. Madden, *J. Geophys. Res.* **94**, 12449 (1989).

75. K. Schätzel, W. Weise, A. Sobotta, and M. Drewel, *J. Colloid Interf. Sci.* **143**, 287 (1991).

76. E. S. Sprunt, T. B. Mercer, and N. F. Djabbarah, *Geophysics* **59**, 707 (1994).

77. R. J. Finno, K. Chung, J. Yin, and J. R. Feldkamp, *J. Geotech. Engineering* (May 1966), 355.

78. J. Yin, R. J. Finno, J. R. Feldkamp, and K. Chung, *J. Geotech. Engineering* (May 1966), 346.

79. A. H. Thompson and G. A. Gist, *The Leading Edge* (Dec. 1993), 1169.
80. S. R. Pride and F. D. Morgan, *Geophysics* **56**, 914 (1991); S. Pride, *Phys. Rev. B* **50**, 15678 (1994).
81. L. Jouniaux and J.-P. Pozzi, *J. Geophys. Res.* **100**, 10197 (1995).
82. L. Onsager, *Phys. Rev.* **37**, 405 (1931); **38**, 2265 (1931).
83. D. G. Miller, *Chem. Rev.* **60**, 20 (1960).
84. See, for example, S. R. deGroot and P. Mazur, *Non-Equilibrium Thermodynamics* (North-Holland, Amsterdam, 1962).
85. U. Saxén, *Ann. Physik Chemie* **47**, 46 (1892).
86. M. R. J. Wyllie, *Petro. Trans. AIME* **192**, T. P. 2940 (1951).
87. R. G. Packard, *J. Chem. Phys.* **21**, 303 (1953).
88. C. E. Cooke, Jr., *J. Chem. Phys.* **23**, 2299 (1955).
89. A. R. Sears and J. N. Groves, *J. Colloid Interf. Sci.* **65**, 479 (1978).
90. Stanford Research Systems, Inc., 1290 D Reamwood Avenue, Sunnyvale, CA 94089.
91. Hewlett-Packard Co., P.O. Box 10301, Palo Alto, CA 94303-0890.
92. D. B. Pengra and P.-z. Wong, in *Statistical Mechanics in Physics and Biology*, D. Wirtz and T. C. Halsey, eds., *MRS Symp. Proc.* **463**, 233 (MRS, Pittsburgh, 1997).
93. J.-Z. Wei and O. B. Lile, in *Advances in Core Evaluation: Accuracy and Precision in Reserves Estimation*, P. F. Worthington, ed. (Gordon and Breach, Philadelphia, 1990).

This Page Intentionally Left Blank

5. ACOUSTICS AND ULTRASONICS

Peter B. Nagy

Department of Aerospace Engineering and Engineering Mechanics
University of Cincinnati
Cincinnati, Ohio

5.1 The Role of Acoustics in Characterizing Porous Media

Acoustics is the science of mechanical waves, including their generation, detection, propagation, and interaction with the elastic medium. Generally, "the term sound implies not only the phenomena in air responsible for the sensation of hearing but also whatever else is governed by analogous physical principles" [1]. Mechanical waves with frequencies below the bottom (≈ 16 Hz) and above the top (≈ 20 kHz) of the audible range are called infrasound and ultrasound, respectively. The main goal of this chapter is to review the most important applications of acoustics and ultrasonics in materials characterization for porous media. The larger the inspection frequency, the shorter the length scale of the materials properties obtained from these measurements. Infrasonic elastic wave propagation is used in the closely related field of seismology, where material properties on very large scales (hundreds of meters to hundreds of kilometers) are of interest. We consider only relatively short-range and localized measurements ranging from approximately 100 Hz to 1 MHz. These applications exploit the fact that transmission of sound is strongly affected by the medium through which it propagates. The other side of wave–material interaction — namely, the physical effects of sound on the material — is not considered throughout this chapter.

Originally, ultrasonic materials testing was used almost exclusively for detecting macroscopic discontinuities in structures after they have been in service for some time. It has become increasingly evident that it is practical and cost effective to expand the role of ultrasonic nondestructive testing (NDT) to include all aspects of materials production and application. Research efforts are being directed at developing and perfecting NDT capable of monitoring (i) material production processes; (ii) material integrity following transport, storage, and fabrication; and (iii) the amount and rate of degradation during service. In addition, efforts are underway to develop techniques capable of quantitative discontinuity sizing, enabling

EXPERIMENTAL METHODS IN THE PHYSICAL SCIENCES
Vol. 35
ISBN 0-12-475982-3

ISSN 1079-4042/99 $30.00

determination of material response using fracture mechanics analysis, as well as techniques for quantitative materials characterization to replace the qualitative techniques used in the past. Ultrasonic techniques play a prominent role in these developments because they afford useful and versatile methods for evaluating microstructures and associated mechanical properties as well as detecting microscopic and macroscopic discontinuities in solid materials.

In homogeneous elastic solids, sound propagates either as a transversely polarized shear wave or as a longitudinally polarized dilatational wave. Since fluids cannot sustain elastic shear stress, only longitudinally polarized dilatational waves can propagate in fluids. In a fluid-saturated porous solid, there are three bulk modes: the shear wave supported by the rigidity of the solid frame and the combined masses of the solid and the saturating fluid and two dilatational waves, which are called the "fast" and "slow" compressional waves.

Acoustic evaluation of porous materials can take advantage of some very specific acoustic phenomena that occur only in fluid-saturated consolidated solids of continuously connected pore strucure. Certain material properties of the porous frame such as the degree of consolidation or grain size can be readily evaluated from the velocity or attenuation of the shear and longitudinal waves in the dry skeleton or those of the fast compressional wave in the fluid-saturated material. The common feature of these wave modes is that the porous skeleton and the interstitial fluid move essentially in phase — that is, the relative motion of the fluid within the pore channels is relatively less important — therefore these modes are fairly similar to the corresponding modes in nonpermeable solids. Other parameters such as tortuosity; permeability; porosity; and pore size, shape, and surface quality are inherently connected to the porous nature of the material and can be evaluated much better from the propagation properties of the slow compressional wave and related wave phenomena. In the slow compressional wave, the porous skeleton and the interstitial fluid move essentially out of phase, therefore the relative motion of the fluid within the pore channels is very important. Naturally, the slow compressional wave is usually very weak due to high attenuation caused by viscous drag between the fluid and the solid frame. In such cases, conventional acoustic velocity and attenuation measurements of the relatively less affected fast and shear modes can be used to characterize the porous material. In this chapter, we focus on acoustic methods based on the primary effect when, owing to the relatively high permeability of the porous frame, the low-viscosity saturating fluid moves significantly within the porous skeleton and the motion is restrained primarily by viscous forces between the two constituents.

5.2 Review of Acoustic Wave Propagation

Acoustics is the study of time-varying deformations or vibrations in elastic media. It is concerned with material particles that are small but yet contain many atoms. Within each particle, the atoms move in unison. Therefore, acoustics deals with macroscopic phenomena and is formulated as if matter were a continuum. Structure at the microscopic level is of interest only insofar as it affects the medium's macroscopic properties. When the particles of a medium are displaced from their equilibrium positions, internal restoring forces arise. It is these restoring forces between particles, combined with the inertia of the particles, that lead to oscillatory motions of the medium. To formulate a mathematical description of these vibrations, which may be either traveling waves or localized oscillations, it is first necessary to introduce quantitative definitions of particle displacement, material deformation, and internal restoring forces. Detailed discussions of the fundamental relationships governing wave propagation in elastic media can be found in numerous textbooks (e.g., [2, 3]) and are only very briefly summarized here.

The deformation of the continuum is described by the displacement–strain relation. In a system of fixed rectangular Cartesian coordinates the position vector is given as

$$\boldsymbol{x} = \boldsymbol{e}_1 x_1 + \boldsymbol{e}_2 x_2 + \boldsymbol{e}_3 x_3 = \boldsymbol{e}_i x_i, \tag{1}$$

where $\boldsymbol{e}_i$ denotes the unit vector in the ith direction (in the indicial notation, a repeated index implies summation over the values of $i = 1, 2, 3$). The strain tensor ε_{ij} can be calculated from the displacement vector $\boldsymbol{u} = \boldsymbol{e}_i u_i$ by the symmetric gradient operator as follows:

$$\varepsilon_{ij} = \tfrac{1}{2}(u_{i,j} + u_{j,i}), \tag{2}$$

where partial differentiation is denoted by a comma; that is, $\partial u_i / \partial x_j = u_{i,j}$. The restoring elastic forces produced by a given deformation can be calculated from the constitutive equation describing the stress–strain relation. For a linear, homogeneous elastic material, the constitutive equation is

$$\tau_{ij} = C_{ijkl} \varepsilon_{kl}, \tag{3}$$

where C_{ijkl} denotes the fourth-order stiffness tensor. For isotropic materials, however, only two elements of the stiffness tensor are independent, and the constitutive equation (Hooke's law) simplifies to

$$\tau_{ij} = \lambda \varepsilon_{kk} \delta_{ij} + 2\mu \varepsilon_{ij}, \tag{4}$$

where λ and μ are the Lamé constants and δ_{ij} is the so-called Kronecker

delta ($\delta_{ij} = 1$ if $i = j$ and $\delta_{ij} = 0$ else). Newton's second law states that

$$\tau_{ij,j} = \rho \frac{\partial^2}{\partial t^2} u_i, \tag{5}$$

where ρ denotes the density of the material. Here, we neglected body force contributions to the balance of momentum as they are usually of static nature and therefore irrelevant in acoustical problems. Finally, the displacement–strain and stress–strain relations can be combined with the balance of momentum equation to write the elastic wave equation as

$$(\lambda + \mu)u_{j,ji} + \mu u_{i,jj} = \rho \frac{\partial^2}{\partial t^2} u_i. \tag{6}$$

Plane wave solutions of the wave equation can be found in the general form of

$$\boldsymbol{u} = A\boldsymbol{p} \exp[i(\boldsymbol{k}\boldsymbol{x} - \omega t)]. \tag{7}$$

Here, A is the displacement amplitude; $\boldsymbol{p}$ denotes the polarization unit vector; ω is the angular frequency; and $\boldsymbol{k}$ denotes the wave vector, $\boldsymbol{k} = \boldsymbol{d}k$, where $\boldsymbol{d}$ denotes the propagation unit vector. The magnitude of the wave vector k, or wave number, is related to the phase velocity v via $k = \omega/v$. Substitution of the preceding plane–wave solution into the wave equation yields two different nontrivial solutions in the case of homogeneous isotropic materials. These are frequency-independent (nondispersive) longitudinal (dilatational) and transverse (shear) waves with phase velocities

$$v_d = \sqrt{\frac{\lambda + 2\mu}{\rho}} \tag{8}$$

and

$$v_s = \sqrt{\frac{\mu}{\rho}}, \tag{9}$$

respectively. Of course, in a viscosity-free fluid ($\mu \equiv 0$), only dilatational waves can exist, which are also called compressional waves.

Pure longitudinal and shear plane waves are uncoupled vibrations of the infinite elastic medium. The ratio between the shear and longitudinal wave velocities can be expressed as

$$\xi = \frac{v_s}{v_d} = \left[\frac{1 - 2\nu}{2(1 - \nu)}\right]^{1/2}, \tag{10}$$

where ν denotes the Poisson ratio of the medium. For most materials $\nu \approx 0.25$–0.35 and the longitudinal velocity is roughly twice the shear wave velocity. Propagation velocities depend on the material, and may range from 10^3 to 10^4 m/s for most liquids and solids, while the sound velocity in air is about 340 m/s. The basic natures of longitudinal and shear waves are shown in Fig. 1. The longitudinal wave (also called dilatational, pressure, or compressional wave) may exist in solids, liquids, and gases, and it is the familiar wave of acoustic theory. We see that the particle motion is in the same direction as the propagation direction. A shear wave (also called transverse wave or equivoluminal wave), on the other hand, can exist only in a solid. We see that the particle motion is at right angles, or transverse, to the direction of propagation.

The ratio of the stress and velocity amplitudes is called the characteristic impedance of the medium and can be expressed as the product of the density and sound velocity; that is, $Z = \rho v$. Nearly all applications of acoustics and ultrasonics involve the interaction of waves with boundaries. Even the most basic studies of material properties, usually involving the velocity and attenuation of waves, in the final analysis require accounting for boundary interactions. The simplest situation of reflection and transmission occurs when waves are impinging normal to the interface between two materials, as shown in Fig. 2.

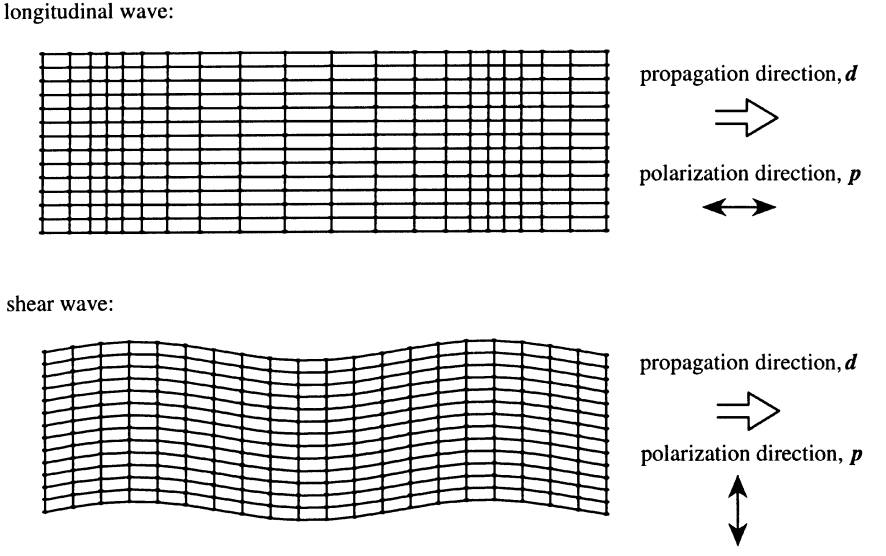

FIG. 1. Longitudinal and shear wave modes.

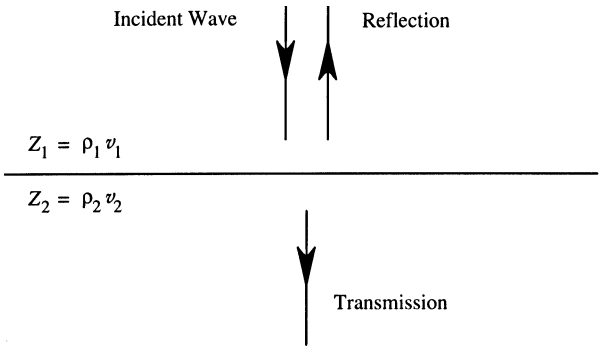

FIG. 2. Reflection and transmission of an acoustic wave at normal incidence to a plane boundary.

This situation can be described mathematically in terms of three propagating waves:

$$u_i = A_i \exp[i(k_1 x - \omega t)], \tag{11}$$

$$u_r = A_r \exp[i(-k_1 x - \omega t)], \tag{12}$$

$$u_t = A_t \exp[i(k_2 x - \omega t)]. \tag{13}$$

The amplitude of the reflected and transmitted waves can be found by noting that the displacements and stresses must be continuous at the interface. Thus, for $x = 0$, it is required that

$$u_i + u_r = u_t \quad \text{and} \quad \tau_i + \tau_r = \tau_t. \tag{14}$$

This leads directly to the result

$$R = \frac{A_r}{A_i} = \frac{Z_1 - Z_2}{Z_1 + Z_2} \tag{15}$$

and

$$T = \frac{A_t}{A_i} = \frac{2Z_1 Z_2}{Z_1 + Z_2}. \tag{16}$$

Here R and T are known as the displacement reflection and transmission coefficients. We see that these results are in terms of the respective characteristic impedances of the materials. A more general situation of reflection and transmission of waves at an interface occurs when the incident wave strikes at an oblique angle. A large number of possibilities exist, depending on the combinations of solid, fluid, and "vacuum" for the two media and, if the incident media is a solid, whether the incident wave is a longitudinal or

shear wave. Generally, mode conversion occurs; that is, an incident longitudinal wave produces not only reflected and transmitted longitudinal waves but also reflected and transmitted shear waves. A detailed discussion of elastic wave interaction with a plane interface separating two media can be found, for example, in Auld's book [3].

The longitudinal and shear waves are the only two types of elastic waves that can exist in an extended homogeneous isotropic medium. If a free surface exists, a surface or Rayleigh wave may also propagate. Such a wave has a complicated elliptical particle motion at the surface with an amplitude that rapidly decays away from the surface; that is, the vibration is limited to a shallow layer of approximately one wavelength below the surface. Figure 3 shows the vibration pattern produced by a Rayleigh wave propagating on the free surface of a solid.

A detailed discussion of Rayleigh waves can be found, for example, in Viktorov's book [4]. The normalized Rayleigh wave velocity $\eta = v_R/v_s$ can be determined from the exact Rayleigh equation:

$$\eta^6 - 8\eta^4 + 8(3 - 2\xi^2)\eta^2 - 16(1 - \xi^2) = 0. \tag{17}$$

Figure 4 shows the normalized Rayleigh velocity as a function of the ratio between the shear and longitudinal wave velocities, ξ. For most materials, the Rayleigh wave velocity is between 92 and 94% of the shear velocity. Since the Rayleigh characteristic equation cannot be explicitly solved for the surface wave velocity, we often use the following approximate expression, which gives the normalized surface wave velocity as a function of Poisson's ratio:

$$\eta \approx \frac{0.87 + 1.12\nu}{1 + \nu}. \tag{18}$$

Figure 4 also shows the results of this approximate formula.

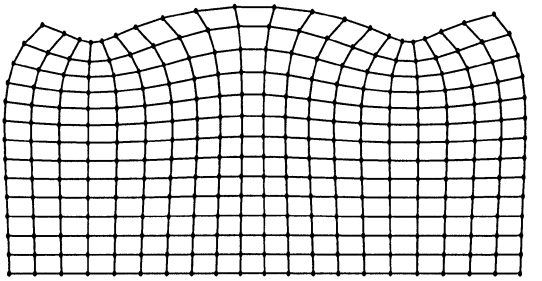

FIG. 3. Vibration pattern produced by a Rayleigh wave propagating on the free surface of a solid.

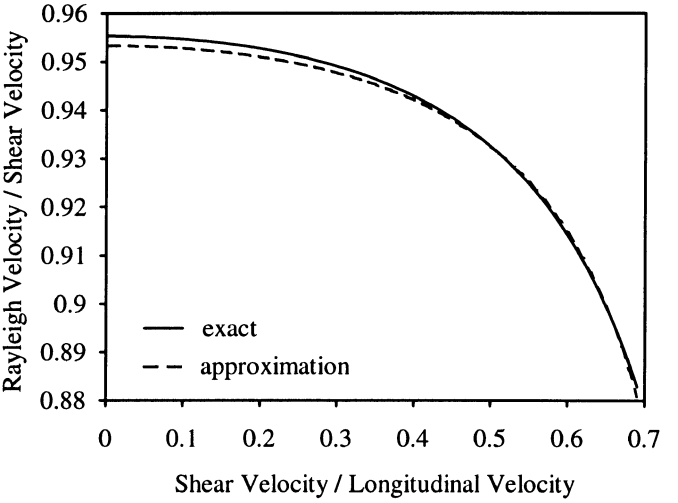

FIG. 4. Normalized Rayleigh velocity as a function of the ratio between the shear and longitudinal wave velocities.

Two types of interface waves can propagate along the fluid-loaded surface of an immersed solid; there is a true mode called a Scholte wave and a pseudomode called a leaky Rayleigh wave. The true wave is always slower than all the bulk waves in the solid and the fluid, and it produces evanescent fields only as it propagates along the interface; that is, the vibration is limited to a shallow layer on both sides of the interface. Typically, the Scholte wave carries most of its energy on the fluid side and its velocity is less than 1% below the compressional bulk wave velocity in the fluid. The leaky Rayleigh wave is slightly faster than the true Rayleigh wave that would propagate on the free surface of the same solid. This mode exists only if the shear velocity of the solid is higher than the compressionl wave velocity in the fluid, which is true for most ordinary solids, but not necessarily for highly porous materials, for example, for numerous natural rocks. The leaky Rayleigh wave velocity is lower than the shear velocity of the solid, therefore it generates only evanescent vibrations on the solid side, but it is higher than the compressional wave velocity in the fluid, therefore it generates propagating waves in the fluid. Via these propagating waves, the mode "leaks" energy into the fluid as it propagates along the interface therefore it becomes strongly attenuated.

Only one true interface wave, the so-called Stoneley wave, can propagate along the plane interface separating two solid half-spaces [5]. This mode exists only for certain combinations of materials properties [6] and its

velocity always lies between the Rayleigh and shear velocities of the denser medium.

In ideal homogeneous, elastic media the already reviewed bulk, surface, and interface waves are all dispersion free. Dispersion means that the propagation velocity is frequency dependent. In the case of dispersive wave propagation, the phase relation between the spectral components of a broadband signal varies with distance, therefore the pulse shape becomes distorted and generally widens as the propagation length increases. There are two main causes for dispersive wave propagation of acoustic waves. First is inherent material behavior such as relaxation in polymers, which is best described by a characteristic time constant. In porous materials, viscous fluid flow through the pore channels often results in such effects. In these cases, the degree of dispersion is generally rather weak and the dispersion is dependent on the ratio of the relaxation time constant to the time period of the ultrasonic vibration. Second, geometrical and size effects can cause a completely different type of dispersion even in specimens made of ideal homogeneous, elastic materials. Guided waves in thin plates and rods are typical examples of such geometrical dispersion. In this case, the degree of dispersion can be very high and it is dependent on the ratio of the specimen's characteristic dimension (e.g., plate thickness or rod diameter) to the acoustic wavelength.

Plates and rods are often used in laboratory tests to characterize porous solids. In low-frequency vibration measurements, the resonance frequencies and damping factors of the specimen can be accurately measured and evaluated for the sought for materials properties. In high-frequency acoustic and ultrasonic measurements, wave propagation properties such as dispersion and attenuation are measured and used to assess the same properties. In this case, the measured dispersion is mainly determined by the smallest characteristic dimension of the specimen.

Dispersive guided waves propagating in plates are called Lamb modes. The modes are classified as symmetric or asymmetric depending on whether the in-plane vibration components of the particles are identical or opposite on the two sides of the plate. Figure 5 shows the vibration pattern produced by the lowest-order symmetric (a) and asymmetric (b) Lamb waves in a plate. Guided wave modes can also propagate in rods. There are three types of modes that can propagate along a rod of circular cross section: (i) axially symmetric longitudinal wave modes, which involve both radial and axial displacements that do not depend on the azimuthal angle; (ii) torsional wave modes, which involve circumferential displacement only that also does not depend on the azimuthal angle; and (iii) flexural modes, which involve radial, axial, and circumferential displacements that do depend on the azimuthal angle. At low frequencies, when the acoustic wavelength is much

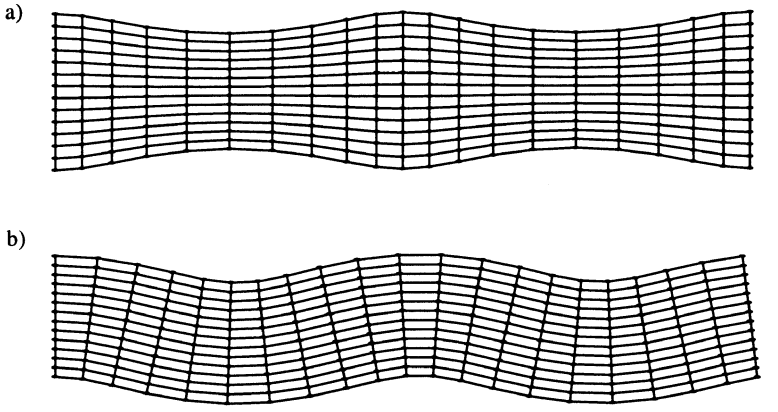

FIG. 5. Symmetric (a) and asymmetric (b) Lamb waves in a thin plate.

higher than the rod radius, only the lowest-order of each mode can propagate. The zeroth-order axisymmetric longitudinal wave propagates at a phase velocity of $v_0 = \sqrt{E/\rho}$, where E denotes Young's modulus. Due to the Poisson effect, this velocity is significantly lower than the longitudinal velocity in the same material and further decreases with increasing frequency. The lowest-order torsional mode is not dispersive and propagates with the shear wave velocity of the bulk material. The lowest-order flexural mode propagates at a very low phase velocity that can be approximated as $v \approx \sqrt{a\omega v_0/2}$. At low frequencies, the velocity of the lowest-order flexural mode is also determined by Young's modulus through v_0 and the mode is strongly dispersive.

5.3 Acoustic Wave Propagation in Fluid-Saturated Porous Materials

The previously reviewed laws of acoustic wave propagation were postulated for homogeneous continua. Their adaptation to permeable porous media is rather difficult because of three major complications. First, porous media are inherently two-phase materials consisting of a solid skeleton and a gas or liquid phase that can flow through the pore channels. Second, fluid-saturated porous media are intrinsically composite in nature, where coupling between the solid and fluid must be accounted for. In the simpler case of air-saturated porous media, the density and stiffness differences between the fluid and the solid phases are so large that this coupling might

be neglected, but in the case of liquid-saturated porous solids, the effect is usually very significant. Finally, most porous media are inherently highly heterogeneous with a random structure that can be described only statistically. Modeling of acoustic wave propagation in porous materials must always balance carefully between the rigor of the description and the complexity of the resulting model. Only a couple of monographs are dedicated solely to the problem of acoustics of porous media [7–10], while most of the relevant literature is distributed in numerous research papers. In the following, we review the most basic aspects of acoustic wave propagation in fluid-saturated porous media.

The most interesting feature of acoustic wave propagation in fluid-saturated porous media is the appearance of a second compressional wave, the so-called slow wave. The existence of a slow compressional wave in an isotropic and macroscopically homogeneous fluid-saturated porous medium was predicted by Biot in 1956 [11, 12]. The main characteristic of this mode is that its velocity is always lower than both the compressional wave velocity in the fluid and the longitudinal velocity in the solid frame. Below a critical frequency, which depends on the pore size in the frame and the viscosity of the fluid, the slow compressional wave is highly dispersive and strongly attenuated over a single wavelength. Above this critical frequency, it becomes a dispersion-free propagating wave with increasing but fairly low attenuation. The slow compressional wave represents a relative motion between the fluid and the solid frame. This motion is very sensitive to the viscosity of the fluid and the dynamic permeability of the porous formation. Naturally, low-viscosity liquids such as water are the fluids most often used in experimental studies of slow wave propagation. We see in this chapter, however, that it also makes good sense to use gaseous fluids such as air to saturate the porous specimens.

Since 1980, when Plona was able to observe slow wave propagation in water-saturated porous ceramics [13], the question of why slow waves cannot be detected in low-permeability materials such as natural rocks has been one of the major issues in the acoustics of fluid-saturated porous materials. Klimenatos and McCann [14] showed that this lack of perceivable slow wave propagation is probably due to inherent internal impurities, such as submicron clay particles, found in all types of natural rocks. These clay particles, deposited both within the pore throats and on the surfaces of the rock grains, greatly increase viscous drag between the fluid and solid frame, which results in excessive attenuation and usually complete disappearance of the slow wave. The excess viscous drag explains the difficulty in detecting the slow wave in fluid-saturated rocks as well as the observed correlation between ultrasonic attenuation and clay content in sandstones. One way to reduce the excessive attenuation of slow waves in porous

materials is to use special fluids of very low viscosity to saturate the specimen. For instance, superfluid ^{4}He below 1.1 K has been shown to work very well in fused glass bead samples [15], in superleak materials consisting of compacted powders [16, 17], and in sandstones [18]. Compared to the solid frame, liquids such as water usually have a lower, but still comparable density ρ_f and bulk modulus K_f. Although their viscosity η is also relatively high, which makes saturation of the porous sample somewhat troublesome, their kinematic viscosity η/ρ_f is fairly low. On the other hand, gaseous fluids such as air have very low density, bulk modulus, and viscosity, while their kinematic viscosity is usually rather high. Therefore, it is very simple to saturate a porous sample by air, but the slow wave is expected to be highly dispersive and strongly attenuated. In spite of these adverse effects, slow waves can be readily observed in air-filled porous samples, including certain natural rocks, using airborne ultrasonic waves [19].

5.3.1 Sound Propagation in Air-Filled Porous Materials with Rigid Frames

Generally, sound propagation in fluid-saturated porous materials is strongly affected by acoustic coupling between the solid skeleton and the interstitial fluid. In the case of air saturation, however, even highly flexible materials such as fibrous polymers can be considered as rigid frames with respect to the saturating fluid (rare exceptions are discussed in Chap. 6 of Ref. [9]). Assuming viscous flow through the connected pores of a motionless skeleton greatly simplifies the acoustical problem, but there is also an additional complication with respect to the case of liquid-filled porous materials. In air-filled porous materials, thermal losses associated with heat conduction between the saturating fluid and the solid frame are not entirely negligible and must be incorporated into the wave propagation model.

Based on Kirchhoff's theory of sound propagation in cylindrical tubes, Zwikker and Kosten [7] developed a simple method in which viscous and thermal effects are treated separately and incorporated in the frequency-dependent complex density $\tilde{\rho}(\omega)$ and bulk modulus $\tilde{K}(\omega)$ of the fluid, respectively. For the simple case of air-saturated permeable solids containing cylindrical pores of circular cross section, the equation of motion can be exactly solved by assuming that the velocity of the fluid in contact with the motionless cylindrical wall must vanish. The average fluid velocity $\bar{v}$ within a single pore satisfies the familiar equation of motion

$$-\frac{\partial p}{\partial x} = i\omega\tilde{\rho}\bar{v}, \tag{19}$$

where $\partial p/\partial x$ is the fluid pressure gradient and ω is the angular frequency. The complex density $\tilde{\rho}$ includes the effect of viscosity

$$\tilde{\rho}(\omega) = \frac{\rho_f}{1 - t(\xi)}. \tag{20}$$

Here, ρ_f is the real-valued fluid density and t is a simple form function:

$$t(\xi) = \frac{2J_1(\sqrt{-i}\,\xi)}{\sqrt{-i}\,\xi J_0(\sqrt{-i}\,\xi)}, \tag{21}$$

where J_0 and J_1 are the zeroth- and first-order Bessel functions and $i = \sqrt{-1}$ is the imaginary unit. The normalized pore size for circular cross sections is

$$\xi = a[\omega\rho_f/\eta]^{1/2}, \tag{22}$$

where a denotes the actual pore radius and η is the viscosity of the fluid.

Similarly, the equation of thermal conduction can be also exactly solved for cylindrical pores of circular cross section by requiring that the temperature of the fluid in contact with the frame be constant. The average compression $\bar{\varepsilon}$ in the pore fluid satisfies the familiar constitutive relation for fluids:

$$\bar{\varepsilon}\tilde{K} = p. \tag{23}$$

The complex bulk modulus $\tilde{K}$ includes the effect of heat conduction in air:

$$\tilde{K}(\omega) = \frac{K_f}{1 + (\gamma - 1)t(P^{1/2}\xi)}. \tag{24}$$

Here, K_f is the real-valued bulk modulus of the fluid, γ denotes the specific heat ratio, and P is the Prandtl number. For air at room temperature, $\gamma \approx 1.4$ and $P \approx 0.74$, while the adiabatic bulk modulus can be calculated from the atmospheric pressure $p_0 \approx 1 \times 10^5$ Pa as $K_f = \gamma p_0 \approx 1.4 \times 10^5$ Pa.

Zwikker and Kosten's model can be used to determine both the complex wave number k and the complex acoustic impedance Z in the fluid-saturated porous solid as follows:

$$k(\omega) = \omega[\tilde{\rho}(\omega)/\tilde{K}(\omega)]^{1/2} \tag{25}$$

and

$$Z(\omega) = \frac{1}{\phi}[\tilde{\rho}(\omega)\tilde{K}(\omega)]^{1/2}, \tag{26}$$

where ϕ denotes the connected porosity.

For the purposes of materials characterization, these acoustical parameters must be related to macroscopic properties of interest such as permeability and porosity. For a porous material having n cylindrical pores of radius a per unit area of cross section, the porosity is $\phi = n\pi a^2$ and the static permeability can be calculated from

$$\kappa_0 = \frac{a^2\phi}{8}. \tag{27}$$

For parallel cylindrical holes, Eq. (22) can be rewritten as

$$\xi = \left[\frac{8\kappa_0\omega\rho_f}{\phi\eta}\right]^{1/2}. \tag{28}$$

In Eq. (28), we can recognize the flow resistivity $\sigma = \eta/\kappa_0$ of the permeable solid for the given saturating fluid.

Very similar results can be obtained for porous materials having prismatic pores of other regular geometries such as triangular, rectangular, and hexagonal cross sections [20, 21]. In spite of the very different geometries of these cross sections, the corresponding exact solutions can be shown to give form functions with rather similar functional dependence on the principal macroscopic material parameters and frequency. Therefore the preceding results for cylindrical pores can be generalized by using the form function given by Eq. (21) for arbitrary cross sections with an equivalent normalized pore radius:

$$\xi = c\left[\frac{8\kappa_0\omega\rho_f}{\phi\eta}\right]^{1/2}, \tag{29}$$

where c is an appropriate shape factor. Of course, for a circular cross section, c is unity. The advantage of the universal approximation of Eq. (29) is that the shape factor turns out to be close to unity for a great number of different geometries. For example, for a narrow slit, a square, and an equilateral triangle, the shape factor is respectively 0.82, 1.07, and 1.14.

The preceding results can be further generalized for porous materials having prismatic pores of oblique orientation. Let us denote the angle between the axes of the pores and the pressure gradient producing the fluid flow through the porous solid by θ. For a porous material having n cylindrical pores of radius a per unit area of cross section, the porosity is $\phi = n\pi a^2/\cos\theta$; that is, inversely proportional to the direction cosine of the pores. Equation (19) can be used only if the complex density previously given by Eq. (20) is also modified to account for the reduced pressure gradient along the pore direction and the reduced flow velocity component

parallel to the direction of the macroscopic pressure gradient:

$$\tilde{\rho}(\omega) = \frac{k_s \rho_f}{1 - t(\xi)}, \tag{30}$$

where $1/\cos^2\theta = k_s$ is called the structure form factor. The frequency-dependent complex bulk modulus $\tilde{K}(\omega)$ can be still calculated from Eq. (24), as the compressibility is not affected by the pore orientation. The static permeability also decreases with respect to the case of pores aligned parallel to the pressure gradient ($\theta = 0$) and Eq. (27) becomes

$$\kappa_0 = \frac{a^2 \phi}{8 k_s}. \tag{31}$$

With this generalization, Eq. (29) can be rewritten to calculate the equivalent normalized pore radius for oblique pore channels as follows:

$$\xi = c \left[\frac{8 k_s \kappa_0 \omega \rho_f}{\phi \eta} \right]^{1/2}. \tag{32}$$

For real porous materials of random pore geometry, there are no corresponding exact solutions. Based on the apparently universal nature of Eqs. (24) and (30) combined with the equivalent normalized pore radius of Eq. (32), Attenborough suggested that the same formulas could be used to approximate the complex density and bulk modulus of porous materials having random pore geometries with an appropriate choice of the normalized pore size [22, 23]. The normalized pore radius should be calculated as

$$\xi = \left[\frac{2 k_s \kappa_0 \omega \rho_f}{\phi \eta s_p^2} \right]^{1/2}, \tag{33}$$

where s_p is the so-called pore shape factor ratio, which is usually between 0.1 and 0.5. Again, the complex density and bulk modulus can be calculated from Eqs. (30) and (24), respectively. By comparing Eqs. (32) and (33) we can verify that Attenborough's approximate model for random porous media gives identical results to those of the previously discussed generalized model for prismatic pores of oblique orientation if the relevant pore shape factors are related through $c = 1/(2s_p)$.

A more rigorous generalization of these analytical models can be achieved by the so-called dynamic permeability model of Johnson *et al.* [24]. Equation (19) can be shown to be exactly valid for steady flow of inviscid fluids ($\tilde{\rho} \to k_s \rho_f$):

$$-\frac{\partial p}{\partial x} = i\omega k_s \rho_f \bar{v} \tag{34}$$

in any porous material of random pore structure if the form factor is defined as follows [24]:

$$k_s = \frac{\langle v_m^2 \rangle}{\langle v_m \rangle^2}. \tag{35}$$

Here v_m denotes the microscopic velocity distribution in the pores and the angle brackets indicate spatial averaging over a pore volume containing several pores. Clearly, the structure form factor is a purely geometrical parameter of the solid skeleton alone. For viscous fluids, Eq. (34) is valid only at very high frequencies. However, this limitation can be formally removed by introducing $\tilde{\rho}(\omega) = \tilde{\alpha}(\omega)\rho_f$ as follows:

$$-\frac{\partial p}{\partial x} = i\omega\rho_f \tilde{\alpha}(\omega)\bar{v}, \tag{36}$$

where $\tilde{\alpha}(\omega)$ is called the frequency-dependent dynamic tortuosity. The high-frequency asymptotic limit of the complex tortuosity is equal to the structural form factor as defined in Eq. (35); that is,

$$\lim_{\omega \to \infty} \tilde{\alpha}(\omega) = \alpha_\infty = k_s. \tag{37}$$

It has been shown that α_∞ can be measured in permeable solids of random pore structure by the electric conductance method [25]. The dynamic permeability can be defined by

$$\phi\bar{v} = -\frac{\tilde{\kappa}(\omega)}{\eta}\frac{\partial p}{\partial x}. \tag{38}$$

A comparison with Eq. (36) reveals that $\tilde{\kappa}(\omega)$ is related to the frequency-dependent dynamic tortuosity $\tilde{\alpha}(\omega)$ via

$$\tilde{\kappa}(\omega) = \frac{\eta\phi}{i\omega\rho_f \tilde{\alpha}(\omega)}. \tag{39}$$

The previously used static permeability κ_0 is the real-valued low-frequency limit of this dynamic permeability.

To simplify the relationship between the acoustic parameters of fluid-saturated porous solids of rigid skeleton, Johnson *et al.* [24] introduced a characteristic dimension Λ of the pore channels by using the microscopic fluid velocity distribution without viscosity $v_i(r)$ as follows:

$$\Lambda = \frac{2\int_V v_i^2(r)\, dV}{\int_A v_i^2(r)\, dA}. \tag{40}$$

The integrals in the numerator and the denominator are carried out over the pore volume V and pore surface A, respectively. Thus, Λ is a characteristic size calculated as the weighted volume-to-surface ratio of the pores, which depends on the shape of the pore. Like the tortuosity α_∞, the characteristic pore size Λ is independent of fluid properties and can be deduced from the attenuation of the sound measured at very high frequencies or, alternatively, using superfluid ^{4}He saturation.

The concept of viscous characteristic dimension was subsequently adapted to the complex bulk modulus of air at high frequencies to account for thermal losses by Champoux and Allard [26, 27]. At high frequencies, the temperature is constant over the pore's cross section except in a narrow layer at the pore wall where it changes exponentially. The thermal characteristic dimension Λ' is defined by

$$\Lambda' = \frac{2V}{A}, \tag{41}$$

that is, $\Lambda'/2$ is the actual volume-to-surface ratio of the pores without any weighting.

For cylindrical pores, both characteristc lengths are equal to the pore radius. For other cross sections, the previously introduced shape factor c can be used to relate the characteristic dimensions to macroscopic material parameters such as porosity ϕ, static permeability κ_0, and high-frequency tortuosity α_∞. The viscous characteristic length can be written as

$$\Lambda = \frac{1}{c}\left[\frac{8\alpha_\infty \kappa_0}{\phi}\right]^{1/2}. \tag{42}$$

Similarly, the thermal characteristic length can be given as

$$\Lambda' = \frac{1}{c'}\left[\frac{8\alpha_\infty \kappa_0}{\phi}\right]^{1/2}. \tag{43}$$

where c' is a second shape factor that must be smaller or equal to c.

Johnson *et al.* [24] suggested a heuristic model for the dynamic density in terms of the characteristic dimension

$$\tilde{\rho} = \rho_f \alpha_\infty \left[1 + \frac{\phi\delta^2}{i2\alpha_\infty \kappa_0}\left(1 + \frac{i8\alpha_\infty^2 \kappa_0^2}{\phi^2 \Lambda^2 \delta^2}\right)^{1/2}\right], \tag{44}$$

where $\delta = (2\eta/\rho_f \omega)^{1/2}$ is the viscous skin depth. In an analogous fashion, the dynamic bulk modulus can be expressed with the thermal characteristic dimension as [26]

$$\tilde{K} = \frac{K_f}{\gamma - (\gamma - 1)/[1 + (4\delta^2/i\Lambda'^2 P)(1 + i\Lambda'^2 P/8\delta^2)^{1/2}]}. \tag{45}$$

Figure 6 shows a comparison between experimental results and theoretical predictions of the dynamic tortuosity $\tilde{\alpha}(\omega) = \tilde{\rho}(\omega)/\rho_f$ and normalized dynamic bulk modulus $\tilde{K}(\omega)/p_0$ for a porous ceramic [26]. The experimental technique is described later in the next section.

The dynamic bulk modulus is normalized in this way to demonstrate that its low-frequency limit is the isothermic rather than adiabatic bulk modulus of air, that is, p_0. The independently measured values of the physical

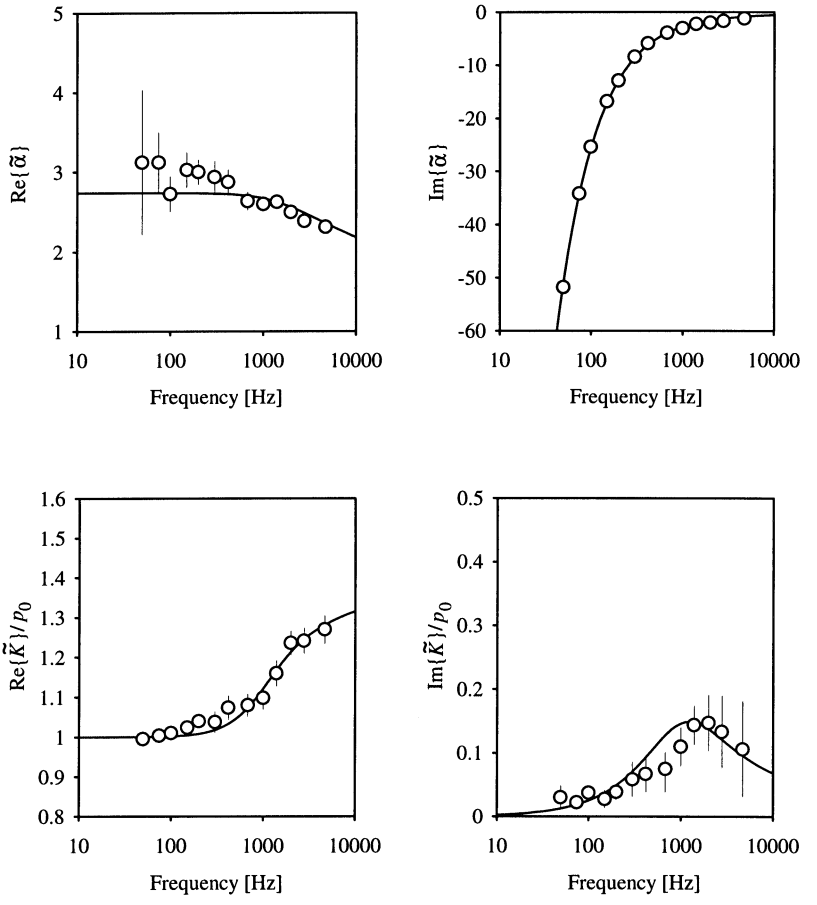

FIG. 6. Comparison between experimental results (symbols) and theoretical predictions (solid lines) of the dynamic tortuosity and normalized dynamic bulk modulus for a porous ceramic. The theoretical curves were calculated by using Eqs. (42)–(45). Reprinted with permission from Y. Champoux and J. F. Allard, *J. Appl. Phys.* 70, 1975–1979 (1991).

parameters used in the calculations were $\phi = 0.432$, $\alpha_\infty = 1.7$, and $\sigma = \eta/\kappa_0 = 44.500\,\mathrm{N \cdot s/m^4}$. The shape factors were chosen as $c = 1.563$ and $c' = 0.746$ by best fitting the analytical results to the experimental data. The corresponding characteristic dimensions are $\Lambda \approx 75\,\mu\mathrm{m}$ and $\Lambda' \approx 150\,\mu\mathrm{m}$. The significant difference between these dimensions is due to the fact that viscous losses are dominated by the smallest cross sections (i.e., pore throats), while thermal losses are associated with the largest pore dimensions.

5.3.1.1 Experimental Techniques. Acoustic characterization of material properties of air-filled permeable porous materials is usually based on impedance measurements in reflection mode. At ultrasonic frequencies, through-transmission measurements are also feasible to determine the sound velocity and attenuation in the material. These two techniques are discussed separately.

5.3.1.2 Acoustic Impedance Measurements. The basic principle of acoustic impedance measurement in a so-called Kundt tube is shown in Fig. 7. A loudspeaker generates a plane wave in a tube that is terminated by the porous specimen to be characterized. The reflection coefficient is determined from the sound pressure measured at different points along the tube with a moving probe or with several fixed ones [28–30]. The acoustic impedance then can be easily calculated from the measured reflection coefficient.

The acoustic pressure in the tube can be written as

$$p(x) = A \exp(ik_f x) + RA \exp(-ik_f x), \tag{46}$$

where A is the complex amplitude of the incident wave, R denotes the reflection coefficient of the specimen, $k_f = \omega/v_f$ is the acoustic wave number in air, and x denotes the distance from the surface of the specimen. By measuring the pressure at two different distances from the surface, the

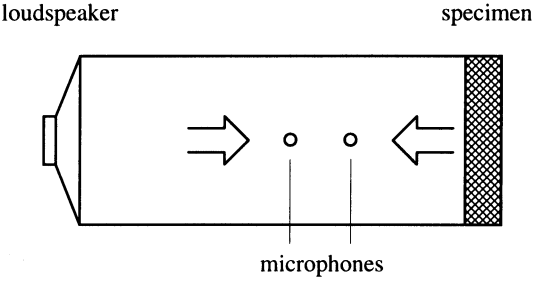

FIG. 7. Schematic diagram of acoustic reflection measurement in the Kundt tube.

reflection coefficient can be obtained from

$$R = \frac{p(x_1)\exp(ik_f x_2) - p(x_2)\exp(ik_f x_1)}{p(x_2)\exp(-ik_f x_1) - p(x_1)\exp(-ik_f x_2)}. \tag{47}$$

Assuming that the transmitted energy is absorbed in the porous material without any significant reflection from the back wall of the specimen, this reflection coefficient is determined by the characteristic impedance of the specimen Z and that of air $Z_f = (\gamma p_0 \rho_f)^{1/2}$:

$$R = \frac{Z - Z_f}{Z + Z_f}. \tag{48}$$

Equations (47) and (48) can be solved for the unknown impedance of the specimen as

$$Z = iZ_f \frac{p(x_2)\sin(k_f x_1) - p(x_1)\sin(k_f x_2)}{p(x_1)\cos(k_f x_2) - p(x_2)\cos(k_f x_1)}. \tag{49}$$

The thereby determined characteristic impedance of the porous specimen is related to the frequency-dependent dynamic density and modulus via Eq. (26).

The characteristic impedance and propagation constant become much more difficult to measure for porous materials of high flow resistivity. Ideally, the specific (surface) impedance of the sample as well as its transfer function along its length must be measured. Figure 8 shows a schematic diagram of the modified system capable of simultaneous specific impedance and transfer function measurements [31].

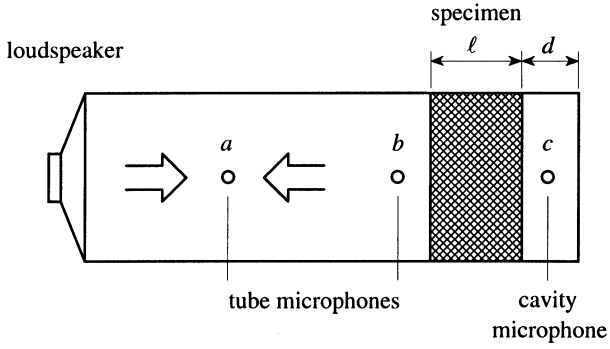

FIG. 8. Schematic diagram of the modified system capable of simultaneous specific impedance and transfer function measurements.

Assuming that the acoustic attenuation over the finite length ℓ of the specimen is not too high, the specific or surface impedance Z_s of the specimen is different from the characteristic impedance Z and can be calculated according to the waveguide equation

$$Z_s = Z\frac{Z_d + Z\tanh(k\ell)}{Z + Z_d\tanh(k\ell)}, \tag{50}$$

where Z_d denotes the input impedance of the backing cavity of length d:

$$Z_d = -i\rho_f v_f \cot(k_f d). \tag{51}$$

Here v_f, ρ_f, and k_f denote the sound velocity, density, and wave number, respectively, in air. The specific impedance is measured by the tube microphones a and b in the previously described conventional way. The transfer function H is measured by comparing the signal of microphone b directly in front of the specimen to that of microphone c behind the specimen, that is, $H = p_c/p_b$. After compensating for the phase shift caused by the inevitable small distance between these microphones and the specimen, the characteristic impedance Z and the wave number k can be separately determined from Z_s and H [31]. In practice, all three microphones will have slightly different frequency responses, therefore they must be calibrated against each other after removing the specimen. This method, which was used by Champoux and Allard [26] to obtain the experimental data previously shown in Fig. 6, works very well in the 100 Hz to 4 kHz frequency range on as large as 8-cm-long specimens of higher than 50 darcy (D) permeability.

5.3.1.3 Ultrasonic Measurements. Impedance measurements based on the described reflection technique are usually done in the 10-Hz to 10-kHz frequency range. In low-permeability porous materials, the wave propagation is essentially diffuse and both the characteristic impedance and wave number are determined by the same properties of the medium. Through-transmission measurements are also feasible at higher frequencies where the attenuation of the wave is low enough to enable penetration depths of many wavelengths. Transmission measurements through porous specimens of lower permeability such as natural rocks can be done in the 10-kHz to 1-MHz ultrasonic frequency range [19, 32]. Figure 9 shows a block diagram of the experimental system used to characterize porous materials by acoustic wave transmission in the ultrasonic frequency range between 10 kHz and 500 kHz. The transmitter is driven by a tone burst of a few cycles. The received signals with and without the specimen placed between the transducers are digitally stored. The computer selects the first five cycles of the signal, from which it determines the insertion loss L_i and insertion delay t_i. The thickness of the specimen is usually varied between 1 and 5 mm to

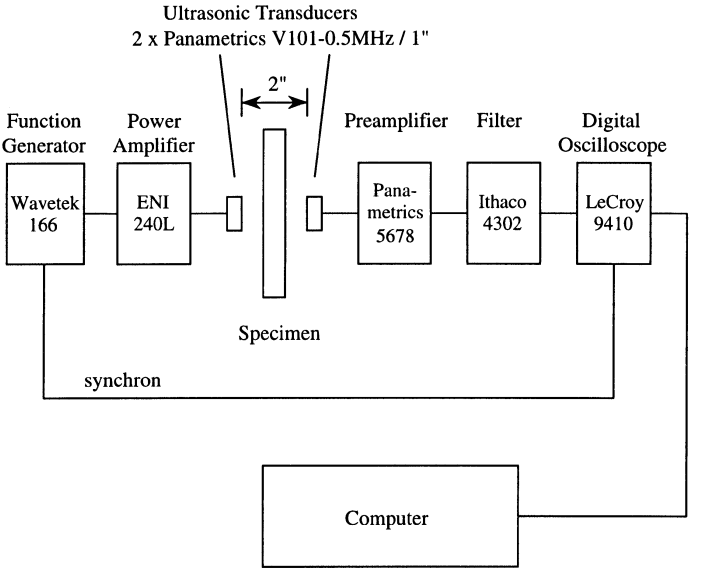

FIG. 9. Block diagram of the experimental system used to characterize porous materials by acoustic wave transmission in the ultrasonic frequency range between 10 kHz and 500 kHz. Reprinted with permission from P. B. Nagy, *J. Acoust. Soc. Am.* 93, 3224–3234 (1993).

accommodate different permeabilities over the widest possible frequency range. Because of the very high attenuation in low-permeability specimens, resonance peaks in the transmission are generally very weak but sometimes, especially at lower frequencies, faintly visible.

Because of the tremendous acoustical mismatch between the incident compressional wave and the porous solid, all the incident energy is either reflected or transmitted via the slow wave without generating appreciable fast compressional or shear transmitted waves. In spite of the excellent coupling between the incident compressional wave and the transmitted slow wave, slow waves cannot propagate in air-saturated porous samples as easily as in water-saturated ones [33]. Since the kinematic viscosity of air is so large and the velocity of sound so small, there is only a very narrow frequency window where the attenuation coefficient is sufficiently low to observe a more or less dispersion-free, scattering-free slow wave. This "window" is set by the conditions that the viscous skin depth $\delta = (2\eta/\rho_f \omega)^{1/2}$ be less than the pore size a_p and, simultneously, the wavelength λ be larger than the grain size a_g. It can be shown that in typical air-filled porous specimens there is usually no frequency window where more or less

dispersion-free and attenuation-free slow wave propagation can be expected. However, strongly dispersive and attenuated slow wave propagation can be observed over a much larger ultrasonic frequency range [19].

In the low-frequency diffuse regime, where transmission-type measurements are not feasible because of the very high attenuation coefficient, we must determine the complex characteristic impedance from reflection-type measurements. In the high-frequency propagating regime, we can use through-transmission measurements to determine the velocity and attenuation coefficient of the slow compressional wave. Even then, but especially in the transition region between the diffuse and propagating regimes, one must take into account the total transmission loss T_0 caused by the significant acoustical impedance mismatch between the air and the air-filled specimen:

$$T_0(\omega) = \frac{4}{2 + Z(\omega)/Z_f + Z_f/Z(\omega)}. \tag{52}$$

At very high frequencies, the dynamic density and bulk modulus given in Eqs. (44) and (45) approach $\tilde{\rho} \approx \rho_f \alpha_\infty$ and $\tilde{K} \approx K_f$, respectively. From Eqs. (25) and (26) the sound velocity and characteristic impedance then can be approximated respectively as $v \approx v_f/\sqrt{\alpha_\infty}$ and $Z \approx Z_f\sqrt{\alpha_\infty}/\phi$ so that the total transmission loss can be written as follows:

$$T_0 \approx T_h = \frac{4}{2 + \alpha_\infty^{1/2}/\phi + \phi/\alpha_\infty^{1/2}}. \tag{53}$$

For example, for $\phi = 0.3$ and $\alpha_\infty = 1.79$, the transmission loss $20 \log_{10} T_0 \approx -4.5$ dB. By taking the high-frequency limits, we inevitably underestimate the total transmission loss and, consequently, slightly overestimate the attenuation coefficient. Also, because of the phase shift caused by the complex nature of $T_0(\omega)$, we slightly underestimate the slow wave velocity in samples of small thickness. To achieve better agreement between the experimental measurements and theoretical calculations, we can correct our analytical results for the difference between the actual transmission loss $T_0(\omega)$ and its real valued asymptote T_h [32]. The normalized velocity and attenuation coefficient are then directly calculated from the actually measured insertion loss L_i and insertion delay t_i of airborne ultrasonic waves through thin slabs of porous materials.

Figure 10 shows an example of the comparison between theoretical and experimental results for a grade 55 porous glass specimen of $\kappa_0 \approx 11$ D [32]. Generally, there is a good agreement between the theoretically predicted and experimentally measured slow wave velocities. For the attenuation coefficient, the agreement is less perfect. Figure 11 shows a comparison between

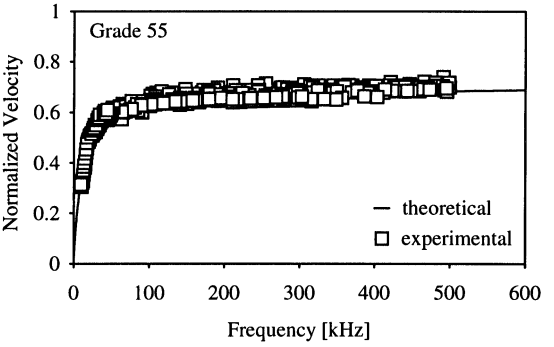

FIG. 10. Example of the comparison between theoretical and experimental results for a grade 55 porous glass specimen of $\kappa_0 \approx 11$ D. Reprinted with permission from P. B. Nagy, *J. Acoust. Soc. Am.* 93, 3224–3234 (1993).

the theoretical and experimental results for grades 40 through 175. As the pore size is gradually increased, viscous losses decrease, while scattering losses become stronger. At first only at higher frequencies (grades 40 and 55), then throughout the whole frequency range (grades 90 and 175), the experimentally observed attenuation coefficient significantly overshoots the theoretical prediction and approaches a linear asymptote (dashed lines in Fig. 11). Similar excess attenuation was also observed in a very high porosity (98%) air-filled absorbent above 300 kHz by Leclaire *et al.* [34]. In this frequency region, the scattering-induced attenuation plays an important role in the total attenuation in these samples. For example, the diameter of the sintered glass beads in porous glass grade 175 is $d_g \approx 600\,\mu$m; that is, $kd_g \geqslant 1$ above 60 kHz.

The same ultrasonic technique can be also adapted to the characterization of porous natural rocks of permeability between 100 mD and 1 D. Basically, the results are fairly similar to those obtained for synthetic materials, although the scatter of the data is usually larger due to inherent macroscopic inhomogeneities found in most natural rocks. Figure 12 shows the normalized slow wave velocity and attenuation coefficient in a 2.1-mm-thick Sunset Blush Massillon sandstone specimen of $\phi = 15\%$ porosity and $\kappa_0 = 600$ mD permeability [32]. The tortuosity was determined by best-fitting the theoretical curve to the measured experimental velocity data as $\alpha_\infty = 2.8$. Again, the experimentally measured velocity agrees quite well with the analytical results, while the attenuation exhibits higher than predicted attenuation and more of less linear frequency dependence.

5.3.1.4 Slow Wave Imaging. At ultrasonic frequencies, the observed acoustic attenuation in porous materials is usually dominated by viscous losses, but elastic scattering can also contribute. Probably the most basic

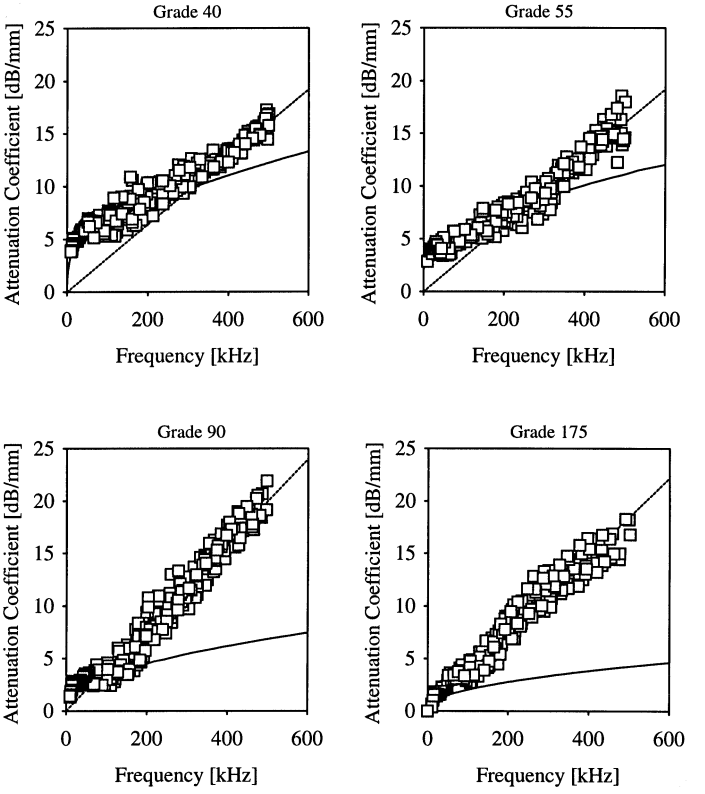

FIG. 11. Slow wave attenuation coefficient as a function of frequency for four different grades of air-filled cemented glass bean specimens. Symbols are experimental data, solid lines are theoretical curves, and dotted lines are linear asymptotes. Reprinted with permission from P. B. Nagy, *J. Acoust. Soc. Am.* 93, 3224–3234 (1993).

difference between viscous and elastic scattering is exhibited through their substantially different effect on the total acoustic energy carried by the slow compressional field. Viscous and thermal losses directly reduce the total acoustic energy by dissipation into heat. On the other hand, elastic or geometrical scattering simply converts the well-collimated coherent acoustic wave into a diffusely propagating incoherent wave without reducing the total acoustic energy. One way to differentiate between viscous and elastic scattering is by considering the frequency dependence of the total field at any particular point. In the case of viscous scattering, a dark spot of higher than average attenuation remains highly attenuated at all frequencies as the signal becomes progressively weaker with increasing frequency. In compari-

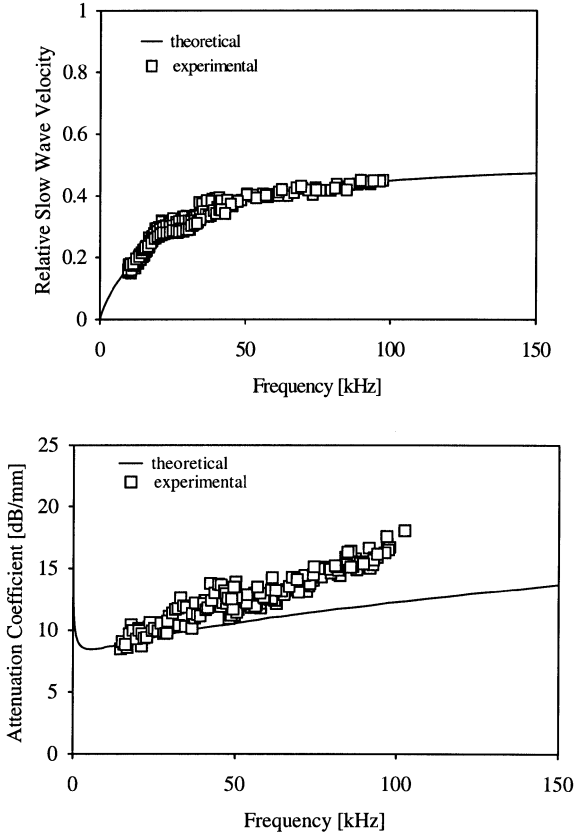

FIG. 12. Normalized slow wave velocity and attenuation coefficient in a 2.1-mm-thick Sunset Blush Massillon sandstone specimen. Reprinted with permission from P. B. Nagy, *J. Acoust. Soc. Am.* 93, 3224–3234 (1993).

son, in the case of elastic or geometrical scattering, a dark spot is generally due to destructive interference between otherwise strong incoherent components. The same spot often becomes brighter or less attenuated at higher frequencies, where the previously destructive interference changes to constructive one, a clear sign of dominantly incoherent transmission, which cannot happen in the case of viscous scattering. Whenever the attenuation is dominated by viscous losses, localized attenuation measurements can be used to obtain a map of the specimen, which corresponds to the permeability distribution of the porous formation.

Such imaging experiments were conducted in a number of synthetic materials and natural rocks [35, 36]. The irregularly shaped pore channels

and the macroscopic inhomogeneity of the porous frame result in a highly uneven flow pattern, which increases the viscous losses and effectively decreases the dynamic permeability of the material. In slow wave imaging, both transmitter and receiver transducers must be equipped with special Plexiglas lenses that focus the ultrasonic beams to the plane of the thin specimen to be inspected to assure close to diffraction limited lateral resolution. Figure 13 shows the slow wave image of a 1.1-mm-thick Berea sandstone slice of 400 mD average permeability with a horizontal crack (bright stripe) close to the bottom part. Figure 14 shows the slow wave image of a 2.5-mm-thick Massillon sandstone sample of 600 mD average permeability at 140 kHz. This specimen exhibits a rather uneven attenuation distribution with a very distinct dark stripe running in a more or less vertical direction on the left side of the picture. This feature was identified as a highly consolidated streak of low-porosity material. This kind of layered behavior is fairly typical to natural rock specimens. As a further example, Fig. 15 shows the slow wave image of a Massillon sandstone specimen of 600 mD permeability at 85 kHz with a characteristic stitching pattern formed by low-permeability areas. Slow wave imaging directly measures the transport properties of the permeable material and requires no inherent postprocessing at all. Of course, the evaluation of these slow wave images in terms of meaningful geophysical material parameters requires further studies of the contrast mechanism as well as extensive comparison of the acoustic pictures with other conventional images to better interpret the data.

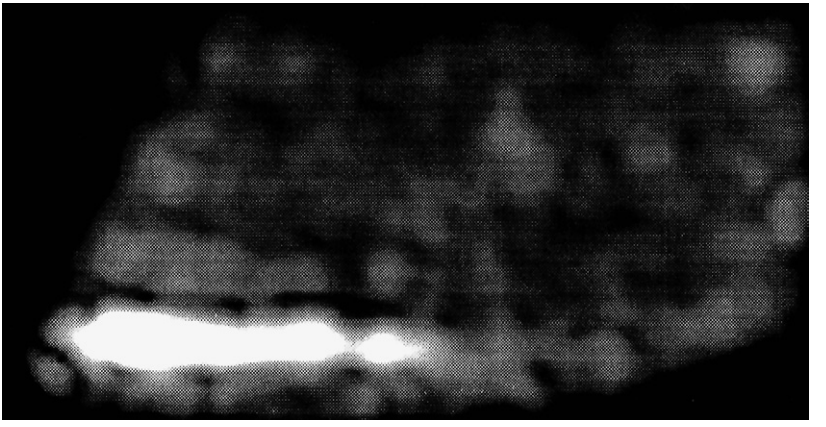

FIG. 13. Slow wave image of a 1- × 2-in., 1.1-mm-thick Berea sandstone sample of 400 mD average permeability at 210 kHz. Reprinted with permission from P. B. Nagy, B. P. Bonner, and L. Adler, *Geophys. Res. Lett.* 22, 1053–1056 (1995).

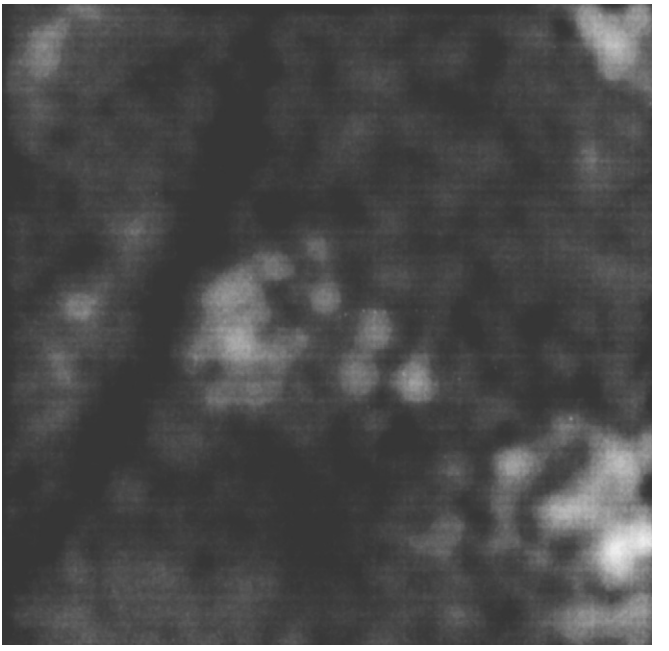

FIG. 14. Slow wave image of a 2.2- × 2.2-in., 2.5-mm-thick Massillon sandstone sample of 600 mD average permeability at 140 kHz. Reprinted with permission from P. B. Nagy, B. P. Bonner, and L. Adler, *Geophys. Res. Lett*. 22, 1053–1056 (1995).

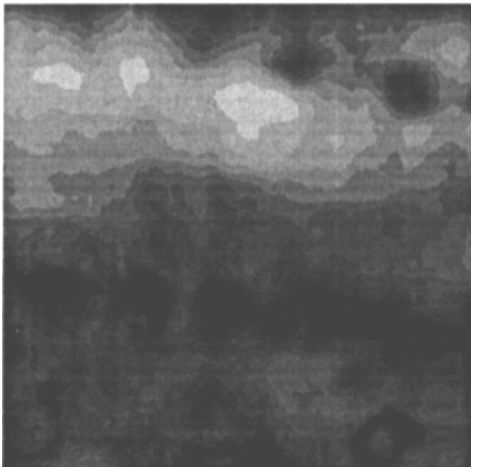

FIG. 15. Slow wave image of a 2.4- × 2.4-in. Massillon sandstone sample of 600 mD average permeability at 85 kHz. Reprinted with permission from P. B. Nagy, B. P. Bonner, and L. Adler, *Geophys. Res. Lett*. 22, 1053–1056 (1995).

5.3.1.5 Pressure Dependence. The total attenuation of slow waves through air-filled permeable solids can be attributed to absorption and scattering effects. As we have seen before, the absorption loss is mainly due to viscous friction and partly to thermal effects. Generally, the viscous loss is a function of the pore size as measured by the viscous skin depth. Similarly, the usually lower thermal loss is a function of the pore size, as measured by the relevant yardstick: the diffusion length in the gas. In the previously discussed models, these losses are separately accounted for in the complex density and bulk modulus of the material. In most cases, the inspection frequency is chosen to be low enough (below 5 kHz) to neglect scattering losses. However, in pursuit of better imaging resolution, it is usually necessary to increase the inspection frequency well above the scattering limit, therefore we must either eliminate or account for the additional scattering losses in our measurements. The scattering loss is another function of the pore size, as measured by the relevant yardstick: the acoustic wavelength. It is well known that the viscosity, thermal conductivity, and sound velocity of gases are all independent of pressure and are functions of temperature only. Therefore, the viscous skin depth and diffusion length are strongly pressure-dependent because they are inversely proportional to the square root of density. In comparison, the acoustic wavelength is independent of pressure. As a result, absorption losses are also pressure-dependent, while scattering losses are not [37]. Although the exact pressure dependence of the absorption loss is not known generally, certain assumptions can be made. In a wide range of applications, both the low- and high-frequency absorption coefficients are proportional to the square root of the kinematic viscosity η/ρ_f of the gas, therefore the absorption is expected to be inversely proportional to the square root of pressure. The pressure dependence of the total attenuation is then of the form $\alpha_{\text{total}} = \alpha_a p^n + \alpha_s$, where α_a is the absorption loss at unit pressure, α_s is the constant scattering loss, and the power n is close to -0.5.

Figure 16 shows the slow wave attenuation coefficient as a function of air pressure for four different grades of air-filled porous glass specimens at 350 kHz. The frequency-dependent attenuation of these specimens at ambient pressure was previously shown in Fig. 11. Symbols are experimental data and the solid lines are best-fitting polynomials of the form of $\alpha(p) = \alpha_s + \alpha_a p^{-1/2}$. There is a very good fit between the experimentally observed pressure dependence of the slow wave attenuation and the best-fitting polynomial with the inverse square root pressure term. If we fit the data by a more general polynomial containing an arbitrary power of pressure the best fitting parameter turns out to be $-\frac{1}{2}$ within the statistical error.

The α_a of the best-fitting polynomial represents the experimentally determined absorption coefficient for $p = 1$ atm, that is, at atmospheric pressure. On the other hand, α_s can be regarded as the experimentally determined

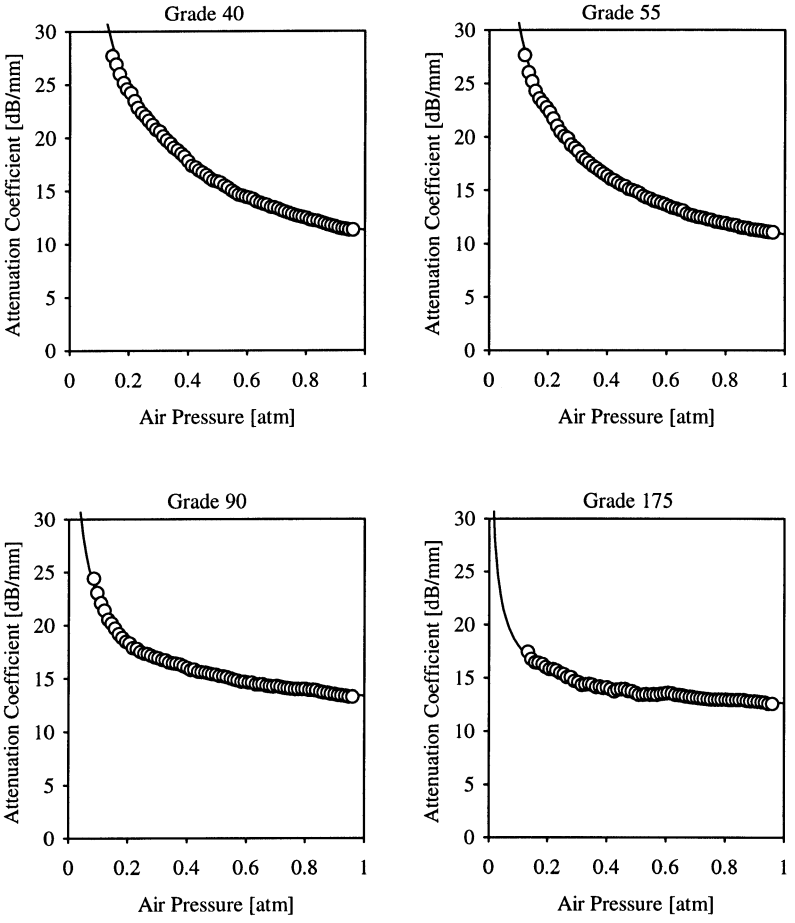

FIG. 16. Slow wave attenuation coefficient as a function of air pressure for four different grades of air-filled cemented glass bead specimens at 350 kHz. Reprinted with permission from P. B. Nagy and D. L. Johnson, *Appl. Phys. Lett.* 68, 3707–3709 (1996).

scattering coefficient, which is independent of pressure. Figure 17 shows the total attenuation coefficient and its absorption component for four grades of air-filled porous glass specimens as determined from the best-fitting polynomial. For both low and high frequencies, the functional dependence of the theoretical absorption coefficient on the principal material properties can be summarized as $\alpha_a \propto \sqrt{\omega\eta/\rho_f\kappa_0}$, where κ_0 denotes the static permeability of the frame [32]. Without varying the air pressure, we must rely on

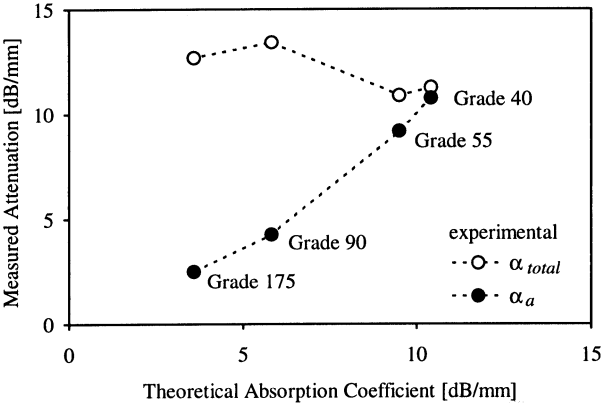

FIG. 17. Comparison between measured and calculated attenuation coefficients for four different grades of air-filled porous glass bead specimens at 350 kHz. Reprinted with permission from P. B. Nagy and D. L. Johnson, *Appl. Phys. Lett.* 68, 3707–3709 (1996).

the measured total attenuation coefficient, which correlates very poorly with the theoretical absorption coefficient calculated from the permeability of the material. Clearly, the absorption coefficient, as determined from the pressure-dependent component of the measured total attenuation, correlates much better with the theoretical prediction. In coarse-grain materials, only the thereby determined absorption coefficient can be regarded as a reliable measure of dynamic permeability. The significant excess attenuation observed in the two largest grades appears to be mainly due to scattering as indicated by the weak pressure dependence of the total loss.

The already demonstrated pressure dependence can be exploited to further enhance the slow wave inspection method for air-saturated porous solids. In particular, using high-pressure air as the saturating fluid can significantly expand the applicability of the technique. For slow wave propagation, an ideal saturating fluid should really have physical properties somewhere between those of water and air so that the viscous losses would be low, but the fluid motion still would not cause significant vibrations in the frame. Although there is no such natural fluid, ordinary high-pressure air combines the best of both worlds. Figure 18 shows the measured slow wave attenuation coefficient through a 2-mm-thick Berea sandstone sample of 200 mD permeability at 350 kHz. This is a relatively low permeability specimen that could not be inspected above 150–200 kHz at atmospheric pressure since the insertion loss exceeded the 70-dB dynamic range of the system. The slow wave attenuation in such low-permeability materials is dominated by viscous absorption, which greatly decreases with increasing

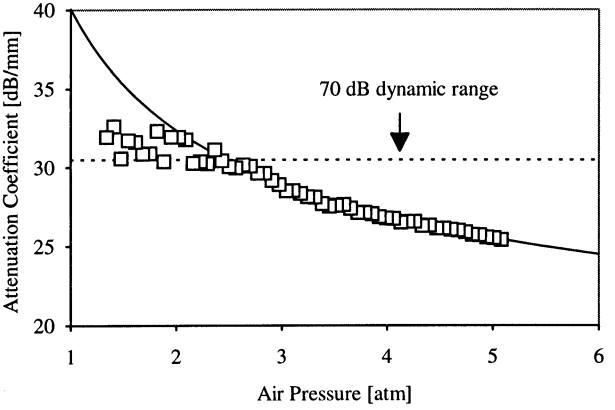

FIG. 18. Measured slow wave attenuation coefficient through a 2-mm-thick Berea sandstone of 200 mD permeability at 350 kHz. Reprinted with permission from P. B. Nagy and D. L. Johnson, *Appl. Phys. Lett.* 68, 3707–3709 (1996).

pressure. Above approximately 3 atm, the insertion loss drops into the measurable dynamic range. Based on this method, a high-pressure slow wave imaging technique can be developed in the future for very low permeability specimens such as natural rocks.

5.3.2 Sound Propagation in Water-Filled Porous Materials with Elastic Frame

In general, sound propagation in air-filled porous materials can be modeled by assuming an ideal rigid frame without any significant loss of accuracy. In contrast, sound propagation in water-saturated porous materials cannot be modeled without properly accounting for acoustic coupling between the fluid and the elastic frame. The most widely used phenomenological acoustic model for fluid-saturated porous materials was developed by Biot [11, 12]. In the following, we present a short summary of Biot's theory.

The stresses are defined as normal and tangential forces acting on the frame or the fluid per unit area of the porous solid. In particular, the stress in the fluid can be written as $\sigma_{ij}^{f} = -\phi p \delta_{ij}$, where p denotes the pressure in the fluid, ϕ is the porosity, and δ_{ij} is the so-called Kronecker delta. Biot derived the following constitutive equations from the strain energy density in the fluid-filled material:

$$\sigma_{ij}^{s} = [(P - 2N)\theta^{s} + Q\theta^{f}]\delta_{ij} + 2N\varepsilon_{ij}^{s} \tag{54}$$

and

$$\sigma_{ii}^{f} = Q\theta^{s} + R\theta^{f}. \tag{55}$$

Here, ε_{ij} denotes the strain tensor, $\theta = \varepsilon_{11} + \varepsilon_{22} + \varepsilon_{33}$ is the dilatation, the superscripts s and f refer to the solid and fluid phases, respectively; P, N, Q, and R are elastic constants that can be determined from independent measurements [38]; and N is the shear modulus of the porous frame, which is not affected by the fluid at all. The other three parmeters can be calculated from

$$P = \frac{(1-\phi)(1-\phi-K_b/K_s)K_s + \phi(K_s/K_f)K_b}{1-\phi-K_b/K_s+\phi(K_s/K_f)} + \frac{4}{3}N, \tag{56}$$

$$Q = \frac{\phi(1-\phi-K_b/K_s)K_s}{1-\phi-K_b/K_s+\phi(K_s/K_f)}, \tag{57}$$

and

$$R = \frac{\phi^2 K_s}{1-\phi-K_b/K_s+\phi(K_s/K_f)}, \tag{58}$$

where K_b, K_s, and K_f are the bulk moduli of the porous frame, the solid, and the fluid, respectively.

Biot showed that one shear wave and two compressional waves, namely the fast and slow modes can propagate in a fluid-saturated porous medium [11, 12]. The complex wave numbers of these three modes can be calculated as follows:

$$\tilde{k}_{\text{shear}} = \sqrt{\frac{\omega^2(\tilde{\rho}_{11}\tilde{\rho}_{22} - \tilde{\rho}_{12}^2)}{N\tilde{\rho}_{22}}}, \tag{59}$$

$$\tilde{k}_{\text{fast}} = \sqrt{\frac{\omega^2(P\tilde{\rho}_{22} + R\tilde{\rho}_{11} - 2Q\tilde{\rho}_{12} - S)}{2(PR-Q^2)}}, \tag{60}$$

$$\tilde{k}_{\text{slow}} = \sqrt{\frac{\omega^2(P\tilde{\rho}_{22} + R\tilde{\rho}_{11} - 2Q\tilde{\rho}_{12} + S)}{2(PR-Q^2)}}, \tag{61}$$

where

$$S = \sqrt{(P\tilde{\rho}_{22} + R\tilde{\rho}_{11} - 2Q\tilde{\rho}_{12})^2 - 4(PR-Q^2)(\tilde{\rho}_{11}\tilde{\rho}_{22} - \tilde{\rho}_{12}^2)} \tag{62}$$

The frequency-dependent complex densities are defined as $\tilde{\rho}_{11} = \rho_{11} - iF(\omega)$, $\tilde{\rho}_{22} = \rho_{22} - iF(\omega)$, and $\tilde{\rho}_{12} = \rho_{12} + iF(\omega)$, where $F(\omega)$ is a frequency-dependent correction term representing viscous losses in the saturating fluid; $\rho_{11} + \rho_{12} = (1-\phi)\rho_s$ and $\rho_{22} + \rho_{12} = \phi\rho_f$ are the densities of the solid

and fluid phases normalized according to their volume fractions, respectively; and $\rho_{12} = \rho_f \phi(1 - \alpha_\infty)$ is a frequency-independent inertia coupling term determined by the tortuosity of the specimen. There are numerous models that can be used to relate $F(\omega)$ to macroscopic properties of the permeable solid. For example, according to the previously discussed dynamic permeability model of Johnson *et al.* [24].

$$F(\omega) = \frac{4\rho_f \phi \alpha_\infty}{c^2} \frac{\delta^2}{\Lambda^2} \left(1 + i \frac{c^4 \Lambda^2}{8\delta^2}\right)^{1/2}. \tag{63}$$

At sufficiently high frequencies when the viscous skin depth δ becomes negligible with respect to the relevant pore size Λ, $F(\omega)$ diminishes, therefore the three density terms become real and all three bulk modes become nondispersive and attenuation free. Even when viscous losses are significant and the waves, especially the slow compressional one, is strongly attenuated, the actual dispersion is relatively small and the velocities can be well estimated from Eqs. (59)–(61) by the real-valued high-frequency asymptotic densities.

The most interesting feature of acoustic wave propagation in fluid-saturated porous media is the appearance of a second compressional wave, the so-called slow wave. The main characteristic of this mode is that its velocity is always lower than both the compressional wave velocity in the fluid and the longitudinal velocity in the solid frame. Below a critical frequency, which depends on the pore size in the frame and the viscosity of the fluid, the slow compressional wave is highly dispersive and strongly attenuated over a single wavelength. Above this critical frequency, it becomes a dispersion-free propagating wave with increasing but fairly low attenuation. The transition point between low-frequency and high-frequency behavior can be estimated as

$$\omega_c \approx \frac{2\eta\phi}{\rho_f \alpha_\infty \kappa_0}, \tag{64}$$

which is typically around 1–10 kHz for water-saturated porous solids of around 1 D permeability. The slow compressional wave represents a relative motion between the fluid and the solid frame. This motion is very sensitive to the viscosity of the fluid and the dynamic permeability of the porous formation. Naturally, low-viscosity liquids such as water are the fluids most often used in experimental studies of slow wave propagation. As mentioned before, another way to reduce the excessive attenuation of slow waves in porous materials is to use special fluids of very low viscosity to saturate the specimen [15–18].

5.3.2.1 Ultrasonic Transmission Measurements in Immersion. Plona was the first to observe slow wave propagation in water-saturated porous ceramics at ultrasonic frequencies [13]. His simple approach is based on acoustic refraction at a fluid–solid interface at the surface of an immersed specimen. The experimental arrangement is shown in Fig. 19. The porous solid is cut into a thin plate of parallel surfaces and placed between the well-aligned transmitter and receiver operated in broadband pitch-catch mode. Generally, the incident wave produces three bulk waves in the solid with varying amplitudes, depending on the properties of the porous specimen and the angle of incidence. When these bulk waves hit the opposite side of the solid plate they give rise to three separate through-transmitted compressional pulses, which are recorded at different angles of incidence. Figure 20 shows the slow, fast, and shear wave transmission coefficients through a water-saturated porous glass plate. The physical parameters of the glass bead specimen and details of the calculation are given in the paper by Wu *et al.* [39]. At normal incidence, only fast and slow compressional waves are generated in the porous solid, but the slow wave pulse is usually overshadowed by multiple reflections of the stronger fast wave within the plate. As the angle of incidence is increased, the first arriving pulse due to the fast wave moves forward, while the slow one moves backward. However, a shear component also appears, and it becomes stronger as the angle of incidence is increased. The pulse train becomes much clearer above the first

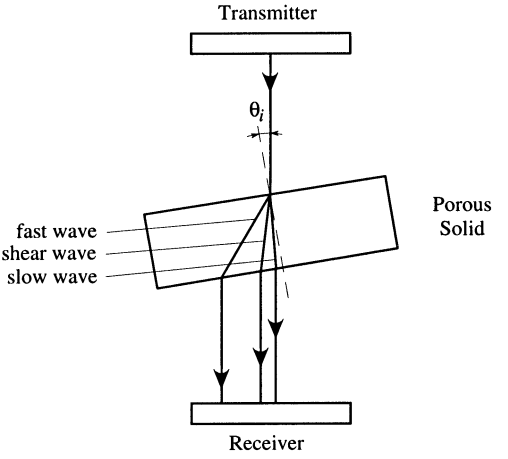

FIG. 19. The experimental arrangement of Plona's through-transmission immersion measurement.

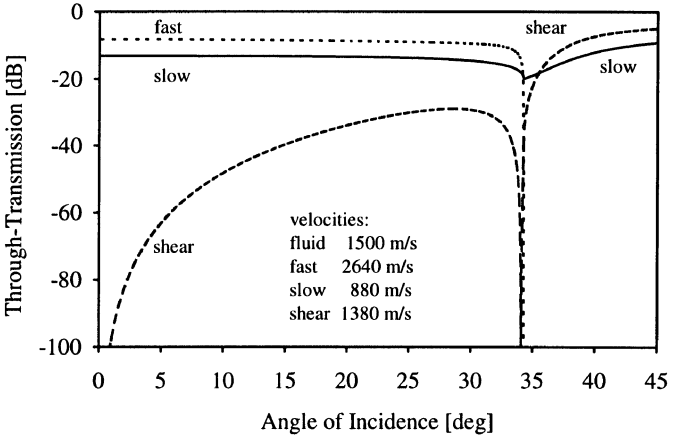

FIG. 20. Slow, fast, and shear transmission coefficients through a water-saturated porous glass plate.

critical angle $\theta_{c1} = \sin^{-1}(v_f/v_{\text{fast}})$, where the fast compressional wave in the fluid-saturated solid becomes evanescent and does not contribute to the through-transmitted signal. In this range, the slow compressional wave usually becomes separable from the shear component as it moves backward; that is, it arrives later when the angle of incidence is increased. In many porous solids, the shear velocity is also higher than the compressional velocity in the fluid, therefore there exists a second critical angle $\theta_{c2} = \sin^{-1}(v_f/v_{\text{shear}})$ above which the shear wave also becomes evanescent and the slow wave becomes the sole vehicle for sound transmission through the plate (in Fig. 20, the sharp minimum at about 34° corresponds to the first critical angle and there is no second critical angle since the shear velocity is lower than the compressional velocity in the fluid).

Plona's experimental results [13] were immediately shown to be in excellent agreement with the predictions of Biot's theory as stated in Eqs. (56)–(62). Figure 21 shows the comparison of theoretical predictions and experimental results for the fast compressional, slow compressional, and shear waves in sintered porous glass [40]. Both fast and shear wave velocities decrease with increasing porosity, while the slow compressional wave velocity increases. The main reason for the increasing slow wave velocity is the decreasing tortuosity; that is, a purely geometrical effect. For the sake of simplicity, let us assume a perfectly stiff frame. Then Eq. (61) can be approximated as $\tilde{k}_{\text{slow}} \approx \sqrt{\omega^2 \tilde{\rho}_{22}/R}$, where $R \approx \phi K_f$. At ultrasonic

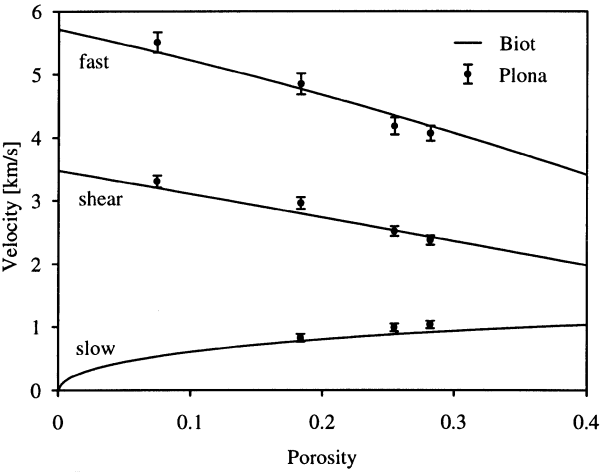

FIG. 21. Comparison of theoretical predictions and experimental results for the fast compressional, slow compressional, and shear waves in sintered porous glass. Reprinted with permission from J. G. Berryman, *Appl. Phys. Lett.* 37, 382–384 (1980).

frequencies where the viscosity-induced dispersion becomes negligible, the complex density $\tilde{\rho}_{22} \approx \rho_{22} = \alpha_\infty \phi \rho_f$ can be approximated by its real-valued high-frequency asymptote, and the slow wave velocity becomes simply $v_{\text{slow}} = \omega/\tilde{k}_{\text{slow}} \approx v_f/\sqrt{\alpha_\infty}$. For cemented or slightly sintered spherical beads, the tortuosity can be estimated from the porosity as $\alpha_\infty \approx (1 + \phi^{-1})/2$ [40]. For relatively low levels of porosity, the combination of these approximations predicts that the slow compressional wave velocity is proportional to the square root of porosity, as shown in Fig. 21.

The strength of the Biot theory lies in its predictive power, that is, that the frequency-dependent acoustic properties (velocity, attenuation, reflection, and transmission coefficients) of a permeable solid saturated with a Newtonian fluid can be calculated from 11 material parameters that can be measured independently. These parameters are porosity (ϕ), tortuosity (α_∞), permeability (κ_0), viscous characteristic length (Λ), fluid density (ρ_f), fluid bulk modulus (K_f), viscosity (η), solid density (ρ_s), solid bulk modulus (K_s), frame bulk modulus (K_b), and frame shear modulus (N). By measuring the frequency dependence of the ultrasonic transmission through two slabs of different thicknesses, Johnson *et al.* were able to separate bulk losses from reflection and transmission losses and found excellent agreement between theoretical predictions and experimental measurements without requiring any adjustable parameters [41, 42].

The attenuation coefficient can be calculated from the imaginary part of the complex wave number as follows:

$$\alpha_{\text{slow}} = -\text{Im}\{\tilde{k}_{\text{slow}}\} \approx \frac{\omega\,\text{Re}\{F(\omega)\}}{2v_f\sqrt{\alpha_\infty}\,\phi\rho_f}. \tag{65}$$

From Eq. (63), the high-frequency asymptote of the viscous coupling term is $F(\omega) \approx (1+i)\rho_f\phi\alpha_\infty\delta/\Lambda$ and the viscosity-induced attenuation can be approximated as

$$\alpha_{\text{slow}} \approx \frac{\omega\sqrt{\alpha_\infty}\,\delta}{2v_f\Lambda} = \sqrt{\frac{\eta\omega\alpha_\infty}{2v_f^2\Lambda^2\rho_f}}. \tag{66}$$

We can also express the viscous characteristic length Λ by the shape factor c from Eq. (42) and rewrite the attenuation coefficient as follows:

$$\alpha_{\text{slow}} \approx \frac{c}{4v_f}\sqrt{\frac{\eta\omega\phi}{\kappa_0\rho_f}}. \tag{67}$$

The attenuation coefficient is proportional to the square root of frequency. As for the crucial material parameters of the porous solid, the attenuation coefficient is proportional to the shape factor and the square root of porosity and inversely proportional to the square root of permeability.

As an example, Fig. 22 shows the experimental slow wave attenuation spectra in porous solids made of consolidated spherical beads [43]. Biot's

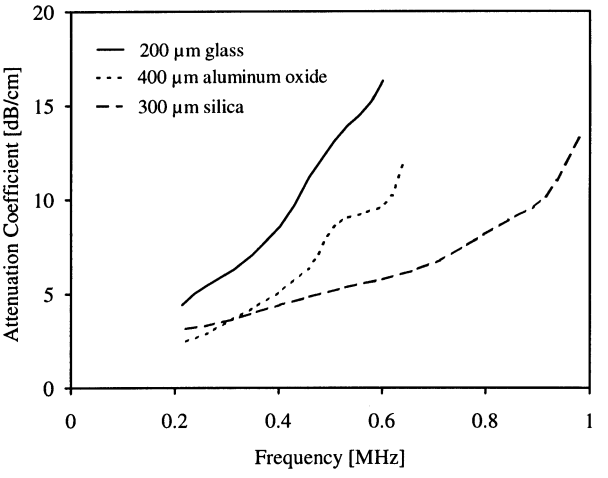

FIG. 22. Experimental slow wave attenuation spectra in porous solids made of consolidated spherical beads. Reprinted with permission from T. J. Plona and K. W. Winkler, *Multiple Scattering of Waves in Random Media and Random Surfaces*, pp. 341–356, The Pennsylvania State University, 1985.

theory proved to be very successful in predicting the velocity of the slow compressional wave, but the slow wave attenuation was found generally much higher than the theoretical value. For example, the viscosity-induced attenuation in the 300-μm-diameter silica bead specimen is predicted by Eq. (67) to be around 0.1 dB/cm at 500 kHz; that is, more than one order of magnitude lower than the experimentally determined value. One obvious reason why the measured attenuation coefficient is so high is excess loss due to scattering. Plona and Winkler showed that the slow wave attenuation in coarse-grained porous materials becomes proportional to the fourth power of frequency, which is a clear indication of Rayleigh-type elastic scattering [43]. The observed discrepancy in fine-grained materials is partly due to irregular pore geometry and partly to pore-wall roughness, which substantially reduce the high-frequency dynamic permeability of the specimens.

In comparison with the previously discussed air-saturation method, slow wave propagation in water-saturated porous solids is generally more difficult to adapt for materials characterization. Saturation must be done with extreme care either in a centrifuge or in a vacuum, since even the lowest level of residual air saturation can prevent slow wave propagation in the specimen. Theoretically, the slow compressional wave in immersion experiments is only 5–10 dB weaker than the fast compressional or shear modes, but it is much more attenuated. Also, because of its lower velocity, it arrives later than the other modes and it is often overshadowed by multiple reflections and scattered components of these stronger signals. The only exception is when the shear velocity is sufficiently high so that we can work above the second critical angle where the slow compressional wave becomes the only propagating mode in the fluid-saturated sample (unfortunately, this does not happen in most natural rocks, where the shear velocity is rather low). On the other hand, in the case of air saturation, the slow compressional wave is at least 70 dB stronger than all other modes and, due to the very low sound velocity in air, the shear critical angle drops below 15°, above which only the slow wave is transmitted through the sample [32]. This means that the highly attenuated slow wave will be submerged in electrical noise rather than spurious signals so it can be easily recovered by simple time averaging. In the case of air saturation, because of the tremendous acoustic mismatch between the incident compressional wave and the porous solid, all of the incident energy is either reflected or transmitted via the slow wave without generating appreciable fast compressional or shear transmitted waves.

5.3.3 Guided Wave Propagation in Water-Filled Porous Materials

Our previous examples involved bulk acoustic wave propagation in infinite fluid-saturated media. In the presence of a boundary separating two half-spaces, interface wave propagation along this boundary can also occur.

If the interface wave velocity is lower than any of the bulk velocities in the neighboring media, only evanescent waves are generated and the acoustic energy is concentrated into a narrow boundary layer around the interface. Such waves are called true interface waves as they can propagate without losing energy into the bulk of the material. If the interface wave velocity is higher than at least one of the bulk velocities in the neighboring media, propagating waves are also generated and the acoustic energy is not strictly concentrated into the boundary layer. Such waves are called leaky interface waves as they lose some of their energy to the bulk of the surrounding material as they propagate along the interface. A special form of interface waves occurs on the free (or essentially free, such as air-loaded) surface of fluid-saturated solids. If the surface curvature is low, such interface and surface waves follow the boundary contour, therefore they are also called guided waves. Other types of guided waves are normal modes of thin rods and plates, which exhibit additional strong dispersion due to structural resonances in the specimens.

5.3.3.1 Surface and Interface Waves. Acoustic wave interaction with a plane interface separating a superstrate fluid and a fluid-saturated porous solid substrate is governed by four boundary conditions [44]. Three of them — namely, the continuity of normal stress and displacement and the disappearance of the transverse stress at the interface — are the usual conditions required at ordinary fluid–solid interfaces. The only conceptual difference in the case of permeable solids is that the continuity of the normal displacement must be modified to express the conservation of fluid volume:

$$U_n' = \phi U_n + (1 - \phi) u_n, \tag{68}$$

where U_n', U_n, and u_n are the normal displacement components of the superstrate fluid, and the substrate fluid and solid, respectively, and ϕ denotes the porosity. The fourth boundary condition is Darcy's law applied to the surface pores of the permeable solid. The surface impedance Z_s is defined as the ratio between the discontinuity in pressure and the relative volume velocity of the fluid with respect to the frame below the interface [44, 45]:

$$p - p' = i\omega Z_s \phi (U_n - u_n), \tag{69}$$

where p and p' denote the fluid pressure in the pore space below the surface and in the superstrate fluid just above it, respectively, and ω is the angular frequency. Generally, Z_s is complex and the definition of Eq. (69) must be used. In the case of a fluid–fluid-saturated porous solid interface (e.g., in borehole Stoneley wave experiments to be discussed later), the finite surface impedance is due to the flow resistivity of the surface pores and its value depends on the viscosity of the fluid. The surface impedance can be also high

because of an elastic boundary layer such as the so-called mudcake in geophysical inspection of natural rocks. It has been also shown that, due to surface tension, practically closed-pore boundary conditions can prevail at an interface between a nonwetting fluid (e.g., air) and a porous solid saturated with a wetting fluid (e.g., water) [46]. In this case, the surface impedance is very high because of the stiffness of the microscopic fluid membranes extended by capillary forces over the otherwise open surface pores. When the surface impedance is purely imaginary, it is advantageous to introduce a surface stiffness parameter $T_s = i\omega Z_s$ so that the discontinuity in pressure is proportional to the average surface displacement of the fluid:

$$p - p' = T_s \phi (U_n - u_n). \tag{70}$$

In the case of ordinary solids, the previously mentioned three boundary conditions can be satisfied by three bulk waves, namely, the reflected compressional wave in the fluid and the longitudinal and shear transmitted waves in the solid. In the case of a permeable solid, an additional boundary condition is necessary to account for the presence of a fourth component; that is, the slow compressional wave in the fluid-saturated solid. Naturally, the most obvious effect of the increasing surface impedance is the sharp decrease in the transmitted slow compressional wave [39, 42, 47]. Interestingly, surface modes propagating along the interface are even more crucially dependent on the surface impedance. Feng and Johnson showed that there exists a new slow surface mode on a fluid–fluid-saturated porous solid interface with closed surface pores [48, 49]. They found that a maximum of three different types of surface modes can exist on a fluid–fluid-saturated porous solid interface depending on (i) the shear velocity of the frame and (ii) the surface conditions; that is, whether the pores are open or closed. In most cases, however, the pores are open at the surface, therefore the slow surface wave cannot be observed. The corresponding slow surface wave propagating along the free surface of a fluid-saturated porous solid seems to be easier to observe experimentally because the pores, which are naturally open when fully submerged in a wetting fluid, are essentially closed by capillary forces [46]. In the ideal case of completely closed surface pores and viscosity-free fluid, two types of surface wave can propagate: There is a pseudo-Rayleigh mode, which leaks its energy into the slow compressional wave, and a "true" surface mode with velocity slightly below that of the slow wave. The second mode is a simple form of the new interface mode predicted by Feng and Johnson [48, 49] when the superstrate fluid is extremely rare and highly compressible like air (theoretically, the slow interface mode also becomes slightly leaky, since its velocity is higher than the sound velocity in air, although the actual energy loss is negligible because of the large density difference between the two fluids).

The effect of completely "open" ($T_s = 0$) and completely "closed" ($T_s = \infty$) surface pores on the interaction of an acoustic wave with the fluid–fluid-saturated porous solid interface is quite easy to understand, but intermediate cases are much more complicated. A question of great practical importance is where and how the transition between these limiting cases occurs. Figure 23 shows the calculated velocity of the "true" slow surface wave and the leaky Rayleigh wave propagating on the surface of water-saturated porous glass as functions of the surface stiffness [50]. The "true" slow surface wave appears only above $T_s \approx 10^7$ N/m^3, where its velocity is equal to that of the slow bulk velocity. The velocity of this mode slightly decreases with increasing surface stiffness, but it flattens off above $T_s = 10^8$ N/m^3, and the total change is only approximately 5%. The Rayleigh velocity slightly increases as the surface stiffness increases and the transition is also around $T_s = 10^7$ N/m^3. It should be mentioned that Wu *et al.* obtained roughly the same transition value for the surface stiffness between open- and closed-pore boundary conditions by analyzing the reflection coefficient of a water–water-saturated porous glass interface at normal incidence [39].

At a fluid–solid interface, surface waves are most commonly excited and their velocities measured by simple immersion techniques. If the surface

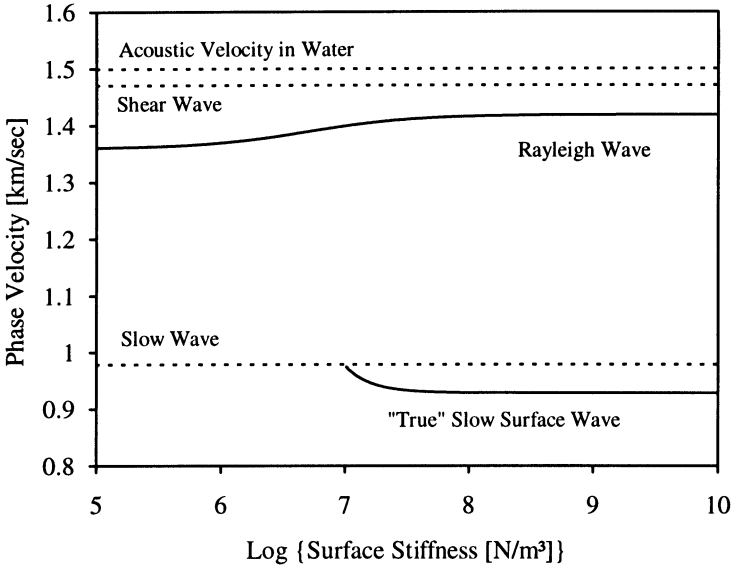

FIG. 23. Surface wave velocity versus surface stiffness on the free surface of water-saturated porous glass. Reprinted with permission from P. B. Nagy and G. Blaho, *J. Acoust. Soc. Am.* 95, 828–835 (1994).

wave velocity is higher than the fluid bulk velocity, the so-called Rayleigh angle phenomena occur due to mode conversion [51]. The excitation of the leaky Rayleigh wave can be detected in different ways, such as observing the Schoch displacement [52], beamsplitting [53, 54], or detecting increased backscattering [55, 56]. The Rayleigh velocity is easily calculated from the Rayleigh angle using Snell's law.

Clearly, when the surface wave does not leak into the fluid (its velocity is less than the fluid velocity), as in the case of the Scholte wave, other techniques must be applied. One way to generate both Rayleigh- and Stoneley-type surface modes on a liquid–solid interface is to make the surface slightly corrugated so that these modes become leaky into both media at particular frequencies where the periodicity of the corrugation is an integer multiple of the surface wavelength. These resonances produce sharp minima in the reflection coefficient of the interface, which can be used to calculate the surface wave velocities [57, 58]. The advantage of this technique over the conventional Rayleigh angle method is that it can be used to generate surface modes of very low phase velocities, which do not leak (or leak only at a very high angle) as they propagate along a smooth liquid–solid interface. This technique was later adapted to studying surface wave propagation on fluid-saturated porous materials by Mayes *et al.* [59].

Surface and interface waves can be also generated by direct excitation using conventional contact transducers [60]. This method is a modification of the edge-excitation method [4] and also can be readily used to generate and detect Scholte waves on a liquid–solid interface. Figure 24 shows the experimental arrangement of the direct generation technique of surface

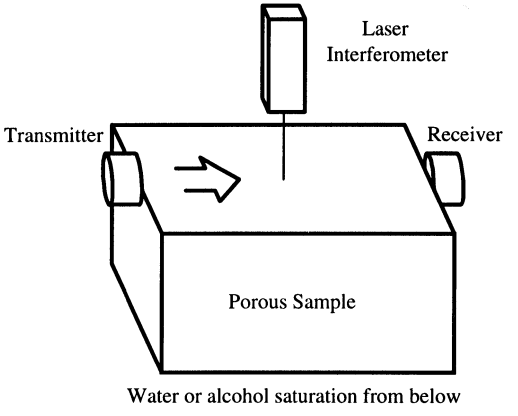

FIG. 24. Experimental arrangement for surface wave generation and detection on fluid-saturated porous materials.

waves. A vertically polarized shear transducer is mounted directly over the corner region so that it can generate an interface wave along the boundary. Saturation is achieved simply by soaking the specimen from below. Capillary forces pull the wetting fluid in the pores and evaporation at the top surface maintains a slow but continuous circulation of the fluid in the pore channels. The transmitter is driven by a tone-burst of two to three cycles between 100 and 300 kHz. Two detection techniques can be used. The normal component of the surface vibration can be measured by a laser interferometer at different locations or by a second vertically polarized shear transducer mounted at the opposite edge of the specimen.

Figure 25 shows the measured surface wave velocity in water-saturated Massillon and Berea sandstones between 100 and 600 mD [61]. The surface wave velocity measured in the wet specimen was normalized to the shear velocity in the dry specimen. The dashed line represents the overall trend in the data. In natural rocks, from 2 to 5 days are necessary to achieve full saturation with water at room temperature. It should be mentioned that during saturation, the velocity and attenuation of the compressional bulk wave both significantly increase. The shear velocity is basically unaffected by water saturation, although it drops 2–3% as a result of the added inertia of the liquid. In comparison, in the most permeable rocks, the surface wave velocity drops as much as 40% due to the presence of the slow surface mode. In low-permeability samples, below approximately 200 mD, the fluid is essentially immobilized in the pores by viscous forces. Such rocks behave

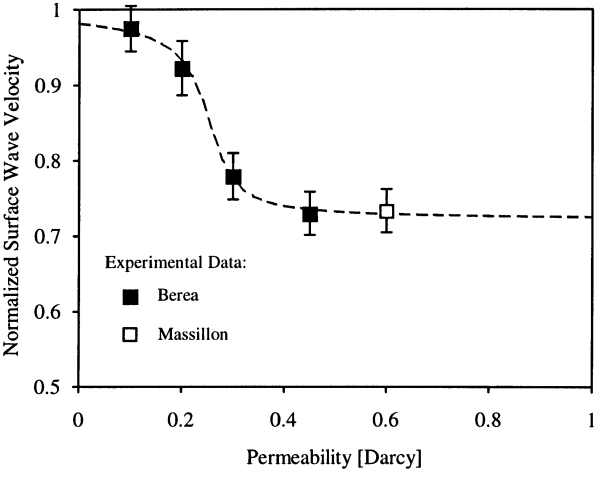

FIG. 25. Measured surface wave velocity in water-saturated Massillon and Berea sandstones between 100 and 600 mD. From L. Adler and P. B. Nagy, *J. Geophys. Res. Solid Earth*, 99, 17863–17869 (1994).

like ordinary solids; the surface wave velocity is only a few percent lower than the shear velocity regardless whether the sample is saturated or not.

These experimental results indicate that the primary relationship between the slow surface wave and permeability is governed by the viscous drag rather than by the surface stiffness. In low-permeability specimens, the fluid is kept immobile by viscous forces, therefore the dominant surface mode is the ordinary Rayleigh-type surface wave, while the slow surface mode is badly attenuated. In high-permeability specimens, assuming that the surface stiffness is still above the minimum required for closed-pore boundary conditions, the dominant surface mode is the slow surface mode, while the ordinary Rayleigh mode is strongly attenuated by leakage into the slow bulk mode. Theoretically, both Rayleigh and slow surface modes contribute to the detected surface vibration. Unfortunately, these two principal modes cannot be clearly separated in spite of their rather different velocities. Better separation could be achieved by either increasing the propagation time or decreasing the pulse length, that is, by increasing the bandwidth of the signal. Both avenues are essentially closed by the extremely high attenuation of these modes. For example, in the case of a relatively less attenuating porous glass specimen, roughly 100 mm of propagation distance is needed to produce the 30 to 40-μs difference in the time of arrival required to resolve the two principal modes. Such a long propagation distance would produce an attenuation in excess of 100 dB. In reality, the propagation distance is limited to 10–20 mm; that is, it is not longer than one or two wavelengths. The resulting composite signal is a linear combination of both modes and the average velocity measured from the phase of the pulse-train is also a linear combination of the two velocities.

5.3.3.2 Rod and Plate Waves. Elastic wave propagation in cylindrical rods was first studied by Pochhammer [62] and Chree [63] more than a hundred years ago. In fluid-filled porous cylinders, Biot's theory can be adapted to account for the relative motion between the fluid and solid phases. The attenuation of fluid-filled solids is usually extremely high because of viscous losses between the saturating fluid and the solid frame, therefore acoustic measurements are limited to relatively low frequencies. Gardner used Biot's theory to study long-wavelength extensional waves in thin rods when the slow compressional mode is diffusive in nature [64]. Berryman extended this theory to high frequencies where the slow compressional mode becomes propagatory and considered not only open but also closed surface pores [65]. Generally, the dispersion of the fast extensional mode does not differ significantly from that of the longitudinal mode in isotropic cylinders. In addition, a slow extensional mode can propagate when the surface pores are closed, but not when they are open. This slow

mode is always slower than the bulk slow wave, although the difference is usually small.

Gardner's theory was experimentally verified by Mörig and Burkhardt, who measured the attenuation in fluid-saturated porous rods of different radii [66]. More recently, Johnson and Kostek showed that the Gardner theory of extensional modes in porous fluid-saturated cylinders is not exactly the low-frequency limit predicted by Biot's theory [67]. The attenuation is significantly underestimated by Gardner's theory for permeabilities above a critical value κ_c that depends on the radius b of the rod:

$$\kappa_c = \frac{\eta \phi b v_E}{\sqrt{8}\, K_f}, \tag{71}$$

where η and K_f denote the viscosity and bulk modulus of the fluid, respectively: ϕ is the connected porosity; and v_E denotes the velocity of the extensional mode. For typical sizes of $b = 1$ cm, the critical frequency is around 1 D, above which Biot's full theory predicts orders of magnitude higher attenuation than Gardner's approximation.

In low-permeability specimens when the slow compressional wave is badly attenuated, Plona's immersion technique does not work since the different pulses cannot be resolved if either the plate thickness is chosen to be very thin or the inspection frequency is reduced. In an effort to overcome this limitation, Xue *et al.* studied Lamb-type guided waves in thin fluid-saturated porous plates [68]. First, the reflected signal from the plate is recorded at different angles of incidence. Then, this signal is spectrum analyzed to find the minima corresponding Lamb wave generation in the plate. The phase velocity of these modes can be calculated from the angle of incidence by using Snell's law. By monitoring how the reflection minima change as the angle of incidence is varied, a dispersion curve containing numerous modes can be obtained. Xue *et al.* found that the lowest-order mode exhibits a cutoff frequency determined by the slow wave velocity therefore it can be used to detect the slow compressional mode and to assess its velocity in thin plates. Although the Lamb wave technique can be used to extend the range of slow wave studies to thinner plates than allowed by Plona's original immersion technique, the improvement is not sufficient to adapt the technique to natural rocks where the first reflection minimum was rendered too weak by excessive attenuation even through the otherwise very thin plates.

5.3.3.3 Tube Waves. One of the most often used guided modes in acoustic characterization of porous solids is the low-frequency fundamental mode of a fluid-filled hole in a fluid-saturated permeable matrix. This wave is known in the geophysics community as the tube wave or Stoneley wave

(in general acoustics, the interface wave propagating along the plane boundary between two elastic half-spaces is called a Stoneley wave). In the low-frequency approximation, the tube wave speed for a circular bore in a nonpermeable matrix reduces to $v \approx \sqrt{K_n/\rho_f}$, where the effective stiffness K_n can be calculated from the bulk modulus K_f of the fluid and the shear modulus N of the elastic matrix surrounding the borehole [69]:

$$\frac{1}{K_n} = \frac{1}{K_f} + \frac{1}{N}. \tag{72}$$

In geophysical inspection, the fluid-filled bore often contains a logging tool, which generally reduces the tube velocity [70]. In addition, the porous matrix containing the fluid-filled bore is not infinite but rather a concentric layer of finite thickness surrounded by a thin casing, usually made of steel, which can further reduce the tube velocity [71].

The velocity of the tube wave is slightly reduced and, more important, it is strongly attenuated by viscous losses when the elastic host is a fluid-filled porous solid, which can be exploited to assess the formation permeability [45, 72–77]. For a permeable matrix, the effective stiffness K_p can be calculated from

$$\frac{1}{K_p} = \frac{1}{K_f} + \frac{1}{N} + \frac{1}{T_s}, \tag{73}$$

where the previously introduced surface stiffness parameter T_s is defined as the ratio between the fluid pressure and the relative average radial fluid displacement at the surface of the borehole with respect to the solid frame. The generally complex surface stiffness can be calculated from

$$T_s = \frac{2b\eta\omega}{\kappa_0 E}, \tag{74}$$

where κ_0 denotes the permeability of the formation, b is the bore radius, and

$$E(\xi) = 2i\xi \frac{H_1^{(1)}(\sqrt{i\xi})}{H_0^{(1)}(\sqrt{i\xi})}. \tag{75}$$

Here, $H_0^{(1)}$ and $H_1^{(1)}$ are zeroth- and first-order Hankel functions of the first kind and

$$\xi = \frac{b^2\omega}{C}, \tag{76}$$

where C is a modified diffusion coefficient, which is slightly lower than the standard diffusion coefficient $C_0 = \kappa K_f/\eta\phi$ [76]. Assuming that the bore

radius is much larger than the diffusion depth in the permeable formation (i.e., $b^2\omega/C \gg 1$), the complex velocity of the tube wave can be approximated as

$$v \approx v_f \sqrt{\frac{N}{N+K_f}} \left(1 - \phi \sqrt{\frac{C_0}{C}} \frac{N}{N+K_f} \sqrt{\frac{iC_0}{b^2\omega}}\right). \tag{77}$$

If the slight dependence of C_0/C on porosity is ignored, the imaginary part of the tube velocity scales as $\sqrt{\phi\kappa/b^2}$; that is, the attenuation of the tube wave increases with porosity and permeability and decreases with bore radius [76]. Of course, there is a parallel drop in the real part of the tube velocity, which can be also exploited to assess the physical parameters of the porous formation.

A schematic diagram of the experimental arrangement used in tube wave measurements is shown in Fig. 26. In laboratory experiments, a scaled-down specimen of approximately 20–30 cm in length can be used. The borehole diameter is around 1 cm so that it can accommodate a small hydrophone receiver, which is scanned up and down along the hole. The outside diameter of the specimen must be large enough to model an infinite host. The sample is saturated with a liquid and a transmitter is positioned at the

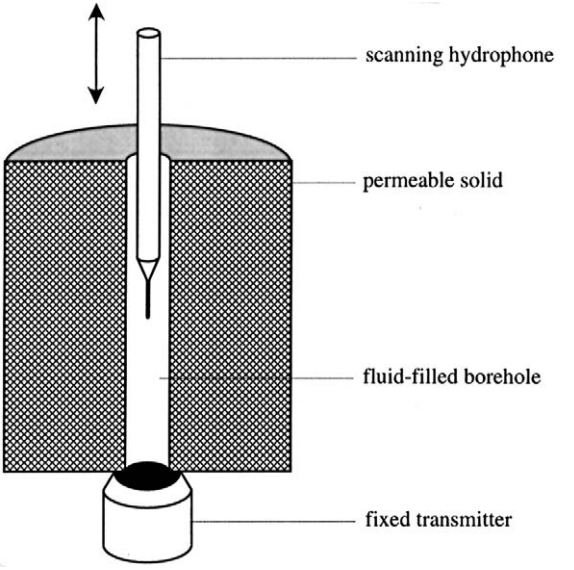

FIG. 26. Schematic diagram of the experimental arrangement used in tube wave measurements.

end of the borehole. First, a reference signal is recorded close to the transmitter, then, the receiver is moved back and the signal is recorded again at different distances from the transmitter. The recorded data is Fourier analyzed to determine how its amplitude and phase change with distance at different frequencies.

As an example, Fig. 27 shows the tube wave velocity and attenuation versus frequency in a borehole filled with silicon oil in Berea sandstone [75].

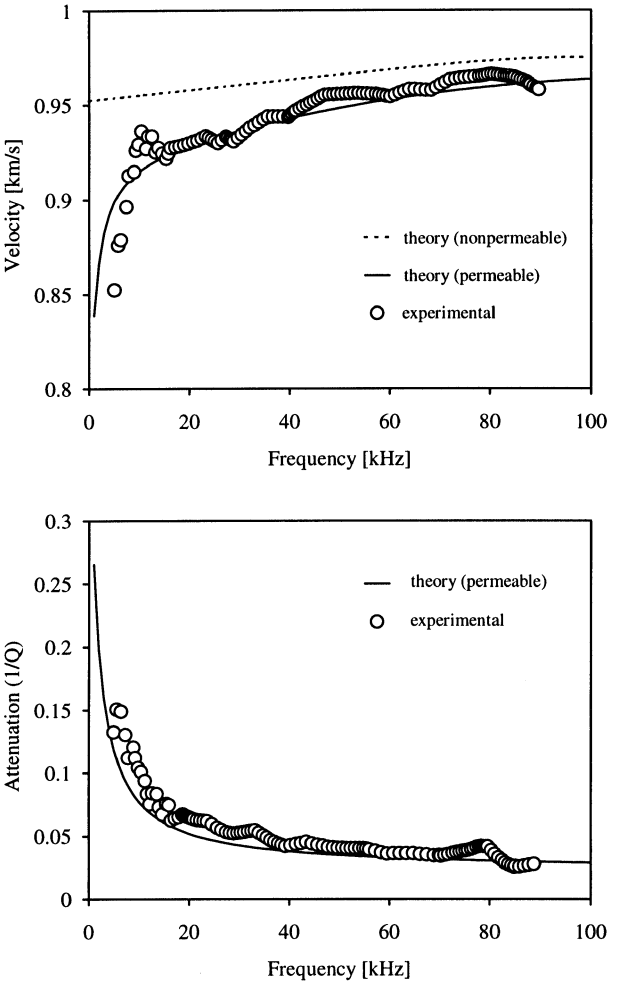

FIG. 27. Tube wave velocity and attenuation versus frequency in a borehole filled with silicon oil in Berea sandstone. Reprinted with permission from K. W. Winkler, H. L. Lin, and D. L. Johnson, *Geophys.* 54, 66–75 (1989).

The porosity and permeability of the sandstone were $\phi = 0.21$ and $\kappa_0 = 220\,\text{mD}$, respectively, while the viscosity and sound velocity in the silicon oil were $\eta = 0.93\,\text{Ns/m}^2$ and $v_f = 999\,\text{m/s}$. The dashed line indicates the theoretical prediction without the effect of permeability. The velocity slightly increases with frequency maintaining a more or less constant slope over the whole frequency range up to 100 kHz. Of course, there is no attenuation without permeability as the only source of loss considered here is due to friction loss between the porous solid and the saturating fluid. The solid line indicates the theoretical prediction with the added effect of formation permeability. The diffusion depth of the fluid vibration in the porous host is inversely proportional to the square root of frequency. At low frequencies, where the penetration depth becomes very large, the tube velocity sharply decreases while the normalized attenuation increases. The normalized attenuation or inverse quality factor is defined as the total loss over a distance equal to the acoustic wavelength divided by π. Generally, at low frequencies, the tube wave behaves similarly to the diffuse slow compressional bulk wave in fluid-saturated permeable solids. However, the tube wave is much easier to observe and study experimentally as the effect of viscous drag between the fluid and the porous host can be controlled, and thereby kept under an acceptable level, by changing the borehole diameter.

5.3.4 Ultrasonic Surface Stiffness Measurements

We have shown that acoustic wave interaction with fluid–fluid-saturated solid interfaces is strongly affected by the boundary conditions, namely, whether the surface pores are open or closed [39, 42, 47–49, 65, 67]. The surface stiffness T_s of a fluid-saturated porous solid can also be directly measured to characterize the porous formation [50]. The geometrical configuration of a single surface pore and the curved boundary between the nonwetting superstrate fluid and the saturating substrate fluid are shown in Fig. 28. The acoustic pressure changes the radius of the surface membrane and thereby the fluid volume in the underlying pore. For the boundary between a fluid-saturated solid and a nonwetting fluid, T_s is the ratio between a small change in capillary pressure and the average displacement of the boundary due to the resulting rise or fall of the fluid level in the pore channels. When the surface pores are structurally open, the surface stiffness is entirely due to the stiffness of the microscopic fluid membranes extended by capillary forces over the surface pores. Due to interfacial tension between the immiscible wetting fluid in the pores and the nonwetting fluid (air) above the surface, essentially closed-pore boundary conditions can prevail at the interface. The surface stiffness of a porous material containing cylindrical pores can be calculated simply as the surface tension σ of the

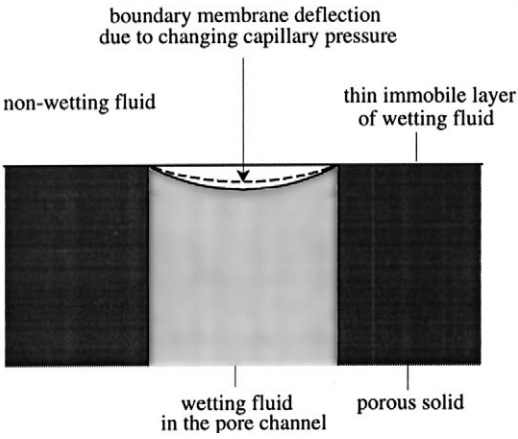

FIG. 28. Schematic diagram of the boundary between a nonwetting fluid and a fluid-saturated porous solid with cylindrical pores.

saturating fluid divided by the static permeability κ_0 of the porous solid; that is, $T_s = \sigma/\kappa_0$ [46].

The same simple relationship can be generalized for the surface stiffness of fluid-saturated porous media containing parallel prismatic pore channels of any number, size, or shape [78]. An immediate benefit of this result is the convenience of directly calculating the surface stiffness of fluid-saturated porous solids containing parallel prismatic pore channels from the static permeability, which is well known for a large number of geometries [79]. Similar relationships for other regular formations, such as ordered spherical beads, are much more difficult to obtain. As the pore shape becomes more irregular in the axial direction, the permeability is determined by the smallest cross sections, causing viscous friction while the surface stiffness depends more on the largest dimensions dominating the compliance of the surface membranes. Still, for a given pore shape, both the surface compliance $1/T_s$ and the static permeability κ_0 are proportional to the square of the characteristic pore size, and the surface stiffness can be expressed in the general form

$$T_s = s\sigma/\kappa_0, \tag{78}$$

where s denotes a shape factor [50].

A schematic diagram of the experimental arrangement for acoustic surface stiffness measurement of fluid-saturated porous solids is shown in Fig. 29 [50]. The technique is based on the direct measurement of the average surface displacement of the water-saturated specimen upon changing the

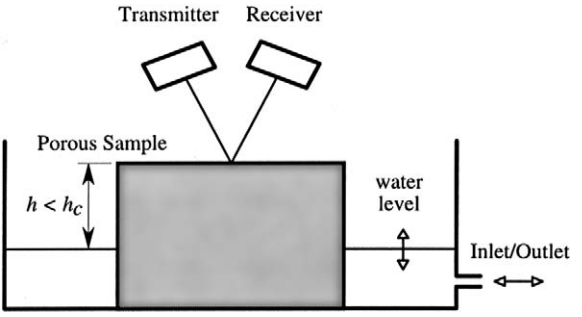

FIG. 29. Schematic diagram of the experimental arrangement for static surface stiffness measurements. Reprinted with permission from P. B. Nagy and G. Blaho, *J. Acoust. Soc. Am.* 95, 828–835 (1994).

hydrostatic pressure in the capillary pores. The porous specimen is soaked from below by water. The fluid level in the pores can rise to a maximum capillary height of $h_c = p_c/\rho_f g$, where p_c denotes the maximum capillary pressure accommodated by the given pore structure and the surface tension of the wetting fluid, ρ_f is the density of the fluid, and g denotes the gravitational acceleration. The pressure difference between the air and the water at the surface is changed by increasing and decreasing the water level in the tank. This is achieved simply by moving an external water tank mounted on a computer-controlled translation stage. This external reservoir is connected to the measuring tank by a flexible rubber tube. The water level in the tank is always kept at least a few millimeters below the surface of the saturated specimen and never lowered more than one-third of the experimentally determined maximum capillary height h_c for a given specimen so that full saturation of the specimen can be maintained throughout the experiment. In this way, the microscopic interface membranes formed over the surface pores are kept intact but are strained sufficiently to produce a measurable surface displacement on the order of a few microns.

The average surface displacement is directly measured by an ultrasonic transmitter–receiver pair working at $f = 100\,\text{kHz}$. Because of the very high acoustic impedance of water with respect to air, the top surface of the porous skeleton and the capillary membranes present a continuous, essentially rigid reflecting interface to the incident airborne ultrasonic pulse. Since the acoustic wavelength $\lambda \approx 3.3\,\text{mm}$ is significantly larger than the combined surface roughness of this interface, the received signal from the surface appears to be reflected from a plane reflector positioned at the average height of the slightly irregular surface. The porous solid is rigidly mounted so that the changing buoyancy of the specimen cannot produce any displacement of the skeleton ($u_n = 0$) and the average surface displacement

ΔU is entirely due to the water level rising and falling in the surface pores $\Delta U = \phi U_n$. The pressure difference between the air and the water at the interface is periodically changed by $\Delta p = \Delta h \rho_f g$. Finally, the surface stiffness can be calculated from the measured average surface displacement as $T_s = \Delta p / \Delta U$.

Figure 30 shows the measured surface stiffness as a function of interstitial pore diameter in cemented glass bead specimens for five different grades. EP Brand Porous Structures are porous engineering materials consisting of tiny, precisely sized spherical particles rigidly bonded together. These samples have an evenly distributed network of interstitial pores that are of uniform size, completely open, and interconnected. This material is available in five standard grades, which also denote the maximum interstitial pore diameter in microns. Because of the self-similar nature of this material and the more than one order of magnitude size range covered by the five standard grades, it is especially suitable to test the validity of the general relationship between surface stiffness and static permeability for a given pore geometry and to find an empirical estimate for the shape factor in the case of spherical grains. From theoretical considerations, one would expect that the surface stiffness is inversely proportional to the square of the interstitial pore diameter. Instead, the experimental data seem to indicate a significantly lower power of 1.45. Interestingly, the same anomaly can also be observed in the relationship between static permeability and pore size. As a result, the surface stiffness is still inversely proportional to the static permeability, as demonstrated in Fig. 31, where we plot the shape factor as a function of the static permeability. The shape factor can be calculated from Eq. (78). Over

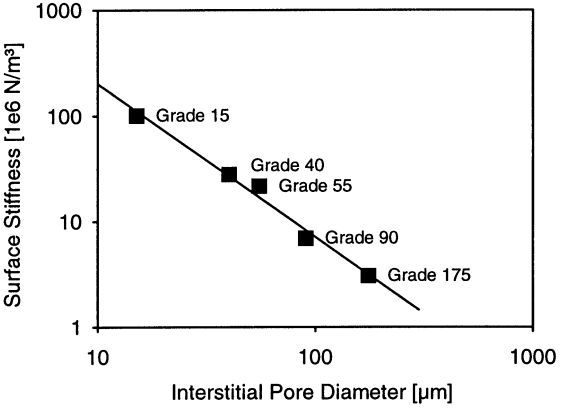

FIG. 30. Measured surface stiffness versus interstitial pore diameter in cemented glass bead specimens. Reprinted with permission from P. B. Nagy and G. Blaho, *J. Acoust. Soc. Am.* 95, 828–835 (1994).

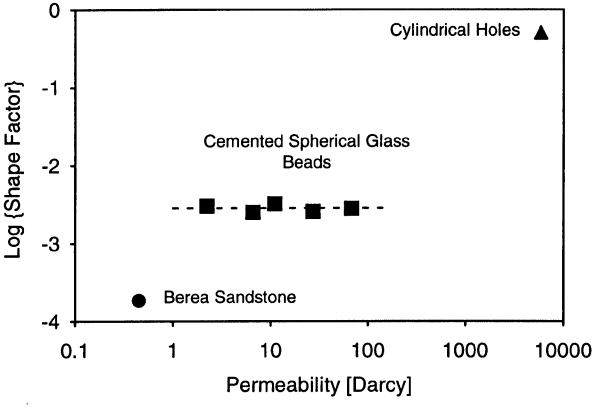

FIG. 31. The product of the measured surface stiffness and the static permeability versus permeability for different porous materials. Reprinted with permission from P. B. Nagy and G. Blaho, *J. Acoust. Soc. Am.* 95, 828–835 (1994).

the wide permeability range of approximately $1\frac{1}{2}$ decades represented by these five standard grades, the shape factor is constant at $s \approx 2.7 \times 10^{-3}$ within $\pm 15\%$. In comparison, for a porous structure of cylindrical pores, the shape factor was found to be $s \approx 0.51$, somewhat lower than the predicted unit value but almost two orders of magnitude higher than for spherical beads.

Figure 31 also shows the surface stiffness of a water-saturated Berea sandstone specimen of 450 mD static permeability. The surface stiffness was found to be only 3×10^7 N/m^3, much less than expected based on the permeability of the specimen. The measured value corresponds to a shape factor of $s \approx 2 \times 10^{-4}$; that is, roughly one order of magnitude lower than the empirical value for spherical beads.

The shape factor, which is calculated from the measured surface stiffness and static permeability, does indeed appear to be independent of pore size for self-similar cemented glass bead specimens over more than one order of magnitude, and it becomes less than one as the pore structure becomes more irregular and random. In light of the analytical predictions [78], the decreasing shape factor is mainly caused by the axial irregularity of the pore channel (i.e., its changing cross section) rather than by its lateral irregularity (i.e., the particular shape of the cross section). In addition, the assumption that the fluid moves only in the pores while it is kept completely immobile by its viscosity in the continuous thin layer covering the top of the solid frame remains in question. Fluid motion in this layer can make a significant contribution to the total surface compliance and might be responsible for the observed reduction in surface stiffness. This effect is expected to be

significant whenever the pore channels smoothly widen on the surface instead of ending in a well-defined meniscus of sharp corners. The significance of this very thin fluid layer covering the entire solid frame greatly depends on frequency. This surface layer is so thin that dynamic motion in it is effectively prevented by the viscosity of the wetting fluid but very slow exchange with the pore fluid can occur. As a result, the quasi-static stiffness of the surface can be much lower than the high-frequency dynamic stiffness.

5.4 Summary

In this chapter, we reviewed the most important applications of acoustics and ultrasonics in materials characterization of porous media. We considered only measurements between 100 Hz to 1 MHz where individual pores are not resolved and the obtained material properties represent localized averages on the scale of the acoustic wavelength. We further limited our review to specific acoustic phenomena that occur only in fluid-saturated consolidated solids of continuously connected pore structure. Our primary interest was to characterize certain material properties of the porous frame — such as tortuosity, permeability, porosity, and pore size and shape — that are inherently connected to the permeable nature of the material. These properties are best evaluated from the propagation properties of the slow compressional wave and related phenomena. In the slow compressional wave, the porous skeleton and the interstitial fluid move essentially out of phase, therefore the relative motion of the fluid within the pore channels is particularly sensitive to material parameters associated with permeability. The price we pay for exploiting the relative fluid motion within a porous solid as a sensitive probe to assess various aspects of permeability is that the acoustical wave is inherently highly attenuated by viscous drag between the fluid and the solid frame. In this chapter, we focused on materials of relatively high permeability saturated with a low-viscosity fluid that moves more or less freely within the pores. In materials of relatively low permeability, such as natural rocks, other, more conventional shear or fast compressional wave velocity and attenuation measurements, which are much less affected by viscous losses than the slow compressional mode, can be used to characterize the porous material within certain limits.

Four major areas of acoustic wave propagation in fluid-saturated porous media were reviewed. In Section 5.3.1, we considered sound propagation in air-filled porous materials with rigid frame. Acoustic impedance measurements made from 100 Hz to 10 kHz were shown to provide information on the porosity, permeability, tortuosity, and characteristic thermal and viscous

pore sizes of the material. Ultrasonic velocity and attenuation measurements made from 10 to 500 kHz can be used to obtain similar data with much higher spatial resolution that can be exploited for slow wave imaging of the permeable solid.

In Section 5.3.2, we reviewed the problem of sound propagation in water-filled porous materials with elastic frame. In this case, there are three bulk modes: the shear wave supported by the rigidity of the solid frame and the combined masses of the solid and the saturating fluid and two dilatational waves, which are called the "fast" and "slow" compressional waves. Acoustic wave propagation in such media are well modeled by Biot's theory that can accurately predict the frequency-dependent acoustic properties of a permeable solid saturated with a Newtonian fluid from a finite number of material parameters that can be measured independently. By measuring the frequency dependence of the ultrasonic transmission through slabs of fluid-saturated solids material parameters such as tortuosity, permeability, and viscous characteristic length can be assessed.

In Section 5.3.3, we considered guided wave propagation in water-filled porous materials. Surface wave propagation on fluid filled permeable solids was shown to be particularly sensitive to the interfacial stiffness of the surface pores. One of the most often used guided modes in acoustic characterization of porous solids is the low-frequency fundamental mode of a fluid-filled hole in a fluid-saturated permeable matrix. The velocity of this so-called tube wave is slightly reduced and, more important, its attenuation is strongly increased by viscous losses when the elastic host is a fluid-filled porous solid, which can be exploited to assess the formation permeability of the material.

Finally, in Section 5.3.4, we reviewed the feasibility of using ultrasonic surface stiffness measurements for materials characterization in permeable solids. For relatively low permeability materials, the interfacial tension between the wetting fluid inside the pores and the nonwetting fluid outside can produce essentially closed pore boundary conditions. Direct acoustic measurement of the resulting surface stiffness was shown to be strongly related to the average interstitial pore size and also to be affected by the shape of the pore channels. In conclusion, acoustic and ultrasonic techniques play an important role along with other physical methods reviewed elsewhere in this book in materials characterization of permeable solids and are expected to find further applications in the future.

References

1. A. D. Pierce, *Acoustics: An Introduction to Its Physical Principles and Applications*, pp. 1–3, Acoustical Society of America, New York, 1989.

2. J. D. Achenbach, *Wave Propagation in Elastic Solids*, North-Holland, Amsterdam, 1973.
3. B. A. Auld, *Acoustic Fields and Waves*, John Wiley & Sons, New York, 1973.
4. I. A. Viktorov, *Rayleigh and Lamb Waves*, Plenum, New York, 1967.
5. R. Stoneley, "Elastic waves at the surface of separation of two solids," *Roy. Soc. Proc. London, Series A* 106, 416–428 (1924).
6. J. G. Scholte, "The range of existence of Rayleigh and Stoneley waves," *Roy. Astron. Soc. London, Monthly Notices Geophys. Suppl.* 5, 120–126 (1947).
7. C. Zwikker and C. W. Kosten, *Sound Absorbing Materials*, Elsevier, New York, 1949.
8. T. Bourbié, O. Coussy, and B. Zinszner, *Acoustics of Porous Media*, Gulf, Houston, 1987.
9. J. F. Allard, *Propagation of Sound in Porous Media*, Elsevier, New York, 1993.
10. R. D. Stoll, *Sediment Acoustics*, Springer-Verlag, Berlin, 1989.
11. M. A. Biot, "Theory of propagation of elastic waves in a fluid-saturated porous solid. I. Low frequency range," *J. Acoust. Soc. Am.* 28, 168–178 (1956).
12. M. A. Biot, "Theory of propagation of elastic waves in a fluid-saturated porous solid. II. Higher frequency range," *J. Acoust. Soc. Am.* 28, 179–191 (1956).
13. T. J. Plona, "Observation of a second bulk compressional wave in a porous medium at ultrasonic frequencies," *Appl. Phys. Lett.* 36, 259–261 (1980).
14. T. Klimenatos and C. McCann, "Why is the Biot slow compressional wave not observed in real rocks?" *Geophys.* 53, 1605–1609 (1988).
15. D. L. Johnson, T. J. Plona, C. Scala, F. Pasierb, and H. Kojima, "Tortuosity and acoustic slow waves," *Phys. Rev. Lett.* 49, 1840–1844 (1982).
16. K. A. Shapiro and I. Rudnick, "Experimental determination of the fourth sound velocity in helium II," *Phys. Rev. A* 137, 1383–1391 (1965).
17. D. L. Johnson and P. N. Sen, "Multiple scattering of acoustic waves with application to the index of refraction of fourth sound," *Phys. Rev. B* 24, 2486–2496 (1981).
18. D. L. Johnson, T. J. Plona, and H. Kojima, in *Physics and Chemistry of Porous Media* (J. R. Banavar, J. Koplik, and K. W. Winkler, eds.), pp. 243–277, American Institute of Physics, New York, 1987.
19. P. B. Nagy, L. Adler, and B. Bonner, "Slow wave propagation in air-filled porous materials and natural rocks," *Appl. Phys. Lett.* 56, 2504–2506 (1990).
20. A. Craggs and J. G. Hildebrandt, "Effective densities and resistivities for acoustic propagation in narrow tubes," *J. Sound Vib.* 92, 321–331 (1984).
21. A. Craggs and J. G. Hildebrandt, "The normal incidence absorption coefficient of a matrix of narrow tubes with constant cross section," *J. Sound Vib.* 105, 101–107 (1986).
22. K. Attenborough, "Acoustical characteristics of rigid fibrous absorbents and granular materials," *J. Acoust. Soc. Am.* 73, 785–799 (1983).

23. K. Attenborough, "On the acoustic slow wave in air-filled granular media," *J. Acoust. Soc. Am.* 81, 93–102 (1987).

24. D. L. Johnson, J. Koplik, and R. Dashen, "Theory of dynamic permeability and tortuosity in fluid-saturated porous media," *J. Fluid Mech.* 176, 379–402 (1987).

25. R. J. S. Brown, "Comparison between formation factor of electrical resistivity and fluid–solid coupling factor in Biot's equations for acoustic waves in fluid-filled porous media," *Geophys.* 45, 1269–1275 (1980).

26. Y. Champoux and J. F. Allard, "Dynamic tortuosity and bulk modulus in air-saturated porous media," *J. Appl. Phys.* 70, 1975–1979 (1991).

27. J. F. Allard and Y. Champoux, "New empirical equations for sound propagating in rigid frame fibrous materials," *J. Acoust. Soc. Am.* 91, 3346–3353 (1992).

28. A. F. Seybert and D. F. Ross, "Experimental determination of acoustic properties using a two-microphone random excitation technique," *J. Acoust. Soc. Am.* 61, 1362–1370 (1977).

29. J. Y. Chung and D. A. Blaser, "Transfer function method of measuring in-duct acoustic properties," *J. Acoust. Soc. Am.* 68, 907–921 (1980).

30. W. T. Chu, "Single-microphone method for certain applications of the sound intensity technique," *J. Sound Vib.* 101, 443–445 (1985).

31. Y. Champoux and M. R. Stinson, "Measurement of the characteristic impedance and propagation constant of materials having high flow resistivity," *J. Acoust. Soc. Am.* 90, 2182–2191 (1991).

32. P. B. Nagy, "Slow wave propagation in air-filled permeable solids," *J. Acoust. Soc. Am.* 93, 3224–3234 (1993).

33. D. L. Johnson and T. J. Plona, "Acoustic slow waves and the consolidation transition," *J. Acoust. Soc. Am.* 72, 556–565 (1982).

34. P. Leclaire, L. Kelders, W. Lauriks, G. C. Glorieux, and J. Thoen, "Determination of the viscous characteristic length in air-filled porous materials by ultrasonic attenuation measurements," *J. Acoust. Soc. Am.* 99, 1944–1948 (1996).

35. P. B. Nagy, B. P. Bonner, and L. Adler, "Slow wave imaging of permeable rocks," *Geophys. Res. Lett.* 22, 1053–1056 (1995).

36. P. B. Nagy, "Local variations of slow wave transmission in permeable materials," *J. Acoust. Soc. Am.* 99, 914–919 (1996).

37. P. B. Nagy and D. L. Johnson, "Improved materials characterization by pressure-dependent ultrasonic attenuation in air-filled permeable solids," *Appl. Phys. Lett.* 68, 3707–3709 (1996).

38. M. A. Biot and D. G. Willis, "The elastic coefficients of the theory of consolidation," *J. Appl. Mech.* 24, 594–601 (1957).

39. K. Wu, Q. Xue, and L. Adler, "Reflection and transmission of elastic waves from a fluid-saturated porous solid boundary," *J. Acoust. Soc. Am.* 87, 2349–2358 (1990).

40. J. G. Berryman, "Confirmation of Biot's theory," *Appl. Phys. Lett.* 37, 382–384 (1980).

41. D. L. Johnson, D. L. Hemmick, and H. Kojima, "Probing porous media with first and second sound. I. Dynamic permeability," *J. Appl. Phys.* 76, 104–114 (1994).

42. D. L. Johnson, T. J. Plona, and H. Kojima, "Probing porous media with first and second sound. II. Acoustic properties of water-saturated porous media," *J. Appl. Phys.* 76, 115–125 (1994).

43. T. J. Plona and K. W. Winkler, in *Multiple Scattering of Waves in Random Media and Random Surfaces* (V. V. Varadan and V. K. Varadan, eds.), pp. 341–356, The Pennsylvania State University, University Park, 1985.

44. H. Deresiewicz and R. Skalak, "On uniqueness in dynamic poroelasticity," *Bull. Seismol. Soc. Am.* 53, 783–788 (1963).

45. J. H. Rosenbaum, "Synthetic microseismograms: logging in porous formations," *Geophys.* 39, 14–32 (1974).

46. P. B. Nagy, "Observation of a new surface mode on a fluid-saturated permeable solid," *Appl. Phys. Lett.* 60, 2735–2737 (1992).

47. P. N. J. Rasolofosaon, "Importance of interface hydraulic condition on the generation of second bulk compressional wave in porous media," *Appl. Phys. Lett.* 52, 780–782 (1988).

48. S. Feng and D. L. Johnson, "High-frequency acoustic properties of a fluid/porous solid interface. I. New surface mode," *J. Acoust. Soc. Am.* 74, 906–914 (1983).

49. S. Feng and D. L. Johnson, "High-frequency acoustic properties of a fluid/porous solid interface. II. The 2D reflection Green's function," *J. Acoust. Soc. Am.* 74, 915–924 (1983).

50. P. B. Nagy and G. Blaho, "Experimental measurements of surface stiffness on water saturated porous solids," *J. Acoust. Soc. Am.* 95, 828–835 (1994).

51. H. L. Bertoni and T. Tamir, "Unified theory of Rayleigh-angle phenomena for acoustic beams at liquid-solid interfaces," *Appl. Phys.* 2, 157–172 (1973).

52. A. Schoch, "Seitliche Versetzung eines total reflektierten Strahls bei Ultraschallwellen," *Acustica* 2, 18–19 (1952).

53. W. G. Neubauer, "Ultrasonic reflection of a bounded beam at Rayleigh and critical angles for a plane liquid-solid interface," *J. Appl. Phys.* 44, 48–55 (1973).

54. M. A. Breazeale, L. Adler, and L. Flax, "Reflection of a Gaussian ultrasonic beam from a liquid-solid interface," *J. Acoust. Soc. Am.* 56, 866–872 (1974).

55. S. Sasaki, "Back reflection of ultrasonic wave obliquely incident to a solid surface in water," *Jpn. J. Appl. Phys.* 3, 198 (1963).

56. M. deBilly, L. Adler, and G. Quentin, "Parameters affecting backscattered ultrasonic leaky-Rayleigh waves from liquid-solid interfaces," *J. Acoust. Soc. Am.* 72, 1018–1020 (1982).

57. A. Jungman, L. Adler, and G. Quentin, "Ultrasonic anomalies in the spectrum of acoustic waves diffracted by periodic interfaces," *J. Appl. Phys.* 53, 4673–4680 (1982).

58. A. Jungman, L. Adler, J. D. Achenbach, and R. Roberts, "Reflection from a boundary with periodic roughness: Theory and experiment," *J. Acoust. Soc. Am.* 74, 1025–1032 (1983).

59. M. Mayes, P. B. Nagy, L. Adler, B. P. Bonner, and R. Streit, "Excitation of surface waves of different modes at fluid-porous solid interface," *J. Acoust. Soc. Am.* 79, 249–252 (1986).

60. P. B. Nagy and L. Adler, in *Physical Acoustics* (O. Leroy and M. A. Breazeale, eds.) pp. 529–535, Plenum, New York, 1991.

61. L. Adler and P. B. Nagy, "Measurements of acoustic surface waves on fluid-filled porous rocks," *J. Geophys. Res. Solid Earth* 99, 17863–17869 (1994).

62. L. Pochhammer, "Über die Fortpflanzungsgeschwindingkeiten kleiner Schwingungen in einem unbegrenzten isotropen Kreiscylinder," *J. Reine Angew. Math.* 81, 324–336 (1876).

63. C. Chree, "The equations of an isotropic elastic solid in polar and cylindrical coordinates, their solutions and applications," *Trans. Cabridge Phil. Soc.* 14, 250–289 (1889).

64. G. H. F. Gardner, "Extensional waves in fluid-saturated porous cylinders," *J. Acoust. Soc. Am.* 34, 36–40 (1962).

65. J. G. Berryman, "Dispersion of extensional waves in fluid-saturated porous cylinders at ultrasonic frequencies," *J. Acoust. Soc. Am.* 74, 1805–1812 (1983).

66. R. Mörig and H. Burkhardt, "Experimental evidence for the Biot-Gardner theory," *Geophys.* 54, 524–527 (1989).

67. D. L. Johnson and S. Kostek, "A limitation of the Biot-Gardner theory of extensional waves in fluid-saturated porous cylinders," *J. Acoust. Soc. Am.* 97, 741–744 (1995).

68. Q. Xue, K. Wu., L. Adler, A. Jungman, and G. Quentin, in *Review of Progress in Quantitative Nondestructive Evaluation* (D. O. Thompson and D. E. Chimenti, eds.), Vol. 8, pp. 213–220, Plenum, New York, 1989.

69. M. A. Biot, "Propagation of elastic waves in a cylindrical bore containing a fluid," *J. Appl. Phys.* 23, 997–1005 (1952).

70. C. H. Cheng and M. N. Toksöz, "Elastic wave propagation in a fluid-filled borehole and synthetic acoustic logs," *Geophys.* 46, 1042–1053 (1981).

71. A. N. Norris, "The speed of a tube wave," *J. Acoust. Soc. Am.* 87, 414–417 (1990).

72. J. E. White, *Underground Sound*, Elsevier, New York, 1983.

73. A. T. Hsui and M. N. Toksöz, "Application of an acoustic model to determine in situ permeability of a borehole," *J. Acoust. Soc. Am.* 79, 2055–2059 (1986).

74. S. K. Chang, H. L. Liu, and D. L. Johnson, "Low-frequency tube waves in permeable rocks," *Geophys.* 53, 519–527 (1988).

75. K. W. Winkler, H. L. Liu, and D. L. Johnson, "Permeability and borehole Stoneley waves: Comparison between experiment and theory," *Geophys.* 54, 66–75 (1989).

76. A. N. Norris, "Stoneley-wave attenuation and dispersion in permeable formations," *Geophys.* 54, 330–341 (1989).
77. X. M. Tang, C. H. Cheng, and M. N. Toksöz, "Dynamic permeability and borehole Stoneley waves: A simplified Biot-Rosenbaum model," *J. Acoust. Soc. Am.* 90, 1632–1646 (1991).
78. P. B. Nagy and A. H. Nayfeh, "Generalized formula for the surface stiffness of fluid-saturated porous media containing parallel pore channels," *Appl. Phys. Lett.* 67, 1827–1829 (1995).
79. A. N. Norris, "On the viscodynamic operator in Biot's equations of poroelasticity," *J. Wave Mat. Interact.* 1, 365–380 (1986).

This Page Intentionally Left Blank

6. SMALL-ANGLE SCATTERING FROM POROUS MATERIALS

Sunil K. Sinha

Advanced Photon Source
Argonne National Laboratory
Argonne, Illinois

Abstract

We review the basic theoretical methods used to treat small-angle scattering from porous materials, treated as general two-phase systems, and also the basic experimental techniques for carrying out such experiments. We discuss the special forms of the scattering when the materials exhibit mass or surface fractal behavior and review the results of recent experiments on several types of porous media. Finally, we discuss SANS experiments probing the phase behavior of binary fluid mixtures or polymer solutions confined in porous materials.

6.1 Introduction

One of the conceptually simplest ways to study porous media is to carry out small-angle scattering experiments, typically using neutrons or x rays as the incident radiation. The technique can be applied *in situ*, under a wide variety of environmental conditions, and does not usually require special sample preparation techniques or optically transparent samples. Small-angle scattering has thus been widely used to investigate the basic morphology of the pore structure and of the internal pore surfaces. Because of finite instrumental resolution effects, however, such experiments can reveal structural information only up to length scales of typically a few tens of nanometers. Special high-resolution methods — for example, employing multiple-bounce perfect crystal monochromators and analyzers — can be used in certain cases to study length scales of up to microns. At these rather large length scales, however, multiple scattering effects can sometimes cloud the interpretation of the scattering data. A particular advantage of small-angle neutron scattering (SANS), as opposed to small-angle x-ray scattering (SAXS), is the ability to contrast-match selected portions of the sample, and this has been exploited in several SANS studies of the properties of fluids confined inside pores.

EXPERIMENTAL METHODS IN THE PHYSICAL SCIENCES
Vol. 35
ISBN 0-12-475982-3

ISSN 1079-4042/99 $30.00

The basic methodology of small-angle scattering has been discussed in a variety of excellent reviews [1–4], and we simply review that part of the formalism that is relevant to the study of porous materials. Neglecting any inelasticity in the scattering (which is discussed in the next chapter), the number of particles per second scattered by a sample into a detector is given by

$$I = S(\vec{q})(I_0/A)(\Delta\Omega), \tag{1}$$

where I_0 is the number of particles per second in the incident beam of cross-sectional area A, $\Delta\Omega$ is the solid angle subtended at the sample by the detector, $S(\vec{q})$ is the scattering function characterizing the sample, and $\vec{q}$ is the so-called wave vector transfer defined by

$$\vec{q} = \vec{k}_1 - \vec{k}_0, \tag{2}$$

where $\vec{k}_0$ and $\vec{k}_1$ are the wave vectors of the incident and scattered radiation, respectively. The magnitude of q is given by $q = 2k_0 \sin\theta$, where 2θ is the angle of scattering (see Fig. 1) and $k_0 = 2\pi/\lambda$, where λ is the wavelength of the incident radiation. The small-angle regime is generally defined by $q \ll k_0$. In general, $S(\vec{q})$ is a function of the average of the instantaneous positions of all the particles in the scattering system, but in the small-angle regime (defined roughly by the range $0 < q < 3\,\mathrm{nm}^{-1}$) we can ignore the atomic and molecular structure of the constituents and deal only with the spatial

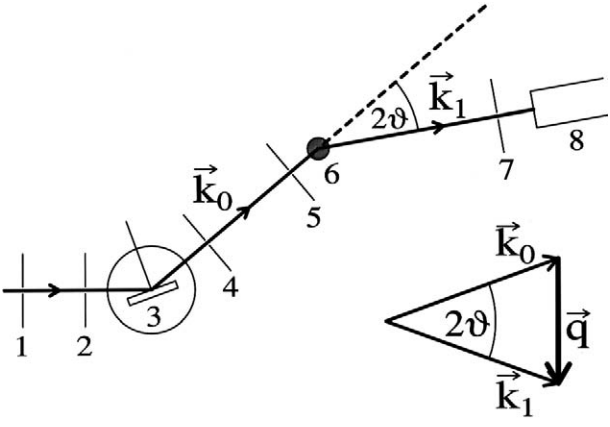

FIG. 1. Schematic diagram of an x-ray scattering instrument. The incident beam is provided by an x-ray tube or rotating anode source. Slits 1, 4, and 7 denote collimating slits, while slits 2 and 5 are guard slits. Label 3 denotes the monochromating crystal, 6 is the sample, and 8 is the x-ray detector.

variations (on length scales from a few nanometers on up) of the *scattering length density* (SLD) $\rho(\vec{r})$ of the sample. For SANS experiments, $\rho(\vec{r})$ is defined by

$$\rho(\vec{r}) = \Sigma\, b_i n_i(\vec{r}), \tag{3}$$

where b_i is the nuclear scattering length [5] of a type I nucleus, and $n_i(\vec{r})$ is the associated number density of such nuclei, while for SAXS experiments, $\rho(\vec{r})$ is defined by

$$\rho(\vec{r}) = (e^2/mc^2) n_{\mathrm{el}}(\vec{r}), \tag{4}$$

where the factor (e^2/mc^2) is the Thompson scattering length of the electron, and $n_{\mathrm{el}}(\vec{r})$ is the electron number density. Since a *uniform* scattering length density does not scatter radiation (except in the forward direction), $S(\vec{q})$ will depend only on the deviations of $\rho(\vec{r})$ about its *mean*, or what is referred to as the *contrast*. The kinematic or Born approximation to the scattering [6], where multiple scattering effects are neglected, then yields for the scattering function $S(\vec{q})$ the expression

$$S(\vec{q}) = \iint d\vec{r}\, d\vec{r}' \langle \delta\rho(\vec{r})\delta\rho(\vec{r}')\rangle e^{i\vec{q}(\vec{r}'-\vec{r})} \equiv \iint d\vec{r}\, d\vec{r}' \gamma(\vec{r}-\vec{r}') e^{i\vec{q}(\vec{r}'-\vec{r})} \tag{5}$$

where the statistical average is taken over the whole system. (This statement has to be modified if the incident radiation is highly *coherent*, as discussed in the last section of this chapter.) It is commonly assumed that such an average depends only on the magnitude of $\vec{R} \equiv \vec{r} - \vec{r}'$, for an isotropic and translationally invariant random porous medium. In Eq. (5), $\delta\rho(\vec{r})$ is defined as the fluctuation from the average SLD, as already explained. If we are dealing with a particulate system (or a system of random cavities) and these are far enough apart that the interference effects between the scattering from different particles (which will occur at values of q typically of order $(2\pi/d)$, where d is the average interparticle distance) is not important in the range of q studied in the experiment, then Eq. (5) simplifies to

$$S(q) = (\Delta\rho)^2 \sum_i v_i^2 f_i^2(\vec{q}) \tag{6}$$

where the sum is over all particles, v_i is the volume of the ith particle, $\Delta\rho$ is its SLD contrast with the average medium (assumed uniform throughout the particle and the same for all particles), and f_i is its form factor defined by

$$f_i(\vec{q}) = \frac{1}{v_i} \int_{v_i} d\vec{r}\, e^{-i\vec{q}\cdot\vec{r}}, \tag{7}$$

where the integral is over the particle volume. In general, one can make a spherical average of $f_i^2(q)$ and assume some law of polydispersity in size of

the particles to carry out the weighted sum in Eq. (6). In such a restrictive case (dilute system of random particles), by making an expansion for small $\vec{q}$, one finds that

$$S(q) = S(0) - \tfrac{1}{3}R_g^2 q^2 + \cdots, \tag{8}$$

where

$$R_g^2 = R_g^2 \sum_i (1/v_i) \int_{v_i} d\vec{r} \cdot r^2 \tag{9}$$

is the average *radius of gyration* of the particles. Equation (8) suggests (at least for small q) in this case the approximation

$$S(q) = S(0) \exp(-\tfrac{1}{3}R_g^2 q^2), \tag{10}$$

which is the famous Guinier approximation [1] for scaling from a dilute system of uniform particles. As we see in Section 6.3, this is of limited usefulness in the case of a real random porous medium.

6.2 Experimental Methods

A detailed description of instrumentation for small-angle scattering and the methods of treating data is given in several books and review articles [1–4]. Here we content ourselves with a much briefer description of the experimental methods used to obtain SAXS and SANS data. With conventional tube x-ray sources, due to intensity limitations, the usual configuration is to use the so-called "slit geometry" in which the beam (usually after reflection from a monochromating crystal to remove polychromatic radiation components) is collimated by slits in one direction only (e.g., in the plane of scattering) and similarly the beam scattered from the sample is also collimated by slits in the same plane, as the detector scans across the scattering angle 2θ. The monochromating crystals usually used are perfect silicon, germanium, or (for lower resolution) low-mosaic-spread pyrolytic graphite crystals. A schematic diagram for such a setup is shown in Fig. 1. Usually a pair of guard slits placed between the first slits and the sample is used to reduce parasitic small-angle scattering contamination from the collimating slits themselves. For higher resolution, especially with higher-flux rotating anode sources, an analyzer crystal (usually a perfect silicon or germanium crystal) is inserted in the scattered beam to Bragg reflect the scattered beam into the detector. Higher-order contamination from $\lambda/2$, $\lambda/3$, etc. components in the incident beam can be eliminated by choosing monochromators such as Si (111) crystals, which have zero structure factors for the second-order reflections, or appropriately adjusting the discriminator

level for the pulse-height spectrum from the detector. For efficient data collection, sometimes a position-sensitive detector is used so that $I(q)$ at many values of 2θ are measured simultaneously. With slit geometry, one is actually not measuring $S(\vec{q})$ but $S(\vec{q})$ integrated over the component of $\vec{q}$ perpendicular to the scattering plane (in principle, up to values determined by the detector size, but effectively over all wave vectors in this direction for the purposes of small-angle scattering), so that any model for $S(\vec{q})$ must be so treated before fitting to the experimental data, or alternatively some method of "unfolding" the resolution from the measured spectra must be employed [2]. For many in-house x-ray sources, the so-called Kratky camera [2] is one of the most popular pieces of apparatus used for small-angle scattering. At higher brightness synchrotron sources, reactor neutron sources and some rotating anode x-ray sources, so-called "pinhole" or "point geometry" is used, where the incident beam is collimated in *both* perpendicular directions (usually by slits, but sometimes by slits in one direction and multiple-slit Soller collimators in the perpendicular direction [2]) so that what is measured is the true $S(q)$ rather than its integral over one direction. (Of course, in principle, this is still smeared with a finite instrumental resolution function, but often this is so narrow in comparison with the features in $S(q)$ that it is ignored). Since we have the relation $q = (4\pi/\lambda)\sin\theta$, by differentiation we can obtain the independent contributions of the wavelength and angular spread of the beam to the resolution broadening in q. We have (since $\theta \ll 1$)

$$\overline{\Delta q^2} = q^2(\overline{\Delta\lambda^2}/\lambda^2) + (4\pi/\lambda)^2\overline{\Delta\theta^2}. \tag{11}$$

From this equation, we can see that the contribution of the wavelength spread in the beam is not appreciable unless q itself becomes fairly large. Thus, for intensity reasons, it is efficient to use a fairly broad bandpass monochromator for small-angle scattering experiments. For synchrotron x-ray sources and some neutron sources, multilayer monochromators or supermirrors [7], which provide a fairly large $(\Delta\lambda/\lambda)$, are often used. At reactor sources, mechanical velocity selectors for the incident neutrons are often employed, with $(\Delta\lambda/\lambda)$ as large as 20%. One then collimates the beam with pinhole geometry, as mentioned, with appropriate guard slits to protect against slit scattering, and the scattered beam is usually collected in a two-dimensional (2-D) area detector placed downstream from the sample. The angular resolution of the scattered beam is determined by the detector pixel size, illuminated sample-size and sample-detector distance, which is consequently quite large (typically 2–20 m). A beam stop is positioned in front of the center of the detector to protect the detector from damage from the intense primary beam transmitted (but not scattered) by the sample. The

size of the beam stop determines $q_{\min}$ and should be chosen consistent with the instrumental resolution function, or just large enough to kill the primary beam spot.

At most synchrotron x-ray sources and increasingly at reactor-based neutron sources, the effect of the angular spread of the beam and the effect of finite sample size can be mitigated and higher resolution obtained (without sacrifice of intensity) by using a curved mirror (or a bent monochromating crystal) to *focus* the incident beam at the detector. A schematic setup of a small-angle beamline at a synchrotron x-ray source or a reactor neutron source is indicated in Fig. 2. In general, in measuring small-angle scattering, one must correct for the scattering from the container, which itself is attenuated by the transmission of the sample when the latter is placed in the container. In addition, one must correct for the "dark noise" or "room background" signal, and thus one has

$$I_{\text{ts}} = [(I_s - I_d)/T] - (I_c - I_d), \tag{12}$$

where I_{ts} is the true signal, I_s is the measured signal with the sample present in the container, I_c is the measured signal from the empty container, I_d is the measured "dark current" signal, and T is the transmission of the sample (measured in a subsidiary experiment).

In addition, one usually must calibrate the sensitivity of the 2-D detector array, which may vary across the pixels, in a subsidiary measurement. Typical ranges of q accessible with such small-angle beamlines are 0.02 to $2\,\text{nm}^{-1}$, corresponding to length scales ($1/q$) of roughly 0.5 to 50 nm. Larger q values are simultaneously accessible at small-angle scattering instruments at pulsed-neutron sources. In this kind of instrument, a pulsed white beam is incident on the sample, scattered into a 2-D detector, and the counts in each pixel are sorted by time of arrival relative to the pulse at the source.

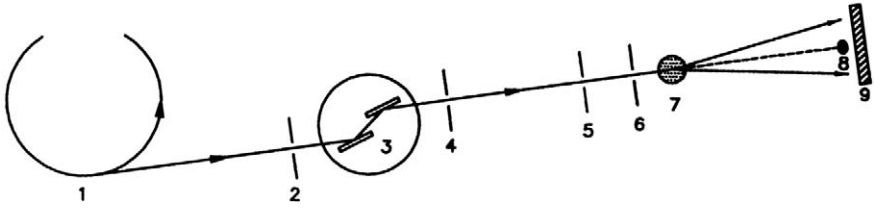

FIG. 2. Schematic diagram of a SAXS setup at a synchrotron radiation source (denoted by 1). Labels 2, 4, 5, and 6 denote collimating and guard slits; 3 is a double crystal monochromator (typically in the vertical plane); 7 is the sample; 9 is a linear or 2-D detector; and 8 is a beam stop to prevent the main transmitted beam hitting its detector.

The time of arrival of the neutron in a particular pixel determines its velocity and thus its wavelength and the corresponding q of the scattering process. By accumulating all such processes (and normalizing relative to the wavelength spectrum in the incident pulse) one builds up the $S(q)$ function. Of course, pinhole collimation requirements still apply, but obviously no monochromator is needed, and the shorter wavelengths present in the beam can yield data at q values out to greater than $5\,\mathrm{nm}^{-1}$.

To go to smaller q values — that is, to probe length scales of microns or larger — one must use a special type of small-angle scattering instrument based on Bonse–Hart multiple bounce monochromators [8] and analyzers, as indicated schematically in Fig. 3. (The high resolution is typically achieved only in the plane of scattering.) The monochromators and analyzer crystals employed are channel-cut perfect crystals of Si or Ge employed in the multiple-bounce mode (typically 2 to 3 bounces are employed) and arranged in the nondispersive configuration relative to each other. The typical Darwin width of the multiple bounce monochromators have their "tails" strongly clipped by the repeated reflections, and a small deviation of the scattered beam from the incident direction can be detected by a slight rotation of the analyzer crystal. Such Bonse–Hart-type small-angle beamlines exist at several current synchrotron x-ray and reactor neutron sources and have been used to measure the small-angle scattering from structural features of sizes as large as microns. While the increase of $S(q)$ at small q for large scattering features helps to make up for the loss of intensity due to the multiple-bounce monochromation, one can sometimes run into the problem of multiple scattering from the sample when $S(q)$ becomes very large, unless the sample is made very thin. In some experiments, this multiple scattering from large pores, in the form of Gruneisen–Mie scattering has been explicitly calculated to interpret the scattering from certain mesoporous ceramics [9].

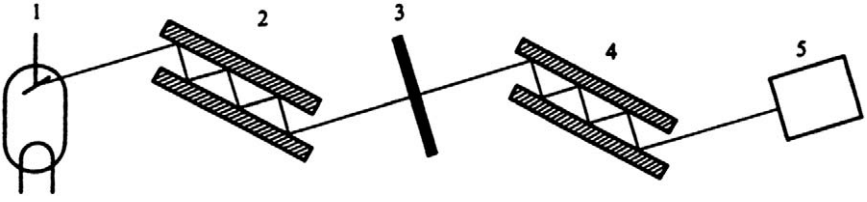

FIG. 3. Schematic of a Bonse–Hart camera: 1, x-ray source; 2, channel-cut multiple-bounce perfect crystal monochromator; 3, sample; 4, multiple-bounce analyzer (mounted nondispersively); and 5, detector.

6.3 Scattering from Porous Media

Contrary to what one might think initially, it is rare to find a porous material that consists of tiny isolated voids randomly embedded in a solid material. For such a simple (but unrealistic) case, one can employ Babinet's principle and use the formula for scattering from a collection of particles and include polydispersity to obtain the dependence of $S(q)$ on the pore size distribution, as discussed in the previous section. A more realistic representation for a porous solid is in terms of a two-phase random or bicontinuous medium (see Fig. 4) where one phase is simply the pore space and the other the solid phase, assumed to be of uniform scattering length density at least for length scales $> 1/q_{\max}$. Since we can imagine the pore space being filled with liquid in some cases, let us generally assume the SLD in these two

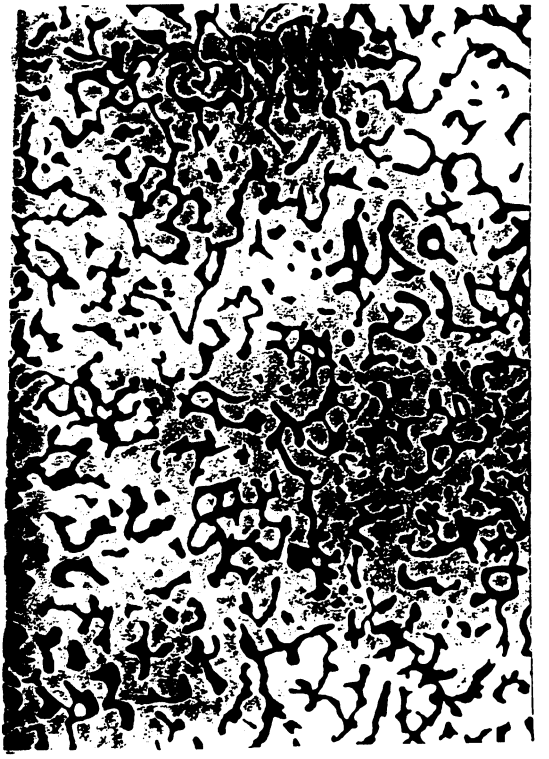

FIG. 4. Transmission electron micrograph (TEM) of a thin section of Vycor glass. Reprinted with permission from P. Levitz, G. Ehret, S. K. Sinha, and J. M. Drake, *J. Chem. Phys.* **95**, 6151. Copyright 1991, American Institute of Physics.

phases to be ρ_1 and ρ_2, respectively. Following Ref. [11], let the volume fractions of the two phases be ϕ_1 and ϕ_2, respectively, ($\phi_1 + \phi_2 = 1$). The average SLD of the system ρ_1 is given by

$$\bar{\rho} = \phi_1\rho_1 + \phi_2\rho_2. \tag{13}$$

The effective SLD contrasts for phases 1 and 2 are given by

$$\begin{aligned} \eta_1 &= \rho_1 - \bar{\rho} = \phi_2(\rho_1 - \rho_2) = \phi_2\Delta\rho, \\ \eta_2 &= \rho_2 - \bar{\rho} = -\phi_1(\rho_1 - \rho_2) = -\phi_1\Delta\rho. \end{aligned} \tag{14}$$

Let us pick at random two points (A, B) in the system separated by a distance $\vec{R}$. Let $P_{11}(\vec{R})$ be the *conditional* probability that if point A is in phase 1, then point B is also in phase 1. The situation is similar for $P_{12}(R)$, $P_{21}(R)$, and $P_{22}(R)$. Obviously, by definition

$$P_{11}(\vec{R}) + P_{12}(\vec{R}) = 1$$

and

$$P_{21}(\vec{R}) + P_{22}(\vec{R}) = 1. \tag{15}$$

The absolute probability that both points are in phase 1 can be called $\tilde{P}_{11}(\vec{R})$ and must be given by

$$\tilde{P}_{11}(\vec{R}) = \phi_1 P_{11}(\vec{R}). \tag{16}$$

Similarly,

$$\tilde{P}_{12}(\vec{R}) = \phi_1 P_{12}(\vec{R}) = \tilde{P}_{21}(\vec{R}) = \phi_2 P_{21}(\vec{R}) \qquad \text{(by symmetry)} \tag{17}$$

and

$$\tilde{P}_{22}(\vec{R}) = \phi_2 P_{22}(\vec{R}). \tag{18}$$

Let us define a function $\gamma_0(R)$ such that

$$P_{11}(\vec{R}) = \phi_1 + \phi_2\gamma_0(\vec{R}). \tag{19}$$

Then by Eq. (15),

$$P_{12}(\vec{R}) = \phi_2 - \phi_2\gamma_0(\vec{R}). \tag{20}$$

By Eq. (17),

$$P_{21}(\vec{R}) = \phi_1 - \phi_1\gamma_0(\vec{R}), \tag{21}$$

and again by Eqs. (20) and (15),

$$P_{22}(\vec{R}) = \phi_2 + \phi_1\gamma_0(\vec{R}). \tag{22}$$

From the preceding arguments, we have from Eq. (5),

$$\gamma(R) \equiv \langle \delta\rho(\vec{r})\delta\rho(\vec{r}) \rangle = \langle \delta\rho(0)\delta\rho(\vec{R}) \rangle$$
$$= \eta_1^2 \tilde{P}_{11}(R) + 2\eta_1\eta_2 \tilde{P}_{12}(R) + \eta_2^2 \tilde{P}_{22}(R), \tag{23}$$

where $\vec{R} = \vec{r}' - \vec{r}$ and we have assumed overall statistical translational invariance.

By Eqs. (14)–(22), after some algebra, we thus have

$$\gamma(R) = (\Delta\rho)^2 \phi_1 \phi_2 \gamma_0(\vec{R}), \tag{24}$$

so that

$$S(\vec{q}) = V(\Delta\rho)^2 \phi_1 \phi_2 \int d\vec{R} \gamma_0(\vec{R}) e^{-i\vec{q}\cdot\vec{R}}, \tag{25}$$

where V is the sample volume.

Assuming $\gamma_0(\vec{R})$ to be isotropic, Eq. (25) can be simplified to

$$S(q) = V(\Delta\rho)^2 \phi_1 \phi_2 \int_0^\infty dR 4\pi R^2 \gamma_0(R) \left(\frac{\sin qR}{qR} \right). \tag{26}$$

Note that, by definition, $P_{11}(0) = P_{22}(0) = 1$ and $P_{12}(0) = P_{21}(0) = 0$, which by Eqs. (19)–(22) implies that $\gamma_0(0) = 1$. Note also that by Eq. (26),

$$S(0) = V(\Delta\rho)^2 \phi_1 \phi_2 v_c, \tag{27}$$

where

$$v_c = \int_0^\infty dR 4\pi R^2 \gamma_0(R) \tag{28}$$

and is called the *correlation* volume. If this volume is larger than the finite *coherence* volume of the radiation (typical neutron coherence lengths being approximately a few tens of nanometers at best for such experiments), then the integral in Eq. (28) is reduced to being over only the radiation coherence volume. The inverse Fourier transform of Eq. (26) yields a way of obtaining $\gamma_0(R)$ directly from the measured $S(q)$:

$$\gamma_0(R) = \frac{1}{2\pi^2 V(\Delta\rho)^2 \phi_1 \phi_2} \int_0^\infty dq q^2 S(q) \left(\frac{\sin qR}{qR} \right). \tag{29}$$

Using the relation $\gamma_0(0) = 1$, we obtain

$$Q \equiv \int_0^\infty dq q^2 S(q) = 2\pi^2 V(\Delta\rho)^2 \phi_1 \phi_2, \tag{30}$$

where Q, proportional to the integral of $S(q)$ over all $\vec{q}$, is called the *Porod*

invariant [2] and does not depend on the detailed morphology of the pore structure.

The correlation volume can be obtained from $S(0)$ if it can be reliably extrapolated from finite q values, and Q can be obtained from Eq. (30). Let us now consider the small R expansion of $\gamma_0(R)$. It can be proved [2, 10] that for *smooth* internal surfaces,

$$\gamma_0(R) = 1 - R/\bar{\ell} + \cdots, \tag{31}$$

where

$$\frac{1}{\bar{\ell}} = \frac{1}{4\phi_1\phi_2}(S/V), \tag{32}$$

where $\bar{\ell}$ is a mean chord length (averaged across the pores and the solid), and S is the internal surface area of the pores. Then, substituting in Eq. (25) for $S(q)$, integrating by parts, and keeping the leading term as $q \to \infty$ (for this purpose we neglect oscillatory terms in the integral, which average out except for perfectly regular systems), we obtain the large $q(q \gg 1/\bar{\ell})$ behavior of $S(q)$:

$$S(q) \approx 2\pi(\Delta\rho)^2 S/q^4, \tag{33}$$

which is the famous Porod law for the asymptotic form of the scattering at large q [2, 10] (see Fig. 5a). A useful relation using Eqs. (33) and (30) is

$$S/V = \pi\phi_1\phi_2/Q \lim_{q\to\infty} [q^4 S(q)]. \tag{34}$$

Thus the internal surface-to-volume ratio for a porous material can be found from scattering experiments alone (if ϕ_1 and ϕ_2 are known) and can be checked for consistency against separate measurements of the internal surface area and porosity (e.g., from vapor pressure isotherm and porosimetry measurements). Porod's law is not always obeyed in the sense that for many porous materials, asymptotic power laws for $S(q) \sim q^{-\nu}$ have been observed, where ν varies between 3 and 4 (see Fig. 5b). This can be explained in terms of a rough internal surface, which at these length scales (of order q^{-1}) behaves like a *self-similar fractal* surface. This is discussed in the next section. For such surfaces, S/V changes with $1/q$ in Eq. (34), reflecting the fact that for a fractal surface the area depends on the length scale chosen.

Turning now to specific models for $\gamma_0(R)$, one of the best-known expressions is due to Debye, Anderson, and Brumberger [11], who basically used a statistical model for the porous medium so that $\gamma_0(R)$ was given by the expression resulting from Poisson statistics:

$$\gamma_0(R) = e^{-R/a}, \tag{35}$$

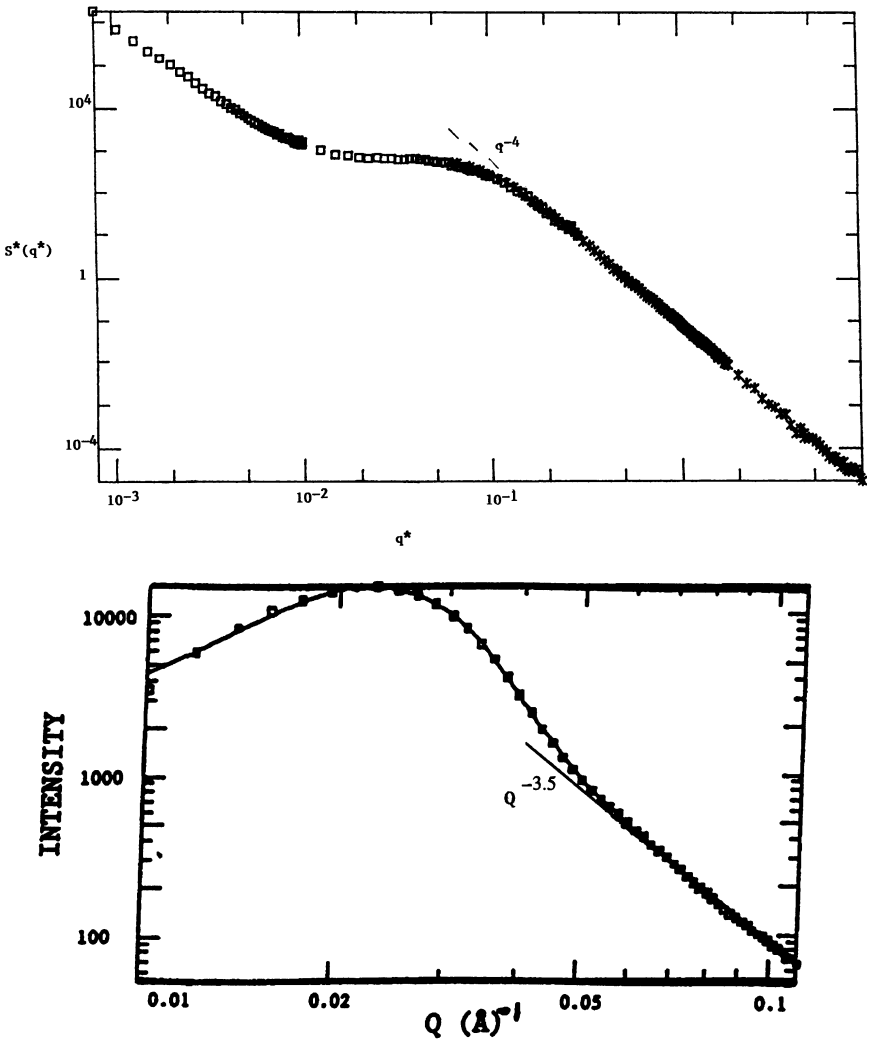

FIG. 5. (a) Scaled $S(q)$ for several silica gels on a log-log plot, showing asymptotic q^{-4} behavior (from Ref. [12]). (b) The $S(q)$ for dry Vycor glass on a log-log plot (open squares) showing a deviation from Porod's law above $0.05\,\text{Å}^{-1}$ with $q^{-3.7}$ behavior (from Ref. [17]).

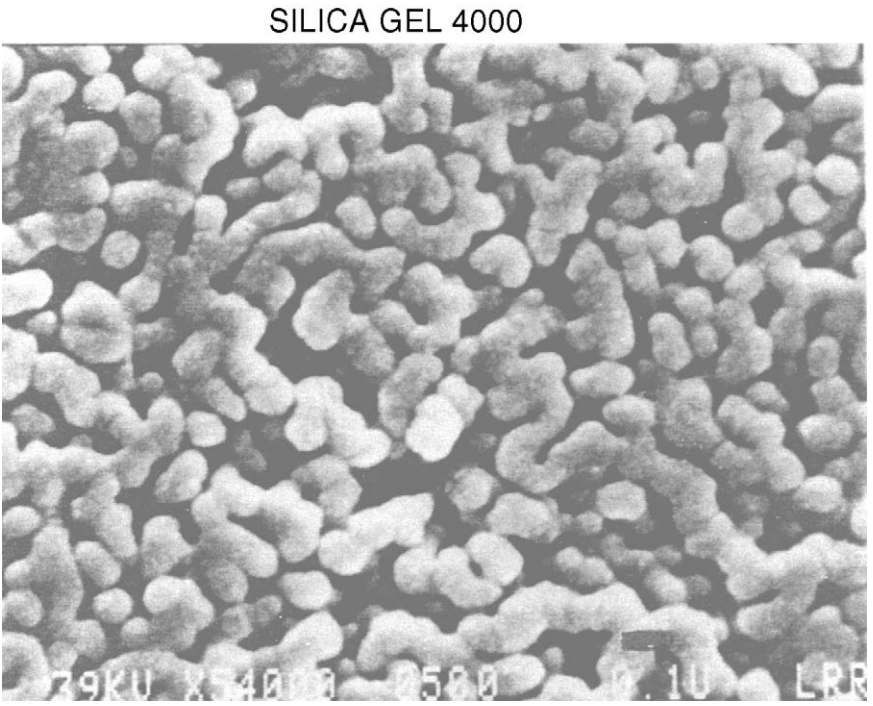

FIG. 6. Electron micrograph of silica gel Si-4000 at 20,000× (from Ref. [12]).

where a is a length that can be taken as characterizing either the average pore size or grain size (for a porous medium consisting of compacted grains). This results in an expression for $S(q)$ given by

$$S(q) = 8\pi V(\Delta\rho)^2\phi_1\phi_2 a^3/(1 + q^2a^2)^2, \tag{36}$$

which has the asymptotic form of Porod's law (Eq. [33]) and is equivalent to putting $\bar{\ell} = a$ in Eqs. (31) and (32).

Figure 5(a) shows small-angle x-ray scattering from a series of silica gels [12], which are porous materials produced by sintering aggregations of silica particles, as exhibited in the micrograph in Fig. 6. The curves in Fig. 5(a) show superpositions of $S(q)$ for several such gels (with appropriate scaling for each of the axes) and are seen to collapse on a single curve, showing that scattering from each member of this family of gels has the same form, except for a single adjustable length scale, the size of the "building block particles." This length scale is obtained by fitting the intermediate to large q parts of $S(q)$ to the form of Eq. (36). (Porod's law is obeyed quite well here, indicating relatively smooth internal surfaces.) At small q, the $S(q)$

rises according to a different power law, which is related to a mass-fractal structure of inhomogeneities existing at large length scales (discussed later).

Vycor glass is extremely popular as a "model porous medium" for a variety of experiments. It is produced by spinodal decomposition on quenching a borosilicate melt from high temperature, resulting in a phase separation of a boron-rich phase and a silica-rich phase. The former is then removed by acid leaching leaving the pore space, and the material resembles that shown in Fig. 4; that is, a bicontinuous two-phase system resulting from the late stages of spinodal decomposition. As might be expected, a characteristic quasi-periodicity exists in this structure (the distribution of distances from an internal surface into a pore through the solid and to the next pore surface is peaked around a characteristic length of ~ 25 nm, the average pore diameter being ~ 8 nm and the porosity being typically 28%), and $S(q)$ for Vycor [13–15] shows a peak as illustrated in Fig. 5b (as measured by SANS). Note that the asymptotic slope (on a log-log plot of $S(q)$) shows an exponent of 3.5 instead of the Porod exponent of 4, indicating a fractally rough surface at small length scales, as discussed in the next section. (However, this deviation may also be due to compositional inhomogeneities at the interface.)

A simple and intuitively appealing method of characterizing the morphology of a two-phase porous medium is in terms of *chord* distributions across each of the two phases (e.g., solid-occupied space and pore space), as indicated schematically in Fig. 7; that is, the probability distribution of lengths along a particular direction between one interface and the next. (For an isotropic porous medium, these distributions will obviously be independent of the direction chosen.) There are obvious similarities to the definition of the Debye function $\gamma_0(\vec{R})$. It has not proved possible, however, to rigorously express $S(\vec{q})$ in terms of such chord distributions without further restrictive assumptions. For a random bicontinuous porous medium, the most obvious assumption that suggests itself is that the probabilities of intersecting successive solid–pore and pore–solid interfaces depend *only* on the chord distributions and are otherwise totally uncorrelated with previous or successive intersections. It is then possible to devise a formal expression for $\gamma_0(\vec{R})$ [16], but writing down an explicit closed-form expression for $S(q)$ is difficult except in special cases. An explicit form for $S(q)$ was devised by Lin and Sinha [17] using a simple phenomenological model similar in spirit to that of Mering and Tchoubar [16], but with more restrictive assumptions. The derivation of this is sketched in Appendix A.

The result obtained for $S(q)$ is

$$S(q) = V(\Delta\rho)^2 \frac{1}{[\langle \ell_p \rangle + \langle \ell_s \rangle]} \left[\frac{2 - f_p(q) - f_s(q)}{1 - f_p(q) f_s(q)} + \text{c.c.} - 2 \right] \frac{F(q)}{q^2}, \quad (37)$$

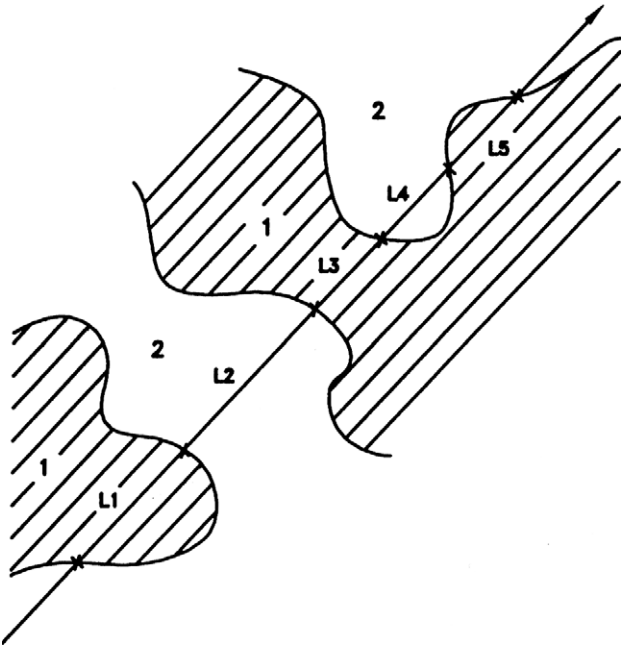

FIG. 7. Schematic of chord distribution model representing a bicontinuous medium composed of media 1 and 2. L_1, L_3, L_5 are chords in medium 1 and L_2, L_4 are chords in medium 2.

where $f_p(q)$ and $f_s(q)$ are, respectively, the Fourier transforms of the pore and solid chord distributions whose averages are (ℓ_p) and (ℓ_s), respectively, and $F(q)$ is an average shape factor for the interface between pore and solid. We can now choose $F(q)$ to give the correct asymptotic form to $S(q)$ at large q; that is, depending on whether we have smooth or rough interfaces, since $f_p(q)$ and $f_s(q) \to 0$ at large q.

Thus, for smooth interfaces where we must obtain Porod's law in the limit, we must have

$$F(q) \cong 2\pi/q^2, \tag{38}$$

whereas for fractally rough surfaces where $S(q) \sim q^{-\nu}$, $F(q)$ must be chosen appropriately. One can now parametrize the chord distributions through the solids and pores respectively. This was done for Vycor glass by Lin and Sinha [17], who chose the following forms for the real-space chord distributions

$$f_{p,s}(z) = z^{\nu}(A_1 e^{-\alpha z} + B_1 e^{-\beta z}), \tag{39}$$

where for each phase the parameters ν, A_1, B_1, α, and β are adjusted to fit the data, one of them being determined by the normalization condition.

Figure 8 shows the deduced pore and solid chord distributions from fitting to the observed $S(q)$ of Vycor. An excellent fit is observed to the data. The fitted parameters yield for the average pore size $\langle \ell_p \rangle$ a value of 8.46 nm, the average chord length through the solid $\langle \ell_s \rangle$ is 17.76 nm, and the porosity $\phi_1 = \langle \ell_p \rangle / (\langle \ell_p \rangle + \langle \ell_s \rangle) = 0.32$. These values are in good agreement with the results of other measurements, such as nitrogen description. Because of the approximations made in the theory that leads to Eq. (37), however, one should perhaps think of such inferred quantities as semi-quantitative rather than rigorous.

A more sophisticated model has been given by Berk [18] starting from the so-called Cahn construction for an internal surface, resulting from choosing contours of the function

$$F(\vec{r}) = \frac{1}{\sqrt{N}} \sum_i \cos(\vec{k}_i \cdot \vec{r} + \phi_i), \tag{40}$$

where $\vec{k}_i$ are a set of N vectors random in direction but having a narrow distribution in length, and ϕ_i are a set of random phases. One then chooses a cutoff value for this function, so that all points for which $F(\vec{r})$ is smaller than this cutoff can be called "pore space" and all points for which $F(\vec{r})$ is greater can be called "solid." For the special case of so-called isometric topology, where this cutoff has the value zero and $\phi_2 = \phi_2$, Berk proves the

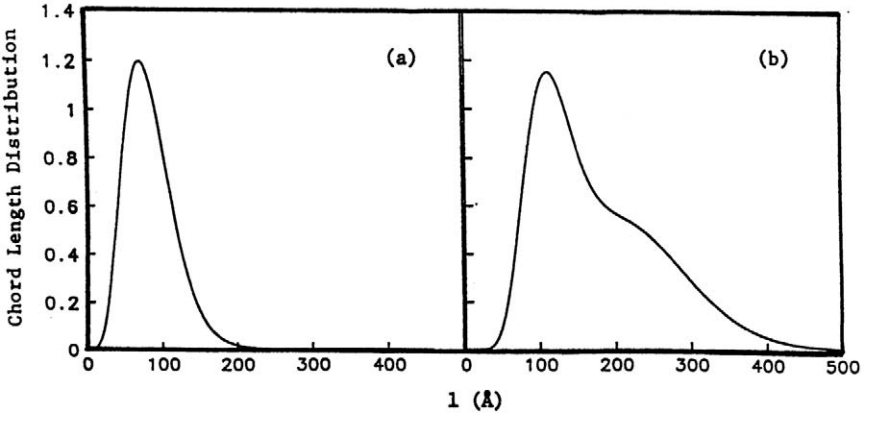

FIG. 8. Chord distribution derived by fitting Eq. (46) to the $S(q)$ for dry Vycor (Fig. 5b): (a) pore chord distribution and (b) solid chord distribution (from Ref. [17]).

remarkably elegant result

$$\gamma_0(R) = (2/\pi) \arcsin[j_0(kR)], \tag{41}$$

while for the general case, he derives an expression for $\gamma_0(R)$ in terms of a power-series expansion of $j_0(kR)$. Here j_0 is the spherical Bessel function, and k is the magnitude of the wave vectors $\vec{k}_i$. In practice, one averages $j_0(kR)$ over a narrow distribution of k centered about some mean value. Using this formalism, Berk has calculated $S(q)$ functions that remarkably resemble the scattering from spinodally decomposed systems, such as Vycor, as well as bicontinuous microemulsion phases [18]. These show the characteristic peak at finite q seen in the scattering from such systems.

Another analytic form for $S(q)$ for such systems has been given by Teubner and Strey [19] based on Ginsburg–Landau free-energy theory and can be written as

$$S(q) = V(8\pi/\zeta)(\Delta\rho)^2 C_2/(a_1 + C_1 q^2 + C_2 q^4), \tag{42}$$

where ζ is the correlation length and a_1, C_1, and C_2 are constants. This corresponds to a Debye correlation function:

$$\gamma_0(R) = \frac{d}{2\pi R} e^{-R/\zeta} \sin(2\pi R/d), \tag{43}$$

where d is a typical domain size. The form of $\gamma_0(R)$ reflects the quasi-periodicity of the medium, and Eq. (42) has been successfully used to fit bicontinuous microemulsion data. It possesses the characteristic peak (as seen in Vycor, for instance).

Chen *et al.* [20] have introduced a modification of Berk's model that borrows some concepts also from the Teubner–Strey model. Their $\gamma_0(R)$ is obtained from an expression similar to Eq. (41) but with $j_0(kR)$, which in Berk's model is really the two-point autocorrelation function of $F(\vec{r})$ in Eq. (40), replaced by the Fourier transform of an inverse sixth-order polynomial in k that contains three parameters a, b, and c. These authors also derive an expression for the average Gaussian curvature of the interface in terms of these parameters and are thus able to obtain values for this curvature by fitting $S(q)$ for an isometric bicontinuous microemulsion [20].

Another model for a spinodally decomposed system at late times has been developed by Li and Ross [21]. These authors use arguments to show that if magnitudes of allowed wave vectors have a very narrow range centered on k_0, then $S(\vec{q})$ can be written as

$$S(q) = C\langle F^2(\vec{q})\rangle \frac{1}{qk_0} \{\zeta/[1 + (q - k_0)^2\zeta^2] - \zeta/[1 + (q + k_0)^2\zeta^2]\}, \tag{44}$$

where C is a constant, $F(\vec{q})$ is a "pore form factor," and ζ represents a correlation length for the decay of the sinusoidal concentration fluctuations associated with the spinodal decomposition. Using this form, Li and Ross were able to get a remarkably good fit to the scattering from dry Vycor glass [21].

It is to be noted that since all these forms are based on smooth internal surfaces, they cannot reproduce anything except an asymptotic q^{-4} behavior for $S(q)$, although the model of Ref. [17] gives a prescription for modifying the $S(q)$ in the case of roughness.

6.4 Scattering from Fractal Systems

We next consider porous solids produced by the rather tenuous aggregation of small or colloidal particles, which often have local mass-fractal structure. Many types of silica gels, xerogels, and aerogels are of this type. Scattering experiments can often provide valuable clues regarding the process of formation of such porous solids. These materials can have extremely high (up to $\sim 98\%$) porosity and still stay amazingly rigid. For such systems, Eq. (5) can be written as

$$S(q) = Nf^2(q)(\Delta\rho)^2 \int d\vec{R} g(\vec{R}) e^{-i\vec{q}\cdot\vec{R}}, \tag{45}$$

where N is the total number of particles, $f(q)$ is the average form factor (or the Fourier transform of the shape function of the individual particles), $\Delta\rho$ is the contrast between the SLD of the particle and that of the embedding medium (usually vacuum or some solvent), and $g(\vec{R})$ is the pair-distribution function for the centers of the particles; that is, the probability per unit volume that given a particle center at the origin, another center can be found at a distance $\vec{R}$. This is a function of the magnitude R only and, for a fractal object, can be obtained from the definition that within a radius R there are on the average CR^D particles (where C is a constant and D is the mass fractal dimension) [22]. By differentiating, we obtain

$$4\pi R^2 g(R)\, dR = DCR^{D-1}\, dR, \tag{46}$$

or

$$g(R) \sim R^{D-3}. \tag{47}$$

In general, $0 < D < 3$, so that the 3-D Fourier transform of $g(R)$ yields an $S(q)$ that goes as q^{-D}. However, fractal correlations exist only up to a finite length scale (a typical cluster size) and may also not be obeyed at short length scales (e.g., nearest neighbor distances).

Neglecting the latter effect (which affects only the large q behavior of $S(q)$), we can take finite cluster sizes into account by choosing instead of Eq. (47), a modified form for $g(R)$; that is [23, 24],

$$g(R) = \delta(R) + AR^{D-3}e^{-R/\xi} + C', \tag{48}$$

where the delta function at the origin is due to the particle correlation "with itself," A and C' are constants, and ξ represents the correlation length of the fractal. This expression can be Fourier transformed to yield for Eq. (45) the expression (neglecting the forward scattering at $q = 0$),

$$S(q) = Nf^2(q)\Delta\rho^2 \left[1 + \frac{A}{(1+q^2\xi^2)^{D/2}} \frac{(1+q^2\xi^2)^{1/2}}{q\xi} \frac{\sin[(D-1)\tan^{-1}(q\xi)]}{D-1}\right]. \tag{49}$$

As expected, provided q is much less than the inverse of the particle size a, $S(q)$ behaves like q^{-D} for $q \gg \xi^{-1}$ and saturates when $q \sim \xi^{-1}$. For q^{-1} much less than the particle size, $S(q)$ behaves like the square of the single particle form factor $f^2(q)$ and eventually rolls off as q^{-4} if the particles are smooth (Fig. 9) or as $q^{-\nu}$ $(3 < \nu < 4)$ if the particles are fractally rough [25]. The preceding expression has been successfully used to fit the scattering from a variety of fractal systems and to study the dependence of D and ξ on porosity. Figure 9 shows $S(q)$ for a series of acid-catalyzed aerogels by Frisken *et al.* [26] fitted to the preceding expression and indicating the corresponding values of the parameters D and ξ. We can see that there is a slight tendency for both D and ξ to *increase* as the pH of the solution from which these samples were grown *decreases*, at constant porosity. By studying silica gels *in situ* during the formation process, the evolution of ξ with time as the fractal clusters grow and saturate has also been studied [27].

As discussed in the previous section, the asymptotic form at large q of $S(q)$ for many porous solids in practice does not obey Porod's law (q^{-4}) but rather $q^{-\nu}$, where ν is an exponent between 3 and 4. This was first explained by Bale and Schmidt [25] in terms of an internal surface that is not smooth (as assumed by the Porod theory) but is actually a self-similar *fractal* surface [22]. From the "tiling" definition of such a surface [22], these authors were able to show that the small R expansion of $\gamma_0(R)$ in Eq. (31) should be replaced by

$$\gamma_0(R) = 1 - CR^{3-D_s} + \cdots, \tag{50}$$

where D_s is the surface fractal dimension of the internal surface, and C is a constant. Wong and Bray [30] have pointed out that Eq. (50) needs to be considered more carefully as it gives completely the wrong result as $D_s \to 3$, predicting vanishing small-angle scattering. In fact, they showed that the

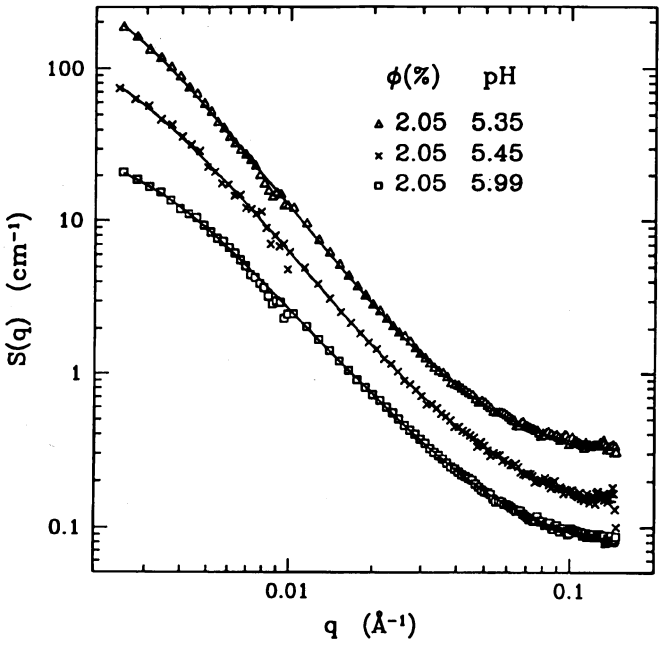

FIG. 9. The $S(q)$ for a series of silica gels made in D_2O at different pH, as indicated. The silica volume fraction for each sample is also denoted on the graph. The solid curves are fits of Eq. (49) to the data with $D = 2.22$, 2.13, and 2.03 for the pH 5.35, 5.45, and 5.99 samples, respectively. Reprinted with permission from B. J. Frisken, F. Ferri, and D. S. Cannell, *Phys. Rev. Lett.* **66**, 2754. Copyright 1991 by the American Physical Society.

factor C contains $3 - D_s$ in the denominator, and deduced for $S(q)$ in the asymptotically large q limit,

$$S(q) = \frac{\pi(\Delta\rho)^2 S_2 \ell_2^{D_s-2} \Gamma(5 - D_s) \sin[\pi(3 - D_s)/2]}{(3 - D_s) q^{6-D_s}} \tag{51}$$

which must replace Eq. (33). In this expression, S_2 is the "smooth" surface area, measured at the length scale ℓ_2, where the surface fractal behavior cuts off, and Γ is the gamma function. Equation (51) yields finite scattering as $D_s \to 3$, as it should. Measurements on porous media by Hurd *et al.* [32] have found that inclusion of the $3 - D_s$ factor in the prefactor to Eq. (51) yields the correct (BET) surface area from scattering data.

Note that for a smooth surface, $D_s = 2$ and Porod's law is recovered. In general $2 \leqslant D_s \leqslant 3$ so that measurement of the exponent ν can be used to

obtain the surface fractal dimension. Schmidt and coworkers have shown that a variety of porous systems particularly coals and charcoals [25, 28] have fractal dimensions greater than 2. In a series of SANS experiments on various rocks, Wong *et al.* [29] have shown that these also have surface fractal dimensions larger than 2 (and often close to 3). Most measured samples of Vycor [13–15] also exhibit a value of the exponent ν close to 3.5, indicating a value of D_s of ~ 2.5.

Self-similar fractal surfaces are, however, only one possible kind of rough surface. Another common form of roughness (typically seen in films and other surfaces) is self-affine roughness, defined by [30, 31]

$$g(R) \equiv \langle [\delta z(\vec{R}) - \delta z(0)]^2 \rangle = CR^{2h}, \tag{52}$$

where h is the self-affine roughness exponent and has the range $0 < h < 1$ and $\delta z(\vec{R})$ is the height fluctuation above the average surface at lateral position $\vec{R}$. The root-mean-square height deviation $[g(R)]^{1/2}$ always becomes much less than R for large enough R so that such surfaces look flat at large enough length scales, but at small length scales, $R \leqslant C^{1/2(1-h)}$, such surfaces approach self-similar fractal surfaces. Their surface fractal dimension D_s is related to h by

$$D_s = 3 - h. \tag{53}$$

Wong [33] first showed that the asymptotic form of $S(q)$ for an isotropic average of such surfaces had the form

$$S(q) \sim A/q^4 + B/q^{3+h}. \tag{54}$$

The first term is Porod's law arising from the larger length scale (smooth) behavior, while from Eq. (53), the second term is seen to be identical to the Bale–Schmidt form in Eq. (51). Equation (54) was also derived by Sinha *et al.* [31] using a different method. Clearly the second term will dominate the asymptotic behavior at large enough q, although the q^{-4} term may get mixed up with other behavior at intermediate q, and thus it is often difficult to decide whether an internal surface is self-similarly or self-affinely rough.

In any case, we have the general behavior for $S(q)$ for a large class of porous materials produced by aggregation (and sintering) of colloidal or granular particles first sketched by Schaeffer and coworkers [32] and shown schematically in Fig. 10. At large q, where we are sensitive only to the shortest length scales (i.e., the internal surfaces), we see power-law behavior characteristic of surface fractals (with Porod's law being the limiting case of $D_s = 2$) and at intermediate q ($q^{-1} \geqslant$ the particle size), we cross over to the power-law characteristic of the mass fractal behavior of the particle aggregates, while at small q ($q^{-1} \geqslant$ aggregate cluster size), $S(q)$ saturates.

In general, it is not possible to have a regime of length scales over which nontrivial and *different* surface and mass fractal dimensions simultaneously pertain to the solid, although the general form for $S(q)$ in this regime has

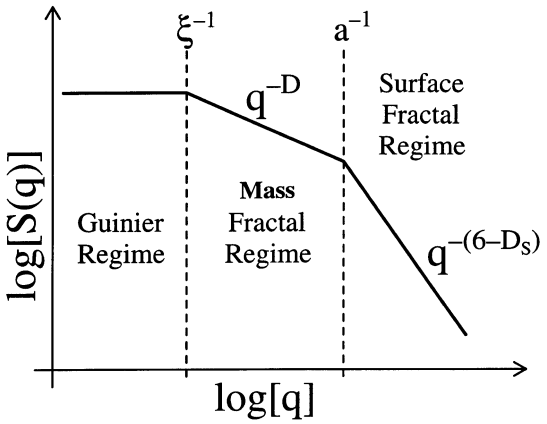

FIG. 10. Schematic diagram for $S(q)$ of a system of fractal clusters, where ξ is the cluster size and a is the size of a constituent solid particle in the cluster.

been derived by Ball and Sinha [34] and has the form

$$S(q) \sim 1/q^{2D-D_s}. \tag{55}$$

The proof of this result is sketched in Appendix B. In all known physically realizable cases, however, this result reduces to those discussed earlier in the chapter. For instance, for a fractal aggregate of particles of dimension D, at length scales greater than the particle size $D_s = D$, the surface area contained inside a radius R is obviously proportional to the number of particles inside this radius, and thus we obtain $S(q) \sim q^{-D}$. On the other hand, for length scales smaller than the particle size, the particle looks solid and thus $D = 3$, while D_s is given by the particle surface fractal dimension and we recover $S(q) \sim q^{-(6-D_s)}$. A nontrivial limit occurs when D and $D_s \to 3$. This corresponds to the case of a porous solid that is sufficiently compacted that both the mass and the internal surface become *uniformly* space filling. Such solids should yield a scaling law of $S(q) \sim q^{-3}$, as also predicted by the theory of Wong and Bray [30] but not the result of Bale and Schmidt [25]. Wong and Cao [35] have discussed the result in Eq. (55) in more detail. They correctly point out that Eq. (55) is derived under the assumption that the surface of the material arises as the natural surface of the mass fractal (see Appendix B). They have pointed out that if, however, a mass fractal is truncated by an imposed and uncorrelated boundary that is a surface fractal of a *different* and nontrivial fractal dimension D_s, then the scattering should consist of two terms, the first being the normal $S(q)$ for a mass fractal and the second having the form $q^{-(3+D-D_s)}$ If $(qL) \gg 1$, where $L \sim$ object size,

then this term becomes negligible, unless D_s approaches the value 3. These authors point out the need for caution in general in evaluating mass and surface fractal dimensions from scattering data if these are likely to be different and close to the value 3.

It is to be noted that the surface fractal dimension for the internal pore surface can in principle also be determined from the *tiling* definition of such a dimension, namely, that the number of molecules of linear diameter d adsorbed on such a surface is proportional to d^{-D_s} assuming the adsorption is determined only by geometrical constraints. This idea has been used by Avnir and coworkers [36] to derive D_s for a variety of porous materials based on adsorption measurements. Unfortunately, as shown by Drake [37] and others [38], this value of D_s may be misleading (or even in some cases greater than 3, which is clearly nonphysical) due to interaction effects between the adsorbate molecules and between these molecules and the surface. Scattering measurements of D_s should be much more reliable since they are determined by purely geometrical factors.

An interesting question is what happens when in the intermediate q (fractal) regime $a \ll q^{-1} \ll \xi$ (where $f(q) \sim 1$) when $D \to 3$, but ξ remains finite. In such a limit, Eq. (49) yields the Lorentzian-squared form of Eq. (36) or q^{-4} rather than q^{-3}, as might be initially expected. In this limit, however, the particles have formed a compact solid with an external surface so that Porod's law comes into play. Nevertheless, close to q^{-3} behavior is actually observed for many porous solids, particularly porous rocks [29]. By comparing the expressions q^{-D} for a mass fractal of dimension D and $q^{-(6-D_s)}$ for a surface fractal of dimension D_s, one can see that they tend to the same scattering law as $D \to 3$; that is, q^{-3}. In fact, in this limit, there is no difference between the mass and surface fractal regimes, and this situation corresponds to the case where the internal surface has not disappeared but the material is sufficiently compacted that both the mass and the internal surface become uniformly space filling. Once compaction proceeds further and the internal surface disappears, q^{-4} behavior is recovered, as observed in experiments on sintered aerogels [39].

6.5 Small-Angle Scattering Studies of Fluids Confined in Porous Media

The behavior of fluids in confined pore spaces is of obvious interest and most conveniently susceptible to study by SANS techniques. This is because it is possible to fill the pores with a fluid whose SLD exactly matches that of the solid, thus removing the scattering from the pore structure itself, thereby reducing the two-phase system to a one-phase system. The only

fluctuations that will then scatter radiation are deviations from the *average* density, which will be fluctuations in the fluid itself.

A problem that has been studied by several groups by both SANS and light-scattering techniques is that of the phase separation of a binary fluid mixture confined in a porous medium, such as Vycor glass or an aerogel [40–49]. A convenient system for such studies is a mixture of water and (2,6) lutidine, which in bulk has an inverted phase diagram (with a homogeneous phase at low temperatures, and phase separation occurring at *higher* temperatures). The critical concentration in the bulk mixture is 31.2% lutidine, and the critical temperature is 33°C. In the vicinity of the critical point in the single phase region, a bulk mixture shows critical fluctuations obeying 3-D Ising-like behavior. The behavior in Vycor glass as seen by light scattering [45, 49] is very different and indicative of the effects of confinement and preferential wetting of the pores (typically 8 nm in diameter), with weak or nonexistent critical fluctuations and long-time relaxation and hysteresis effects with temperature in the two-phase region. SANS data from such a system [44, 45] as a function of temperature are shown in Fig. 11.

To study the concentration fluctuations in the fluid alone, without the complications from the scattering due to the solid–liquid contrast, the homogeneous phase was taken to be contrast-matched with the Vycor using the appropriate mixture of H_2O, D_2O, and lutidine. (The fact that Vycor preferentially absorbed lutidine from the supernatant solution complicated

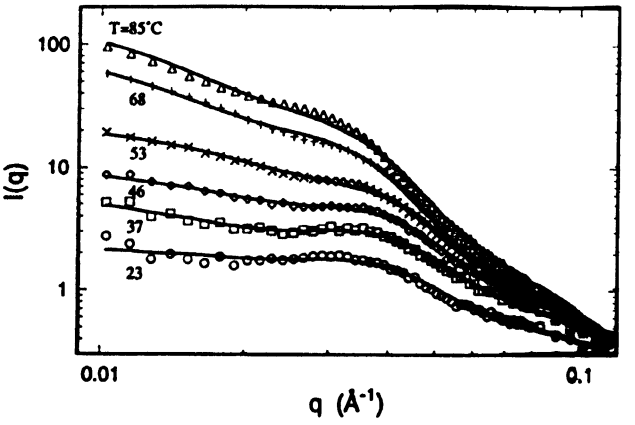

FIG. 11. The $S(q)$ in arbitrary units for a contrast-matching binary lutidine–water mixture near the critical concentration inside Vycor glass, as a function of temperature. Reprinted with permission from Lin *et al.*, *Phys. Rev. Lett.* **72**, 2207. Copyright 1994 by the American Physical Society.

the task of ensuring that the final single-phase mixture inside the Vycor was nominally critical and contrast-matched, but this was achieved by a systematic study of different initial mixtures [44]). The "Vycor peak" at $q \sim 0.025$ (see Fig. 5b) is absent due to the contrast-matching with the silica (see Fig. 11), but a peak at a larger value of q ($\sim 0.035\,\text{Å}^{-1}$) was observed in the data. This peak was identified as due to a "skin" of lutidine-rich liquid adsorbed on the internal pore surfaces, as proved by a complementary experiment in which a similar layer of hydrocarbon chains was attached to the internal pore surface of Vycor inside a contrast-matching solution of H/D toluene in the pores. The peak at the same q was clearly observed (see Fig. 12) and was used to subtract off the "skin" scattering from the observed $S(q)$ from the Vycor–water–lutidine mixture; that is, from the observed data in Fig. 11. The remaining scattering was fitted by the sum of a Lorentzian to represent the critical fluctuations (which turned out to have a very small amplitude) and a Lorentzian-squared term (with a different length scale) to represent the formation of microdomains of phase-separated water-rich and lutidine-rich phases in the two-phase region (see Eq. [36]).

The fitted curves are shown in Fig. 11. A good fit was obtained, with the domain size saturating in the two-phase region at the 8-nm length-scale of

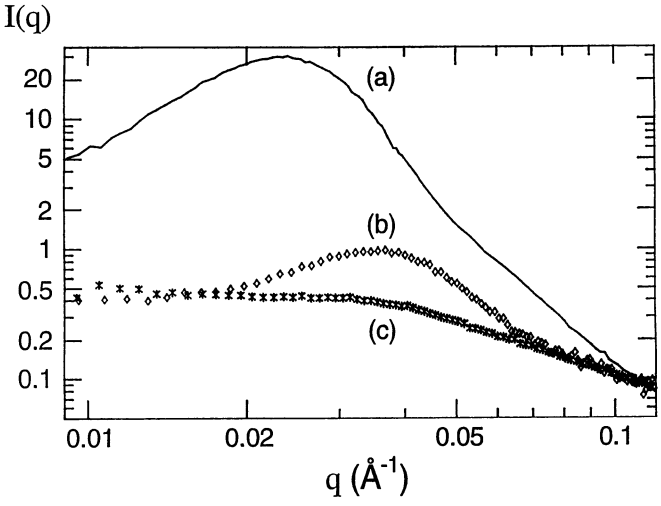

FIG. 12. Log-log plot of $S(q)$ in arbitrary units for (a) dry Vycor glass, (b) Vycor derivalized with a C_{18}-alkylsiloxane surface layer and filled with contrast-matching hexane–*d*-hexane mixture, and (c) Vycor with contrast-matching binary lutidine–water mixture. Reprinted with permission from Lin *et al.*, *Phys. Rev. Lett.* **72**, 2207. Copyright 1994 by the American Physical Society.

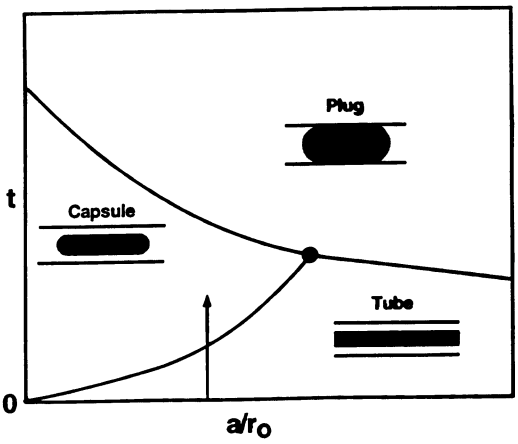

FIG. 13. Phase diagram of the single-pore model of Liu *et al.* (Ref. [48]) for phase separation inside a confined pore geometry. The arrow indicates the observed behavior of the water–lutidine system in Vycor deduced from SANS data, t is the reduced temperature, r_0 is the tube radius, and a is a molecular length.

the Vycor pores. This provided partial confirmation of the phase diagram obtained theoretically by Liu *et al.* [48] for a fluid mixture phase separating inside a finite tube. In their phase diagram (see Fig. 13), the system goes from a "tube" phase (lutidine-rich "skin" lining the pore walls) to a "capsule"-like phase ("skin" and capsules of water-rich phase within the tubes) as the temperature is raised into the two-phase region.

A similar study was carried out by Frisken *et al.* [47] in the much more open structures of a series of silica gels using a D_2O lutidine mixture. In this case, the scattering was interpreted as that from a dispersed fractal structure of the silica framework, together with the associated static concentration variations induced in the fluid by the preference of the silica for wetting itself with lutidine, in addition to spontaneous critical fluctuations in the fluid. Thus this model is similar in spirit to the well-known "random field Ising model," which was initially proposed for such systems [40, 41].

Following Eq. (5), we can write

$$S(q) = \frac{1}{V}\langle \delta\rho(\vec{q})\delta\rho^*(\vec{q})\rangle, \tag{56}$$

where $\delta\rho(\vec{q})$ is the Fourier transform of the SLD fluctuation $\delta\rho(\vec{r})$. If $\phi_s(r)$, $\phi_l(r)$, and $\phi_w(r)$ are, respectively, the local volume fractions of silica, lutidine, and D_2O and their fluctuations from the mean are $\delta\phi_s$, $\delta\phi_l$, and $\delta\phi_w$, then

$$\rho(\vec{q}) = \rho_s\phi_s(\vec{q}) + \rho_l\phi_l(\vec{q}) + \rho_w\phi_w(\vec{q}), \tag{57}$$

where ρ_s, ρ_l, and ρ_w are the SLDs of silica, lutidine, and water, respectively.

Since

$$\delta\phi_s + \delta\phi_l + \delta\phi_w = 0, \tag{58}$$

we obtain from Eq. (57)

$$\delta\rho(\vec{q}) = (\rho_s - \rho_w)\delta\phi_s(\vec{q}) + (\rho_l - \rho_w)\delta\phi_l(\vec{q}). \tag{59}$$

Let us ignore spontaneous critical concentration fluctuations in the liquid for the moment and concentrate on the response of the lutidine concentration to the silica concentration via the "wetting" interaction. Assuming linear response, this can be formally written as

$$\delta\phi_l(\vec{q}) = \alpha(\vec{q}, T)\delta\phi_s(\vec{q}), \tag{60}$$

where $\alpha(\vec{q}, T)$ can be written in the Ornstein–Zernike form

$$\alpha(\vec{q}, T) = -\frac{\bar{\phi}_l}{\bar{\phi}_l + \bar{\phi}_w} + \frac{\alpha_0(T)}{1 + q^2\zeta^2}. \tag{61}$$

(The constant term in Eq. (61) is there to account for the excluded volume decrease of lutidine concentration due to the presence of the silica, even in the absence of wetting, i.e., when $\alpha_0 = 0$).

Using Eqs. (59)–(61) in Eq. (56), we obtain

$$S(q) = \frac{1}{V}[(\rho_s - \rho_w) + (\rho_l - \rho_w)\alpha(\vec{q}, T)]^2\langle\delta\phi_s(\vec{q})\delta\phi_s^*(\vec{q})\rangle. \tag{62}$$

But the scattering from the silica gel itself in pure D_2O can be written as

$$S_{sg}(q) = \frac{1}{V}[\rho_s - \rho_w]^2\langle\delta\phi_s(\vec{q})\delta\phi_s^*(\vec{q})\rangle, \tag{63}$$

so that the scattering from the binary fluid mixture can be expressed in terms of $S_{sg}(q)$ (measured in a separate experiment) and $\alpha(\vec{q}, T)$ as

$$S(\vec{q}) = \left[1 + \frac{\rho_l - \rho_w}{\rho_s - \rho_w}\alpha(\vec{q}, T)\right]^2 S_{sg}(\vec{q}). \tag{64}$$

To this must be added the pure critical fluctuations in the fluid given by

$$S_{crit}(\vec{q}) = (\rho_l - \rho_w)^2\chi/(1 + q^2\xi^2) \tag{65}$$

and a background term. Such an expression was found to provide an extremely good fit (Fig. 14) to the data for a wide range of temperatures and concentrations throughout the one-phase region of the pure system. The four fitting parameters used were χ, ξ, α_0, and a constant background term B.

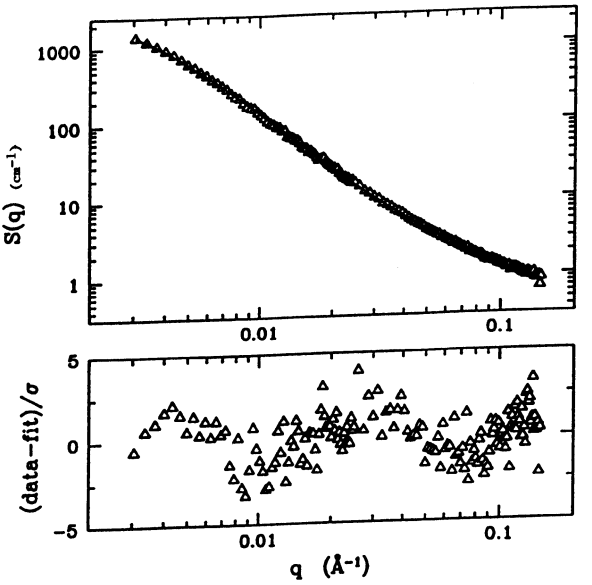

FIG. 14. Result of fitting the theoretical expression given in Eqs. (63) and (64) to the measured $S(q)$ (in absolute units) for a silica gel–water–lutidine sample containing 2.05% silica and 40 volume of lutidine at 26.80°C. The residuals in units of the standard deviation of the data are shown in the bottom portion of the figure. Reprinted with permission from Frisken *et al.*, *Phys. Rev. E* **51**, 5866. Copyright 1995 by the American Physical Society.

The results showed that ξ increased toward the critical temperature, as did α_0 and χ, although the accuracy was not sufficient to determine any critical exponents (in addition to the fact that the concentration of the "free" fluid, that which is not "frozen" in the wetting layers, also changes with temperature). This behavior appears to be different from the behavior observed in Vycor. Note also that α_0 was found *not* to scale with χ, which would be expected from a simple linear response theory indicating that the wetting response of the fluid near the silica surface is probably nonlinear, as might be expected. In the two-phase region, $S(\vec{q})$ could be represented by

$$S(q) = \frac{C_1}{(1 + q^2\xi_d^2)} + C_2 S_{sg}(q), \tag{66}$$

plus a constant background term; that is, scattering due to the silica gel in an effective uniform fluid plus scattering from domains (see Eq. [36]), indicating that sharp interfaces between phase separated domains had

formed. Equation (66) is similar in spirit to the model of Debye *et al.* [11], and the models used by Wong *et al.* [50] and Lin *et al.* [44] to describe frozen domains. The value of ξ_d was too large to measure accurately. Within the instrumental resolution, the first term in Eq. (66) effectively looked like Porod scattering. These domains also appeared to coarsen with increasing time, as observed by an increase in the amplitude of the q^{-4} term (proportional to the interfacial area by Eq. [33]).

In addition to binary fluid mixtures, the condensation of a single fluid into a porous medium is also a subject of considerable interest that has been studied with simultaneous vapor pressure adsorption isotherm and SANS measurements. Li *et al.* [51, 52] used SANS to study the condensation of a contrast-matched D_2O/H_2O mixture into Vycor glass, thus selecting the scattering from only the network of unfilled pores. For adsorption, they found an extra diffuse component in $S(q)$ at small q, which seemed to decrease as $q^{-0.5}$, while for the case of desorption they found a strong power-law component in $S(q)$, which behaved like $q^{-1.75}$, initially increased with increasing desorption and then decreased as desorption neared completion. This component was fitted rather well with a model for scattering from a mass fractal (see Eq. [49]), and indeed it is tempting to associate this mass fractal with the "percolation cluster" opened by the network of unfilled pores. The fractal dimension 1.75 is problematic, however, since percolation clusters in three dimensions are expected to have a fractal dimension of 2.4 [53]. The authors rationalize this as due to some as yet unclear influence of the pore geometry in Vycor glass.

Similar SANS studies of capillary condensation in Vycor glass using contrast-matched hexane were carried out by Lin *et al.* [54]. The behavior of the scattering on adsorption was similar to that reported by Li *et al.* [51, 52], but the desorption process was not studied.

The conformation of polymers confined inside pore spaces is also of interest. At first thought it would appear difficult to get a polymer whose equilibrium radius of gyration R_g in solution is greater than a typical pore size to enter the porous medium. However, it turns out, as predicted theoretically [55] that from a sufficiently concentrated (semidilute or more concentrated) polymer solution osmotic pressure will force the polymer chains to enter the pores, the criterion being roughly that the correlation length ξ in the semidilute solution be comparable to the pore size. This was observed in SANS experiments by Lal *et al.* [56] where polystyrene (PS) chains of equilibrium radius of gyration as large as 30 nm were imbibed into cleaned Vycor glass from semidilute solutions in times ranging from hours (for the smallest chains) to 65 days (for the largest chains). This was verified by first studying the SANS from the virgin Vycor sample with a contrast-matched solvent (deuterated dichloromethane) in the pores (which showed

no characteristic "Vycor peak") and comparing it with the imbibed Vycor in which the Vycor peak had reappeared, indicating that PS chains entering the Vycor had destroyed the contrast-matching condition.

For the SANS experiments a mixture of hydrogenated and deuterated PS chains of equal molecular weights (MW) (h-PS and d-PS respectively), and hydrogenated and deuterated toluene solvent (*h*-toluene and *d*-toluene) was used. The SANS experiment can be made sensitive to the conformation of *individual* PS chains inside the Vycor if the following two conditions are simultaneously met:

1. The *h*-, *d*-toluene mixture exactly contrast matches the silica of the Vycor. (This was determined by careful subsidiary contrast matching experiments using varying *h*-, and *d*-toluene concentrations.)
2. The concentration of *h*-PS and *d*-PS chains is chosen such that the averaged SLD of the chains exactly matches that of the solvent.

Under these conditions it can be shown [56] that only single chain fluctuations will contribute to the observed $S(q)$, which thus measures the form factor or conformation of simple chains. Experiments were done for a variety of PS molecular weights. A typical $S(q)$ curve for PS of MW 75K in toluene in Vycor is shown in Fig. 15. The results were compared with the $S(q)$ for the same chains in dilute solution in toluene (i.e., "free" chains). A Debye function fit (appropriate to free Gaussian chains in a good solvent) [55] was made to both sets of data. Such a procedure is valid to obtain a radius of gyration from the small q region where the fit is reasonably good, although at large q, both curves deviate. The radius of gyration of the confined chains were obtained to be always smaller than the radius of gyration of the free chains in the equivalent bulk solution. The free chains in dilute solution yield an $S(q)$ that deviates from the $1/q^2$ Debye-like behavior due to excluded volume effects (yielding $q^{-1/\nu}$, where ν is the Flory exponent [55]).

The chains in the Vycor deviate due to conformational changes arising from confinement in the tubelike pores. These were interpreted in terms of the theory developed by Daoud and de Gennes [57] and Brochard and de Gennes [58]. Briefly, the theory takes into account four main effects that govern the behavior of chains confined in nonadsorbing cylindrical pores. These are the confinement of the chains by the cylinder walls, which squeezes the chains laterally; the intrachain excluded volume effect, which swells the chains and stretches them along the cylinder axis; the entropic elasticity of the chains, which limits this stretching; and the interchain interactions, which can also lead to segregation of the chains. Thus the polymer chains are stretched out into "cigars" along the tubes, which may

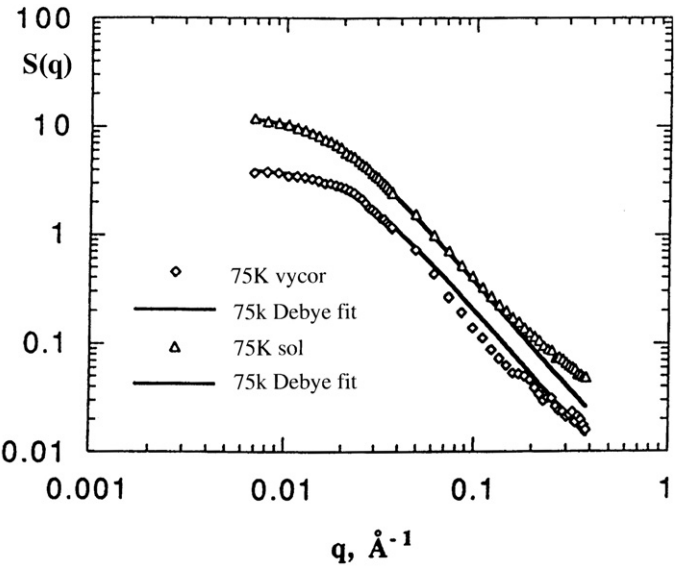

FIG. 15. The $S(q)$ in arbitrary units for 75K MW polystyrene chains in dilute solution (Δ) in toluene and in toluene in Vycor ($\diamond$). The solid lines are corresponding fits of the Debye function for ideal polymer chains (from Ref. [56]).

at high concentrations segregate from each other (strong confinement limit) or overlap in an entangled manner (moderate confinement regime) and thus no longer be stretched along the cylinder axis. In the latter cases $R_{gz}^2 = R_g^2/3$, where R_{gz} is the radius of gyration along the cylinder axis, and R_g is that of the chain in bulk solution. One then has the relation

$$R_{gv}^2 = D^2/8 + R_{gz}^2, \tag{67}$$

where R_{gv} is the radius of gyration as measured in the Vycor pore space, and D is the pore diameter of Vycor (known to be ~ 7 nm). Thus Eq. (67) provides a method for testing the relationship of the measured radii of gyration of the individual chains in Vycor and in the bulk solution, and was found to be satisfied extremely well for the different molecular weights studied. Thus one can conclude that the chains were in the conformation of ideal overlapping squeezed cigars. This conclusion was confirmed by also fitting the $S(q)$ of the individual chains in the regime $D < q^{-1} < R_g$ to a "cylindrical" Guinier model.

6.6 Conclusion

This chapter has discussed the experimental methods for studying small-angle scattering from porous media and a variety of theoretical models for understanding the observed $S(q)$. Over the years these types of experiments have yielded a great deal of insight into the morphology of various kinds of porous media and the area and roughness of the internal pore surfaces, including information about their fractal structure (if such structure is present). In turn, this information has yielded insights into the ways in which such porous media are formed. Small-angle scattering experiments have also been used to probe the behavior of fluids (including wetting of the internal pore surfaces and phase separation) and polymers inside porous media.

With the advent of third-generation synchrotron sources with brightnesses several orders of magnitude greater than achievable hitherto, one may expect qualitatively new kinds of information to be available from such experiments in the future. Thus, the fast kinetics of internal conformational changes (e.g., wetting, phase separation, or gelation) can be expected to be studied via SAXS experiments in real time, in which complete $S(q)$ spectra are obtained in milliseconds or less. In addition, the highly coherent radiation from such sources, which is incident on the sample, should make it possible to study equilibrium dynamics (e.g., of single molecules diffusing through the pore spaces, or of dynamic concentration fluctuations of phase-separating fluids inside porous media) using the techniques of photon intensity correlation spectroscopy (cf. Ref. [59] also Ref. [60]. For static SAXS measurements, the radiation may be coherent over most of the sample, and thus one is no longer measuring a statistical average of the density autocorrelation function as in Eq. (5), but the actual Fourier transform of the actual correlation function over the whole sample. Without going into details, this leads to at least the possibility of *direct* holographic *imaging* of the porous medium down to the nanometer length scale, rather than a measurement of $S(q)$. Similar advances may be expected when higher-brightness neutron sources are finally available.

Acknowledgments

I wish to acknowledge the collaborations and discussions I have enjoyed on much of this work with Mike Drake, Pierre Levitz, Min Lin, Paul Schmidt, Torsten Freltoft, Jorgen Kjems, Barbara Frisken, Dave Cannell, Andrea Liu, Gary Grest, Po-zen Wong, Zoran Djordjevic, Charles Glinka, Sushil Satija, Halina Stanley, Xiaolung Wu, P. Thiyagarajan, Jyotsna Lal, and Loic Auvray.

This work has been supported by the U.S. Department of Energy Basic Energy Sciences under contract numbers W-31-109-Eng-38 and W-7405-Eng-36.

Appendix A

Let us assume we have a bicontinuous medium where each of the phases (which we can characterize as "solid" and "pore," respectively) is characterized by uniform SLD contrasts η_1 and η_2, respectively (as in Eqs. [14]). We can write

$$S(q) = (\Delta\rho)^2 \int_v d\vec{r}\,' \int_v d\vec{r}\,' e^{i\vec{q}\cdot(\vec{r}\,'-\vec{r})}, \tag{A1}$$

where v indicates the volume enclosing *one* of the phases (e.g., solid). This is equivalent to Eq. [5] if one subtracts the scattering from a uniform SLD equal to that of the other phase throughout the sample volume and uses $(\eta_1 - \eta_2)^2 = \Delta\rho^2$.

Since the medium is isotropic, we can choose an arbitrary direction of $\vec{q}$ and call it the z axis. Then carrying out the z integration explicitly in Eq. (A1), we obtain

$$S(q) = \frac{(\Delta\rho)^2}{q^2} \iint dx\,dy \iint dx'\,dy' \sum_{ij} e^{iq[z_i(x',y') - z_j(x,y)]} p_i p_j, \tag{A2}$$

where $z_i(x_1, y)$ is the intersection of the ith sheet of the interface with the vertical (i.e., parallel to the z axis) line through the point (x, y), and $p_i = +1$ if one goes from *solid* to *pore* through the interface as z increases, and equal to -1 if one goes from *pore* to *solid*. Since, in general, these experiments are not carried out with perfectly coherent radiation and thus represent an average over many "coherence volumes" in the sample, we can make a statistical average over the expression in Eq. (A2). Now $z_i(x', y')$ can be written as $z_i(x, y) + [z_i(x', y') - z_i(x, y)]$, and we assume that these two components (perpendicular and parallel to q) fluctuate independently and that the expectation value of the latter on a single sheet of the interface depends only on the *relative* separation (x, y) of (x, y) and (x', y'). We can then average independently over all possible initial points (x, y), which we can call $(0, 0)$ for convenience. Denoting this average by $\langle\ \rangle_0$, we may write Eq. (A2) as

$$S(q) = \frac{A(\Delta\rho)^2}{q^2} \sum_{ij} p_i p_j \langle e^{iq[z_i(0,0) - z_j(0,0)]} \rangle \iint dX\,dY \langle e^{iq[z_i(X,Y) - z_i(0,0)]} \rangle_I, \tag{A3}$$

where A is the cross-sectional area of the sample, and the symbol $\langle\ \rangle_I$

denotes a statistical average over interfaces. In general, the integral over (X, Y) will have contributions only from those points on the interface laterally within a *persistence* length of the interface from $(0, 0)$. We write the integral over (X, Y) in Eq. (A3) as an average shape factor $F(q)$ for the interface. Then we have

$$S(q) = \frac{\Delta\rho^2}{q^2} AF(q) \sum_{ij} p_i p_j \langle e^{iq[z_i(0,0) - z_j(0,0)]} \rangle_0. \tag{A4}$$

Now the quantity $\langle e^{iq[z_i(0,0) - z_{i+1}(0,0)]} \rangle_0$, where $[z_i(0, 0) - z_{i+1}(0, 0)]$ is the distance between successive intersections of the (i)th and $(i + 1)$th interfaces with a line parallel to the z axis is equal to $f_p(q)$ or $f_s(q)$, depending on whether $i \to i + 1$ spans a "pore" phase or a "solid" phase and $f_p(q)$ and $f_s(q)$ are defined by the Fourier transforms

$$f_{p,s}(q) = \int_0^\infty dz\, e^{-iqz} f_{p,s}(z), \tag{A5}$$

where $f_p(z)$ and $f_s(z)$ are the (normalized) pore and solid chord distributions, respectively. Let us choose i as some particular interface (say solid–pore in the direction of z), and consider the sum over j as we include successive interfaces along the z axis. The first item will be the next pore–solid interface (with $p_j = -1$), the next will be the following solid–pore interface with $p_j = +1$, etc., and dropping the argument $(0, 0)$, which is implicit in the average, we have

$$\sum_{j>i} p_j \langle e^{iq(z_i - z_j)} \rangle = -\langle e^{-iq(z_{i+1} - z_i)_p} \rangle + \langle e^{-iq(z_{i+2} - z_{j+1})_s} \rangle \langle e^{-iq(z_{i+1} - z_i)_p} \rangle - \cdots \tag{A6}$$

where $(z_{i+1} - z_i)_p$ and $(z_{i+2} - z_{i+1})_s$ denote distances across pore and solid spaces, respectively, using the definitions of Eq. (A5), we can write

$$\begin{aligned} \sum_{j>i} p_j \langle e^{iq(z_i - z_j)} \rangle &= -f_p(q) + f_p(q) f_s(q) - f_p(q) f_s(q) f_p(q) + \cdots \\ &= -f_p(q)[1 - f_s(q)][1 + f_p(q) f_s(q) + f_p^2(q) f_s^2(q) + \cdots] \\ &= \frac{-f_p(q)[1 - f_s(q)]}{1 - f_p(q) f_s(q)}. \end{aligned} \tag{A7}$$

We now consider the sum over successive interfaces in the *negative* z direction, which yields simply the complex conjugate of the preceding expression:

$$\sum_{j<i} p_j \langle e^{iq(z_i - z_j)} \rangle = \frac{-f_p^*(q)[1 - f_s^*(q)]}{1 - f_p^*(q) f_s^*(q)}. \tag{A8}$$

Finally, we add the term $j = i$, which gives unity. A little reflection shows that if we had started with i at a pore–solid interface instead, we would have obtained the above results with $f_p(q)$ and $f_s(q)$ interchanged. Thus, finally,

$$\sum_{i,j} p_i p_j \langle e^{iq(z_i - z_j)} \rangle = \frac{N}{2}\left[\frac{2 - f_p(q) - f_s(q)}{1 - f_p(q) f_s(q)} + \text{c.c.} - 2\right]. \tag{A9}$$

Also if $\langle \ell_p \rangle$ and $\langle \ell_s \rangle$ are the expectation values of the chords through the pore and solid phases respectively, and L is the sample dimension along the direction of $\vec{q}$, we have

$$L = \frac{N}{2}[\langle \ell_p \rangle + \langle \ell_s \rangle], \tag{A10}$$

so by Eq. (A4), we get the result in Eq. (37) of the main text.

Appendix B

Here we sketch the proof [34] of the result given in Eq. (55) for a system with a hypothetical mass fractal dimension D and a different surface fractal dimension D_s (leaving aside the question of whether these can coexist at the same length scales).

Assuming a constant SLD contrast $\Delta\rho$ within the particles of the system, we have

$$S(q) = (\Delta\rho)^2 \int_V \int_V d\vec{r}\, d\vec{r}\,' e^{i\vec{q}\cdot(\vec{r} - \vec{r}\,')}, \tag{B1}$$

where V is the volume, which defines the object. We have the vector identity

$$i\vec{q} \int_V d\vec{r}\, e^{i\vec{q}\cdot\vec{r}} = \int_S d\vec{S} e^{i\vec{q}\cdot\vec{r}}, \tag{B2}$$

when S is the surface bounding volume V. Thus,

$$\int_V \int_V d\vec{r}\, d\vec{r}\,' e^{i\vec{q}\cdot(\vec{r} - \vec{r}\,')} = \frac{1}{q^2} \int_S \int_S (d\vec{S} \cdot d\vec{S}\,') e^{i\vec{q}\cdot(\vec{r} - \vec{r}\,')} \tag{B3}$$

$$= \frac{1}{q^2} \int_S \int_S dS\, dS' [\vec{n}(\vec{r}) \cdot \vec{n}'(\vec{r}\,')] e^{i\vec{q}\cdot(\vec{r} - \vec{r}\,')}, \tag{B4}$$

where $\vec{n}(\vec{r})$ is the unit vector normal to the surface S at $\vec{r}$. Let us assume the scaling form

$$[\vec{n}(\vec{r}) \cdot \vec{n}'(\vec{r}\,')] \sim |\vec{r} - \vec{r}\,'|^{-\chi}, \tag{B5}$$

where χ is an exponent to be determined. Then

$$S(q) = \frac{1}{q^2} \int_S \int_S dS\, dS' |\vec{r} - \vec{r}'|^{-\chi} e^{i\vec{q}\cdot(\vec{r}-\vec{r}')}. \tag{B6}$$

Since the integral depends only on $(\vec{r} - \vec{r}')$, one integral over S can be done, yielding a measure of the total (fractal) surface area. The other can be reduced to dimensionless form by substituting

$$R' = q|\vec{r} - \vec{r}'|.$$

Then,

$$S(q) \sim \frac{1}{q^2} q^{-D_s} q^{\chi} \left[\int_{S'} d^2R' \frac{1}{(R')^{\chi}} e^{iR' \cos\theta} \right], \tag{B7}$$

where θ is the angle between $\vec{q}$ and $(\vec{r} - \vec{r}')$, and we have used the fact that the fractal surface elemental area dS scales as $q^{D_s}\, dS$ under a length scale transformation $r' \to qr$. The last factor in square brackets in Eq. (B7) is independent of q, so that

$$S(q) \sim 1/q^{2D_s - \chi}. \tag{B8}$$

To obtain χ, consider a plane intersecting the object, the *linear* dimension of this intersection being R (see Fig. 16). Consider the surface that encloses this plane and the surface of the object that it intersects on one side of the plane — that is, the surfaces $(S_1 + S_2)$ in Fig. 16 — we have

$$\int_{S_1 + S_2} d\vec{S} = 0, \tag{B9}$$

or

$$\int_{S_1} d\vec{S} = -\int_{S_2} d\vec{S} \sim \vec{n}_p R^{D-1}, \tag{B10}$$

where $\vec{n}_p$ is the unit vector normal to the plane (surface S_2), and we have used the result that the area of intersection of a plane with an object of fractal dimension D is an object of fractal dimension $(D - 1)$ [22]. From Eq. (B10),

$$\int_{S_1} \int_{S_1} d\vec{S} \cdot d\vec{S}' = \int_{S_1} \int_{S_1} dS\, dS' \frac{1}{|r - \vec{r}'|^{\chi}} \sim R^{2D-2}. \tag{B11}$$

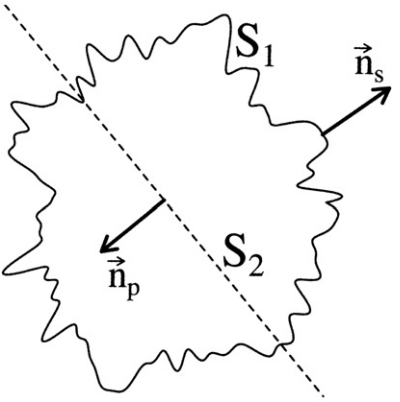

FIG. 16. Schematic of a fractal object intersected by a plane surface with cross-sectional area S_2, where S_1 represents the surface area of the object on one side of S_2, and $\vec{n}_p \vec{n}_s$ represents the normals to these respective surfaces.

Now consider length scale transformations $r \to \chi r$, $r' \to \alpha r'$. Then $dS \to \alpha^{D_s} dS$ and $dS' \to \alpha^{D_s} dS'$ so that the left-hand side of Eq. (B11) is multiplied by a factor $\alpha^{2D_s - \chi}$. The right side is multiplied by a factor α^{2D-2}. Thus,

$$\chi = 2D_s - 2D + 2, \tag{B12}$$

and hence by Eq. (B8),

$$S(q) \sim 1/q^{2D-D_s}. \tag{B13}$$

References

1. A. Guinier and D. C. Fournet, *Small-Angle Scattering of X-Rays* (Wiley, New York, 1955).
2. O. Glatter and O. Kratky, *Small-Angle X-Ray Scattering* (Academic Press, New York, 1982).
3. T. P. Russell, in *Handbook of Synchrotron Radiation*, Vol. 3 (G. Brown and D. E. Moncton, Eds.), North Holland, Amsterdam, 1991).
4. L. A. Feigin and D. I. Svergun, *Structure Analysis by Small Angle X-Ray and Neutron Scattering* (Plenum Press, New York, 1987).
5. G. E. Bacon, *Neutron Diffraction*, 3rd ed. (Clarendon Press, Oxford, 1975).
6. G. L. Squires, *Introduction to the Theory of Thermal Neutron Scattering* (Cambridge University Press, Cambridge, 1978).

7. F. Mezei, *Commun. Phys.* **1**, 81 (1976); F. Mezei and P. Dagleish, *Commun. Phys.* **2**, 41 (1977); O. Scharpf, *Physica B* **156–157**, 639 (1989); O. Scharpf, *Physica B* **174**, 514 (1991).
8. U. Bonse and M. Hart, *Z. Phys.* **189**, 151 (1966).
9. K. A. Hardman-Rhyne, K. G. Frase, and N. F. Berk, *Physica* **136 B&C**, 223 (1986).
10. G. Porod, in *Small-Angle X-Ray Scattering* (H. Brumberger, Ed., Proc. of Conf. held at Syracuse Univ., 1965, p. 1.
11. P. Debye, H. R. Anderson, and H. Brumberger, *J. Appl. Phys.* **28**, 679 (1957).
12. J. M. Drake, P. Levitz, and S. Sinha, *Mat. Res. Soc. Symp. Proc.* **73**, 305 (1986).
13. D. W. Schaefer, B. C. Bunker, and J. P. Wilcoxon, *Phys. Rev. Lett.* **58**, 284 (1987).
14. P. Wiltzius, F. S. Bates, S. B. Dierker, and G. Wignall, *Phys. Rev. A* **36**, 2991 (1987).
15. P. Levitz, G. Ehret, S. K. Sinha, and J. M. Drake, *J. Chem. Phys.* **95**, 6151 (1991).
16. J. Mering and D. Tchoubar, *J. Appl. Cryst.* **1**, 153 (1968); D. Tchoubar and J. Mering, *J. Appl. Cryst.* **2**, 128 (1969).
17. M. Y. Lin and S. K. Sinha, *Mat. Res. Soc. Symp. Proc.* **195**, 485 (1990).
18. N. F. Berk, *Phys. Rev. Lett.* **58**, 2718 (1987) and *Phys. Rev. A* **44**, 5069 (1991).
19. M. Teubner and R. Strey, *J. Chem. Phys.* **87**, 3195 (1987).
20. S. H. Chen, D. D. Lee, K. Kimishima, H. Jinnai, and T. Hashimoto, *Phys. Rev. E* **54**, 6526 (1996).
21. J.-C. Li and D. K. Ross, *J. Phys. Condens. Matter* **6**, 352 (1994).
22. B. B. Mandelbrodt, *The Fractal Geometry of Nature* (Freeman, New York, 1982).
23. S. K. Sinha, T. Freltoft, and J. Kjems, in *Kinetics of Aggregation and Gelation* (F. Family and D. Landau, Eds., North-Holland, Amsterdam, 1984), pp. 87–90.
24. T. Freltoft, J. K. Kjems, and S. K. Sinha, *Phys. Rev. B* **33**, 269 (1986).
25. H. D. Bale and P. W. Schmidt, *Phys. Rev. Lett.* **53**, 596 (1984).
26. B. J. Frisken, F. Ferri, and D. S. Cannell, *Phys. Rev. Lett.* **66**, 2754 (1991).
27. G. Vacca, W. B. Dozier, A. Ellison, J. M. Drake, and S. K. Sinha (1994, unpublished).
28. P. W. Schmidt, *J. Appl. Cryst.* **15**, 567 (1982).
29. P.-z. Wong, *Phys. Today* **41**(12), 24 (1988) and references therein.
30. P.-z. Wong and A. Bray, *J. Appl. Cryst.* **21**, 786 (1988) and *Phys. Rev. B* **37**, 7751 (1988).
31. S. K. Sinha, E. B. Sirota, S. Garoff, and H. B. Stanley, *Phys. Rev. B* **38**, 2297 (1988).
32. D. W. Schaefer, J. E. Martin, P. Wiltzius, and D. S. Cannell, *Phys. Rev. Lett.* **52**, 2371 (1984); A. J. Hurd, D. W. Schaefer, D. M. Smith, S. B. Ross, A. Lemauté, and S. Spooner, *Phys. Rev. B* **39**, 9742 (1989).

33. P.-z. Wong, *Phys. Rev. B* **32**, 7417 (1985).
34. R. C. Ball and S. K. Sinha (1986, unpublished); S. K. Sinha, *Phys. D* **38**, 310 (1989).
35. P.-z. Wong and Q.-z. Cao, *Phys. Rev. B* **45**, 7627 (1992).
36. D. Avnir, D. Farin, and P. Peiffer, *J. Chem. Phys.* **79**, 3566 (1983) and *Nature Lond.* **308**, 261 (1984).
37. J. M. Drake, P. Levitz, and J. Klafter, *Israel J. Chem.* **31**, 135 (1991).
38. K. B. Gavrilov, A. G. Okiener, and Y. I. Aristov, *Reaction Kim Catal. Lett.* **58**, 39 (1996).
39. S. K. Sinha and Z. Djordjevic (1988, unpublished).
40. F. Brochard and P. G. de Gennes, *J. Phys. Lett.* **44**, L-785 (1983).
41. D. Andelman and J. F. Joanny, in *Scaling Phenomena in Disordered Systems* (R. Rynn and A. Skjeltarp, Eds., Plenum, New York, 1985), p. 163.
42. W. I. Goldberg, in *Scaling Phenomena in Disordered Systems* (R. Pynn and A. Skjeltorp, Eds., Plenum, New York, 1985), p. 151.
43. M. C. Goh, W. J. Goldburg, and C. M. Knobler, *Phys. Rev. Lett.* **58**, 1008 (1987).
44. M. Y. Lin, S. K. Sinha, J. M. Drake, X. L. Wu, P. Thiyagarajan, and H. B. Stanley, *Phys. Rev. Lett.* **72**, 2207 (1994).
45. S. B. Dierker and P. Wiltzius, *Phys. Rev. Lett.* **58**, 1865 (1987); ibid. **62**, 804 (1989); ibid. **66**, 1185 (1991).
46. B. J. Frisken and D. S. Cannell, *Phys. Rev. Lett.* **69**, 632 (1992).
47. B. J. Frisken, D. S. Cannell, M. Y. Lin, and S. K. Sinha, *Phys. Rev. E* **51**, 5866 (1995).
48. A. J. Liu and G. Grest, *Phys. Rev. A* **44**, R7894 (1991); L. Monette, A. J. Liu, and G. Grest, *Phys. Rev. A* **46**, 7614 (1992); A. J. Liu, *et al.*, *Phys. Rev. Lett.* **65**, 1897 (1990).
49. J. V. Maher, W. I. Goldberg, D. W. Pohl, and M. Lenz, *Phys. Rev. Lett.* **53**, 60 (1984).
50. P.-z. Wong, J. W. Cable, and P. Dimon, *J. Appl. Phys.* **55**, 2377 (1984).
51. J.-C. Li, D. K. Ross, and M. J. Benham, *J. Appl. Cryst.* **24**, 794 (1991).
52. J.-C. Li, L. D. Howe, M. J. Benham, D. K. Ross, J. P. A. Fairclough, and K. Ibel, *Phys. Rev. B* **49**, 5911 (1994).
53. D. Stauffer, *Introduction to Percolation Theory* (Taylor & Francis, London and Philadelphia, 1985).
54. M. Y. Lin, S. K. Sinha, J. S. Huang, B. Abeles, J. W. Johnson, J. M. Drake, and C. J. Glinka, *Mat. Res. Soc. Symp. Proc.* **166**, 449 (1990).
55. P. G. de Gennes, *Scaling Concepts in Polymer Physics* (Cornell University Press, Ithaca, NY, 1985), p. 95.
56. J. Lal, S. K. Sinha, and L. Auvray, *J. Phys. II* **7**, 1597 (1997).
57. M. Daoud and P. G. de Gennes, *J. Phys.* **38**, 85 (1977).
58. F. Brochard and P. G. de Gennes, *J. Phys.* **40**, L-399 (1979).

59. G. Grübel, J. Als-Nielsen, D. Abernathy, G. Vignaud, S. Brauer, G. B. Stephenson, S. G. J. Mochrie, M. Sutton, I. K. Robinson, R. Fleming, R. Pindak, S. Dierker, and J. F. Legrand, *ESRF Newsletter* **20**, 14–15 (1994); M. Sutton, S. G. J. Mochrie, T. Greytak, S. E. Nagler, L. E. Berman, G. A. Held, and G. B. Stephenson, *Nature Lond.* **352**, 608 (1991).

60. S. B. Dierker, R. Pindak, R. M. Fleming, I. K. Robinson, L. Berman, *Phys. Rev. Lett.* **75**, 449 (1995); T. Thurn-Albrecht, W. Steffen, A. Patkowski, G. Meier, E. W. Fischer, G. Grubel, D. L. Abernathy, *Phys. Rev. Lett.* **77**, 5437 (1996).

7. LIGHT SCATTERING AND OTHER OPTICAL METHODS

Kenneth H. Langley
Department of Physics and Astronomy
University of Massachusetts
Amherst, Massachusetts

Iwao Teraoka
Department of Chemical Engineering, Chemistry, and Materials Science
Polytechnic University
Brooklyn, New York

7.1 Introduction

Initially it would seem that the application of optical methods or light scattering to the study of porous materials is nearly impossible. With a few important exceptions (such as optically transparent gels) porous materials generally appear quite opaque. This results either from direct absorption or, in a more transparent material, from the high concentration of discontinuities in the index of refraction at the pore walls. Since these discontinuities are abrupt over distances comparable to the wavelength of visible light, incident light is scattered very strongly and the propagation of a well-defined beam in the material is hopeless. Despite these difficulties, a number of studies employing various optical techniques have been carried out in porous materials in recent years. Generally these fall into two categories:

1. If the matrix material is transparent and uniform in index of refraction, and the pore spaces can be filled with a fluid having an index of refraction that closely matches that of the matrix material, the porous material is rendered transparent. So-called "index matching" removes the discontinuities at the pore–matrix boundaries to such an extent that the effects of multiple scattering and attenuation can be essentially ignored. Conventional imaging is employed and the detected light is considered as affected only by single scattering. The most common example of this is the study of macromolecular diffusion in optically transparent polymer gels in which the fluid component of the gel (or solvent) is chosen to match the index of the polymer. A second example is the measurement of diffusion in porous glasses.

EXPERIMENTAL METHODS IN THE PHYSICAL SCIENCES
Vol. 35
ISBN 0-12-475982-3

ISSN 1079-4042/99 $30.00

2. In complete contrast to the first category, in systems that scatter light strongly, the propagation of light can be described by a diffusion approximation. The key idea is that light that reaches the detector has been scattered within the medium so many times that the phases of the scattered fields have been completely randomized and only the intensity of the light reaching the detector must be considered. An equivalent description is that the path of each scattered photon can be considered to be a random walk through the medium. The statistics of these random walks is well understood and can be used in the analysis of the scattered light.

Dynamic light scattering (DLS), fluorescence recovery after photobleaching (FRAP), forced Rayleigh scattering (FRS), and interferometric methods belong to the first category. Diffusing-wave spectroscopy (DWS) belongs to the second category, is relatively new to this field and will be discussed in Section 7.5. The distinguishing characteristics of each method are described briefly next; details are explained in the later sections of this chapter.

DLS has been the most useful optical technique to investigate what is occurring in a system of interest contained in the cavities of a porous medium. DLS has been applied to studies of various diffusion processes of polymer molecules in the interior of a porous medium, phase transitions in a confining geometry, and dynamic modes of a nonrigid porous medium itself. The diffusion coefficient obtained is the isotropic mean. The advantages of DLS include: (1) DLS can selectively pick up a signal from the system in the pore space, leaving signal components from the solid phase of the porous medium in the background; (2) there is no need to chemically modify the molecules or choose labeled species; (3) the system is not exposed to an external field that may cause an unintended change to the system such as a temperature increase; and (4) DLS enables measurement within a small volume inside a porous medium. Furthermore, DLS reveals the tortuosity of a given porous medium, a measure of resistivity for diffusional transport of small molecules through the medium.

FRAP is a method of measuring the diffusion coefficient of fluorescent molecules in reasonably transparent media, and hence its use has been limited primarily to studies of the movement of macromolecules or particles in polymers, polymer solutions or gels, and biological materials rather than in rigid porous materials, which tend to be more opaque. The method generally requires direct imaging of the scattering volume (in common with DLS) or at least direct reception, without scattering, of the fluorescent light. The diffusion modes detected are limited to those in the plane of focus within the sample of interest. Improvements such as spatial Fourier analysis,

modulation detection, and holographic pattern photobleaching have enabled the use of the method even in somewhat turbid materials.

FRS, also called holographic grating relaxation spectroscopy, is a powerful tool in the measurement of diffusive dynamics of condensed phases using dye-molecules or dye-labeled molecules as a probe. The term FRS is due to the fact that the light is scattered by the classical Rayleigh mechanism, but the intensity is greatly enhanced by writing or "forcing" the modulation pattern. FRS has been applied to study of dye diffusion in a swollen cross-linked polymer gel and diffusion of dye-labeled polymer chains in concentrated solutions and melts. More recently, FRS has been applied to the study of probe diffusion in polyacrylamide gels and diffusion of dye molecules in Vycor porous glass. FRS is sensitive only to the diffusion component normal to the modulation pattern.

Interferometric methods utilize the difference in the refractive index between a sample and a reference to create the fringe pattern. Analysis of the distortion in the image provides information on the diffusivity of solutes in the porous matrix. The methods have been used to study of the partitioning of a solute with a porous medium and diffusion over the interface between regions of different solute concentrations.

In the following discussion, each section opens with an introduction to the basic theory and practice of a particular technique and is followed by a few examples of what has been learned through application of the method. The examples are intended to be illustrative and are by no means exhaustive.

7.2 Dynamic Light Scattering

7.2.1 Discussion of the Method

As the name suggests, dynamic light scattering makes use of dynamics or fluctuations in the intensity of scattered light to derive information about physical processes occurring inside a scattering medium. In principle, any process that causes the intensity of the scattered light to vary with time is a possible candidate to be studied by DLS. In practice, however, diffusion or some other structural relaxation modes are usually studied.

The method has been extensively reviewed [1–4], but for the sake of completeness it is worthwhile to recall here essential features. Light from a laser is brought to a focus in a small region (typically 100 μm in diameter) at the center of a glass cell (see Fig. 1). Light scattered from a small region (scattering volume) of the sample into a small range of angles near the scattering angle θ falls on a photodetector operated in the photon-counting mode. The scattering volume is an intersection between the path of the

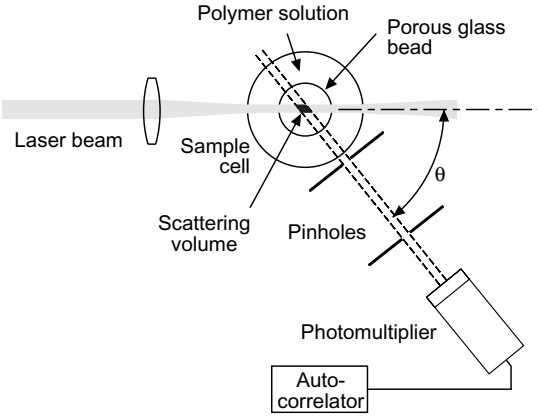

FIG. 1. Configuration of a dynamic light scattering system for study of diffusion processes in the interior of a porous silica bead.

incident beam and the solid angle determined by the pinholes or the two slits.

The detected light intensity (photon count rate) fluctuates dramatically as the electric field of the light wave scattered by each of the scattering particles fluctuates relative to the electric field of the light wave scattered by other particles. The fluctuations are due to the Brownian motion or other modes of motion of the particles. Pulses from the photodetector are processed by a digital correlator which computes the autocorrelation function of the intensity of the scattered light. In this homodyne detection configuration, it can be shown [3] that the autocorrelation function $g_{\mathrm{HO}}(t)$, after normalization by its long time limit, is related to the normalized electric-field autocorrelation function $g_{\mathrm{E}}(t)$ by

$$g_{\mathrm{HO}}(t) = 1 + b_{\mathrm{HO}}|g_{\mathrm{E}}(t)|^2, \tag{1}$$

where t is time, and b_{HO} is a constant of the apparatus, called a coherence factor, related to the coherence of the scattered light over the aperture of the detector. If the light scattering is by identical particles making independent diffusional motions, then $g_{\mathrm{E}}(t)$ is a decaying exponential:

$$|g_{\mathrm{E}}(t)| = \exp(-\Gamma t), \tag{2}$$

with the decay rate Γ given by $\Gamma = Dq^2$, where D is the diffusion coefficient of the particles, and q is the scattering wave vector of the light. The latter is related to the scattering angle θ by $q = (4\pi n/\lambda)\sin(\theta/2)$, where n is the index of refraction of the solvent, and λ is the vacuum wavelength of the light. Equivalently, if the decay rate of $|g_{\mathrm{E}}(t)|$ is proportional to q^2 in measure-

ments at different scattering angles, then it can be said that the motion of each particle follows the diffusion equation. An alternative way to think of this situation is to consider the scattered light as selecting the Fourier component of the thermal particle density fluctuations corresponding to the wave vector **q**. The component experiences an almost negligible shift in the wavelength when scattered (Doppler shift). This is why DLS is also called quasi-elastic light scattering.

The hydrodynamic radius of a molecule or a particle in suspension R_H is defined as the radius of a sphere that has the same diffusion coefficient in a given solvent. It is calculated from the Stokes–Einstein law:

$$D = \frac{k_B T}{6\pi\eta R_H}, \tag{3}$$

where k_B is the Boltzmann constant, T the temperature, and η the solvent viscosity. When the scatterers are not rigid, rotational motions contribute to the autocorrelation function. For the decay of $g_E(t)$ to be solely due to the center of mass motion, the scattering angle must be sufficiently low; that is, $qR_H \ll 1$.

The single exponential decay in Eq. (2) is observed only for a system of identical scatterers with negligible interactions between them. Otherwise, the decay deviates from the single exponential and is expressed, in general, as a superposition of exponential decays with different decay rates:

$$|g_E(t)| = \int_0^\infty \exp(-\Gamma t) G(\Gamma)\, d\Gamma. \tag{4}$$

Two analysis methods are commonly used to estimate the distribution function $G(\Gamma)$. One is a cumulant expansion method in which a polynomial fit of $\ln|g_E(t)|$ (often second order) is used to calculate the average, variance, and higher-order cumulants of Γ. The other is a direct deconvolution of $|g_E(t)|$ with additional conditions on the shape of $G(\Gamma)$. Computer program packages as represented by CONTIN [5] carry out the inverse-Laplace transform.

7.2.2 Application of DLS to Diffusion of Polymers in Porous Silica

DLS was used to study various diffusion processes [6–14] of polymer molecules in a solution filling controlled pore glass [15] that has a uniform, bicontinuous network structure of the pore space. The solid phase of the porous glass is amorphous silica. A typical configuration around the sample cell is shown in Fig. 1. A porous silica bead immersed in a solution of the polymer is fixed in a sample cell. A laser beam is focused inside or near the silica bead. The scattering volume determined by the two pinholes is entirely

contained in the silica bead and consists of three components: silica, solvent, and polymer. To minimize scattering by the silica, an organic solvent with a refractive index close to that of silica (1.457) is selected. The porous silica bead is then almost invisible, and the polymer is the only species that has an index of refraction different from the rest. Table I is a partial list of solvents that can be made isorefractive with silica. Depending on minority components in the silica phase, the refractive index of the silica can vary slightly. Fine-tuning of the index match can be accomplished by temperature adjustment.

Even at the best index match, however, spatial fluctuations in the refractive index of the solid phase cause most of the scattering, much stronger than the scattering from molecules of interest in the pore channels. The static scattering by the solid phase creates an irregular speckle pattern with spatially alternating bright and dark spots. Scattered light can be collected within one of the bright spots. A darker region can be selected as well; the decaying component of the autocorrelation function will be the same except that a longer accumulation time is required.

The light scattered by a volume in the interior of the porous medium has two components: elastic, static scattering by the immobile silica phase, and quasielastic, fluctuating scattering by diffusants moving in the pore space. The wavefronts of the two components are well matched in phase. Therefore the first component serves as a local oscillator in this optical mixing (heterodyne) configuration. Bishop *et al.* [6, 7] applied the theory of heterodyne detection to derive the intensity autocorrelation function $g_{HE}(t)$, normalized by its long time limit, as

$$g_{HE}(t) = 1 + b_{HE}|g_E(t)| + O(|g_E(t)|^2), \tag{5}$$

where $b_{HE}(\ll 1)$ is the coherence factor, and $|g_E(t)|$ is due to the scatterers in the pore channels. Later a liquid-filled porous medium was treated more generally as a nonergodic medium. See Section 7.2.3. [16, 17].

TABLE I. Typical Solvents Isorefractive with Silica [77]

Solvent	n_D^{20}	Boiling point (°C)
Cyclohexanone	1.4500	155
Carbon tetrachloride	1.4600	76–77
Cycloheptanone	1.4610	179
Fluorobenzene	1.4650	85
Trans-decahydronaphthalene	1.4690	185
N-methyl pyrrolidone	1.4700	202
2-Fluorotoluene	1.4730	113–114

The porous medium has a characteristic wavenumber of $\sim 1/R_p$, where R_p is the average pore radius. For $|g_E(t)|$ to represent macroscopic diffusion of polymer in the porous medium, another condition $qR_p \ll 1$ must be satisfied in addition to $qR_H \ll 1$. Bishop *et al.* [7] studied diffusion of polystyrene in pieces of controlled pore glass with different pore radii to see how $|g_E(t)|$ depends on qR_p. At low scattering angles—for example, at $qR_p = 0.35$ (see Fig. 2b), $|g_E(t)|$ decayed as a single exponential with a diffusion coefficient D_I smaller than the diffusion coefficient D_E of the same polymer in the exterior solution (see Fig. 2a). The D_I represents diffusion over a distance that smears out pore structure details. They also verified that, in the range of $qR_p \lesssim 1$, the decay rate in $|g_E(t)|$ is proportional to q^2. At $qR_p = 1.85$, the decay showed a deviation from a single exponential (Fig. 2c). At $qR_p = 5.3$, the initial decay rate was close to $D_E q^2$, signifying that DLS explored diffusional motion of a polystyrene molecule within a single pore channel before the molecule senses the presence of pore walls (Fig. 2d).

Bishop *et al.* [7] also explored the dependence of D_I on the dimension of polystyrene fractions for $R_H/R_p \lesssim 0.2$. For all combinations of R_H and R_p studied, D_I/D_E decreased as R_H/R_p increased. In the limit of $R_H/R_p \to 0$, D_I/D_E approached a value smaller than unity, a result ascribed to tortuosity of the porous medium. The limiting value χ_0 is the intrinsic conductivity (reciprocal of the tortuosity) of the medium and depends on R_p and the structure of the medium. They showed that the data points lie on a master curve when $D_I/(\chi_0 D_E)$ was plotted as a function of R_H/R_p. Use of the formula

$$D_I/D_E = \chi_0 F_d^{-1}(R_H/R_p), \tag{6}$$

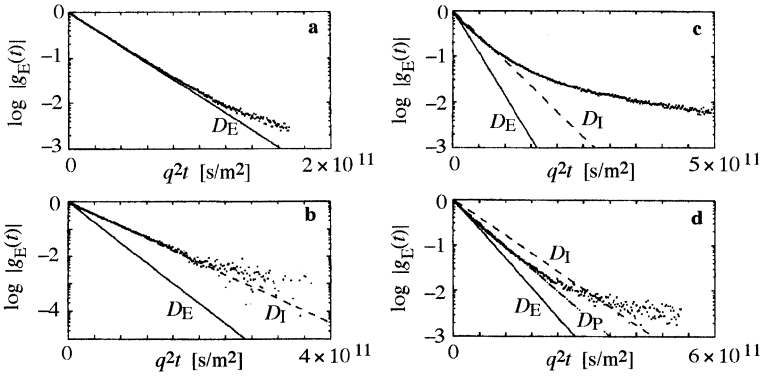

FIG. 2. Normalized electric-field autocorrelation function $|g_E(t)|$ plotted as a function of q^2t, measured in the exterior solution (a) and in the porous silica bead at $qR_p = 0.35$ (b), 1.85 (c), and 5.3 (d). Adapted with permission from M. T. Bishop *et al.*, *Macromolecules* **22**, 1220. Copyright 1989 American Chemical Society.

which separates a geometrical factor χ_0 and the hydrodynamic drag [18, 19] F_d^{-1} for a molecule of R_H in a single, straight pore channel of radius R_p was thus justified.

The range of R_H/R_p was subsequently extended to 1.4 [8, 9]. Figure 3 is a plot of D_I as a function of the molecular weight M of polystyrene fraction for porous silica beads of $R_p = 27.5$ and 7.5 nm. Toward the high end of the molecular weight for each bead — that is, in the strong confinement, $R_H/R_p \gtrsim 1$ — D_I decreased sharply as M increased. The entropy barrier model [20, 21] that ascribes the decrease to the presence of bottlenecks of the pore space in the network-structured porous medium was found to explain the dependence.

The examples of DLS studies already shown are in dilute solution conditions, or more precisely, the extrapolation to zero concentration. At finite concentrations, interactions between solute molecule cause the diffusion coefficient to be different. The diffusion mode explored by DLS for solutions at nonzero concentrations is called mutual diffusion, as DLS detects fluctuations in the total solute concentrations at a given wave vector. It is often the case that repulsive interaction between solvated molecules increases the mutual diffusion coefficient D_m at higher concentrations. At concentrations higher than the overlap concentration (semidilute regime), monomer density fluctuates on a length scale shorter than the chain dimension. The diffusion detected by DLS is called the cooperative (or

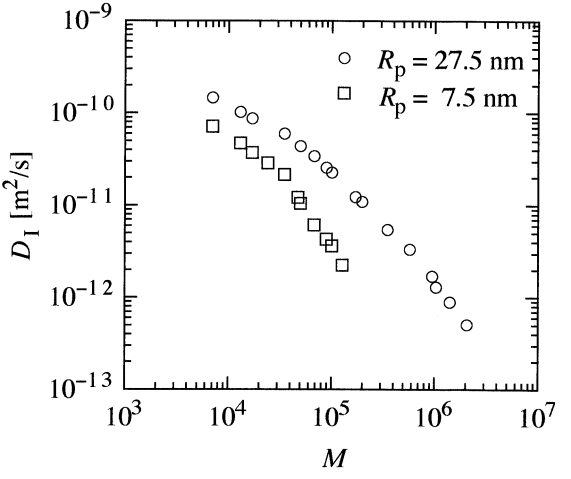

FIG. 3. Diffusion coefficient D_I of polystyrene in a porous silica bead for different molecular weights M of the polymer. Porous silica beads of two different pore radii $R_p = 7.5$ and 25 nm were used. Adapted with permission from Y. Guo *et al.*, *Macromolecules* **23**, 2022. Copyright 1990 American Chemical Society.

collective) diffusion, and its coefficient is denoted by D_c. Past studies show that D_c depends little on the molecular weight and rather is determined by the total monomer concentration of the solution. The apparent hydrodynamic radius calculated from Eq. (3) gives the dynamic correlation length ξ of the fluctuations:

$$D_c = \frac{k_B T}{6\pi\eta\xi}. \tag{7}$$

Applying DLS to a porous silica bead immersed in a semidilute solution of polystyrene, Teraoka *et al.* [14] found that D_m increased in the porous medium for each of the three fractions of the polymer (see Fig. 4) more rapidly than in the surrounding solution. The arrows indicate the overlap concentrations for the three fractions. A large difference in D_m for polymer fractions with different molecular weights at low concentrations almost disappeared when the exterior concentration became semidilute. This observation was explained as a change in the partitioning of polymer molecules with the porous medium. At low concentrations, each polymer chain is partitioned independently according to the size exclusion principle. At concentrations higher than the overlap concentration, however, the high osmotic pressure of the polymer solution forces the chains to migrate into the pores at a proportion much higher than at low concentrations. Thus as

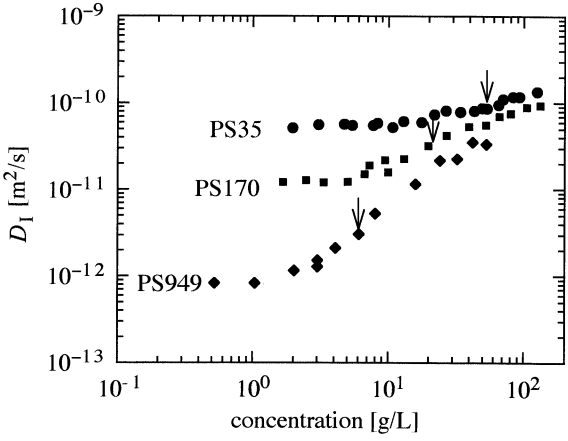

FIG. 4. Diffusion coefficient D_I of polystyrene (mutual diffusion) in a porous silica bead of $R_p = 25$ nm plotted as a function of polystyrene concentration in the surrounding solution. The arrows in the figure indicate the overlap concentrations of the three polystyrene fractions. Reprinted with permission from Teraoka *et al.*, *Macromolecules* **26**, 287. Copyright 1993 American Chemical Society.

the surrounding solution becomes semidilute, the solution in the pore channels also becomes semidilute. With the transition in the partitioning, concentration fluctuations in the pore shows a crossover. Slow macroscopic diffusion of long chains hindered by the pore tortuosity gives way to concentration fluctuations with a length scale much shorter than R_p.

7.2.3 Application of DLS to the Dynamics of Gels

A chemical gel that consists of crosslinked polymer chains is a type of porous medium. Unlike solid porous materials such as silica gels, the polymeric gel usually exists in a liquid. Depending on the interaction between the solvent and the polymer, the gel is either swollen or shrunken. The interaction can be manipulated by changing temperature, solvent composition, and, in some gels, pH. When swollen, the volume fraction of the polymer network is as small as 0.001, and the network consists of a sparsely jointed thin thread locally fluctuating around the equilibrium position. This mode of motion can be considered as overdamped phonons.

DLS has been vital to investigate the dynamics of the swollen gels at equilibrium and the statics and kinetics of the volume phase transition (between swollen and shrunken states). The technique has also been extensively used to study motions of large molecules impregnated into the gel. A brief review of applications of DLS to gels is given in the following.

According to Tanaka *et al.* [22], the electric-field autocorrelation function of light scattered by the gel matrix is given as

$$|g_{\mathrm{E}}(t)| \propto \left[\frac{\partial n^2}{\partial \ln(1-\phi)}\right]^2 \frac{k_{\mathrm{B}}T}{K+4/3\mu}\exp(-Dq^2t), \tag{8}$$

with a collective diffusion coefficient D given by $D = (K + 4/3\mu)/f$, where n is the refractive index of a whole gel, $1 - \phi$ is the volume fraction of the gel matrix, K and μ are the bulk and shear moduli ($K + 4/3\mu$ is the longitudinal modulus), and f is the friction coefficient. The collective diffusion is caused by local concentration fluctuations of the matrix. In a UCST-type gel (swollen at temperatures higher than a critical temperature T_s), the longitudinal modulus depends on the temperature T as

$$K + \tfrac{4}{3}\mu \propto T - T_s. \tag{9}$$

Figure 5 shows the diffusion coefficient D and the intensity I of the light scattered at 90° for 2.5% polyacrylamide gel in water, plotted as a function of T [22]. As T approaches T_s from above, I diverges, and D approaches zero. Equation (9) was found to hold except near T_s.

Later Tanaka *et al.* [23] used DLS to study critical dynamics of volume phase transition in an isopropylacrylamide gel in water. This gel has an LCST-type phase diagram. Figure 6 is a plot of the collective diffusion

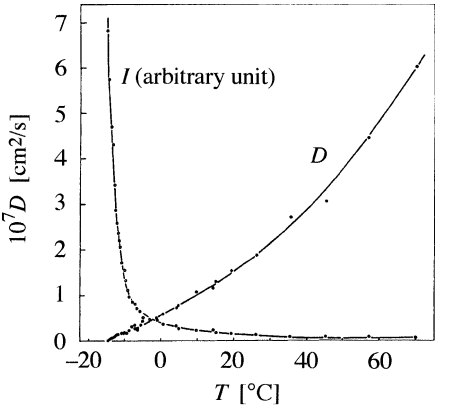

FIG. 5. Intensity I and the diffusion coefficient D of collective diffusion in a 2.5% polyacrylamide gel measured at temperatures above the volume phase transition temperature. Adapted with permission from T. Tanaka *et al.*, *Phys. Rev. Lett.* **38**, 771. Copyright 1977 American Physical Society.

coefficient obtained from the decay rate in $|g_E(t)|$. The critical slowing down is evident. The diffusion coefficient agreed with the one estimated from the rate of change in the radius of the spherical gel, indicating that the collective diffusion coefficient dictates also the motion of the network during the volume change.

Gels are typical nonergodic media — the time averages of the scattering intensity and its autocorrelation function measured at a specific solid angle of scattering are not identical to their ensemble averages over all possible

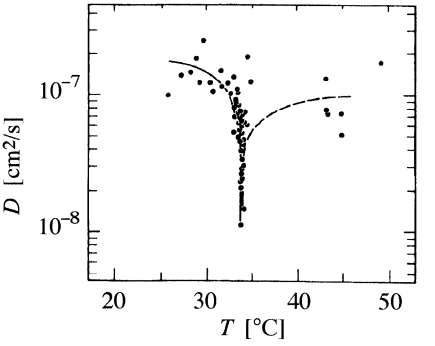

FIG. 6. Collective diffusion coefficient D of poly(isopropylacrylamide) gel determined from DLS measurements. Reproduced with permission from T. Tanaka *et al.*, *Phys. Rev. Lett.* **55**, 2455. Copyright 1985 American Physical Society.

configurations. Joosten *et al.* [16, 17] applied general discussion of light scattering from nonergodic media, developed by Pusey and van Megen [24], to the scattering from gels. They decomposed $g_E(t)$ into a fluctuating component that arises from concentration fluctuations of the gel network and a constant component due to macroscopic inhomogeneities of the network. The latter serves as a local oscillator in this heterodyne configuration. The apparent diffusion coefficient D_A, obtained from the initial decay rate of the total scattering intensity I by regarding it as purely homodyne, is related to the diffusion coefficient D_N, to be obtained from the initial decay rate in the autocorrelation function of the fluctuating component I_F by

$$D_N/D_A = 2 - \langle I_F \rangle_T / \langle I \rangle_T, \tag{10}$$

where $\langle \cdot \rangle_T$ denotes the time average. The ratio ranges between 1 (pure homodyne) and 2 (heterodyne limit).

Shibayama *et al.* [25] used the preceding formulation to analyze the light scattering from different speckles in a poly(isopropylacrylamide-*co*-acrylic acid) (NIPA/AAc) gel. Figure 7 shows spatial fluctuations of $\langle I \rangle_T$, measured at different locations in a gel sample prepared with different acrylic acid (AAc) contents. Apparently, the polyelectrolyte component suppresses the inhomogeneity of the gel. To apply Eq. (10), they rewrote it as

$$\frac{\langle I \rangle_T}{D_A} = \frac{2}{D_N} \langle I \rangle_T - \frac{\langle I_F \rangle_T}{D_N}. \tag{11}$$

Figure 8 shows D_A as a function of $\langle I \rangle_T$, and the inset is a plot of $\langle I \rangle_T / D_A$

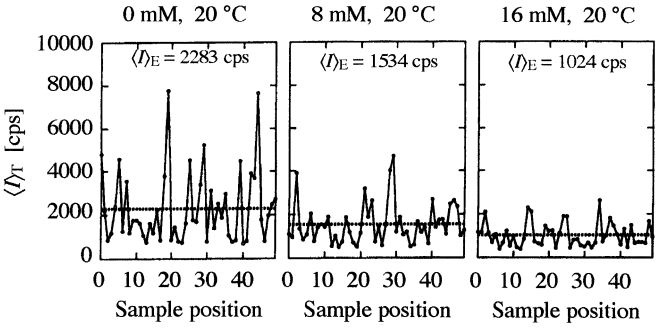

FIG. 7. Spatial fluctuations of the time-average scattering intensity $\langle I \rangle_T$ measured at different positions in a NIPA/Acc gel sample prepared with different acrylic acid contents (indicated above each plot). Reprinted with permission from M. Shibayama *et al.*, *Macromolecules* **29**, 6535. Copyright 1996 American Chemical Society.

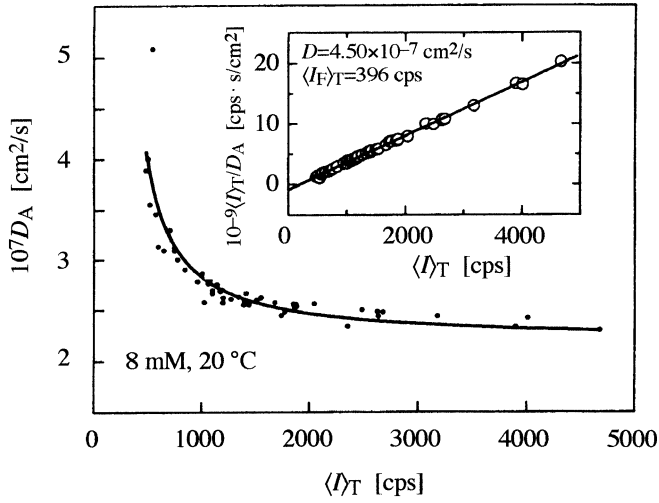

FIG. 8. Apparent diffusion coefficient D_A, obtained from the analysis of the scattering intensity, as a function of $\langle I\rangle_T$. The inset is a plot of $\langle I\rangle_T/D_A$ as a function of $\langle I\rangle_T$. Reprinted with permission from M. Shibayama *et al.*, *Macromolecules* **29**, 6535. Copyright 1996 American Chemical Society.

as a function of $\langle I\rangle_T$. The linearity of the latter indicates that the formulation by Joosten *et al.* correctly describes the nonergodic nature of the gel. From the slope and the intercept, D_N and $\langle I_F\rangle_T$ can be evaluated, as shown in the figure.

Diffusion of probe polymers in a network of polymeric gel has been studied extensively by applying DLS to the gel immersed in an index-matching solvent. The swollen gels include a crosslinked polydimethylsiloxane (PDMS) gel in tetrahydrofuran [26] and a crosslinked poly(vinyl methyl ether) gel in toluene [27]. The dependence of the tracer diffusion coefficient on the matrix concentration and the probe molecular weight was analyzed using the reptation model. In these studies, the light intensity autocorrelation functions were not analyzed in the view of nonergodicity.

7.2.4 Application of DLS to Critical Phenomena in a Porous Medium

Typical DLS studies of critical phenomena in porous media include liquid–vapor phase separation [28] and phase separation of binary liquid mixtures. Most of the concern has been directed toward the effects of the confinement on the phase diagram, and the appearance of different modes of compositional fluctuations. Here we discuss some of the results observed for confined binary mixtures.

In binary liquid critical mixtures in confining geometry, the correlation length ξ competes with the pore radius R_p. When $\xi < R_p$, preferential wetting by one of the components dictates the state of the fluid. When $\xi > R_p$, in contrast, the pore geometry and surface chemistry apply a quenched random field (pinning) to the fluid that tries to separate into domains larger than the pore size. The latter nature has been formulated in the random-field Ising model [29]. DLS takes advantage of its unique capability to measure ξ even when most of the scattering comes from the solid phase of the porous medium, as explained in Section 7.2.2.

Dierker and Wiltzius [30] applied DLS to critical dynamics of a binary mixture (lutidine and water) in porous Vycor with a pore diameter of 6 nm. The fluid's LCST was lower in Vycor compared with the bulk counterpart. They analyzed $|g_E(t)|$ as a sum of nonactivated and activated relaxations and found that the activated relaxation is explained in the random-field Ising model [29].

Aliev *et al.* [31] studied critical dynamics of a carbon disulfide–nitromethane mixture in porous silica of pore diameter 100 nm. They took advantage of the bulk critical mixture (60.1% of carbon disulfide by volume) being nearly isorefractive with silica, whereas the two constituent liquids have a greatly different indices. The UCST in the pore was lower than that of the bulk T_c. The DLS relaxation time measured at scattering angles of 15 and 90° showed critical slowing down as T approaches T_c from either side. A crossover from diffusional relaxation at large scattering angles to q-independent relaxation at low angles was also observed. The latter was explained as diffusional relaxation in a finite-size well [31].

7.3 Fluorescence Recovery after Photobleaching

7.3.1 Discussion of the Method

Photobleach recovery techniques have evolved considerably since the original presentation by Poo and Cone [32] and Axelrod *et al.* [33], but the basic idea remains the same. A small patch of sample containing naturally fluorescent molecules (e.g., vitamin A) or dye (e.g., dansylchloride)-labeled diffusant particles is illuminated by a low-intensity laser beam and the fluorescence signal is monitored by a detector. The laser is then switched briefly to an intensity sufficiently high to photobleach labeled particles in the illuminated region. By using the attenuated laser beam, the subsequent growth of the fluorescent signal from the bleached region is monitored as it recovers to a significant fraction of its original level. The bleached region is erased during recovery due to replenishment of intact fluorophore in the illuminated region by diffusional transport from the surrounding region.

Typical dimensions of the illuminated region over which diffusion is averaged is tens or hundreds of micrometers, but as we shall see, the measured diffusion coefficient can characterize diffusion on a length scale ranging from hundreds of micrometers down to half the wavelength of light in the sample.

There are several possible variations on each aspect of this method. The pattern of the photobleached region may be any one of several different configurations such as a simple round spot or cylinder, an array of stripes, or a holographically created grating. The recovery of the signal may be monitored in a number of different ways: straightforward measurement of the total fluorescence signal or detailed spatial Fourier analysis of the sample image. The signal-to-noise improvement advantages of lock-in detection techniques can be gained by bleaching a transient grating and then scanning it with a spatially periodic illumination pattern to produce a modulated signal.

7.3.2 "Spot" or Direct Photometric Analysis FRAP

Perhaps the most straightforward to understand of the photobleaching techniques is the "spot" method originally used by Axelrod *et al.* [33] to measure the two-dimensional lateral diffusion of a fluorescent probe associated with a membrane (Fig. 9). In their approach, a laser beam is focused in the sample. The collected fluorescent light from the small circular illuminated area is monitored by a photodetector. Note that in this experiment, the sample is a thin membrane that limits the scattering volume (the illuminated region) to a small distance along the axis of the beam. In many later applications to bulk samples, the optical system of a microscope is used

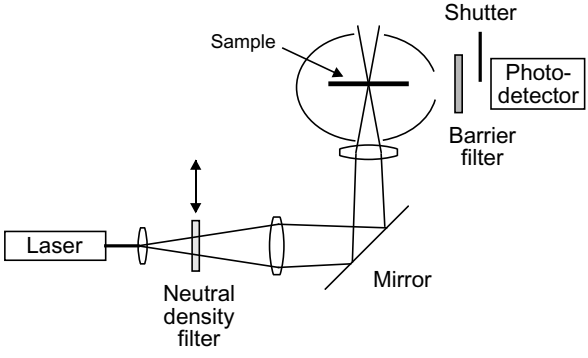

FIG. 9. Schematic of spot photometric analysis FRAP by Axelrod *et al.* [33]. The sample is a solution contained in a quartz cuvette of 100 μm path length. The barrier filter is a saturated solution of potassium dichromate. Adapted with permission from D. Axelrod *et al.*, *Biophys. J.* **16**, 1315. Copyright 1976 Biophysical Society.

to focus the laser beam to a small cylindrical region inside the sample. The objective thus images the scattering volume and an aperture is used to discriminate against fluorescent light not originating in the scattering volume.

In either the thin membrane or the imaged volume case, only the diffusion perpendicular to the axis of the beam is considered. The intensity of the beam $I(r)$ at radial distance r from the center axis has a Gaussian profile $I(r) \propto \exp(-2r^2/w^2)$, where w is the radius at the e^{-2} power point. Bleaching to a nonfluorescent species is assumed to be a simple irreversible first-order reaction occurring over a time short compared to characteristic times of transport. Thus, during the bleach pulse, the concentration of remaining fluorescent molecules, $c(r, 0)$, is reduced to a fraction of the initial uniform concentration. During recovery, the concentration $c(r, t)$ of labeled (fluorescing) molecules in the illuminated region at time t is governed by Fick's second law of diffusion with diffusion coefficient D. The total fluorescence signal is given by

$$F(t) = (Q/A_{\text{att}}) \int_0^\infty c(r, t) I(r) 2\pi r \, dr. \tag{12}$$

The prefactor is the product of the quantum efficiencies of light absorption, emission, and detection, Q, divided by the attenuation factor of the laser beam during recovery, A_{att}. Substituting the solution of the diffusion equation into Eq. (12), the following is obtained:

$$F(t) = F_i \sum_{n=0}^{\infty} \frac{(-K_b)^n}{n!} \frac{1}{1 + n(1 + t/t_{\text{D}})}, \tag{13}$$

where F_i is the measured value of F before photobleaching; t_{D} and K_b are fitting parameters. These expressions assume that the signal recovers completely to its prebleach value after a sufficiently long time. The diffusion coefficient is related to t_{D} and the beam radius by $t_{\text{D}} = w^2/(4D)$. Note that the measured diffusion coefficient does depend on the beam radius, but the prefactor Q/A_{att} need not be known. In many experimental situations, the fluorescence signal does not recover completely to the value before photobleaching, indicative that only a fraction of the labeled macromolecules are actually mobile.

7.3.3 Spatial Fourier Analysis

The spot fluorescence photobleaching method requires that the sample be thin and without strong light scattering characteristics. Otherwise the image will be contaminated by out-of-focus light and the effects of scattering and absorption. If the method is carried out through the objective lens of a

microscope, as is typical, the sample must be thin compared to the focal depth of the microscope, a rather severe restriction. A modification to the original spot FRAP technique has been demonstrated [34] in which the diffusion coefficient is calculated from the decay of spatial Fourier coefficients in successive fluorescence images. The theory of image formation is used to show that the decay rate of the observed fluorescent intensity is identical to the decay rate of the concentration distribution in the sample and hence the diffusion coefficient can be measured without explicit knowledge of the optical distortion of the image or determination of the true spot size or bleach depth. The technique also takes advantage of simplifications to the solution of the diffusion equation in Fourier space and requires no assumptions concerning the initial distribution of fluorescence.

Using the spatial Fourier analysis (SFA), Berk *et al.* [34] verified that, for a range of labeled proteins and dextrans, the diffusion coefficients measured in aqueous solution were in agreement with previous measurements by other methods. In weakly scattering agarose gel, a direct comparison to FRAP showed that the results were more accurate and were independent of sample thickness. In the most stringent test, albumin was placed in a simulated tissue consisting of a suspension of cancer and red blood cells in agarose gel. Although the SFA results did exhibit some pathlength dependence, the technique eliminated most of the image distortion and scattering effects that would impair conventional photometric analysis FRAP.

7.3.4 Periodic Pattern Photobleaching and Modulation Detection

An elegant and simple improvement to the spot FRAP technique was introduced by Smith and McConnell [35], who were concerned with the very slow movement of particles associated with synthetic and biological membranes [36–38]. The laser source shining through a mask and forming the bleaching stripe pattern was switched to a much lower intensity after photobleaching, thus providing spatially matched periodic illumination. In this case, the total fluorescence signal grows in real time with the same time constant as determined photographically. Anisotropic diffusion was studied by projecting a two-dimensional grid instead of stripes [39].

In a later development, diffusion was measured in a polymer film cast on the mask with a photolithography created pattern of stripes [40, 41]. This method eliminates the possibility of a phase shift between the bleaching and the reading patterns. In the Frank *et al.* experiment [41], diffusion coefficients in the range of 10^{-13} cm^2/s were measured in films only a fraction of a micrometer thick, which contained 1–10% labeled polymer.

While periodic pattern photobleach offers many advantages, particularly the ability to detect anisotropic diffusion, it is still susceptible to problems

common to DC detection schemes: low-frequency noise, long-term drift, and further bleaching of the labeled species during the recovery. Lanni and Ware [42] invented a method that overcomes the principal shortcomings of the DC detection schemes. They devised a system in which the fluorescence signal of interest is a sinusoid of decaying amplitude. A coarse striped mask (a Ronchi ruling) was used as the fixed field stop in a fluorescence microscope. The periodic set of alternating bright and dark bands of laser light imaged in the sample was used to photobleach a striped pattern. During the recovery, the same pattern, at reduced intensity, was scanned across the bleached region in a direction perpendicular to the stripes by translating the Ronchi ruling at a constant speed. A periodic signal is generated as the illumination falls in and out of phase with the bleached region in the sample. The theory of the method is reviewed in the following.

Immediately after photobleaching the concentration of fluorescence in the sample, $c(x, t)$, at x along the pattern can be described by a constant plus a square-wave fluctuation:

$$c(x, 0) = c_0 + [-1 + f(x)]\Delta c/2, \tag{14}$$

where $f(x)$ is a unit-amplitude square-wave of period d. Diffusion of fluorescent molecules relaxes the contrast in $c(x, t)$ as the sum of spatial Fourier components each of which decays exponentially:

$$c(x, t) = c_0 + \frac{\Delta c}{2}\left[1 + \frac{4}{\pi}\sum_{n:\text{odd}}^{\infty}\frac{1}{n}\exp(-Dq^2n^2t)\,\sin(nqx)\right], \tag{15}$$

where $q = 2\pi/d$. The illumination pattern moving at the speed of v is also a square-wave function. The detector output contains a DC component plus a set of decaying AC components. A typical component of the signal is

$$F(t) \propto \exp(-Dq^2n^2t)\,\cos(nqvt). \tag{16}$$

As long as the ratio of pattern speed to spatial period is large compared to the decay constant (i.e., $v/d \gg Dq^2$) each of the lowest frequency components will be well separated (compared to its bandwidth) from the others as well as from the DC component for easy analysis.

There are several distinct advantages to the modulation detection: The ratio of the DC photodetector signal just after photobleach to that just prior to the photobleach yields the actual extent of the photobleaching. The use of high-gain, tuned amplification means that the extent of photobleaching need not be great, minimizing photodamage to delicate sample material such as proteins. The ratio of the mobile fluorescent probe fraction to the immobile fraction may be determined from the ratio of the DC signal to the amplitude of the decaying AC signal just after bleaching. Further bleaching

due to illumination during the fluorescence recovery is not a problem if the experiment is operated in the "ratio mode." The DC as well as the oscillating signal is reduced by illumination bleaching, and therefore by monitoring the ratio of these two, the effect of bleaching is canceled out. The method has been applied extensively to diffusion of probes in polymer solution [43, 44].

7.3.5 Holographic FRAP

Holographic FRAP, first practiced by Davoust *et al.* [45], combines many aspects of pattern photobleaching and modulation detection, and indeed has many features in common with forced Rayleigh scattering and other transient grating techniques [46]. The principal difference is that the periodic bleach and readout patterns are produced holographically by crossed laser beams. The basic method is illustrated in Figs. 10 and 11 [47]. Two intense laser beams are crossed inside the sample to "write" a parallel fringe pattern. The fluorescence of probe molecules located at regions of constructive interference of the two beams is selectively destroyed during the writing pulse. The same two beams, greatly attenuated, are used to "read" the periodic fluorescence pattern during recovery. The phase of one of the reading beams is effectively swept so that the reading pattern advances continuously across the bleached pattern at constant velocity. Maxima in the fluorescence signal will occur whenever the reading and written gratings are out of phase; that is, when maxima in the reading grating coincide with the unbleached stripes of the written pattern. As the written grating fades because of translational diffusion of the probe molecules, the modulated fluorescence signal decays exponentially.

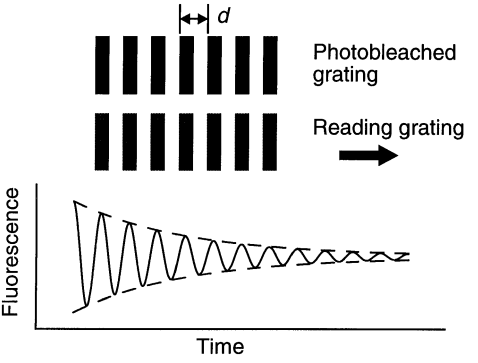

FIG. 10. Pictorial representation of the holographic FRAP experiment. Adapted with permission from M. T. Cicerone *et al.*, *Macromolecules* **28**, 8224. Copyright 1995 American Chemical Society.

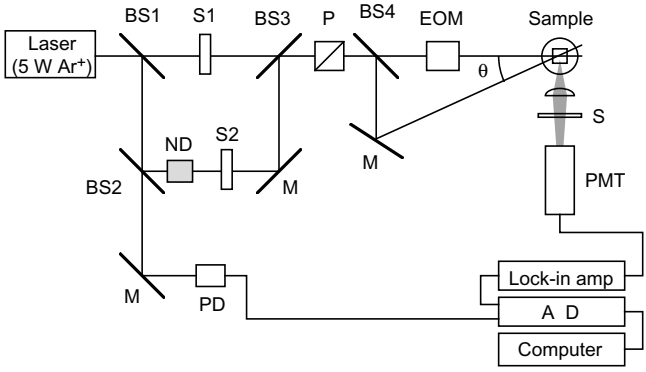

FIG. 11. Schematic of holographic FRAP apparatus; BS, beamsplitter; P, polarizer; S, shutter; M, mirror; ND, neutral density filter; EOM, electro-optic modulator; PMT, photomultiplier tube; and PD, photodiode. Adapted with permission from M. T. Cicerone *et al.*, *Macromolecules* **28**, 8224. Copyright 1995 American Chemical Society.

In the earlier realizations of holographic FRAP, Davoust *et al.* [45] used an oscillating mirror to effect a sinusoidal phase modulation. Cicerone *et al.* [47] instead used an electro-optic modulator to repetitively ramp the phase exactly from 0 to 2π at a rate of 10 kHz (Fig. 11), effecting a reading grating that translates linearly at a constant velocity. The signal with the spatial modulation frequency is concentrated in a very narrow frequency band at the fundamental phase modulation frequency, unlike the situation with sinusoidal modulation. Elimination of vibration effects from FRAP experiments is the major advantage of this modulation scheme. Once again, if the signal is taken as the grating contrast ratio, division by the DC signal compensates the signal of interest for residual bleaching by the illuminating light. If the translation of unbleached probe molecules is governed by translational diffusion, the contrast ratio decays exponentially at a rate of Dq^2, where $q = 4\pi \sin(\theta/2)/\lambda$ (θ and λ are both measured in the same medium, either in air or in the sample). Cicerone *et al.* used holographic FRAP to measure the diffusion of small probe molecules of rubrene and tetracene in polystyrene. By using the counterpropagating beam configuration, they reduced d to 0.153 μm and hence were able to measure diffusion coefficients below the glass transition temperature as small as a few times 10^{-16} cm^2/s.

7.3.6 Application of FRAP to a Porous Gel

FRAP has been used extensively to measure diffusion coefficients of labeled polymers, proteins, and particles in a wide variety of matrix

materials [44, 47, 48], but here we will use just one typical study to illustrate the kind of information that can be learned about a porous material.

Tong and Anderson [49] measured the partition and diffusion coefficients of globular proteins and linear polymers in cross-linked polyacrylamide gels by using the classic "spot" FRAP technique. Slabs of 0.76-mm-thick transparent gel were loaded either with (1) spherical proteins bovine serum albumin (BSA) or ribonuclease-A (RNase) labeled with fluorescein-5-isothiocyanate or (2) poly(ethylene glycol) (PEG) of two different molecular weights labeled with 5-([4,6-dichlorotriazin-2-yl]amino)-fluorescein. The partition coefficient K, the ratio of the concentration inside the gel to the concentration in the surrounding solution, was determined by comparing the intensities of the fluorescence signal from slabs of the loaded gels in equilibrium with buffer solution and from the buffers alone. Partition coefficients for the proteins as a function of polymer fiber volume fraction $1 - \phi$ of the gel were analyzed in terms of the theory of Ogston [50] which models the medium as infinitely long fibers of radius a_f placed randomly to interact with a dilute diffusant of hard spheres of radius a_s:

$$K = \exp[-(1\text{-}\phi)(1 + a_s/a_f)^2] \tag{17}$$

The solute permeability of a gel is proportional to the product of the partition coefficient and the diffusion coefficient in the gel, D_{gel}. The measured products KD_{gel} were compared to the theory (Fig. 12) using the Ogston expression for the partition coefficient and a modified Brinkman

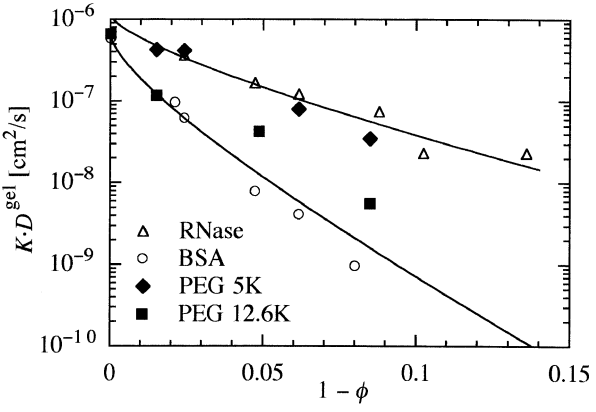

FIG. 12. Product of the partition coefficient K and the diffusion coefficient D^{gel} in the gel, for RNase, BSA, and two fractions of PEG, plotted as a function of the gel volume fraction $1 - \phi$. Solid lines represent the Ogsten-Brinkman model. Adapted with permission from J. Tong and J. L. Anderson, *Biophys. J.* **70**, 1505. Copyright 1996 Biophysical Society.

expression [48] for the diffusion coefficient. It was noted that, first, the gel fiber volume fraction $1 - \phi$ has a striking effect on solute permeability, amounting to two or three orders of magnitude and, second, there is a significant effect of solute size. At a given concentration, the gel is much more selective against BSA as compared to RNase, even though the molecular radii differ only by a factor of 1.8. The first feature is mostly due to a sharp decrease in the partition coefficient as $1 - \phi$ increases.

7.4 Forced Rayleigh Scattering

7.4.1 Discussion of the Method

The basic experimental layout is illustrated in Fig. 13 [51]. Coherent light of wavelength λ from the "writing" laser source is pulsed on briefly, often by a mechanical shutter. The laser light is divided by a beamsplitter into two beams of approximately equal intensity. These two beams are made to cross at angle θ in the sample where they form a spatial interference pattern of fringe spacing $d = \lambda/[2\sin(\theta/2)]$. The fringes are in planes perpendicular to the plane of the two writing beams, and are separated by distance d in a direction perpendicular to the bisector of the angle between the beams. Near the maxima in the fringe pattern, the intense electric field induces a change in the local index of refraction, thus "writing" an index of refraction grating. This pattern can be detected in various ways. Typically a second laser beam is incident on the sample in an appropriate direction such that its light is Bragg-scattered from the planes of the spatial grating. This reading of the

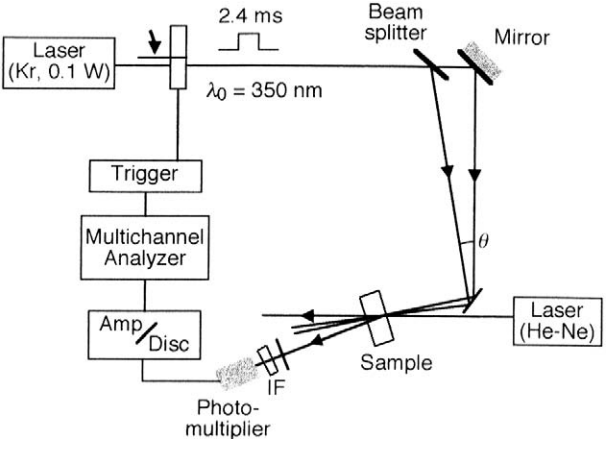

FIG. 13. Schematic of FRS measurement system. Adapted with permission from L. Léger *et al.*, *Macromolecules* **14**, 1732. Copyright 1981 American Chemical Society.

grating by diffraction, as opposed to monitoring the fluorescent emission, is the distinguishing feature of the FRS technique. The intensity of the Bragg-scattered light is monitored by a photodetector. The photodetector output is the signal of interest; as the grating decays by diffusion, Bragg-scattered light declines in intensity.

In general, FRS can utilize any process that alters the real or imaginary part of the index of refraction. In cases of interest to us, the sample contains a few percent of a photochromic dye or polymers labeled with such a dye. Photons of the writing pulse cause a reaction to change the absorption of light at the wavelength used in the Bragg-scattered beam, so the grating is essentially an absorption grating, which provides relatively high contrast and enables measurement of the diffusion of labeled molecules present in a low concentration.

Several different optical configurations have been used to deliver the intersecting beams to the sample and bring the Bragg-scattered light to the photodetector. In one arrangement, the two writing beams converge on the sample symmetrically with respect to the monitor beam, a helium-neon laser beam incident parallel to the planes of the fringes [52]. Guo *et al.* [53], following Amis, used a system of translating prisms and reflected the writing beams from an off-axis parabolic mirror to accomplish convenient adjustment of the beam-crossing angle. In any apparatus, the distance traveled by the two writing beams from the laser to the sample must be identical to within the coherence length of the laser, otherwise no interference pattern will be formed. The reading beam can be a separate laser of wavelength chosen near the region of strong absorption of the dye, as in Fig. 13, or can be one of the writing beams attenuated by a factor of 1000 or so [54]. The latter can be convenient because the writing beam automatically satisfies the Bragg condition.

After the pattern is written, it relaxes by diffusion of the optically modified molecules present in bright stripes at the moment of writing. Note this situation is in contrast to the one in FRAP where the unbleached fluorescent molecules are detected. The response of dye molecules to the writing light may not be linear, and the grating may contain spatial Fourier components at harmonics as well as the fundamental of the grating period. If the grating decay is monitored by Bragg scattering, however, there will be a different diffracted beam produced for each spatial frequency present and the intensity of each diffracted beam will decay in time with a unique decay rate

$$I_j(t) = I_j(0) \exp[-D(2\pi j/d)^2 t] \qquad (j = 1, 2, 3, \ldots), \tag{18}$$

where D is the diffusion coefficient of the dye molecules. The preceding assumes that there is no further chemical reaction after the writing pulse and the only relaxation mechanism is the diffusion of photochemically altered

molecules. In practice, if the lifetime of photochemical activation is τ, then the observed decay rate τ_{obs} is instead

$$1/\tau_{obs} = D(2\pi j/d)^2 + 1/\tau. \tag{19}$$

The actual experimentally observed signals are more complicated and difficult to interpret. Often the model function

$$I(t) = [A \exp(-t/\tau) + B]^2 + C^2 \tag{20}$$

is used, where B and C are constants. Furthermore it often happens that there is a short interval after the pump is switched off during which the signal increases before it decays [55, 56].

7.4.2 Application of FRS to Polymer Diffusion in a Porous Material

A study of the diffusion of polymer in solution within a gel of fumed silica is used to illustrate the application of FRS to dynamics in a porous material. The rate of hindered diffusion was measured for two molecular weights of polymer as a function of the silica volume fraction [53].

Gels were formed from mixtures of fumed silica, also called pyrogenic silica. These silica powders are formed in the hydrolysis of silicon tetrachloride in a hydrogen–oxygen flame and have an extremely large surface area. Basic 10–20-nm-diameter subunit "beads" are clustered into fractal structures several hundred angstroms in characteristic dimension [57]. In the FRS study, silica particles were modified by treatment with hexamethyl disilazane to remove surface hydroxyl groups, which would otherwise tend to bind the dye-labeled diffusant. Modified silica, placed in fluorobenzene solution at concentrations above approximately 6% volume fraction, formed weak gels after several hours to days, depending on the concentration.

Two fractions of polystyrene were labeled at random sites (one per 1000 monomer units) along the polymer chain with 4-dimethylaminoazobenzene-4′-isothiocyanate. Fluorobenzene was chosen as a solvent because it is a good solvent for polystyrene and has an index of refraction close to that of silica. Gels were formed by simply mixing a labeled polystyrene solution with fumed silica on a test tube mixer and allowing the solutions to stand until no appreciable flow was observed in a tilted tube over several minutes.

In the FRS apparatus, fringe spacing could be varied from 3 to 30 μm by changing the beam convergence angle θ. The transient diffracted optical intensity from labeled polystyrene in a gel of modified silica is shown in Fig. 14. The transient signal begins to decay immediately after the writing beam pulse and decays to the prewriting level baseline according to Eq. (20). In contrast, the signal from the same polymer moving in a gel of unmodified

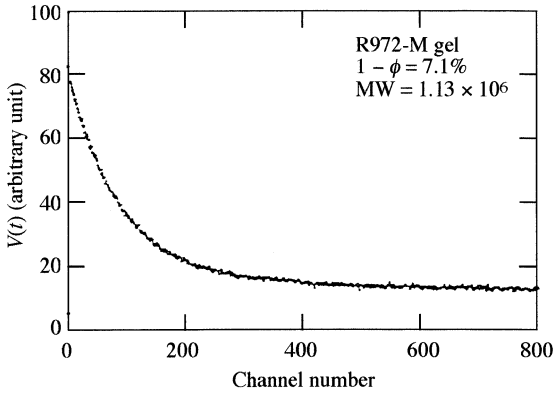

FIG. 14. Transient diffracted optical intensity after excitation by a writing beam pulse. Labeled polystyrene is diffusing in a gel of surface-modified fumed silica. Adapted with permission from Y. Guo *et al.*, *Phys. Rev. A* **46**, 3335. Copyright 1992 American Physical Society.

silica in which some surface adsorption is present, typically showed a rapid rise after exposure to the writing beams, followed by slower relaxation to the baseline.

The decay rate $1/\tau$ observed at different scattering wave vectors for the same labeled polymer in free solution and in the modified silica was proportional to q^2 (Fig. 15), characteristic of normal diffusion behavior. The ratio of the diffusion coefficient in a silica matrix to that in free solution, D/D_0, often referred to as the hindrance factor, is plotted as a function of volume fraction $1 - \phi$ of modified silica in Fig. 16 for the two fractions of polystyrene. At low volume fractions, a gel did not form, and the hindrance factor was measured in a uniform suspension. Lacking a truly appropriate model for this system, the results were compared with the hydrodynamic theory developed by Neale and Nader [58] for a much simpler system—a homogeneous swarm of spherical particles of arbitrary size distribution, but nonoverlapping range of hydrodynamic interactions. Assuming that each particle experiences the remainder as a uniform fluid, the model predicts that $D/D_0 = 2\phi/(3 - \phi)$. At low volume fractions, the results are reasonably consistent with the Neale–Nader theory (solid line in Fig. 16) probably because the silica particles can be regarded as a collection of spherical objects even though the spherical units are aggregated into ramified clusters. At higher volume fractions, departure from the model becomes evident. The results were also compared with a theory developed by Prager [59] for a homogeneous and isotropic suspension of solid particles of arbitrary shape. In Prager's model the principle of minimum entropy production was applied

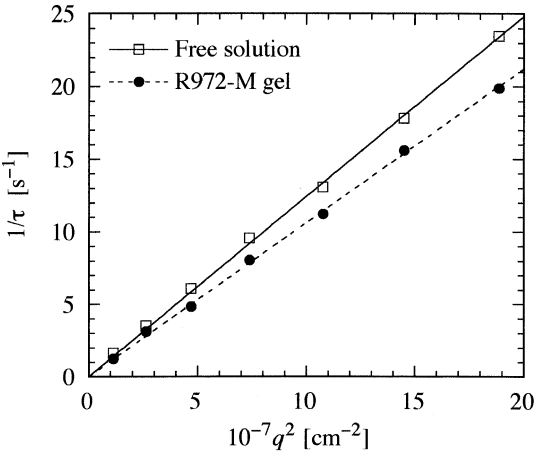

FIG. 15. Decay rate $1/\tau$ plotted as a function of q^2, square of the scattering wave vector, for polystyrene in free solution (squares) and in modified fumed silica (circles). Adapted with permission from Y. Guo *et al.*, *Phys. Rev. A* **46**, 3335. Copyright 1992 American Physical Society.

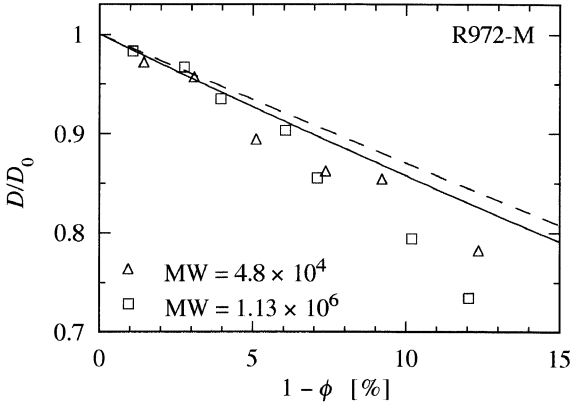

FIG. 16. Hindrance to the diffusion of polystyrene in modified fumed silica gel of different volume fractions $1 - \phi$. The solid line is the prediction by the Neale–Nader theory, and the dashed line is the upper limit of the hindrance factor in the Prager's model. Adapted with permission from Y. Guo *et al.*, *Phys. Rev. A* **46**, 3335. Copyright 1992 American Physical Society.

to obtain an upper bound of the hindered diffusion rate: $D/D_0 < (\phi/3)(2+\phi)$ (dashed line in Fig. 16). The data clearly satisfy the predicted inequality.

7.5 Diffusing-Wave Spectroscopy

7.5.1 Discussion of the Method

Diffusing-wave spectroscopy is a relatively recent development of dynamic light scattering (see Section 7.2), which extends the power of DLS analysis to strongly scattering media such as concentrated suspensions [60], foams [61, 62], and streams of flowing particles [63]. Because DWS is sensitive to movement of the scatterers over distances small compared to the wavelength of light, it also offers the opportunity to explore particle dynamics and interaction at small length scales not previously attainable. Another advantage of the technique arises from the fact that the light arriving at the detector has been scattered repeatedly, sampling large spatial regions of the sample. This means that events that are rare in time and widely separated in space are nonetheless included into the data. While most of the applications to date have been concerned with concentrated suspensions of particles, and foams are the only materials studied that are considered as conventional porous materials, the technique is relatively early in its development. There is still the hope of useful application to many more relatively opaque porous materials. DWS has been reviewed by Weitz and Pine [64].

The experimental apparatus for DWS is very similar to that used in DLS: Light from a laser impinges on a sample, where it is scattered (in this case many times) before it arrives at a detector, which provides single-photon pulses to a digital correlator for computation of the autocorrelation function of the scattered light intensity. The collection optics is arranged such that scattered light from approximately one single speckle is allowed to reach the detector, a much stricter requirement than in DLS. In principle, the total angle through which light is scattered between entering and leaving the sample is not an important consideration, since there are many individual scattering events along each photon path from source to detector. In fact, theoretical understanding of the method demands that each photon experiences a number of scattering events large enough so that the passage of the light through the sample can be interpreted as a diffusion process. That is, all knowledge of the scattering wave vector, polarization, structure factor, etc. in each single scattering is lost, and a photon path can be considered to be a large number of equivalent events, each making equal contributions to the correlation function [65–67]. Indeed, there is a considerable latitude in choosing the detector orientation in an experiment, but for simplicity of the

theory and other practical reasons, only two geometries are commonly used: transmission (forward scattering) and backscattering (Fig. 17).

Transmission DWS (Fig. 17, apertures 3 and 4) offers several advantages in the interpretation of the resulting autocorrelation functions, but obviously suffers due to great loss in light intensity in more opaque samples. There is a somewhat delicate trade-off between making the sample thin enough and laser power high enough (without sample heating) to obtain sufficient light at the detector, and making the sample thick enough to reduce the transmission of unscattered direct light to an acceptable level. Eliminating unscattered direct light is extremely important, however, as only then is it assured that all photon paths through the sample are long compared with the transport mean free path, l^*, defined as the length scale over which the direction of light propagation is randomized. The functional form of the correlation function for transmission DWS from a collection of monodisperse scatterers with diffusion coefficient D in suspension is:

$$g_E(t) = \frac{\dfrac{L/l^*4/3}{z_0/l^* + 2/3}\left[\sinh\left(\dfrac{z_0}{l^*}\sqrt{\dfrac{6t}{\tau}}\right) + \dfrac{2}{3}\sqrt{\dfrac{6t}{\tau}}\cosh\left(\dfrac{z_0}{l^*}\sqrt{\dfrac{6t}{\tau}}\right)\right]}{\left(1 + \dfrac{8t}{3\tau}\right)\sinh\left(\dfrac{L}{l^*}\sqrt{\dfrac{6t}{\tau}}\right) + \dfrac{4}{3}\sqrt{\dfrac{6t}{\tau}}\cosh\left(\dfrac{L}{l^*}\sqrt{\dfrac{6t}{\tau}}\right)}, \qquad (21)$$

where L is the sample thickness, $\tau = k_0^2 D)^{-1}$ with $k_0 = 2\pi/\lambda$, z_0 is the distance from the sample surface at which the propagation direction of the

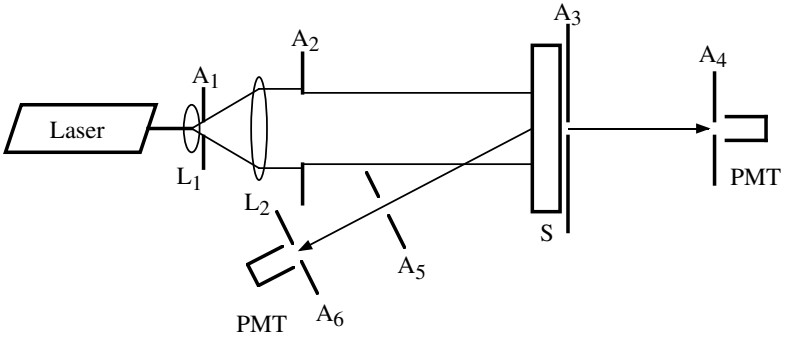

FIG. 17. Transmission and backscattering setup for DWS measurements. After the laser beam is spatially filtered and expanded, aperture A_2 selects the uniform part of the beam to illuminate sample S. Apertures A_3 and A_4 select a single speckle for transmission detection. Apertures A_5 and A_6 are used in the backscattering mode. Adapted from D. A. Weitz and D. J. Pine, in *Dynamic Light Scattering*, W. Brown, Ed., by permission of Oxford University Press.

light is considered to be randomized (it turns out that the results are quite insensitive to the value of z_0), and l^* can be determined experimentally from the transmittance. This rather formidable expression is nearly an exponential decay of characteristic time $\tau(l^*/L)^2$, reflecting the fact that there is a characteristic number of random steps $(L/l^*)^2$ in a typical photon path. Expressions have also been developed for illumination of the sample by a point source and by a Gaussian beam. Since the time scale of the decay is set by the time it takes a typical path length to change by one wavelength, it can be shown that the expression for the autocorrelation function can be expressed in terms of the root-mean-square displacement of the scattering particles as approximately $g_E(t) = \exp[-(L/l^*)^2 k_0^2 \langle \Delta \mathbf{r}^2(t) \rangle]$. This expression has been used to analyze DWS obtained from a stream of flowing sand [63].

Backscatter geometry for DWS (Fig. 17, apertures 5 and 6) in principle has several advantages: Independent knowledge of l^* is not required for interpretation of the autocorrelation function, access to the sample from only one side is required (convenient for monitoring material in an industrial process, for example), and many different photon path lengths are probed at once. In practice, however, it turns out that because much of the contribution to the correlation function comes from near the surface of the sample where the path lengths are comparable to l^*, the diffusion approximation is not well obeyed and correlation functions must be interpreted with caution. The expression for $g_E(t)$ of light scattered in the backward direction from a uniformly illuminated sample is

$$g_E(t) = \frac{\sinh\left[\sqrt{\frac{6t}{\tau}}\left(\frac{L}{l^*} - \frac{z_0}{l^*}\right)\right] + \frac{2}{3}\sqrt{\frac{6t}{\tau}}\cosh\left[\sqrt{\frac{6t}{\tau}}\left(\frac{L}{l^*} - \frac{z_0}{l^*}\right)\right]}{\left(1 + \frac{8t}{3\tau}\right)\sinh\left(\frac{L}{l^*}\sqrt{\frac{6t}{\tau}}\right) + \frac{4}{3}\sqrt{\frac{6t}{\tau}}\cosh\left(\frac{L}{l^*}\sqrt{\frac{6t}{\tau}}\right)}, \quad (22)$$

which reduces, in the case of an infinitely thick sample, to a simple stretched exponential:

$$g_E(t) = \left(1 + \frac{2}{3}\sqrt{\frac{6t}{\tau}}\right)^{-1} \exp\left(-\frac{z_0}{l^*}\sqrt{\frac{6t}{\tau}}\right), \quad (23)$$

which in turn can be well approximated by $g_E(t) = \exp[-\gamma(6t/\tau)^{1/2}]$, where $\gamma = z_0/l^* + 2/3$. In practice, γ varies by a factor of about 2 depending on particle size and polarization state [68]. Presumably these variations are due to different contributions of short paths under different experimental conditions.

7.5.2 Application of DWS

DWS has been used to study the coarsening of a foam [61] using both the transmission and backscattering geometries. The decay times of $g_E(t)$ were interpreted in a model of intermittent foam bubble rearrangement. They showed that the temporal increase of average bubble diameter in a coarsening foam could be followed by DWS as well as by static light transmission (Fig. 18) because of the consistency between values of l^* derived from the two methods. The dashed line in the figure is the $t^{1/2}$-power-law growth of average bubble size predicted for an assumed statistically self-similar distribution of densely packed bubbles.

Menon and Durian [63] used DWS to study the short time dynamics of grains in the interior of a three-dimensional gravity-driven flow of sand. Plots of the mean-square displacement of the particles $\langle \Delta \mathbf{r}^2 \rangle$ versus time obtained in both the forward and the backward scattering geometries were identical, verifying the validity of the method. Since the two geometries measure grains in different spatial regions of the sample, it was also verified that the short-term particle dynamics are identical in different parts of the flowing stream. It was found that at short times, particle motion is dominated by ballistic flight of grains from collision to collision, with a wide range of random velocities (Fig. 19). Diffusional flow of particles in the long time limit was confirmed by independent video microscopy.

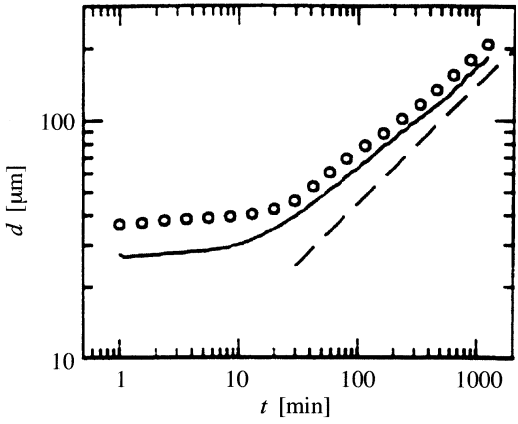

FIG. 18. Average bubble diameter as a function of foam age: circles, DWS measurements; solid curve, static light transmission. Dashed line has a slope of 0.5. Reprinted with permission from D. J. Durian *et al.*, *Phys. Rev. A* **44**, R7902. Copyright 1991 American Physical Society.

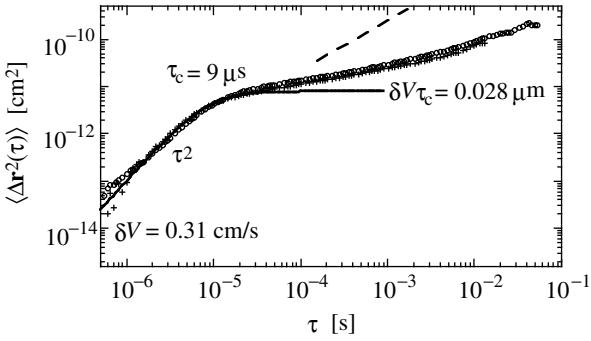

FIG. 19. Mean-square displacement of particles in a gravity-driven flow of sand. At short times particle movement is ballistic; in the long time limit, the motion becomes diffusional (dashed line). From N. Menon, unpublished, used with permission.

7.6 Other Optical Methods

7.6.1 Interferometry

Unlike other optical techniques reviewed in this chapter, the interferometry method discussed here images a porous medium as a whole. With interferometry it is possible to measure the average porosity of the medium [69, 70]. Its built-in spatial resolution provides information about inhomogeneity of the medium [71]; that is, distribution of the porosity and composition of the solid phase of the medium. When interferometry is applied to a porous medium immersed in a solution, it enables us to evaluate the solute concentration within the medium [69, 70, 72]. Imaging of the porous medium at different times in a process that involves a change of the medium gives us information on the kinetics of the process [71]. To utilize the spatial resolution, the porous medium must have a simple shape such as a sphere or a cylinder.

Sernetz *et al.* [69, 72] constructed a micro-Mach-Zehnder interferometer, as illustrated in Fig. 20a. An example of the image of a hydrogel bead immersed in an aqueous solution of linear polymer is shown in Fig. 20b. For the bead portion of the image, the parallel fringe pattern is displaced and distorted. The pattern depends on the geometry of the porous medium. For a spherical gel, it is elliptic [70]. The maximum displacement Δx_m occurs for a fringe that passes through the center of the gel bead. It is related to the difference δn in the refractive index between the porous medium and the surrounding solution by $\Delta x_m/\xi = d\delta n/\lambda$, where ξ is the fringe period, and d the thickness of the gel bead.

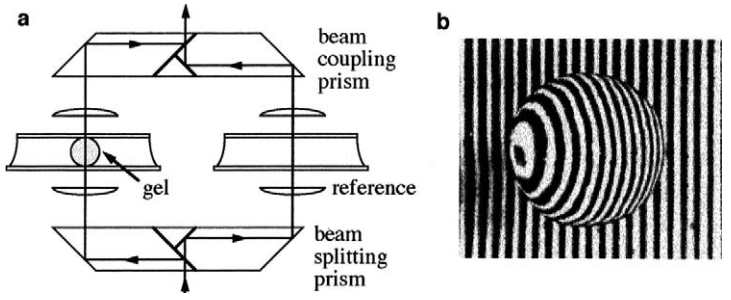

FIG. 20. (a) Micro-Mach-Zehnder interferometer constructed to find the porosity of a hydrogel and the partition coefficient of polymer in the gel and (b) example of interferogram of a hydrogel. From M. Sernetz *et al*., in *The Fractal Approach to Heterogeneous Chemistry*, D. Avnir, Ed., 1989. Copyright John Wiley & Sons Limited. Reproduced with permission.

The refractive index of a solution at concentration c is expressed as $n_S + (dn/dc) \times c$ with n_S being the index of the solvent; dn/dc is a differential refractive index. When the porosity ϕ is defined as the volume fraction of the pore space in the entire porous medium, δn is expressed as

$$\delta n = (1 - \phi)(n_G - n_S) + \phi \Delta n(c_I) - \Delta n(c_E), \tag{24}$$

where n_G is the refractive index of the solid phase of the porous medium (or the matrix of the gel bead), and c_I and c_E are the solute concentrations in the pore channels and in the surrounding solution, respectively. The first term in Eq. (24) can be estimated from the fringe pattern for the same porous medium immersed in the pure solvent, which produces $(\Delta x_m/\xi)_0$. Thus, c_I at a given c_E can be estimated by using

$$(\lambda/d)[(\Delta x_m/\xi) - (\Delta x_m/\xi)_0] = \phi \Delta n(c_I) - \Delta n(c_E). \tag{25}$$

Teraoka [70] constructed a Jamin interferometer (Fig. 21) to measure the partition coefficient of polystyrene in a porous silica bead. A single crystal of calcite was used as a beamsplitter, and another single crystal as a coupler. The bottom beam illuminates the porous medium immersed in a solution, and the top beam travels through the exterior solution. The interferometer was used to measure the concentration c_I of the polymer in the interior of a porous silica bead (bead diameter $\cong 2$ mm; pore diameter $\cong 50$ nm) as a function of the concentration c_E in the surrounding solution. Figure 22 shows the partition coefficient $K \equiv c_I/c_E$ as a function of c_E/c^* for six fractions of polystyrene standard, where c^* is the overlap concentration of the fraction. By using the same interferometer for the silica bead immersed in mixtures of two liquids at different mixing ratios, the porosity of the bead was also evaluated.

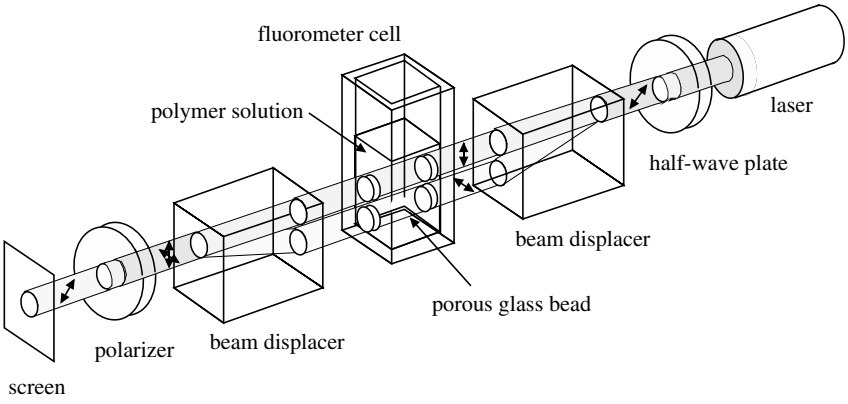

FIG. 21. Jamin interferometer used to measure the partition coefficient of polymer in a porous silica bead. Reprinted with permission from I. Teraoka, *Macromolecules* **29**, 2430. Copyright 1996 American Chemical Society.

Spatial resolution of the interferometry was utilized to study infusion of polymer into the silica bead [71]. Analysis of $\Delta x/\xi$ for all fringes along a diameter of the bead image made it possible to obtain the radial distribution of the polymer concentration within the bead at different times during the infusion. A deviation of the profile from a semiellipse was translated into the distribution of the solute polymer within the porous medium. Two distinct

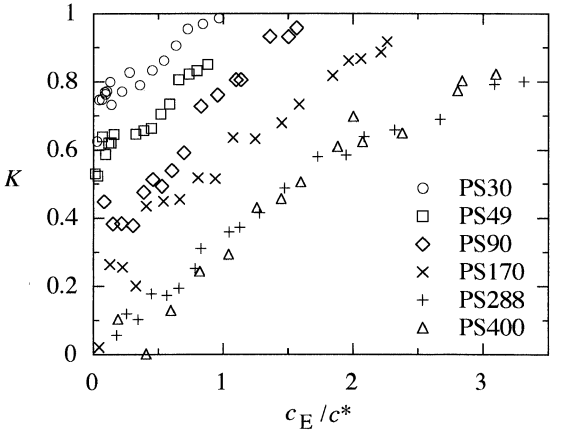

FIG. 22. Partition coefficient K in a porous silica bead, plotted as a function of the reduced polymer concentration c_E/c^* in the exterior solution for six fractions of polystyrene standard. Adapted with permission from I. Teraoka, *Macromolecules* **29**, 2430. Copyright 1996 American Chemical Society.

patterns were observed. When the polymer chain was larger than the pore size, the profile increased in unison, a result indicating that the entrance of polymer chains into the pore openings on the bead surface was rate-limiting. When the polymer chain was smaller, in contrast, the profile increased gradually from the bead edge and advanced toward the center. In the latter, intrapore diffusion was the rate-limiting process. They also showed that the spatial resolution is useful to find the origin of nonuniformness of the porous medium itself.

7.6.2 Holographic Interferometry

There are many classical methods for determining the diffusion coefficient of a solute in an optically transparent solution or gel by measuring the time evolution of the boundary between two regions of different concentration. In a typical arrangement, a flat, sharp interface is created, solute-containing solution being on one side and solute-depleted solution on the other. Light is passed through the sample parallel to the interface region and then combined with reference light to form an interference pattern. The nature of the pattern is determined by the characteristics of the light, how it is combined with the reference beam, and, most important, the index of refraction profile near the interface. In turn, the index of refraction distribution is directly related to the solute concentration profile. Hence, as the spatial distribution of solute concentration evolves in time due to diffusion, the light pattern also evolves and can be analyzed to extract the diffusion coefficient. The holographic interferometry explained in the following has a particular advantage in the details of the way light is used to form the pattern.

In classic laser interferometry measurements of diffusion, a laser beam is divided by a beamsplitter into a test beam, which passes through the sample, and a reference beam, which does not. A series of interference fringes is formed when the two beams are recombined. The diffusion coefficient is determined from the fringe shape and spacing. In holographic interferometry, a holographic image of the diffusion cell is recorded at an initial time. At each successive later time, the initial image is reconstructed to make the reference needed to form interference fringes with the beam passing through the diffusion cell. The primary advantage is that the test beam passing through the sample at the later time is identical to the beam passing through the cell at the initial time, except for changes in the optical path distance that have occurred because of diffusion of the solute. Because the fringes are essentially formed by comparing initial and later test beams, which both travel along a single path, spurious fringe shifts due to slight inhomogeneities in the glass or gel matrix are eliminated.

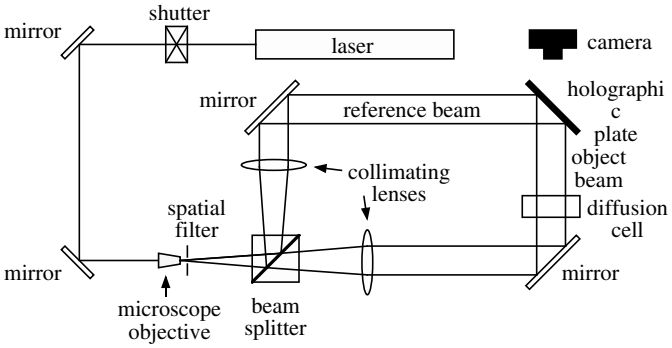

FIG. 23. Apparatus for holographic interferometry. Reproduced with permission from T. F. Kosar and R. J. Phillips, *AIChE J.* **41**, 701. Copyright 1995 American Institute of Chemical Engineers, all rights reserved.

Figure 23 illustrates the apparatus for holographic interferometry used by Kosar and Phillips [73] to examine the effect of ionic strength, polymer concentration, and polymer molecular weight on the diffusion of bovine serum albumin in dextran solutions, and later, the diffusion of proteins and nonionic micelles in agarose gels [74]. After exposure of the initial holographic image, the photographic plate is removed, developed, and then replaced into its holder. The holder must return the plate precisely to its original position. After the initial image is recorded, the reference beam is tilted slightly in the horizontal direction so that each later image contains a series of parallel fringes oriented perpendicular to the plane of the interface. These fringes are straight lines far from the interface, but are displaced into an S shape near the interface. The diffusion coefficient is determined simply from the distance d between the extrema of the S shape and the time between initial hologram at time t_1 and the later at time t_2 [75, 76]:

$$D = (d^2/8)(t_1^{-1} - t_2^{-1})[\ln(t_2/t_1)]^{-1}. \tag{26}$$

We can see that for an experiment of a few hours duration, practical considerations establish a lower limit to diffusion coefficients that can be measured by this method at about $10^{-7}\,\mathrm{cm}^2/\mathrm{s}$.

References

1. B. Berne, R. Pecora, *Dynamic Light Scattering with Applications to Chemistry, Biology, and Physics*; Wiley, New York, 1976.
2. K. S. Schmitz, *An Introduction to Dynamic Light Scattering by Macromolecules*; Academic Press, San Diego, 1990.

3. B. Chu, *Laser Light Scattering*; Academic Press, San Diego, 1991.
4. W. Brown, *Dynamic Light Scattering*; Clarendon, Oxford, 1995.
5. S. W. Provencher, *Macromol. Chem.* **180**, 201 (1979).
6. M. T. Bishop, K. H. Langley, F. E. Karasz, *Phys. Rev. Lett.* **57**, 1741 (1986).
7. M. T. Bishop, K. H. Langley, F. E. Karasz, *Macromolecules* **22**, 1220 (1989).
8. N. Easwar, K. H. Langley, F. E. Karasz, *Macromolecules* **23**, 738 (1990).
9. Y. Guo, K. H. Langley, F. E. Karasz, *Macromolecules* **23**, 2022 (1990).
10. Y. Guo, K. H. Langley, F. E. Karasz, *Macromolecules* **25**, 4902 (1992).
11. I. Teraoka, K. H. Langley, F. E. Karasz, *Macromolecules* **26**, 287 (1993).
12. Z. Zhou, I. Teraoka, K. H. Langley, F. E. Karasz, *Macromolecules* **27**, 1759 (1994).
13. Z. Zhou, I. Teraoka, K. H. Langley, F. E. Karasz, *Macromolecules* **27**, 7402 (1994).
14. I. Teraoka, Z. Zhou, K. H. Langley, F. E. Karasz, *Macromolecules* **29**, 37 (1996).
15. W. Haller, *Nature* **206**, 693 (1965).
16. J. G. H. Joosten, J. L. McCarthy, P. N. Pusey, *Macomolecules* **24**, 6690 (1991).
17. J. G. H. Joosten, *Progr. Colloid Polym. Sci.* **91**, 149 (1993).
18. W. M. Deen, *AIChE J.* **33**, 1409 (1987).
19. I. Teraoka, *Progr. Polym. Sci.* **21**, 89 (1996).
20. M. Muthukumar, A. Baumgärtner, *Macromolecules* **22**, 1937 (1989).
21. M. Muthukumar, A. Baumgärtner, *Macromolecules* **22**, 1941 (1989).
22. T. Tanaka, S. Ishikawa, C. Ishimoto, Phys. *Rev. Lett.* **38**, 771 (1977).
23. T. Tanaka, E. Sato, Y. Hirokawa, S. Hirotsu, *Phys. Rev. Lett.* **55**, 2455 (1985).
24. P. N. Pusey, W. van Megen, *Physica A* **157**, 705 (1989).
25. M. Shibayama, Y. Fujikawa, S. Numura, *Macromolecules* **29**, 6535 (1996).
26. M. R. Aven, C. Cohen, *Polymer* **31**, 778 (1990).
27. N. A. Rotstein, T. P. Lodge, *Macromolecules* **25**, 1316 (1992).
28. A. P. Y. Wong, S. B. Kim, W. I. Goldburg, M. H. W. Chan, *Phys. Rev. Lett.* **70**, 954 (1993).
29. P.-G. de Gennes, *J. Phys. Chem.* **88**, 6469 (1984).
30. S. B. Dierker, P. Wiltzius, *Phys. Rev. Lett.* **58**, 1865 (1987).
31. F. Aliev, W. I. Goldburg, X.-I. Wu, *Phy. Rev. E* **47**, R3834 (1993).
32. M.-m. Poo, R. A. Cone, *Nature* **247**, 438 (1974).
33. D. Axelrod, D. E. Koppel, J. Schlessinger, E. Elson, W. W. Webb, *Biophys. J.* **16**, 1315 (1976).
34. D. A. Berk, F. Yuan, M. Leunig, R. K. Jain, *Biophys. J.* **65**, 2428 (1993).
35. B. A. Smith, H. M. McConnell, *Proc. Natl. Acad. Sci. USA* **75**, 2759 (1978).
36. L. M. Smith, B. A. Smith, H. M. McConnell, *Biochemistry* **18**, 2256 (1979).
37. L. M. Smith, J. W. Parce, B. A. Smith, H. M. McConnell, *Proc. Natl. Acad. Sci.*

USA **76**, 4177 (1979).

38. H. R. Petty, L. M. Smith, D. T. Fearon, H. M. McConnell, *Proc. Natl. Acad. Sci. USA* **77**, 6587 (1980).
39. B. A. Smith, W. R. Clark, H. M. McConnell, *Proc. Natl. Acad. Sci. USA* **76**, 5641 (1979).
40. B. A. Smith, *Macromolecules* **15**, 469 (1982).
41. B. Frank, A. P. Gast, T. P. Russell, H. R. Brown, C. Hawker, *Macromolecules* **29**, 6531 (1996).
42. F. Lanni, B. R. Ware, *Rev. Sci. Instr.* **53**, 905 (1982).
43. M. R. Wattenbarger, V. A. Bloomfield, Z. Bu, P. S. Russo, *Macromolecules* **25**, 5263 (1992).
44. M. B. Mustafa, D. L. Tipton, M. D. Barkley, P. S. Russo, F. D. Blum, *Macromolecules* **26**, 370 (1993).
45. J. Davoust, P. F. Davaux, L. Leger, *EMBO J.* **1**, 1233 (1982).
46. H. J. Eichler, P. Günter, D. W. Pohl, *Laser-Induced Dynamic Gratings*; Springer, Berlin, 1986.
47. M. T. Cicerone, F. R. Blackburn, M. D. Ediger, *Macromolecules* **28**, 8224 (1995).
48. E. M. Johnson, D. A. Berk, R. K. Jain, W. M. Deen, *Biophys. J.* **70**, 1017 (1996).
49. J. Tong, J. L. Anderson, *Biophys. J.* **70,** 1505 (1996).
50. A. G. Ogston, *Trans. Faraday Soc.* **54**, 1754 (1958).
51. L. Léger, H. Hervet, F. Rondelez, *Macromolecules* **14**, 1732 (1981).
52. J. A. Wesson, H. Takezoe, H. Yu, S. P. Chen, *J. Appl. Phys.* **53**, 6513 (1982).
53. Y. Guo, S. J. O'Donohue, K. H. Langley, F. E. Karasz, *Phys. Rev. A* **46**, 3335 (1992).
54. W. Schaertl, K. Tsutsumi, K. Kimishima, T. Hashimoto, *Macromolecules* **29**, 5297 (1996).
55. K. W. Rhee, D. A. Gabriel, C. S. Johnson, Jr. *J. Phys. Chem.* **88**, 4010 (1984).
56. J. A. Wesson, I. Noh, T. Kitano, H. Yu, *Macromolecules* **17**, 782 (1984).
57. D. W. Schaefer, A. J. Hurd, D. K. Christen, S. Spooner, J. S. Lin, in *Better Ceramics Through Chemistry III*; Materials Research Society, Pittsburgh, Pa., 1988; p. 305.
58. G. H. Neale, W. K. Nader, *AIChE J.* **19**, 112 (1973).
59. S. Prager, *Physica* (*Utrecht*) **29**, 129 (1963).
60. D. A. Weitz, J. X. Zhu, D. J. Durian, H. Gang, D. J. Pine, *Phys. Scripta* **T49**, 610 (1993).
61. D. J. Durian, D. A. Weitz, D. J. Pine, *Science* **252**, 686 (1991).
62. D. J. Durian, D. A. Weitz, D. J. Pine, *Phys. Rev. A* **44**, R7902 (1991).
63. N. Menon, D. J. Durian, *Science* **275**, 1920 (1997).
64. D. A. Weitz, D. J. Pine, in *Dynamic Light Scattering*; W. Brown, Ed.; Clarendon, Oxford, 1995.

65. G. Maret, P. E. Wolf, *Phys. B* **65**, 409 (1987).
66. D. J. Pine, D. A. Weitz, P. M. Chaikin, E. Herbolzheimer, *Phys. Rev. Lett.* **60**, 1134 (1988).
67. D. J. Pine, D. A. Weitz, J. X. Zhu, E. Herbolzheimer, *J. Phys.* (*Paris*) **51**, 2101 (1990).
68. F. C. MacKintosh, J. X. Zhu, D. J. Pine, D. A. Weitz, *Phys. Rev. B* **40**, 9342 (1989).
69. M. Sernetz, H. R. Bittner, C. Baumhoer, S. Schwarz, H. Willems, in *Characterization of Porous Solids*; K. K. Unger, J. Rouquerol, K. S. W. Sing, H. Kral, Eds.; Elsevier, Amsterdam, 1988; Vol. 39.
70. I. Teraoka, *Macromolecules* **29**, 2430 (1996).
71. A. Dube, I. Teraoka, *Macromolecules* **30**, 5352 (1997).
72. M. Sernetz, H. R. Bittner, H. Willems, C. Baumhoer, in *The Fractal Approach to Heterogeneous Chemistry*; D. Avnir, Ed.; John Wiley, New York, 1989.
73. T. F. Kosar, R. J. Phillips, *AIChE J.* **41**, 701 (1995).
74. D. D. Kong, T. F. Kosar, R. J. Phillips, S. R. Dungan, *AIChE J.* **43**, 25 (1997).
75. N. Bochner, J. Pipman, *J. Phys. D* **9**, 1825 (1976).
76. J. Szydlowska, B. Janowska, *J. Phys. D* **15**, 1385 (1982).
77. Catalog/Handbook of Fine Chemicals, Aldrich Chemical Co., Milwaukee and Acros Organics Handbook of Fine Chemicals, Fisher Scientific, Pittsburgh.

8. X-RAY IMAGING

Mary E. Coles
Mobil Exploration and Production Technical Center
Dallas, Texas

8.1 Introduction

X-ray imaging was originally developed within the medical sector [1–5] and has since found wide applications within the petroleum [6–26] and other [22, 23, 28, 29] industries. X-ray imaging has been shown to be a valuable tool because it provides the ability to nondestructively identify and evaluate internal structural characteristics and fluid distributions within porous media systems. X-ray imagers offer researchers the capability of rapid, nondestructive visualization and analysis of the internal structure of porous materials and experiments involving porous material systems. Within petroleum industry, x-ray imaging is used to study porous rock samples (cores) obtained from oil and gas reservoirs, with applications in both the area of core analysis and petrophysics and multiphase fluid flow.

X-ray images of sleeved and preserved cores, are used to select representative samples as well as to identify and characterize fractures, inhomogeneities, and zones of mud invasion [9, 11, 12, 17]. Bedding planes or other depositional features, identified in x-ray scans, are often used to orient the core for proper slabbing [9, 17]. X-ray scanning of core plugs for nonuniformities or induced damage prior to special core analysis tests helps to ensure the validity of results. The ability to spatially quantify the distribution of fluids using x-ray imaging is utilized in a wide variety of fluid flow experiments [7, 10, 13–15] and also to verify experimentally measured quantities [16, 21, 22].

This chapter discusses the use of x rays to characterize porous media systems and to quantify fluid distributions within these systems. The process of x-ray attenuation within sample materials, which is the basis of all x-ray imaging, is presented. This is followed with a description of one-dimensional x-ray profile measurement and two-dimensional digital radiographic imaging. Computed tomography (CT) scanning which provides three dimensional information is also presented. Specific examples of x-ray imaging and applications are presented.

EXPERIMENTAL METHODS IN THE PHYSICAL SCIENCES
Vol. 35
ISBN 0-12-475982-3

ISSN 1079-4042/99 $30.00

8.2 Nature and Attenuation of X Rays

As illustrated in Fig. 1, during the x-ray imaging process, the attenuation of an x-ray beam is measured as it passes through a sample material. The detector may be a single element, a linear array, a two-dimensional array, or a charge-coupled device (CCD) with an image intensifier, depending on the specific imaging system and application. X rays are a specific form of electromagnetic radiation as are radio waves; microwaves; and infrared, visible light, ultraviolet, and gamma rays [1, 30]. In the energy range typical of the x rays utilized in most x-ray imaging systems (generally 50–150 keV), there are two mechanisms by which x rays interact with and are attenuated by matter. These mechanisms are the photoelectric effect and Compton scattering [1, 30].

In photoelectric scattering, if the binding energy (energy that holds the electron to the atom) of the photon is greater than the binding energy of the electron, the photon may interact with the electron, giving up all of its energy. During the interaction, the photon ceases to exist and the electron acquires enough energy to escape from its shell around nucleus. The probability of a photoelectric interaction varies inversly as the third power of the energy in excess of the binding energy of the atom and is proportional to the third power of the atomic number [1, 30]. This means that the amount of attenuation that results from photoelectric absorption is very dependent on the chemical composition of the material (higher atomic mass, higher attenuation) as well as the energy of the x ray. As the energy is lowered, photoelectric absorption increases. This is shown schematically in Fig. 2a.

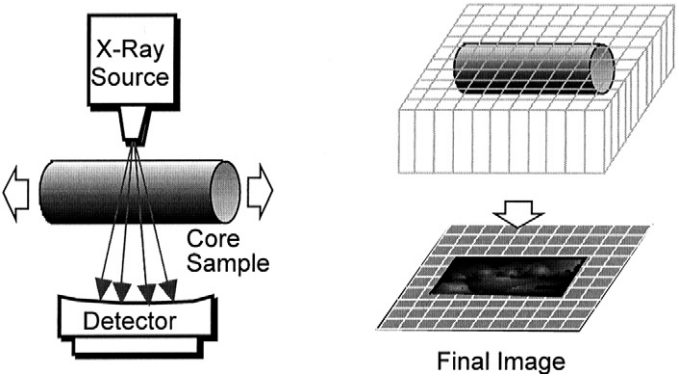

FIG. 1. X-ray attenuation measurement. During the x-ray imaging process, the attenuation of an x-ray beam is measured as it passes through a sample material.

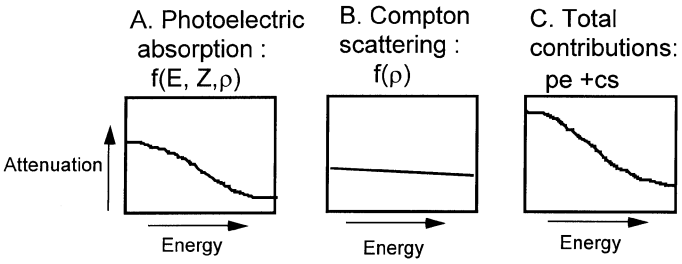

FIG. 2. Components of x-ray attenuation. (a) The amount of x-ray attenuation that may arise as a result of photoelectric interaction with the material is critically dependent on the energy of the x-ray beam and is a function of both the atomic number and the bulk density of the material. (b) The x-ray attenuation that results from Compton scattering within the material is relatively independent of the scanning energy of the x-ray beam and is primarily a function of the bulk density of the material scanned. (c) With the relative contributions of photoelectric absorption and Compton scattering, the total signal depends on the bulk density and atomic number of the material and on the x-ray energy.

During Compton scattering, a photon strikes an electron, knocking the electron out of the atom. The incident photon does not disappear, but is deflected or scattered with some partial loss of energy and may interact with subsequent atoms. The probability for a Compton interaction depends on the electron density of the material and is relatively independent of the atomic number [1, 30]. A Compton interaction is somewhat dependent on energy but less so than with photoelectric interaction (Fig. 2b).

When a parallel monochromatic x-ray beam passes through a substance of uniform density and atomic number, it is attenuated in an exponential manner such that:

$$I/I_0 = \exp^{-\mu x} \tag{1}$$

where I/I_0 is the attenuation or the fractional decrease in x-ray intensity per unit length of the specific material, x is the thickness of the material, and μ is defined as the total linear attenuation coefficient such that

$$\mu = \eta(\sigma_{pe} + \sigma_{cs}), \tag{2}$$

where η is the number of atoms per unit length and σ_{pe} and σ_{cs} are the photoelectric and Compton cross sections for the material. The total linear attenuation coefficient μ is governed by the extent to which both photoelectric and Compton scattering occurs and is therefore a function of the atomic number and bulk density of the material and the energy of the prob-

ing x rays and can be calculated for a given material and photon energy [31].

The attenuation of a beam of x rays through a mixture of different materials is given by

$$A = \left(\ln \frac{I}{I_0} = \sum_i - \mu_i \phi_i \chi_i \right) \tag{3}$$

where μ_i and χ_i are the linear attenuation coefficient and path length of the ith material, and ϕ_i is the volume fraction of the ith material in the path of the x ray. The x-ray attenuation, as measured with a specific source, sample, detector location, and x-ray energy is referred to as x-ray projection data.

For x-ray attenuation through a heterogeneous sample, an average attenuation coefficient can be defined as

$$\bar{\mu} = \sum_i \phi_i \mu_i, \tag{4}$$

where ϕ_i is the volume fraction of the item material in the path of the x ray.

8.3 X-Ray Profile Measurement

One-dimensional, x-ray attenuation profiles can be obtained by translating the x-ray source and detector with respect to the sample material and measuring the x-ray projection data as a function of distance (see Fig. 1). Here, an x-ray attenuation profile can be obtained using a single element detector and measuring the attenuation through the sample as the sample is translated relative to the source and detectors. The x-ray radiation passes a single time through the entire thickness of the sample and the x-ray attenuation is recorded as a function of the position.

X-ray attenuation profiles provide rapid nondestructive, noninvasive, and easily automated probing of core material systems. Porosity, bulk density and *in situ* fluid saturation profiles (such as those shown in Chapter 4 of this book) are easily obtained. Often, x-ray profiles are obtained in combination with other experimental data to ensure the validity of experimental conditions. For example, Potter and Groves [16] utilized x-ray attenuation measurements to determine saturation profiles. This information was used to decide when steady-state conditions had been reached and instigated changing of fluid injection ratios in automated permeability measurements. Maloney and Dogget [26] were able to identify and correct dehydration occurring during desaturation of a core sample for resistivity measurements. X-ray profiles obtained in conjunction with electrical resistivity experiments revealed [22], under some conditions, nonuniform saturations along the

length of the core that could be correlated to anomalies in the log–log crossplot of resistivity vs water saturation.

8.4 Digital Radiographic Imaging

Two-dimensional radiographic imaging has long been in use within the medical sector (chest radiographs) and the nondestructive testing arena [28, 29]. Here, x-ray radiation is generated, passed through a test object, and imaged on radiographic film. Differences in the attenuation of the x-ray beam resulting from atomic number and density differences within the test object are recorded on the radiographic film.

For many applications, it is more convenient to collect and store the digital projection attenuation information using a moving linear array or CCD array detector with an image intensifier, producing a two-dimensional image, as shown in Fig. 1. This is referred to as digital radiographic imaging. Digital radiographic imaging is a very rapid and, under some conditions, a very accurate method of determining two-dimensional porosity and fluid distributions within porous material [24, 25].

Although digital radiographic imaging is very rapid, true three-dimensional internal spatial detail may at times be difficult to distinguish, as separate features within the porous material may overlap in the projected image, thereby reducing the effective resolution. Accuracy may also be compromised if the size of the detector elements are not at least as small as the features of interest [25]. Geometry effects, such as differences in the thickness of the test object, may be significant and may obscure features of interest.

8.5 Computed Tomography Imaging

Computed tomography imaging is a technique for obtaining cross-sectional images of an object from multiple projections of a collimated beam of radiation (x rays) passing through that object. Use of CT has increased dramatically in recent years for a variety of applications within the petroleum industry. Computed tomography enables three-dimensional images to be obtained of porous media systems in a nondestructive, noninvasive, and rapid manner. Often medical scanners are utilized because of their availability and ease of use.

As shown in Fig. 3, during the course of a single tomographic scan, multiple x-ray projection data sets are obtained by measuring the x-ray attenuation induced by the sample material for a multitude of locations

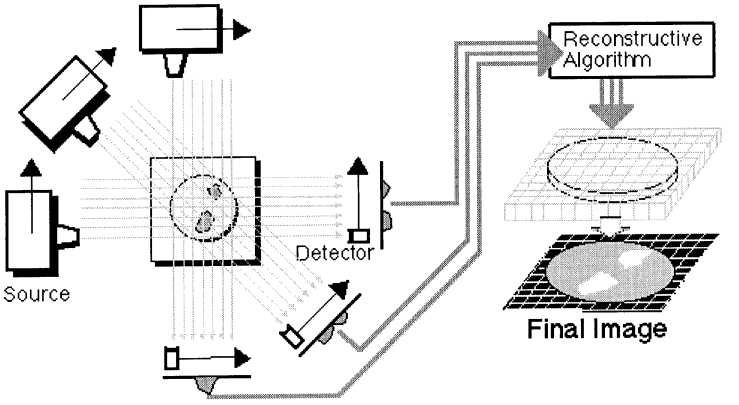

FIG. 3. X-ray computed tomography. Projection data are obtained about a sample in a plane perpendicular to the motion of the scan. A cross-sectional reconstructed image is generated representing the x-ray attenuation in specific volume elements of the material.

around the sample, within a plane perpendicular to the motion of the scan. Using the x-ray projection profiles, a cross-sectional reconstructed image is generated that represents the x-ray attenuation in specific voxels (three-dimensional volume elements) of the material [32]. A computer system controls the CT scanning, receives attenuation information, reconstructs the CT image, and presents the image on a computer screen.

In the tomographic image shown in Fig. 4, light areas represent high x-ray attenuation (high density or atomic number) and darker areas represent low x-ray attenuation (low density or atomic number). Although the tomographic image is represented as pixels, having no thickness, it is important to recall that each attenuation value portrayed in the CT image is associated with a specific cross-sectional pixel size and finite slice thickness (creating the voxel). Slice thickness can vary from 1.5 to 10 mm. For voxels that contain more than one component, the measured CT number will depend on the volume fraction occupied by each component. This partial volume effect [1] serves to limit the sensitivity and resolution when scanning (Eq. [4]) many heterogeneous systems.

The geometrical scanning arrangement employed in obtaining x-ray projection data at different angles is often referenced to one of five successive generations of CT scanners [1]. Changes in successive generations have been primarily driven by the need to reduce scan and exposure times for medical applications and may not necessarily reflect sensitivity or resol-

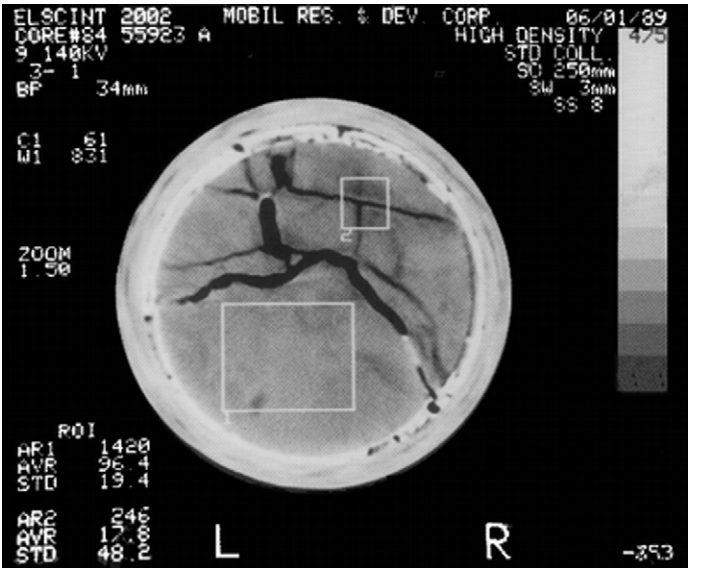

FIG. 4. A CT Image. Light indicates high density–atomic number areas (relatively opaque to x rays), and dark indicates low density–atomic number areas (relatively transparent to x rays). Information concerning scanning conditions is often placed directly on the x-ray image. Knowledge of the scanning conditions is necessary for a comparison of images.

utions enhancements for nonmedical applications. Schematic diagrams representing the movements associated with different generational scanning geometries are provided by Morgan [1].

Hard copy output is often x-ray film. Most systems now allow access to an auxiliary image processing system for digital image manipulation and processing. Often image processing is carried out on a separate system, after transfer of the image data.

Most medical scanners can operate up to 140 keV (voltage on the x-ray tube) with a lower limit established by the attenuation of the material to be scanned. Access to high x-ray energies is important for petroleum applications, because core material is highly attenuative compared to samples for which most medical scanners were designed. Some high-energy systems (greater than 300 keV) are entering the market, but are relatively cost and accessibility prohibitive.

Generally, the linear attenuation coefficient μ is normalized to that of a standard material (such as water). This is defined as the CT number of the

material:

$$\text{CT number} = \frac{\mu_{\text{material}} - \mu_{\text{standard}} \cdot K}{\mu_{\text{standard}}}, \tag{5}$$

where K is a scaling factor, set as a matter of convention to either 500 or 1000. This converts all the attenuation coefficients into integers, where the baseline or reference value is assigned to the linear attenuation coefficient of the standard for the specific x-ray voltage used. CT values that are less than the CT value of the standard imply an attenuation value less that the attenuation of the standard. CT values greater than the CT value of the standard imply an attenuation value less that of the standard. This is discussed in more detail by Morgan [1].

In addition to a tomographic or slice image, many scanners are enabled to produce an x-ray digital radiographic image by holding the position of the source and detectors constant and translating the sample with respect to the plane containing the source and detectors. This (Fig. 1) is often referred to as a preview or surview scan. As with all digital radiographic imaging, the x-ray radiation passes a single time through the entire thickness of the sample and the x-ray attenuation is recorded as a function of the position. Medical scanners that are able to produce this type of projection radiograph, in addition to the tomographic or slice type image, are called "full-body scanners." With the digital radiographic mode, a large amount of core material can be scanned and imaged very rapidly; however, the ability to obtain spatial information or discern regions with small differences in x-ray attenuation is greatly diminished.

Features of tomographic and digital radiographic images are compared in Table I. Generally, both scanning modes are employed. Digital projection

TABLE I. Comparison of Tomographic and Digital Radiographic Scanning

Scanning Mode	Motion	Image produced	Notes
Slice	Source detectors move	Cross-sectional	Obtains full spatial information; able to discern regions of low attenuation contrast
Digital radiography	Sample translates	Traditional radiograph	Rapid scan of entire core; often used to preview, locate position; does not provide true 3-D information, gives 2-D average

images are obtained to identify areas of interest or to view rapid processes; tomograms (slices) are obtained for full spatial information or to view areas of lower attenuation contrast.

8.6 X-Ray Imaging Techniques

8.6.1 Effect of X-Ray Energy

Core material is very attenuative compared with typical biological tissue samples. The use of an x-ray beam that is too low in energy often results in overattenuation of the x-ray beam, insufficient signal-to-noise level measured at the x-ray detector system, and a grainy image when scanning core material. Generally, to optimize the image quality, it is helpful to use the maximum voltage (creates highest energy) and current (creates maximum photon flux) possible for a given imaging system. Use of lower-energy x rays is necessary, however, when photoelectric attenuation must be optimized (for example, in scanning for atomic energy differences or dual energy scanning where differences in the Compton and photoelectric attenuation of the material enables one to solve two simultaneous equations). Because attenuation is highly dependent on the energy of the x rays utilized, this information must always be provided.

8.6.2 Spatial and Contrast Resolution

X-ray images represent discrete x-ray attenuation information within specific volume elements of a sample. Therefore, inherent in each image are the concepts of spatial resolution and contrast resolution.

Spatial resolution refers to the ability to resolve as distinct two or more closely spaced high contrast objects. This is illustrated in Fig. 5a. Objects within the sample will not appear as resolved as separate features if the distance between them is less than the resolution of the system. Separate features present within the core material may not be identifiable as separate, but will appear as a single, spatially averaged feature. The theoretical resolution limit for any imaging system is controlled by the spatial specificity and accuracy of ray paths through the sample. The uncertainty is determined by the operative size of the source and detectors, their distance from the sample, and the ability to obtain sufficient independent projection information. In digital radiographic scanning, only one projection is obtained; therefore, the attenuation represents the average along the x-ray pathlength and the ability to separate overlapping features is significantly reduced.

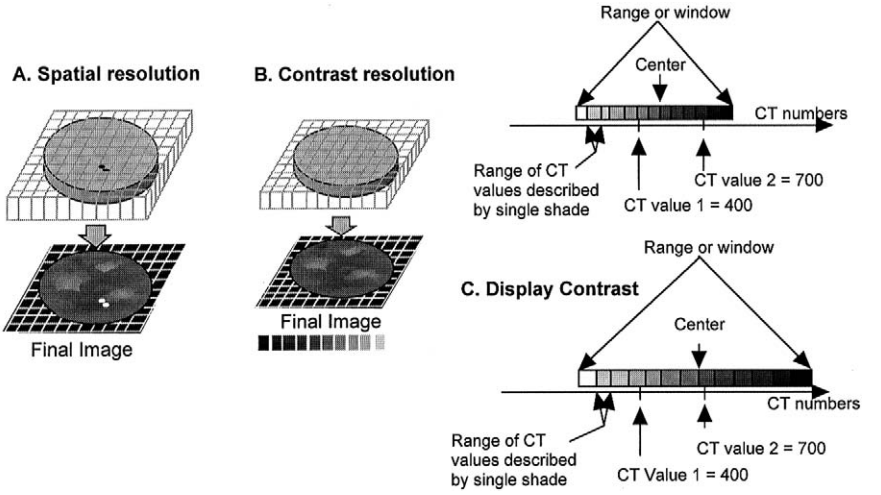

FIG. 5. Spatial and contrast resolution and display contrast: (a) spatial resolution refers to the ability to resolve as distinct two or more closely spaced high-contrast objects, (b) contrast resolution refers to the ability of the imaging system to distinguish small differences in contrast (linear attenuation coefficient) in relation to a homogeneous background, and (c) display contrast or image gray-scale mapping concerns different window (range) and center assignments. Notice that a given shade of gray can represent different CT values with each mapping. Note also that a given CT value can appear as different shades of gray with different mapping (range and center) assignments.

The inability to maintain a sufficient signal-to-noise ratio at small source and detector appatures ($<0.25\,\mu m$) is what actually limits the resolution of commercial medical imagers. Ultra-high-resolution imaging using a very high flux source is described in Section 8.8. Reconstruction and display resolution are generally chosen to match the theoretical limit to minimize unnecessary cost and computation.

8.6.3 Contrast Resolution

Contrast resolution (also referred to as contrast sensitivity) is the capability of the x-ray scanning system to distinguish small differences in contrast (linear attenuation coefficient) in relation to a homogeneous background. This is illustrated in Fig. 5b. The intrinsic resolution in measuring the intensity is a function of the size, shape, and characteristic attenuation of the object; the collimation of the x-ray beam; and detector sensitivity. Contrast resolution is typically expressed as either the smallest difference in x-ray

attenuation that can be discriminated for an object of a particular diameter, or as the smallest diameter of an object with a particular contrast that can be detected. A low-contrast object can be identified if it is large, whereas small objects can be identified if they have a large contrast relative to a homogeneous background. This is due to the partial volume effect, wherein the smaller object must be of significant attenuation contrast to affect the volume or voxel average (Eq. [4]). Knowledge of the contrast resolution (sensitivity) of a given x-ray imaging system enables one to estimate, for example, the smallest difference in bulk density that can be identified with a given instrument.

8.6.4 Display Contrast

The range of attenuation values or CT numbers displayed in a given image is often referred to as the image "window." This range is then mapped to and represented by a discrete number of gray levels to create the image. Generally, many attenuation values or CT numbers are "mapped" to each gray level in an image. For example, in Fig. 4, the window is 831 CT units wide, centered at 61 CT units (listed as "C1" and "W1"). In this image, the range is broken down into 16 bins (shades of gray), where each gray level represents $831/16 = 52$ CT units.

It is important to realize that the gray-scale mapping assignments in a given image are usually optimized by the operator for each image and may not be consistent for several images or image sets. Therefore (since the mapping is rather arbitrary and different imagers have different attenuation response profiles); a given shade of gray on one image may or may not represent the same attenuation value as that same shade of gray in another image. Conversely, a given attenuation value may appear as different colors or shades of gray in different images. This is illustrated in Fig. 5c. This lack of uniformity can make it difficult to compare or quantify images.

The display contrast is affected by the gray-scale-mapping window. As the window of CT numbers (represented by a given number of gray-scale bins) is increased or decreased, the actual number of CT values mapped to the same shade of gray increases or decreases. If the range (window) is large, two CT values that are slightly different in value may appear as the same shade of gray. As the range of numbers (window) is decreased, a smaller range of CT values is represented by a single shade of gray, and these same two CT numbers may be represented by different shades of gray. Therefore, the effective display contrast may be increased up to that allowed by the intrinsic contrast resolution. With a small window, however, it is often difficult to cover the entire range of CT values present in the image. The optimal mapping assignment in any given image is generally a trade-off,

wherein the entire dynamic range (total range of CT numbers of interest) is represented with optimal display contrast (smallest range of CT numbers per shade of gray). Additional mapping options, designed to expand the dynamic range specifically the area of interest are available with external image processing techniques.

Knowledge of the spatial and attenuation resolution of the specific imaging system and of the x ray energy, scanning geometry and display contrast mapping used is needed for proper assessment and analysis of the image.

8.6.5 Beam Hardening

Equation (1) and (3) (in Section 8.2) describes the x-ray attenuation for a monochromatic (single energy or wavelength) source of x rays. However, the x rays produced in any commercially available x-ray scanner are polychromatic (more than one energy). Recall from Section 8.2 that the x-ray attenuation resulting from the photoelectric interaction with a given material significantly increases as the energy decreases. Therefore, with a polychromatic x-ray beam, attenuation (which is the sum of the photoelectric effect and Compton scattering) is not constant for all energies of the x-ray beam, but is higher for the lower energy components of the x-ray beam. This preferential attenuation of the lower energy components of the x-ray beam leads to an effect known as beam hardening. Beam hardening, if not accounted for, results in incorrectly measured attenuation and CT values, which can significantly decrease the accuracy of quantative results.

Beam hardening becomes especially pronounced when dealing with higher attenuating samples such as core material. As the polychromatic x-ray beam passes from the edge of the core material toward the center of the sample, the lower energy components of the x-ray beam are preferentially attenuated, changing the energy distribution of the x-ray beam. When the x-ray beam reaches the center of the sample, the lower energy component could be significantly decreased compared to the higher energy ones. This is referred to as "hardening" of the beam. The net result of this changing beam energy profile, as it passes through the sample, is an increased attenuation at the edges (lower energy components present) with an effectively larger attenuation coefficient and decreased attenuation at the center (less lower energy components present) with a lower attenuation coefficient. Beam hardening can be seen in CT images as a significantly higher attenuation ring or "cupping" at the edges of a core material sample (such an image is shown in Fig. 6).

Beam hardening can be compensated for with improved prereconstruction algorithms [9], or interpolation methods (see Chapter 4). It is often

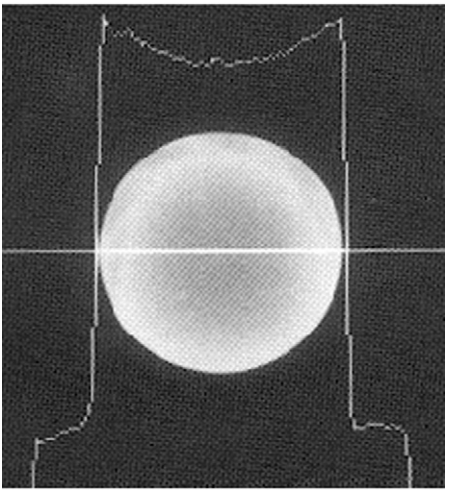

FIG. 6. The Beam hardening effect is seen as a higher attenuation ring or "cupping" at the edge of an imaged object. A profile of the values across the center of the image is shown. Beam harden significantly affects the ability to obtain quantitative information from an x-ray image.

easier to preharden the x-ray beam by surrounding the sample with sand, an attenuating fluid [12], or aluminum when CT scanning. Aluminum rings or an aluminum core holder have been found to adequately preharden the beam and minimize beam-hardening effects [20].

For digital radiographic scanning it is important to maintain consistency in the geometry through which the attenuating x-ray beam travels. Here, differences in attenuation resulting from beam hardening can lead to apparent and incorrect differences in measured x-ray attenuation.

8.6.6 Use of Attenuation Standards

Because of differences in x-ray sources, detectors, and scanning arrangements, attenuation values obtained for a given sample using different imagers will show variation [1]. Additionally, the x-ray source and detectors are prone to day-to-day instrumental drift in their attenuation responses. The effect of the drift on measured attenuation is not predictable and is itself a function of the absolute attenuation measured (greater drift for greater attenuation) [33–35]. This leads to inconsistent and unreliable attenuation values, which, if not corrected, can result in significant errors when these values are used in quantitative calculations. Calibration with attenuation

standards is vital if calculation or comparisons are to be carried out with x-ray attenuation data.

Conventionally, in medical x-ray attenuation measurements, a water sample is used as an attenuation standard. However, this is not sufficient for scanning of higher attenuating core material. Additional standards are necessary for reference attenuating media. A method has been developed to compensate for instrumental differences and drift utilizing secondary attenuation standards to calibrate the attenuation data [33–35]. This method uses secondary attenuation standards to identify and characterize the day-to-day drift of the x-ray source and detectors. Compensating for the drift serves to standardize all attenuation measurements taken in multiday experiments to the same baseline attenuation.

The reference material must be of uniform density and composition and should exhibit attenuation characteristics close to that of the material to be measured. To compensate for differing beam-hardening effects, the standard should be the same diameter as the sample material. Several laboratories have previously used aluminum as a secondary reference because it is uniform in composition and attenuates slightly more than most core systems [11, 12, 20]. Fused quartz has also come to be utilized as a secondary reference [11, 33, 35]. The density and x-ray attenuation characteristics of fused quartz are close to those of many sandstones. Fused quartz is uniform in composition and is readily available through optical supply distributors.

The use of both fused quartz and aluminum provides us with standards of attenuation both lower and higher than most core systems and enables us to adequately compensate for instrumental differences and drift [33–35]. Correction is done prior to calculation of bulk density, porosity, or saturation. Results show significant increases in the accuracy and precision of calculated values when calibration with external attenuation standards is employed [33–35].

Scans of the standards may indicate only a small drift over the period of several days and therefore may require only a small correction, while other sets of standard scans may indicate a rather large drift and require greater correction to maintain accuracy. Calibration is especially important when instrumental drift is large for a series of scans that are subsequently used as a baseline to other scanning days, when the error induced by the instrumental drift is propagated through all subsequent calculations.

Uncorrected instrumental drift leads to inconsistent and unreliable values and underestimation of the accuracy of the x-ray attenuation method. Calibration with external attenuation standards has resulted in significant increases in the accuracy and precision of quantitative values calculated from x-ray attenuation data.

8.6.7 Chemical Dopants

For experiments involving the calculation of fluid saturations, to increase measurement sensitivity, chemical dopants (compounds highly attenuating to x rays due to their high atomic number) are often added to one or more phases or fluids to increase the x-ray attenuation of that phase. Examples of commonly employed dopant materials are listed in Table II. An iodated hydrocarbon can generally be used to dope the oil phase and a bromide or iodide salt can be used to dope the aqueous phase. Xenon gas can be used to tag the gas phase.

When doped solutions are used, care must be taken to ensure that the system to be scanned falls within the working dynamic range of the instrument and is linear in concentration of the dopant. A typical attenuation response as a function of concentration of dopant as shown in Fig. 7. Too low a dopant level does not produce sufficient attenuation contrast, and too high a dopant concentration may decrease the photon flux on the detector to below its detection limits. A nonlinear attenuation response (common with high dopant concentrations) results in a significant error in quantitative calculations.

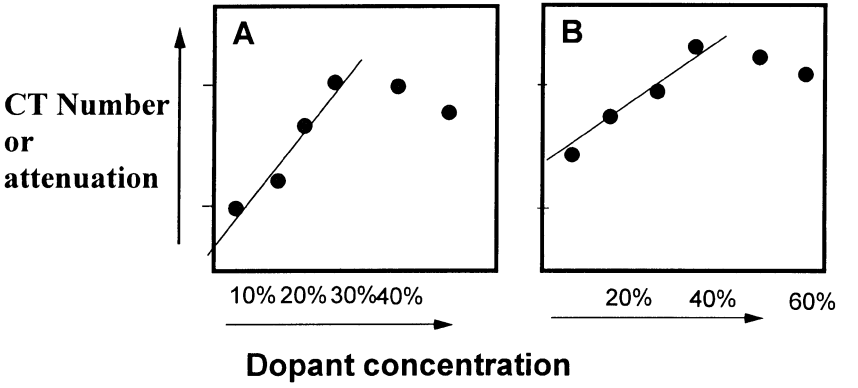

FIG. 7. Dopant linearity: The typical attenuation response as a function of concentration of dopant material for (a) CT number vs concentration of a typical dopant solution and (b) CT number vs concentration of a typical dopant and core material system with approximately 20% porosity. When doped solutions are used, care must be taken to ensure that the system to be scanned falls within the working dynamic range of the instrument and is linear in concentration of the dopant. Too low a dopant level does not produce sufficient attenuation contrast, and too high a dopant concentration may decrease the photon flux on the detector to below its detection limits. Beam-hardening effects increase with dopant concentration.

TABLE II. Common Dopants

Material	CT Number
Barium bromide (10% solution)	295
Sodium bromide (10% solution)	−249
Sodium tungstate (10% solution)	214
Iododecane–hexadexane (50–50)	806
Sodium iodide (saturated)	1477

Measurements made relative to water = −500 CT units.

High levels of dopant materials can significantly increase beam-hardening effects (increased photoelectric attenuation). Any changes in beam hardening induced by the dopant materials must be minimized or corrected if accuracy is to be maintained.

8.7 Applications of X-Ray Imaging

X-ray scanning can be applied to obtain either qualitative (visual) or quantitative (numerical) data. Historically, much of the information obtained from x-ray scanners utilized in both the medical and other industries has consisted primarily of a qualitative, or visual, assessment of the images. In this capacity, the scanner has been utilized within the petroleum industry to identify and evaluate internal structural characteristics and discontinuities of core material and fluid distributions within core material systems.

Qualitative applications are those that require only a visual assessment of the resulting x-ray images. Due to their availability and ease of use, medical imagers are often utilized. The use of such scanners, if they have the appropriate resolution is quite adequate for qualitative applications. Applications include evaluation of core for samples selection, evaluation of core damage, establishment of bedding plane orientation, and plug screening.

8.7.1 Qualitative Application of X Ray Imaging

8.7.1.1 Sample Selection. Perhaps the most common application for CT or radiographic scanning within the petroleum industry is screening of the core prior to sample selection. If samples selected for core analysis tests are not representative of the reservoir material, subsequent work to charac-

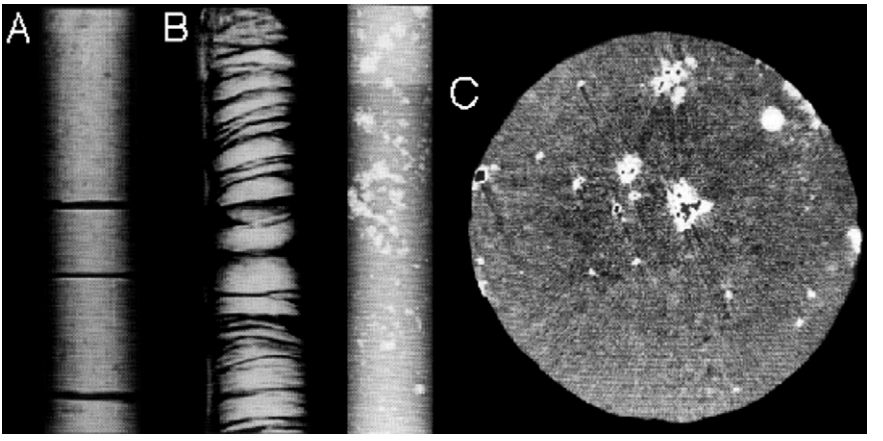

FIG. 8. X-ray screening is often utilized to evaluate a core prior to sampling (a) and to identify and avoid areas of damage (b). Samples need not be removed from rigid PVC or fiberglass core barrel liners, as the x rays pass through the liners with minimal attenuation. Screening for sampling locations is rapid and nondestructive. (c) Pyrite inclusions are readily identifiable in these digital radiographic and tomographic scans as intense white areas. Black areas appearing in the center of the areas of white and streaking of the image in c is due to the intense attenuation of the mineral inclusions.

terize the storage and flow properties of the reservoir utilizing the samples may be of little value. X-ray screening is often utilized to evaluate core prior to sampling (Fig. 8a) and to identify and avoid areas of damaged core (Fig. 8b), thereby facilitating the selection of appropriate sampling intervals. X-ray scanning is also used to identify a core containing nonrepresentative mineralogical inclusions (Fig. 8c), which might bias core analysis measurements. Samples do not need to be removed from rigid PVC or fiberglass core barrel liners as the x rays pass through the liners with minimal attenuation. Screening for sampling locations is rapid and nondestructive.

8.7.1.2 Mud Invasion. Barite, contained in many drilling muds, is highly attenuative to x rays due to the high atomic number of barium. Invasion of drilling mud into porous core material samples is clearly observable in the CT scans shown in Fig. 9. Figure 9a shows mud invaded into the open pore structure of a carbonate sample, and Fig. 9b shows mud invading predominately from lower right side of this image of a pebbly coarse grained sandstone sample. X-ray scanning has been used to identify areas of mud invasion and also to evaluate the utility of improved mud systems, thereby improving core quality.

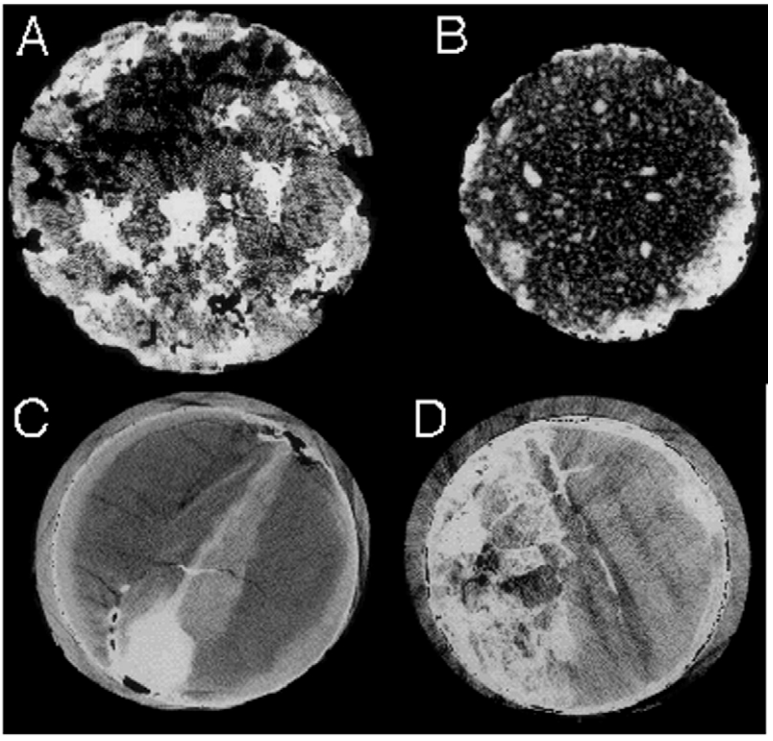

FIG. 9. Mud invasion. Barite, contained in many drilling muds, is highly attenuative to x rays. The presence of drilling mud invasion is clearly observable in these CT images: (a) mud (white) invaded into the open pore structure (black) of a carbonate sample and (b) mud invading predominantly from lower right side of this image of a pebbly coarse grained sandstone sample. (c) and (d) Invasion of barite mud is evident in these CT scans of unconsolidated core (areas of white). In (c), the invasion of a mud filtrate is also evident as lighter areas around the core and across the diagonal of the image.

CT slice images can be stacked together to provide full three-dimensional characterization of core data. Figure 10 shows a image of a three-dimensional data set created by stacking together 19 consecutive tomographic images of a limestone. The open pore space appears as dark, while drilling mud, which has invaded the open pore space, appears opaque white.

8.7.1.3 Core Damage in Unconsolidated Core. The x-ray scanning of core samples has been shown to be particularly useful when dealing with cores obtained from unconsolidated or friable formations, which are especially susceptible to damage or alteration imposed during the coring or

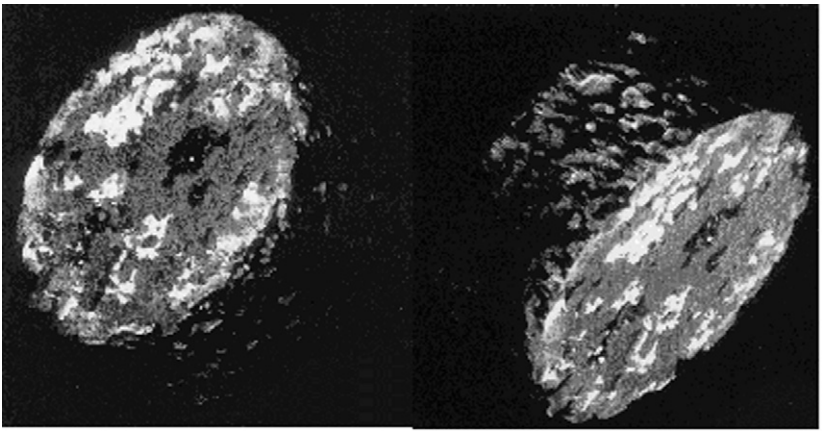

FIG. 10. A 3-D CT. CT slice images can be stacked together to provide full three-dimensional characterization of core data. Shown are images of a three-dimensional data set created by stacking consecutive tomographic images of limestone. The open pore space appears as dark, while drilling mud appears in opaque white.

handling process [17, 27]. X-ray imaging can be utilized to provide clear evidence of fractures (Fig. 11) and invasion of barite mud (Fig. 9c and 9d). Evaluation of damage in fragile, unconsolidated core material utilizing CT scans, has assisted in the identification of those processes that are responsible for damage to the core material and therefore min-

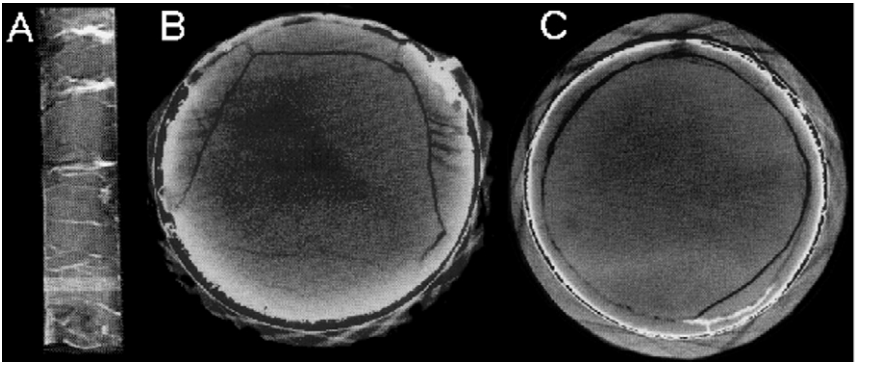

FIG. 11. Core damage. These digital radiographic (a) and CT scans (b and c) of an unconsolidated core show clear evidence of fractures and can assist in the identification of those processes that lead to damage and the minimization of subsequent coring damage [17].

imization of core damage in subsequent coring and core-handling operations.

8.7.1.4 Bedding Plane Orientation. Bedding planes or other depositional features are often apparent in x-ray images (Figs. 12a and 12b). Here density and atomic number differences in sand as opposed to shale gives rise to different x-ray attenuations and appears as alternating light and dark bands in the image. Special core analysis identification of depositional features can be used to orient the core for the proper slab angle [11, 17], thereby enhancing the prediction of reservoir performance from core analysis data.

8.7.1.5 Plug Screening. The special core analysis of core plug samples is relatively expensive. It is estimated that approximately 30% of core plugs obtained from fragile, unconsolidated core material are severely damaged during the plugging process. Damage is generally severe enough to invalidate any special core analysis results. X-ray scanning can be used to identify and evaluate plugging induced damage (see Fig. 12c) or any inhomogenie-

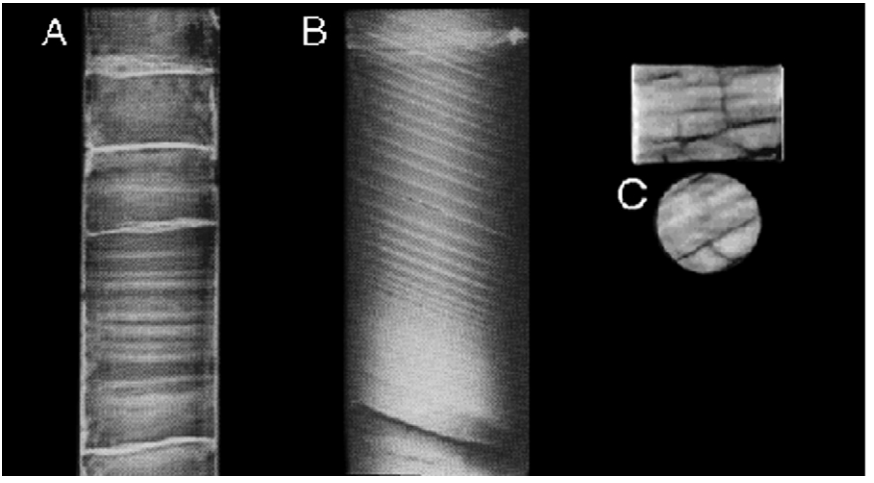

FIG. 12. Bedding planes and other depositional features are often apparent in x-ray images. Density and atomic number differences in sand as opposed to shale give rise to different x-ray attenuations and appear as alternating light and dark bands in these digital radiographic images (a and b). Identification of depositional features can be used to orient the core for the proper slab angle. (c) CT scanning can be used to identify and evaluate plugging-induced damage. Here a fracture is clearly evident down the length and across the face of a core plug, which could affect the validity of special core analysis [17].

ties in the sample, and therefore maintain the validity of special core analysis results.

8.7.2 Quantitative Applications of X-Ray Imaging

X-ray images represent discrete x-ray attenuation information of the material scanned. In addition to qualitative assessment of the x-ray images, quantitative information such as density, atomic number, porosity, and saturation values and distributions can be extracted from CT scan images with appropriate processing and calculations [10, 11, 13, 17, 19, 20, 22–27, 33–39].

Quantitative applications may or may not be possible utilizing scanners located within a medical facility and would depend on scan optimization and consistency, the use of external reference attenuating media, and the ability to access numerical values within the image.

To obtain quantitative (numerical) information, the scanning must be carried out in a careful and consistent manner, followed by some amount of external calculation or manipulation. Significant improvements in the accuracy and reliability of quantitative analysis have been achieved over the last several years [17, 21, 22, 33–36].

As discussed in Section 8.6, to obtain accurate and reliable values, it is necessary to minimize beam-hardening effects and ensure appropriate use of attenuation standards and chemical dopants,

8.7.2.1 Calculation of Bulk Density. Bulk density values can be obtained from x-ray attenuation measurements [9, 11, 20]. For sandstones, bulk density is conveniently estimated utilizing a calibration curve that defines the measured attenuation values for the fused quartz standard and aluminum standards as a function of bulk density. A similar procedure, with appropriate standards (for example, calcite and CaCl solutions), can be used to calculate bulk density for carbonate samples. A fit of the calibration plot can then be used to calculate the bulk density of a sample material from the measured attenuation value. Examples of such calibration plots are shown in Fig. 13. Here, two calibration plots are shown: one for sandstones and one for carbonates. This approach is empirical and depends on the knowledge and consistency of the mean atomic number of the sample material (here one for carbonates, and one for sandstones). This method will not work, for example, if the mean atomic number is different from the standards used to create the calibration line (for example, excessive mineralization of pyrite or hematite or saturation with a doped material).

Bulk density values obtained from CT scan data of several consolidated samples agree well with values obtained utilizing conventional techniques (see Table III). The ability to measure bulk density in specific undamaged

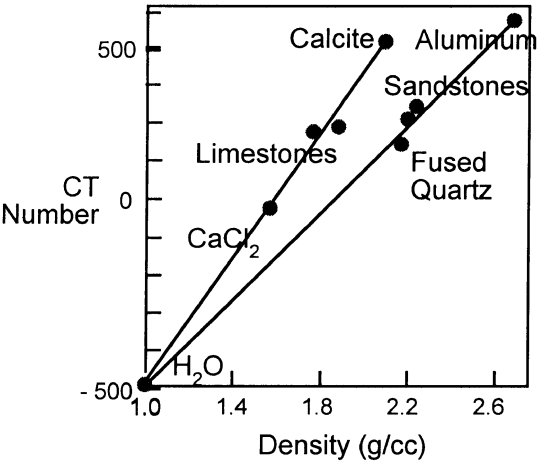

FIG. 13. Bulk density calculations. Bulk density can be calculated from attenuation values by comparison to known standards [33, 34].

or noninvaded areas of a core is particularly useful in the area of unconsolidated core analysis. Specific areas of the image can be selected and utilized to calculate bulk density values. In this manner, erroneous values due to damage or mud invasion of the core material can be avoided. For example, in Fig. 14 bulk density values can be calculated from the CT value within any area of this CT image (see boxes labeled 1 and 2 in the figure). Note the high attenuation of the mud-invaded area (567.6 CT units) verses that of the noninvaded area (112.2 CT units).

As already discussed, if the mean atomic number or composition of the core material system is unknown or highly variable, a simple calibration may not be obtainable or appropriate. A more complicated technique,

TABLE III. Bulk Density Values Calculated from CT Data Compared to Values Obtained with Conventional Techniques

	Measured	
Sample Calculated	Bulk Density (g/cm^3)	Bulk Density (g/cm^3)
Sandstone	2.17	2.11
Sandstone	2.17	2.12
Limestone	2.20	2.26

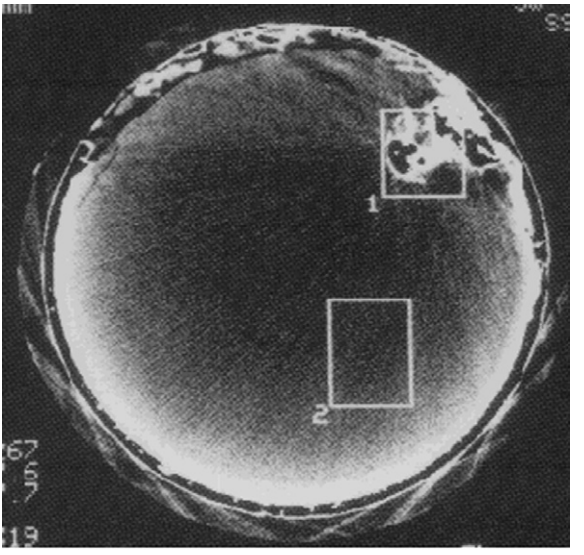

FIG. 14. Specific areas of the image can be selected and utilized to calculate bulk density values. In this manner, erroneous values due to damage or mud invasion of the core material can be avoided. For example, a bulk density value can be calculated from the CT number from area 2 of this CT image. Note the high attenuation of the mud-invaded area within box 1 (567.6 CT units) verses the attenuation within box 2 (112.2 CT units).

involving attenuation measurements obtained at two different scanning energies has been developed [32–34] and is successfully utilized. The use of this method has been found to provide accuracy to within 0.06 g/cm^3 and does not require a priori knowledge of the composition or saturation of the core material.

Bulk density values can be correlated to the density well log [9, 11] and can be used to verify or supplement well log information. Bulk density values were calculated from CT scans of unconsolidated core and were found to agree with the density well log information (recognizing sampling size differences) [11, 36–38].

8.7.2.2 Calculation of Porosity. For CT applications, the CT number (CT_{total}) of a volume element containing rock matrix material and a single fluid can be expressed as a linear combination of the attenuation from each component such that [13]

$$CT_{total} = (1 - \phi)CT_r + \phi CT_f \tag{6}$$

where ϕ porosity of the rock, and CT_r and CT_f are the CT values for the

rock and fluid. If two measurements are made, each with a different fluid occupying the pore space of the rock, these can be described as

$$\mathrm{CT}^1_{\mathrm{total}} = (1-\phi)\mathrm{CT}^1_r + \phi\,\mathrm{CT}^1_f, \tag{7}$$

$$\mathrm{CT}^2_{\mathrm{total}} = (1-\phi)\mathrm{CT}^2_r + \phi\,\mathrm{CT}^2_f, \tag{8}$$

where the superscripts indicate the values obtained when saturated with different fluids. If the x-ray source is assumed to be monochromatic (which we know is an approximation), then the attenuation contributed by the rock material, the $(1-\phi)\ \mathrm{CT}_r$ term, is the same in each case. Subtracting these two equations and rearranging enables one to solve for porosity:

$$\phi = \frac{\mathrm{CT}^1_{\mathrm{total}} - \mathrm{CT}^2_{\mathrm{total}}}{\mathrm{CT}^1_f - \mathrm{CT}^2_f}. \tag{8}$$

If one of the saturation states is the dry rock and the other is fully saturated, Eq. (9) simplifies to

$$\phi = \frac{\mathrm{CT}_{\mathrm{sat}} - \mathrm{CT}_{\mathrm{dry}}}{\mathrm{CT}_f - \mathrm{CT}_{\mathrm{dry}}}. \tag{10}$$

Using this equation, some error may be realized when dealing with extremely attenuating (very highly doped) fluids due to the differences in attenuation imposed by the fluid within the core material, which are not accounted for in the simplifying assumptions. Error will also be realized if the CT values of the two saturated states are not significantly different (for example, low porosity or insignificant attenuation differences of the fluids).

For digital radiography and x-ray attenuation profiling, an analogous relation can be developed [24, 25]:

$$\phi = [(A_f - A_a)/(\mu_a - \mu_f)]/L, \tag{11}$$

where A_f and A_a are the attenuations measured (defined in Eq. [3]) when the sample is air and fluid filled, μ_a and μ_f are the linear attenuation coefficients of the air and fluid, and L is the sample diameter. Here, A_f and A_a are the (averaged) projected attenuation values measured at the detector for a one-dimensional profile or a two-dimensional digital radiographic image.

8.7.2.3 Calculation of Fluid Saturation. Using x-ray attenuation measurements we can accurately determine the saturation and distribution of fluids within a core sample [7, 10, 13–16, 18–25]. The spatial details of fluid saturations can provide information about the effects of viscous fingering, fluid segregation, and the relative permeability of fluids within core materials. Accurate determination of the distribution of fluids is often important when considering the effect on experimentally measured quanti-

ties [16, 22, 26]. Prior to the advent of x-ray technology, this information was determined gravimetrically or volumetrically assuming the saturations were distributed uniformly throughout the test sample. Development of x-ray techniques in recent years has enabled *in situ* determination of fluid saturation distributions and, with appropriate standardization, accurate quantitative saturation values for two- and three-phase systems.

8.7.2.3.1 Two-Phase Saturation. For CT applications, when two immiscible phases (for example oil and water) are present within a core sample, the measured CT number at a given saturation can be described as [9, 11]

$$\mathrm{CT}_{\mathrm{sat}} = \mathrm{CT}_o S_o + \mathrm{CT}_w S_w, \tag{12}$$

where S_o and S_w are the oil and water saturations and CT_o and CT_w represent the CT numbers for the core when it is fully saturated with oil or with water. The entire pore volume is assumed to be totally filled with the fluids, therefore,

$$1 = S_o + S_w. \tag{13}$$

By combining Eqs. (12) and (13), the water saturation can be easily calculated from x-ray attenuation data:

$$S_w = \frac{\mathrm{CT}_{\mathrm{sat}} - \mathrm{CT}_o}{\mathrm{CT}_w - \mathrm{CT}_o}. \tag{14}$$

For digital radiography and x-ray profile measurements, the analogous equation is [24, 25]

$$S_w = \frac{A_{\mathrm{sat}} - A_o}{A_w - A_o}, \tag{15}$$

where A_{sat}, A_o, and A_w are the attenuation values obtained at a given saturation and for the core fully saturationed with oil and water. Oil saturation is calculated as

$$S_o = 1 - S_w. \tag{16}$$

Note $\mathrm{CT}_{\mathrm{sat}}$, CT_o, and CT_w and the analogous, A_{sat}, and A_o and A_w, are measurements obtained at different times. A displacement experiment to change S_w can be very slow, even though the images can be obtained very quickly. Therefore even a moderate uncorrected drift would decrease the accuracy of the calculated saturations [33]. Saturation values along the length of a core, calculated using Eqs. (14) and (16), showed agreement between volumetric and CT results to within one saturation percent when attenuation standards are used [33–35].

Accurate determination of the distribution of fluids is often important when considering the effect on experimentally measured quantities. For example, a primary assumption in obtaining electrical resistivity for calculation of fluid exponent is that the fluid saturation saturation is uniform during electrical measurement. Under some conditions, CT scans have revealed nonuniform saturation along the length of the core sample [22]. Saturation values at specific locations along the core length were calculated using Eq. (14) during the desaturation process. The saturation profiles (see Fig. 15a) showed the formation of a moving front that could be correlated to nonlinearities in the log-log resistivity index–water saturation crossplot. The use of x-ray imaging to characterize saturation distribution during resistivity measurements is also discussed in Chapter 4 of this book.

8.7.2.3.2 Three-Phase Saturation. For CT applications, extending Eq. (13) to a system containing three immiscible phases (gas, oil, and water), the CT number at a given saturation can be described as [10, 39]

$$\mathrm{CT}_{\mathrm{sat}} = \mathrm{CT}_o S_o + \mathrm{CT}_w S_w + \mathrm{CT}_g S_g, \tag{17}$$

where S_o, S_w, and S_g are the oil, water, and gas saturations, and CT_o, CT_w, and CT_g represent the CT number for the core when it is fully saturated with oil, water, or gas. As in the two-phase system, the entire pore volume is

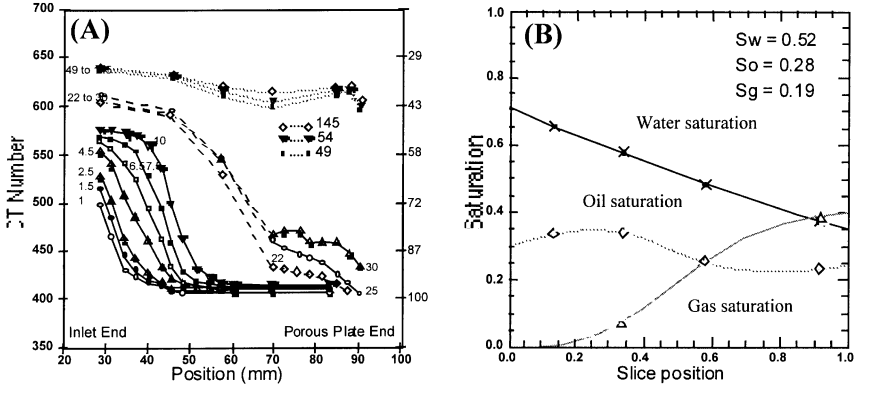

FIG. 15. Two- and three-phase saturation distributions can be obtained from x-ray measurements: (a) two-phase saturations along the length of a core sample during a porous plate desaturation process, where the different profiles were obtained at subsequent times, [22] and (b) the results of dual-energy measurement of three-phase saturation, showing residual oil and gas saturation distributions subsequent to a water flood [35].

assumed to be totally filled with the fluids, therefore,

$$1 = S_o + S_w + S_g. \tag{18}$$

Equations (17) and (18) describe a system that contains three unknowns. To solve for all variables, an additional equation is needed and is generally obtained by scanning the sample at an additional x-ray probing energy. For x-ray scanning at energies 1 and 2, the CT number at each energy can be described as [10]

$$\mathrm{CT}_1 = \mathrm{CT}_{o1} S_o + \mathrm{CT}_{w1} S_w + \mathrm{CT}_{g1} S_g \tag{19}$$

and

$$\mathrm{CT}_2 = \mathrm{CT}_{o2} S_o + \mathrm{CT}_{w2} S_w + \mathrm{CT}_{g2} S_g, \tag{20}$$

where S_w, S_o, and S_g are the saturations of water, oil, and gas; CT_{ij} is the measured CT number of sample fully saturated with fluid i for x-ray energy j; and CT_j is the measured attenuation value (or CT number) of sample of unknown saturation for x-ray energy j.

If we define $\mathrm{CT}' = \mathrm{CT} - \mathrm{CT}_g$, then the saturations are

$$S_w = \frac{\mathrm{CT}'_{o2}\mathrm{CT}'_1 - \mathrm{CT}'_{o1}\mathrm{CT}'_2}{\mathrm{CT}'_{o2}\mathrm{CT}'_{w1} - \mathrm{CT}'_{o1}\mathrm{CT}'_{w2}}, \tag{21}$$

$$S_o = \frac{\mathrm{CT}'_{w1}\mathrm{CT}'_2 - \mathrm{CT}'_{w2}\mathrm{CT}'_1}{\mathrm{CT}'_{o2}\mathrm{CT}'_{w1} - \mathrm{CT}'_{o1}\mathrm{CT}'_{w2}}, \tag{22}$$

$$S_g = 1 - S_w - S_o. \tag{23}$$

Analogously, three-phase saturation values can be calculated from x-ray attenuation measurements obtained from x-ray profile or digital radiographic information as [24, 25]

$$S_w = \frac{A'_{o2}A'_1 - A'_{o1}A'_2}{A'_{o2}A'_{w1} - A'_{o1}A'_{w2}} \tag{24}$$

and

$$S_o = \frac{A'_{w1}A'_2 - A'_{w2}A'_1}{A'_{o2}A'_{w1} - A'_{o1}A'_{w2}}, \tag{25}$$

A' is defined as $A - A_g$ and the subscripts o and w and 1 and 2 refer to the fully saturated measurements at different energies.

Vinegar and Wellington [10] reported a technique for calculating saturation distributions in a three-phase system using dual-energy scanning techniques and discuss the dopant requirements for maximum sensitivity. As shown in Fig. 15b, Sandor and Hove [39] have accomplished three-phase

saturation measurements to obtain residual oil and gas saturation distributions subsequent to a water flood. A brine doped with sodium tungstate and oil doped with iododecane were utilized. Energies employed were 70 and 110 keV.

When obtaining three-phase information using these dual-energy saturation techniques, dopant type and concentration levels and scanning energies must be optimized for the relative saturation ranges of the fluids. As a practical matter, it is not always possible to obtain maximum sensitivity for all concentration ranges in a given three-phase system. Alternatively, a flow strategy can be designed in which one of the fluid phases can be maintained constant and immobile. Such a strategy has been employed by maintaining irreducible water saturation constant and immobile within a Berea core sample and flooding with gas, then with oil [21, 33]. The calculated saturations compare well with volumetric measurements to within one saturation unit.

Figure 16 shows a volume data set created by stacking together the CT slices obtained of S_{iw} subsequent to oil and gas flooding. Notice the nonuniform saturation along the length and across the face of the core. This

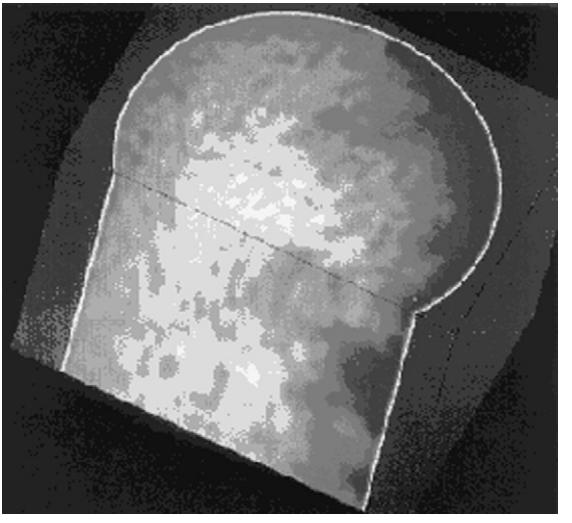

FIG. 16. Volume data set of three-phase distributions created by stacking together subsequent CT slices [33]. Light, medium, and dark shades indicate oil, water, and gas saturations. Notice the nonuniform saturation along the length and across the face of the core. This spatial information concerning saturation distributions facilitates quality control and understanding of experimental results.

spatial information concerning saturation distributions was not available before CT techniques and facilitates quality control and understanding of experimental results.

8.8 Ultra-High-Resolution CT

Computed microtomography [40–43] (CMT) offers unique imaging capabilities compared with conventional optical and electron microscopes or nuclear magnetic resonance (NMR) imaging. CMT is analogous to medical x-ray CT scanning and produces images with a much higher spatial resolution. Synchrotron x rays, generated in a storage ring for relativistic electrons, provide an x-ray beam of extremely high flux (about 10^6 times higher than conventional x-ray tube sources). This high flux (in photons per square centimeter) enables the operative size of the source and detector to be very small (slit width of the order of a micron) and still maintain a sufficient signal-to-noise ratio, making synchrotron x rays ideal for microtomography. With synchrotron x-ray CMT, three-dimensional maps of linear x-ray attenuation coefficients inside small samples can be obtained with about 1% accuracy and resolution approaching 1 μm [40, 43].

There has been interest in using synchrotron x-ray CMT for the characterization of porous media for geological applications [44–49]. Advantages include very high spatial resolution (reported 5 μm), narrow energy band (less artifacts), and tunability (increased sensitivity and mineralogical information). CT and microtomographic images of three sandstones are shown in Fig. 17. Histograms, showing the frequency of attenuation values contained within the respective images are also presented. The CT spatial resolution was $0.25 \times 0.25 \times 3\,\text{mm}^3$ and the spatial resolution for the CMT was $5 \times 5 \times 5\,\mu\text{m}^3$. The microtomograms clearly show pores, structural features, and mineralogical distributions not visible with the resolution of the CT scanner. The higher resolution of the CMT images are reflected in their histograms, which show clearer feature separation than the CT histograms. The high resolution offered by CMT enables porosity calculations directly from the histogram of a single microtomographic image. Mineral distributions can be identified as different attenuation values (different shades) in the microtomographic images of Fig. 17.

Three-dimensional characterization of core samples can be obtained by stacking together multiple CMT slices or imaging using a high-resolution CCD array [50, 51]. A volume data set, created from consecutive CMT slices of a 3-mm-diameter sandstone sample is shown in Fig. 18a. A large set of information useful in modeling properties of and processes in porous media can be obtained from CMT data. Spatial correlation and pore space

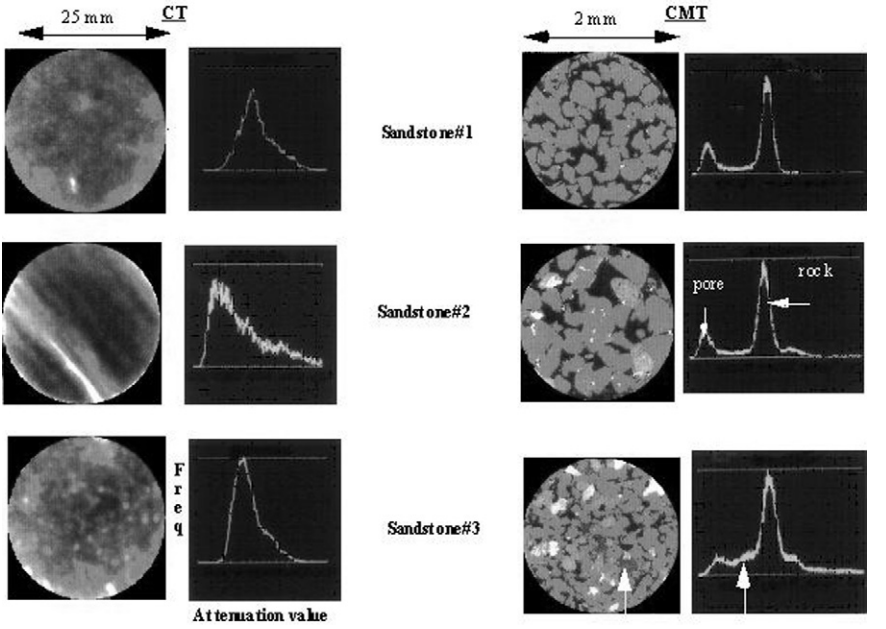

FIG. 17. CT scans and microtomograms of sandstone samples. CT samples were 2.54 cm and CMT samples were 2 mm in diameter. Note the greatly increased resolution and measurement sensitivity in the CMTs. Arrows on "Sandstone # 3" image indicate the effect of porosity arising from pores smaller than the resolution of the microtomogram. Different minerals evident in the computed microtomograms can be identified by comparing their attenuation coefficients represented in the image to those obtained from microtomograms of known mineral samples [46, 47].

interconnectivity can be conveniently represented and characterized with such volumetric tomographic data [52, 53]. For visualization of the pore space using computer image processing, the rock matrix material can be set to be transparent and the pore space can be represented as interconnecting pathways. This is illustrated in Fig. 18b. Here, different shades correspond to connected pathways of the pore network.

Simulation of capillary-dominated displacements is possible on arbitrarily complex CMT pore systems using percolation and network modeling concepts [52–54]. Microtomographic images of real rock can serve as boundary conditions for rigorous fluid flow modeling [50, 54–56]. Pore level images of endpoint saturations (Fig. 19) have been obtained with microtomographic techniques [50, 55–56], providing for the first time three-dimensional imaging and characterization of fluid transport through the pore structure. Pore level images of endpoint saturations were found to

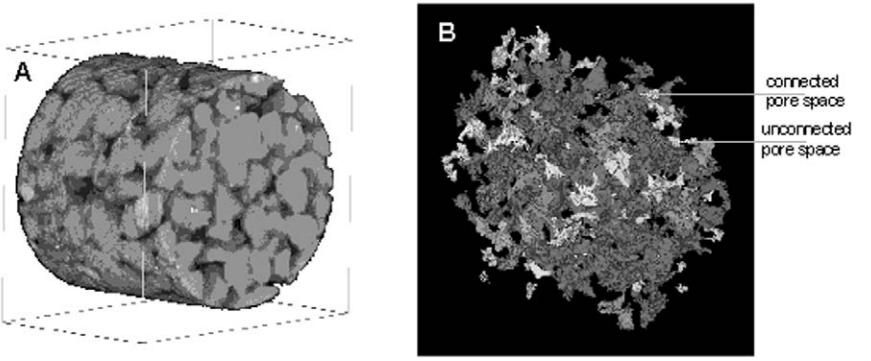

FIG. 18. Volume computed microtomography. (a) A three-dimensional microtomographic image data set of a 3-mm-diameter 1 D (darcy) sandstone sample. Resolution is $20 \times 20 \times 20\,\mu$m. (b) The rock matrix has been made transparent and interconnectivity is shown as the number of independent clusters of porosity elements. Calculated permeabilities compare well with plug permeabilities [46, 47].

agree well with predictions using computational fluid dynamics and network modeling techniques. With computed microtomography, opportunities therefore exist to significantly impact the description and understanding of fluid transport properties within core material systems.

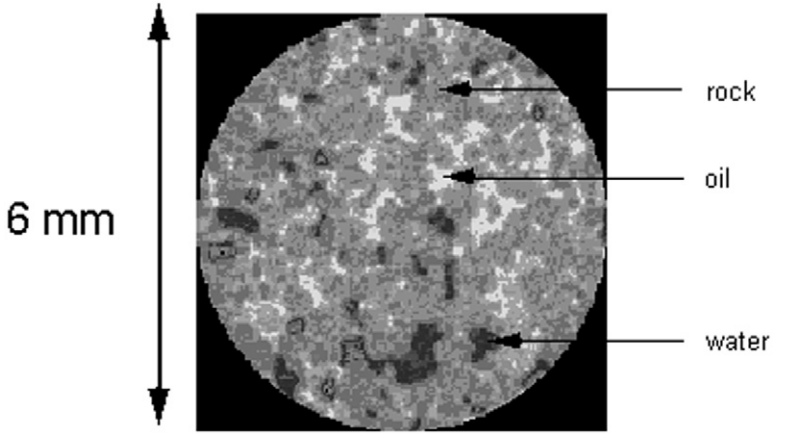

FIG. 19. Endpoint saturation images following a displacement process obtained using synchrotron x rays. This image was obtained after flooding to residual oil under capillary-controlled conditions. Oil and water are clearly visible within the core material (as indicated) in this 20 D sandstone [51].

8.9 Summary

X-ray imaging is invaluable in providing information about the internal structure and saturation distributions within porous materials. X-ray scanning is versatile, rapid, and noninvasive and can be utilized to address problems in the area of core analysis and petrophysics as well as fluid displacement processes in reservoir core material. X-ray scans provide qualitative (visual) assessment of core materials and with the proper use of attenuation standards and dopant materials, quantitative information such as bulk density, porosity, and fluid saturations can be calculated from x-ray attenuation data. The development of ultra-high-resolution computed microtomography provides three-dimensional, pore level characterization and imaging of core material and fluid transport processes.

References

1. C. L. Morgan, 1983, *Basic Principles of Computed Tomography*, University Park Press.
2. A. C. Kak and M. Slaney, 1987, *Principles of Computerized Tomographic Imaging*, IEEE Press.
3. R. A. Brooks and G. Di Chiro, 1975, "Theory of Image Reconstruction in Computed Tomography," *Comput. Tomogr.*, 177, 561–715 (December 1975).
4. R. A. Rutherford, B. R. Pullan, and I. Isherwood, "Calibration and Response of an EMI Scanner," *Neuroradiology* 11, 7–13 (1976); "Measurement of Effective Atomic Number and Electron Density Using an EMI Scanner," *Neuroradiology* 11, 15–21 (1976).
5. L. Dubal and U. Wiggli, "Tomochemistry of the Brain," *J. Comput. Assist. Tomogr.*, 1:300–307, (1977).
6. Y. Wang, S. Ayral, and C. C. Gryte, "Computer-Assisted Tomography for the Observation of Oil Displacement in Porous Media," *Soc. Petr. Eng. J.*, pp. 53–55 (February 1984).
7. S. L. Wellington and H. J. Vinegar, "CT Studies of Surfactant-Induced CO_2 Mobility Control," SPE, 14393, presented at the 60th Annual SPE of AIME Tech. Conf., Las Vegas, September 22–25, 1985.
8. S. Y. Wang, Y. B. Huang, V. Pereira, and C. C. Gryte, "Application of Computed Tomography to Oil Recovery from Porous Media," *Appl. Opt.* 24(23), (1985).
9. H. J. Vinegar, "X-Ray CT and NMR Imaging of Rocks," *JPT*, pp. 257–259 (March 1986).
10. H. J. Vinegar and S. L. Wellington, "Tomographic Imaging of Three Phase Flow Experiments," *Rev. Sci. Inst.* 58(1), 96–107 (1987).
11. S. L. Wellington and H. J. Vinegar, "X-Ray Computerized Tomography," *JPT*, 885–898 (August 1987).

12. P. K. Hunt, P. Engler, and C. Bajsarowicz, "Computed Tomography as a Core Analysis Tool: Applications and Artifact Reduction Techniques," SPE, 16952, presented at the 62nd Annual Tech. Conf. of Soc. of Pet. Eng., Dallas, September 27–30, 1987.
13. E. M. Withjack, "Computed Tomography for Rock-Property Determination and Fluid-Flow Visualization," SPE 16951, presented at the 62nd Annual Tech. Conf. of Soc. of Pet. Eng., Dallas, September 27–30, 1987.
14. A. O. Hove, J. K. Ringen, and P. A. Read, "Visualization of Laboratory Corefloods with the Aid of Computerized Tomography of X-Rays," *SPE Res. Eng.* pp. 148–154 (May 1987).
15. A. O. Hove, V. Nilsen, and J. Leknes, "Visualization of Xanthan Flood Behavior in Core Samples by Means of X-Ray Tomography," SPE–DOE 17342, presented at the SPE–DOE Enhanced Oil Recovery Symposium, Tulsa, April 17–20, 1998.
16. G. Potter and D. Groves, "Displacements, Saturations, and Porosity Profiles from Steady-State Permeability Measurements." SPE 19679 presented at the 64th Annual Technical Conference and Exhibition of the SPE, October 8–11, 1989.
17. R. E. Gilliland and M. E. Coles, "Use of CT Scanning in the Investigation of Damage to Unconsolidated Core," SPE 19408, presented at the 9th SPE Formation Damage Contr. Symp., Lafayette, La., February 2–23, 1990.
18. E. J. Peters and W. D. Hardham, "Visualization of Fluid Displacements in Porous Mediausing Computed Tomography Imaging," *J. Petr. Sci. Eng.*, 4, 155–168 (1990).
19. A. Kantas, "Investigation of Physical Properties of Porous Rock and Fluid Flow Phenomia in Porous Media Using Computer Assisted Tomography," *In Situ* 14(1), 77–132 (1990).
20. M. E. Coles, E. L. Muegge and E. S. Sprunt, "Applications of CAT Scanning for Oil and Gas Production Research," *IEEE Trans. Nucl. Sci.* 38(2), 510–515 (1991).
21. B. F. Marek, K. J. Hartman, and A. E. McDonald, "Three Phase Relative Permeability of Limestones Having Bimodal Pore Size Distributions," SPE 21374, Middle East Oil Show, Bahrain, 1991.
22. E. S. Sprunt, K. P. Desai, M. E. Coles, R M. Davis, and E. L. Muegge, "CT Scan Monitored Electrical Resistivity Measurements Show Problems Achieving Homogeneous Saturation," SPE 21433, Middle East Oil Show, Bahrain, 1991.
23. E. J. Peters and N. Afzal, "Characterization of Heterogeneities in Permeable Media with Computed Tomography Imaging," *J. Petr. Sci. Eng.* 7, 283–296 (1992).
24. P. Engler, M. W. Santana, and R. Narayanan, "Characterization of the Distribution of Fluid Content and Porosity in Reservior Cores by Using Digital Radiography," *Mater. Eval.* 50, 516–524 (1992).

25. P. Engler, M. W. Santana, and R. Narayanan, "Determination of Two Dimensional Fluid Distribution and Porosity by Digital Radiography," SPE 25817, unsolicited paper, February 1993.

26. D. Maloney and K. Dogget, "New Procedure and Apparatus for Combined reservior Condition Gas-Brinerelative Permeability, Capillary Pressure and Electrical Property Measurements," SCA 9427, presented at the Society of Core Analysts Annual Technical Meeting, September 12–14, 1994.

27. E. L. Muegge, Jorge J. Faz, and Eve S. Sprunt, "Method for Identifying Porosity and Drilling Mud Invasion of a Core Sample From a Subterranean Formation," U.S. Patent 4,722,095, January 26, 1988.

28. G. L. Becker, ed., J. K. Aman, G. L. Becker, H. Berger, L. E. Bryant, Jr., W. E. J. McKinnen, and F. J. Sattler, 1990, *Radiographic NDT*, DuPont NDT Systems, E. I. du Pont de Nemours & Co.

29. L. E. Bryant and P. McIntire, eds., 1985, *Nondestructive Testing Handbook*, *Vol. 3: Radiography and Radiation Testing*, American Society for Nondestructive Testing.

30. R. D. Evans, 1955, *The Atomic Nucleus*, McGraw-Hill Book Company.

31. XCOM: Photon Crossection on a Personal Computer, 1987, NBSIR 87-3597, M. J. Berger and J. H. Hubbell, Center for Radiation Research, National Bureau of Standards, Gaithersburg, Md.

32. R. H. Huseman, G. T. Gullberg, W. T. Greenberg, and T. F. Budinger, "Donner algorithm for Reconstruction Tomography," LBL PUB-214, Lawrence Berkley Lab., Berkley, Calif., 1977.

33. M. E. Coles, E. L. Muegge, and B. F. Marek, "Use of Attenuation Standards for CAT Scanning Applications Within Oil and Gas Production Research," 1992 Society of Core Analysts Conference Paper 9223.

34. M. E. Coles, "Image and Attenuation Standards for CT Scanning," CT Workshop, Society of Core Analysts, September 12, 1994.

35. M. E. Coles, E. L. Muegge, F. M. Auzeraia, P. Phrulla, and A. Kantas, "Use of Attenuation Standards for CT Scanning," 1995 Society of Core Analysts Conference Poster, 9513, September 12–14, 1995.

36. M. E. Coles and E. L. Meugge, "Method for Determining Density of Samples of Materials Employing X-Ray Energy Attenuation Measurements," U.S. Patent 5063509, November 5, 1991.

37. M. E. Coles and E. L. Meugge, "Method for Evaluating Core Samples from X-Ray Energy Attenuation Measurements," U.S. Patent 5164590, December 1992.

38. M. E. Coles and E. L. Meugge, "Method for Determining Density of Samples of Materials Dual Energy X-Ray Energy Attenuation Measurements," CT Workshop, Society of Core Analysts, September 12, 1994.

39. R. Sandor and A. Hove, "Three Phase Saturation Quantification Using CT," CT Workshop, Society of Core Analysts, September 12, 1994.

40. P. Spanne and M. Rivers, "Computerized Microtomography using Synchrotron Radiation from the NSLS," *Nucl. Instr. Meth. Phy. Res.*, 24(25), pp. 1063–1067 (1987).

41. B. P. Flannery, H. W. Deckman., W. G. Roberge, and K. I. D'Amico, "Three Dimensional X-ray Microtomography," *Science* 237(18), pp. 1439–1444 (1987).

42. M. C. Nichols, J. H. Kinney, Q. C. Johnson, R. A. Saroyan, U. Bonse, R. Nusshardt, and R. Pahl, "Synchrotron Microtomography of Supported Catalysts," *Rev. Sci. Inst.* 60(7), pp. 2475–2477 (1989).

43. K. W. Jones, P. Spanne, S. W. Webb, W. C. Conner, R. A. Beyerlein, W. J. Reagan, and F. M. Dautzenberg, "Catalyst Analysis Using Synchrotron X-ray Microscopy," *Nucl. Inst. Meth. Phy. Res.*, 56(57), pp. 427–432 (1991).

44. J. Jasti, G. Jesion, and L. Feldkamp, "Microscopic Imaging of Porous Media using X–Ray Computed Tomography," SPE 20495, presented at SPE Annual Technical Conference September 23–26, 1990.

45. J. H. Dunsmuir, S. R. Ferguson, K. L. D'Amico, and J. P. Stokes, "X-Ray Microtomography: A New Tool for the Characterization of Porous Media," *Soc. Pet. Eng.* 22860, presented at the 66th Annual Tech. Conf., Dallas, October 6–9, 1991.

46. M. E. Coles, P. Spanne, E. L. Muegge, and K. W. Jones, "Computed Microtomography of Reservoir Core Samples," SCA 9401, presented at Society of Core Analysts Annual Technical Conference, September 12–14, 1994.

47. M. E. Coles, R. D. Hazlett, P. Spanne, E. L. Muegge, and M. J. Furr, "Characterization of Reservoir Core Using Microtomography," Poster at 1994 Gordon Conference on Flow in Permeable Media, August 8–12, 1994.

48. F. M. Auzerais, J. Dunsmuir, B. B. Ferréol, N. Martys, J. Olson, T. S. Ramakrishnan, D. H. Rothman, and L. M. Schwartz. "Transport in Sandstone: A Study Based on Three Dimensional Microtomography," *Geophys. Res. Lett.* **23**(7), 705–708 (1996).

49. P. Spanne, J. F. Thovert, C. J. Jacquin, W. B. Lindquist, K. W. Jones, and P. M. Adler, "Synchrotron Computed Microtomography of Porous Media: Topology and Transports," *Phys. Rev. Lett.* **73**(14), 2001–2004 (1994).

50. R. D. Hazlett, M. E. Coles, K. W. Jones, B. Andrews, B. Dowd, P. Siddons, and A. Peskin, "Developments in Synchrotron X-Ray Microtomography for Application to Flow in Porous Media," SCA 9630, presented at Society of Core Analysts Annual Technical Conference, September 8–10, 1996.

51. M. E. Coles, R. D. Hazlett, E. L. Muegge, K. W. Jones, B. Andrews, B. Dowd, P. Siddons, A. Peskin, P. Spanne, and W. E. Soll, "Developments in Synchrotron X-Ray Microtomography with Applications to Flow in Porous Media," SPE 50985, *SPE Reserv. Eval. Eng.*, p. 288, August 1998.

52. R. D. Hazlett, "Stastical Characterization and Stochastic Modeling of Pore Networks in Relation to Fluid Flow," *Math. Geol.* 29(6), 801–822 (1997).

53. R. N. Vaidya, R. D. Hazlett, J. J. Buckles, and M. E. Coles, "Simulation of Wettability Effects on Displacement Processes by Cellular Automata Methods,"

presented at Third International Symposium on Evaluation of Reservoir Wettability and Its Effect on Oil Recovery, September 21–23, 1994.

54. J. J. Buckles and R. D. Hazlett, "Application of Lattice Boltzmann Simulation to Oil Reservoir Engineering," presented at the First International Connection Machine Users Meeting, Sante Fe, February 16–18, 1994.
55. M. E. Coles, R. D. Hazlett, P. Spanne, E. L. Muegge, W. E. Soll, and K. W. Jones, "Pore Level Imaging of Fluid Transport," SCA 9628, presented at Society of Core Analysts Annual Technical Conference, September 8–10, 1996.
56. M. E. Coles, R. D. Hazlett, P. Spanne, W. E. Soll, E. L. Muegge, and K. W. Jones, "Pore Level Imaging of Fluid Transport Using Synchrotron X-ray Microtomography," *J. Petr. Sci. Eng.*, 19, 55–63 (1998).

9. NUCLEAR MAGNETIC RESONANCE

Robert L. Kleinberg
Schlumberger-Doll Research
Ridgefield, Connecticut

9.1 Introduction

Nuclear magnetic resonance (NMR) has long been used to characterize condensed matter. Chemical shift spectroscopy, relaxation studies of kinetic processes, and three-dimensional imaging are familiar ways of using NMR to probe properties of gases, liquids, and solids. The use of NMR to investigate porous media has primarily focused on measurements of the fluids in the pore space. Because the common pore fluids are rich in hydrogen, most applications are based on proton NMR measurements.

The application of NMR to porous media has been accompanied by the development of new measurement modalities, enabling the study of mesoscopic properties that are difficult or impossible to determine by other techniques. One of the most useful of these properties is the pore size or, more generally, the pore size distribution. An NMR relaxation time measurement can be used to determine a volumetrically weighted distribution of pore sizes spanning several orders of magnitude. Properties that have been derived from the NMR-determined pore size distribution include hydraulic permeability and the capillary pressure curve.

Quantitative measurement of signal amplitude plays a much more important role in the characterization of porous media than in most other magnetic resonance investigations. Calibrated proton spin density measurements can be the simplest and most accurate way to measure the volume fraction of pore space (porosity). Processes such as freezing, drying, and hydration are easily monitored by amplitude measurements.

This chapter reviews methods and applications of NMR measurements of porous media. The emphasis is on amplitude and relaxation techniques developed specifically for porous media. Other reviews cover magnetic resonance imaging, pulsed field-gradient techniques, and characterization of fluid flows by NMR [1–3]. Here, special attention is paid to sedimentary rocks, which present a broad range of difficulties to the experimentalist and are in many respects "worst-case" porous media. Measurements have been made in the laboratory and, in some cases, by "inside-out" NMR equipment

EXPERIMENTAL METHODS IN THE PHYSICAL SCIENCES
Vol. 35
ISBN 0-12-475982-3

ISSN 1079-4042/99 $30.00

operating as much as 10 km underground for the purpose of measuring properties of subsurface geological formations *in situ*.

A number of important porous systems are not discussed in this chapter. Where the pore openings are on a molecular scale, such as in intercalation compounds and zeolites, the guest phases behave as individual molecules not as continuous fluids. Methods that are useful for characterizing these materials are in some respects distinct from those presented here.

9.2 NMR Relaxation

There is a multitude of types of NMR measurements. In fact, one of the main attractions of the technique is the variety of measurements that can be made with basic apparatus. Measurements of magnetic relaxation have proved particularly helpful in porous media studies. For details concerning the relaxation measurement technique, the reader is urged to consult one of many excellent books [4–7].

To make an NMR measurement, magnetic nuclei are first aligned by a static magnetic field B_0. Then they are irradiated by an antenna broadcasting radio frequency pulses. The pulses reorient the magnetic moments of the nuclei. The carrier (Larmor) frequency, f_0, of the pulses is

$$f_0 = \frac{\gamma}{2\pi} B_0, \tag{1}$$

where γ is the gyromagnetic ratio of the nucleus. Each isotope has a unique gyromagnetic ratio; for protons, $\gamma/2\pi = 42.58$ MHz/T. It is this frequency selectivity that makes NMR a resonance technique.

The transverse relaxation (T_2) measurement consists of a series of pulses. The first is a 90° pulse, during which the nuclei are rotated 90° from the B_0 direction. This is followed by a long series of 180° pulses. The sequence is called a CPMG after its inventors, Carr and Purcell [8] and Meiboom and Gill [9]. When irradiated with this series of pulses, a nuclear spin system will return a series of equally spaced spin echoes [10], one after each 180° pulse. The echo spacing is called T_E and is typically of the order of a millisecond.

The transverse magnetization decay is monitored by measuring the amplitudes of the echoes during the CPMG sequence. The entire decay curve is acquired during one echo train, which makes this measurement a very efficient one. The characteristic decay time for echo amplitude is called T_2, the transverse relaxation time. The amplitude of the nth echo, occurring

at time $t = n \cdot T_E$, is

$$M(t) = M_0 \exp\left(-\frac{t}{T_2}\right). \tag{2}$$

After the end of a CPMG acquisition sequence, the spins are free to return to equilibrium along the static field B_0. The process of realignment is often relatively slow. It is characterized by a time constant T_1, called the longitudinal relaxation time. Methods of measuring T_1 have been reviewed by Sezginer *et al.* [11].

Both T_1 and T_2 arise from molecular processes, but there is not necessarily any relationship between them. For liquids measured in bulk, it is often the case that $T_1 = T_2$. For solids, it is often the case that $T_1 \gg T_2$. It is always true that T_1 is greater than or equal to T_2. The relaxation processes of greatest interest for porous media studies are described here. The references should be consulted for a more complete overview [4–6, 12, 13].

Bulk Fluid Process: Magnetic relaxation occurs when a nucleus is subjected to any magnetic disturbance that has an oscillating component at the Larmor frequency. One such disturbance is the fluctuation of local magnetic fields arising from the random motion of neighboring nuclei. This mechanism is quite weak; for water, $T_1 = T_2 = 3$ s at room temperature.

Surface Relaxation: Brownian motion causes fluid molecules to diffuse substantial distances during an NMR measurement. The equation for diffusion is

$$\langle x^2 \rangle = 6Dt, \tag{3}$$

where $\langle x^2 \rangle$ is the mean square distance a molecule diffuses in time t, and D is the molecular diffusion coefficient. For water at room temperature, $D = 2 \times 10^{-9}$ m^2/s; in one second, the typical length of time for an NMR measurement, a molecule can diffuse 110 μm. Diffusion gives a molecule the opportunity to collide with nearby solid surfaces, and each collision of a molecule with a surface provides an opportunity for spin relaxation. This mechanism contributes to T_1 and T_2, but not necessarily with the same strength.

Diffusion in Magnetic Field Gradients: In the presence of gradients in the static magnetic field, molecular diffusion causes transverse relaxation. Longitudinal relaxation is not affected. For bulk liquids T_2 resulting from this effect is [8]

$$\left(\frac{1}{T_2}\right)_D = \frac{D(\gamma G T_E)^2}{12}, \tag{4}$$

where D is the molecular diffusion coefficient, γ is the gyromagnetic ratio of the nucleus, and G is the gradient strength in Teslas per meter. The B_0 gradient can originate either in the apparatus or in the sample itself, as explained in Section 9.3.5.

Summary: The relaxation processes act in parallel, and so the rates add:

$$\left(\frac{1}{T_2}\right)_{\text{total}} = \left(\frac{1}{T_2}\right)_S + \left(\frac{1}{T_2}\right)_D + \left(\frac{1}{T_2}\right)_B, \tag{5}$$

where $(1/T_2)_S$ is the surface contribution, $(1/T_2)_D$ is the diffusion in field gradient contribution, and $(1/T_2)_B$ is the bulk contribution. The corresponding equation for T_1 is

$$\left(\frac{1}{T_1}\right)_{\text{total}} = \left(\frac{1}{T_1}\right)_S + \left(\frac{1}{T_1}\right)_B. \tag{6}$$

Note there is no diffusion contribution to T_1.

9.3 NMR Properties Peculiar to Porous Media

9.3.1 Fluid–Solid Interaction

Because bulk relaxation processes can be very inefficient in liquids and gases, T_1 and T_2 of nuclear spins of fluids confined in porous media are frequently controlled by the fluid–solid interaction at the surfaces of the pore space [14, 15]. The macroscopic theory of magnetic relaxation at a fluid–solid interface is now very well established. The basic concept is that fluid molecules diffuse, eventually reaching a grain surface where there is a finite probability they are relaxed. The rate-limiting step can either be the relaxation process at the surface or the rate at which unrelaxed spins can be transported to the surface [16–20].

If the rate-limiting step is relaxation at the surface, fluid molecules can transit the pore several times before being relaxed. Then the magnetization decay in an individual pore is spatially uniform and monoexponential and depends not on pore shape but only on the surface-to-volume ratio. This is referred to as the fast-diffusion or surface-limited regime. In the absence of other relaxation mechanisms, the relaxation rates can be expressed by

$$\left(\frac{1}{T_1}\right)_S = \rho_1 \left(\frac{S}{V}\right)_{\text{pore}}, \tag{7a}$$

$$\left(\frac{1}{T_2}\right)_S = \rho_2 \left(\frac{S}{V}\right)_{\text{pore}}, \tag{7b}$$

where $(S/V)_{\text{pore}}$ is the surface-to-volume ratio of the pore, and ρ_1 and ρ_2 are

constants that depend on the strength of the interactions between fluid nuclear spins and the solid surfaces they encounter.

In the opposite case, magnetic relaxation occurs at the grain surface, but the decay of macroscopic magnetization is controlled by the transport of molecules to the surface [17, 18]. This is likely to be the case when pores are relatively large and/or surface relaxation is strong. Molecules usually will be relaxed at their first encounter with the surface. This is called the slow-diffusion or diffusion-limited regime. In this regime, there is a time-dependent nonuniform spatial distribution of magnetization in the pore. This gives rise to a magnetization decay, which in a single pore has a multiexponential character and depends on the shape of the pore. As long as both longitudinal and transverse relaxation are diffusion limited, their rates are equal, even if the microscopic processes governing relaxation at the surface are different. To lowest order,

$$\left(\frac{1}{T_1}\right)_S = \left(\frac{1}{T_2}\right)_S = c\frac{D}{a^2}, \tag{8}$$

where a is the pore radius, D is the bulk diffusion coefficient of the fluid, and c is a constant of order unity that depends on the shape of the pore. Spin diffusion [4], by which nuclear magnetism is transported by magnetic interactions between neighboring nuclei, is negligibly slow compared to molecular transport in liquids.

Experimentally, surface- and diffusion-dominated regimes sometimes can be distinguished by measuring the temperature dependence of the relaxation rates. In the absence of strong temperature dependence, the relaxation cannot be diffusion dominated, since the diffusion coefficient of the fluid, which explicitly appears in Eq. (8), always depends strongly on temperature [21]. However, an increase of relaxation rate with increasing temperature could arise from either of two causes. The relaxation could either be diffusion dominated or, if surface dominated, the surface relaxivity might be strongly temperature dependent [12, 22].

There are several mechanisms by which fluid molecules can be relaxed by solid surfaces. They are described in the following paragraphs.

Homonuclear Dipole–Dipole Coupling. This is the principal relaxation mechanism in bulk fluids such as water. NMR relaxation rates of nuclei in bulk fluids are typically low because inter- and intramolecular magnetic interactions are modulated at the frequency of the molecular motions, which is typically orders of magnitude higher than the Larmor frequency [23]. The presence of a solid surface increases the rate of relaxation by reducing the frequency of molecular motion [24, 25].

Cross-Relaxation by Other Nuclear Spins. Nuclear spins residing in molecules that are fixed at the surface have short relaxation times. The fixed spins can then efficiently relax the spins on itinerant fluid molecules. All nuclear spins can relax each other by this mechanism, but proton–proton interactions are the strongest. A striking example of this effect was demonstrated by Fung and McGaughy [26]. Surface coatings of silicone were applied to glass beads for the purpose of making them hydrophobic and therefore presumably less efficient at relaxing pore water. However, water proton relaxation was accelerated because the fixed silicone protons were a better relaxer than the silica surface.

Relaxation by Paramagnetic Ions. The magnetic moments of electron spins are 10^3 times larger than those of nuclear spins and therefore tend to dominate nuclear relaxation [12, 13]. Even small concentrations of paramagnetic ions at the solid surface can have a large effect on the relaxation of pore fluids, but these ions must be immediately at the surface to be effective [27]. Relaxivity depends linearly on the surface density of the ions [28]. It also depends on their identity, oxidation state, and electron relaxation time; these properties may be different at the surface than in the bulk of the solid. Kenyon and Kolleeny [29] observed a saturation of relaxivity at high concentrations of manganese on calcite surfaces. Roose *et al.* [30] found that when Mn^{2+} is adsorbed on silica, it retains its primary hydration shell, thus behaving very much unlike a lattice ion.

Relaxation by Free Electrons. The paramagnetic relaxation mechanism does not require the presence of a paramagnetic ion. A crystallographic point defect is formed when an atom is lost from a solid surface. Such defects are known to be relatively common on oxide surfaces. These defects can be populated by localized unpaired electron spins that efficiently relax nuclear spins of adsorbed fluid molecules [28].

Apparently, subtle differences in material preparation can substantially affect the relaxivity of a surface. Gallegos *et al.* [31] measured the surface relaxivities of a series of controlled-pore silica glasses and a series of silica sphere packings. The longitudinal relaxation rates were linearly proportional to surface-to-volume ratio for both series, but the relaxivities differed considerably. Analogous results were found for two series of calcium silicates that had been synthesized at high temperatures in different atmospheres [28]. It was hypothesized that different processing conditions led to different numbers and types of surface defects capable of trapping unpaired electrons.

9.3.2 Heterogeneity of Pore Space

In many synthetic materials, the pore space is uniform. Perhaps more interesting are those materials whose pore sizes and shapes vary significantly

within a sample. In many cases, relaxation is surface limited and Eqs. (7) apply. Then, when the pores are isolated from each other, there will be a one-to-one mapping from the distribution of pore sizes to a distribution of relaxation times.

For open cell materials — those in which pores are not isolated from each other — the term pore is more a semantic construct than a well-defined volume. For materials having a fractal fluid–solid interface [32, 33], or even simply a pitted one, the identity of a pore may depend on the size scale being investigated. Because NMR is not a steady-state measurement, the measurement itself introduces one or more length scales. Molecules sample only a limited volume of pore space before they are relaxed. The radius of the volume sampled cannot be larger than the root mean square distance the molecule diffuses in the NMR relaxation time, $\sqrt{6DT_1}$ or $\sqrt{6DT_2}$, where D, the diffusion coefficient, is itself a function of observation time in porous media [34] (see Section 9.3.4). If mixing occurs between pores of different sizes on this time scale, the spectrum of relaxation times will narrow [35–38].

In the limit that molecules are able to sample all pore sizes in the pore space before relaxing, the relaxations become single exponential with the decay rates

$$\left(\frac{1}{T_1}\right)_S = \rho_1 \left(\frac{S}{V}\right)_0, \tag{9a}$$

$$\left(\frac{1}{T_2}\right)_S = \rho_2 \left(\frac{S}{V}\right)_0, \tag{9b}$$

where $(S/V)_0$ is the surface to pore volume ratio of the whole sample. Note that this limit does not imply that each molecule has sampled the entire pore space. It is only required that, on average, molecules sample the entire range of pore sizes before being relaxed [39]. Haranczyk *et al.* [40] report transition from a single exponential decay to multiexponential decay as water is evaporated from a controlled pore glass. They interpret this as a transition from a regime in which water can sample the whole range of pore sizes during the decay of magnetization to one in which water molecules are effectively isolated in droplets.

The presence of pore coupling can be tested by varying the temperature at which the NMR relaxation measurement is made. Pores are coupled by means of molecular diffusion. If a broad distribution of relaxation times is not narrowed as temperature is increased, then diffusion, which is strongly temperature-dependent, cannot be a factor in the relaxation, and thus pore coupling cannot be an important factor in spin relaxation.

Porous sedimentary rocks are extreme examples of materials with heterogeneous pore spaces. In a typical sandstone rock, pore sizes vary over many orders of magnitude. There is no typical pore shape in such materials. NMR relaxation of fluids in rocks is characterized by broad distributions of relaxation times that do not generally change with temperature [41]. Thus, it can be concluded that water in the rocks investigated relaxed by a surface-dominated process, that the surface relaxation process was temperature-independent, and that pore coupling was not important.

9.3.3 Secular Alteration of Microgeometry

The pore space can be time varying as well as spatially heterogeneous. The solid matrix is not always impervious to chemical attack, and the most common pore fluid, water, is a good solvent, particularly at elevated temperature. Therefore the experimenter should not assume that his sample is unchanging over the course of time. There can be changes in the oxidation state of the surface, which will affect, for example, the NMR relaxing strength of paramagnetic ions at the fluid–solid interface.

Changes in the fine or gross geometry of the pore space are also possible. In one experiment, ordinary spherical borosilicate glass beads were immersed in water, sealed in an NMR tube, and stored at room temperature for approximately 1 year. At the end of the year, the NMR relaxation time of the water was found to be much shorter than it was originally. The tube was broken open, and the beads were found welded together. Microscopy showed the glass surface had been radically reworked by dissolution and reprecipitation [C. Straley, private communication].

The rate of chemical processes depends on the nature of the surface. Glass, which has a disordered structure, is unstable at room temperature. When quartz, which is chemically identical but structurally distinct, is stored under water in the laboratory, it appears to be stable, although even quartz will undergo alteration in geological contexts. Grinding creates abundant high-energy sites at the surface, and these sites are readily attacked by water. A water-saturated packing of a ground mineral will therefore undergo structural changes at accelerated rates, as has been observed for freshly pulverized calcite ($CaCO_3$) in the author's laboratory.

9.3.4 Restriction of Diffusion

The diffusion coefficient can be defined as the ratio of the mean square displacement of a particle to the time over which that displacement takes place:

$$D = \langle x^2 \rangle / 6T. \tag{10}$$

The observation time T is well defined in NMR measurements. The diffusion coefficient can be determined by transverse relaxation measurements [8, 10, 42] or by pulsed field-gradient measurements [7, 43, 44].

The presence of solid matter has an important effect on the diffusion of fluid molecules. Two distinct cases are common. In one, the pore space is connected over relevant length scales—an open cell material. In the opposite case, the pores are isolated from each other—a closed cell material.

Diffusion in open cell materials has been investigated theoretically [45] and experimentally [34]. In the limit that the observation time goes to zero, the diffusion coefficient attains its bulk fluid value. However, the diffusion coefficient drops very rapidly as observation time is increased, asymptotically reaching a limit determined by the tortuosity of the pore space (see Fig. 1). The tortuosity is defined as the ratio of the diffusion coefficient of a fluid in bulk to the steady-state diffusion coefficient of that fluid in the porous medium. It is related to a number of other transport properties, such as electrical conductivity [46].

The asymptotic limit is approached only when variation in pore size and connectivity is adequately sampled by each diffusing fluid molecule [39]. In

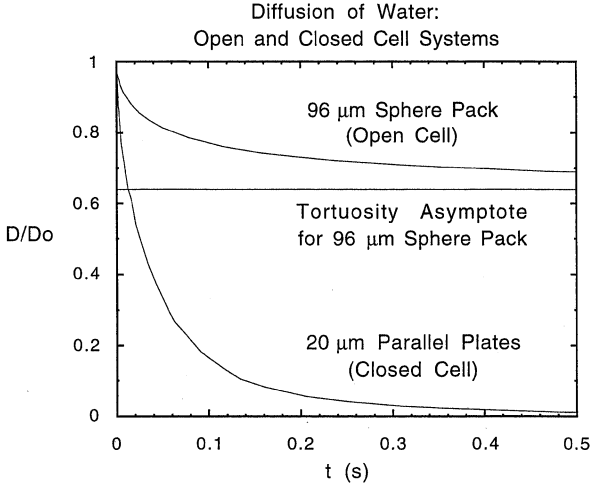

FIG. 1. Diffusion coefficient as a function of observation time; D_0 is the diffusion coefficient of the bulk fluid. In open cell systems, the reduced diffusion coefficient asymptotes to the tortuosity at long observation times; in closed cell systems, it goes to zero in that limit. Sphere pack data from Latour *et al.* [34]. Parallel plate data from Wayne and Cotts [48]. Reprinted with permission from Latour *et al.*, *J. Magn. Reson.* **A101**, 342–346 (1993) [39].

a very heterogeneous material, such as natural rock, this limit may not be reached in observation times experimentally accessible by NMR; that is, a few times T_1. In the presence of magnetization relaxation at grain surfaces, the apparent diffusion coefficient is affected proportionately to the strength of the surface relaxivity. Surprisingly, the effect can be either positive or negative, depending on the geometry of the pore space [47].

The diffusion coefficient has a very different dependence on observation time in closed cell materials [48–50]. As in the open cell case, in the limit of zero diffusion time, the diffusion coefficient approaches its bulk value. As observation time increases, the diffusion coefficient decreases; in the limit of infinite observation time, the diffusion coefficient goes to zero, as shown in Fig. 1.

9.3.5 Internal Magnetic Field Gradients

A further complication in performing and interpreting NMR experiments in porous media is the presence of magnetic field gradients that are induced by the granular nature of the material. The influence of magnetic field gradients is mainly on T_2 relaxation.

If pores were spheres or ellipsoids, the field inside them might differ from the applied field B_0, but there would be no gradient of the magnetic field within the pore. In real materials, however, the irregularity of the pore space coupled with a contrast in magnetic susceptibility between grain solid and pore fluid allows the existence of magnetic field gradients in the pore space.

The internal gradients produced by magnetic susceptibility contrasts can be roughly estimated by [51]

$$G = \Delta\chi_v B_0/R, \tag{11}$$

where B_0 is the applied static field, and $\Delta\chi_v$ is the difference in volumetric magnetic susceptibility between grain and pore substances. For water $\chi_v = -9.26 \times 10^{-6}$ in SI units. For magnetically dilute solids, χ_v depends linearly on the content of paramagnetic ions. For 5000 ppm by weight Fe^{3+} in a typical metal oxide, $\chi_v = +30 \times 10^{-6}$ in SI units [28]. Here R is a characteristic length scale of the pore space, and R is usually rather indefinite, and so this equation is generally useful only to indicate the scaling of factors that contribute to the gradients.

The computation of the spatial distribution of gradients, or even their statistical distribution, is a nontrivial problem for any real material. In an irregular pore, the gradient will vary from point to point; thus there will be a distribution of gradients. The gradients surrounding an isolated spherical grain have been computed [52], as have the statistics of gradients in a dilute solution of solid spheres in a uniform fluid background [53]. A detailed

microscopic model has been treated by Brown and Fantazzini [54]. Le Doussal and Sen [55] proposed a simplified but appealing model in which the local field varies parabolically within each pore.

Magnetization decays of spins diffusing through a distribution of gradients can be distinctly nonexponential [56]. Several studies have shown how pore size, diffusion coefficient, susceptibility contrast, and static magnetic field strength influence the relaxation rates of fluids in porous media [57–62].

9.4 Pore Size Distribution

9.4.1 NMR Relaxation Rate and Surface-to-Volume Ratio

One of the most important parameters characterizing a porous medium is the pore size or, more generally, the pore size distribution. Pore size distribution can be very difficult to measure by conventional means, especially if the pore space is irregular or the grain surfaces are rough. NMR provides a simple, fast, nondestructive, and volumetrically averaged method of measuring pore sizes that range over several orders of magnitude. The NMR measurement is made on fluid-saturated samples. This is an important feature when measuring a material that is altered by drying. Most other pore-sizing methods, such as mercury porosimetry, gas adsorption, or electron microscopy, require a dry sample.

The basis of the measurement is the relaxation of pore fluid spins at the solid surface. As explained in Section 9.3.1, the NMR relaxation rate is proportional to the surface-to-volume ratio in the surface-limited relaxation regime:

$$\left(\frac{1}{T_1}\right)_S = \rho_1 \left(\frac{S}{V}\right)_{\text{pore}}, \tag{12a}$$

$$\left(\frac{1}{T_2}\right)_S = \rho_2 \left(\frac{S}{V}\right)_{\text{pore}}. \tag{12b}$$

The connection between a surface–volume distribution and a pore size distribution is poorly defined for some porous media. Pore spaces have been modeled as spheres connected by throats, an interconnected network of tubes, and an interconnected network of sheets. None of these models has universal applicability. Thus the term “pore size” should be understood to mean a quantity, inversely proportional to the local surface-to-volume ratio, which measures the smallest dimension of a locality in the pore space [63].

For diffusion-limited situations, the magnetization decays are shape-dependent and multiexponential [17], and therefore it is more difficult to

relate NMR measurements to pore size. Fortunately, the diffusion-limited case seems to be less common than the surface-limited case. In many materials, the surface relaxation is sufficiently weak that diffusion-limited relaxation can be expected only in large pores where bulk relaxation is a competing, and often dominant, mechanism.

9.4.2 Limitations of the Measurement

There are limitations on the range of pore sizes that can be measured by this technique. The minimum detectable pore size is determined by the minimum detection time of the experiment, which is usually the spectrometer dead time. The largest pore that can be accurately sized depends on the competition between surface-mediated relaxation and other relaxation mechanisms:

$$\left(\frac{1}{T_1}\right)_{\text{total}} = \left(\frac{1}{T_1}\right)_S + \left(\frac{1}{T_1}\right)_B, \tag{13a}$$

$$\left(\frac{1}{T_2}\right)_{\text{total}} = \left(\frac{1}{T_2}\right)_S + \left(\frac{1}{T_2}\right)_D + \left(\frac{1}{T_2}\right)_B, \tag{13b}$$

where S signifies surface relaxation, D signifies diffusion relaxation, and B signifies bulk relaxation. There is no diffusion contribution to T_1, because that process is strictly a dephasing mechanism. Only the surface relaxation mechanism depends directly on pore size.

Pore size can be determined only when the pore space is fully saturated with the wetting phase fluid. If some liquid is removed, T_1 and T_2 are typically shifted to shorter times: the volume of fluid in a pore is decreased while the solid surface area remains the same. If two fluids are present in the pore space, the wetting phase will be relaxed by the surface while the nonwetting phase relaxes at its bulk relaxation rate: the fluid–fluid interface is often an inefficient relaxer [64]. An example is shown in Section 9.9.3.

9.4.3 Distributions of Pore Sizes and Relaxation Times

Porous media with broad distributions of pore sizes have nonexponential NMR magnetization decays. Timur [65] analyzed his nonexponential NMR relaxation data in terms of a three-exponential decay. The three-exponential fit suggests the pore space can be partitioned into volumes with distinctly different surface-to-volume ratios.

Kenyon *et al.* [66] used the stretched exponential form [67–69] to analyze inversion recovery longitudinal relaxation data:

$$\frac{1}{2}\left(1 - \frac{M(t)}{M(\infty)}\right) = \exp\left[-\left(\frac{t}{T_{1\alpha}}\right)^{\alpha}\right]. \tag{14}$$

This approach implicitly assumes a particular form of pore size distribution, the width of which is measured by the stretching exponent α:

$$m_1(T_{1i}) \propto \exp\left[-\left(\frac{T_{1i}}{\sigma}\right)^{\alpha/(1-\alpha)}\right], \tag{15a}$$

where

$$\sigma = \frac{T_{1\alpha}}{\alpha}(1-\alpha)^{(\alpha-1)/\alpha}. \tag{15b}$$

Here $m_1(T_{1i})$ is proportional to the number of spins relaxing with time constant T_{1i}. The stretched exponential form has an infinite slope at $t = 0$; Peyron *et al.* [70] proposed a modification that circumvents this problem.

The most general way of analyzing relaxation data is to calculate a spectrum of relaxation times [71]:

$$M(t) = \sum_i m_1(T_{1i})\left[1 - 2\exp\left(-\frac{t}{T_{1i}}\right)\right] \tag{16a}$$

and

$$M(t) = \sum_i m_2(T_{2i})\exp\left(-\frac{t}{T_{2i}}\right) \tag{16b}$$

for longitudinal and transverse relaxation, respectively. Each $m_1(T_{1i})$ and $m_2(T_{2i})$ is proportional to the number of spins with relaxation times T_{1i} and T_{2i}, respectively.

Assuming the sample consists of a collection of disconnected pores and relaxation is surface limited, this distribution of relaxation times corresponds to a distribution of surface-to-volume ratios with the time constants given by

$$\frac{1}{T_{1i}} = \rho_1\left(\frac{S}{V}\right)_i \tag{17a}$$

and

$$\frac{1}{T_{2i}} = \rho_2\left(\frac{S}{V}\right)_i. \tag{17b}$$

In this simple case (which is not uncommon), there is a direct mapping from the spectrum of pore sizes or, more precisely, the spectrum of surface-to-volume ratios to a spectrum of relaxation rates.

9.4.4 Pore Sizes from T_1 versus T_2

Either T_1 or T_2 can be used to determine pore size. Where there is a broad distribution of pore sizes, T_2 is a much more efficient way of generating the

relaxation time distribution. This is because a single CPMG acquisition (see Section 9.2) is sensitive to relaxation times that range from the echo spacing T_E to the total acquisition time NT_E, where N is the number of echoes in the sequence. There is in principle no limit to the size of N, and in the author's laboratory N is typically selected to be more than 4000.

Using T_1 has the advantage that it is unaffected by relaxation by diffusion in magnetic field gradients (see Section 9.3.5). This is particularly important when the internal gradients in porous media are large; that is, at a high magnetic field or when there is a large magnetic susceptibility contrast between solid and fluid phases. It has the disadvantage that it takes much longer to vary the recovery time over the many orders of magnitude necessary to measure a wide range of relaxation times [11].

An example of a T_2 magnetization decay for water in a porous rock is shown in Fig. 2a. The measurements were made at an applied static

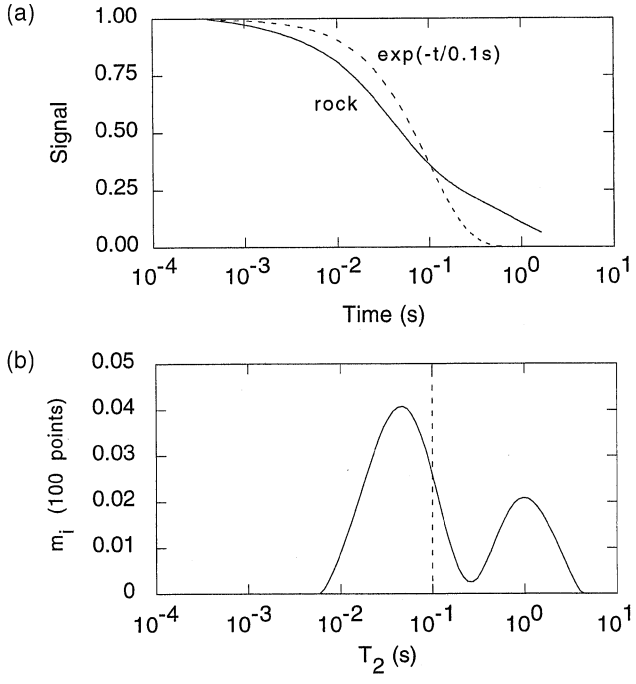

FIG. 2. NMR transverse relaxation for a material characterized by a broad distribution of relaxation times: (a) multiexponential magnetization decay (solid line) and single exponential decay (dashed line) and (b) corresponding distributions of relaxation times, m_i.

magnetic field of 0.05 T (Larmor frequency of 2 MHz for protons). For the CPMG measurement of T_2, the echo spacing was 0.4 ms and 4095 echoes were collected for an echo acquisition time of 1.64 s. Note the unusual way of plotting the recovery: The signal $M(t)$ is plotted linearly while echo time is plotted logarithmically, the reverse of the usual practice. This is sensible when relaxation times span orders of magnitude. The distribution of transverse relaxation times derived from the data in Fig. 2a is shown in Fig. 2b.

When the shapes of the T_1 and T_2 distributions are similar, a T_1/T_2 ratio can be determined from them. The cross correlation of two functions, $m_1(T_{1i})$ and $m_2(T_{2i})$, with logarithmically spaced abscissas is

$$C(\xi) = \sum_i m_1(T_{1i}) \cdot m_2(\xi T_{2i}). \tag{18}$$

When the two distributions have approximately the same shape but are displaced from one another on the logarithmic abscissa, the cross-correlation function is a maximum for a particular multiplier ξ, the T_1/T_2 ratio. For sedimentary rocks, a very wide class of porous media in itself, the T_1/T_2 ratio is generally between 1 and 3 [72]. For a series of synthetic oxides containing known quantities of iron or manganese, the ratio is in the range 1 to 4 [28].

The T_1/T_2 ratios discussed here are derived from measurements made at a static field strength of 0.05 T and an CPMG echo spacing of 0.16 ms. At low fields and short echo spacings, both longitudinal and transverse relaxation are dominated by the surface relaxation mechanism. At higher fields or larger echo spacings, T_2 is increasingly controlled by relaxation by molecular diffusion in the internal magnetic field gradients of rocks, and so one expects the T_2 distributions to be significantly altered. For rocks, significant effects of internal gradients have been noted at 0.25 T [73]. Long echo spacings in even lower magnetic fields also have significant effects [74, 75].

9.5 Determination of Surface Relaxivity

A number of mechanisms accelerate the magnetic relaxation of fluid spins at solid surfaces, as detailed in Section 9.3.1. Regardless of the mechanism, the surface relaxivity coefficients ρ_1 and ρ_2 are specific for each combination of solid and fluid and are almost always difficult or impossible to calculate *ab initio*. Therefore, relaxivities must be experimentally determined by comparing NMR relaxation measurements to surface-to-volume measurements made by other techniques on standard samples.

9.5.1 Synthetic Materials

Numerous studies have been made of the relaxivity of solid surfaces in contact with fluids. Most frequently, the fluid has been water. The measurement of relaxivity requires a measurement of NMR relaxation time (T_1 or T_2) and a measurement of pore space surface-to-volume ratio. Artificial packings of uniformly sized grains produce narrow pore size distributions. Such porous media are generally characterized by single-exponential magnetization decays and a single surface-to-volume ratio that characterizes the whole sample. Various methods of measuring S/V produce consistent results. In imperfect packings, if diffusion allows fluid molecules to visit pores of different sizes during the relaxation time, a distribution of pore sizes can be averaged, resulting in a single-exponential decay (see Section 9.3.2). This situation is most likely to occur in well-mixed synthetic materials.

Surface relaxivities have been determined for a number of synthetic materials such as porcelain, powdered minerals, or packed glass beads, which have uniform pore sizes and single-exponential NMR decays. Table I reports relaxivity values in the literature [76–81]. Usually, the longitudinal relaxivity ρ_1 is reported. This is because prior to the introduction of low-field techniques, T_2 had limited value for estimating pore sizes, as discussed in Section 9.4.4. Usually, little or no information has been given about the exact compositions of the solids.

9.5.2 Natural Materials

It is much more difficult to determine ρ_1 and ρ_2 for natural materials. Pore sizes can vary by orders of magnitude within a single sample, and while nuclear magnetic resonance has the capability of measuring a broad

TABLE I. Longitudinal Relaxivities of Materials with Well-Defined Surface Areas

Material	ρ_1(μm/s)	Reference
Fe_xCaSiO_3	4–12	28
Mn_xCaSiO_3	0.4–3	28
Quartz sand	3	76
Silica gel	1–13	77
Porcelain	4	78
Glass beads	5	79
Alumina	3	79
Glass beads	11	80
Quartz sand	3	81

distribution of relaxation times, there are few other techniques with a comparable capability. It is therefore difficult to find a proper independent determination of a spectrum of surface-to-volume ratios. While many methods have been used to obtain the S/V distribution, or an interpretable measure of it, none is completely adequate.

Optical and electron microscopy [82, 83] are limited to the examination of surfaces or thin sections. Therefore, they lack the three-dimensional information necessary for the characterization of irregular pore geometries. Furthermore, these techniques have a very limited dynamic range in practice: It is not possible to quantitatively characterize porous materials with a broad range of pore sizes that extends into the submicrometer range.

Mercury porosimetry [84] is capable of measuring the volume associated with pore openings over many orders of magnitude of the latter. However, to derive information on the surface-to-volume ratio of the pore space, a microgeometric model must be assumed. Typically, the model is one of a well-connected network of cylindrical tubes, although this is not always stated explicitly. A model-dependent cumulative surface area can be defined at any value of injection pressure (e.g., 500 psi [3.4 MPa] or 30,000 psi [210 MPa]). Alternatively, a differential pore volume versus pore opening spectrum can be computed and compared directly to the NMR T_2 distribution.

Capillary pressure [85] measurements, based on draining water from a porous medium by means of a porous plate or centrifuge, are closely related to mercury porosimetry. While lacking the detail of mercury injection porosimetry, water drainage measurements can provide a similar connection between an NMR relaxation time distribution and volumes associated with pore opening radii. Again, to obtain the relaxivity, a pore space geometry must be assumed.

Adsorption isotherm [84] measurements, exemplified by the Brunauer, Emmett, and Teller (BET) [86] method, measure the total internal surface area of a porous medium. To determine S/V, pore volume is measured by conventional buoyancy porosity methods (see Section 9.7). The result is a single surface-to-volume ratio for the entire pore space.

NMR pulsed field-gradient (PFG) [34, 45, 87–89] methods also provide a single surface-to-volume ratio, rather than a volumetric distribution. The result can differ from that obtained by the adsorption isotherm–buoyancy porosity method in the presence of surfaces that are rough on a submicrometer length scale. Adsorption isotherm methods measure surface areas on a molecular scale, while NMR PFG has a measurement scale length of the order of a micrometer.

9.5.3 Case Study: Sandstones

Rock grain surfaces are unusually difficult to characterize because they can have a rough or fractal character [32, 33]. That is, the apparent surface area depends on the characteristic scale length of the measurement: Independent methods of measuring the internal surface area give widely differing results [90]. Accordingly, measurements of ρ for sedimentary rocks have varied by orders of magnitude, depending on the method used (see Fig. 3).

The fractal nature of the rock grain surfaces is due to the presence of clay [91]. Generically, clays are minerals that have a fibrous or platy structure. For example, montmorillonite clay, commonly found in geologic forma-

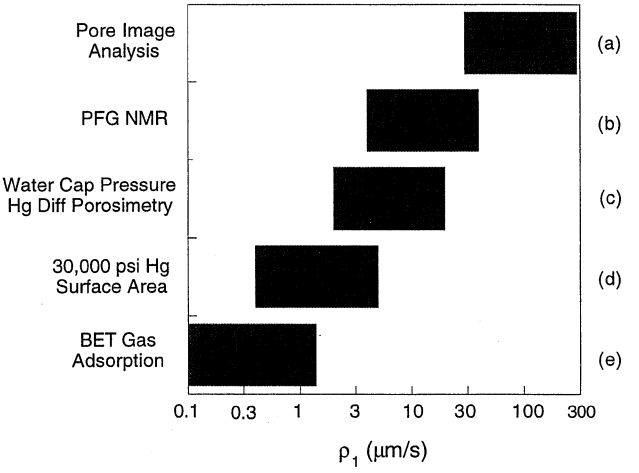

FIG. 3. The apparent relaxivity of natural materials depends on the method used to determine the surface-to-volume ratio. Each bar represents the range of values of longitudinal relaxivities found for sandstones. The determinations were made by various laboratories on various samples. (a) Pore Image Analysis: Distributions of three-dimensional surface-to-volume ratios are estimated from microscopic measurements of two-dimensional areas and perimeters of individual pores viewed in thin section. (b) PFG NMR: Mean S/V is determined from NMR pulsed field-gradient measurements of the time-dependent diffusion coefficient. (c) Water Cap Pressure: Volumes associated with pore radii are determined from the retention of water during centrifugation. Hg Diff porosimetry: Volumes associated with pore radii are determined from mercury injection. (d) 30,000-psi Hg Surface Area: Total internal surface area is determined from the work expended in injecting mercury into the porous medium; total pore volume is equal to volume of mercury injected. (e) BET Gas Adsorption: Total internal surface area is determined from nitrogen adsorption isotherms; total pore volume is found from the difference between dry and water-saturated weights.

tions, is composed of platelets 1 nm thick. When exfoliated, the surface area is as large as $750\,m^2/g$; when dry, the surface area measured by nitrogen absorption BET [84, 86] is one or two orders of magnitude smaller [92]. This can be compared to a quartz grain (the main constituent of sandstones) which, at the fineness of silt (50-μm grain diameter) has a surface area of the order of $0.1\,m^2/g$. Thus, a problem arises when measuring relaxivities of rocks having even modest clay content. The surface area as measured by the nitrogen adsorption BET method is usually several square meters per gram, which is dominated by the surface area of the clay and may have no relation to pore size.

It is instructive to estimate relaxivity from the initial slope of the NMR decay, the sample volume V_0 and the total internal surface area from BET S_0:

$$\rho = -\frac{V_0}{S_0}\left(\frac{1}{M}\frac{dM}{dt}\right)_{t=0}. \tag{19}$$

For CPMG measurements of transverse relaxation, M is the envelope of echo amplitudes; for inversion recovery measurements of longitudinal relaxation, M is the function given on the left side of Eq. (14). Using this method, ρ_1 of a number of sandstones is found to be in the range 0.1 to 0.8 μm/s [36]. This range of values is consistent with the Korringa–Seevers–Torrey [16] expression $\rho_1 = h/T_{1a}$, where h is the thickness of the first fluid monolayer on the surface, and T_{1a} is the longitudinal relaxation time of a fluid molecule adsorbed on the surface. For $h = 0.35$ nm and T_{1a} in the range of 1 to 5 ms, appropriate for water on a clay surface [93–95], ρ_1 of a few tenths of micrometers per second is expected. Thus, when applied to sandstones, the BET–initial decay method measures the relaxivity of water intimately associated with clay.

Water in the interlayer spaces of clay packets appears not to communicate with pore water, even though diffusion measurements suggest the two populations should be in rapid exchange [96]. Published neutron diffraction measurements report the surprising observation that clay-trapped water exchanges with surrounding bulk water on a time scale of thousands of seconds [96, 97]. Therefore, clay-trapped and pore water constitute distinct populations on the NMR time scale.

Not all clay forms packets. Water on the surface of dispersed clay appears to efficiently exchange with pore water (D. Allen, personal communication, 1998). In such cases water in even large pores relaxes relatively rapidly, and NMR relaxation will be a poor estimator of pore size.

A good way to test the proposition that NMR measures pore size in rock is to compare the NMR relaxation time distribution to an independent

pore-sizing method that is relatively insensitive to the presence of clay. Probably the best such method is mercury injection porosimetry. In many sandstones there is a quantitative connection between T_2 relaxation time distributions and differential mercury intrusion spectra [64, 79, 98–100] (see Fig. 4). For sandstones, the mercury injection pressure P and the relaxation time T_2 are usually related by $P \cdot T_2 = 10$ psi-s $= 70$ kPa-s.

The NMR relaxivity parameter ρ_2 can be determined from a comparison of NMR T_2 distributions and mercury injection porosimetry curves [101]. Consider an array of well-connected cylindrical tubes, which is the model normally used to analyze mercury porosimetry data. (An analogous argument can be made for an array of slitlike pores.) The injection pressure P is related to the tube radius r:

$$P = \frac{2\gamma \cos \theta}{r}, \tag{20}$$

where γ is the surface tension, and θ is the contact angle. The NMR

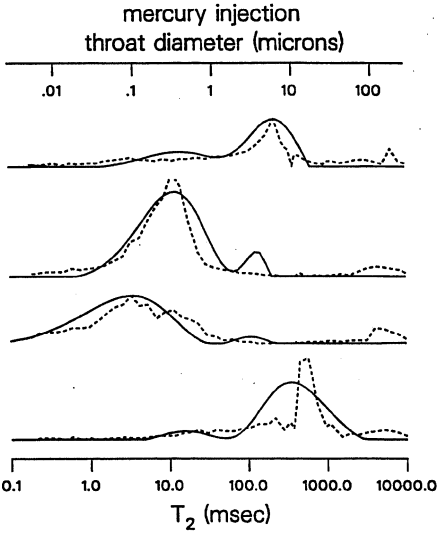

FIG. 4. Comparison of NMR T_2 distributions (solid lines) with differential mercury porosimetry (dashed lines) for four sandstones. Although NMR relaxation measures volume associated with pore body surface-to-volume ratio, and mercury porosimetry measures volume associated with a pore throat diameter, the curves are often in semiquantitative agreement (Schlumberger).

transverse relaxation rate for cylindrical capillaries is

$$\frac{1}{T_2} = \rho_2 \frac{S}{V} = \rho_2 \frac{2}{r}. \tag{21}$$

Then,

$$\rho_2 = \frac{\gamma \cos \theta}{P \cdot T_2}. \tag{22}$$

For mercury displacing vacuum in sandstone, $\gamma = 0.4855$ Pa-m, $\theta = 140^\circ$, $P \cdot T_2 = 10$ psi-s, and 1 psi = 6895 Pa; we find $\rho_2 = 5$ μm/s.

The relaxivity can also be determined from centrifuge desaturation measurements using Eq. (22). Straley *et al.* [102] found an air–brine capillary pressure of 100 psi is associated with a T_2 of 0.033 s for many sandstones. The parameters for air displacing water in sandstone are $\gamma = 0.07172$ Pa-m, $\theta = 0^\circ$, and $P \cdot T_2 = (100 \text{ psi})(0.033 \text{ s})$, and so we find $\rho_2 = 3$ μm/s. It is encouraging that similar values of ρ_2 are determined from two very different capillary pressure measurements.

The value of ρ_2 depends on the relaxing strength of the surface and therefore on the mineralogy of the porous medium [27, 28]. Iron-rich rocks have higher values of ρ_2. Moreover, the match between mercury porosimetry and NMR relaxation curves is not universal. In a pore-and-throat model of the pore space, mercury porosimetry is sensitive to the throat opening, whereas NMR relaxation measures the size of the pore body. These techniques give the same information only when there is no distinction between pores and throats or when there is a fixed multiplicative relationship between their sizes. It appears that such a relation exists for many sandstones. However, carbonate rocks subject to dissolution–reprecipitation processes under geological conditions are less likely to have a predictable relationship between pore and throat sizes.

9.6 Multiexponential Decay Signal Processing

A multiexponential longitudinal magnetization decay can in general be written

$$M(t) = \sum_i m_1(T_{1i}) \left[1 - 2 \exp\left(-\frac{t}{T_{1i}} \right) \right], \tag{23}$$

where $m_1(T_{1i})$ is proportional to volume of fluid relaxing at a rate $1/T_{1i}$ and is constrained to be nonnegative. This equation assumes perfect spin-tipping pulses, but it can be easily generalized to account for experimental imper-

fections. For transverse relaxation the equation is

$$M(t) = \sum_i m_2(T_{2i}) \exp\left(-\frac{t}{T_{2i}}\right). \tag{24}$$

All comments and equations that follow apply equally to T_1 and T_2, with the respective coefficients generically called m_i.

Modern practice is to preselect values of T_{2i} and find the corresponding coefficients m_i. Typically, 10 to 100 values of T_{2i} are used, equally spaced on either linear or logarithmic scales. How the T_{2i} are chosen does more than stretch or compress the horizontal axis of the relaxation time spectrum; it also changes the values of the m_i. On a linear scale the proportion of spins with relaxation times between T_{2i} and $T_{2i} + dT_2$ is $[m(\text{linear})_i]dT_2$. On a logarithmic scale, the proportion of spins with relaxation times between $\log T_{2i}$ and $\log T_{2i} + d \log T_2$ is $[m(\log)_i]d \log T_2$. Note that $m(\text{linear})_i$ and $m(\log)_i$ are related because appropriate integrals over both quantities must have the same value, proportional to the total fluid volume. Thus

$$V = \int m(\text{linear})_i \, d(T_{2i}) = \int m(\log)_i \, d(\log T_{2i}). \tag{25}$$

Since

$$d(\log T_2) = \frac{dT_2}{T_2}, \tag{26}$$

then

$$m(\text{linear})_i = \frac{m(\log)_i}{T_{2i}}. \tag{27}$$

For materials whose pore sizes range over several orders of magnitude, the logarithmic spacing is a more natural way to present the relaxation time spectrum.

The relaxation time distribution can be obtained by using the least-squares method. We find the m_i that minimize the difference ε between measurement data $M(t_j)$ and the fit to the data. For a CPMG decay,

$$\varepsilon = \sum_j \left[M(t_j) - \sum_i m_i \exp\left(-\frac{t_j}{T_{2i}}\right)\right]^2. \tag{28}$$

In practice, the inversion of magnetization data $M(t)$ to the spectrum m_i poses significant mathematical problems. The functions $\exp(-t/T_{2i})$ span the space of monotonically decaying functions, but they are not orthogonal. Hence, the inversion is not unique when $M(t)$ is noisy or when the mathematical computation has finite precision; in practice, both are limitations. In the past either the number of terms in Eq. (24) was limited to two

or three — a sparse spectrum indeed — or many terms were used, which resulted in spiky, nonphysical spectra.

Regularization is a mathematical technique that circumvents these problems [103, 104]. A functional is added to the right side of Eq. (28), which adds a constraint to the distribution. A cost function that discriminates against spikes in the distribution is

$$\varepsilon = \sum_j \left[M(t_j) - \sum_j m_i \exp\left(-\frac{t_j}{T_{2i}} \right) \right]^2 + \alpha \sum_i (m_i)^2. \tag{29}$$

Similarly, a cost function that discriminates against jumps in the distribution is

$$\varepsilon = \sum_j \left[M(t_j) - \sum_i m_i \exp\left(-\frac{t_j}{T_{2i}} \right) \right]^2 + \alpha \sum_i (m_{i+1} - m_i)^2. \tag{30}$$

The variety of such cost functions is limited only by the imagination of practitioners. There are now many papers on regularized inversion in the literature; only a small sampling is cited here [71, 79, 105–110].

Regularization has the effect of smoothing the spectrum, which removes spikes and makes the inversions reproducible in the presence of random noise. The obvious disadvantages are that the distributions are artificially broadened and that real, narrow features can be filtered out of the results. When the regularization parameter α is very small, the multiexponential fit is given great freedom to reduce the difference between the fit and the data. This can result in fitting the noise, which results in spiky relaxation time distributions that are not reproducible. When α is large, the distributions are forced to be very smooth, which can lead to rather poor fits to the data.

An insidious hazard of regularization is arbitrary selection of the regularization parameter; that is, the amount of smoothing. If the same amount of regularization is used for all experimental data sets, high-quality data will be represented by unnecessarily broadened spectra or low-quality data will not be inverted reproducibly. If a regularization parameter is arbitrarily selected for each data set, it is possible the results will reflect the preconceived notions of the analyst.

To avoid the problems of arbitrary smoothing, it is essential to use an algorithm that selects the regularization parameter in a data-dependent but objective manner. There are various sensible prescriptions for choosing α. One is to select the largest α consistent with a preselected fit error; another is to select an α such that $d\varepsilon/d\alpha$ does not exceed a certain bound. Clearly these criteria themselves introduce a certain arbitrariness into the processing, but they do at least ensure that all data sets are treated in a consistent manner.

Unfortunately, there has been some overenthusiastic use of the multiexponential decomposition algorithms, resulting in the publication of relaxation time distributions that lack credibility. One example of the pitfalls of the technique is illustrated by Fig. 5. The noiseless model input relaxation time distribution is shown as a heavy line; it consists of a sharp peak at long T_2 and a low amplitude tail that extends to very short T_2. This is a difficult combination for the algorithm in use in the author's laboratory. The distributions computed for various values of α are shown as lighter curves. Large values of α unduly broaden the spike, while at small values of α, the long low-amplitude tail breaks up into discrete peaks. The incautious user may overinterpret these features.

At a minimum, the stability of processing techniques should be checked by numerical simulations. A manifestation of Gaussian white noise is added to a model noiseless decay, and the result is inverted to give a relaxation time distribution. This operation is then repeated many times at the same signal-to-noise ratio. A properly tuned algorithm should give stable results at a variety of noise levels, the computed distributions becoming progressively smoother and more featureless as the signal-to-noise ratio decreases.

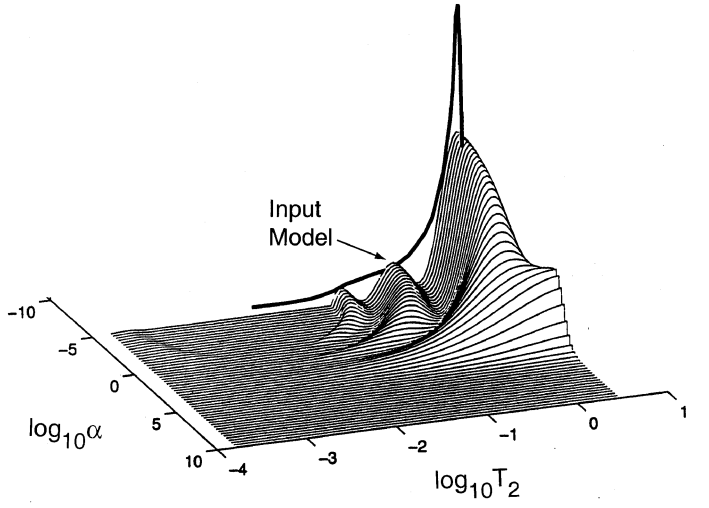

FIG. 5. Computed relaxation time distributions depend on the magnitude of the regularization parameter α. A noiseless model relaxation time distribution (heavy line) is used to generate a model noiseless magnetization decay (not shown). The decay is then inverted to a relaxation time distribution using various values of α (light curves, foreground) (courtesy of A. Sezginer).

Some tests of this type are documented in the literature [101, 111, 112]. Comparisons of the T_2 distributions from experiments and random walk simulations are also instructive [113].

9.7 NMR Porosity

The simplest NMR measurement made on porous media is the fraction of sample volume that consists of fluid-filled pore space, commonly referred to as porosity.

A typical conventional measurement of porosity is based on the buoyancy (Archimedes) principle. Porosity is determined by weighing a small sample three times. First, the sample must be cleaned: Any material left in the pore space that will not vaporize with water (e.g., tar) will contribute to the grain space. Then, the sample is thoroughly dried in an oven and weighed. It is weighed a second time after being fully saturated with water. Finally, the saturated rock is weighed a third time while suspended in a water bath. The density of the solid, the volume of water imbibed during saturation, and the total volume of the sample can be determined. The ratio of the latter two quantities is the buoyancy porosity. The method is simple and reliable, but it is time consuming and can be performed only on samples available for laboratory preparation and measurement.

The NMR porosity measurement depends on the fact that the amplitude of a proton NMR measurement is directly proportional to the amount of hydrogen in the material investigated. Protons are present in both water and oils, in clay minerals, and in some solids such as gypsum (calcium sulfate hydrate). However, the transverse relaxation time T_2 is sufficiently short in solids, of the order of 10 μs, that the signal from those protons can be eliminated from the measurement by ignoring very fast components of the signal. On the other hand, the relaxation times of protons in pore fluids are greater than 1 ms for many interesting materials, and so these protons are visible in the signal. Relaxation times of water trapped in very small pores or clays have intermediate values; such protons can be visible or invisible, depending on hardware and signal processing choices.

To obtain absolute values of porosity it is necessary to calibrate the NMR spectrometer. The usual method is to make a one-point calibration using a standard sample of known proton density. Differences in proton concentrations of the pore fluid and the calibration sample must be considered: Very saline water and many oils have a significantly lower proton density than pure water. Temperature control is also important, because signal amplitude obeys the Curie law [4] and is therefore proportional to the inverse absolute temperature, amounting to a variation of 0.3%/°C at room temperature.

To the extent that B_1 and B_0 vary over the sample volume, it is useful for the standard to be the same size and shape as the unknown to be measured and for the standard and the unknown to be placed in the identical location in the apparatus. Obviously, the provision of homogeneous fields reduces the amount of care needed to match size, shape, and placement. For example, it is helpful to use a B_1 coil substantially larger than the sample.

To ensure a quantitative amplitude measurement, it is essential that the system gain be constant when measuring the standard and the unknown. Differences in magnetic susceptibility (common in porous media) necessitate Larmor frequency tuning. Resistive losses and capacitive coupling between the RF coil and the sample can change the tuning characteristics and thus the sensitivity of the coil. To minimize these effects, the Q of the coil should be kept relatively low; in the author's laboratory, a probe with $Q = 30$ is used. A large RF coil is also helpful, since capacitive coupling between coil and sample is reduced relative to a smaller coil.

The problems of calibration and probe tuning are linked and are best considered together. One approach is to select a standard for which the resistivity and capacitive coupling to the probe are nearly the same as that for the unknown. If the unknown has a porosity in a given range and is saturated with a saline solution of a certain electrical conductivity, a standard having a known porosity in the same range, saturated with the same solution, may be selected.

A second approach is to calibrate the apparatus with bulk water. However, bulk water typically has a dielectric constant and conductivity signficantly larger than that of a porous medium with which it is saturated. The proton spin density of a bulk water sample can be adjusted with D_2O, and its relaxation time can be reduced to a convenient value by adding NiCl or other soluble paramagnetic salt.

Some porous media have a significant magnetic susceptibility contrast between grain material and pore fluid, which causes an inhomogeneous broadening of the NMR line. The bandwidth of the transmitted pulse must be large enough so that the entire line is resonated, or signal will be lost and the porosity underestimated; a low-Q coil is helpful. This problem becomes more severe at higher static magnetic fields [102, 114].

Sometimes excursions of antenna Q or amplifier sensitivity are unavoidable. An example is the borehole NMR instrument (Section 9.11), which is required to measure signal amplitude with an absolute accuracy of 1% of full scale while both the sensor and the electronic circuitry are subjected to large temperature variations. The product of antenna and receiver gains is monitored by injecting a known current at the Larmor frequency through a test loop embedded in the antenna. The overall sensitivity of the receiver system is proportional to the response to this fixed magnetic moment. The

test loop is calibrated by comparing its magnetic moment to that of an NMR signal of a standard sample at a stable, known temperature. When changes of antenna Q are substantial, the pulse lengths may require adjustment to maintain their nominal values.

Quantitative amplitude measurements can only be made when the nuclear magnetism is completely polarized. Commonly, this is ensured by waiting $5T_1$ between acquisition sequences. Because relaxation times of fluids in porous media can be broadly distributed, it is necessary to wait five times the longest expected relaxation time, not just five times the average relaxation time.

There have been many comparisons of NMR porosity with buoyancy porosity. Often, excellent agreement between the methods is found when care is taken in both measurements. In one example [115], not atypical, the root-mean-square scatter of the measurements was less than 1% of full scale.

9.8 Materials Processing Applications

Nuclear magnetic resonance is very useful in following the fate of fluids during the processing of porous materials. During drying, liquid is replaced by vapor with a much lower spin density. Freezing and hydration are accompanied by large changes in both T_1 and T_2. Filtration is accompanied by significant changes in surface-to-volume ratio and therefore relaxation times. Physical alteration that changes the internal microgeometry, or chemical alteration that changes the solid-fluid interaction, can be monitored by NMR. These processes are important in industrial, chemical, and civil engineering contexts. Numerous applications are described in a review article [116].

9.8.1 Saturation and Desaturation

As a bulk property, the moisture content of a porous or granular material is easily monitored by weight, electrical conductivity, dielectric constant, or sound propagation. NMR has the advantage that it is noncontacting and noninvasive. It can be performed on a batch basis or continuously on a process stream by passing a nonmetallic pipe containing the material through the magnet and RF coil [117]. The amplitude of the NMR signal is directly proportional to liquid content; the technique is identical to that used to determine fluid-filled porosity, as described in Section 9.7. The amplitude method is readily combined with magnetic resonance imaging to measure water saturation and drying profiles of porous media [118–121]. For example, NMR studies have shown that a porous medium can be

saturated by vapor transport only to a vapor percolation limit. At that limit, liquid water blocks the pore throats, with no further ingress of vapor possible [122].

The sensitivity of NMR to the structure of the pore space means much more powerful ways of monitoring fluid saturations are possible. As water leaves, the surface-to-volume ratio of the remaining pore fluid increases and the relaxation time decreases [25]. Deviations from the expected behavior indicate material heterogeneities, which can be particularly significant in the preparation of catalysts [119, 123]. A transition from a single-exponential decay to a multiexponential decay has been interpreted as the loss of continuity of the water phase as drying progressed [40]. Soga *et al.* [124] pointed out that dissolution of iron from a glass surface can depend on the degree of unsaturation, thereby affecting the water proton relaxation time.

In a material with a distribution of pore openings, one expects water to preferentially leave the largest pores, where the capillary forces are the weakest. If one measures the distribution of relaxation times (see Section 9.4) as a function of drying, the longest relaxation time components would be expected to disappear first, followed subsequently by ever faster components [122, 125]. This was demonstrated in the context of centrifuge desaturation of rock samples, in which pore sizes range over several orders of magnitude [64]. Rock specimens were fully saturated with water and the spectrum of longitudinal relaxation times determined. Then, each rock was centrifuged at a number of rotor speeds. At successively higher speeds, water was progressively expelled from the samples as the centrifugal pressure overcame the capillary pressure of successively smaller pore spaces. At each step the NMR relaxation spectrum was remeasured. At low centrifuge speed, the components with the longest T_1 disappeared from the spectrum, while the short T_1 components were unaffected. As the centrifuge speed was increased, progressively faster components disappeared.

9.8.2 Freezing

The freezing transition is marked by T_2 becoming very short, of the order of 10^{-5} s, while T_1 becomes very long, of the order of 10^2 s, making it easy to monitor. In microporous materials, with pore sizes of the order of nanometers, the freezing temperature depends on pore size and some water appears not to freeze at all [126, 127]. Similar behavior has been observed in coals [128]. This phenomenon can be used to determine the pore size distribution [129].

9.8.3 Hydration

The process of hydration involves water being taken out of the liquid state and being incorporated into a solid. From the standpoint of NMR, the

process is akin to freezing. The most important, and probably the most complicated, material of practical significance that undergoes hydration is cement. The proton NMR signal arises from crystalline phases, a gel phase, and from water in micropores, the proportions of which change over a period of months. These phases have quite distinct relaxation times, and it is possible to follow the curing of cement in a nondestructive time-lapse fashion [130–132].

9.8.4 Filtration

Filtration is the process by which solids in suspension are separated from a liquid when the latter is passed through a filter. The solids build up on the upstream surface of the filter to form a filter cake. An internal filter cake is created when the solid particles are smaller than the pores of the filter; the smaller the particles, the farther they will invade. Because external and internal filter cakes are generally the main impedance to subsequent fluid flow through the filter, characterizing them is of great importance to the chemical and water purification industries. They are also of interest to the petroleum industry, since the formation of internal filter cakes causes permeability reduction of oil-bearing rock formations.

A filter cake, aside from being formed adjacent to a porous medium, is itself a porous medium, with the same relaxation processes. As the filter cake is compressed by the continued pressure of liquid, it densifies, its surface-to-volume ratio increases, and its NMR relaxation time decreases [133, 134]. Internal filter cakes can also be monitored by the changes they induce in the NMR relaxation times of the porous medium. By finding a distribution of relaxation times as a function of position in a rock core, Fordham *et al.* [110] showed that an internal filter cake developed in a porous sandstone invaded by clay fines.

9.8.5 Physical and Chemical Alterations

The dependence of NMR relaxation time on pore space surface-to-volume ratio makes the technique a good one to quickly and nondestructively assess a variety of materials processing operations. For example, the pore structure of ceramics depends sensitively on firing temperature, an effect that can be probed by measuring relaxation time distributions of subsequently imbibed liquids [135].

Chemical alterations can also be detected. NMR relaxation mechanisms are very short range and fluid relaxation has little if any sensitivity to the solid past the first or second layer of atoms at the surface. It is therefore possible to change the surface relaxivity by coating the surface with foreign matter. Catalyst deactivation by coking has been imaged by this means

[119]. Similarly, the relaxivity can be changed by altering the wettability of the surface [136–138] or possibly by changing the oxidation state of paramagnetic ions on grain surfaces.

9.9 Petrophysical Applications

Petrophysics is the study of physical properties of rocks. Because petroleum is found in porous sedimentary rock, there have been considerable efforts to understand the relationships between porous rocks and the fluids saturating their pore spaces. Nuclear magnetic resonance has some unique capabilities in the study of these relationships. Several review articles [73, 139–141] and extensive bibliographies [142, 143] are available.

9.9.1 Partitioning of Porosity

One of the principal strengths of the NMR measurement is its ability to discriminate among waters of hydration bound in minerals, water trapped in clay layers, and pore fluids.

Protons in the solid matrix are characterized by their very long longitudinal relaxation times, of the order of 10^2 s, and very short transverse relaxation times, typically in the range 10^{-5} s. The signal from this population can be suppressed by a short repetition time of the measurement cycle, the small remainder being lost in the dead time of many NMR instruments. Matrix protons are of no interest to petroleum engineers, and therefore there is little motivation to use a machine capable of solids work for petrophysical applications.

A second group of protons is associated with water trapped within clay packets. Clays are fibrous or lamellar minerals with very large surface areas [92, 144]. The molecular structures of clays typically carry a negative charge, which must be balanced by associated cations, which are often exchangeable. Clays are hydrophilic, and owing to their high surface area can physisorb large amounts of water. This clay-trapped water has NMR relaxation times of about 10^{-3} s [93–95, 102]. Clays are ubiquitous in sandstones and, because of their affinity to water and mobile ions, have a profound effect on the electrical conductivity and hydraulic permeability of rocks. Surprisingly, clay-trapped water does not mix with other fractions of pore water on the NMR time scale, as explained in Section 9.5.3. On the other hand, water on the surface of dispersed clay is exchangeable with pore water.

A third group of protons is associated with pore fluids. Protons in fluids diffuse freely in the pore space, transported by the Brownian motion of the

molecules in which they reside. When molecules encounter solid surfaces, they are momentarily attached, in which condition their nuclei can be relaxed by magnetic interactions with spins in the solid, as discussed in Section 9.3.1. Their relaxation times are related to pore size.

Relaxation in sandstones is summarized in Fig. 6. Each pore constitutes a system of two rapidly exchanging populations: bulk water and water adsorbed on magnetic sites at the surface. Thus, each pore is characterized by a single relaxation time, which is a weighted average of the relaxation times of the two populations. Pores are coupled weakly, if at all, to other pores on the time scale of the NMR measurements. Water trapped in clay packets constitutes a separate reservoir that is uncoupled from the pore water, and therefore it has a distinct relaxation time.

Petrophysicists subdivide pore water into movable and irreducible fractions. The irreducible water saturation is the fraction of water that cannot be flushed from the rock at a given pressure gradient. An example of how NMR discriminates between producible and nonproducible water is shown in Fig. 7. Four rock samples are shown. In each case, the solid line shows the distribution of relaxation times for the water-saturated rock. The dashed

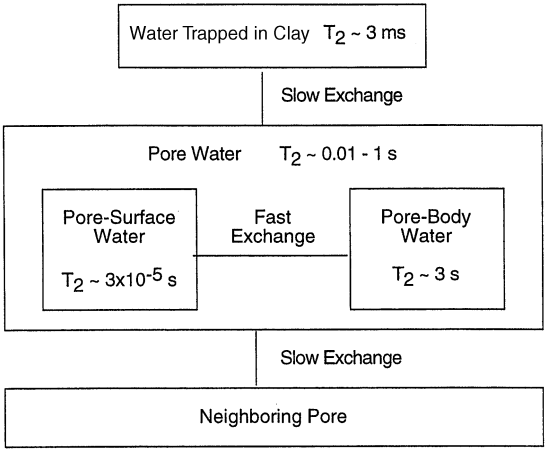

FIG. 6. Water occupies NMR-distinct sites in a sandstone pore. Rapidly relaxing water at the pore-grain interface is in fast exchange with the rest of the pore water, upon which bulk relaxation processes are acting; the resulting population-weighted average relaxation time is generally in the range of 0.01 to 1 s. Water trapped in clay packets relaxes rather rapidly, but does not exchange with pore water on the time scale of the NMR measurement. Neighboring pores are relatively isolated from each other.

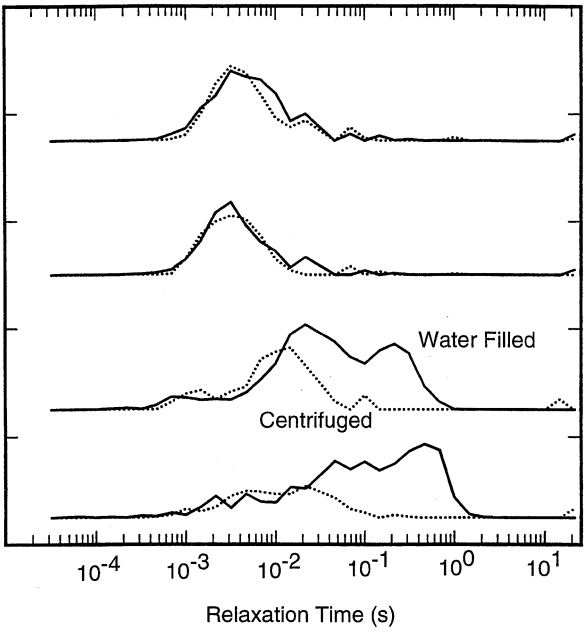

FIG. 7. NMR relaxation time distributions for four rocks. Solid curves are for fully water saturated rocks. Dashed curves are for the same rocks after being centrifuged at a capillary pressure of approximately 100 psi (700 kPa). Centrifuging expels water from the largest pores, resulting in a decrease of magnetization relaxing with long time constants (after Straley *et al.*, reprinted with permission from [64]).

line shows the distributions after the samples were centrifuged at a capillary pressure of 100 psi. In this case, the nonwetting phase is air. Water is expelled from the largest pores, but it is held in the small pores by capillary pressure. If one measures the full spectrum and applies a 33-ms cutoff, one can predict the fraction of the porosity that contains movable water. This is of great interest to the petroleum engineer, who normally will avoid an oil-bearing zone if it will also produce large quantities of water.

9.9.2 Hydraulic Permeability

Permeability is defined by Darcy's law [145, 146],

$$Q = \frac{k}{\eta} \nabla P, \tag{31}$$

where Q is the volume rate of flow per unit cross-sectional area, k is the

permeability, η is the viscosity of the fluid, and ∇P is the pressure gradient that drives the flow. A practical unit of permeability is the darcy (D), which is approximately $10^{-12}\,m^2$. Sedimentary rocks have permeabilities up to 10 D. It is usually not economic to produce oil from reservoirs with permeabilities smaller than about 0.01 D.

Since permeability has dimensions of length squared, it is obvious that k cannot be reliably predicted from a knowledge of porosity, which is dimensionless. Semiempirical formulas for permeability always incorporate a length scale parameter. The best known of these is the Kozeny equation, for which the permeability is inversely proportional to the square of the surface-to-volume ratio [145, 146]. Since the NMR relaxation rate is proportional to the surface-to-volume ratio, permeability is expected to be proportional to relaxation time squared.

This hypothesis has been substantiated by a large body of measurements [66, 76, 147]. A widely used equation has the form (66, 102)

$$k \sim \phi^4 T_2^2, \tag{32}$$

where ϕ is the porosity, and T_2 is any convenient one parameter measure of the relaxation time distribution.

Correlations such as Eq. (32) appear to depend on constancy of the surface relaxivity across a wide variety of sandstones, a surprising conclusion in view of the varied concentration of paramagnetic ions in rocks. Experiments on synthetic porous materials have shown that while the surface relaxivity is linearly proportional to the concentration of paramagnetic ions, as expected, there is a substantial relaxivity due to the oxide surface itself, independent of paramagnetic concentration [28]. This may explain the success of the correlations.

Attempts to establish similar correlations for carbonate rocks have been less successful. The microgeometry of carbonates is much more diverse than that of sandstones, as a result of dissolution and reprecipitation of calcium carbonate in groundwater. Therefore the Kozeny equation is not expected to be broadly applicable to carbonates. However, the versatility of the NMR measurement has led to clever application-specific correlations of local utility [148].

9.9.3 Oil–Water–Gas Discrimination

Many rock surfaces are hydrophilic: When water and nonpolar hydrocarbon coexist in the pore space, the water phase is relaxed at the grain surfaces which are not accessible to the nonwetting phase.

The hydrocarbons of most interest to the petroleum industry have low viscosities and therefore relatively long relaxation times: It is not unusual

for a light hydrocarbon to have bulk relaxation times of several tenths of a second or more [149]. Thus there can be a reasonable relaxation time contrast between water in a rock with small pores and a low-viscosity oil [64, 150].

Figure 8 shows how the T_2 distribution changes as the oil–water ratio in a porous sandstone is varied [64]. As the proportion of kerosene in the pore space increases (parts c–f, reading up), the kerosene peak grows in amplitude but remains at the relaxation time of bulk kerosene (part a). Simultaneously, the water peak shrinks and moves to shorter values of T_2, because the solid surface area exposed to water remains the same but the volume of water in each pore decreases.

This situation is complicated by two effects. First, crude oils tend to have reasonably broad distributions of relaxation times in bulk [150]. This is presumably because these oils are not pure substances but are complex mixtures of aliphatic and aromatic species; however, the physical chemistry has not been thoroughly explored.

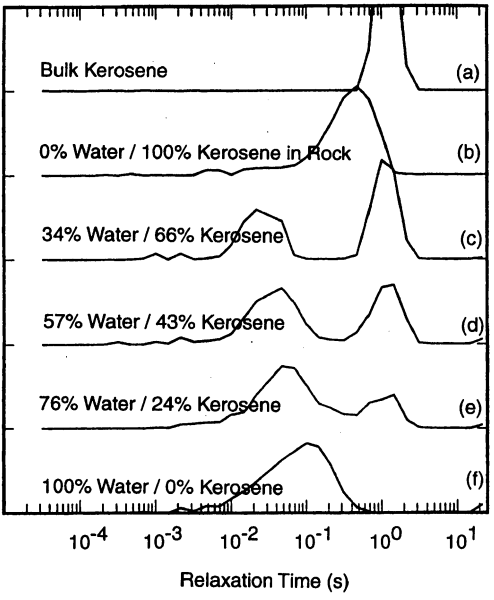

FIG. 8. Immiscible fluids in rock. (a) Relaxation of bulk kerosene, (b) relaxation of kerosene after being imbibed into oven-dried rock, and (c)–(f) relaxation time distributions for water-wet rock with various amounts of water and kerosene. Relaxation of wetting fluids (kerosene in [b], water in [c]–(f)] is accelerated by grain surfaces. When not in contact with grain surfaces, kerosene relaxes at its bulk rate (compare [c]–[e] to [a]) (after Straley *et al.*, reprinted with permission from [64]).

The second complicating effect is that low-viscosity fluids can have large diffusion coefficients, and so molecular diffusion in magnetic field gradients can contribute to transverse relaxation (see Sections 9.2 and 9.3.5). Because the internal magnetic field gradients in rocks are unknown, vary spatially, and are difficult to determine, this effect can be difficult to predict. When instrument gradients are large compared to internal gradients, the situation is considerably simplified.

Gas also exists in the pore space of rocks in the deep subsurface. Owing to its high pressure, subsurface methane can have a proton density as much as half that of liquid water. It is therefore a likely target for NMR investigations. The longitudinal relaxation of gas is predominantly controlled by bulk processes [151], although the high solubility of gas in water or oil at high pressure also gives it access to the relaxing power of the grain surfaces [152]. The transverse relaxation time is dominated by diffusion in the magnetic field gradients of porous media. The very large diffusion coefficient of gas at high pressure [153] implies the transverse relaxation rate is sensitive to the pulse spacing in the CPMG pulse sequence. This technique is used to distinguish gas from light oils [154]. Conversely, the maximum internal gradient in a porous medium can be determined by similar means [155].

9.10 Instrumental Requirements

There is abundant literature on the specification and construction of NMR apparatus [6, 156–163]. Spectrometer requirements for studying porous media are not particularly onerous, although there are some special considerations. The nuclei investigated are in the liquid (or sometimes gas) phase, and so the transverse relaxation is normally observable without undue demands on the speed of receiver recovery after transmitter pulses. Except where gases are used as long-lived spin probes, longitudinal relaxation times are usually shorter than their bulk values, which is convenient for signal accumulation. Although the nuclei of interest are diluted by solid material, the spin density is more than 10% of the bulk fluid value for many materials of interest.

The presence of internal magnetic field gradients leads to special requirements. To measure transverse relaxation rates dominated by surface relaxation — and therefore carry interesting information on the microgeometry of the pore space — it is necessary to minimize the relaxation due to diffusion in a magnetic field gradient. Therefore, there has been a trend toward measurements at magnetic fields as low as 0.01 to 0.05 T. In this respect, NMR applied to porous media has moved in a direction opposite

to other material science disciplines, which are probing matter in fields of 7 T and above.

Fields in the 10- to 100-mT range can be produced by arrays of permanent magnets. These magnets are relatively inexpensive and require no power or cooling systems. They should be thermostated, but this requirement is not onerous because modern materials such as samarium cobalt alloys have temperature coefficients of the order of 0.03%/°C. The properties of permanent magnet materials have been reviewed [164].

Good static field homogeneity is in many cases unnecessary. The inhomogeneous linewidth of a porous or granular material is of the order of

$$\Delta B/B_0 = |\Delta\chi_v|, \tag{33}$$

where $\Delta\chi_v$ is the magnetic susceptibility contrast between pore fluid and solid matrix. The susceptibility used is the SI volumetric susceptibility, which is dimensionless but 4π times larger than the cgs volumetric susceptibility, which is also dimensionless. Note that modest levels of paramagnetic impurities can significantly change the magnetic susceptibility of a solid or liquid.

Tipping pulses are governed by

$$\theta = \gamma B_1 t_p, \tag{34}$$

where θ is the tip angle in radians, γ is the nuclear gyromagnetic constant, B_1 is half the linearly polarized RF field strength, and t_p is the length of the tipping pulse. Normally, the experimenter is free to choose B_1 and t_p for convenience, as long as the product satisfies Eq. (34). However, in the presence of large inhomogeneous broadening, the RF amplitude must be large enough to satisfy $B_1 > \Delta B_0$, which is the requirement if all the spins are to be resonated. This becomes increasingly difficult at high fields [114].

The two most important problems associated with low fields are low signal levels and long receiver dead times. Conventional analysis shows that the signal-to-noise ratio goes as approximately the square of the field [6, 159]. While this rule of thumb does not take into account all the frequency variation in the efficiency of RF magnetic field reception, it suggests the magnitude of the problem. Good receiver design is very important [165]. The use of large samples and long averaging times are other obvious ways to mitigate the problem of low signal levels.

At low fields, the proton resonance can be in or just above the commercial AM radio band. Good RF shielding and grounding technique is sometimes needed to avoid interference from cultural sources, and between various parts of the NMR spectrometer [166, 167]. The coil should be impedance matched to the transmission line [168, 169].

For materials containing fine pores or in which strong relaxation processes are operative, it is best to extend relaxation measurements to times as short as possible. This means the dead time of the coil and receiver combination must be minimized. This problem becomes more difficult as the frequency is reduced. Amplifiers sensitive to low-frequency signals recover more slowly than high-frequency components. When a large current is used to generate the transmitted pulse, it must be removed from the coil before the received signal can be detected; *Q*-switches [163, 170] or active damping [171] have proved useful.

Diode detection has the undesirable effect of rectifying noise and thereby generating an artificial voltage bias. Therefore, a standard feature of modern NMR spectrometers is the provision for phase-sensitive detection [172]. In the laboratory, a phase shifter is used to rotate the signal into one channel of a dual phase-sensitive detector (PSD), while the other channel contains noise. When manual tuning is not practical, the phase can be estimated in real time and an appropriate mathematical rotation of the in-phase and quadrature signals performed [108]. It is important to use only the in-phase component. Squaring and summing the channels rectifies the noise and produces a baseline signal that considerably complicates the extraction of accurate multiexponential relaxation time fits.

9.11 Inside-Out NMR

NMR properties of porous media can be studied not only in the laboratory, but in the field as well. Earth's field ground-penetrating NMR apparatus has detected aquifers [173, 174]. A large loop is laid on the surface and after application of a 2-kHz pulse, which resonates protons in the 0.05-mT field of the earth, the free induction decay is monitored. The depth of investigation is at best comparable to the radius of the loop. Crude depth profiling is possible. The technique works best in arid regions, since the conductivity of the earth limits the penetration of the oscillating field. Earth's field NMR has been the subject of several other studies as well [175–177].

A pulsed NMR device that reads a few centimeters below the surface uses a horseshoe permanent magnet and an RF coil [178, 179]. The device produces conventional spin echoes at 3 MHz, using 200-kW pulses. It was used on a prototype basis to measure the moisture content of soils on farms.

It is also possible to make NMR measurements of subsurface formations *in situ*, from within boreholes drilled deep into the earth. Instead of putting a sample inside a magnet and a radio frequency coil, the apparatus is mounted inside a cylindrical sonde, from which fields are projected to an

exterior volume. The earliest such device dates from the 1950s [180]. Formation spins around the borehole were polarized by direct current in a coil having several thousand turns. After the current was turned off, the spins precessed around the earth's field [4]. This device was commercialized and used in oil fields in various parts of the world until the late 1980s.

More recently, a number of "inside-out" pulse NMR instruments have been developed for borehole application [181–185]; these have been reviewed elsewhere [141]. The literature on stray field (STRAFI) measurements can also be consulted [186–188]. At present, the most significant commercial applications of inside-out NMR are to petroleum exploration.

Section 9.9 described ways in which NMR can provide economically significant information about the pore space of rocks and the fluids residing there. The methods described can be used to characterize samples of rock brought to the surface and measured in the laboratory. However, the real value of NMR is that the measurements can be made *in situ* deep within the earth, using inside-out techniques. Geologists and petroleum engineers need continuous measurements of physical properties of formations over hundreds or thousands of meters of depth interval. Since these measurements are performed at drilling rigs, which can cost as much as $100,000 per day to operate, speed and efficiency are of the utmost importance. Rock samples can be brought to the surface, but this process is time consuming and does not provide the information in a depth-continuous or timely manner. The use of inside-out NMR techniques (along with inside-out measurements of electrical, acoustic, nuclear, and other properties [189, 190]) is the best way to acquire detailed information about hydrocarbon reservoirs [141, 191]. The process of making these measurements is called well logging.

NMR well logging instruments are presently deployed worldwide, helping to characterize oil and gas reservoirs. They output a well log, which records processed data as a function of depth and is normally available in real time. A portion of a typical well log is shown in Fig. 9. The depth scale (in feet) is at the extreme left; the most significant digit has been replaced by an X. The first panel is a mineralogical analysis of the rock formation determined from a combination of neutron and γ-ray scattering techniques [190]. The rock is primarily dolomite and illite clay, with streaks of other minerals.

In the fourth panel there are a series of T_2 distributions as a function of depth. The horizontal scale is logarithmic and ranges from 1 to 3000 ms. Below X410 almost all the weight in the distributions is at short values of T_2, indicating water-saturated rocks with very small pores. Above X410 the weight is predominantly at long T_2, which signals the presence of large pores and possibly of light oil [191]. A geologist can look at the NMR data and immediately recognize a change in rock texture at an unconformity in a formation thousands of feet underground and thus normally hidden.

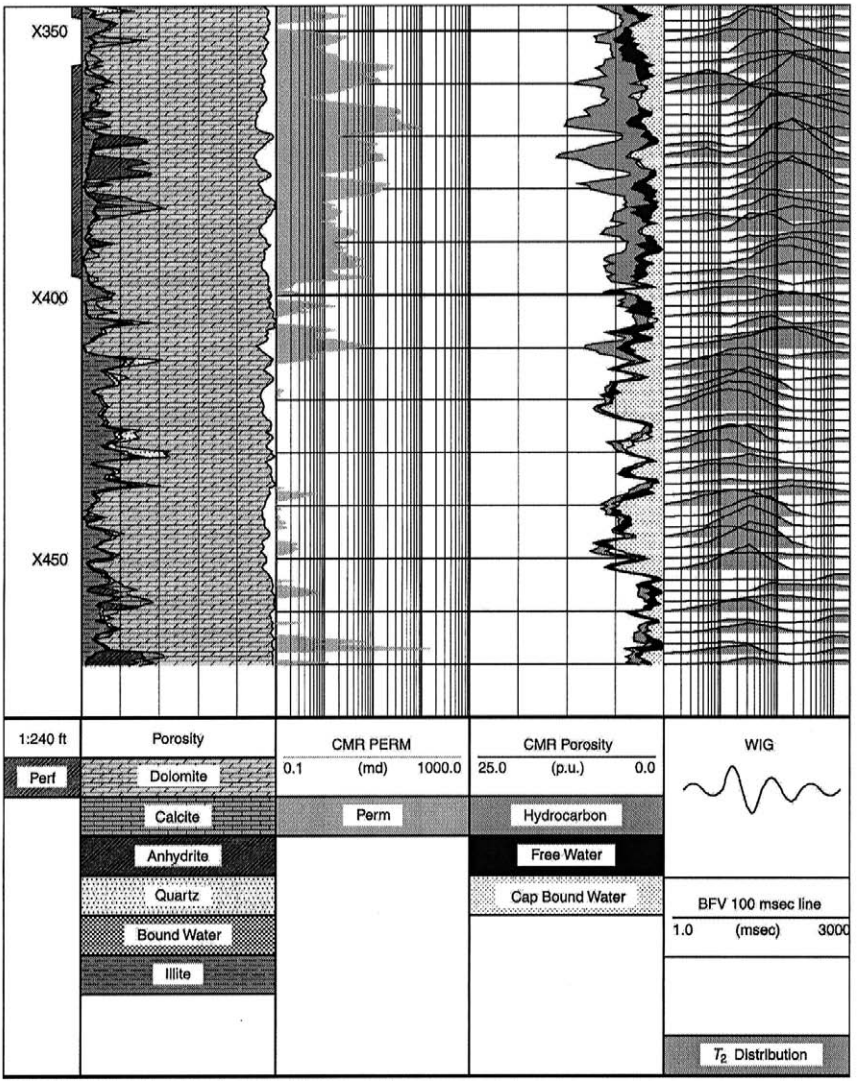

FIG. 9. NMR well log. The depth scale (in feet) is at the extreme left; the most significant digit has been replaced by an X. First panel: Mineralogical analysis of the formation, based on neutron and γ-ray scattering measurements. Second panel: Log of NMR-derived permeability, plotted on a logarithmic scale in units of millidarcies ($1\,\text{mD} \sim 10^{-15}\,\text{m}^2$). Third panel: NMR porosity measurement, partitioned into irreducible water (stipple) movable water (black), and light oil (gray). Fourth panel: T_2 distributions; the horizontal scale is logarithmic and ranges from 1 to 3000 ms. Reprinted with permission from *Schlumberger Oilfield Review*, Autumn 1995, p. 22.

The third panel contains porosity information. The horizontal scale ranges from 0 to 25%, plotted from right to left. The envelope (leftmost line in the track) is the total porosity, found at each depth by integrating the curves of the fourth panel. The porosity is partitioned into several fractions. The stippled area is the irreducible water saturation described in Section 9.9.1. It is found by integrating the panel 4 curves from 1 to 100 ms (as is appropriate for dolomite formations). The balance is the movable fluid fraction, which is further subdivided into water (black) and hydrocarbon (gray), as determined by a resistivity measurement. There is little oil below X410 because oil cannot enter small pores of the water-wet rock.

A log of NMR-derived hydraulic permeability is shown in the second panel. Permeability is plotted on a logarithmic scale and changes by orders of magnitude in this section. In the fine-grained formation the permeability is negligible, while in the upper section it is substantial. These results were used by petroleum engineers to institute an efficient production program for this well.

NMR is an excellent technique for noninvasively monitoring moisture content, the progress of polymerization reactions, and the curing of materials such as cements and ceramics. Inside-out techniques enable these well-established applications to move out of the laboratory and onto the factory floor, food processing plant, or construction site. Large objects can be efficiently inspected by noncontacting means, through piping or protective coatings (which must be nonmetallic), and in remote and/or hostile environments. One such device [192] is simple and compact and appears to have considerable potential in industrial and field applications.

9.12 Conclusion

Nuclear magnetic resonance is capable of providing quantitative, isotope-specific, volumetrically averaged information about fluids imbibed in porous media. Because NMR relaxation rates depend on the freedom of molecules to move, they are a sensitive indicator of chemical or physical changes. Interactions at the fluid–solid interface also influence relaxation rates, thereby making the NMR decay curve a probe of scale length.

Rapidly growing numbers of academic and engineering publications have shown how these capabilities can be exploited in industrially useful applications, such as measurements of moisture content and distribution, the monitoring of drying and hydration, and the quantitation of immiscible fluid phases residing in the pore space. Because NMR is a noncontacting and reasonably rapid measurement, it can be used to monitor processes on a continuous basis in a flowline.

Nuclear magnetic resonance is used on a commercial basis only when its value exceeds the cost of purchase, operation, and maintenance. That threshold has been passed in the petroleum industry, where NMR measurements routinely determine properties of hydrocarbon reservoirs in all parts of the world. It is also being used as an analytical tool in many industrial laboratories for development of processes and for quality control. The availability of low-cost and easy-to-use benchtop and inside-out NMR machines will contribute to more widespread use of the technique.

Acknowledgments

I thank my colleagues at Schlumberger-Doll Research for years of help, discussion, and disputation about NMR of porous media.

References

1. A. T. Watson and C. T. P. Chang, *Prog. NMR Spectros.* 31, 343–386 (1997).
2. C. T. P. Chang, A. T. Watson, and C. M. Edwards, this volume.
3. J. P. Hulin and D. Salin, this volume.
4. A. Abragam, *Principles of Nuclear Magnetism*, Clarendon Press, Oxford, 1961.
5. T. C. Farrar and E. D. Becker, *Pulse and Fourier Transform NMR*, Academic Press, New York, 1971.
6. E. Fukushima and S. B. W. Roeder, *Experimental Pulse NMR*, Addison-Wesley, Reading, Mass., 1981.
7. P. T. Callaghan, *Principles of Nuclear Magnetic Resonance Microscopy*, Clarendon Press, Oxford, 1991.
8. H. Y. Carr and E. M. Purcell, *Phys. Rev.* 94, 630–638 (1954).
9. S. Meiboom and D. Gill, *Rev. Sci. Instrum.* 29, 688–691 (1958).
10. E. L. Hahn, *Phys. Rev.* 80, 580–594 (1950).
11. A. Sezginer, R. L. Kleinberg, M. Fukuhara, and L. L. Latour, *J. Magn. Reson.* 92, 504–527 (1991).
12. H. Pfeifer, in *NMR: Basic Principles and Progress* (P. Diehl *et al.*, eds.), vol. 7, pp. 53–153, Springer-Verlag, New York, 1972.
13. I. Bertini and C. Luchinat, *NMR of Paramagnetic Molecules in Biological Systems*, Benjamin/Cummings, Menlo Park, Calif., 1986.
14. F. Bloch, *Phys. Rev.* 83, 1062–1063 (1951).
15. R. J. S. Brown and I. Fatt, *Petrol. Trans. AIME*, 207, 262–264 (1956).
16. J. Korringa, D. O. Seevers, and H. C. Torrey, *Phys. Rev.* 127, 1143–1150 (1962).
17. K. R. Brownstein and C. E. Tarr, *Phys. Rev. A* 19, 2446–2453 (1979).
18. P.-G. de Gennes, *C. R. Acad. Sci. Paris*, 295, 1061–1064 (1982).

19. M. H. Cohen and K. S. Mendelson, *J. Appl. Phys.* 53, 1127–1135 (1982).
20. D. J. Wilkinson, D. L. Johnson, and L. M. Schwartz, *Phys. Rev. B* 44, 4960–4973 (1991).
21. H. J. V. Tyrrell, *Diffusion and Heat Flow in Liquids*, Butterworths, London, 1961.
22. K. J. Packer, in *Progress in Nuclear Magnetic Resonance Spectroscopy* (J. W. Emsley *et al*., eds.), vol. 3, pp. 87–128, Pergamon, Oxford, 1967.
23. N. Bloembergen, E. M. Purcell, and R. V. Pound, *Phys. Rev.* 73, 679–712 (1948).
24. D. E. Woessner, *J. Magn. Reson.* 39, 297–308 (1980).
25. F. D'Orazio, S. Bhattacharja, W. P. Halperin, K. Eguchi, and T. Mizusaki, *Phys. Rev. B* 42, 9810–9818 (1990).
26. B. M. Fung and T. W. McGaughy, *J. Magn. Reson.* 43, 316–323 (1981).
27. R. L. Kleinberg, W. E. Kenyon, and P. P. Mitra, *J. Magn. Reson.* A108, 206–214 (1994).
28. I. Foley, S. A. Farooqui, and R. L. Kleinberg, *J. Magn. Reson.* A123, 95–104 (1996).
29. W. E. Kenyon and J. A. Kolleeny, *J. Colloid Interface Sci.* 170, 502–514 (1995).
30. P. Roose, J. Van Craen, G. Andriessens, and H. Eisendrath, *J. Magn. Reson.* A120, 206–213 (1996).
31. D. P. Gallegos, K. Munn, D. M. Smith, and D. L. Stermer, *J. Colloid Interface Sci.* 119, 127–140 (1987).
32. P.-z. Wong, *Phys. Today* 41, 24–32 (1988).
33. A. H. Thompson, *Annu. Rev. Earth Planet. Sci.* 19, 237–262 (1991).
34. L. L. Latour, P. P. Mitra, R. L. Kleinberg, and C. H. Sotak, *J. Magn. Reson.* A101, 342–346 (1993).
35. K. S. Mendelson, *J. Electrochem. Soc. Solid-State Sci. Technol.* 133, 631–633 (1986).
36. W. P. Halperin, F. D'Orazio, S. Bhattacharja, and J. C. Tarczon, in *Molecular Dynamics in Restricted Geometries* (J. Klafter and J. M. Drake, eds.), Chap. 11, Wiley, New York, 1989.
37. K. R. McCall, D. L. Johnson, and R. A., Guyer, *Phys. Rev. B* 44, 7344–7355 (1991).
38. T. S. Ramakrishnan, L. M. Schwartz, E. J. Fordham, W. E. Kenyon, and D. J. Wilkinson, *Transactions of the SPWLA 39th Annual Logging Symposium*, Paper SS (1998).
39. L. L. Latour, R. L. Kleinberg, P. P. Mitra, and C. H. Sotak, *J. Magn. Reson.* A112, 83–91 (1995).
40. H. Haranczyk, R. G. Soga, R. J. Rumm, and M. M. Pintar, *Magn. Reson. Imaging* 9, 723–726 (1991).

41. L. L. Latour, R. L. Kleinberg, and A. Sezginer, *J. Colloid Interface Sci.* 150, 535–548 (1992).
42. D. E. Woessner, *J. Phys. Chem.* 67, 1365–1367 (1963).
43. E. O. Stejskal and J. E. Tanner, *J. Chem. Phys.* 42, 288–292 (1965).
44. E. O. Stejskal, *J. Chem. Phys.* 43, 3597–3603 (1965).
45. P. P. Mitra, P. N. Sen, L. M. Schwartz, and P. Le Doussal, *Phys. Rev. Lett.* 68, 3555–3558 (1992).
46. P.-z. Wong, in *AIP Conference Proceedings 154: Physics and Chemistry of Porous Media II* (J. R. Banavar, J. Koplik, and K. W. Winkler, eds.), American Institute of Physics, New York, 1987.
47. P. N. Sen, L. M. Schwartz, P. P. Mitra, and B. I. Halperin, *Phys. Rev. B* 49, 215–225 (1994).
48. R. C. Wayne and R. M. Cotts, *Phys. Rev.* 151, 264–272 (1966); erratum *Phys. Rev.* 159, 486 (1967).
49. D. E. Lauffer, *Phys. Rev. A* 9, 2792–2798 (1974).
50. S. Frey, J. Karger, H. Pfeifer, and P. Walther, *J. Magn. Reson.* 79, 336–342 (1988).
51. L. E. Drain, *Proc. Phys. Soc.* 80, 1380–1382 (1962).
52. J. A. Glasel and K. H. Lee, *J. Am. Chem. Soc.* 96, 970–978 (1974).
53. S. Majumdar and J. C. Gore, *J. Magn. Reson.* 78, 41–55 (1988).
54. R. J. S. Brown and P. Fantazzini, *Phys. Rev. B* 47, 14823–14834 (1993).
55. P. Le Doussal and P. N. Sen, *Phys. Rev. B* 46, 3465–3485 (1992).
56. P. P Mitra and P. Le Doussal, *Phys. Rev. B* 44, 12035–12038 (1991).
57. P. Hardy and R. M. Henkelman, *Magn. Reson. Med.* 17, 348–356 (1991).
58. S. D. Stoller, W. Happer, and F. J. Dyson, *Phys. Rev. A* 44, 7459–7477 (1991).
59. R. M. Weisskoff, C. S. Zuo, J. L. Boxerman, and B. R. Rosen, *Magn. Reson. Med.* 31, 601–610 (1994).
60. G. C. Borgia, R. J. S. Brown, and P. Fantazzini, *Phys. Rev. E* 51, 2104–2114 (1995).
61. M. D. Hurlimann, K. G. Helmer, T. M. DeSwiet, P. N. Sen, and C. H. Sotak, *J. Magn. Reson.* A113, 260–264 (1995).
62. M. A. Horsfield, S. A. Clark, and T. J. Norwood, *J. Magn. Reson.* A122, 222–229 (1996).
63. R. L. Kleinberg, *Magn. Reson. Imaging* 12, 271–274 (1994).
64. C. Straley, C. E. Morriss, W. E. Kenyon, and J. J. Howard, *Transactions of the SPWLA 32nd Annual Logging Symposium*, Paper CC (1991); *Log Analyst*, pp. 40–56 (January–February 1995).
65. A. Timur, *J. Petrol. Tech.* 21, 775–786 (1969).
66. W. E. Kenyon, P. I. Day, C. Straley, and J. F. Willemsen, *Soc. Petrol. Eng. Form. Eval.* 3, 622–636 (1988); erratum: *Soc. Petrol. Eng. Form. Eval.* 4, 8 (1989).

67. J. Klafter and M. F. Shlesinger, *Proc. Natl. Acad. Sci. USA* 83, 848–851 (1986).

68. P. A. Beckmann, *Phys. Reports* 171, 85–128 (1988).

69. S. H. Chung and J. R. Stevens, *Am. J. Phys.* 59, 1024–1030 (1991).

70. M. Peyron, G. K. Pierens, A. J. Lucas, L. D. Hall, and R. C. Stewart, *J. Magn. Reson.* A118, 214–220 (1996).

71. D. P. Gallegos and D. M. Smith, *J. Colloid Interface Sci.* 122, 143–153 (1988).

72. R. L. Kleinberg, S. A. Farooqui, and M. A. Horsfield, *J. Colloid Interface Sci.* 158, 195–198 (1993).

73. W. E. Kenyon, *Nucl. Geophys.* 6, 153–171 (1992).

74. R. L. Kleinberg and M. A. Horsfield, *J. Magn. Reson.* 88, 9–19 (1990).

75. R. L. Kleinberg, C. Straley, W. E. Kenyon, R. Akkurt, and S. A. Farooqui, Society of Petroleum Engineers Paper 26470 (1993).

76. D. O. Seevers, *Transactions of the SPWLA 7th Annual Logging Symposium*, paper L (1966).

77. B. I. Tul'bovich, F. A. Slisarenko, V. I. Klyaev, and S. I. Sorokin, *Izv. Vyssh. Ucheb. Zavel., Khim. Khim. Tekknol.* 9, 735–737 (1966).

78. J. D. Loren and J. D. Robinson, *Soc. Petrol. Eng. J.* 10, 268–278 (1970).

79. J. A. Brown, L. F. Brown, J. A. Jackson, J. V. Milewski, and B. J. Travis, Society of Petroleum Engineers Paper 10813 (1982).

80. C. Straley, A. Matteson, S. Feng, L. M. Schwartz, W. E. Kenyon, and J. R. Banavar, *Appl. Phys. Lett.* 51, 1146–1148 (1987).

81. Z. R. Hinedi, A. C. Chang, M. A. Anderson, and D. B. Borchardt, *Water Res. Res.* 33, 2697–2704 (1997).

82. T. G. Rochow and E. G. Rochow, *An Introduction to Microscopy by Means of Light, Electrons, X-Rays, or Ultrasound*, Plenum, New York, 1978.

83. J. I. Goldstein and H. Yakowitz, eds. *Practical Scanning Electron Microscopy*, Plenum, New York, 1975.

84. S. Lowell and J. E. Shields, *Powder Surface Area and Porosity*, Chapman and Hall, New York, 1984.

85. J. W. Amyx, D. M. Bass, Jr., and R. L. Whiting, *Petroleum Reservoir Engineering*, McGraw-Hill, New York, 1988.

86. S. Brunauer, P. H. Emmett, and E. Teller, *J. Am. Chem. Soc.* 60, 309–319 (1938).

87. M. D. Hurlimann, K. G. Helmer, L. L. Latour, and C. H. Sotak, *J. Magn. Reson.* A111, 169–178 (1994).

88. E. J. Fordham, S. J. Gibbs, and L. D. Hall, *Magn. Reson. Imaging* 12, 279–284 (1994).

89. H.-K. Liaw, R. Kulkarni, S. Chen, and A. T. Watson, *Am. Inst. Chem. Eng. J.* 42, 538–546 (1996).

90. T. Skjetne, T. E. Southon, B. Hafskjold, O. Selle, I. Svorstol, A. T. Buller, H. Rueslatten, A. Brayshaw, and M. Z. Kalam, *Magn. Reson. Imaging* 9, 673–679 (1991).
91. P.-z. Wong, J. J. Howard, and J.-S. Lin, *Phys. Rev. Lett.* 57, 637–640 (1986).
92. G. Sposito, *The Surface Chemistry of Soils*, Chap. 1, Oxford University Press, New York, 1984.
93. D. E. Woessner and B. S. Snowden, Jr., *J. Colloid Interface Sci.* 30, 54–68 (1969).
94. J. Hougardy, W. E. E. Stone, and J. J. Fripiat, *J. Chem. Phys.* 64, 3840–3851 (1976).
95. O.-M. Nes, P. Horsrud, and T. Skjetne, *Society of Exploration Geophysicists Expanded Abstracts, 1993 Technical Program*, pp. 88–91 (1993).
96. D. J. Cebula, R. K. Thomas, and J. W. White, *J. Chem. Soc. Faraday I* 76, 314–321 (1980).
97. J. M. Adams, C. Breen, and C. Riekel, *J. Colloid Interface Sci.* 68, 214–220 (1979).
98. W. E. Kenyon, J. J. Howard, A. Sezginer, C. Straley, A. Matteson, K. Horkowitz, and R. Ehrlich, *Transactions of the SPWLA 30th Annual Logging Symposium*, Paper LL (1989).
99. C. E. Morriss, J. MacInnis, R. Freedman, J. Smaardyk, C. Straley, W. E. Kenyon, H. J. Vinegar, and P. N. Tutunjian, *Transactions of the SPWLA 34th Annual Logging Symposium*, Paper GGG (1993).
100. D. Marschall, J. S. Gardner, D. Mardon, and G. R. Coates, *Proceedings of the 1995 International Symposium of the Society of Core Analysts*, Paper SCA-9511 (1995).
101. R. L. Kleinberg, *Magn. Reson. Imaging*, 14, 761–767 (1996).
102. C. Straley, D. Rossini, H. Vinegar, P. Tutunjian, and C. Morriss, *Proceedings of the 1994 International Symposium of the Society of Core Analysts*, Paper SCA-9404 (1994).
103. A. N. Tikhonov and V. Y. Arsenin, *Solutions of Ill-Posed Problems*, V. H. Winston & Sons, Washington, D.C., 1977.
104. J. P. Butler, J. A. Reeds, and S. V. Dawson, *SIAM J. Numer. Anal.* 18, 381–397 (1981).
105. S. W. Provencher, *Comput. Phys. Commun.* 27, 213–227 (1982); S. W. Provencher, *Comput. Phys. Commun.* 27, 229–242 (1982).
106. W. H. Press, S. A. Teukolsky, W. T. Vetterling, and B. P. Flannery, *Numerical Recipes in C*, 2nd ed. Chap. 18, Cambridge University Press, New York, 1992.
107. P. C. Hansen, *Numerical Algorithms* 6, 1–35 (1994).
108. R. Freedman, U.S. Patent 5,291,137 (1994).
109. M. G. Prammer, Society of Petroleum Engineers Paper 28368 (1994).
110. E. J. Fordham, A. Sezginer, and L. D. Hall, *J. Magn. Reson.* A113, 139–150 (1995).

111. K. P. Whittall, M. J. Bronskill, and R. M. Henkelman, *J. Magn. Reson.* 95, 221–234 (1991).

112. R. Freedman and C. E. Morriss, Society of Petroleum Engineers Paper 30560 (1995).

113. C. Straley and L. M. Schwartz, *Magn. Reson. Imaging* 14, 999–1002 (1996).

114. M. Peyron, G. K. Pierens, A. J. Lucas, L. D. Hall, G. F. Potter, R. C. Stewart, and D. W. Phelps, *Magn. Reson. Imaging* 12, 295–298 (1994).

115. G. C. Borgia, V. Bortolotti, A. Brancolini, R. J. S. Brown, and P. Fantazzini, *Magn. Reson. Imaging* 14, 751–760 (1996).

116. L. F. Gladden, *Chem. Eng. Sci.* 49, 3339–3408 (1994).

117. W. L. Rollwitz and G. A. Persyn, *J. Am. Oil Chem. Soc.* 48, 59–66 (1971).

118. R. J. Gummerson, C. Hall, W. D. Hoff, R. Hawkes, G. N. Holland, and W. S. Moore, *Nature* 281, 56–57 (1979).

119. L. F. Gladden, *Trans. Inst. Chem. Eng.: Chem. Eng. Res. Des.* 71A, 657–674 (1993).

120. K. Kopinga and L. Pel, *Rev. Sci. Instrum.* 65, 3673–3681 (1994).

121. P. J. McDonald, T. Pritchard, and S. P. Roberts, *J. Colloid Interface Sci.* 177, 439–445 (1996).

122. S. P. Roberts, P. J. McDonald, and T. Pritchard, *J. Magn. Reson.* A116, 189–195 (1995).

123. L. F. Gladden, *Chem. Eng. J.* 56, 149–158 (1995).

124. K. G. Soga, H. Haranczyk, R. J. Rumm, and M. M. Pintar, *Magn. Reson. Imaging* 9, 727–731 (1991).

125. S. Chen, H.-K. Liaw, and A. T. Watson, *J. Appl. Phys.* 74, 1473–1479 (1993).

126. R. T. Pearson and W. Derbyshire, *J. Colloid Interface Sci.* 46, 232–248 (1974).

127. R. Schmidt, E. W. Hansen, M. Stocker, D. Akporiaye, and O. H. Ellestad, *J. Am. Chem. Soc.* 117, 4049–4056 (1995).

128. D. G. Levine, R. H. Schlosberg, and B. G. Silbernagel, *Proc. Natl. Acad. Sci. USA* 79, 3365–3370 (1982).

129. J. H. Strange and J. B. W. Webber, *Meas. Sci. Technol.* 8, 555–561 (1997).

130. L. J. Schreiner, J. C. MacTavish, L. Miljkovic, M. M. Pintar, R. Blinc, G. Lahajnar, D. Lasic, and L. W. Reeves, *J. Am. Ceram. Soc.* 68, 10–16 (1985).

131. W. P. Halperin, J.-Y. Jehng, and Y.-Q. Song, *Magn. Reson. Imaging* 12, 169–173 (1994).

132. M. Bogdan, B. J. Balcom, T. W. Bremner, and R. L. Armstrong, *J. Magn. Reson.* A116, 266–269 (1995).

133. M. A. Horsfield, E. J. Fordham, C. Hall, and L. D. Hall, *J. Magn. Reson.* 81, 593–596 (1989).

134. E. J. La Heij, P. J. A. M. Kerkhof, K. Kopinga, and L. Pel, *Am. Inst. Chem. Eng. J.* 42, 953–959 (1996).

135. G. C. Borgia, P. Fantazzini, C. Palmonari, and G. Timellini, *Magn. Reson. Imaging* 14, 899–901 (1996).
136. G. C. Borgia, P. Fantazzini, and E. Mesini, *J. Appl. Phys.* 70, 7623–7625 (1991).
137. G. Guillot, C. Chardaire-Riviere, S. Bobroff, A. Le Roux, J. C. Roussel, and L. Cuiec, *Magn. Reson. Imaging* 12, 365–368 (1994).
138. D. M. Marschall and G. Coates, Society of Petroleum Engineers Paper 38739 (1997).
139. J. R. Banavar and L. M. Schwartz, in *Molecular Dynamics in Restricted Geometries* (J. Klafter and J. M. Drake, eds.), Chap. 10, Wiley, New York, 1989.
140. C. Chardaire-Riviere and J. C. Roussel, *Rev. Inst. Francais Petr.* 47, 503–523 (1992).
141. R. L. Kleinberg, in *Encyclopedia of Nuclear Magnetic Resonance* (D. M. Grant and R. K. Harris, eds.), vol. 8, pp. 4960–4969, Wiley, Chichester, 1996.
142. J. A. Jackson and M. Mathews, *Log Anal.* 34(3), 35–69 (1993).
143. S. E. Prensky, *Log Anal.* 39(2), 93–98 (1998).
144. C. E. Weaver, *Clays, Muds, and Shales*, Elsevier, Amsterdam, 1989.
145. A. E. Scheidegger, *The Physics of Flow Through Porous Media*, Macmillan, New York, 1960.
146. A. E. Scheidegger, in *Encyclopedia of Physics* (C. Truesdell, ed.), vol. VIII/2, pp. 625–662, Springer-Verlag, Berlin, 1963.
147. A. H. Thompson, S. W. Sinton, S. L. Huff, A. J. Katz, R. A. Raschke, and G. A. Gist, *J. Appl. Phys.* 65, 3259–3263 (1989).
148. D. Chang, H. Vinegar, C. Morriss, and C. Straley, *Transactions of the SPWLA 35th Annual Logging Symposium*, Paper A (1994).
149. R. L. Kleinberg and H. J. Vinegar, *Log Anal.* 37(6), 20–32 (1996).
150. C. E. Morriss, R. Freedman, C. Straley, M. Johnston, H. J. Vinegar, and P. N. Tutunjian, *Transactions of the SPWLA 35th Annual Logging Symposium*, Paper C (1994).
151. S. Rajan, K. Lalita, and S. V. Babu, *J. Magn. Reson.* 16, 115–129 (1974).
152. C. Straley, *Transactions of the SPWLA 38th Annual Logging Symposium*, Paper AA (1997).
153. K. R. Harris, *Physica* 94A, 448–464 (1978).
154. R. Akkurt, H. J. Vinegar, P. N. Tutunjian, and A. J. Guillory, *Transactions of the SPWLA 36th Annal Logging Symposium*, Paper N (1995).
155. M. D. Hurlimann, *J. Magn. Reson.* 131, 232–240 (1998).
156. A. G Redfield and R. K. Gupta, in *Advances in Magnetic Resonance* (J. S. Waugh, ed.), vol. 5, Academic Press, New York, 1971.
157. J. D. Ellett, Jr. , M. G. Gibby, U. Haeberlen, L. M. Huber, M. Mehring, A. Pines, and J. S. Waugh, in *Advances in Magnetic Resonance* (J. S. Waugh, ed.), vol. 5, Academic Press, New York, 1971.
158. D. I. Hoult and R. E. Richards, *Proc. Roy. Soc. Lond. A* 344, 311–340 (1975).

159. D. I. Hoult and R. E. Richards, *J. Magn. Reson.* 24, 71–85 (1976).

160. D. I. Hoult, *Prog. NMR Spectros.* 12(1), 41–77 (1978).

161. R. F. Karlicek and I. J. Lowe, *J. Magn. Reson.* 32, 199–225 (1978).

162. K. Jurga, E. C. Reynhardt, and S. Jurga, *J. Magn. Reson.* 96, 302–306 (1992).

163. D. D. Griffin, R. L. Kleinberg, and M. Fukuhara, *Meas. Sci. Tech.* 4, 968–975 (1993).

164. H. R. Kirchmayr, *J. Phys. D* 29, 2763–2778 (1996).

165. C. D. Motchenbacher and F. C. Fitchen, *Low-Noise Electronic Design*, Wiley, New York, 1973.

166. H. W. Ott, *Noise Reduction Techniques in Electronic Systems*, Wiley, New York, 1976.

167. W. E. Timms, *J. Med. Eng. Tech.* 16, 69–78 (1992).

168. A. B. Przedpelski, *Electron. Design* 5, 54–62 (1978).

169. R. L. Thomas, *A Practical Introduction to Impedance Matching*, Artech, Dedham, Mass., 1978.

170. E. R. Andrew and K. Jurga, *J. Magn. Reson.* 73, 268–276 (1987).

171. D. I. Hoult, *Rev. Sci. Instrum.* 50, 193–200 (1979).

172. D. P. Blair and P. H. Sydenham, *J. Phys. E* 8, 621–627 (1975).

173. M. Schirov, A. Legchenko, and G. Creer, *Expl. Geophys.* 22, 333–338 (1991).

174. O. A. Shushakov, *Geophys.* 61, 998–1006 (1996).

175. B. Favre, J. P. Bonche, H. Mehier, and J. O. Peyrin, *Magn. Reson. Med.* 13, 299–304 (1990).

176. J. Stepisnik, V. Erzen, and M. Kos, *Magn. Reson. Med.* 15, 386–391 (1990).

177. G. J. Bene, in *Encyclopedia of Nuclear Magnetic Resonance* (D. M. Grant and R. K. Harris, eds.), vol. 7, pp. 4697–4702, Wiley, Chichester, 1996.

178. R. F. Paetzold, G. A. Matzkanin, and A. De Los Santos, *Soil Sci. Soc. Am. J.* 49, 537–540 (1985).

179. R. F. Paetzold, A. De Los Santos, and G. A. Matzkanin, *Soil Sci. Soc. Am. J.* 51, 287–290 (1987).

180. R. J. S. Brown and B. W. Gamson, *Petrol. Trans. AIME* 219, 199–207 (1960).

181. R. K. Cooper and J. A. Jackson, *J. Magn. Reson.* 41, 400–405 (1980).

182. L. J. Burnett and J. A. Jackson, *J. Magn. Reson.* 41, 406–410 (1980).

183. J. A. Jackson, L. J. Burnett, and J. F. Harmon, *J. Magn. Reson.* 41, 411–421 (1980).

184. Z. Taicher, G. Coates, Y. Gitartz, and L. Berman, *Magn. Reson. Imaging* 12, 285–289 (1994).

185. R. L. Kleinberg, A. Sezginer, D. D. Griffin, and M. Fukuhara, *J. Magn. Reson.* 97, 466–485 (1992).

186. P. Kinchesh, E. W. Randall, and K. Zick, *J. Magn. Reson.* 100, 411–415 (1992).

187. J. H. Strange and M. R. Halse, in *Encyclopedia of Nuclear Magnetic Resonance*, (D. M. Grant and R. K. Harris, eds.), vol. 4, pp. 2476–2477, Wiley, Chichester, 1996.

188. P. J. McDonald, *Prog. NMR Spectros.* 30, 69–99 (1997).

189. J. R. Hearst and P. H. Nelson, *Well Logging for Physical Properties*, McGraw-Hill, New York, 1985.

190. D. V. Ellis, *Well Logging for Earth Scientists*, Elsevier, New York, 1987.

191. R. L. Kleinberg and C. Flaum, in *Spatially Resolved Magnetic Resonance* (P. Blumler *et al.*, eds.), Chap. 54, Wiley-VCH, Weinheim, Germany, 1998).

192. G. Eidmann, R. Savelsberg, P. Blumler, and B. Blumich, *J. Magn. Reson.* A122, 104–109 (1996).

This Page Intentionally Left Blank

10. NMR IMAGING OF FLUIDS AND FLOW IN POROUS MEDIA

C. T. Philip Chang and A. Ted Watson

Department of Chemical Engineering and Engineering Imaging Laboratory
Texas A&M University
College Station, Texas

Carl M. Edwards

Baker Atlas, Division of Baker Hughes, Inc.
Houston, Texas

10.1 Introduction

Many processes of interest to industry and society involve the flow of fluids through porous media. For example, filtration is used to purify water and treat sewage, membranes are used to separate gases, and chemical reactions are carried out in reactors packed with porous catalyst supports. Large-scale processes in nature include the flow of petroleum in underground reservoirs and the flow of water in aquifers.

It is often desired to simulate the flow of fluids in porous media to design processes or make decisions regarding operation and control. Such simulations require suitable mathematical models that relate various fluid states, as well as various porous media properties that may be defined within the models. The considerable efforts that have been directed to such endeavors have been significantly limited by the lack of means for observing fluid states *within* porous media. Nuclear magnetic resonance (NMR) provides many exciting new opportunities for probing fluid states and flow within porous media. It is a noninvasive method that is sensitive to molecular-level events within fluids, and with imaging, fluid states and properties can be resolved spatially. While other techniques such as optical, ultrasonic, and x-ray methods can be used to visualize fluid saturations and flow patterns, nuclear magnetic resonance imaging (MRI) provides unique and effective methods for obtaining quantitative information on the distribution and flow of fluids within porous media.

MRI can image nuclear spin density, NMR relaxation processes, chemical compositions, and the fluid transport processes of diffusion and flow.

EXPERIMENTAL METHODS IN THE PHYSICAL SCIENCES
Vol. 35
ISBN 0-12-475982-3

ISSN 1079-4042/99 $30.00

This chapter deals with the application of these techniques to probe fluids and flow in porous media, for which the imaging methods and interpretations of image data are often complicated due to the effects that the solid matrix has on the fluid. We will assume that the reader has some familiarity with NMR, but not imaging. For further information about the use of NMR with porous media, we recommend Ch. 9 of this text, the text by Callaghan [1], and the review article by Watson and Chang [2]. Of course, there are many good texts on NMR principles and experimental methods, and we recommend Farrar and Becker [3] and Fukushima and Roeder [4]. Mansfield and Morris [5] have written a monograph on the application of NMR imaging in medicine and biology that provides a good description of imaging.

Although the fundamental imaging principles used in biomedical imaging are generally applicable to imaging fluid flow in porous media, obtaining quantitative images sensitive to only one of the desired NMR parameters in porous solids requires special considerations. The challenges as well as those experimental techniques developed to probe fluids and flow in porous media are covered in Section 10.2. Some applications of MRI to processes in porous media are provided in Section 10.3.

10.2 Imaging in Porous Media

The general objectives of NMR imaging are to obtain a number of NMR parameters, such as spin density and relaxation times, as functions of their spatial positions. Most imaging methods use magnetic field gradients of one sort or another to accomplish spatial discrimination. Various imaging methods have been classified into three regimes — point, line, and plane — according to the manner in which the spatial element of the image data is acquired. Generally, it is advantageous from signal-to-noise considerations to select a method in which the largest number of spins are detected at each step of the data acquisition. The Fourier imaging method, which encodes the spatial information in the phase of the NMR signal in a plane-by-plane scan in Cartesian coordinates, has been shown to be optimal with respect to signal-to-noise [6] and the data processing to form an image is straightforward. If the magnetization of the sample is perturbed by slice-selective excitation, the image can be reconstructed in the two dimensions of the plane of the slice.

Porous media are ubiquitous. Within living beings, for example, skin, vessels, and bone as well as many organs are porous materials. For many medical applications, the properties of the porous media need not be explicitly considered or determined for diagnostic purposes. However,

imaging within porous solids, such as sedimentary media that make up petroleum reservoirs and aquifers, requires particular considerations. The solid matrix material can have a profound effect on relaxation and can also cause significant gradients of the magnetic field. This can limit the resolution of standard imaging methods and complicate issues of quantification. Since samples observed within the laboratory are not part of the actual process of interest, which occurs underground, diagnostic analysis is of little value. Instead, determination of understandings of the complex processes that may occur, and properties useful for describing those processes, is important. This necessitates the development of quantitative means for analyzing measured NMR signals. Many processes of interest may involve multiple fluid phases. For example, the recovery of fluids from petroleum reservoirs may involve the flow of two fluid phases, such as oil and water, or three fluid phases, such as oil, water, and gas, through porous media. Thus, an important consideration is to be able to observe the fluid phases separately, or to distinguish the portion of the measured signals corresponding to the various fluid phases. In short, such porous materials provide many challenges to the effective use of MRI for noninvasive probes of the media and flow processes.

In the first part of this section (Section 10.2.1), a brief overview of the basic physical principles of NMR imaging is provided. The unique aspects and challenges of imaging fluids in porous media are discussed in Section 10.2.2. The remainder of this section addresses the use of contrast techniques to obtain maps of specific molecular species (Section 10.2.3), practical techniques used for quantitative imaging (Section 10.2.4), and imaging of molecular translational motion (Section 10.2.5).

10.2.1 Imaging Background

A typical Fourier imaging pulse sequence is shown in Fig. 1. It is a variant of the spin-warp [7] pulse sequence. This particular sequence generates a two-dimensional map of the spin density using two Fourier transforms. It is composed of three building blocks that we discuss in detail: (1) selective excitation, (2) frequency encoding, and (3) phase encoding. These fundamental imaging concepts provide a foundation for understanding many of the various NMR imaging methods.

The pulse sequence shown, which is composed of two radio-frequency (RF) pulses, uses a spin echo to produce images. The RF pulses are selective pulses. Their energy is distributed only over a limited range of frequencies, which can be contrasted with nonselective pulses that distribute energy over a large frequency range, usually much larger than the frequency range of interest. When a selective RF pulse is applied simultaneously with a field

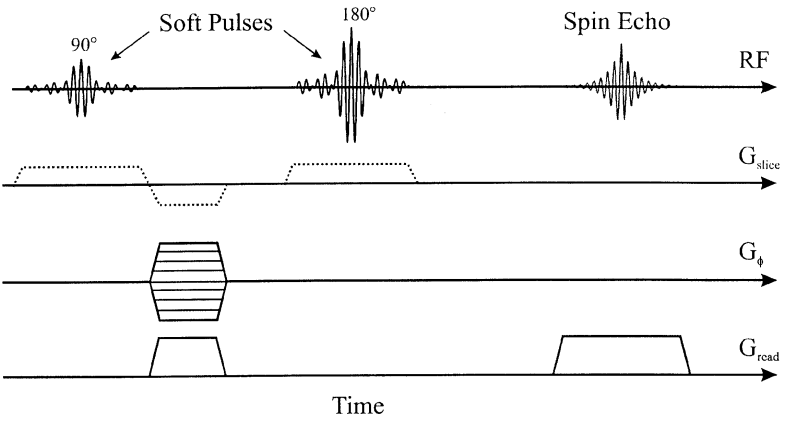

FIG. 1. Example of a typical two-dimensional Fourier transform spin-echo imaging pulse sequence, which is a variation of the spin-warp sequence. The top line represents the time variation of both the applied RF and the received spin-echo signal. When the spectral-selective pulses, also known as *soft* pulses, are applied in the presence of the slice gradients, only those spins within a slice of the sample are affected. The bottom three lines represent the time variation of three magnetic field gradients. They are usually perpendicular to each other, although this is not required.

gradient, the result is a slice-selective pulse. The gradient is used to generate a distribution of Larmor frequencies that is much larger than the limited frequency range of the selective pulse. The pulse then selectively excites nuclei that have Larmor frequencies in the pulse's frequency band. The result is the excitation of spins in a plane normal to the direction of the magnetic field gradient. For this reason, the gradient is commonly known as the slice gradient and we denote it here by G_{slice}. The thickness and position of the plane depend on the details of the RF pulse and strength of the field gradient.

The second important building block is the application of a magnetic field gradient during data acquisition. This gradient, G_{read}, is sometimes referred to as the readout (or read) gradient. We refer to it as the frequency-encoding gradient, which is precisely what it does. It encodes spatial information in the Larmor frequency at which each spin in the sample resonates. It is normally orthogonal to G_{slice}. The frequency-encoding gradient is applied for a time period that includes the spin echo (see Fig. 1).

The third building block is the application of a pulsed field gradient that is usually perpendicular to both the slice selective gradient and the frequency-encoding gradient. The purpose of this gradient is to encode spatial

information in the phase of the NMR signal. To acquire the data necessary for a complete image, the sequence shown in Fig. 1 must be repeated many times. A different amplitude of the phase-encoding gradient is applied each time the sequence is repeated. This is shown by the cross-hatching in the diagram.

A complete set of image data is comprised of m digitized spin echoes. If each digitized echo has n complex points (quadrature detection), then the data can be thought of as a 2-D matrix with rows corresponding to time evolution of the signal in the presence of the read gradient G_{read} and columns corresponding to different values of the gradient amplitude G_{ϕ}. The image is constructed by a 2-D discrete Fourier transform of the rows and columns of this matrix.

These building blocks can be well described by the Bloch equations. In fact, they can be adequately described neglecting the relaxation terms in the Bloch equations, as shown in the following.

10.2.1.1 Precession of Nuclear Magnetization in a Magnetic Field Gradient. While conventional NMR spectroscopy requires the use of a homogeneous magnetic field $\mathbf{B}_0$, NMR imaging is accomplished by making the magnetic field vary linearly across the sample space. This is accomplished by applying an additional small field B, which is in the direction of $\mathbf{B}_0$ and has a constant gradient, $\mathbf{G} = \nabla B$. The field gradient is switched on and off in an imaging sequence. We use $\mathbf{g}(t)$ to denote the time-varying gradient amplitude associated with the gradient pulses. When the gradient pulse is on, $\mathbf{g}(t) = \mathbf{G}$, while $\mathbf{g}(t) = 0$ when it is off. The field gradient gives rise to a spatially dependent distribution of Larmour frequencies, $\omega(\mathbf{r}) = -\gamma(B_0 + \mathbf{g}\cdot\mathbf{r})$. Under the on-resonance condition—that is, the frequency of the RF field $\Omega = -\gamma\mathbf{B}_0$—the magnetization is no longer static in the rotating frame but precesses with a frequency

$$\omega'(\mathbf{r}) = -\gamma\mathbf{g}\cdot\mathbf{r}, \tag{1}$$

depending on the position $\mathbf{r}$. In the absence of relaxation and the RF magnetic field, the Bloch equations for a volume element at $\mathbf{r}$ simplify to

$$\begin{aligned} \frac{dM_{z'}}{dt} &= 0, \\ \frac{dM_{x'}}{dt} &= \gamma M_{y'}\mathbf{g}\cdot\mathbf{r}, \\ \frac{dM_{y'}}{dt} &= -\gamma M_{x'}\mathbf{g}\cdot\mathbf{r}, \end{aligned} \tag{2}$$

in the rotating frame, where M_i are the components of the magnetization

vector. These equations are immediately solved using the complex notation

$$M_+(\mathbf{r}, t) \equiv M_{x'}(\mathbf{r}, t) + iM_{y'}(\mathbf{r}, t) = M_0(\mathbf{r}) \exp(-i2\pi\mathbf{k}\cdot\mathbf{r}), \tag{3}$$

where the reciprocal space vector $\mathbf{k}$ is defined as

$$\mathbf{k} = (2\pi)^{-1}\gamma \int_0^t \mathbf{g}(t')\, dt'. \tag{4}$$

The signal produced by the nuclear magnetization is a linear superposition of the signal from each elemental volume of the entire sample. Accordingly, the detected signal is the integral of $M_+(\mathbf{r}, t)$ over the whole sample volume:

$$S(\mathbf{k}) = \int M_0(\mathbf{r}) \exp(-i2\pi\mathbf{k}\cdot\mathbf{r})\, d\mathbf{r}. \tag{5}$$

The result forms the basis for understanding both frequency encoding and phase encoding of spatial information in the NMR signal. In practice, $S(\mathbf{k})$ is sampled in the $\mathbf{k}$-space by varying either the duration or amplitude of the gradient pulse. The reconstruction of $M_0(\mathbf{r})$ can be obtained by Fourier transforming the detected signal with respect to $\mathbf{k}$. In a real experiment, an additional phase factor resulting from the inhomogeneities in B_0 and other instrumentation factors (e.g., the receiver phase) may contribute to the integrand in Eq. (5). To obtain $M_0(\mathbf{r})$ free from this phase factor, one can take the magnitude of each point in the Fourier transformed complex array. In principle, the magnitude of $M_0(\mathbf{r})$ is proportional to the spin density $\rho(\mathbf{r})$. However, it is always affected by the contrast effects such as spin relaxations.

10.2.1.2 Selective Excitation. Selective excitation is a procedure whereby the applied RF pulse is tailored so that only a well-specified range of the NMR frequency spectrum is affected. When this is done in the presence of a magnetic field gradient, the selective RF pulse excites only those spins within a slice of the physical sample.

The width of the excited frequency band is inversely proportional to the duration of the RF pulse. For a given tip angle, the duration of an RF pulse determines the pulse intensity since the angle through which the magnetization tips is $\gamma B_1 t_p$ for an RF pulse of duration t_p and field amplitude B_1. It is easy to see that a broadband 90° pulse will have a larger B_1 than a narrow-band pulse. For this reason, a nonselective broadband RF pulse is called a *hard* pulse and a selective narrow-band pulse is termed a *soft* pulse.

A number of RF amplitude modulation and multiple-pulse schemes have been used to accomplish the selective excitation. For example, a Gaussian amplitude modulation pulse has been used in chemical shift-selective excitations. In general, the corresponding frequency spectrum of an RF pulse is

given by the Fourier transform of its time domain profile. A rectangular frequency spectrum is required if a rectangular slice is to be excited. This implies that the RF amplitude in the time domain should be modulated as a sinc function, $\sin(ct)/(ct)$. Since the duration of a sinc function is infinite, a truncated sinc pulse is actually used.

For a selective 90° RF pulse of duration t_p applied in the presence of a slice-selective gradient G_{slice} taken to be in the z direction, the Bloch equations in the rotating frame yield

$$\frac{dM_{z'}}{dt} = 0,$$

$$\frac{dM_{x'}}{dt} = \gamma M_{y'} G_{\text{slice}} z,$$

$$\frac{dM_{y'}}{dt} = \gamma M_{z'} B_1(t) - \gamma M_{x'} G_{\text{slice}} z, \tag{6}$$

where the RF field $B_1(t)$ defines the x' direction of the rotating frame. The time evolution of the magnetization can be solved analytically [8] after transforming Eq. (6) into another frame of reference that rotates about the negative z direction at a frequency of $\gamma G_{\text{slice}} z$ with respect to the frame $(x', y' z')$. As a result, the signal contributed by the spins on a plane at z is expressed as

$$M_+(z) = i\gamma M_0(z) \exp(-i\gamma G_{\text{slice}} z t_p/2) \int_{-t_p/2}^{t_p/2} B_1(t') \exp(i\gamma G_{\text{slice}} z t')\, dt'. \tag{7}$$

The integral in Eq. (7) is the Fourier transform of the RF field, which represents the frequency spectrum of the RF pulse. For a sinc profile in the time domain, the spectrum, which has a frequency variable of $\gamma G_{\text{slice}} z$, is rectangular. This means that only those spins within a slice of finite thickness are affected. If the phase of the RF field is modulated with a constant angular frequency ω_m — that is, the RF field becomes $B_1(t)\exp(i\omega_m t)$ — then the conjugate variable of the Fourier transform of the RF field in Eq. (7) becomes $\gamma G_{\text{slice}} z + \omega_m$. This procedure results in an offset of the slice location by an amount $\Delta z = \omega_m/\gamma G_{\text{slice}}$. The z-dependent phase twist, $-\gamma G_{\text{slice}} z t_p/2$, in Eq. (7) is annoying but can easily be removed. In Fig. 1, an inverted gradient of amplitude $-G_{\text{slice}}$ for a duration $t_p/2$ is applied following the slice-selective gradient pulse. Note that no additional reversing gradient pulse is required for the selective 180° RF pulse because it is self-rephasing.

Using the basic spatial encoding and slice selection principles, a number of different techniques are available, both in terms of imaging schemes (e.g.,

1-D, 2-D, or 3-D) and pulse sequences (e.g., spin-echo, stimulated-echo, or gradient-echo) that enhance or suppress different contrast mechanisms and produce images of NMR parameters that relate directly or indirectly to parameters of interest in regard to fluid flow in porous media. An understanding of the basic physical principles and nomenclature of NMR imaging is thus important in evaluating different imaging strategies and in appreciating the advantages and limitations of these techniques.

10.2.2 Considerations for Imaging in Porous Media

The use of NMR imaging to investigate and characterize the properties of fluids and flow in porous media is carried out by detecting the signals from the fluid phase. Protons are the most commonly observed nuclei. The primary challenge presented by fluid-saturated porous systems in terms of NMR imaging is the fast transverse relaxation, which is sensitive to the pore size and saturation. Imaging sequences have a certain minimum time from excitation of the spin system to acquiring image data. Thus, some relaxation will have occurred before data are acquired. This makes quantification of porosity or fluid saturation difficult. Furthermore, some fluid may reside in pores so small as to be unobservable by NMR imaging techniques, even at an echo time as short as only a few milliseconds. But if due care is taken in selecting samples and designing the experiment, useful NMR imaging studies can be performed.

The enhancements in T_2 relaxation due to the surfaces and diffusion of molecules in the presence of internal magnetic-susceptibility-derived gradients result in a more rapid dephasing of transverse magnetization and therefore act as additional line-broadening mechanisms. The line broadening imposes a fundamental limitation to the spatial resolution Δr in NMR imaging [9]:

$$\Delta r = \frac{2\pi\Delta f}{\gamma G}, \tag{8}$$

where G is either the strength of the readout gradient or the maximum strength of the phase-encoding gradient, and Δf is the NMR linewidth. The image resolution employed in most studies of porous systems to date has been considerably larger than the pore size.

The signal-to-noise ratio (S/N) provides another limitation to spatial resolution in NMR imaging since the signal available from each volume element (voxel) decreases as the voxel size is reduced. Moreover, the fluid content for each voxel in porous media is usually less than 30% by volume depending on the porosity, which makes the signal sensitivity even worse. Since the S/N of an NMR imaging experiment increases with the strength

of the applied magnetic field, it would seem desirable to perform at the strongest possible static field. However, the internal gradients arising from the magnetic susceptibility variations also increase with the strength of the operating field. As a consequence, the choice of field strength for imaging experiments is compromised between the signal sensitivity and imaging resolution. Many imaging experiments on fluid-saturated porous media have employed a field strength of 2 T, which corresponds to a proton resonance frequency of 85 MHz.

Equation (8) suggests that the linewidth-limited resolution can be improved by using higher gradient strengths. The field gradients are the most essential elements of an NMR imaging system, in addition to the standard NMR spectrometer design. Field gradients of sufficient strength and stability are critical for effective performance of both conventional and pulsed field-gradient NMR imaging experiments. The pulse sequences used for imaging porous media often require rapid switching of gradient pulses so that observations at shorter echo times with correspondingly greater signal-to-noise are allowed. In principle, the switching speed is mainly determined by the voltage and bandwidth of the power amplifier. However, the rapid change of magnetic fields can induce eddy currents in the surrounding conductors, such as the cylindrical tubes in superconducting magnets. These currents can persist after the gradient pulses are turned off and produce unwanted field gradients. It has always been a challenge in the design of gradient coils and pulse circuitry to provide increased gradient strength while switching the gradients on and off in a faster and squarer fashion. Interested readers are referred to the book by Callaghan [1] for a discussion on field gradient hardware.

A further effect of line broadening in porous media is to make the discrimination of water and oil based on their chemical shift difference more difficult. Indeed, the line broadening found in many porous media precludes the use of simple chemical-shift-imaging methods when quantitative measurements are desired. A number of discrimination approaches to obtaining images from the different fluid components are introduced in the following subsection, including methods using the contrasts in chemical shift, relaxation time, diffusion, and nuclear species. Quantitative determination of porosity and saturation distributions requires consideration of the spatial variation and saturation dependence of transverse relaxation, as well as selection of an appropriate model for representation of the relaxation process. These issues are addressed in Section 10.2.4. Pulsed field-gradient NMR detects molecular displacement over a well-defined time scale and can be an excellent approach to the characterization of structural features and transport processes. Section 10.2.5 discusses the imaging of fluid molecular translation using pulsed magnetic field-gradient techniques to encode the

displacements of fluid molecules and their coupling with a suitable imaging sequence.

10.2.3 Liquid Phase Discrimination

MRI has shown the potential to provide a means to determine the spatial distribution of fluid saturations within porous media, with obvious applications in rock physics, fluid–solid interfacial processes, and porous media fluid dynamics, especially liquid–liquid displacement mechanics. To study multiphase flow, where several fluid phases may be present within the pore space, it is necessary to distinguish between fluids of different chemical compositions. Nuclear spins experience a variety of electric and magnetic fields, which are sensitive to the physical and chemical differences of the fluids. Several approaches for discrimination between oil and water phases in porous rocks have been investigated based on the chemical or spin relaxation contrasts. Separately imaging the individual fluids in rock cores using chemical shift contrasts is challenging due to the resonance line broadening of the NMR signal. Depending on the nature of the rock, the broadening can be sufficient to prevent the spectral resolution of the NMR signals for oil and water phases. For those samples for which the resonance line broadening is moderate and spectral separation between oil and water is still resolvable, a number of approaches utilizing the chemical shift contrast can be used to obtain fluid-selective images. For those with severe line broadening, substantial additional effort is required. In addition, other contrast techniques such as spin relaxation, diffusion, or multinuclei can be used if sufficient contrast is available.

10.2.3.1 Chemical Shift Contrast. The nuclei in fluids are surrounded by molecular electrons that interact with the nuclear spin angular momentum. The magnetic coupling of the orbital motion of electrons to the nucleus gives rise to the so-called chemical shift. The chemical shift causes Larmor frequencies to be slightly displaced in a manner that is characteristic of the chemical environment. Chemical shifts depend strongly on the atomic number and are of the order of a few parts per million in protons. The shift of about 3.5 ppm between oil and water proton resonances is of particular interest in NMR imaging. This separation represents 300 Hz at 85 MHz. In samples where both oil and water contribute to the image, this offset in frequency can enable separate images from the different molecular species to be obtained. This facility has been termed chemical shift imaging. Chemical shift imaging has several advantages over relaxation-weighted imaging for fluid phase resolution in porous media studies because the chemical shift is insensitive to bulk physical property variations (such as pore geometry, magnetic susceptibility, temperature, and fluid phase interactions). There-

fore, chemical shift imaging is well suited to the study of multiphase flow in porous media and to even more complicated systems such as miscible or chemically interacting fluid phases.

The various methods for chemical shift imaging can be classified into two major categories. The first category consists of methods that selectively excite or saturate water (or oil) protons before a conventional image pulse sequence is applied. The second category involves methods of spectroscopic chemical shift imaging, in which a chemical shift dimension is added to each pixel and the chemical shift information can be frequency encoded or phase encoded.

10.2.3.1.1 Spectrally Selective Methods. Selective excitation involves applying an RF pulse that affects only a specific region of the NMR frequency spectrum so that only nuclei of a certain chemical shift may be disturbed. The simplest method to obtain chemically selective excitation in the spin-echo imaging sequence is to make the 90° RF pulse a narrow-band frequency-selective pulse (so-called soft pulse) while the 180° pulse is slice selective. The chemical-shift-selective (CHESS) pulse has a low intensity and long time profile in the time domain and is applied at some chosen frequency in the NMR spectrum. Unlike slice-selective pulses, the chemically selective pulse is applied in the absence of a magnetic field gradient. An example of the use of selective excitation to obtain fluid-selective images for two dolomite samples saturated with single fluid phases has been demonstrated by Edelstein *et al.* [10].

Selective saturation, or selective suppression, represents an inverse approach to selective excitation in the imaging of chosen chemical species. This method is very effective when all resonances in the spectrum except one are to be observed. One approach of selective saturation to obtain water- or oil-selective images is to add a CHESS pulse and a homospoil gradient pulse to the beginning of any imaging pulse sequences to null the water or oil NMR signal. The advantage of this method is that it involves only a minor modification of the standard imaging pulse sequences. Dechter *et al.* [11] have demonstrated the use of the selective saturation method to obtain chemically selective, fluid-specific images of refined oil and aqueous brine in carbonate and sandstone cores. The spectrally selective methods yield images of only one fluid phase at a time, and sometimes suffer from low sensitivity in the presence of short transverse relaxation times because the necessarily long RF pulses lengthen the echo time T_E.

10.2.3.1.2 Spectroscopic Methods. Full-scale spectroscopic imaging involves an increase of dimensionality in the data acquisition process so that the frequency spectrum becomes a fourth dimension in addition to the three spatial dimensions. This is achieved by spatially encoding the signal with phase-encoding magnetic field gradients after a nonselective RF pulse is

used to excite the spins. All magnetic field gradients are turned off during data acquisition to provide chemical shift information. Once acquired and processed, the image data can be sliced to produce displays that show the distribution of each individual chemical species in any defined plane. A serious disadvantage of this four-dimensional method is that it requires more imaging time. Unless one of the spatial dimensions is sacrificed, the addition of a full spectral dimension to each pixel of the image is too time consuming to be practically applied to many investigations.

A chemical-shift-imaging technique reported by Hall *et al.* [12] to obtain the spatial mapping of water and dodecane in a composite Berea sandstone sample involves a modification of the conventional spin-warp sequence. The pulse sequence uses a slice-selective RF pulse followed by two perpendicular phase-encoding gradients, and the spin-echo signal is collected after a 180° pulse. After three-dimensional Fourier transformation of the acquired data set, each chemical shift frequency corresponding to a selected fluid can be displayed as a separate image. The number of spin echoes required for this technique is $m \times n$, where m and n are the number of pixels in the respective spatial dimensions of the images. Experimental time considerations may thus prohibit high-resolution measurements. Another drawback of this method is that any magnetic field inhomogeneity can lead to a distortion in the spectral dimension. The field inhomogeneity depends not only on the magnet shimming but also on the magnetic susceptibility, shape, and orientation of the sample in the magnet.

The experimental time can be reduced by phase encoding the chemical shift and frequency encoding one of the spatial dimensions. This is because each phase-encoding step involves a repetition of the entire pulse sequence, whereas an increase in frequency-encoding resolution does not increase the experimental time significantly. Since the generation of a spectral dimension is only to resolve the different fluids, high spectral resolution is not important. As demonstrated by Dixon [13], two steps of phase encoding the spectral information may be adequate to resolve water and lipid in biological systems. However, this simple method suffers from some limitations [14, 15] with respect to quantitative accuracy when applied to fluids in porous solids where the linewidths are typically broader than those in biological systems.

In a conventional spin-echo imaging sequence, the phase is usually encoded in the spectral dimension by varying the time of the 180° pulse while keeping the time between excitation and acquisition constant (see Fig. 2). As a result, a time delay τ is introduced between the Hahn spin echo and the gradient echo, allowing the nuclear magnetization vectors to evolve out of phase with each other by an amount dependent on the spectral frequency differences as well as the inhomogeneity in magnetic field. Assum-

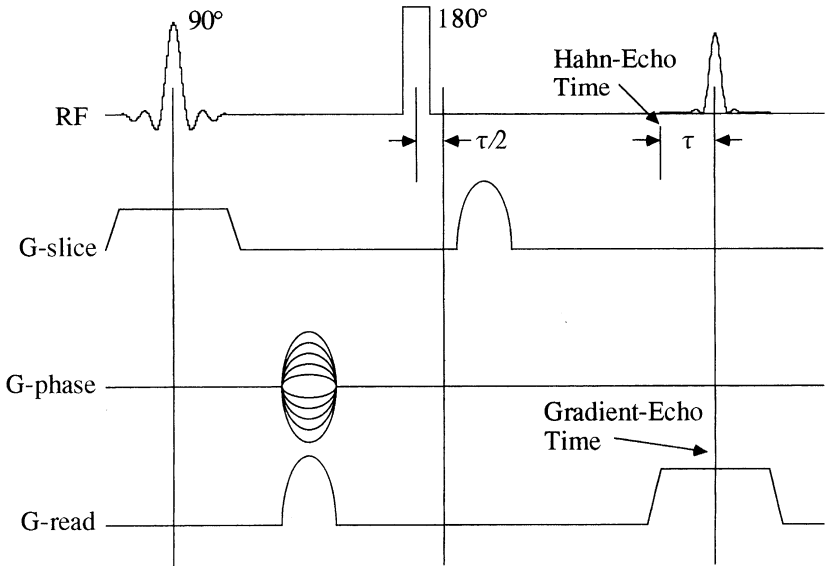

FIG. 2. Timing diagram for a phase-encoding chemical-shift-imaging pulse sequence. A time delay τ is introduced between the spin echo and the gradient echo to phase encode the spectral information. Reprinted with permission from C. T. Chang and C. M. Edwards, *Log Anal.* **34**, 20 (1993).

ing that the imaging gradients are sufficiently strong so as to compress the frequency separation within a single pixel, the image signal intensity for a pixel at (x, y) can be written as [15]

$$I(x, y) = \exp[i\phi_0(x, y)] \int \rho(x, y, \omega)\exp\{i[\omega + \Delta\omega_0(x, y)]\,\tau\}\, d\omega, \qquad (9)$$

where $\Delta\omega_0(x, y) = \gamma\Delta B_0(x, y)$ is the frequency offset due to the magnetic field inhomogeneity $\Delta B_0(x, y)$, and $\phi_0(x, y)$ is the nonuniform phase delay caused by instrumentation factors. The expression $\rho(x, y, \omega)$ is the spin density including the relaxation effects, where ω is written explicitly to specify that the image signal is subject to the linewidth and chemical shift effects.

If the effect of field inhomogeneity can be ignored, $I(x, y)$ is the Fourier transform of the spin density $\rho(x, y, \omega)$ which contains the spectral information. Reconstruction of the spectral dimension from $I(x, y)$ simply requires calculating the inverse Fourier transform, provided that an image data set with regularly incremented τ is acquired. Majors *et al.* [16] reported the use

of this technique to study the displacement of oil by water-flooding in a dolomite core sample. They found that this spectroscopic imaging modality is particularly useful for systems where T_2 is short but the chemical shift separations are still large compared with the linewidths. The distortion in the spectral dimension caused by the magnetic field inhomogeneity is apparent in their images because no correction was made on the phase errors $\Delta\omega_0(x, y)\tau$. Horsfield *et al.* [14] developed an estimation method to separate oil and water images in porous rocks. This method uses at least eight chemical-shift-encoded images with different values of τ and requires well-characterized spectra for the oil and water resonances and a large amount of computation. The phase errors caused by magnetic field inhomogeneities were corrected using an estimated inhomogeneity function and a least-squares algorithm. The scheme aimed to provide an ability to distinguish water and oil signals even when their spectral lines cannot easily be resolved.

An improved technique for chemical shift imaging that provides the capability to rapidly and easily quantify the oil and water distributions in porous media has been presented by Chang and Edwards [15]. This technique is applicable to separating oil and water signals even when their spectral lines cannot be resolved. When a sample consists of only two chemical components, Eq. (9) can be expressed in terms of their relative chemical shift σ and reduced to

$$I(x, y) = [h_w(\tau) M_w(x, y) + h_o(\tau) M_o(x, y) \exp(i\sigma\tau)] \exp\{i[\Delta\omega_0(x, y)\tau + \phi_0]\}, \tag{10}$$

where subscripts w and o refer to the water and oil components, respectively, and $h(\tau)$ is the Fourier transform of the lineshape function and represents a signal decay factor during the period τ. For a Lorentzian lineshape, $h(\tau)$ is simply an exponential decay. With this expression, the oil signal is regarded as being a resultant magnetization vector M_o shifted by a phase angle $\sigma\tau$ from the water magnetization vector M_w. Using the knowledge of the chemical shift between oil and water σ, any phase shifts of the respective signals can be achieved by suitable adjustment of Hahn spin-echo time relative to gradient echo time (i.e., the value of τ). Four images with phase shift $\sigma\tau = 0$, π, and $\pm\pi/2$ are acquired. In the following discussion, the signal intensity for a pixel at (x, y) is expressed as $I(\sigma\tau)$ to explicitly indicate the phase shift between the water and oil magnetizations. The in-phase and opposed-phase images are used to determine the position-dependent phase factor caused by the field inhomogeneity. The in-phase signal is given by setting $\tau = 0$ in Eq. (10),

$$I(0) = [h_w(0) M_w + h_o(0) M_o] \exp(i\phi_0), \tag{11}$$

and setting $\tau = \pi/\sigma$ yields the opposed-phase signal

$$I(\pi) = [h_w(\pi/\sigma) M_w - h_o(\pi/\sigma) M_o] \exp[i(\Delta\omega_0 \pi/\sigma + \phi_0)]. \quad (12)$$

A phase map of $\Delta\omega_0(x, y)\pi/\sigma$ can be produced from the argument of $I(\pi)/I(0)$ on a pixel-by-pixel basis. Since calculated phase values lie between $+\pi/2$ and $-\pi/2$, phase unwrapping is required in the case when the phase factor is of such magnitude that the phase wraparound problem must be confronted, which often occurs for images of large cross-sectional area or for samples with large magnetic susceptibilities.

The separated water and oil images are calculated from the two images with $\sigma\tau = \pm\pi/2$ where the oil magnetization vector is shifted symmetrically with respect to the water vector by $\pm\pi/2$:

$$I(\pm\pi 2) = \left[h_w\left(\frac{\pi}{2\sigma}\right) M_w \pm i h_o\left(\frac{\pi}{2\sigma}\right) M_o \right] \exp\left[i\left(\pm \Delta\omega_0 \frac{\pi}{2\sigma} + \phi_0 \right)\right]. \quad (13)$$

The images are first phase corrected to eliminate the phase factor $\pm\Delta\omega_0\pi/2\sigma$ using the phase map obtained from the in-phase and opposed-phase images. By complex addition and subtraction of the phase corrected $I(\pm\pi/2)$, the final separated images of $h_w M_w$ and $h_o M_o$ can then be formed in magnitude to remove the phase factor ϕ_0. The water and oil images are now separated, but it should be noted that the signal intensity in these images is subjected to the relaxation effects.

A cylindrical sample of carbonate rock (2.5 cm in diameter, 5.5 cm long) was used to demonstrate the ability of this method to quantitatively map water and oil distributions during a drainage process. Figure 3 shows separated water and oil images when the oil front was approximately halfway through the core. The water-saturated core was injected with machine oil from the top. The peaks of the proton resonances for water and oil are shifted by 3.5 ppm and the linewidth at half maximum for each resonance was estimated to be approximately 2.8 ppm. Using only four phase-encoded images, the water and oil images were correctly separated even though their resonance lines overlap significantly.

10.2.3.2 Relaxation Contrast. Relaxation contrast is crucial to the observation of structural features in medical MRI where the spin density exhibits only a small variation between the various types of human tissue. Relaxation-weighted imaging for fluid phase selection in porous media relies on the difference in T_1 or T_2 values of the fluid phases to eliminate or reduce the signal from one phase while detecting the signal from the other phase. For a spin-echo imaging sequence, the signal intensity in a pixel is determined by the signal amplitude at the echo center for spins corresponding to that pixel. With a 90° RF excitation pulse, and assuming the dephasing of

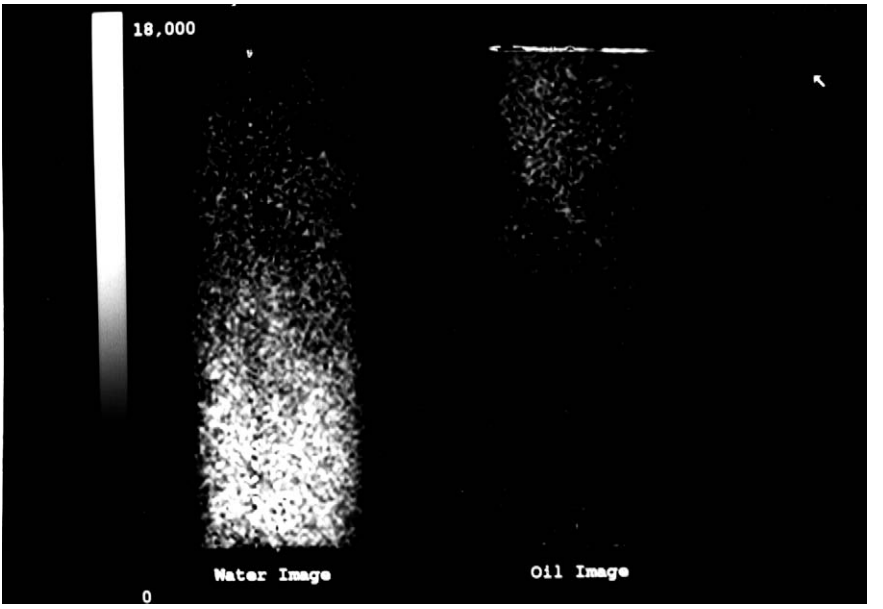

FIG. 3. Proton chemical-shift images of water and oil in a carbonate rock sample when the oil front was approximately halfway through the core in a primary drainage experiment. Machine oil was injected from the top into the completely water-saturated sample. The scale at left indicates image intensity in arbitrary units. Reprinted with permission from C. T. Chang and C. M. Edwards, *Log Anal.* **34**, 20 (1993).

the transverse magnetization by the read gradient is small, the signal amplitude at the echo center measured in the xy plane can be expressed as:

$$M = M_0\{1 - 2\exp[-(T_R - T_E/2)/T_1] + \exp(-T_R/T_1)\}\exp(-T_E/T_2), \tag{14}$$

where M_0 represents the intrinsic magnetization. The T_1 and T_2 weighting in images can be obtained by appropriate selections of T_R and T_E values. For fluids in porous media, the single-exponential relaxation represented in Eq. (14) should be used with caution because many systems exhibit multi-exponential features.

10.2.3.2.1 T_2 Contrast. For $T_R \gg T_1$, the signal intensity is proportional to the number of protons and subject to the transverse relaxation factor, $\exp(-T_E/T_2)$. The introduction of substances that enhance proton relaxation contrast provides a useful means for differentiating liquid phases if these substances are soluble in one phase but not in the other. Contrast

agents such as transition metal or lanthanide cations, which contain unpaired paramagnetic electrons, are commonly used in medical imaging. An application to porous media has been reported by Baldwin and Yamanashi [17] in which oil is distinguished from water in reservoir cores. The water was doped with manganese ions (Mn^{2+}) to reduce its transverse relaxation time, thereby enabling only the oil signal to be observed. In a study of oil and water invasion in a model porous medium with MRI, Chen *et al.* [18] used Ni^{2+} ions to suppress the water signal so that the images are sensitive only to the oil distribution.

In addition to the spin-echo sequence, a Carr–Purcell–Meiboom–Gill (CPMG) sequence can be used to obtain a series of T_2 weighted images (see Section 10.2.4). The spin-lattice recovery term $\exp[-(T_R - T_E/2)/T_1]$ in Eq. (14) is absent, and the influence of T_1 relaxation can be completely removed by choosing $T_R \gg T_1$. A suitable relaxation model can then be used to compute a T_2 distribution for each pixel by least-squares fitting to the decay of the CPMG images. Oil and water are resolved on the basis of their T_2 values. An example of this is presented by Majors *et al.* [16] in an MRI study of immiscible displacements in porous media for which a paramagnetic dopant, $CuSO_4$, was added to water to enhance the T_2 contrast of the water and oil signals.

10.2.3.2.2 T_1 Contrast. The inversion–recovery sequence that is widely used for T_1 measurement can be used for the selective suppression of unwanted spin signals as well. A unique feature of this method is the growth of the longitudinal magnetization from a negative signal to a positive signal. The crossover through zero magnetization occurs at a time $T_1 \ln 2$ if the spin–lattice relaxation behavior is exponential. When a difference in T_1 values exists for protons in different fluids, an inversion pulse can be applied followed by a time delay to remove the magnetization of a particular component before the imaging pulse sequence [19]. Several researchers have reported separate oil and water images taking advantage of different T_1 values for the protons in the oil and water phases within porous rock samples [10, 12, 20]. It should be noted that the fluids in porous media usually exhibit a broad distribution of relaxation times that makes it very difficult to remove either the oil or the water signal completely.

10.2.3.3 Diffusion Contrast. Diffusion imaging [21] is another technique that can be useful for separating the oil signal from the aqueous signal. For many viscous oils, the diffusion contrast for distinguishing the oil from water is available. When the diffusional motion is observed in a heterogeneous system such as interconnected pores in rocks, however, the degree of mobility of fluid molecules depends on the length of the diffusion time, and the observed diffusion coefficient is not always the same as that of the bulk fluid. At short enough times, the diffusive motion is not restricted signifi-

cantly by the solid matrix and the observed motion is characteristic of the fluid alone. At long enough diffusion times, a uniform average mobility would be observed because the molecules have the opportunity to repeatedly sample all of the different environments, and the apparent diffusion coefficient asymptotically approaches a new value that depends on the pore geometry as well as the viscosity of the fluid.

The pulsed field-gradient stimulated-echo method has been used to distinguish the aqueous and oil distributions in porous media [22]. The use of stimulated echo enables the diffusion to be observed over a range of times such that a considerable change in apparent diffusion coefficient can be observed. A gradient pulse of amplitude G is applied in each of the two transverse evolution periods of the stimulated echo sequence (see Fig. 4). The molecular diffusion results in an additional attenuation of the echo amplitude:

$$A = \exp[-\gamma^2 G^2 \delta^2 (\Delta - \delta/3) D_{\text{eff}}], \tag{15}$$

where D_{eff} is the effective diffusion coefficient, δ is the duration of each gradient pulse, and the separation of the pulses Δ is the diffusion time. The difference in the attenuation factors provides a contrast that can be used to separate the water and oil signals. The successful use of this technique depends on the availability of the contrast in the attenuation factor.

10.2.3.4 Multinuclear MRI. Another way to discriminate oil and water in porous media is to detect the oil phase by regular proton MRI and to

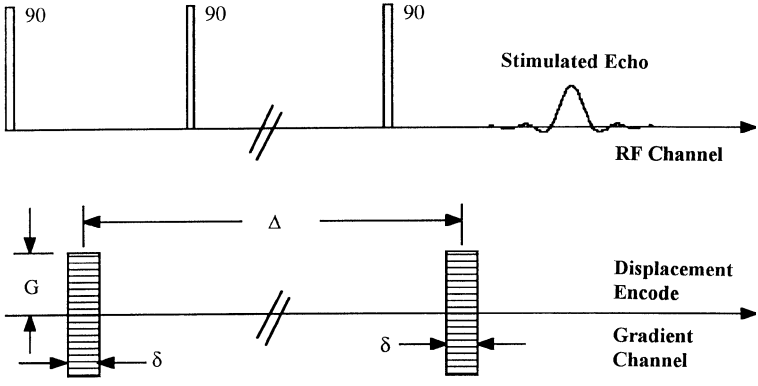

FIG. 4. The RF and displacement-encoding field gradient pulses in a typical stimulated-echo imaging pulse sequence. The spatial encoding for imaging can be performed in the usual ways and is not shown. The time Δ between the field-gradient pulses is the time that fluid molecules are tracked.

detect the aqueous phase by imaging the brine nuclei other than protons. These nuclei include ^{23}Na from the NaCl brine [23], ^{7}Li from LiCl brine [24], and ^{19}F from $C_6H_5CF_3$ [25]. The oil phase can also be detected by ^{13}C [26] or by ^{19}F if fluorinated hydrocarbons are present [24]. Moreover, the H_2O phase can be replaced by D_2O and one can use deuterium NMR techniques to detect directly the aqueous phase while using proton to detect the oil phase.

The intrinsic NMR S/N of a nucleus is related to its gyromagnetic ratio γ and spin quantum number I by the proportionality [5]:

$$\xi_0 \propto \gamma^{11/4} I(I+1), \tag{16}$$

at constant field. Therefore, the S/N can be a critical concern for detecting any nuclei other than protons because of the small γ values involved. For equal abundance and identical instrumental factors, the ξ_0 for protons is about 65 times that for deuterons. In principle, one may have to spend about 65^2 times more experimental time for deuteron NMR experiments as compared to protons to achieve the same S/N. However, the sensitivity penalty may be partially compensated in porous media due to other advantages often available in nonproton NMR modalities [23, 24]. In any imaging experiment, the actual S/N depends on the echo time T_E as well as the repetition time T_R, and it increases with the square root of the number of acquisitions. For a spin-echo imaging experiment with tip angle α and total experimental time t, the S/N is

$$\xi(t) = \xi_0 \exp\left(-\frac{T_E}{T_2}\right)\left[1 - \exp\left(-\frac{T_R}{T_1}\right)\right]\sqrt{t/T_R}\sin\alpha. \tag{17}$$

Under the conditions of identical tip angle α and T_R being a constant multiple of T_1, the relative S/N for nuclear species a and b is

$$\frac{\xi_a}{\xi_b} = \frac{\xi_{0a}}{\xi_{0b}} \exp\left[T_E\left(\frac{1}{T_{2b}} - \frac{1}{T_{2a}}\right)\right]\sqrt{\frac{T_{1b}}{T_{1a}}}. \tag{18}$$

From a series of imaging experiments on sand packs and natural rocks [27], it has been found that deuterons in D_2O have shorter T_1 but longer T_2 than those for protons in H_2O. The shorter T_1 enables a faster repetition of the data acquisition and the longer T_2 prevents rapid signal decay during T_E from occurring. As a result, the deuteron S/N is smaller than the proton S/N by a factor of only about 5 to 17, but not 65 as previously discussed.

10.2.4 Quantitative Imaging

One of the most important concerns for utilizing MRI techniques to investigate fluid flow in porous media is the ability to obtain quantitative

values for localized properties. Two important properties are the porosity and the fluid saturation. When only a single fluid phase is present, the porosity distribution can be determined by NMR imaging under static conditions. When multiple fluid phases are present, the individual fluid saturations can be determined provided that there are suitable methods to discriminate the fluid phases, such as the methods described in Section 10.2.3. To obtain quantitative values of porosity and fluid saturation, it is essential to remove all relaxation effects from the image as well as to calibrate the NMR signal intensity of the fluid.

The use of NMR imaging techniques to determine fluid saturation is based on the fact that the intrinsic image signal intensity $M_0(\mathbf{r})$ is proportional to the spin density in the corresponding volume element of the sample:

$$M_0(\mathbf{r}) = c\rho(\mathbf{r}). \tag{19}$$

The proportionality constant c depends on the apparatus and material under study and may change during the experiment since the change of fluid states may result in changes in the coil quality factor Q. For the purpose of determining c, a reference material with a known number of nuclei can be inserted into the receiver coil together with the sample to be studied [28]. The signals of the reference material and the studied sample are separated on the basis of spatial location. The constant c can thus be determined by comparing the image intensity and the number of nuclei in the reference material. However, the observed image signal intensity is always subject to T_2 relaxation. The extent of signal attenuation depends on the relative lengths of T_2 and the echo time T_E. In addition, T_1 effects will also be present with T_1 weighting, depending on the ratio of T_R to T_1. The effects of T_1 relaxation can be readily eliminated if sufficiently long repetition time T_R is used. The effects of T_2 can be removed if $T_E \ll T_2$. But instrument limitations on the shortest achievable T_E often do not allow T_2 effects to be eliminated completely in many imaging studies on porous media due to their short-T_2 characteristics.

To obtain a spin density map free of T_2 relaxation attenuation, a series of progressively attenuated images can be collected and the signal intensity at each pixel can be extrapolated back to its intrinsic value M_0. Chen *et al.* [29] have reported the use of a single spin-echo imaging sequence and the involvement of repeated imaging with several echo times T_E to obtain the attenuated image set. Procedures are described in which the transverse relaxation during T_E is modeled to obtain accurate estimates of intrinsic signal intensity and, hence porosity and saturation distributions. Another quantitative technique [10, 20, 30] uses a CPMG multiple-spin-echo tech-

nique to obtain a series of relaxation-attenuated images. An obvious advantage of CPMG over the single-spin-echo technique is the shorter imaging time for CPMG. An entire series of relaxation-attenuated CPMG images is collected in about the same time as a single spin-echo image. Another advantage is that CPMG technique allows for the acquisition of transverse relaxation data with the molecular diffusion time controlled by the experimentally selected value of echo spacing. The use of a short echo spacing can minimize the diffusion attenuation rate and improve the interpretation of fitting parameters with suitable relaxation models used.

There are a number of different approaches that have been used to model the relaxation process. The accuracy of the estimates of the intrinsic signal intensity, and hence the porosity and saturation, depends critically on the manner in which the relaxation has been represented. Simple models that have been used include the single exponential-model [31] and the stretched-exponential model [32]. While estimates of the parameters within these models are readily obtained, they generally do not provide for accurate estimates of the intrinsic intensity [33]. A modified stretched exponential has been reported [34]. However, results showing the precision with which the relaxation process is represented were not provided.

A porous medium tends to have a broad distribution of pore sizes, and therefore the magnetization decay of fluids in the porous medium is expected to exhibit a distribution of relaxation times if the relaxation process is controlled by the surface-relaxation mechanism. Methods to estimate the intrinsic intensity can be based on the methods to estimate relaxation distributions. A method using the multiexponential representation for the relaxation process has been reported by Chen *et al.* [33]. A more convenient approach has been developed using the representation of relaxation with a continuous distribution [35]. This approach has considerable computational advantages compared to the use of multiexponentials, and is shown to compare favorably with the multiexponential method.

10.2.5 Imaging of Molecular Translational Motion

The methods described so far have been largely directed to spatially resolving the various fluid phases within porous media, and determining the amounts of those fluids. This provides important information regarding the fluid states within porous media, which can specify the porosity and fluid saturation distributions. However, these methods provide little direct information about fluid transport. The transport of fluids in porous media is a subject of considerable importance in many areas, including oil reservoir characterization, perfusion in biological tissue, and the transport of contaminants in soil.

NMR imaging methods can be extended to the measurement of molecular displacements within porous structures. The work reported in Refs. [36–39] has yielded spatial maps of the fluid velocity in porous media. Distribution functions of molecular displacements arising from self-diffusion and externally driven flow in porous media have also been measured [37, 40–43]. These measurements are dynamic rather than static in nature and provide information about the mechanisms of fluid transport. A number of different flow parameters could be characterized by these measurements. For example, average fluid velocity is proportional to the permeability. Even though the pressure drop is unmeasurable within a porous medium, it may be possible to produce a three-dimensional map of permeability in a porous sample using estimation procedures. The displacement distribution function depends on the pore geometry in a complex way. Nevertheless it may be possible to extract meaningful information about pore structures and hydrodynamic dispersion from these measurements.

Two classes of MRI methods have been commonly employed to measure the fluid molecular motion in porous media. They are broadly categorized as time-of-flight and phase-encoding approaches [1]. There are a variety of methods within each class due to the multitude of techniques that can be used to acquire NMR data. The time-of-flight approach makes use of the magnitude of the nuclear magnetization as a fluid tag and observes the effects on the image intensity due to displacements of excited spins during the time between excitation and signal acquisition. The phase-encoding approach uses magnetic field gradients to phase encode the molecular motion. Since the phase-encoding approach requires an additional dimension for displacement encoding, the imaging time may be longer than that necessary for time-of-flight approach. However, it is more convenient to obtain precise quantification of molecular displacements with the phase-encoding approach. For this reason, the majority of the reports of NMR dynamic imaging of flow in porous media have used the phase-encoding approach.

10.2.5.1 Pulsed Field-Gradient NMR Imaging. The use of phase shifts of nuclear magnetization to measure molecular motion has been investigated for decades [44] and its application to the spatially resolved measurement of flow velocity was first proposed by Moran [45]. Nuclear spins moving in the presence of a magnetic field gradient exhibit a phase shift of the transverse magnetization. This phase shift results from changes in the magnetic field and the associated resonance frequency seen by spins that move in the direction of the magnetic field gradient. Equation (1) indicates that in a field gradient $\mathbf{g}$, the NMR signal for a spin at position $\mathbf{r}$ oscillates at an angular frequency $\omega'(\mathbf{r}) = -\gamma \mathbf{g} \cdot \mathbf{r}$. For a time-dependent

gradient $\mathbf{g}(t')$, the phase of a spin with positional time dependence $\mathbf{r}(t')$ is

$$\varphi(t) = -\gamma \int_0^t \mathbf{g}(t') \cdot \mathbf{r}(t')\, dt'. \tag{20}$$

The measurements of molecular translation involve two primary elements. The first element is the use of magnetic field gradients to impose spatial tags on the spins. The second is the use of spin echoes to detect the effect of phase shifts on the NMR signals. It is conceivable that the molecular motion for fluids in porous media is irregular spatially and temporally. To obtain a measure of molecular displacements that is of practical relevance to the processes described by the usual transport parameters such as permeability and diffusion, the gradients are applied in the form of intense pulses. It is instructive to discuss the so-called bipolar-gradient method here, although other modifications such as multiple alternating gradient pulse methods [46] are useful with porous media since they serve to negate the background gradients arising from magnetic susceptibility heterogeneities. A bipolar gradient sequence is equivalent to two identical pulses that are applied during the dephasing and rephasing periods of a spin-echo sequence [47]. For stimulated-echo experiments, the gradient pulses are inserted in the transverse evolution periods. Figure 4 shows the RF and field-gradient pulses in a typical stimulated-echo imaging pulse sequence. The spatial encoding for imaging can be performed in usual ways and is not shown. The time Δ between the field gradient pulses is the time that fluid molecules are tracked. A remarkable feature of the stimulated echo is that the relaxation decay has a T_1 dependence during the interval between the second and third RF pulses. Longer observation time Δ can be achieved without the usual signal attenuation due to T_2 relaxation, since T_1 is usually longer than T_2 for fluids in porous media.

Now consider the effect of the two gradient pulses of amplitude G, pulse width δ, and separation Δ. In the narrow-pulse approximation where $\delta \ll \Delta$, the pulse duration δ is assumed short enough so that negligible molecular displacement occurs during this period compared to that during Δ. The first pulse imparts a phase shift $-\gamma\delta\mathbf{G}\cdot\mathbf{r}_0$ to a spin located at $\mathbf{r}_0$. This phase shift is inverted by the 180° pulse in a spin-echo sequence or by the last two 90° pulses in a stimulated-echo sequence. Suppose that the spin has moved to position $\mathbf{r}_0 + \mathbf{R}$ at the time of the second gradient pulse. Then, the net phase shift for the spin is $-\gamma\delta\mathbf{G}\cdot\mathbf{R}$. A wave vector $\mathbf{k}$ was defined in Eq. (4), which is used to describe the precession of magnetization in a spatial-encoding gradient. Here we introduce another wave vector:

$$\mathbf{q} = (2\pi)^{-1}\gamma\delta\mathbf{G}. \tag{21}$$

While $\mathbf{k}$ is conjugate to the spin position $\mathbf{r}$, $\mathbf{q}$ is conjugate to the spin displacement $\mathbf{R}$.

By combining the displacement encoding gradients and static imaging, it is possible to obtain a distribution function of spin translation in individual voxels of the sample. We generalize the spin density $\rho(\mathbf{r})$ to a spatial-displacement joint density function [45] defined as

$$\varrho_\Delta(\mathbf{r}, \mathbf{R}) = \rho(\mathbf{r})\mathscr{P}_\Delta(\mathbf{R}, \mathbf{r}), \tag{22}$$

where $\mathscr{P}_\Delta(\mathbf{R}, \mathbf{r})$ is the normalized distribution function of spin displacement over a perod of time Δ for a voxel at location $\mathbf{r}$, satisfying the normalization condition, $\int \mathscr{P}_\Delta(\mathbf{R}, \mathbf{r})\, d\mathbf{R} = 1$. The relaxation effects are absorbed in the definition of $\varrho_\Delta(\mathbf{r}, \mathbf{R})$. The joint density function $\varrho_\Delta(\mathbf{r}, \mathbf{R})$ is proportional to the number of spins per unit spatial volume and per unit displacement volume, at location $\mathbf{r}$ with displacement $\mathbf{R}$ during Δ. The measured NMR signal is modulated by the two wave vectors, $\mathbf{k}$ and $\mathbf{q}$, and can be written, similarly to Eq. (5), as

$$S(\mathbf{k}, \mathbf{q}) = \iint \varrho_\Delta(\mathbf{r}, \mathbf{R}) \exp(-i2\pi\mathbf{k}\cdot\mathbf{r}) \exp(-i2\pi\mathbf{q}\cdot\mathbf{R})\, d\mathbf{r}\, d\mathbf{R}, \tag{23}$$

and the inverse Fourier transformation yields

$$\varrho_\Delta(\mathbf{r}, \mathbf{R}) = \iint S(\mathbf{k}, \mathbf{q}) \exp(i2\pi\mathbf{k}\cdot\mathbf{r}) \exp(i2\pi\mathbf{q}\cdot\mathbf{R})\, d\mathbf{q}\, d\mathbf{k}. \tag{24}$$

Thus the joint density function for a voxel can be reconstructed. Various analysis methods have been used to extract information about fluid motion in porous media using pulsed field-gradient NMR data. These methods include velocity imaging, diffusion, and dispersion measurements. We restrict our discussion to analysis methods for velocity imaging in the next subsection.

10.2.5.2 Velocity Imaging. A number of researchers have reported NMR imaging experiments in which a map of the fluid velocity is obtained in a porous medium using the phase shift induced by spins moving in a magnetic field gradient [36–39, 48, 49]. The key challenge for successful use of NMR velocity-imaging techniques to characterize fluid flow properties is the interpretation of the measured parameters. Different experimental strategies provide information about flow processes at different spatial and dynamic scales in porous media. In principle, the flow velocity can be probed either as a local quantity with an image resolution below the pore level [48, 49], or as a macroscopic flow property corresponding to local volume and temporal averages of fluid molecular displacements [37]. One

must develop a suitable methodology to correctly measure the parameters that best describe the properties of interest.

NMR velocity imaging provides a unique opportunity for estimating permeabilities corresponding to local regions. From a theoretical point of view, the permeability represents a macroscopic empiricism that cannot be measured directly. It is a locally averaged quantity [50] representing tens or hundreds of pores and may vary spatially throughout the media. To obtain velocity-imaging data that represent macroscopic processes described by the transport parameters, special considerations in terms of experimental and data analysis methodologies are required. Due to the complex nature of fluid molecular motion in the pore space, molecular velocities are not constant during the measurement time. Moreover, the velocity field within a voxel is not uniform when the spatial resolution is much larger than the pore dimensions. In the following discussion, we illustrate that naïve assumptions about the interpretation of measurement process may lead to incorrect characterization of the flow process.

In a pulsed field-gradient NMR imaging experiment, molecular displacements over a predetermined observation time are measured, and these measurements can then be interpreted as average velocities. Under the condition of narrow gradient pulses, the time average of each spin's velocity in the direction of the gradient (e.g., z direction) is defined as

$$\bar{v} = \frac{Z}{\Delta}, \tag{25}$$

where $Z = z(\Delta) - z(0)$ is the displacement in the z direction. The NMR signal for a voxel at position $\mathbf{r}$ is the Fourier transformation of Eq. (23) with respect to $\mathbf{k}$, and is calculated as

$$\begin{aligned} S'(\mathbf{r}, q) &= \rho(\mathbf{r}) \int_{-\infty}^{\infty} \mathscr{P}_{\Delta}(Z, \mathbf{r}) \exp(-i2\pi qZ)\, dZ \\ &= \rho(\mathbf{r}) \int_{-\infty}^{\infty} P_{\Delta}(\bar{v}, \mathbf{r}) \exp(-i2\pi q\bar{v}\Delta)\, d\bar{v}, \end{aligned} \tag{26}$$

when the relationships in Eqs. (22) and (25) are used. The velocity distribution function $P_{\Delta}(\bar{v}, \mathbf{r})$ is the probability density of spins that are moving within the velocity range $\bar{v}$ and $\bar{v} + d\bar{v}$. The mean velocity for a voxel is given by

$$\langle \bar{v} \rangle_{\mathbf{r}} = \int_{-\infty}^{\infty} \bar{v} P_{\Delta}(\bar{v}, \mathbf{r})\, d\bar{v}. \tag{27}$$

Two experimental methods can be used to estimate the mean velocity for each voxel: (1) the measurement of the velocity distribution and (2) the

measurement of the phase shift of the NMR signal. In the first, the velocity distribution function $P_\Delta(\bar{v}, \mathbf{r})$ is measured and Eq. (27) is used to calculate $\langle \bar{v} \rangle_\mathbf{r}$. The velocity distribution function is determined by performing the inverse Fourier transform of the NMR signal in Eq. (26) with respect to q. To do this, the NMR data set is acquired with regularly incremented gradient amplitude G. A longer experimental time than in conventional imaging is required because of the addition of a velocity dimension to each voxel. The second method uses the phase of the measured NMR signal in Eq. (26) to estimate the mean velocity. A key advantage of the latter method is that fewer steps of phase encoding the velocity are needed and the experimental time can be shorter. Despite the popularity of this method, determination of $\langle \bar{v} \rangle_\mathbf{r}$ using the phase shift is not straightforward. As seen in Eq. (26), the velocity distribution function plays an important role in the phase as well as the amplitude of the measured NMR signal. The phase spread associated with incoherent motion such as hydrodynamic dispersion and self-diffusion causes signal attenuation whereas coherent flow velocity gives rise to a mean phase shift. Unfortunately, the mean phase shift is not always proportional to the mean velocity.

Several properties of $P_\Delta(\bar{v}, \mathbf{r})$ are useful to know to interpret the results of the phase measurement of NMR signal for fluids in porous media. The measured $P_\Delta(\bar{v}, \mathbf{r})$ depicts the dynamic displacement profile for flow superimposed on diffusion during Δ. For small Δ, velocity of each molecule will undergo little averaging and $P_\Delta(\bar{v}, \mathbf{r})$ will approach the instantaneous velocity spectrum with a component at a maximum velocity corresponding to fluid in the center of the pore throats and a component of zero velocity corresponding to the pore–fluid boundary layer. In the limit of very long Δ such that the molecules undergo significant displacements due to both flow and diffusive motion in the pore space and experience different velocities, $P_\Delta(\bar{v}, \mathbf{r})$ will reflect aspects of the averaging of many velocity streamlines. Figure 5 shows velocity distribution functions of water flowing through a pack of 0.2-mm glass beads in a 20-mm i.d. cylinder at a flow rate of 16 ml/min, which is equivalent to a rate of 0.85 mm/s per unit cross-sectional area of the sample. The voxel size is much larger than the pore dimensions. Three sets of data were obtained at $\Delta = 0.1$, 0.3, and 0.5 s. The data represents $P_\Delta(\bar{v}, \mathbf{r})$ in the mean flow direction. The velocity distribution function is profoundly dependent on the observation time. At $\Delta = 0.1$ s, there is a significant component at zero velocity. As Δ increases, the component at zero velocity disappears and the distribution becomes more symmetric. The behavior of $P_\Delta(\bar{v}, \mathbf{r})$ can be more complicated in natural rocks [37] where the pore structure is heterogeneous and nonflowing pores may exist.

Having examined the properties associated with the measured $P_\Delta(\bar{v}, \mathbf{r})$, we now turn to the analysis procedure involved in estimating $\langle \bar{v} \rangle_\mathbf{r}$ from the

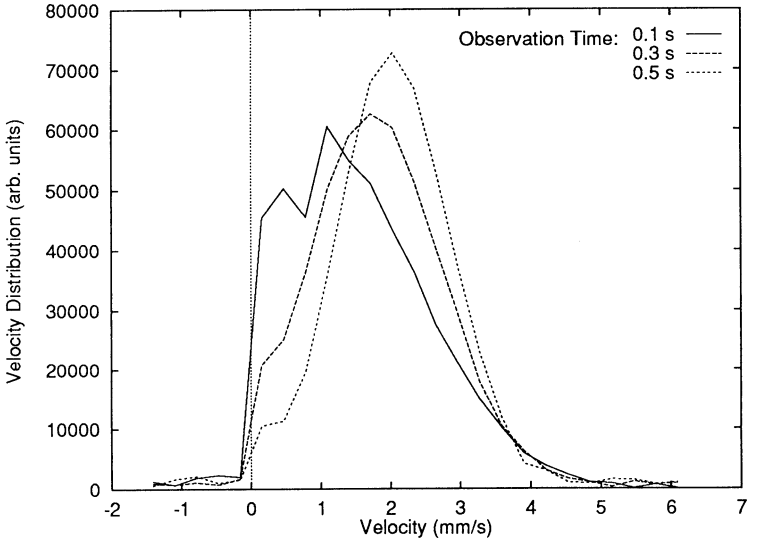

FIG. 5. Velocity distributions for water flow in a 0.2-mm glass bead pack at different observation times Δ. The flow rate per unit cross-sectional area was fixed at 0.85 mm/s.

phase shift of NMR signal. In terms of $\langle \bar{v} \rangle_{\mathbf{r}}$, Eq. (26) can be expressed as

$$S'(\mathbf{r}, q) = \rho(\mathbf{r}) \exp(-i2\pi q \langle \bar{v} \rangle_{\mathbf{r}} \Delta) \int_{-\infty}^{\infty} P_{\Delta}(\bar{v}, \mathbf{r}) \exp[-i2\pi q(\bar{v} - \langle \bar{v} \rangle_{\mathbf{r}})\Delta] \, d\bar{v}. \tag{28}$$

The phase shift of the measured signal is proportional to the mean velocity only if the integral in Eq. (28) is a real number. For this integral to be real, the velocity distribution function must be symmetric about the mean velocity [51]. This is generally not true for flow through porous media. Failure to recognize this behavior may result in severe errors in the determination of velocity.

The mean value as well as the variance of velocity in a voxel can be estimated by expanding the phase factor of the integrand in Eq. (28) in a power series and taking ensemble average (the integral) of each term [52]:

$$S'(\mathbf{r}, q) = \rho(\mathbf{r}) \exp(-i2\pi q \langle \bar{v} \rangle_{\mathbf{r}} \Delta) \cdot \left\{ 1 - \left\langle \frac{1}{2} [2\pi q(\bar{v} - \langle \bar{v} \rangle_{\mathbf{r}})\Delta]^2 \right\rangle + \mathcal{O}(\langle [2\pi q(\bar{v} - \langle \bar{v} \rangle_{\mathbf{r}})\Delta]^3 \rangle) \right\}. \tag{29}$$

If the condition

$$2\pi q(\bar{v} - \langle \bar{v} \rangle_{\mathbf{r}})\Delta \ll 1 \tag{30}$$

is satisfied so that the higher-order terms in Eq. (29) can be ignored, the phase of the signal at location **r** is approximated as

$$\varphi(\mathbf{r}) \simeq -2\pi q \langle \bar{v} \rangle_{\mathbf{r}} \Delta = -\gamma G \delta \Delta \langle \bar{v} \rangle_{\mathbf{r}}, \tag{31}$$

which is proportional to the mean velocity and the first moment of the gradient, $G\delta\Delta$. The attenuation factor $\{1 - \langle \frac{1}{2}[2\pi q(\bar{v} - \langle \bar{v} \rangle_{\mathbf{r}})\Delta]^2 \rangle\}$ is determined by the variance of the velocity, which provides a measure of fluid dispersion. In cases where the voxel size is much smaller than the pore size, Eq. (30) can be a good approximation because of small velocity spreads within voxels. In general cases, the accuracy of this approximation depends on the magnitude of the first moment of the gradient as well as the velocity spread in voxels [37].

In velocity-imaging experiments via phase mapping, a reference phase map at zero velocity is usually required to correct for the phase error caused by inhomogeneities of the magnetic field. There are a number of sources of field inhomogeneities in the velocity-imaging experiment, including the magnet shimming, susceptibility effects, and eddy currents arising from gradient switching. Figure 6 shows the corrected phase shift for a voxel, which is much larger than the mean pore size, as a function of the first moment of the gradient for water flow (1.6 ml/min) through the packing of 0.2-mm glass beads in a 20-mm i.d. cylinder. At small gradient amplitudes where the condition in Eq. (30) is satisfied, the phase shift is linearly proportional to the first moment of the gradient and the mean velocity can be derived from the slope. It is apparent that the data obtained with the shorter Δ deviate from the linearity earlier as the magnitude of G increases. This is consistent with the $P_{\Delta}(\bar{v}, \mathbf{r})$ measurements, which indicate a more asymmetric $P_{\Delta}(\bar{v}, \mathbf{r})$ for the shorter Δ, as illustrated in Fig. 5. The mean velocity so determined is independent of Δ, although the shape of the velocity distribution is dependent on Δ. The fluid velocity at each voxel is expected to be proportional to the flow rate if Darcy's law is satisfied. The effect of changing the flow rate on the phase shift from a voxel is shown in Fig. 7, in which the phase shift normalized to the flow rate for water flow in a Bentheimer sandstone sample is plotted against the gradient amplitude. The sandstone sample is 47 mm long and has a diameter of 25.4 mm. For small gradient amplitudes (< 3 G/cm) the phase shift is proportional to the gradient amplitude, and the mean velocity determined from the slope is proportional to the flow rate. From the preceding discussion, we conclude that estimates of the mean velocity of flow in porous media using the phase shift of NMR signal corresponding to a voxel much larger than the pore size

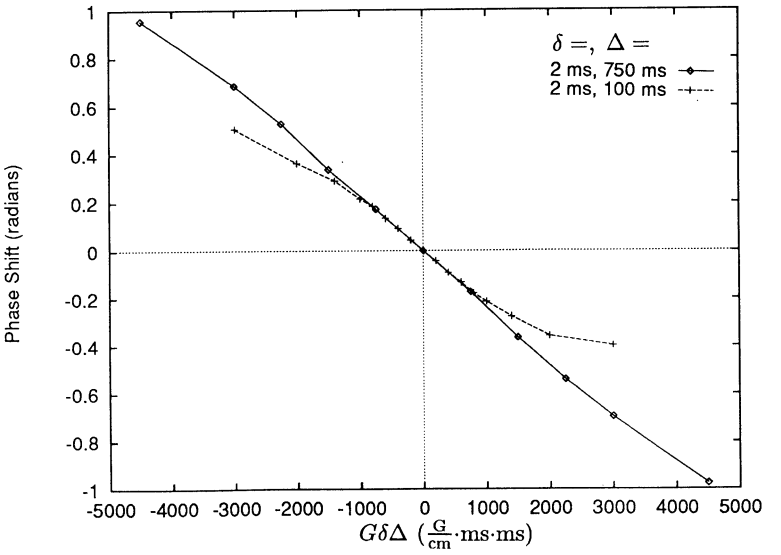

FIG. 6. The phase shift of NMR signal from a voxel as a function of the first moment of the magnetic field gradient $G\delta\Delta$ for water flow in the 0.2-mm bead pack. The linear region is wider for the data set with longer Δ.

depend in a complicated way on the magnitude and time scale of the gradient pulses. To obtain a reliable measurement, special care must be exercised. One must be certain that Eq. (30) is well satisfied, and it is also necessary for the narrow pulse approximation to be valid.

The ability of NMR velocity imaging to make noninvasive measurements probing spatially resolved flow processes makes it an invaluable tool for the study of porous media. No other experimental technique provides such information that can be useful to detect heterogeneities and analyze fluid transport in porous media.

10.3 Applications

A number of papers have presented NMR images of fluids in various porous solids [53]. In particular, experiments of fluid–fluid displacements have been carried out by several groups [e.g., Refs. 18, 31, 32, 54, 55]. Imaging studies of porous media using pulsed field-gradient techniques have been relatively limited despite the unique ability of these techniques to characterize both structure and transport.

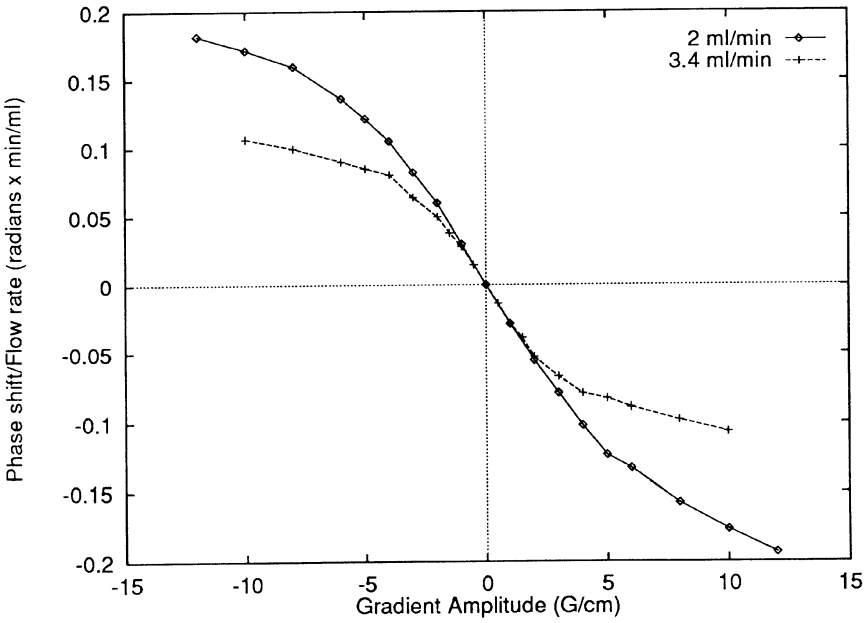

FIG. 7. The phase shift from an image voxel normalized to the flow rate as a function of the amplitude of the magnetic field gradient for water flow in the Bentheimer sandstone sample. The measurements were made with $\delta = 2$ ms and $\Delta = 100$ ms. The mean flow velocity determined from the linear region is proportional to the flow rate.

Although NMR imaging has been applied to investigations of fluids in porous media for more than a decade, the potential of using image data to determine properties that are useful for modeling and simulating fluid flow behavior has not been fully explored. We present here some applications of NMR imaging techniques that have been used to study fluid flow in porous media. We first give an example of how the imaging technique has been used to estimate multiphase flow functions, and then we discuss some of more recent applications of the pulsed field-gradient techniques to the study of transport phenomena in porous media.

10.3.1 Estimation of Multiphase Flow Functions

Estimation of capillary pressure and relative permeability functions is an important inverse problem in studies of multiphase flow through porous media. The mathematical model for multiphase dynamic flow through porous media is a set of coupled nonlinear partial differential equations [56]

and the unknown properties are functions of fluid saturation, a state variable. Conventional dynamic displacement experiments that utilize measurements outside of the porous sample, such as pressure drop and cumulative production, can be insufficient for accurate resolution of capillary pressure and relative permeability functions. These measurements made outside the sample do not allow for sufficient resolution of state variable within the sample. The information about instantaneous distribution of a state variable in the porous sample is very desirable for accurate estimates of the flow functions.

Fluid saturation images provide additional information of fluid states inside a porous sample. The use of NMR imaging measurements of saturation profiles to estimate multiphase flow functions has been demonstrated [57]. In the example presented here, a two-phase dynamic displacement experiment was performed on a Texas Cream limestone sample. Hexadecane was used as the oleic phase and D_2O as the aqueous phase. Oil was injected at a constant flow rate into the sample initially saturated with the aqueous phase. The pressure drop and oil saturation profiles were measured until the steady state was reached. Proton NMR was used to measure the oil saturation profiles as well as the porosity profile. The water saturation profiles could easily be determined because they are complements to the oil saturation profiles. The pressure drop, saturation profile, and water production data were used in a regression-based approach to estimate the capillary pressure and relative permeability functions. Figure 8 shows the measured and estimated water saturation data. The estimated capillary pressure and relative permeability functions are shown in Figs. 9 and 10, respectively. The simultaneous reconciliation of saturation profiles with production and pressure drop data increases the confidence in the accuracy of estimates of flow functions from the parameter estimation methods.

10.3.2 Evaluation of Flow and Transport

A brief survey of the applications of NMR imaging to fluid flow in porous media using pulsed field-gradient techniques is included in this section. These techniques provide spatial information about average flow velocity and average propagator, which can be used to investigate transport properties such as the permeability, dispersion, and diffusion.

Gleeson and Woessner [36] used NMR imaging to examine the connectivity of pores in a limestone. They showed by three-dimensional fluid saturation imaging that the pores in this rock are well connected. However, the flow sensitive image indicates that only part of the pores are effective in conducting fluid flow. Merrill [38] has mapped the average flow velocity inside a brine-filled sandstone sample using a pulsed field-gradient spin-echo

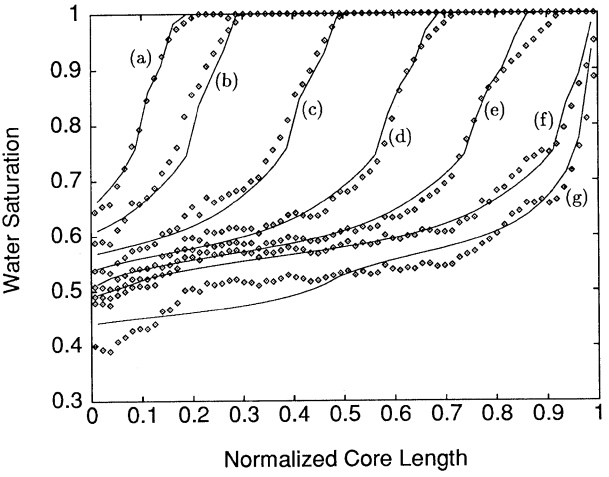

FIG. 8. Measured (dots) and estimated (lines) water (D_2O) saturation profiles in a limestone sample during a two-phase displacement experiment. Oil was injected from the left at a constant flow rate into the sample, which was initially saturated with the aqueous phase. Saturation profiles correspond to different times during the experiment: (a) 4.5, (b) 9.5, (c) 19.5, (d) 29.5, (e) 39.5, (f) 49.5, and (g) 229.5 min. Reprinted with permission of ASME from Kulkarni, *et al.*, *Proc. 2nd. Int. Conf. on Inverse Probl. Eng.: Theory and Practice*, Le Croisic, France, June 1996.

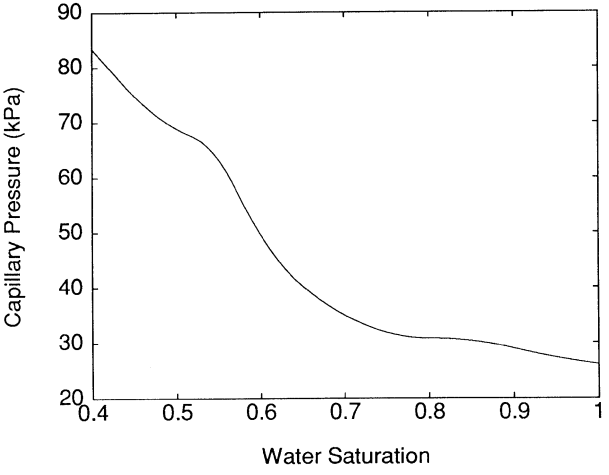

FIG. 9. Capillary pressure function estimated from the two-phase displacement experiment shown in Fig. 8. Reprinted with permission of ASME from Kulkarni, *et al.*, *Proc. 2nd. Int. Conf. on Inverse Probl. Eng.: Theory and Practice*, Le Croisic, France, June 1996.

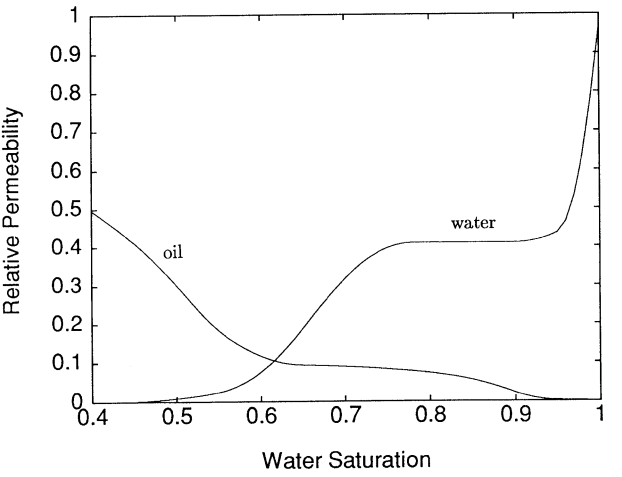

FIG. 10. Relative permeability functions estimated from the two-phase displacement experiment shown in Fig. 8. Reprinted with permission of ASME from Kulkarni, *et al.*, *Proc. 2nd. Int. Conf. on Inverse Probl. Eng.: Theory and Practice*, Le Croisic, France, June 1996.

sequence. The data were statistically analyzed to find the variation of the average velocity as a function of porosity. The results show that the velocity is a linear function of porosity. Thus, higher porosity regions of the core are better contacted by the displacement fluid. More recently, fluid velocity maps of water flowing through a Bentheimer sandstone have been measured using a modified echo-planar imaging (EPI) technique [39]. EPI is a high-speed NMR imaging modality and is capable of measuring motion over very short times, of the order of a tenth of a second. Their results showed that the velocity profiles of the local pixel values are approximately Gaussian in shape and centered about a mean value corresponding to Darcy's law. They also reported that when the same flow state is repeated, the velocity maps change but the characteristics of the velocity profile remain the same. This random nature of the velocity maps led them to propose a stochastic theory of flow in porous media. The stochastic model was based on conservation of energy and momentum over an assembly of voxels. This approach predicts that the flow distribution variance is proportional to the mean flow velocity. In a related work [58], a model for flow coupling between isolated voxel pairs was proposed to provide a complementary explanation of the Gaussian velocity distribution.

Measurements of the displacement (or velocity) distribution of fluid molecules during a predetermined time Δ have also been reported by several researchers. In their pioneer work, Edwards *et al.* [37] found that the

measured velocity distribution in porous media is affected by the observation time. They performed a number of computer simulations to observe the effect of diffusion on the velocity distribution function. In a more recent study, Kutsovsky *et al.* [40] measured the velocity distribution functions of water flow in bead packs. It was demonstrated that the velocity distribution derived from a crude bundle-tube model accounts for the positive part of their measured distributions. Packer and Tessier [42] reported the measurements of the displacement distribution function of an aqueous phase in a Fontainebleau sandstone sample. For displacements measured along the mean flow direction, the shape of the distribution as a function of Δ was modeled in terms of laminar flow within a set of randomly oriented capillaries. The distribution functions for small Δ are asymmetric and dominated by the orientational distribution of the capillaries. At long Δ, the distribution function increasingly shows an evolution to a more Gaussian-like shape. Using the capillary model, the evolution is reproduced only when diffusion of molecules across the velocity gradients within the capillaries is introduced, and when the transfer of spins between differently oriented capillaries is allowed. The distributions for displacements perpendicular to the mean flow direction are symmetric with respect to zero displacement. They show an evolution from a Gaussian-like shape for small Δ to a shape having some slight oscillatory character after longer times. The oscillatory features are likely to arise from structural characteristics of the pore space.

Other interesting applications of pulsed field-gradient NMR imaging include the studies of diffusion and dispersion in porous media. Molecular diffusion is an important physical property carrying information about the structure of porous media and dynamics of fluid flow. A determination of the apparent diffusion coefficient as a function of the diffusion time allows a qualitative probe of restricted diffusion as well as a quantitative detection of pore sizes. Through diffusion imaging, spatial heterogeneities of structure in porous media become accessible [59].

Dispersion has been treated as pseudo-diffusion or random flow, depending on the length scale of the measurement [1]. Despite different mechanisms that cause dispersion, a common feature of these processes is that the dispersion is dependent on fluctuations in velocity. The knowledge of the velocity distribution function enables a calculation of the variance in velocity, a parameter that is directly related to the dispersion coefficient. Therefore, the pulsed field-gradient NMR imaging methods allow not only a map of average velocity to be determined but also a map of mean dispersion for components both parallel and perpendicular to the mean flow direction. Lebon *et al.* [41, 60] measured the velocity distribution of water flow inside unconsolidated glass bead packs. The distribution of the velocity component along the mean flow direction was determined and an exponen-

tial decay of the velocity probability distribution was observed for short Δ. The results are very similar to that obtained from simulations in which the Stokes equation is solved in random sphere packings. At longer displacements, of the order of the pore size, strong distortions of the overall shape of the distribution were observed. The distortions were considered to be related to the dispersion phenomenon. At mean displacements larger than five bead diameters, the displacement distribution is Gaussian and the width of the distribution corresponds to the macroscopic dispersion coefficient as measured by other techniques. A generalized approach for the measurement of flow and dispersion has recently been reported by Seymour and Callaghan [43]. Various pulsed field-gradient NMR techniques have been described in the context of standard theories of dispersion. These techniques provide access not only to the average velocity and dispersion coefficient but also to propagators relevant to spatial and temporal correlations and, thus, provide the potential for studying complex flow properties involving the interplay between hydrodynamic and structural characteristics of porous media.

References

1. P. T. Callaghan, *Principles of Nuclear Magnetic Resonance Microscopy*. Oxford University Press, 1991.
2. A. T. Watson and C. T. P. Chang, *Prog. Nucl. Magnet. Res. Spectrosc.* **31**, 343 (1997).
3. T. C. Farrar and E. D. Becker, *Pulse and Fourier Transform NMR*. Academic Press, 1971.
4. E. Fukushima and S. B. W. Roeder, *Experimental Pulse NMR—A Nuts and Bolts Approach*. Addison-Wesley Publishing Co., 1981.
5. P. Mansfield and P. G. Morris, NMR Imaging in Biomedicine. In J. S. Waugh, editor, *Advances in Magnetic Resonance*, *Suppl. 2*. Academic Press, 1982.
6. P. Brunner and R. R. Ernst, *J. Magn. Reson.* **33**, 83 (1979).
7. W. A. Edelstein, J. M. S. Hutchison, G. Johnson, and T. Redpath, *Phys. Med. Biol.* **25**, 751 (1980).
8. D. R. Bailes and D. J. Byrant, *Contemp. Phys.* **25**, 441 (1984).
9. S. Chen, F. Qin, and A. T. Watson, *AIChE J.* **40**, 1238 (1994).
10. W. A. Edelstein, H. J. Vinegar, P. N. Tutunjian, P. B. Roemer, and O. M. Mueller, *Proc. 63rd Annu. Tech. Conf. Exhibit. Soc. Petrol. Eng.*, p. 101, 1988. SPE 18272.
11. J. J. Dechter, R. A. Komoroski, and S. Ramaprasad, *J. Magn. Reson.* **93**, 142 (1991).
12. L. D. Hall, V. Rajanayagam, and C. Hall, *J. Magn. Reson.* **68**, 185 (1986).

13. W. T. Dixon, *Radiology* **153**, 189 (1984).
14. M. A. Horsfield, C. Hall, and L. D. Hall, *J. Magn. Reson.* **87**, 319 (1990).
15. C. T. Chang and C. M. Edwards, *Log Anal.* **34**, 20 (1993).
16. P. D. Majors, J. L. Smith, F. S. Kovarik, and E. Fukushima, *J. Magn. Reson.* **89**, 470 (1990).
17. B. A. Baldwin and W. S. Yamanashi, *SPE Res. Eng.* **4**, 207 (1989).
18. J.-D. Chen, M. M. Dias, S. Patz, and L. M. Schwartz, *Phys. Rev. Lett.* **61**, 1489 (1988).
19. A. J. Dwyer, V. J. Sank, J. W. Resing, A. M. Hickey, and J. L. Doppman, *Radiology* **168**, 827 (1988).
20. P. D. Majors, P. Li, and E. J. Peters, *Proc. SPE Annu. Tech. Conf. Exhib.*, Dallas, Tex., October 1995. SPE 30557.
21. K.-D. Merbodlt, W. Hanicke, and J. Frahm, *J. Magn. Reson.* **64**, 479 (1985).
22. C. T. Chang and C. M. Edwards, *Bull. Am. Phys. Soc.* **37**, 1159 (1992).
23. P. N. Tutunjian, H. J. Vinegar, and J. A. Ferris, *The Society of Core Analysts Annual Technical Conference Preprints*, *Paper No. 9111*, 1991.
24. S. N. Sarkar, R. A. Komoroski, and J. J. Dechter, *Proc. 43rd Pittsburgh Conf. Annu. Chem. Appl. Spectr., No. 798*, 1992.
25. S. N. Sarker, J. J. Dechter, and R. A. Komoroski, *J. Magn. Reson. Ser. A* **102**, 314 (1993).
26. H. J. Vinegar, P. N. Tutunjian, W. A. Edelstein, and P. B. Roemer, *Proc. Sixth Annu. Tech. Conf. Soc. Petrol. Eng.*, *Paper No. 19590*, 1989.
27. S. N. Sarkar, C. T. Chang, and C. M. Edwards, *Bull. Am. Phys. Soc.* **38**, 165 (1993).
28. C. T. Chang, S. Mandava, A. T. Watson, S. Sarkar, and C. M. Edwards, *Magn. Reson. Imaging* **11**, 717 (1993).
29. S. Chen, K.-H. Kim, F. Qin, and A. T. Watson, *Magn. Reson. Imaging* **10**, 815 (1992).
30. G. K. Pierens, M. Peyron, A. J. Lucas, T. A. Carpenter, L. D. Hall, G. F. Potter, R. C. Stewart, and D. W. Phelps, *Magn. Reson. Imaging* **12**, 323 (1994).
31. S. S. Mandava, A. T. Watson, and C. M. Edwards, *AIChE J.* **36**, 1680 (1990).
32. E. J. Fordham, L. D. Hall, T. S. Ramakrishnan, M. R. Sharpe, and C. Hall, *AIChE J.* **39**, 1431 (1993).
33. S. Chen, F. Qin, K.-H. Kim, and A. T. Watson, *AIChE J.* **39**, 925 (1993).
34. M. Peyron, G. K. Pierens, A. J. Lucas, L. D. Hall, and R. C. Stewart, *J. Magn. Reson. Ser. A* **118**, 214 (1996).
35. R. N. Kulkarni and A. T. Watson, *AIChE J.* **43**, 2137 (1997).
36. J. W. Gleeson and D. E. Woessner, *Magn. Reson. Imaging* **9**, 879 (1991).
37. C. M. Edwards, C. T. Chang, and S. Sarkar, *The Society of Core Analysts Annual Technical Conference Preprints, Paper No. 9310,* 1993.
38. M. R. Merrill, *AIChE J.* **40**, 1262 (1994).

39. P. Mansfield and B. Issa, *J. Magn. Reson. Ser. A* **122**, 137 (1996).
40. Y. E. Kutsovsky, L. E. Scriven, H. T. Davis, and B. E. Hammer, *Phys. Fluids* **8**, 863 (1996).
41. L. Lebon, L. Oger, J. Leblond, J. P. Hulin, N. S. Martys, and L. M. Schwartz, *Phys. Fluids* **8**, 293 (1996).
42. K. J. Packer and J. J. Tessier, *Molec. Phys.* **87**, 267 (1996).
43. J. D. Seymour and P. T. Callaghan, *AIChE J.* **43**, 2096 (1997).
44. K. J. Packer, C. Rees, and D. J. Tomlinson, *Adv. Molec. Relax. Process.* **3**, 119 (1972).
45. P. R. Moran, *Magn. Reson. Imaging* **1**, 197 (1982).
46. R. M. Cotts, M. J. R. Hoch, T. Sun, and J. T. Markert, *J. Magn. Reson.* **83**, 252 (1989).
47. E. O. Stejskal and J. E. Tanner, *J. Chem. Phys.* **42**, 288 (1965).
48. G. J. Nesbitt, T. W. Fens, J. S. van den Brink, and N. Roberts, Evaluation of fluid displacement in porous media using NMR microscopy. In B. Blumich and W. Kuhn, editors, *Magnetic Resonance Microscopy*. VCH, 1992.
49. P. T. Callaghan, K. R. Jeffrey, and Y. Xia, Translational motion imaging with pulsed gradient spin echo methods. In B. Blumich and W. Kuhn, editors, *Magnetic Resonance Microscopy*. VCH, 1992.
50. S. Whitaker, *Transp. Porous Media* **16**, 3 (1986).
51. A. Caprihan, S. A. Altobelli, and E. Benitez-Read, *J. Magn. Reson.* **90**, 71 (1990).
52. Q. S. Xiang and O. Nalcioglu, *IEEE Trans. Med. Imaging* **7**, 364 (1988).
53. For example, *Magn. Reson. Imaging* **9**(5), 1991; **12**(2), 1994; **14**(7/8), 1996; **16**(5/6), 1998.
54. B. A. Baldwin and W. S. Yamanashi, *Magn. Reson. Imaging* **6**, 493 (1988).
55. E. J. Fordham, M. A. Horsfield, C. Hall, and L. D. Hall, *Magn. Reson. Imaging* **9**, 803 (1991).
56. K. Aziz and A. Settari, *Petroleum Reservoir Simulation*. Applied Science Publishers, 1979.
57. R. N. Kulkarni, J. E. Nordtvedt, and A. T. Watson, *Proc. 2nd Int. Conf. on Inverse Probl. Eng.: Theory and Practice,* Le Croisic, France, June 1996.
58. P. Mansfield and B. Issa, *J. Magn. Reson. Ser. A* **122**, 149 (1996).
59. S. J. Gibbs, J. J. Attard, and L. D. Hall, *AIChE J.* **39**, 689 (1993).
60. L. Lebon, J. Leblond, and J. P. Hulin, *Phys. Fluids* **9**, 481 (1997).

This Page Intentionally Left Blank

11. ACOUSTICAL AND ELECTRICAL METHODS FOR THE STUDY OF FLUID MIXING IN POROUS MEDIA

Jean-Pierre Hulin and Dominique Salin

Laboratoire FAST
Pierre et Marie Curie and Paris-Sud Universities and CNRS (UMR 7608)
Orsay, France

11.1 Static Mixing and Tracer Dispersion in Porous Media: An Introduction

11.1.1 How Miscible Fluids Spread and Mix in Porous Media

Miscible fluids in direct contact never remain completely separated, even if they do not flow and/or are localized in a free volume without solid walls. Molecular diffusion always induces some mixing: However, this process is effective only at small distances and quickly becomes extremely slow at larger ones. On the other hand, to induce complete mixing over a significant volume, it is necessary to stretch, fold, and intertwine filaments of the two fluids. In an open geometry and for low-viscosity fluids, as for a drop of cream in a coffee cup, it is generally sufficient to stir the fluids to induce very efficient turbulent mixing. In porous media, on the contrary, flow is almost never turbulent, particularly when the pore size is small. One can no longer rely on flow velocity time variations to induce mixing but only on the spatial disorder of the flow field due to the complex structure of the pore space.

A common example is the mixing of viscous fluids in chemical engineering applications: Inducing turbulence would require a prohibitively large amount of energy and might in addition destroy the internal structure of many complex fluids. Similar processes are encountered in environmental problems such as the spreading of aqueous or nonaqueous pollutants following an accidental discharge; the mixing of these pollutants with surrounding water flows generally includes underground porous layers.

Let us analyze the generic case of two fluids in contact flowing through a porous medium: Mixing is then almost always associated to the random walk of fluid (or tracer) particles through the disordered structure of the pore volume, and thermal molecular agitation is dominant only at very low mean flow velocities. The steps of the random walk are much larger than those of thermal Brownian motion so that the corresponding spreading scale and the width of the dispersion front is correspondingly increased. Of course, the minimum size of heterogeneities of the mixture obtained in this

EXPERIMENTAL METHODS IN THE PHYSICAL SCIENCES
Vol. 35
ISBN 0-12-475982-3

ISSN 1079-4042/99 $30.00

way is also larger; however, if the medium is adequately homogeneous, this size is of the order of the grain diameter so that molecular diffusion can generally complete the mixing.

One generally characterizes the relative influence of the various spreading mechanisms by the Péclet number:

$$\mathrm{Pe} = \frac{Ud}{D_m}, \tag{1}$$

where d is the characteristic size of the grains of the medium, U is the mean flow velocity, and D_m is the molecular diffusion coefficient for the species considered; Pe characterizes the relative influence of convective spreading effect due to the disorder of the medium and of molecular diffusion. For a homogeneous porous packing in which the correlation length of the velocity field is of the order of the grain size, the value $\mathrm{Pe} = 1$ corresponds to the boundary between dominant convective ($\mathrm{Pe} > 1$) and diffusive ($\mathrm{Pe} < 1$) spreading mechanisms.

The mixing of two fluids flowing in a porous medium may be very effective in some cases. Some static mixers contain a set of dividing plates; in fact, they mimick in a simplified and more ordered way the internal structure of porous materials. Two fluids injected side by side inside the mixer flow out as small entangled filaments; if needed, molecular diffusion can then complete the mixing at small length scales. Such devices are well adapted to the mixing of viscous and/or complex fluids for which, as already stated, turbulent mixing is not suitable; they find many applications in the food or polymer industries when one deals with viscous pastes or polymer solutions.

11.1.2 A Simple Mixing Experiment in a Porous Sample

Let us represent (Fig. 1) how a dot of passive, nonreactive tracer, initially concentrated in a very small volume of fluid, will spread out as it is carried through a porous medium by the main flow. If we were inside a fluid volume of velocity $\mathbf{v}$, the local concentration $c(\mathbf{r}, t)$ of tracer would satisfy the classical convection–diffusion equation:

$$\frac{\partial c}{\partial t} + \mathbf{v}.\mathbf{grad}\, c = D_m \nabla^2 c. \tag{2}$$

A dot of passive solute (dye, conducting salt, radioactive component, etc.) would convect with the local velocity $\mathbf{v}$ and spread out in time evenly in all directions over a distance of the order of $\sqrt{D_m t}$. In porous media, one can no longer use the local concentration as a variable due to its fast and random changes. We therefore replace c by the macroscopic variable $C(\mathbf{r}, t)$,

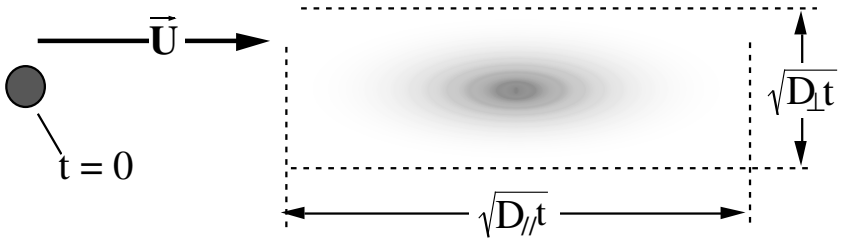

FIG. 1. Schematic view of the spreading of an initially concentrated tracer dot located in a porous medium where a steady uniform flow of velocity U has been established.

which represents the average of c over a representative elementary volume (REV) large enough compared to the pore size. If the medium is not too heterogeneous, C satisfies the macroscopic equation [1–3]:

$$\frac{\partial c}{\partial t} + \mathbf{U}.\mathbf{grad}\, C = D_{||}\frac{\partial^2 C}{\partial x_{||}^2} + D_{\perp}\nabla_{\perp}^2 C, \tag{3}$$

where $\mathbf{U}$ is the mean velocity through the medium (also averaged over a large enough number of pore volumes); $x_{||}$ and $x_{\perp}$ represent the coordinates respectively parallel and perpendicular to the flow, and $\nabla_{\perp}^2$ is the 2-D Laplacian operator associated with these coordinates. Let us note that Eq. (2) remains valid at the local scale but that Eq. (3) is more useful for practical purposes. The two coefficients $D_{||}$ and $D_{\perp}$ are respectively the longitudinal and transverse dispersion coefficient; they are generally different ($D_{||} > D_{\perp}$) so that a pointlike tracer injection will give rise to an elliptical tracer spot. Generally, $D_{||}$ and $D_{\perp}$ are much larger than the molecular diffusion coefficient D_m; they become of the order of D_m only if the Péclet number Pe defined in Eq. (1) is lower than 1 so that molecular diffusion processes become significant.

Figure 2 describes how longitudinal dispersion can be determined practically. We consider a cylindrical porous sample with an arbitrary cross section and establish an evenly distributed flow through it using a low-volume injector. At an initial time $t = 0$, we either induce a stepwise variation of tracer concentration in the flow or perform a pulselike very short injection of tracer. The subsequent tracer concentration variations can be monitored along the flow (if the type of detection allows for it) or detected at the outlet of the sample. For instance, in the latter approach displayed in Fig. 2 with a stepwise tracer injection, concentration variations at the outlet of the sample are shifted by a mean time T_0 reflecting the porous volume of the sample and the initially abrupt concentration variation is spread out over an interval Δt. If the sample is homogeneous

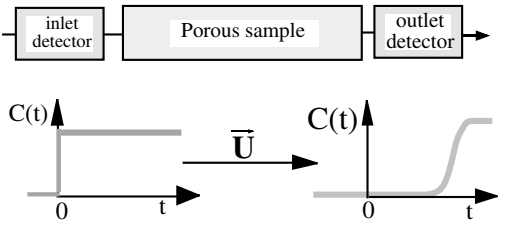

FIG. 2. Schematic view of a typical transmission dispersion experiment through a porous sample with tracer concentration variations induced at the inlet and detected at the outlet under steady flow conditions through the medium.

enough, the dispersion coefficient $D_{||}$ can be determined by fitting the concentration variation to solutions of the Gaussian convection–diffusion Eq. (3). In other cases, other, more refined models are necessary to analyze tracer spreading [4–5].

Many types of tracers and detection techniques can be used. Optical techniques (UV absorption, fluorescence, and differential optical index variations), radioactive tracers, acoustical detection techniques, electromagnetic techniques (conductivity, nuclear magnetic resonance [NMR], and polarography), etc. are all possibilities. Some of these techniques allow for the analysis of spatial tracer distributions inside porous materials. Others can be performed only at the inlet or outlet of the sample. The choice will depend on the particular requirements of the experiments to be performed and on the information being sought. This chapter describes a few of these techniques.

11.1.3 Mixing or Separation

We noted that, for passive tracers, the mean transit time T_0 through the sample is directly related to the porous volume V_p (T_0 is equal to the ratio of the total pore volume V_p and the injection flow rate Q_t). This is no longer the case if the solute interacts physicochemically with the matrix of the porous sample or if sterical exclusion effects prevent the tracer from accessing the full pore volume.

Such properties are put to work by analytical chemists in the extremely important applications of chromatography. Analytical or preparative liquid chromatography, for instance, uses exactly the same type of procedure. One generally performs a pulsewise injection of chemical tracer and uses a suitable detector to monitor the concentration peaks corresponding to the flow of the various mixture components out of the porous sample. The different transit times for the various components may have a large diversity

of origins, including the differences in their physicochemical interactions with the matrix, the varying diffusions of the molecules into some small pores of the sample, and the influence of the various sizes of the molecules. The materials of the porous sample (the so-called "chromatographic column") are chosen according to the type of chemical species to be separated. In this respect, dispersive mixing is a nuisance for analytical chemists. If the dispersion coefficient $D_{||}$ is minimized, the width of the detection peaks is reduced, and this improves the resolution of the technique. The example of chromatography shows that similar experimental setups can be used for mixing or separation, provided, of course, two essential parameters are modified: the interaction between the solutes and the solid matrix, on one hand, and the intrinsic dispersion of the tracer, on the other hand.

11.1.4 Large- and Small-Scale Mixing

Even in the case of passive tracers, the description of dispersion as a mixing process must be complemented by the knowledge of the scale at which mixing is realized. Consider, for instance, a sample that contains large-scale heterogeneities such as strata of various permeabilities and parallel to the flow: For a given pressure difference applied along the sample, the flow velocity in each of the layers is different. Therefore the transit times through the two types of layers will be markedly different. The shape of the separation front between the two tracer volumes of different concentrations will also be strongly distorted and extend over a much longer distance parallel to the main flow. However, while the spatial extent of this mixing front is increased, mixing is actually less uniform and large unmixed patches of each fluid can surround each other. Thus, a good analysis requires not only a measurement of the average solute concentration in a flow section but also a mapping of the concentration variations across the flow.

Similar problems can occur (and are discussed later is this chapter) when the displaced and displacing fluid have different densities and/or viscosities. In some cases, fingering instabilities may appear. In other cases, the contrast of fluid properties may stabilize the displacement front and compete with other instabilities. Generally, hydrodynamic instabilities can create large-scale structures of the displacement front, and a mapping, even an approximate one, of the concentrations may be extremely useful.

Tracer dispersion and miscible mixing are clearly extremely sensitive tools for the analysis of permeability heterogeneities in porous media. We see later in the chapter that monitoring evolutions of the concentration variation front along the flow and visualizing concentration distributions are extremely helpful for understanding the origin and distribution of heterogeneities.

11.1.5 Some Dispersion Measurement Problems in Porous Media

Tracer dispersion in porous media clearly includes a large variety of problems related to many different mechanisms. Some mechanisms act at the pore scale and are associated with the local structure and disorder of the flow field even inside homogeneous porous media. Others correspond to very large scale heterogeneities of the media such as those encountered in stratified soils or natural rocks and in large-scale geological structures. Some mechanisms result primarily from viscosity or density contrasts between the invading and displaced fluids.

Depending on the type of displacement process to be studied, the experimental tools involved can be quite different. We present first in Section 11.2 the essential mechanisms involved in tracer dispersion in porous media. Section 11.3 describes a few high-resolution techniques for characterizing tracer transport and dispersion properties at the pore scale. In contrast, Section 11.4 presents techniques suitable for the study of tracer dispersion associated with large-scale heterogeneities. Examples of applications of such techniques to the study of the problem of anomalous, non-Gaussian dispersion are discussed in Section 11.5. Finally, Section 11.6 presents special problems and techniques dealing with displacement processes involving two fluids of different physical and rheological properties.

11.2 Mechanisms of Miscible Mixing

11.2.1 Main Solute Dispersion Mechanisms

As noted, pure molecular diffusion is dominant only at very low Péclet numbers $\mathrm{Pe} = Ud/D_m \ll 1$. However, it is an important factor to complement mixing on small length scales at any velocity, and it can markedly influence and modify other mechanisms. Finally, the dominant dispersion mechanisms are quite dependent on the topology of the porous medium.

In classical porous media such as rocks or unconsolidated grain packings, the major dispersion mechanism is the random changes of flow direction and velocity associated with the random pore geometry. This process is called geometrical dispersion [6–8]. It can be pictured as a random walk of tracer particles superimposed over a drift velocity U associated to the mean flow (Fig. 3). Let us call l the length of the individual steps, τ their duration, and u the typical fluctuation with respect to the mean velocity U during the step; in the following, u is assumed to be of the same order of magnitude as—although lower than—U so that $l \approx U\tau$. From the laws of random walks, the mean square deviation $\sqrt{\overline{\Delta x^2}}$ with respect to the mean displacement Ut along the mean flow for a set of particles following different paths

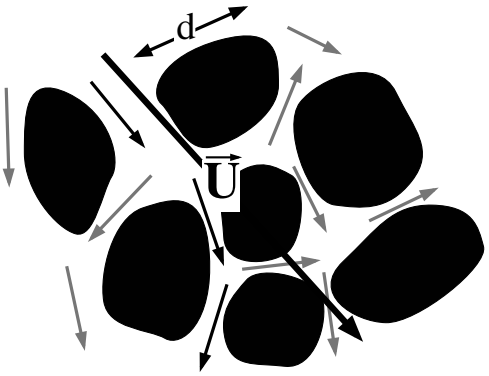

FIG. 3. Schematic view of the trajectories of tracer particles inside a porous medium; these are pictured as a random walk with individual steps of length l and duration τ superimposed over a global drift at the mean velocity U inside the sample.

increases as

$$\sqrt{\overline{\Delta x^2}} \approx \sqrt{D_{||}t}, \tag{4}$$

with

$$D_{||} \cong U^2\tau \cong Ul \cong \frac{l^2}{\tau}. \tag{5}$$

In homogeneously made media (packings of nonporous grains for instance), one can assume that the step length is of the order of the grain size d. Then,

$$D_{||} \cong Ud. \tag{6}$$

One therefore often introduces the dispersivity $l_d = D_{||}/U$, which represents the characteristic length of the dispersion process. Experimental measurements on homogeneous monodisperse bead packings report around Pe = 10 a minimum value of l_d of about half the diameter, in qualitative agreement with Eq. (6). For Pe = 1000, l_d is about 50% higher [1, 9]. At very low Péclet numbers, molecular diffusion is dominant and l_d increases as D_m/U.

More precisely, the dispersivity l_d is equal to the Lagrangian correlation length of the flow velocity field [7], with

$$D_{||} = \left\langle \int_0^t \delta V_{||}(\mathbf{x}(0), 0)\delta V_{||}(\mathbf{x}(t'), t')\, dt' \right\rangle, \tag{7}$$

where $\delta V_{||}x(t'), t')$ and $\delta V_{||}(x(0), 0)$ are the respective deviations $V_{||} - U$ at

times t' and 0 of the velocity component $V_{||}$ along the mean velocity $\mathbf{U}$ for a same given particle. The integral is taken along the 3-D particle trajectory $\mathbf{x}(t)$ between times 0 and t, and $D_{||}$ is obtained from an ensemble average over all particles. Therefore l_d represents the pathlength over which a fluid particle keeps track of an initial deviation from $\mathbf{U}$. Equation (7) demonstrates the nonlocal nature of dispersion since $D_{||}$ is determined by an integral along the whole path of tracer particles and not by an average of local values.

Often l_d is much larger than the grain size in heterogeneous media and rocks where a particle keeps a significant deviation from the mean velocity for the whole time necessary to cross a block of given permeability. Very large dispersivities are measured in stratified media [10] or in porous media with large channels of varying permeabilities. Natural or artificial consolidated porous media also often give very broad dispersion curves, particularly if there is a layered structure [11].

Another important issue in tracer dispersion is the case of porous media with a significant fraction of the pore volume occupied by zero-velocity zones [12]; for instance, this is the case for hydrodynamic dispersion in partially saturated porous media (the flow velocity is kept low enough during the dispersion measurement so that no variation of the saturation occurs). During a dispersion experiment, tracer molecules move by convection along the backbone and by molecular diffusion on the dead ends. The characteristic diffusion time τ_ξ over the dead zones is of the order of $\tau_\xi = \xi^2/D_a$, where ξ is the typical size of the dead zones, and D_a is the effective diffusion constant over these regions. From Eq. (5), the effective dispersion coefficient is then

$$D_{||} = U^2\tau_\xi = \frac{(U\xi)^2}{D_a} \tag{8}$$

so that the dispersion coefficient $D_{||}$ varies in this case as U^2 instead of U. In porous media with a low saturation close to the percolation threshold [13], the effective diffusion coefficient D_a may be much lower than D_m. Strong increases of the dispersion coefficient as well as non-Gaussian dispersion curves are then observed.

11.2.2 Particular Case of Dispersion in Fractures

Fractured media are particularly important because pollutants spread mostly underground by fluid transport through fractures. At the scale of a single fracture, even with rough walls, the flow field differs greatly from that of the flow through an ordinary 3-D porous medium. This is due to the large permeability anisotropy between directions parallel and perpendicular to

the fracture solid walls. Few flow lines penetrate from the fracture into the bounding rock matrix. Also, flow lines remain in the same region of the velocity profile across the aperture (close to the walls or in the maximum velocity zone) throughout their path along the fracture.

As a result, dispersion in a single fracture is similar to that between parallel planes or inside a continuous capillary tube. For such geometries, dispersivity is due to the fluid velocity differences associated with the Poiseuille parabolic profile. Spreading is limited by transverse molecular diffusion across the flow section. In this so-called Taylor dispersion [14], $D_{||}$ verifies for a capillary tube of diameter d [15]:

$$D_{||} = \frac{d^2 U^2}{192 D_m} + D_m. \tag{9}$$

Note that the characteristic molecular diffusion time *across* the capillary tube section is $\tau_m = d^2/D_m$. When the term D_m is negligible in Eq. (9), the diffusion time $\tau_m \approx d^2/D_m$ plays the part, in the case of Taylor dispersion, of the characteristic velocity decorrelation time τ introduced in Eq. (5).

For a fracture with smooth parallel walls [15–16], Eq. (9) remains valid provided the factor 192 is replaced by 210 and the diameter d is replaced by the distance a between the walls. Then the dispersivity $l_D = D_{||}/U$ satisfies

$$l_D = \frac{D_{||}}{U} = \frac{U\tau_m}{210} + \frac{D_m}{U} = \frac{Ua^2}{210 D_m} + \frac{D_m}{U}. \tag{10}$$

If one or both walls are rough, there will be some disorder in the flow field, particularly if the height of the asperities is comparable to the fracture aperture. A dispersion mechanism analogous to geometrical dispersion due to the random splitting of the flow tubes is then present. Roughness mostly introduces a two-dimensional disorder in planes parallel to the fracture surface but does not move tracer away from or toward the solid surfaces. Thus, wall roughness does not suppress Taylor dispersion, but results in an additional, geometrical type term [16].

11.3 Experimental Techniques for Studying Dispersion at Microscopic Scale

11.3.1 Key Issues in the Dispersion Processes at Short Distances

Dispersion can be described by a classical convection–diffusion equation when the spreading process is Gaussian. In this case, it corresponds to a random walk superimposed over a mean drift associated with the global flow through the sample. The process can be considered as Gaussian when

the requirements for the central limit theorem to be valid are met. This implies that a tracer particle has undergone a sufficient number of flow redirections after which its velocity becomes decorrelated from its initial value. In homogeneous media, each step corresponds to the displacement from one pore to another. In heterogeneous media, which can be pictured as an array of blocks of different permeabilities, an individual step corresponds to the path through one block. Mesoscopic changes of velocity from one block to another influence dispersion much more than smaller-scale velocity variations from one pore to another. Reference [17] shows that the dispersion magnitude is determined by a combination of the scale of the heterogeneities and of the amplitude of the corresponding permeability or flow velocity variations.

At very short times, on the contrary, spreading occurs only at the pore scale, and it reflects the velocity probability distribution in the pore volume and not its interpore correlation. These have a variety of origins: parabolic velocity profiles in individual pores, velocity dependence on the orientation of the flow channels with respect to the mean pressure gradient, or variability of flow channel diameters. As the spreading time increases, the pathlength of the tracer particles becomes of the order of the pore size. However, transition toward Gaussian dispersion occurs only after moving through several pores. Analyzing these different spreading regimes helps us to understand mass transport processes at different length scales in porous media.

11.3.2 Particle Velocimetry and Path-Imaging Techniques

One obvious approach to analyzing tracer spreading at small distances is to analyze directly the path of (supposedly) passive tracer particles and their location at regular time intervals. This can be realized using particle image velocimetry techniques [18]: Flow carrying solid particles is imaged using multiple exposures, each obtained through a brief, intense illumination. Since the time interval between exposures is known, the trajectory of individual particles can be identified by the continuous dot sequences, and the velocity can be calculated from the dot spacing. Obviously transparent porous media saturated with fluids of the same optical index are required. A few consecutive images with many particles enable us to determine velocity distributions. Analysis of the early phase of dispersion requires following particle trajectories over a long enough pathlength, which is rather cumbersome. An additional difficulty is the inherently 3-D structure of the flow pattern. Quite often, a plane illumination of the system is used to discriminate particles located in the plane of interest. However, this also makes it difficult to follow particles over a long distance, since they move in and out of the illumination plane.

11.3.3 Tracer Dispersion Analysis Using Pulsed Gradient NMR Techniques

11.3.3.1 Pulsed Gradient NMR Techniques and Velocity Distribution and Dispersion Measurements. NMR measurements provide an interesting approach to the analysis of tracer dispersion at the pore scale. Pulsed magnetic field gradient techniques enable us to determine the displacement of the nuclei (for instance, protons in water) along a chosen direction during a preset measurement time. This time can be varied over a broad range, from a few to several hundred milliseconds [19].

For very short measurement times and low flow velocities, the displacement of the fluid particles is small compared to the pore and the grain size. In this case, these measurements provide the distribution of the velocity component parallel to the field gradient. In the case of simple geometries (monodisperse sphere packings for instance), these measurements can be compared to numerical simulations in which Stokes equation is solved numerically [19–23].

For long measurement times, the molecular displacements can be much larger than the grain diameter d (displacements of up to $7d$ could be obtained practically). This enables us to study the full transition of the spreading mechanisms governing the displacement distribution from pure convection to Gaussian dispersion. We note that in classical dispersion experiments, tracer is injected at the inlet of the porous sample and the concentration variations are monitored at the outlet. In pulsed gradient NMR experiments, all water molecules in the sample are marked simultaneously and the distribution of their displacements can be determined after a selectable time lapse. Compared to the classical technique, pulsed NMR does not introduce any dead volume associated with a tracer injection circuit. Moreover, the time interval and the pathlength can be varied to enable investigations at the microscopic scale.

The principles and the practical implementation of NMR measurements in porous media are described in detail in Chapters 9 and 10 of this book. We present here only the features of these techniques directly related to dispersion or velocity measurements. In particular, we do not discuss the influence of magnetic flow field heterogeneities and relaxation processes due to the complex geometrical and physicochemical structure of porous media. These are important limitations in the use of such techniques in, for instance, natural rock samples.

11.3.3.2 Practical Implementation of Pulsed Gradient Velocity Measurements. Let us describe a typical experimental setup adapted to measurements in small-diameter porous samples. The experiments described here [19, 25] were performed with a 100-MHz Bruker CXP-100 pulsed

NMR spectrometer using a vertical superconducting solenoid. The sample is a nonconsolidated packing of spherical glass beads of diameters ranging between 80 and 800 μm, contained in an 8 mm i.d. glass tube parallel to the magnetic field (Fig. 4). The magnetic field gradient is also parallel to the tube axis. A NMR saddle coil around the tube delivers the radio-frequency pulses and detects the magnetization induction. The measurement volume $\mathscr{V}$ is of the order of 1 cm^3. The flow velocity is always low enough so that the transit time through $\mathscr{V}$ is much larger than the longitudinal spin relaxation time T_1.

During the measurements, space is encoded by magnetic field-gradient pulses of duration δ with an intensity g up to 1 T/m. After a pulse, a magnetization phase shift $\varphi = \gamma\delta g z$ has been induced on fluid elements located at a coordinate z in the direction parallel to the magnetic field gradient (γ is the gyromagnetic ratio of the water molecules protons). The sequences used in the experiments include two field-gradient pulses of same duration δ and amplitude g at an interval Δ and before the second magnetic field pulse, a suitable RF pulse sequence is applied and flips the magnetization so that the effective phase shift φ is exactly reversed at all points. If fluid particles did not move during Δ, the two phase shifts would exactly cancel out after the second pulse. On the contrary, if the fluid particle has moved by a distance Δz in the time lapse between the two pulses, there will be a resultant phase shift $\Delta\varphi(\Delta z)$ of the magnetization:

$$\Delta\varphi(\Delta z) = k\Delta z = \gamma\delta g\Delta z, \tag{11}$$

where $k = \gamma\delta g$ represents the wave number associated to the value g of the

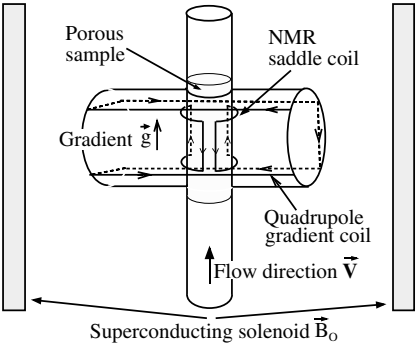

FIG. 4. Experimental setup showing a superconducting magnet, the nuclear magnetic resonance saddle coil for the radio-frequency pulse generation and signal detection and the quadrupole gradient coil for the magnetic field generation parallel to the flow in the porous sample.

magnetic field gradient. The phase shift $k\Delta z$ clearly varies from one fluid particle to another; thus, following Ref. [25], one introduces the probability distribution $P_\Delta(\Delta z)$ of the displacements z during the time lapse Δ. Equation (11) can then be rewritten as

$$M_1(k) = M_0\langle \exp[i\gamma\delta g\Delta z]\rangle = M_0 \int P_\Delta(\Delta z)\exp[i\gamma\delta g\Delta z]\, d\Delta z. \qquad (12)$$

The amplitude $M_1(k)$ of the first echo is then the Fourier transform of the propagation function $P_\Delta(z)$ in which the wave number $k = \gamma\delta g$ is the variable conjugate to the displacement Δz. One first measures the complex value of the magnetization $M_1(k)$ for a large number (typically 100) of different evenly spaced magnetic field-gradient amplitudes. Then, $P_\Delta(\Delta z)$ is obtained by inverse Fourier transform of $M_1(k)$. The technique can be calibrated by analyzing the self-diffusion of water molecules without flow. $P_\Delta(\Delta z)$ follows a Gaussian law from which the molecular diffusion coefficient can be obtained. Each individual measurement for given Δ is very brief, but global averaging times of order 10^4 s are necessary to obtain curves such as those of Fig. 5. Various types of pulse sequences were used, including the pulsed field-gradient Hahn sequence, the pulsed field-gradient stimulated-echo sequence (PFG-SSE), and the Cotts sequence [24–25]. The most elaborate ones can perform measurements for Δz up to several grain sizes and minimize the influence of transverse relaxation and magnetic field heterogeneities during most of the pulse sequence.

An important test of the validity of the measurement is to compare variations of the mean displacement $\langle z\rangle_{\text{nmr}}$ determined from the experimental curves to the macroscopically controlled value $\langle z\rangle_{\text{th}} = Q\Delta/S\varnothing$ (Q is the flow rate, $\varnothing$ and S are the sample porosity and cross-sectional area). Figure 6 displays the variation of $\langle z\rangle_{\text{nmr}}$ as a function of $\langle z\rangle_{\text{th}}$ for a series of measurements. The two values coincide to within $\pm 10\%$ up to very long mean displacements of roughly 600 μm (three sets of experiments corresponding to bead diameters of 80, 145, and 800 μm are superimposed on the figure).

11.3.3.3 Velocity Distribution Measurements Using Pulsed Gradient NMR in Glass Bead Packings. If one chooses a time interval Δ much smaller than the decorrelation time τ_v for the velocity of the tracer particle, then their displacement Δz is small compared to the pore size and their velocity remains roughly constant along Δz. In the limit $\Delta \to 0$, $\Delta z = v_z\Delta$, and Eq. (12) becomes

$$M_1(k) = M_0\langle \exp(i\gamma\delta g\Delta v_z)\rangle = M_0 \int P_\Delta(v_z)\exp(i\gamma\delta\Delta g v_z)\, dv_z, \qquad (13)$$

where $P(v_z)$ (often called the "velocity spectrum") is the probability distribu-

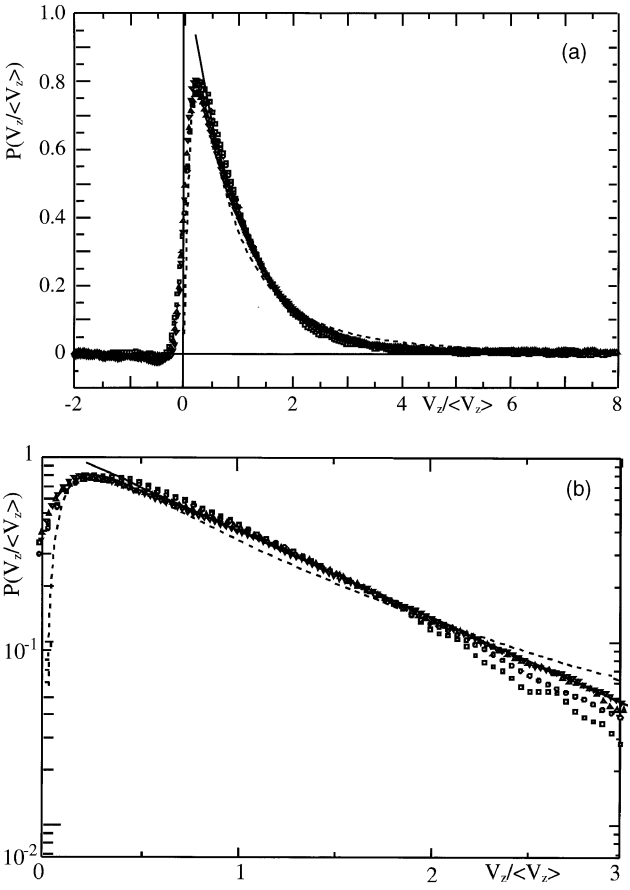

FIG. 5. (a) Normalized velocity distribution $P(v_z/\langle v_z \rangle$ curves obtained with NMR measurements using Hahn-type (H) and stimulated echo pulse sequences (SE) for monodispersive sphere packing ($d = 800 \pm 150$ μm) and a Reynolds number $\mathrm{Re} = 0.9$ and for various measurement times Δ and mean displacements $\langle z \rangle$: (□) and (○) H, $\Delta = 15$ ms, and $\langle z \rangle = 48.7$ μm; (Δ) SE, $\Delta = 15$ ms, and $\langle z \rangle = 64.6$ μm; and (∇) SE, $\Delta = 20$ ms, and $\langle z \rangle = 81.6$ μm. The ratios of the mean displacement and the grain diameter range between 0.06 and 0.1. The solid line is an exponential fit, and the dashed line is a log-normal fit. (b) Shape of the velocity distribution (logarithmic plot). Symbols are identical to those in (a).

tion of the velocity component along the field gradient. In practice, $P(v_z)$ is determined by taking the inverse Fourier transform of the complex echo amplitude $M_1(k)$, where k is varied by changing the field gradient g.

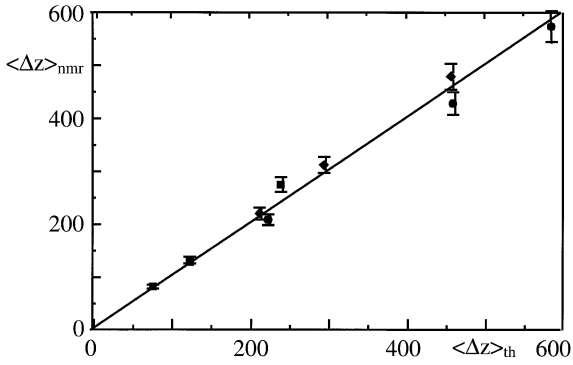

FIG. 6. Variation of the experimental mean displacement $\langle z \rangle$ determined by the pulsed gradient NMR technique as a function of the theoretical value $Q\Delta/S\emptyset$.

Such measurements have been reported in Refs. [19, 24–29]. In some cases, only the overall probability distribution is determined. In others, NMR imaging techniques are used to obtain spatial maps of the velocity field when the resolution is good enough (less precise velocity determination techniques are often used in this case).

Figure 5 compares experimental velocity distributions obtained with different pulse sequences and for mean displacements between 49 and 82 μm. The velocity v_z is normalized by its mean $\langle v_z \rangle$: All curves coincide quite well and normalization compensates for differences between the mean displacements. Data are compared on linear (Fig. 5a) and logarithmic (Fig. 5b) scales to exponential and log-normal distributions [26], as suggested by various authors. Experimental data are consistent with a log-normal function near the peak but are better described by an exponential decay for $v_z/\langle v_z \rangle > 0.5$.

These results can also be compared to numerical simulations using models constructed by dropping randomly, one at time, equal size spheres into a parallelepipedic volume [19–21]. There is a good agreement and the simulated velocity distribution also gives an exponential fall-off at large velocity [19].

11.3.3.4 Dispersion Measurements Using Pulsed NMR Techniques. When the displacement of the fluid particles is no longer small compared to the pore size, the particle displacement is no longer proportional to the velocity components. At the opposite limit, say $\Delta z = 5d$, a Gaussian dispersion regime has been reported using similar techniques [30].

Let us now discuss the transition between these two regimes on displacement distributions measured on three different unconsolidated bead pack-

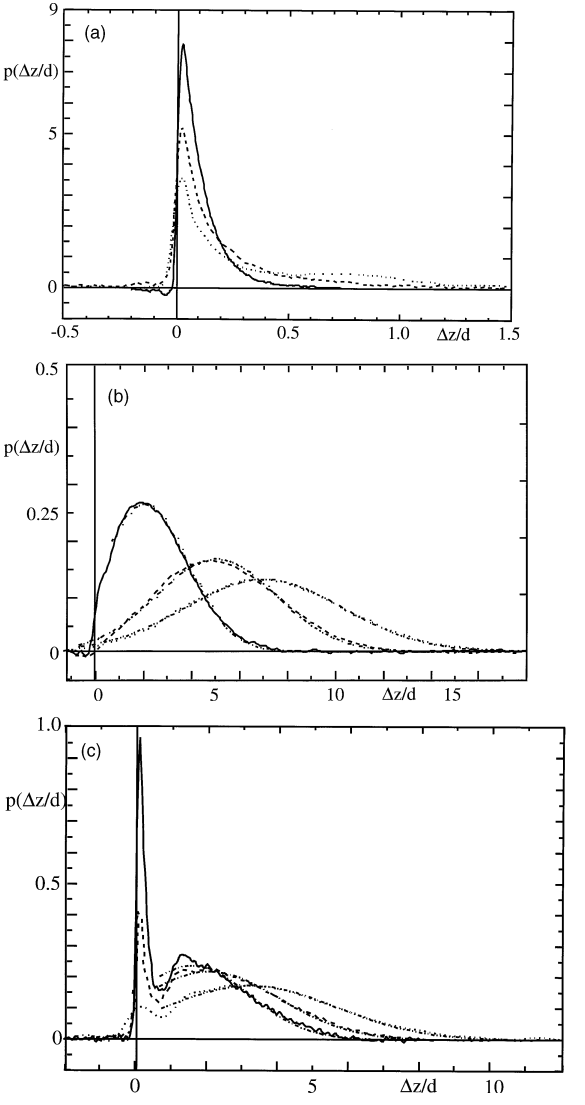

FIG. 7. Normalized displacement probabilities $P(\Delta z/d)$ as a function of the normalized distance $\Delta z/d$ for (a) $d = 800\,\mu\text{m}$, $\text{Re} = 0.89$, (solid line) $\Delta z/d = 0.1$, (dashed line) $\Delta z/d = 0.16$, and (dotted line) $\Delta z/d = 0.3$; (b) $d = 80\,\mu\text{m}$, $\text{Re} = 0.15$–0.19, (solid line) $\Delta z/d = 2.8$, (dashed line) $\Delta z/d = 5.7$, (dotted line) $\Delta z/d = 7.3$, and (dash-dotted) Gaussian fit of the second peak; and (c) $d = 145\,\mu\text{m}$, $\text{Re} = 0.22$–0.24, (solid line) $\Delta z/d = 1.5$, (dashed line) $\Delta z/d = 2.1$, (dotted line) $\Delta z/d = 3.2$, and (dash-dotted line) Gaussian fit of the second peak.

ings of same external geometry as in the preceding [19, 25]. Grain diameters are again $d = 800$, 145, and 80 μm and the mean displacement $\langle \Delta z \rangle$ ranges between 65 and 500 μm. Using three different grain diameters d enables us to vary the ratio $\langle \Delta z \rangle / d$ over a broad range from 0.08 to 7.3.

The mean fluid velocity U varies from 1.310^{-3} to 6.710^{-3} m/s (Reynolds numbers $\mathrm{Re} = Ud/3v$ ranges from 0.89 for 800-μm-diameter beads to 0.16 for 80-μm-diameter beads). Smaller velocities are avoided to keep pure longitudinal molecular diffusion negligible compared to convective dispersion. The physicochemical interaction with the grains can be ignored even for the smallest beads and the packing geometry is assumed to be identical for all sizes. Velocity distributions should therefore be the same for all samples provided scale changes of the grain size d are taken into account.

Figures 7a to 7c show $P(\Delta z/d)$ for Δz parallel to the mean flow velocity through the sample; Δz is normalized by the grain diameter d to enable comparison of the three samples. For each bead size, experiments have been performed [25] with different values of $\langle \Delta z \rangle / d$.

11.3.3.4.1 Mean Displacements Up to 0.3 Grain Diameters. Figure 7a shows the data for the largest beads ($d = 800$ μm). The smallest displacement $\langle \Delta z \rangle / d = 0.1$ reproduces the behavior seen in Fig. 5, and $P(\Delta z/d)$ simply reflects the velocity component distribution parallel to the flow. However, when $\langle \Delta z \rangle / d$ increases to 0.16, the distribution is already strongly distorted; and for $\langle \Delta z \rangle / d = 0.3$, a secondary peak can be seen. The latter corresponds to the fastest particles, which have moved into another pore and have changed velocity markedly. The peak position reflects the mean velocity through the sample and its broadening is a precursor of the dispersive displacement distribution occuring at long times. On the other hand, the slower molecules have moved by only a small amount, and they are represented by the peak near the origin.

11.3.3.4.2 Large Displacements from 2.8 to 7.3 Grain Diameters. This second series of curves (Fig. 7b) was obtained for the sample with the smallest beads ($d = 80$ μm). Since $\langle \Delta z \rangle$ is large compared to the grain size, fluid particles have explored a large enough number of pores for the central limit theorem to apply. The spreading process reaches a steady dispersive regime similar to that observed in macroscopic samples. A small anomaly is barely noticeable near the origin for the two data sets with the smaller $\langle \Delta z \rangle$. The third data set is highly symmetrical and well fitted by a Gaussian function.

As already stated, this measurement differs from a classical dispersion experiment. Fluid particles are marked uniformly in the pores instead of being injected at one end of the sample. Analyzing data in Fig. 7b by assuming that the spreading process follows a Gaussian behavior gives a normalized dispersion law $D_{||}/Ud \approx 0.8$, in good agreement with Eq. (3) and

with experimental results obtained by classical techniques [31] for similar samples in this range of Péclet numbers (Pe $\approx$ 400). This agreement implies that the sample is homogeneous enough so that the different averages of the two measurements give the same results.

11.3.3.4.3 Transition Regime: Distances from 1.5 to 3.2 Grain Diameters. In this range of $\langle z \rangle / d$ values, obtained using the intermediate bead size $d = 145\,\mu m$, double-peaked distributions are observed (Fig. 7c). The first peak corresponds to particles in low-velocity zones such that their displacement during the measurement time is small compared to the pore size. The second peak corresponds to fast particles, which have already moved across one or more pores. Fits of the latter peaks by a Gaussian variation give dispersion coefficients close to the previous ones. As expected, the height of the second peak increases with $\langle z \rangle$ relative to the first; that is, fewer particles remain trapped in slow zones after a long time. We note that the shape of the curve $\langle z \rangle / d = 3.1$ is very similar to the curve with $\langle z \rangle / d = 2.8$ in Fig. 7b. This shows that after suitable normalization, the displacement distribution depends mainly on $\langle z \rangle / d$ and not on the grain size d. The observed behavior of $P(z/d)$ is well reproduced by Monte Carlo simulations, which model the porous medium by a random network of tubes [25].

These NMR results demonstrate the main features of tracer dispersion in porous media. A large fraction of the fluid initially has a low-velocity component in the direction parallel to the mean flow, but after flowing through several pores, the probability density of the displacements displays a Gaussian peak that corresponds to the mean velocity.

11.3.4 Electrochemical Techniques for Measuring Echo Dispersion at Short Distances

11.3.4.1 Reversibility of Tracer Dispersion in Homogeneous Samples. Another way to investigate the transition between convective spreading associated with the local flow velocities and classical macroscopic dispersion is to study the reversibility of the process by the following echo dispersion technique [32]. A tracer concentration variation is introduced at time $t = 0$ at the inlet of the porous sample and carried by a flow. After a time t_i, the front has penetrated a mean distance $L = t_i/U$ into the sample. The flow direction is then reversed and an "echo" of tracer concentration variation is detected at the inlet of the sample at a time $t = 2t_i$. From the shape of the echo curves, one can obtain an effective echo dispersion coefficient D_{echo}. This technique is described in more detail in Section 11.5.

For macroscopic measurements in which L is much larger than the grain size and for homogeneous samples of simple geometry (glass bead packings for instance), D_{echo} is equal to the transmission dispersion coeffi-

cient. The case of heterogeneous media will be discussed later in the present chapter. This result appears to contradict the reversibility for low Reynolds number flows ($\mathrm{Re} \ll 1$). When the mean flow velocity $\mathbf{U}$ is reversed ($\mathbf{U} \to -\mathbf{U}$), the local velocity $\mathbf{v}(\mathbf{r}, t)$ is replaced by its opposite $-\mathbf{v}(\mathbf{r}, t)$ at every point in the fluid and one might expect the tracer to converge back so that one should have $D_{\text{echo}} \ll D_{\text{transmission}}$.

This apparent contradiction can be resolved by considering the spreading of an initially localized dot of tracer [33]. At small penetration depths (one grain diameter or less), spreading is reversible. On the other hand, after going through several pores, the spot splits into very thin filaments. Molecular diffusion causes the particles to follow randomly different filaments. Thus completely different paths are followed when the flow is reversed. This filament division process is exponential and dispersion becomes irreversible above a penetration depth l_T of a few pore diameters. Note that l_T should depend weakly on the Peclet number, possibly as $\ln(\mathrm{Pe})$, due to the exponential decrease of the filament size with distance.

This transition to irreversibility has been studied numerically and experimentally on 2-D arrays of cylinders [34] using dye visualisations. In two dimensions, the influence of molecular diffusion is very much amplified near stagnation points where diffusion is most important. This is the major source of irreversibility. Measurements on more realistic 3-D geometries cannot be performed with standard chromatographic devices because valves and injectors have significant dead volumes. Special measurement techniques are needed to obtain spatial resolutions markedly lower than a grain diameter.

11.3.4.2 Electrochemical Technique for High-Resolution Echo Tracer Dispersion Measurements. Electrochemical techniques can achieve such high spatial resolutions [33, 35]. The tracer is produced *in situ* by the electrochemical oxidation of ferrocyanide $\mathrm{Fe(CN)}_6^{4-}$ ions into ferricyanide $\mathrm{Fe(CN)}_6^{3-}$ ions on a platinum grid placed against the inlet end of the sample. This minimizes dead volume that limits the resolution. In Fig. 8, the porous medium is an unconsolidated packing of monodisperse glass beads (diameter 2 or 4 mm) contained in a 55-mm i.d. vertical cylinder.

Initially, the liquid contains only ferrocyanide ions and a steady constant downward flow is established through the sample. Ferricyanide ions, which act as the tracer species, are generated by passing an electrical current between the platinum grid and a ground electrode. The number of tracer ions generated per unit time is proportional to the current. A short current pulse can create a thin homogenous plane of tracer about 1/10 mm thick. After the tracer has penetrated the desired mean depth into the medium, the flow is reversed. The grid is connected to a potentiostat circuit, which measures a time-dependent current I_d that corresponds to the reduction of

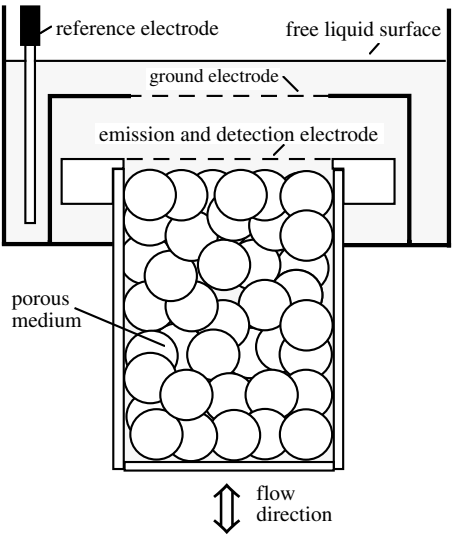

FIG. 8. Experimental setup for the analysis of tracer dispersion reversibility using an electrochemical technique for both the emission and the detection of tracer. The platinum grid electrode used both for tracer emission and detection is made of 0.06-mm o.d. wires with a 0.33-mm mesh size; it is placed at a height of 1.5 mm above the sample.

the ferricyanide tracer ions back into ferrocyanide ions on the grid. Figure 9 shows two experimental curves that correspond to penetration distances of 0.62 and 1.25 times the bead diameter.

The instrumental spatial resolution of the system is estimated by first performing the experiments without the porous medium. In this configuration, one obtains effective dispersion coefficient values as low as one to three times the molecular diffusion coefficient. In all experiments with the same flow velocity, the number of detected ions is independent of the penetration distance and proportional to the injected charges. This confirms that the detection system is linear and that the shapes of the experimental curves are meaningful.

In this example, the main interest is to have a very sharp tracer pulse with essentially no dead volume. It can be extended to obtain tracer injections with arbitrary (for instance, sinusoidal) waveforms [35]. The full transfer function of the system can be determined by changing the excitation frequency and measuring the amplitude and phase shift of concentration variations at the outlet.

11.3.4.3 Transition to Irreversible Dispersion in Glass Sphere Packings. Due to the small number of pores explored, curves such as those of Fig. 9 do not generally follow the convection–diffusion Eq. (3) since they are not in the asymptotic limit. We can estimate the effective dispersivity length l_{dec} and the dispersion coefficient D_{echo} from the first moment $\bar{t}$ and the mean square width $\overline{\Delta t^2}$ of the transit time distribution by the expression

$$l_{dec} = \frac{D_{echo}}{U} = \frac{\overline{\Delta t^2} U}{2\bar{t}}. \tag{14}$$

For a given velocity U, one can determine the effective dispersivities $l_{dec}(L)$ for different penetration depths L into the sample. Figure 10 shows how $l_{dec}(L)$ varies with L/d for two different bead diameters $d = 4$ mm (Fig. 10a) and $d = 2$ mm (Fig. 10b).

In both cases, $l_{dec}(L)$ reaches its limiting value at about $L/d = 15$. The limit value (about 0.2 and 0.1 cm, respectively) is roughly half the bead diameter, in good agreement with transmission (and other echo) measurements in homogeneous samples [31, 32]. From the simple model, assuming an exponential division of the tracer filaments, one expects $l_{dec}(L/d)$ to depend very weakly on the Péclet number, as observed (a logarithmic dependence is predicted). We note that the $l_{dec}(L/d)$ data follow the same curve for the two bead diameters after l_{dec} has been normalized by the diameter d. These results confirm that the transition to irreversibility occurs

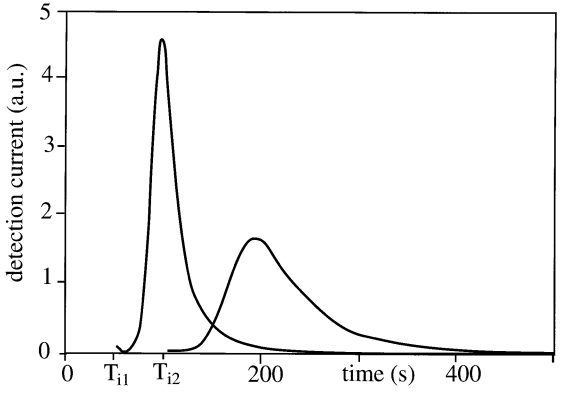

FIG. 9. Typical variations of the detection current in a 4-mm glass bead packing with Pe = 785, Re = 0.57, and $D_m = 7.2\ 10^{-6}$ cm^2/s. Flow inversion times are $t_i = 50$ and 100 s, corresponding to mean penetration distances respectively equal to 2.5 and 5 mm.

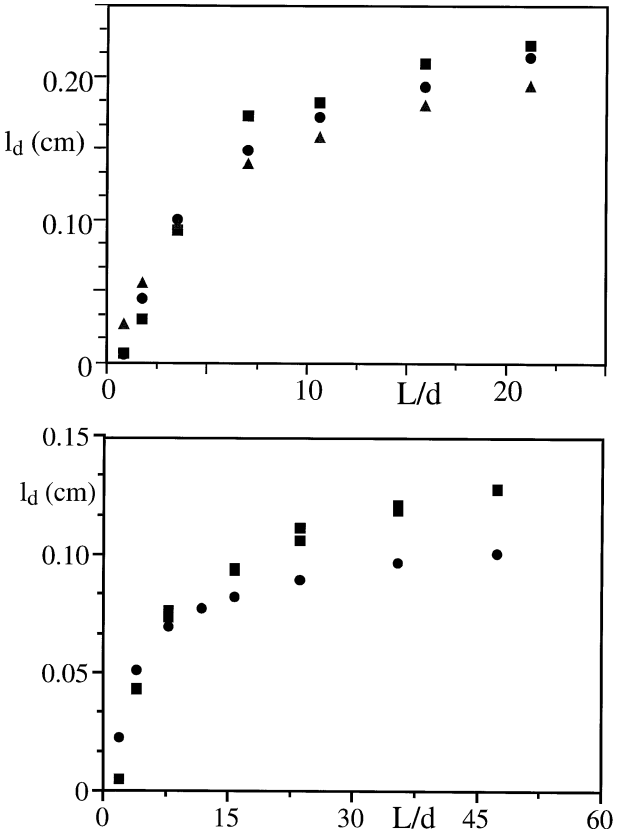

FIG. 10. Variation of the effective dispersivity l_D as a function of the mean penetration distance L normalized by the bead diameter d for (a) $d = 4$ mm, (■) Pe = 1570 and Re = 1.13, (●) Pe = 785 and Re = 0.57, and (▲) Pe = 390 and Re = 0.28, and (b) $d = 2$ mm, (■) Pe = 880 and Re = 0.64 and (●) Pe = 220 and Re = 0.16.

over a small distance of the order of 10 grain layers. However, at short distances ($L/d \ll 1$), l_{dec} is 20 to 80 times smaller than its limiting value; a large part of the spreading is reversible.

11.3.5 Potential Developments of High-Resolution Techniques

In this section, we have studied high-resolution dispersion measurement techniques such as pulsed gradient NMR, particle imaging and elec-

trochemical techniques. We have shown that they can give irreplaceable information concerning the mechanisms of tracer and solute transport at the scale of one pore or less or of a small number of pores. Until now, however, these techniques have been mostly used in homogeneous nonconsolidated samples with simple and well-connected pore geometries. An important issue is the extension of these techniques to consolidated porous materials and natural rocks; in these, other features such as local flow reversals or large-volume dead zones are to be expected. The coupling of such measurements to imaging techniques, enabling us to identify these anomalous flow regions should be an important step forward; however, some problems such as the sensitivity of NMR measurements to magnetic impurities will have to be overcome.

In the following sections we deal, on the contrary, with techniques for analyzing transport or dispersion over distances corresponding to many pore sizes.

11.4 Experimental Techniques for Analyzing Dispersion in Large-Scale Heterogeneities

11.4.1 Acoustic Technique

Experimental studies of transport phenomena in porous media, such as the mixing of miscible fluids or two-phase fluid flows, require a characterization of not only the overall fluid saturations of the sample but also the transient and spatial saturation of each fluid. Although microwave [36, 37], gamma, and x-ray absorption [38, 39] techniques may appear old-fashioned compared to porous media imaging through X rays or NMR computerized tomography [40–42], these techniques, originally designed for medical applications, may be unsuitable for fast-flow experiments and large samples and they cannot be used when temperature and pressure conditions require a metallic sample cell. By contrast, acoustic imaging can accommodate a wide range of sample cell materials transparent to acoustic waves. In this section, we describe in particular how a three-dimensional acoustic scanner can be realized by using sound velocity variations to measure fluid saturations [43–45]. Let us note that the wavelength λ of acoustic waves is much larger than the grain and pore sizes. Therefore this probe is macroscopic and automatically performs volume element (REV), averaging on the porous media at this scale. From a previous work [43, 44], we present the principle, accuracy, and time and space resolutions of saturations determinations. We then describe their application in visualizing saturation profiles and constructing a 3-D acoustic scanner. In both cases, imaging a flowing blob is used as a test.

11.4.1.1 Acoustics of Porous Media. The classical Biot theory [46] gives the best description of acoustic wave propagation in porous media saturated with one fluid. Numerous consequences of this theory have been experimentally verified [47], and it is described in Chapter 5. Here, we report some measurements in porous media saturated with miscible fluids (which is a single fluid phase), and extend Biot's approach to two immiscible phases saturating the medium; for example, oil and water in rocks.

11.4.1.2 Porous Media Saturated with One Fluid Phase. Figure 11 displays sound velocity measurement in a fireproof-brick porous medium [48] saturated with a water–glycerol mixture of various concentrations c. Note that a mixture of miscible fluids behaves as a single phase and that Biot's theory applies. This more or less linear calibration curve shows that for c varying from 0 to 100%, the velocity variation is about 20%. Since our acoustic device can detect relative velocity variations as small as 10^{-4}, the corresponding concentration resolution in miscible fluid is about 0.2%. A similar test has been performed on unconsolidated glass bead packs saturated with water–ethanol mixtures [43].

11.4.1.3 Porous Medium Saturated with Two Fluid Phases. One of most important problems in oil recovery and immiscible flows is to determine the local saturation of oil (S_o) or water (S_w). It is generally accepted that acoustic methods are inappropriate for the determination of saturation profiles in sandstones because the sound velocity in rocks fully saturated with either oil or water are nearly the same. Figure 12 displays experimental values of the sound velocity versus the brine saturation S_w. The data clearly show a strong dependence on the flow history of the sample. The right-hand

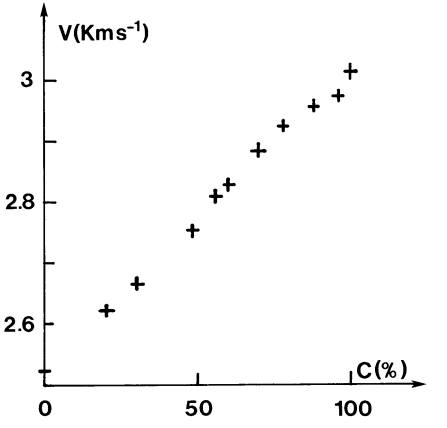

FIG. 11. Sound velocity versus glycerol concentration in the glycerol–water mixture.

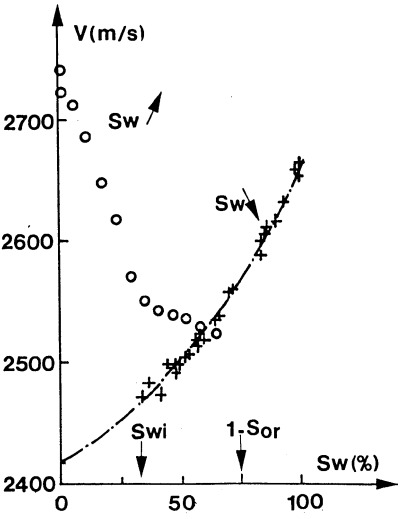

FIG. 12. Sound velocity of a water-wet sandstone versus water saturation for (+) drainage and (o) imbibition.

side curve (+) corresponds to the injection of oil (nonwetting fluid) into a brine saturated sample (a drainage process). The line through the data is our extension of Biot's theory to two immiscible fluids. It combines the two fluids into a single one using an effective medium theory that takes into account oil and water densities and compressibilities (ρ_o, ρ_w, K_o, K_w). The left-hand curve (o) corresponds to the injection of brine into a sample saturated with oil (imbibition process). The decrease of the sound velocity with S_w results from the continuous decrease of the frame moduli due to the modification of the grain contacts by the totally wettting fluid injection [44]. Using these calibration curves with the aforementioned 10^{-4} precision in sound velocity measurements, we can achieve a saturation resolution of 0.5%.

11.4.1.4 Sound Velocity Variation Measurements. To measure sound velocity accurately, we use an automated system whose principle is sketched in Fig. 13. The key element of the system is the transducer probe. It consists of uniformly spaced piezoelectric zirconate titanate (PZT) elements that have been sawed and polished. Each PZT element is 5.6 mm wide, 10 mm long, and 2 mm thick with a resonant frequency of about 350 kHz. The bandwidth is quite narrow because there is no damped backing, which also has the advantage of increasing the sensitivity. A pulse function generator sends a sine-wave pulse (15 V peak to peak) to the transmitter at 350 kHz. It is received by the opposite transducer after a time of flight τ. The received

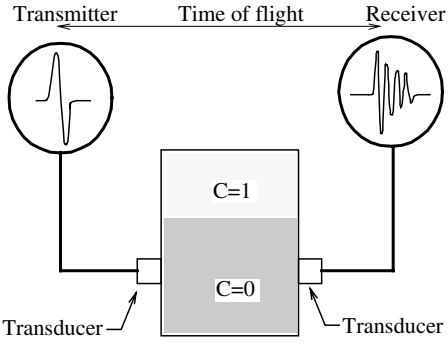

FIG. 13. Principle of sound velocity measurements.

signal, which has been attenuated by successive interfaces, diffraction, and attenuation in the different media is amplified by 60 dB. Changes in the fluid concentration inside the porous medium affect the sound velocity and therefore the time of flight τ. For a typical 2500 m s^{-1} sound velocity and a 4-cm-thick porous medium, $\tau = 16\,\mu s$. This τ value is precisely measured by a counter timer with an accuracy of better than 0.01 μs. All this equipment is computer controlled. The accuracy in τ measurements is limited by the electronic fluctuations of the signal. A typical received signal has a voltage $U = 500$ mV with noise $\delta U = \pm 10$ mV. Over a quarter period $T/4 = 700$ ns, this gives a timing error $\delta\tau = \pm 15$ ns, and thus a precision in τ (or velocity) of 10^{-3}. To obtain the 10^{-4} resolution, the signal is averaged 100 times. With a repetition rate of the transmitted pulse of 1 ms, this is achieved in 0.1 s. The lateral spatial resolution is typically 3 mm, close to the 2-mm transducer thickness. We should emphasize that a large variety of sample holder materials, such as metal and epoxy, are transparent to acoustic waves. Thus, the acoustic technique is well suited for studies at various temperature and pressures.

11.4.1.5 Concentration Profile Measurements. During a flow experiment, fluid concentrations $C(z, t)$ versus time at different z positions from the inlet can be measured using sound velocity. We use a sample core (sandstone) of typical size $4 \times 4 \times 30\,cm^3$ in an epoxy holder. Fluids flow along the vertical z direction. Velocity measurements are performed using 10 transmitter–receiver pairs laid every 2.5 cm along the sample. The 10 pairs are scanned successively using a computer controlled system. This automated procedure records $C(z, t)$ for the 10 z values in less than 2 s.

In a dispersion experiment [48], one fluid in the porous medium is displaced by another miscible one (water–ethanol or water–glycerol mixtures). Figure 14a gives the time dependence of $C(z, t)$, in five cross sections

of a sandstone for a constant 6 cm^3/h flow rate. These profiles show the typical dispersion characteristics, namely, the increase in the width of the transition zone with distance z from the inlet, which is a feature of the longitudinal dispersion effect. From left to right $z = 1.5$, 6.5, 11.5, 16.5, and 21.5 cm. A best fit to these data with solutions of Eq. (3) (Fig. 14b), leads to the longitudinal dispersion coefficient.

Figure 15 shows concentration variations at nine spatial locations in a flow experiment where a 1-cm^3 miscible fluid blob, injected in the porous medium through a small tubing, is displaced at a 3.2-cm/h constant flow rate. Each profile shows the passing of the drop through a particular z plane; the larger distance from the inlet (z varies from 3 to 27 cm in 3-cm steps), the larger the width, the smaller the height of the profile, which is due to both transverse and longitudinal dispersion. These data can be used to determine the transverse dispersion coefficient [13, 48].

11.4.1.6 A 3-D Acoustic Scanner. The acoustic velocity measurement can be used to design a 3-D acoustic scanner for determining the complete

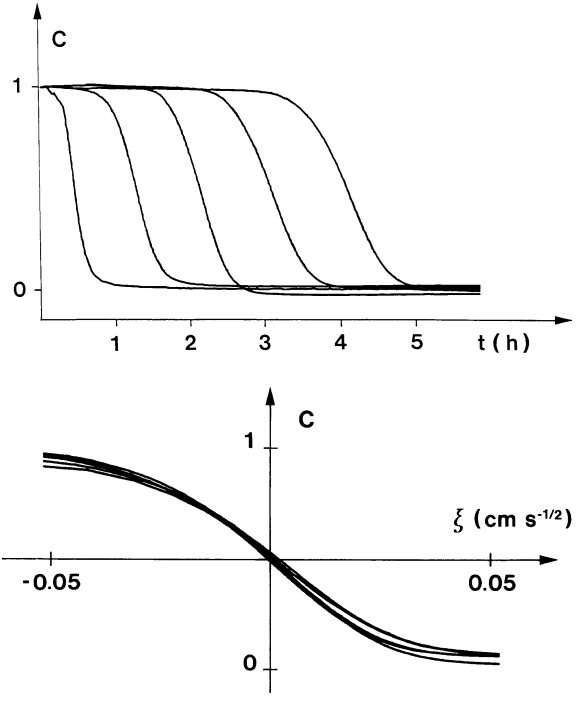

FIG. 14. (a) Hydrodynamic dispersion profiles in five successive planes and (b) the same plot in reduced variables to determine the dispersion coefficient.

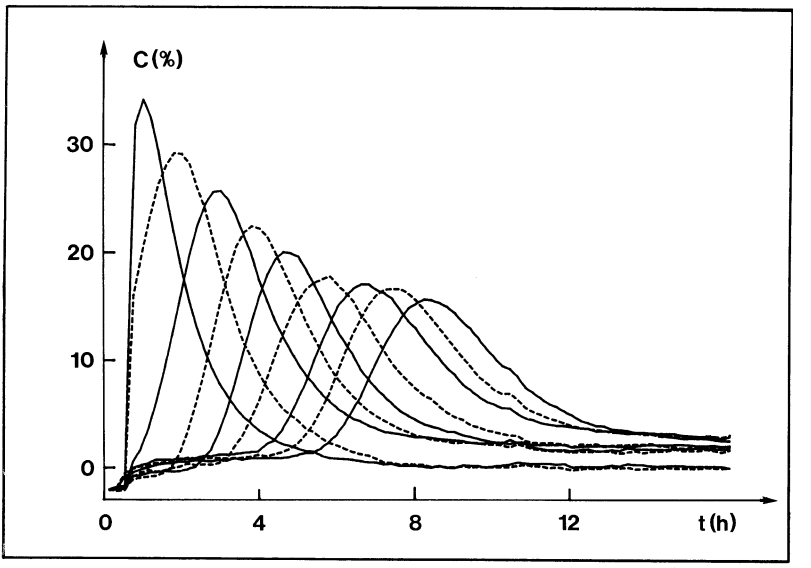

FIG. 15. Concentration variations with time induced by a 1-cm^3 miscible fluid drop moving upward through five measurement planes.

concentration distribution $C(x, y, z, t)$ in the sample. The 3-D concentration determination is realized in the same $4 \times 4 \times 30\,\text{cm}^3$ sandstone core encased in epoxy by an array of 10×10 pairs of transducers set up in the x-y plane and swept along the z direction. This device enables us to obtain 3-D images by a standard imaging reconstruction algorithm and is sketched in Fig. 16. Transducers are laid every 4 mm with their thin dimension in the x-y directions so that the spatial resolution in the x-y plane is $3 \times 3\,\text{mm}^2$. To improve measurement stability, the sample and the detection array are immersed into a constant temperature water bath. The 20 transducer pairs of the grid are scanned in less than 4 s. Displacement of the detector along the vertical direction is accomplished by a stepping motor. It moves at a velocity of 10 cm/s with a 0.05-mm positioning reproducibility. The z spatial resolution is mainly due to the 10-mm length of the transducers in that direction. Since it is possible to sweep as many z values as we need and perform a deconvolution procedure, however, we can also reach a 4-mm spatial resolution along z. The limiting voxel size of the scanner is then $4 \times 4 \times 4\,\text{mm}^3$. A scan of the 30-cm-long sample with 10 slices can be accomplished in 2 min. The data are analyzed using an in-house computer algorithm to determine the fluid saturation at each voxel of the sample. Figure 17 displays the experimental results obtained when a 1-cm^3 miscible

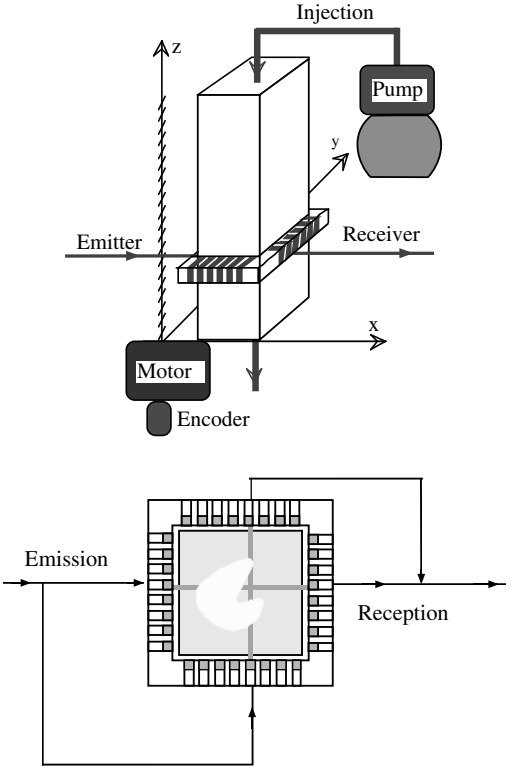

FIG. 16. (a) Sketch of the 3-D acoustic scanner and (b) sketch of the transducers array in an x-y plane.

fluid blob is displaced at a constant flow rate. The contour maps in Fig. 17 show the distributions in a given x-y plane ($z = 6\,\text{cm}$) at five successive times. One clearly sees the blob moving up through the plane.

11.4.2 Other Techniques Applicable to the Analysis of Large-Scale Heterogeneities

Besides acoustic imaging, other techniques can also be used to study dispersion over large scales: NMR imaging is one option, though much more costly. In Section 11.3.3 we showed that pulsed gradient NMR techniques give velocity distributions at the pore scale and at very short times. The NMR imaging apparatus can also be adapted to provide qualitative "images" of the flow velocity.

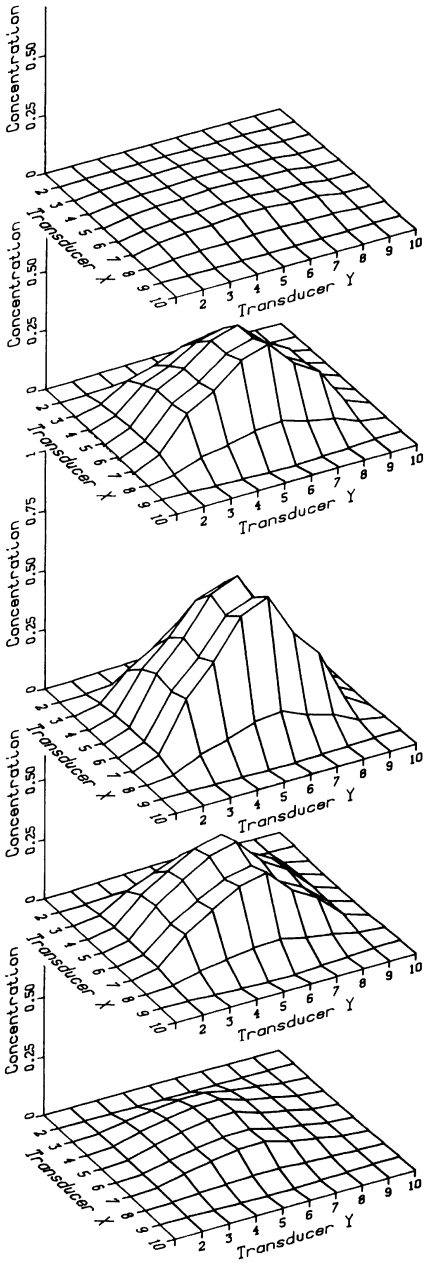

FIG. 17. Concentration maps obtained at five different times in the same horizontal plane during the same blob displacement experiment as in Fig. 15.

Other types of measurements can also be performed with NMR imagers. For example, one can use paramagnetic tracer ions such as Mn^{2+} complexes, which strongly shorten the paramagnetic relaxation times T_1 and T_2 [49], the NMR signal amplitude is then observed to have a maximum with respect to the tracer concentration. Using ion concentrations always higher than that corresponding to the maximum, the amplitude has a monotonous dependence and one obtains either full 3-D images or 1-D profiles of the concentration as needed. The former enables us to visualize large-scale heterogeneities; the latter gives less noisy 1-D data that can be analyzed more quantitatively. Radioactive tracers have also been used for concentration measurements but they have been limited to 1-D profiles so far [50, 51].

11.5 Experimental Analysis of Anomalous Dispersion and Finite Size Effects

Contrary to the ideal data displayed in Fig. 14, anomalous dispersion is often observed. In such experiments, the concentration variation $C(t)$ at the outlet of the sample exhibits a long time tail; an example is shown in Fig. 18, where the dashed lines correspond to the Gaussian curve. Such a profile cannot be fitted by solutions of Eq. (3), even with appropriate boundary

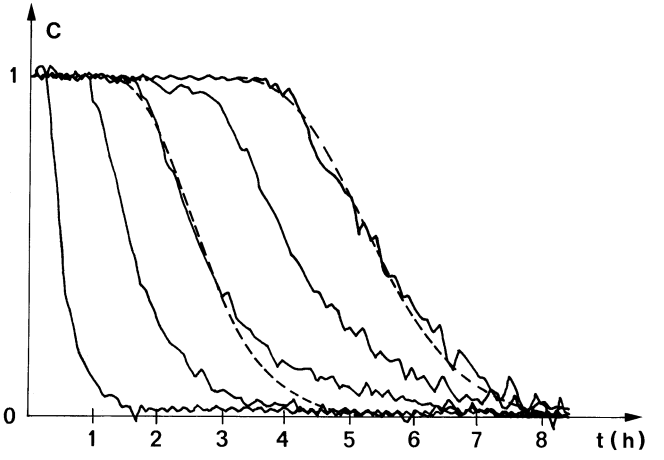

FIG. 18. Finite-size effects: concentration variation vs time at five equidistant locations across the unsaturated millstone porous medium. Dashed lines correspond to a Gaussian dispersion profile; at short distances from the inlet, profiles display a long time tail; at a large distance, they tend toward a Gaussian profile.

conditions [13] because some tracer seems to remain trapped after the front is passed. These effects are observed even with completely passive tracers, which do not interact or become adsorbed on the porous matrix. Much work has been done, mainly in petroleum engineering [4, 52–57], to explain these long tails, including the well-known Coats–Smith [4], porous spheres [53–54], and transverse matrix diffusion models.

The phenomenological Coats–Smith model, which lends itself to our experimental analysis, assumes that a fraction of the pore volume is occupied by stagnant fluid zones. Exchanges between flowing C and stagnant C^* fluids take place with a characteristic time τ_D via molecular diffusion (assuming that adsorption on the pore walls is negligible). The concentration variation $C(L, t)$ at the outlet ($x = L$) is characterized by three parameters [4]: the flowing fraction f, a dispersion coefficient D_f including only the effect the flowing zones, and the stagnation time τ_D (L and U are generally known). Experimental curves can often be fitted precisely by solutions of this capacitance model, especially for a single x/L value, and it has been used intensively in petroleum and chemical engineering [5]. In cases where adsorption is present (as in chromatography), this model can also be applied, but time constants associated to adsorption must also be taken into account. In many porous media, on the other hand, the characteristic time τ_D is flow dependent ($\tau \propto U^{-1}$) and not constant as would be expected for molecular diffusion. Moreover, the coefficient D_f is roughly proportional to U. Thus, the global dispersion coefficient combining the influence of flowing and "dead" zones is proportional to U and not to U^2, as expected when a large fraction of the pore volume is occupied by dead zones [12, 58]. In spite of these shortcomings, these models are a convenient way to characterize dispersion at a finite distance L.

To account for these non-Gaussian profiles, one can think of either a finite-size effect or anomalous dispersion. A finite-size effect means that the number of steps involved in the random walk process leading to dispersion is not large enough to lead to a Fickian behavior. For very long samples, the three parameters in the capacitance model should, for instance, merge into a single asymptotic Gaussian dispersion coefficient [11, 32, 59]. Direct statistical calculations with characteristic lengths [60] or nonlocal dispersion approaches [61, 62] are required. The latter theory leads to predictions in agreeement with experimental longitudinal and transverse diffusivity measurements [63]. If a finite-size effect is the right answer, the profiles $C(x, t)$ must become more Gaussian as the distance x from the inlet increases. A long enough sample should then give a spreading proportional to $\sqrt{t}$.

An alternative hypothesis, in the absence of such a decisive test, is real anomalous dispersion [64–66] due to long-range correlated heterogeneities.

Depending on the behavior of the correlation length of the permeability (and therefore of the velocity field), spreading may grow as t^{α} with $\alpha > 1/2$ (hyperdiffusion) or $\alpha < 1/2$ (hypodiffusion) even for a long sample. For instance, in a model medium consisting of strata of different permeabilities, the value $\alpha = \frac{3}{4}$ has been predicted [66], in reasonable agreement with experimental results (see the references in Ref. [17]).

11.5.1 Acoustic Experiment on Non-Gaussian Dispersion

To clarify the problem of anomalous hydrodynamic dispersion in porous media, we use an acoustic technique that enables us to measure the concentration $C(z, t)$ in 10 cross sections of the same sample at 10 distances z values from the inlet; that is, we can test 10 sample lengths L simultaneously. This technique enables us to observe the long time tail along the sample and to test the possibility of finite-size effects. Moreover, 10 concentration profiles provide a sounder basis for comparisons with a semiphenomenological theory, particularly when three adjustable parameters are introduced. Using the same millstone that leads to Gaussian dispersion at any scale (Fig. 14), we turn it into an unsaturated medium by immiscible displacement. First, we saturate the millstone competely with brine, which serves as a totally wetting fluid. We then inject a nonwetting oil (hexane), beginning at a small flow rate (capillary number $\mathrm{Ca} \sim 10^{-7}$) and then increasing step by step (up to $\mathrm{Ca} \sim 10^{-5}$) to achieve a nearly constant (acoustically tested) oil saturation $So = 60\%$ along the sample. The corresponding water saturation ($\sim 40\%$) is close to the irreducible water saturation. Such a procedure leads to a multiconnected network of oil entangled with the one of water. The topology of this network can be visualized more or less as a percolation network [67]. We perform the dispersion measurements on the hexane network by injecting a second oil (nonane), miscible with hexane. The flow rate is kept lower than for the initial hexane injection so that the wetting fluid (brine) remains stationary. The set of five curves in Fig. 18 correspond to the time-dependent concentration $C(t)$ for five different pairs of transducers at $x = 1.5$, 7.4, 10.8, 15.6, and 20.6 cm from the inlet at a mean flow velocity, $U = 3.6$ cm/h. The increased noise in the data as compared to Fig. 14 is due to the weaker velocity contrast between oil and water saturated media when the fluid distribution is inhomogeneous on a larger scale. Nevertheless, compared to Fig. 18 it is clear that $C(x, t)$ exhibits a long time tail, especially at small x values.

11.5.2. Characterization of the Observed Non-Gaussian Dispersion

One possible way to analyze these data is to compute the different moments of the residence-time distribution from which one obtains the flow velocity

(mean transit time) and the dispersion coefficient (mean-square transit time). However, the noise in the data, especially in the long time tail, excludes this possibility as well as other treatments that require Laplace or Fourier transforms. Following other authors [53–57], we fit the data analytically with appropriate models. The dashed lines in Fig. 18 are best fits of our data with solutions of Eq. (3) of the type

$$C(x,t) = \frac{1 - \mathrm{erf}(x - |V|t)/2\sqrt{D_{||}t}}{2}, \tag{15a}$$

where

$$\mathrm{erf}(\xi) = \frac{2}{\sqrt{\pi}} \int_0^{\xi} e^{-\xi^2} d\xi. \tag{15b}$$

In this process, we have preferentially fitted early time data. There is a large discrepancy for curves corresponding to small x values, but the disagreement is reduced at higher ones; that is, dispersion becomes more Gaussian at larger distances from the injection plane. From these fits, we obtain an x-dependent dispersion coefficient $D(x)$ but, for each x value, $D(x)$ is proportional to U over one and a half decades. The effective dispersion length $l_D(x) = D_{||}(x)/U$ is plotted versus x in Fig. 19. Note that l_D increases and becomes of the order of 1 cm at the largest distances, while the profiles become Gaussian again. This value is much larger than in the fully saturated sample, which is a reasonable result since the scale of heterogeneities is much larger in the partially saturated sample. The dashed lines in Fig. 18 correspond to computations from Eq. (15) using l_D values from Fig. 19. This l_D value corresponds to the dashed lines in Fig. 18 obtained from Eq. (15). To characterize the long time tail, we use a semilogarithmic plot of C versus t. Between $C \sim 0.3$ and 0 we find that $C(x,t) = \exp[-t/\theta(x)]$. The long time tail of the non-Gaussian profiles at small distances can be described as an exponential decay of characteristic time $\theta(x)$ inversely proportional to U, in agreement with other experiments. Our experiment shows that the long time tail is due to the finite-size effect: The characteristic dispersion length $l_D \sim 1$ cm is not small enough compared to observation length x (1.5 to 21 cm). It is basically this transient effect that is described by the nonlocal dispersion theory [61, 62]. From the basic mechanism responsible for dispersion [7], these authors calculated the residence-time distribution (RTD), which is the response $P(x,t)$ of the medium to an impulse source at $x = 0$ and $t = 0$. At a long distance from the inlet, they recovered a classical Gaussian peak, whereas at a short distance, the transient RTD exhibits a long time tail. The characteristic time depends on the mechanism involved in the dispersion process: (i) For hold up dispersion (real dead ends), τ_h is

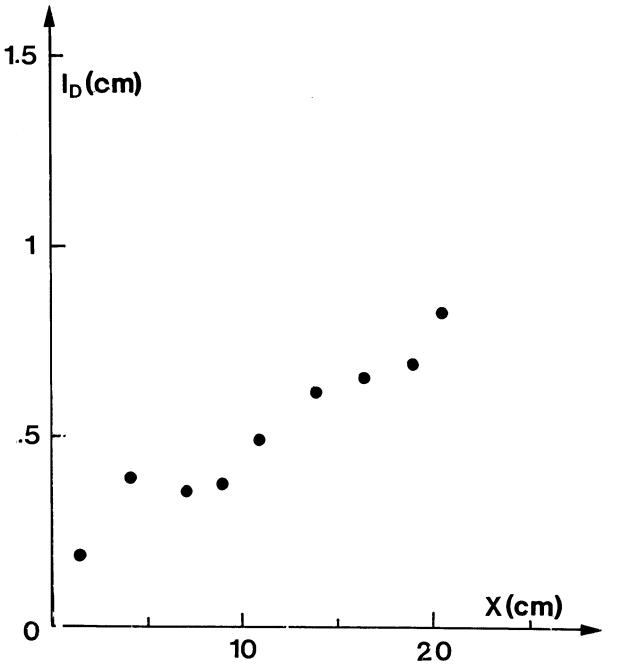

FIG. 19. Dispersion length $l_D = D/U$ versus distance for the Gaussian fit of the previous; l_D increases toward a value $l_D = 0.9$ cm at large enough distances from the inlet.

velocity independent; (ii) for boundary layer dispersion, τ_b is velocity dependent with $\tau_b \propto U^{-2/3}$; and (iii) for mechanical dispersion (convection along different flow passages), τ_m is also flow dependent, but with $\tau_m \sim U^{-1}$. Our data agree with mechanical dispersion and give an asymptotic dispersion coefficient proportional to $U(D = Ul_D)$, as predicted by theory.

11.5.3 Reversibility of non-Gaussian Characteristics of Dispersion

As in the case of high-resolution measurements described in Section 11.3.4, the study of the reversibility of tracer dispersion at longth length scales also provides important additional data. This will particularly be the case when long time tails are present. The reversibility of the tail effect with respect to a change of the flow direction provides information concerning the convective or diffusive nature of tracer exchange with the slow zones.

11.5.3.1 Echo Dispersion Measurement Technique. In classical transmission dispersion, one lets a tracer concentration front induced by a

pulse- or steplike concentration variation at the inlet move all the way through a porous sample, it is then detected at the outlet (Fig. 2). In echo dispersion, the tracer concentration front first moves by a distance x into the sample and the flow direction is reversed at a time T_0: after a time $2T_0$ an "echo" signal is obtained when the front moves back through a detector placed this time at the inlet. Typical experimental curves corresponding to various penetration distances (full lines) are displayed in Fig. 20. They are compared to more classical transmission measurements (dotted line) for which the detector is placed at the sample outlet and the flow is not reversed. Let us note that, while the transmission curve displays a marked tail effect, the echo curves are narrower and can be well fitted by the functions of Eq. (15). Let us now compare echo dispersion measurements in homogeneous samples giving Gaussian transmission dispersion curves and heterogeneous samples displaying anomalous transmission dispersion surves (such as those of Fig. 20).

11.5.3.2 Echo Dispersion in Homogeneous Samples. Figure 21 displays variations with the Péclet number $\mathrm{Pe} = Ud/D_m$ of l_{dec} (dispersion length from echo measurements) compared to the transmission dispersion length l_D in a sample packing of unconsolidated glass beads of diameter $d = 200\,\mu$m (lower sets of points) [32]. Values obtained using both techniques are very similar and l_D is of the order of half the grain size. As discussed in Section 11.3.4, this reflects the fact that dispersion is irreversible

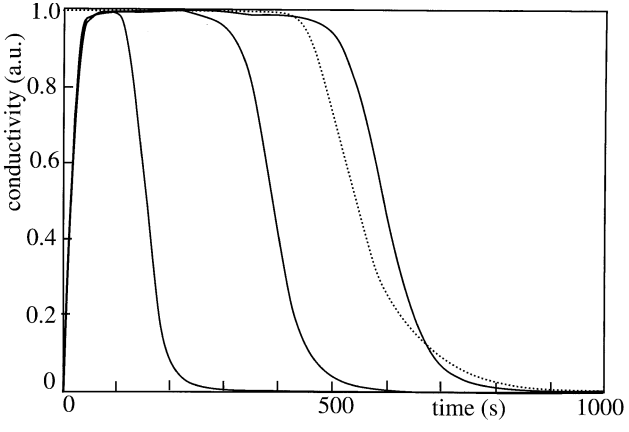

FIG. 20. Experimental echo dispersion curves (solid lines) for three different penetration depths inside a Massilon sandstone porous sample. Dotted line is experimental transmission dispersion curve through the same sample (displays non-Gaussian tail effect).

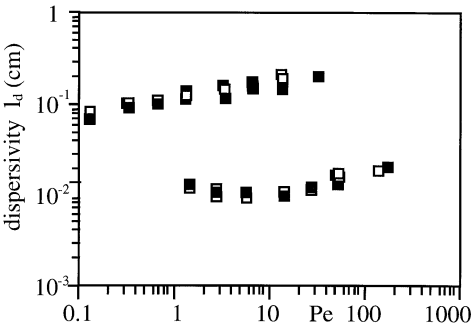

FIG. 21. Dispersion length variations with the Péclet number $\mathrm{Pe} = Ud/D_m$ in transmission (l_d, open squares) and echo (l_{dec}, solid squares) for two Gaussian porous samples: unconsolidated 200 μm-diameter glass beads packing (lower set of points) and Berea sandstone (upper set of points).

with respect to the flow direction after a pathlength of a few grain sizes. The upper set of points corresponds to Berea sandstone samples; l_D is also almost equal to l_{dec}, but both dispersivities range between 1 and 2 mm, that is, 20 times more than the typical grain size (≈ 70 μm). The reason is that Berea sandstone has a slightly layered structure and both l_D and l_{dec} are of the order of magnitude of the layer thickness [68]. This shows that dispersion remains Gaussian provided that heterogeneities are small enough to be sampled over the tracer particle's flow path. Note that the degree of reversibility does not depend on the Péclet number, in agreement with the results of Section 11.3.4.

Different results are obtained for the Massilon sandstone sample on which the dispersion curves of Fig. 20 have been obtained. This rock displayed visible colored layers with a thickness of a few millimeters. The corresponding echo and transmission dispersivity variations are displayed in Fig. 22. At high Péclet numbers, the transmission dispersivity is higher than the echo one by a factor of 2 or 3; transmission dispersion curves are highly non- Gaussian, while echo curves agree well with Eq. (15). At low Péclet numbers, both dispersivity values become similar and the transmission curves are nearly Gaussian. Similar results have been observed on glass bead packings with layers of different permeabilities [10].

Dispersion anomalies (taillike features, for instance) in natural or artificial layered samples can therefore be identified from their partial reversibility in echo dispersion experiments; these give Gaussian curves with smaller dispersivity values than transmision dispersion. Also, the dependence of the relative values of the two types of dispersivities on the Péclet number is

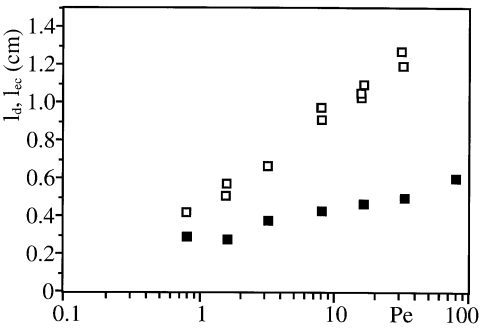

FIG. 22. Dispersion length variations with the Péclet number $\mathrm{Pe} = Ud/D_m$ in transmission (l_d, open squares) and echo (l_{dec}, solid squares) for a non-Gaussian Massilon sandstone sample.

related to the size of the heterogeneities. In this case, one deals with heterogeneities of large sizes but with relatively small contrasts between high- and low-velocity zones: Solute transport is generally convective in both types of regions, which explains the reversibility of the tail effect.

11.5.3.3 Anomalous Tracer Dispersion in Porous Media with a Broad Flow Velocity Distribution or in Double-Porosity Media. We shall now analyze the different case of heterogeneities of smaller size but with a higher permeability contrast between high- and low-velocity zones. In this case, molecular diffusion can play a significant part in the exchange of solute between high- and low-velocity regions. We shall particularly analyze these effects in the case of double-porosity media.

We designate as double-porosity materials porous media where flow may occur both in large connected pores and inside the solid matrix, which is itself porous (but with smaller pores). This problem has applications in petroleum and chemical engineering. The two upper curves of Fig. 23 display transmission dispersivity variations with the Péclet number for nonconsolidated packings of porous grains of internal porosities $\varnothing_{\mathrm{int}} = 30\%$ and 19% [69]: The grains are made of sintered glass beads of initial diameter $d_b = 55\,\mu\mathrm{m}$. The mean grain size is $d_g = 550\,\mu\mathrm{m}$.

At Péclet numbers $\mathrm{Pe} > 10$, $D_{||}/U_g$ increases more with Pe for both double-porosity samples than for single-porosity ones (lower curve) due to the large permeability contrast between the inside and the outside of the grains. For $\mathrm{Pe} \leqslant 5$, spreading is controlled locally by molecular diffusion depending little on the width of flow channels, and $D_{||}$ is similar for single- and double-porosity samples. For very large Péclet numbers, on the contrary, tracer transport is convective everywhere. From Eq. (5), one has

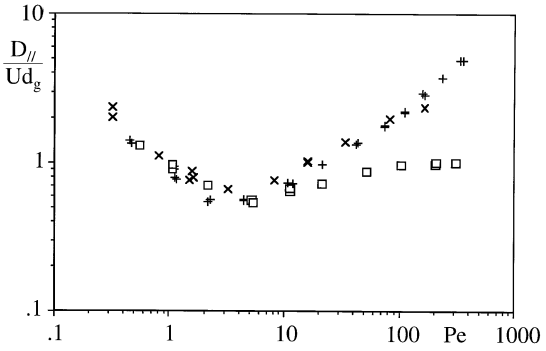

FIG. 23. Variation of the normalized dispersivity $l_D/d_g = D_{||}/Ud_g$ as a function of the Péclet number Ud_g/D_m for three different porous samples: (□) single-porosity packing of 200-μm-diameter beads; (×) double-porosity packing of grains with a high internal porosity $\varnothing_{\text{int}} = 30\%$ ($d_g = 550\,\mu\text{m}$ and $d_b = 55\,\mu\text{m}$); (+) double-porosity packing of grains with a lower internal porosity $\varnothing_{\text{int}} = 19\%$ ($d_g = 550\,\mu\text{m}$ and $d_b = 55\,\mu\text{m}$).

$D_{||} \approx u^2\tau$, where u is the order of the deviations of the fluid velocity with respect to the mean U (in the present case $u \approx U$), and τ is the time during which a tracer particle keeps memory of such a deviation. It is controlled by the transit time through the slowest channels so that $\tau \approx d/(\varepsilon U)$ ($\varepsilon \ll 1$ is the velocity ratio between the inside and the outside of the grains). Thus,

$$D_{||} \approx \frac{Ud}{\varepsilon} \gg Ud. \tag{16}$$

This limit value is reached when the internal velocity $u \cong \varepsilon U$ is high enough so that tracer transport inside the grains is convective with $\varepsilon U d_g/D_m \gg 1$ ($\text{Pe} = Ud_g/D_m \gg 1/\varepsilon$). At intermediate Pe values, $D_{||}/U$ increases until tracer transport is fully convective [60, 70]. In Fig. 23, neither of the two double-porosity curves reaches the plateau regime due to the small ε value giving exceedingly high values for the corresponding Péclet number. We observe, however, that, as expected, the curve corresponding to $\varnothing_{\text{int}} = 30\%$ is more strongly curved downward than that for $\varnothing_{\text{int}} = 19\%$, for which ε is still smaller. A similar increase of the normalized dispersivity $D_{||}/d_g$ has been observed in porous media with a complex cellular structure such as fireproof bricks [48].

Experimental concentration variation curves for $\varnothing_{\text{int}} = 30\%$ are well fitted by Eq. (15a). On the contrary, curves corresponding to $\varnothing_{\text{int}} = 19\%$ display clear non-Gaussian characteristics (Fig. 24a) at high flow velocities ($\text{Pe} = Ud_g/D_m = 430$). At long times, the conductivity becomes much slower

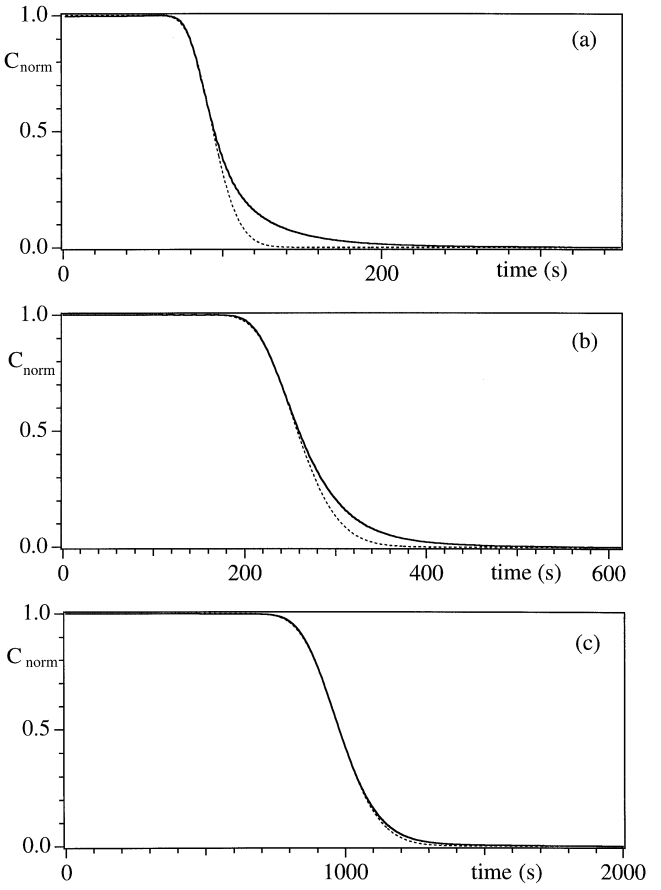

FIG. 24. Experimental tracer transmission dispersion curves showing the variation of the normalized conductivity of the fluid at the outlet of a double-porosity sample following an abrupt salt concentration variation at the inlet ($Ø_{int} = 19\%$, $d_g = 550\,\mu m$, and $d_b = 55\,\mu m$): (a) $Pe = Ud_g/D_m = 430$, (b) $Pe = 160$, and (c) $Pe = 43$. The continuous line represents the experimental variation, and the dotted line corresponds to a fit of a Gaussian solution of Eq. (3) with the early part of the curve.

toward its asymptotic value than the Gaussian solution fitted with the early part of the curve (dotted line). On the other hand, at the lowest velocity ($Pe = 43$), the curve follows the Gaussian variation. At an intermediate velocity value ($Pe = 160$), a weaker deviation from the Gaussian behavior is observed than for $Pe = 430$.

TABLE I. Relative Orders of Magnitude of the Global Transit Time through the Sample and of the Characteristic Exchange Times between the Main Flow and Individual Grains

Pe	U (cm/s)	ε (estimated)	T_0 (s)	$\tau_{di} = d_g^2/D_m$	$\tau_{ci} = \dfrac{d_g}{\varepsilon U}$	τ_i (s)
430	0.11	0.00135	98	67	185	49
160	0.04	0.00135	250	67	497	59
43	0.011	0.00135	980	67	1850	64.5

Table I compares the diffusive (τ_{di}) and convective (τ_{ci}) exchange times between the inside and the outside of the grains to the mean transit time T_0 through the whole sample (the harmonic average τ_i representing an estimation of the resulting exchange time is also indicated). Although figures estimated for the various components of τ_i may differ from real ones by factors of 3 or 4, τ_i is not very small for Pe = 430 compared to the mean transit time. Since τ_i is the characteristic time for individual events in the random spreading process, the central limit theorem no longer applies and non-Gaussian curves are found. For Pe = 43, τ_i remains about the same since molecular diffusion is the dominant exchange process at all velocities; on the contrary, T_0 is much higher, so that one now has $\tau_i \ll T_0$ and dispersion is Gaussian again (Fig. 24c).

We verify in this way that dispersion tails appear when the exchange time between the inside of *individual* grains and the main flow is not negligible any more compared to the global transit time T_0 through the *whole sample*. An important difference between these effects and those reported above for large-scale heterogeneities in Section 11.5.3.2 is the fact that molecular diffusion plays a more important part. Its influence controls the transition between Gaussian and non-Gaussian dispersion as the Péclet number varies. This difference also appears in echo dispersion experiments [69]: Long time tails in Figs. 24a and 24b do not disappear when the flow is reversed, in contrast with the curves of Fig. 20.

11.5.3.4 Echo Dispersion and the Identification of Heterogeneities. Combining informations from echo and transmission dispersion measurements, particularly in the case of non-Gaussian dispersion curves, provides useful information concerning the various types of permeability heterogeneities in porous samples and their sizes. These measurements complement other data obtained, for instance, using acoustical or nuclear resonance imaging techniques.

Non-Gaussian dispersion features appear when transit times through some individual heterogeneous structures become of the order of magnitude of the global transit time through the whole sample. This may be the case when very large heterogeneities with a moderate velocity contrast with the rest of the sample are present (for instance in stratified media); this is also the case for smaller heterogeneities with a very large velocity contrast (for instance double-porosity packings of grains with a very low internal permeability acting as dead zones). In the first case, long-time-tail features observed in the dispersion curves disappear when the flow is reversed in echo dispersion experiments. In the second case, these features are not suppressed by a flow reversal but give instead rise to both short and long time deviations from the Gaussian dispersion shapes.

11.6 Mapping of Miscible Fluid Flow with Viscosity and Density Contrasts

11.6.1 Mixing Modifies the Flow Field Itself

Dispersion of contaminants in porous aquifers, and various processes related to oil recovery, require knowledge of the permeability field and modeling of the associated displacement. In environmental contamination problems, the contaminant is often a passive tracer (e.g., a trace chemical), which is spread following the two modes of advection with the flow and molecular diffusion. The resulting combined transport is the hydrodynamic dispersion already described. However, when the dispersed species is sufficiently concentrated to affect the viscosity and density of the mixture, the flow field itself is modified as the displacement takes place. Understanding the evolution of the flow field in such cases is one of the key issues for the prediction of the fate of the contaminants, the displacement characteristics of oil from oil reservoirs, etc. [10]. At sufficiently large viscosity and/or density contrasts, the interrelation between fluid displacements and permeability fields must be considered [71].

11.6.2 Miscible Flow in a Stratified Porous Media

Many simulation and experimental studies have been conducted to address various aspects of these displacements [71]. Let us examine miscible displacements in mutilayered porous media, in which the flow direction is parallel to the layer planes for two- and four-layer systems. The process is controlled by the mobility ratio, $M = \mu_-/\mu_+$, which here denotes the ratio of the viscosity of the displaced fluid (subscript $-$) to that of the displacing fluid (subscript $+$).

Miscible displacement experiments were performed at different values of the flow rate q in a layered pack of glass beads of length $L = 30$ cm, and of a square cross section ($4.5 \times 4.5\,\text{cm}^2$), corresponding to an aspect ratio of 6.66. The layering was accomplished by first partitioning the system in equally spaced layers, using very thin spacers, which were gently removed after each layer was filled with glass beads of the appropriate size. For the two-layer system, we used glass beads with mean diameters $d_1 = 200\,\mu\text{m}$, and $d_2 = 100\,\mu\text{m}$ respectively, leading to a layer permeability ratio of 4 (based on a permeability scaling as the square of the bead diameter [1–3]). The four-layer medium was made of glass beads with respective mean diameters of 160, 120, 80, and 32 μm, arranged in order of increasing size from one boundary to the other. The sample was placed with the larger dimension aligned with the direction of the gravity vector. The fluids used consisted of mixtures of water and glycerol and/or water and sucrose (at variable initial volume fraction). The variable composition allows for various combinations of viscosity and density contrasts, including the particular cases of equal density-different viscosity and equal viscosity-different density mixtures. The concentration profile was determined acoustically; the overall accuracy in concentration was better than 0.1%. Here K is the arithmetic average of the permeability, and q is the flow velocity. In the experiments, the latter varied over one decade from 5 to 50 cm/h. In all cases, however, the flow rate and the Péclet number were sufficiently large for dispersion not to dominate the displacement. All experiments were conducted at conditions such that the displacement is stable in each layer (see later in the chapter [72]). A typical set of the obtained concentration profiles versus reduced time (injected pore volume) in the five transducer locations for the two-layer system are shown in Fig. 25 for the three different values of the viscosity ratio, $M = 1$, 0.574, and 0.161, respectively, and in absence of gravity effect. For this problem, the displacement is stable in all layers [72]. At values of M near 1 (Fig. 25a), the two different layers are clearly identified in the form of different fronts moving at different speeds. As M decreases, however, this distinction becomes less apparent (Fig. 25b), and at the smallest value of M tested, the two concentration profiles merge into one (Fig. 25c), containing the features of miscible displacement in a homogeneous (single-layer) system. A schematic of the layer arrangement and the notation used is shown in the bottom right in Fig. 25. A similar trend is observed for the four-layer sample. For a more quantitative description, we studied the front velocity in each layer, U_i, defined as the velocity of the inflection point of each layer. Since the fluids have not had a sufficiently long time to diffuse into one another, this velocity is representative of the "interface" separating the two fluids. Alternatively, we can view each "apparent layer," as implied by the concentration profiles, as a phase.

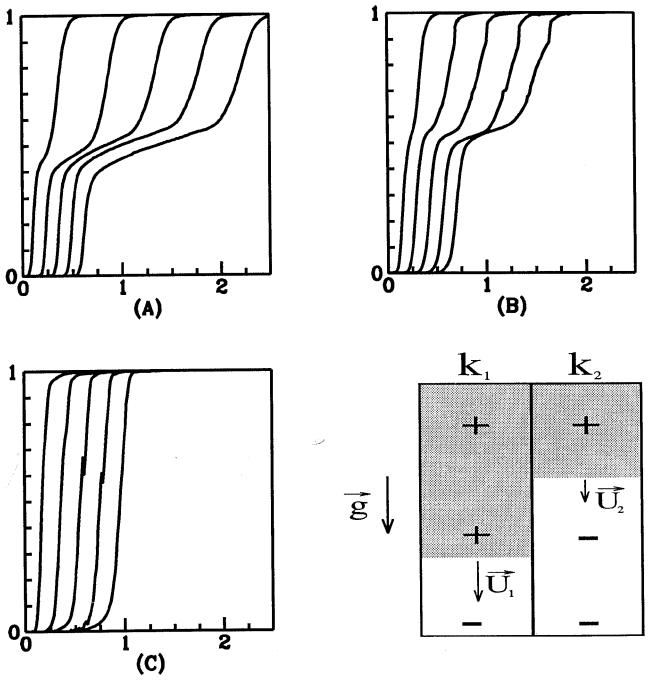

FIG. 25. Concentration versus reduced time (pore volume) at five equidistant locations across a two-layer porous medium with a permeability ratio $k_1/k_2 = 4$. Viscosity ratios are, respectively, (a) $M = 1$ (b) $M = 1.74$, and (c) $M = 6.2$ for these isodensity fluids. The flow rate is $q = 12$ cm/h. The bottom right figure is a schematic of the front velocity distributions.

Then, Fig. 25 can be viewed as successive phase transitions as the control parameters vary. To construct the corresponding phase diagram, we plot the front velocities, U_i, in terms of the parameter $M^* = 1/M$. Figure 26 (top) shows the reduced (with q) velocities plotted versus M^* for the two-layer medium. The existence of two distinct layers is evident at sufficiently small M^*. As this parameter increases, the two velocity branches approach each other, and at a specific value they coincide. The critical "bifurcation" point is a function of the permeability contrast, as discussed in the following. A similar figure can be constructed for the four-layer system (Fig. 26, bottom). We note the successive transitions from four to two to one apparent layers as the parameter M^* increases. It should be noted that the particular sequence shown reflects the specific combination of gravity and viscosity effects in these experiments due to the particular method of preparing the

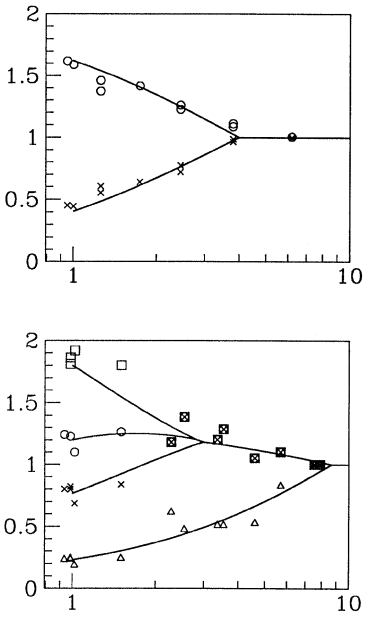

FIG. 26. (Top) Phase diagram for a two-layer porous medium with reduced velocities in each layer versus viscosity ratio M. Full lines are theorical predictions, and $\times$ and o represent the velocities of the fronts U_1 and U_2 observed in Fig. 25. (Bottom) Cut of the phase diagram for a four-layer medium with reduced velocities in each layer versus viscosity ratio M. Full lines are the theoretical predictions; Δ, $\times$, o, and $\square$ represent respectively the velocities of the fronts U_1, U_2, U_3, and U_4; and $\boxtimes$ represents the reduced velocity of the front resulting from the merging of the three latter fronts.

fluid mixtures of different concentrations. In a sense, therefore, Fig. 26, bottom, is a specific cut of the 3-D phase diagram corresponding to the particular experimental set, and does not imply that in such systems the 4–2–1 transition will always occur. Also shown in Fig. (26), are theoretical predictions obtained as follows.

Assuming the transverse flow equilibrium analysis of Yortsos *et al.* [73], the pressure is uniform in planes perpendicular to the flow direction (i.e., no cross flows). Therefore Darcy's law leads to the relationship between the local pressure gradient and the local permeability and viscosity, depending on where we are located in the layered system. For instance, in the two layers porous medium of respective permeability k_1 and k_2, $k_1 > k_2$, (Fig. 25, bottom right), the ratio between the front u and v, respectively in media

1 and 2 is found noting that due to fluid conservation the speed u is also that of the more viscous fluid in the zone in Fig. 25a, whereas v is the velocity of the less viscous zone in Fig. 25b:

$$\boldsymbol{u} = \boldsymbol{q}_a = -\frac{k_1}{\mu_+}\nabla_p, \tag{17a}$$

$$\boldsymbol{v} = \boldsymbol{q}_b = -\frac{k_2}{\mu_-}\nabla_p, \tag{17b}$$

leading to

$$\frac{u}{v} = \frac{k_1}{Mk_2}. \tag{18}$$

For $M = 1$, *this ratio is the permeability ratio. Increasing* M reduces the velocity difference between the two layers and it vanishes for $M_0 = k_1/k_2$. For a larger M value, a single front is observed: The medium behaves as if it were homogeneous. Inversely, for $M < 1$, the velocity ratio is larger than the permeability ratio and the permeability contrast looks as if it is enhanced.

11.6.3 Mapping Heterogeneous Permeability Fields

One of the key issues with porous media is to determine the permeability field to predict or prevent oil recovery, contamination by chemical or nuclear waste, etc. Here we propose to take advantage of using acoustics to follow the interface between two fluids to infer some properties of the permeability field. As an illustration of this conjecture, we analyze two examples in which the permeability heterogeneity leads to a measurable signature in terms of response to flow: miscible fluid flow in a layered porous medium parallel to the flow direction and immiscible fluid flow in a layered porous medium perpendicular to the flow direction. The former case is described in Section 11.6.2. The second one has been described elsewhere [74, 75].

11.7 Discussion and Conclusions

In addition to their intrinsic interest, tracer dispersion and miscible fluid displacements are powerful tools to characterize the heterogeneities of either the structure of porous media or the fluid distribution inside them.

Their study benefits greatly from the development of new tools that enable us not only to study concentration variations at the inlet and outlet of a sample but also to determine the fluid spatial distribution inside it. For

instance, acoustic velocity measurements enable us to obtain saturation profiles along a sample and even 3-D saturation images. Pulse gradient NMR methods can be used to analyze the mechanisms of tracer dispersion and solute transport at the pore scale and below. Selective tracer injection techniques (for instance, electrochemical tracers or selective electrodes) enable us to realize precise dispersion measurements with a very good spatial resolution.

The reversibility of miscible displacement processes is an important issue, even at the very low Reynolds numbers for which Stokes flow reversibility can be assumed to be valid. The degree of irreversibility of the miscible displacement front distorsions with respect to a flow reversal and its dependence with respect to the Péclet number is an important indicator of the type and size of the heterogeneities of the medium.

The interest of dispersion measurements does not correspond only to the case of passive tracers. Miscible displacements in which there is a density or viscosity contrast between the displaced and displacing species are of particular interest: Front displacement instabilities may appear together with a subtle interplay of stabilizing and destabilizing effects and of their interaction with the structural heterogeneities of the porous media. Other important problems and new effects can also be expected by replacing Newtonian fluids by fluids such as polymer solutions with nonlinear characteristics. This will open a new domain of study of the interaction between rheological nonlinearities and permeability heterogeneities.

Acknowledgments

The work presented here has been performed by and/or in cooperation with J. C. Bacri, C. Baudet, M. Chaouche, E. Charlaix, G. Daccord, C. Gauthier, I. Ippolito, J. Leblond, L. Lebon, C. Leroy, D. Loggia, P. Magnico, T. J. Plona, N. Rakotomalala, P. Rigord, and R. Woumeni.

A large part of these studies has been performed in deep interaction with Prof. Y. Yortos from USC. The collaboration between the two groups was made possible by the NATO Grant No. GRC 973049. Other studies have been performed in cooperation with the Grupo de Medios Porosos (A. Calvo, R. Chertcoff, and M. Rosen, University of Buenos Aires) under PICS-CNRS No. 145 and with the Ben Levich Center (J. Koplik, CUNY) thanks to a NATO grant. Discussions with Profs. E. Guyon and E. J. Hinch and with Drs. J. P. Bouchaud, Y. Caristan, A. Georges, G. Guillot, and R. Lenormand are gratefully acknowlegded.

We also thank the Schlumberger Doll Research center, the Schlumberger Dowell Corporation, and the CEA Bruyères le Châtel center for their

cooperation. This work was partly supported by the GDR-CNRS Physique des Milieux Hétérogènes Complexes, the ARC-Géothermie des Roches Fracturées, and the PNRN and PRNH programs; all these sources of support are gratefully acknowlegded.

We finally wish to thank Prof. P.-z. Wong and the referees for their many suggestions and thoughtful comments.

References

1. Bear, J., *Dynamics of Fluids in Porous Media*, Elsevier Publishing Corporation, New York (1972).
2. Dullien, F. A. L., Porous Media, Fluid Transport and Pore Structure, Academic Press, New York (1979).
3. Scheidegger, A. E., The Physics of Flow through Porous Media, Toronto University Press, Toronto (1963).
4. Coats, K. H. and Smith, B. D., *Soc. Petr. Eng. J.* **231** (1964) 73–84.
5. Villermaux, J., in *Percolation Processes: Theory and Applications*, Proceedings of the 1981 E33 NATO Advanced Studies Institute, edited by A. E. Rodrigues and D. Tondeur, Sijthoff and Noordhoff, Dordrecht, the Netherlands (1981) 83–140.
6. Saffman, P. G., *J. Fluid Mech.* **6** (1959) 321–349; Saffman, P. G., *J. Fluid Mech.* **6** (1960) 194.
7. Koch, D. L. and Brady, J. F., *J. Fluid. Mech.* **154** (1985) 399–427.
8. Koplik, J., in *Disorder and Mixing*, Proceedings of the Nato Conference on Disorder and Mixing edited by E. Guyon, Y. Pomeau, and J. P. Nadal, Kluwer, Dordrecht, the Netherlands (1988) 235–248.
9. Pfannkuch, H. O., *Rev. Inst. Fr. Pet.* **18** (1963) 215–270.
10. Leroy, C., Hulin, J. P., and Lenormand, R., *J. Cont. Hydro.* **11** (1992) 51–68.
11. Charlaix, E., Hulin, J. P., and Plona, T. J., *Phys. Fluids* **30** (1987) 1690–1698.
12. De Gennes, P. G., *J. Fluid. Mech.* **136** (1983) 189–200.
13. Bacri, J. C., Rakotomalala, N., and Salin, D., *Phys. Fluids A* **2** (1990) 674–680.
14. Taylor, G. I., *Proc. Roy. Soc. London Ser. A* **219** (1953) 186–203.
15. Aris, R., *Proc. Roy. Soc. London Ser. A* **235** (1956) 67–77.
16. Ippolito, I., Daccord, G., Hinch, E. J., and Hulin, J. P., *J. Cont. Hydro.* **16** (1994) 87–108.
17. Gelhar, L. W., and Axness, C. L., *Wat. Res. Res.* **19** (1983) 161–180 and references therein.
18. Cenedese, A., and Viotti, P., *Water Res. Res.*, **32** (1996) 2329–2344.
19. Lebon, L., Oger, L., Leblond, J., Hulin, J. P., Martys, N. S., and Schwartz, L. M. *Phys. Fluids* **8** (1996) 293–301.
20. Martys, N. and Garboczi, E. J., *Phys. Rev. B* **46** (1992) 6080–6090.

21. Schwartz, L. M., Martys, N., Bentz, D. P., Garboczi, E. J., and Torquato, S., *Phys. Rev. E* **48** (1993) 4584–4591.
22. Adler, P. M., Jacquin, C. G., and Thovert, J. F., *Wat. Res. Res.* **28** (1992) 1571–1576.
23. Salles, J., Thovert, J. F., and Adler, P. M., *J. Contam. Hydrol.* **3** (1993) 3–22.
24. Lebon, L., Leblond, J., and Hulin, J. P., *Phys. Fluids* **9**, (1997) 481–490.
25. Callaghan, P. T., *Aust. J. Phys.* **37** (1984) 359–387.
26. Georgiadis, J., Behringer, R., Shattuck, M., and Johnson, G. A., *Interstitial Velocity and Temperature Fields in Fully-Saturated Porous Media*, Ninth Symposium of Energy Engineering Sciences, Fluid and Dynamical Systems (1991).
27. Shattuck, M., Behringer, R., Georgiadis, J., and Johnson, G. A., Proceedings of Forum on Experimental Techniques in Multiphase Flows, *ASME*, *Fed.* **125** (1991) 39–45.
28. Kutsovsky, Y. E., Scriven, L. E., Davis, H. T., and Hammer, B. E., *Phys. Fluids*, **8** (1996) 863–871.
29. Kutsovsky, Y. E., Alvarado, V., Davis, H. T., Scriven, L. E., and Hammer, B. E., *Magn. Reson. Imaging* **16** (1998) 63–71.
30. Edwards, C. M., Chang, C. T., and Sarkar S., SCA Conference Paper Number 9310 (1993).
31. Fried, J. J., and Combarnous, M., *Adv. Hydrosci.* **7** (1971) 169–282.
32. Hulin, J. P., and Plona, T. J., *Phys. Fluids A* **1** (1989) 1341–1347.
33. Rigord, P., Calvo, A., and Hulin J. P., *Phys. Fluids A* **2** (1990) 681–687.
34. Oxaal, U., Flekkoy, E. G., and Feder, J., *Phys. Rev. Lett.* **72**, (1994) 3514–3517.
35. Baudet, C., Hulin, J. P., and Deslouis, C., *Exp. Fluids* **7** (1989) 329–334.
36. Davis, L. A. SPE 12037, Annual Fall Technical Conference and Exhibition, San Francisco (5–8 Oct. 1983).
37. Aggarwal, S. K., and Johnston, R. H., *IEEE Instrum. Measure.* **35** (1986) 60–67.
38. Boyer, R. L., Morgan, F., and Muskat, M., *Petr. Trans. AIME* 170 (1947) 15–33.
39. Laird, A. D. H., and Putnam, J. A., *Petr. Trans. AIME* 216 (1959) 216–220.
40. Cromwell, V., Kortum, D. J., and Bradley, D. J., SPE 130098, Annual Fall Technical Conference and Exhibition, Houston (16–19 Sept. 1984).
41. Blackband, S., Mansfield, P., Barnes, J. R., Clague, A. D. H., and Rice, S. A., SPE 13401, Annual Fall Technical Conference and Exhibition, Houston (16–19 Sept. 1984).
42. Baldwin, B. A., and Yamanashi, W. S., SPE 14884, SPE/DOE Symposium on Enhanced Oil Recovery, Tulsa (20–23 April, 1986).
43. Salin, D., and Schon, W., *J. Phys. Lett.* **42**, (1981) L–477; Bacri, J.-C., Hoyos, M., Lenormand, R., Rakotomalala, N., Soucemariadin, A., and Salin, D., *J. Phys.* **III**, 1 (1991) 1455.
44. Bacri, J.-C., Salin, D., *Geophys. Res. Lett.* **13** (1986) 326–328.

45. Soucemarianadin, A., Bourlion, M., and Lenormand, R., SPE 16953, Annual Fall Technical Conference and Exhibition, Dallas (27–30 Sept. 1987).
46. Biot, M. A., *J. Acoust. Soc. Am.* **28** (1956) 168–178.
47. Johnson, D. L., and Plona, T. J, *J. Acoust. Soc. Am.* 72 (1982) 556–565.
48. Bacri, J.-C., Rakotomalala, N., and Salin, D., *Phys. Rev. Lett.* 58 (1987) 2035–2038.
49. Guillot, G., Kassab, G., Hulin, J. P., and Rigord, P., *J. Phys. D* **24** (1991) 763–773.
50. Rosen, M., Grattoni, C., Chertcoff, R. and Bidner, M. S., *Chem. Eng. Sci.* **42** (1987) 2055–2059.
51. Gauthier, C., Borgotti, J. C., and Sadoudi, A., *CRAS II* **306** (1988) 1309–1312.
52. Brigham, E., *Soc. Petr. Eng. J. Trans. AIME* **257** (1974) 91.
53. Baker, L. E., *Soc. Petr. Eng. J. Trans. AIME* **263** (1975) 219.
54. Passioura, J. B., *Soil Sci.* **111** (1971) 339.
55. Rao, P. S. C., Rolston, D. E., Jessup, R. E., and Davidson, J. M., *Soil. Sci. Soc. Am. J.* **44** (1980) 1139.
56. Correa, A. C., Pande, K. K., Ramey, H. J., Jr., and Brigham, W. E., *Soc. Petr. Eng.* **16** (1987) 704.
57. Bretz, R. E., Specter, R. M., and Orr, F. M., Jr., in *Reservoir Characterization*, edited by L. W. Lake and H. B. Carroll, Academic, New York (1986).
58. Montroll E. W., and Weiss, G. H., *J. Math. Phys.* **6** (1965) 167.
59. Hulin, J.-P., and Salin, D., in *Proceedings of the Cargese NATO School on Mixing and Disorder*, edited by E. Guyon, J. P. Nadal, and Y. Pomeau, Kluwer, Dordrecht (1988).
60. Bouchaud, J. P., and Georges, A., *C. R. Acad. Sci. Paris II* **307**, (1988) 1431.
61. Koch, D. L., and Brady, J. F., *Chem. Eng. Sci.* **42** (1987) 1377.
62. Koch, D. L., and Brady, J. F., *J. Fluid. Mech.* **180** (1987) 357.
63. Han, N., Bhakta, J., and Carbonell, R. G., *AIChEJ* **31** (1985) 277.
64. Koch, D. L., and Brady, J. F., *Phys. Fluids* **31**, (1988) 965.
65. Bouchaud, J. P., Georges, A., and Le Doussal, P., *J. Phys.* (*Paris*) **48** (1987) 1855.
66. Matheron, G., and de Marsily, G., *Water Res. Res.* **16**, (1980) 901.
67. Sahimi, M., Hughes, B. D., Heiba, A. L., Davis, H. T., and Scriven, L. E., *Chem. Eng. Sci.* **41** (1986) 2103; **41** (1986) 2133.
68. Auzerais, F. M., Ellis, D. V., Luthi, S. M., Dussan, E. B. and Pinoteau, B. J., SPE paper 20602, presented at the 65th annual conference and exhibition of the Society of Petroleum Engineers, New Orleans, LA, 23–26 Sept. (1990).
69. Magnico, P., Leroy, C., Bouchaud, J. P., Gauthier, C., and Hulin, J. P., *Phys. Fluids. A* **5** (1993) 46–57.
70. Bouchaud J. P. and Georges A., *Phys. Rep.* **195** (1990) 127.

71. Waggoner, J. R., Castillo, J. L., and Lake, L. W., *Soc. Petr. Eng.* **21237** (1991); Sorbie, K., Pickup, G. E., Ringrose, P. S., and Jensen, J. L., *Soc. Petr. Eng.* **24140** (1992); Tchelepi, H. A., Orr, F. M., Rakotomalala, N., Salin, D., and Woumeni, R., *Phys. Fluid A.* **5**, (1993) 1558; Kempers, L. J. T. M., and Haas, H., *J. Fluids Mech.* **267** (1994) 299–324.

72. Loggia, D., Rakotomalala, N., Salin, D., and Yortsos, Y. C., *Europhys. Lett.* **32** (1995) 633.

73. Yortsos, Y. C., *Transp. Porous Media* **18** (1995) 107.

74. Chaouche, M., Rakotomalala, N., Salin, D., and Yortsos, Y. C., *Europhys. Lett.* **21** (1993) 19.

75. Chaouche, M., Rakotomalala, N., Salin, D., Xu, B., and Yortsos, Y. C., *Chem. Eng. Sci.* **49** (1994) 2447.

This Page Intentionally Left Blank

Index

C

D

E

F

G

H

I

J

K

L

M

N

T

U

V

W

X

Y

Z

This Page Intentionally Left Blank